SLAC – 283
UC – 34D
(E/I/A)

SLAC LBL Users Organization
Stanford Linear Accelerator Center

Proceedings of the Workshop on e^+e^- Physics at High Luminosities

Stanford Linear Accelerator Center
Stanford, California
November 30 – December 1, 1984
and
April 5–6, 1985

May 1985

Work supported by the Department of Energy, contract DE-AC03-76SF00515

WORKSHOP STEERING COMMITTEE

E. Bloom

C. Buchanan

M. Derrick

W. Hofmann

J. G. Layter

P. Oddone

H. P. Paar, Workshop Chairman

R. Panvini

J. M. Paterson

FOREWORD

This report contains an account of the work done in the Workshop on e^+e^- Physics at High Luminosities. The Workshop was sponsored jointly by the SLAC-LBL Users Organization (SLUO) and the Stanford Linear Accelerator Center. Over 150 physicists participated in 2 sessions, one on 30 November - 1 December 1984 and one on 5-6 April 1985. The motivation for the workshop was provided by the realization that a simple inexpensive upgrade of PEP may lead to a luminosity of order 10^{32} cm^{-2}sec^{-1}. The participants explored the physics opportunities that would become available for experiments logging 1 fb^{-1}. In addition the questions of optimal beam energy and detector upgrades were considered.

Five working groups were formed, each with a convener, on the following subjects: B-physics (W. Hofmann), Two-Photon Physics (J. Layter), Quark and Gluon Fragmentation (C. Buchanan), New Particle Searches (M. Derrick), and Machine Physics (E. Paterson). This report starts with an introduction and summary. The hurried reader may limit himself to reading just this chapter and perhaps refer to later chapters for details. The other chapters elaborate on the above topics, and on the TPC and HRS detector capabilities.

Many thanks go to the participants for their enthusiastic participation and especially to J. Weiss, who organized the first meeting of the Workshop and to R. Panvini, Chairman of SLUO, for his guidance. Nina Adelman and Helen Mogilev ran the Workshop secretariat with great skill.

This report would not have been possible on such a short time scale without the able assistance of our typists Wanda Bradford, Lydia Beers, June Belew, Effie Clewis, Pam Guerra, Robin Shaver, and especially Lucy Cheung of the Publications Office and the able staff of the Illustration Office of Kevin Johnston.

Hans Paar
Workshop Chairman
May 3, 1985

CONTENTS

CHAPTER I. INTRODUCTION AND SUMMARY

H. P. PAAR

and

E. BLOOM, C. BUCHANAN, M. DERRICK, W. HOFMANN,
J. G. LAYTER, P. ODDONE, R. PANVINI, J. M. PATERSON

CHAPTER I. INTRODUCTION AND SUMMARY

CONTENTS

I.1 GENERAL

The Standard Model of electroweak interactions and Quantum Chromo Dynamics of the strong interactions have met with considerable success. It is the task of experimental high energy physics to test all aspects of these theories in order to see whether they are correct and complete. In doing so one measures at the same time some of the many free parameters that appear in the theory and tests our ability to calculate these processes. Electron-positron collisions, hadron-hadron collisions and lepton-hadron collisions all have in the past and will no doubt in the future contribute significantly to this program.

Some of the contributions of the experimental programs at the electron-position colliding beam machines PETRA and PEP are the establishment of the gluon, the lifetime measurements of the τ-lepton and the b and c quark, the measurement of quark and gluon fragmentation into observable hadrons, the measurement of weak-electromagnetic interference and the measurements of branching fractions. No new particles were discovered ('bad luck'). The PETRA and PEP machines have covered center-of-mass energies of 20-45 GeV at luminosities up to 3×10^{31} cm^{-2}sec^{-1}. Measurements are reported based upon integrated luminosities of up to 200 pb^{-1}.

The question arises as to whether the PETRA and PEP experimental programs have fully realized their physics potential. As other electron-positron colliders are operating at lower energies (DORIS II and CESR at around 10 GeV) or are planned at higher energies (SLC and LEP at around 100 GeV), it seems natural to study the physics impact of a high luminosity upgrade of PEP.

A Workshop on e^+e^- Physics at High Luminosities was organized under the auspices of the SLAC-LBL Users Organization and Stanford Linear Accelerator Center. Five working groups were established on B-physics, Two-Photon Physics, Quark and Gluon Fragmentation, Rare Processes and New Physics and PEP Upgrade. All considerations are based on 1 fb^{-1} integrated luminosity which may take 2 years to accumulate if PEP's luminosity is increased by a factor

5. In this chapter the main results of the workshop on these 5 subjects will be summarized. More detail is provided in the following five chapters. After these there are chapters on the TPC and HRS capabilities. These are followed by appendices on the theoretical aspects of B physics and $B\overline{B}$-mixing, and one with the names of the participants.

I.2 B-PHYSICS

I.2.1 General

Systems containing a bound state of a light up or down quark and a heavier strange, charmed or bottom quark are playing an important role in testing the standard theory. Heavy quarks decay into lighter ones by the weak charged current interaction. The experimental study of the kaon system has lead to the observation of $K^0\overline{K^0}$-mixing, CP violation, the Glashow-Iliopoulos-Maiani mechanism, the prediction of the c-quark including its mass, the Kobyashi-Maskawa matrix and the prediction of the (b,t) quark family. These aspects and some new ones, may appear again in the study of b-quark systems.

The following issues will be discussed below: tagging, mixing, lifetimes, $b \rightarrow u$ transitions and CP-violation.

I.2.2 B-Tagging

In 1 fb^{-1} and at 29 GeV CM energy one collects 35000 $B\overline{B}$ events or 70000 B's. According to the LUND model, typical fiducial cuts would leave 25000 charged B's, 25000 neutral B's, 8000 strange B's, 5000 B baryons, and, more speculative, 200-2000 charmed B's. These together form 9% of all hadronic events. B tagging can enhance this fraction, at the expense of efficiency, by using event topolgy, high p_T leptons, high p_T kaons, a specific final state or multiple vertices. The latter requires a vertex chamber with good resolution. Studies show that either the high p_T lepton or a combination of topology and vertex cut lead to B samples

with 70% purity and with 2500 or 6000 events respectively. Requiring a $D^{\pm *}$ in the final state results in a sample over 90% pure of 150 neutral B^0 events (this assumes that $\overline{B^0} \to D^{+*}\ell^-\nu$ dominates over $B^- \to D^{+*}\pi^-\ell^-\nu$) while D^0 or F tags lead to enhancements in charged or strange B's respectively. Baryon tags (p or Λ) select baryonic B's with high purity.

I.2.3 Mixing

In analogy with $K^0\overline{K^0}$-mixing, one may have $B_d^0\overline{B_d^0}$ and $B_s\overline{B_s^0}$-mixing through the diagram of Fig. 1a. Many aspects of the standard model enter in the evaluation of the box diagram, including m_t and K-M matrix elements. Any new physics that involves particles coupled to quarks will contribute to mixing through the box diagram. Thus important constraints are imposed upon such new theories.

One expects B_s-mixing to be larger than B_d-mixing. Mixing is detected by the appearance of equal sign dileptons in the final state. We expect about 100 (200) equal sign dilepton events for 29 (22) GeV CM-energy with signal to background of 0.4 (0.8) leading to a 6 (9) standard deviation effect (see Appendix B). It is interesting to note that this is competitive with CESR running at the $\Upsilon(4S)$, due to the fact that $B_s\overline{B_s}$ production is above threshold at the $\Upsilon(4S)$ and B_dB_d or $\overline{B_d}\ \overline{B_d}$ production in a p-wave is suppressed by Bose-Einstein statistics.

I.2.4 Lifetimes

The measurement of the b-lifetime is important for the determination of the K-M matrix. A more precise measurement of the b-lifetime is needed, for the charged and neutral B-mesons separately, to evaluate the influence of the exchange diagram, which contributes only to B^0 decay, with respect to the spectator diagram, which contributes to both B^0 and $B^\pm$ decays. The considerations below assume a vertex detector based upon the Radial Drift Chamber principle. It is expected to measure impact parameters with a precision in the range $20\mu + 65\mu/\text{p}$ to $40 + 130\mu/\text{p}$. With 1 fb^{-1} of data, one expects to measure the

b-lifetime with a statistical precision of about 0.06 psec and a systematic error of 0.05 to 0.1 psec, depending upon which B tagging method was used. A measurement of the difference of charged and neutral lifetimes, using for example a D-tag, is expected to have an error in the range 0.3 to 0.5 psec. A lifetime difference of this order or larger would be very interesting and it will be possible to measure it.

I.2.5 $V(b \to u)$

At present an upper limit of $|V_{bu}| < 0.014$ exists, derived from the lepton spectrum of semileptonic decay. This limit depends upon the assumption that the lepton's momentum spectrum extends to larger momenta for $b \to u$ decays than for $b \to c$ decays. This seems plausible but depends upon details of hadron formation. A direct measurement of V_{bu} can be made by measuring the branching ratio $BR(B \to \tau\nu_\tau)$ given by the annihilation diagram of Fig. 1b. One expects $BR(B \to \tau\nu_\tau) \lesssim 5 \times 10^{-4}(f_B/200\ \text{MeV})^2 \times (V_{bu}/0.014)^2$, probably too small to measure with 1 fb^{-1}. But if one should find a larger value, say 5×10^{-4} to 5×10^{-3}, then one would conclude that either V_{bu} is larger or that f_B is larger. In the latter case B-mixing would be increased, $\tau(B^\pm)$ would exceed $\tau(B^0)$ by 50% and $BR(F \to \tau\nu) \simeq 0.7 \times 10^{-2}(f_F/200\ \text{MeV})^2 \simeq 8\%$.

I.2.6 CP Violation

CP violation is not expected to be observable with 1 fb^{-1}. To see an asymmetry $(N^+ - N^-)/(N^+ + N^-) \simeq 10^{-3}$ in inclusive leptons from B-decay one needs 10^6 events and one gets fewer than 10^4. To measure CP violation in dilepton charge asymmetry $(N^{++} - N^{--})/(N^{++} + N^{--}) \simeq 10^{-2}$ to 10^{-3} we need 10^4 to 10^6 dileptons. Fewer than 500 are expected.

I.3 TWO-PHOTON PHYSICS

I.3.1 General

Two photon physics has become experimentally feasible at the higher energies of PETRA and PEP. However, measurements have turned out to be very difficult. This is due to the fact that, owing to the low $\gamma\gamma$-CM energies, the final state has a low multiplicity of low energy particles at small polar angles. It is difficult to trigger efficiently and at low rate. To make matters worse, rates are low due to the fact that the $\gamma\gamma$-luminosity $L_{\gamma\gamma} \simeq (10^{-2} - 10^{-5})L_{ee}$. Despite all this, some interesting experimental results have been obtained that motivated much theoretical work. Below we discuss some of them.

I.3.2 Deep-Inelastic eγ Scattering

To observe deep-inelastic $e\gamma \rightarrow e$ had scattering, the outgoing lepton needs to be detected at small angles. Figure 2 shows a possible layout with Q1 in the new closer position. The front face is at 3.5 m, using the TPC/Two-Gamma detector as an example. One measures the structure function $F_2(x, Q^2)$, where x is the fraction of the target photon's momentum found in the struck quark and Q^2 is the four-momentum squared of the probing photon, see Fig. 3.

It was thought initially that this measurement of F_2 constituted one of the best tests of QCD as it predicted both the x dependence of F_2 and its Q^2 development. It was later realized that higher order corrections are important. Furthermore the hadronic vector meson component of the target photon complicates the interpretation of experimental results. Fortunately one is relatively free of these complications for $x > 0.3$ and one expects F_2 to rise linearly with ln Q^2. We show this in Fig. 4, where F_2 has been averaged over x in the interval $0.3 < x < 0.8$. The data are consistent with the required Q^2 dependence but the error bars are very large and the x range used in the averaging is very large. 1 fb^{-1} would allow x bins of 0.1 and smaller error bars. If the beam energy is lowered from 14.5 GeV to 11 GeV, the last point at $Q^2 = 100$ GeV^2 would be lost.

One has a handle on the VMD contribution to the structure function. By using the topology of the final state, the VMD related part (particle production along the beam-axis) can be suppressed relative to the pointlike part (high p_T particle production). The precision of the Λ measurement from F_2^γ is among the most precise of all Λ determinations, underlining the need to clarify the issue of its theoretical interpretation.

I.3.3 Missing Mass Search

Using double tagged events one determines the $\gamma\gamma$-CM energy directly from the scattered leptons. The central detector is used only to define a hadronic final state. Resolutions of 1% at 14.5 GeV have been achieved with NaI shower detectors leading to good missing mass resolution. In Fig. 5 we show what a 12 GeV narrow resonance with a two photon width $\Gamma_{\gamma\gamma} = 0.4$ MeV would look like. Figure 6 gives upper limits that can be set on $\Gamma_{\gamma\gamma}$ for 1 fb^{-1} integrated luminosity. Chiral invariance implies that spin 0 particles couple to fermions proportional to the fermion's mass. This suppresses their production in e^+e^- collisions. On the other hand no such suppression is present in their coupling to two photons. This leads to $\Gamma_{\gamma\gamma} \simeq O(10\ \text{MeV})$ for such particles, well within the sensitivity indicated in Fig. 6. This technique is competitive with untagged resonance detection. The latter relies upon detecting all decay products so one loses by the branching ratio and the acceptance for observing all decay products. The mass resolution at fixed mass improves with lower beam energies: at 22 GeV e^+e^- CM-energy it is typically 30% better than at 29 GeV. This compensates partly for the reduced $\gamma\gamma$-luminosity.

I.3.4 Charmonium

An example of resonance detection by reconstruction of the exclusive final state is given by the $\eta_c \to \pi^+\pi^-\pi^+\pi^-$. Data on this from the TPC/Two-Gamma detector has been reported. With their presently better momentum resolution

and 1 fb^{-1} we expect the effective mass spectrum shown in Fig. 7. The η_c, χ_0 and (χ_2,η_c') are clearly visible. The measurement of their $\gamma\gamma$-widths provides an important test of the potential model of charmonium. Single tagging is expected to reduce the background by a factor 2 and the signal by 20% due to their different Q^2-dependence. The data are consistent with that expectation.

I.3.5 Gluonia

The formation of resonances by $\gamma\gamma$-collisions provides a means for determining their quark and gluon content. Together with their radiative decays, constraints result on the amount of u, d, and s quarks.

As an example, consider the η'. One writes: $|\eta'\rangle = \frac{x}{\sqrt{2}}\left[|u\rangle + |d\rangle\right] + y\,|s\rangle + z\,|G\rangle$ where $|G\rangle$ stands for neutral gluonic content and of course $x^2 + y^2 + z^2 = 1$. One finds, using $\Gamma_{\gamma\gamma}(\eta') = 3.8$ keV that $x = 0.51 \pm 0.05$, $y = 0.77 \pm 0.13$ and $z = 0.39 \pm 0.18$. These values for x and y may be compared with those measured in $J/\psi \to \gamma\eta'$ by the MK III Collaboration: $x = 0.34 \pm 0.05$, $y = 0.72 \pm 0.12$. Standard SU(3) assignments are: $x = 0.82$ and $y = 0.58$, while in octet-singlet mixing with a mixing angle $\theta = -10$ degrees, required by the Gell-Mann-Okubo mass formula, one has $x = y = 0.71$.

A similar analysis can be performed for other neutral resonances.

I.4 Quark and Gluon Fragmentation

I.4.1 General

The fragmentation of quarks and gluons into observable hadrons is described by models based on general ideas of QCD. The models are necessary because it has been impossible thus far to calculate such non-perturbative effects. It is of course hoped that this will be possible eventually. When that happens, it will be useful to have models that describe a large body of data.

Initial experimental results on event topology are described successfully by several models such as the Independent Fragmentation Model (Feynman-Field, Ali-Hoyer), the Clustering Model (Webber) and the String Model (Lund). More recently data with particle identification have become available, and the models are required to accommodate this. It is expected that we can further discriminate between models as high statistics data with high resolution and particle identification become available. Below we review some interesting processes.

I.4.2 Event Topology

Recent experimental work by the JADE and TPC groups have eliminated the Independent Fragmentation Model by studying in detail the particle distribution between jets in 3-jet events. This is shown in Fig. 8. The Independent Fragmentation Model does not describe the data owing to the fact that it predicts too many particles between the two quark jets. The Cluster Model does not describe the data sample that contains a heavy particle as well as the String Model (Fig. 8c), while it is indistinguishable from the String Model in Fig. 8a and b. The Cluster Model has not yet been tuned as extensively as the String Model for this. The effects that are observed are sensitive to particle masses, therefore particle identification is important in these studies.

We note that at 29 GeV center of mass energy 12% of the events contain 3 jets while at 22 GeV this fraction drops to 6%.

I.4.3 Two-Particle Correlations

The study of two-particle correlations gives information on particle production in jets and the mechanism that is responsible for short range and long range flavor correlations. Figure 9 shows the charged K-K rapidity correlations as measured by TPC. Kaons with rapidity between 1.5 and 4.0 are selected; then the density of oppositely charged kaons minus that of the same sign charged kaons is

plotted. There is evidence for both short and long range correlations. The statistical accuracy of the data does not allow for a discrimination between different models at this moment.

The TPC group has presented data on $p\bar{p}$ correlations, clearly ruling out the Cluster Model (see Fig. 10). In this model, the p and $\bar{p}$ are produced isotopically in the $p\bar{p}$ center of mass (dashed line in Fig. 10a). The String Model predicts peaking along the jet axis (solid line in Fig. 10a). Acceptance modifies the curves as shown in Fig. 10b. Although the data favors the String Model, again more statistics would definitely settle it. Furthermore the study of p_T correlations of the two baryons is sensitive to the mechanism for baryon formation within the String Model.

I.4.4 Heavy Particle Production

Heavy particles preserve the momentum information of the fragmentation process better than light particles such as pions which frequently are produced from resonance decays. Λ and other strange baryons, D, F, D^*, F^* are produced in substantial numbers in 1 fb^{-1}. It is expected, on the basis of presently seen event numbers, that TPC will obtain 28000 p ($\bar{p}$), 14000 Λ ($\bar{\Lambda}$), 1500 $\Sigma^{*\pm}$, 600 Ξ^-, 280 Ξ^{*0} and 180 Ω^-. This is a new testing ground for fragmentation models. We show in Fig. 11 the D^* fragmentation function from HRS and TPC and in Fig. 12 the F fragmentation function from HRS. Again the need for more statistics is clear.

I.4.5 Exotic Probes into the Hadronization Process

With high statistics, high resolution data, some unusual effects become measurable. Here we mention two: Λ polarization and the Bose-Einstein interference effect in like-sign pion pairs.

TPC has preliminary evidence for Λ polarization, see Fig. 13, as function of p_T. The effect is only 2σ and therefore polarization is not established; 1 fb^{-1}

is expected to give a larger than 10σ effect. The String Model can account for this, although with large uncertainties; the Cluster Model cannot (yet). The String Model's explanation depends upon the detailed mechanism for production of an $s\bar{s}$ pair and ud diquarks. Conversely, a measurement of the Λ polarization as function of p_T will constrain the String Model's prediction (now a band in Fig. 13). This in turn will affect baryon production in general, if indeed that depends upon diquark production.

The Bose-Einstein interference effect in like-sign pion pairs has been demonstrated among others by the TPC group. It shows up as an enhancement in the production of pairs of identical particles with small relative momenta. In Fig. 14 this enhancement R is plotted as function of Q, twice the momentum of a particle in the rest frame of the pair. The measurement relies upon particle identification: plotting R for equal sign particle pairs, without regard for particle species, diminishes the effect. The effect has a sharp Q dependence near $Q = 0$ and it is important therefore to obtain much more statistics in order to be able to bin the data in smaller bins near $Q = 0$ and obtain a precise value of R at $Q = 0$. None of the hadronization models can account for this effect so far.

I.5 Rare Processes and New Physics

I.5.1 General

Apart from the gluon, no new particles have been discovered at PEP and PETRA. This is in marked contrast to their predecessors SPEAR and DORIS. One can think of several reasons for this: the new particles may be too heavy; the experiments are not looking in the right way for them; the cross sections may be too small or they may not exist. A high luminosity PEP upgrade will ensure that we continue to address at least the second and third items above. Below we mention some possible avenues to pursue with higher luminosity.

I.5.2 Charged Particle Searches

The PEP and PETRA experiments have set mass and cross section limits on a large number of postulated particles. Insofar as a given cross section limit was determined in a process free of background, higher luminosity will lead to lower upper limits on the cross section or the discovery of the particle in question.

An example is the limit on production of stable factionally charged quarks, by the TPC: $R_q \lesssim 10^{-3}$. Another type of search, leading to mass limits larger than the beam energy, is the production of an excited electron e^*. Here one looks for deviations from QED in the reaction $e^+e^- \rightarrow \gamma\gamma$ with e^* exchange. The present limit is $m_e^* > 60 - 70$ GeV. The sensitivity scales as $\mathcal{L}^{\frac{1}{8}}$ so a factor 10 in luminosity improves the limit by a factor 1.3.

I.5.3 Search for SUSY Particles

Limits exist, based upon pair production of such particles. As the cross section is given in this model, the existing mass limits can only be improved by going to higher energy.

Mass limits beyond the beam energy have been obtained by searching for singly produced SUSY particles, but again these limits are hard to improve by going to higher luminosity.

An example is the e^+e^- annihilation into 2 photinos, accompanied by radiation. An $\tilde{e}$ is exchanged; the only particle detected is the radiated photon. The ASP experiment is designed specifically to search for this reaction. This experiment is expected to set a 60 GeV limit on the mass of the $\tilde{e}$. The sensitivity goes as $(3\mathcal{L})^{\frac{1}{4}}$. A factor 10 in luminosity improves the limit by a factor 1.8.

I.5.4 Z^0 Decay

One expects 6000 virtual Z^0 produced in 1 fb^{-1} at 29 GeV (5500 at 22 GeV). These are large numbers and in fact the $Z^0 \rightarrow \nu\overline{\nu}$ decay is expected to be seen at the ASP experiment.

Already at present luminosities, the Z^0 production has given a result complementary to the $p\overline{p}$ collider regarding the production of monojets. If the monojets from UA1 are produced through Z^0 decay, one would expect to have seen 10-20 monojet events at PEP. This is not the case and the Z^0 is therefore ruled out as a source of monojets.

It is desirable to enhance the capability, as exemplified above, to complement results from higher energy machines.

I.5.5 Mass Limit on ν_τ

The present limit is $m(\nu_\tau) < 150$ MeV from MK II ($\tau \rightarrow 3\pi^{\pm}\pi^0\nu_\tau$) and DELCO ($\tau \rightarrow KK\pi\nu_\tau$). This limit can be improved by selecting decays into hadronic final states with the highest possible effective mass. The recent observation by HRS of $\tau \rightarrow 5\pi^{\pm}\pi^0\nu_\tau$ decays, combined with their excellent resolution, resulted in an upper limit of 89 MeV. With an achieved mass resolution of 10-15 MeV and 27 events expected in 1 fb^{-1}, an upper limit in the 10-20 MeV range can be obtained.

I.6 PEP UPGRADE

I.6.1 The Machine

Several possibilities exist for increasing the PEP luminosity. In the mini-maxi scheme, three of the six intersections, equally spaced around the ring, would have their β_x^* and β_y^* reduced by a factor 3 while the other three intersections would get very large β^*. Increasing the number of circulating particles N by $\sqrt{3}$ results

in an increase in luminosity by a factor $3\sqrt{3} \approx 5$ for the same value of the tune shift $\Delta\nu_y$. The chromatic aberrations are also similar to present values. As the present machine operates comfortably at $\mathcal{L} = (2-3) \times 10^{31}$ cm^{-2}sec^{-1}, one may be reasonably confident that this solution will work. An additional increase in luminosity might be obtained with non-zero dispersion in the intersection points. This improvement is more speculative and can be kept in reserve. The mini-maxi scheme requires the construction of twelve new high precision quadrupoles and associated hardware.

Another possibility is to use, as much as possible, existing hardware. The present quadrupoles nearby the intersection can be moved closer to the interaction point and by lowering the beam energy from 14.5 to 11 GeV, one obtains the required shorter focal length. Wigglers are required to keep the beam sizes at the beam crossings the same. To keep $\Delta\nu_y$ constant, one varies N in proportion to E so the luminosity $\mathcal{L}$ (proportional to N^2) goes down by a factor $(14.5/11)^2 = 1.7$. So the net increase in $\mathcal{L}$ is a factor $3\sqrt{3}\,(11/14.5)^2 = 3$. Other schemes are possible and are under study.

I.6.2 Optimal Beam Energy for Physics

In view of the economies obtained by lowering the beam energy from 14.5 to 11 GeV with a concomitant reduction in luminosity by a factor 1.7, we review the physics requirements upon the beam energy.

All processes with cross sections proportional to 1/s will have the same event yield at either beam energy. Lifetime measurements, obtained by measuring impact parameters, do not benefit much from higher beam energies, owing to the fact that the increase in the impact parameter nearly saturates at these energies. The fraction of tracks with p > 1 GeV in the wrong hemisphere is 1% at 11 GeV and drops to 0.3% at 14.5 GeV, small in both cases. Of B decays, 70% have all tracks in one hemisphere at 11 GeV, 85% do so at 14.5 GeV. The number of high momentum tracks from B decay increases from 1.8 at 11 GeV to 2.5 at 14.5

GeV while the number of non-B tracks increase from 7.5 to 9.0. However these are easily discriminated against by a rapidity cut. The number of 3-jet events is larger at the higher energy. This is an advantage in the study of gluon jets.

In conclusion, for annihilation physics, 14.5 GeV is favored over 11 GeV but not overwhelmingly so. This slight preference for the higher energy might be offset by the advantage of obtaining a dataset at a different energy.

The case for Two-Photon physics is clearly in favor of 14.5 GeV. The ratio of $\gamma\gamma$-luminosity $\mathcal{L}_{\gamma\gamma}$ for beam energies of 11 and 14.5 GeV are given in Table I. The entries in the third column are calculated under the assumption that $\mathcal{L}_{ee}^{upgr}(11\text{ GeV}) = 3\sqrt{3}(11/14.5)^2\ \mathcal{L}_{ee}^{now}(14.5\text{ GeV}) = 3\mathcal{L}_{ee}^{now}(14.5\text{ GeV})$. The luminosity upgrade with 11 GeV beam energy gives an increase in $\mathcal{L}_{\gamma\gamma}$ for W $<$ 12 GeV and a decrease for W $>$ 12 GeV.

Table I. Ratio of $\mathcal{L}_{\gamma\gamma}$ at 11 and 14.5 GeV

W ($\gamma\gamma$-CM Energy)	$\mathcal{L}_{\gamma\gamma}(11)/\mathcal{L}_{\gamma\gamma}(14.5)$ (for same $\mathcal{L}_{ee}$)	$\mathcal{L}_{\gamma\gamma}(11)/\mathcal{L}_{\gamma\gamma}$(now)
3	0.82	2.5
5	0.74	2.2
9	0.53	1.6
12	0.37	1.1
15	0.12	0.4

Another case to consider is exemplified by the search for SUSY particles. As long as no background is present, the mass limits one sets are approximately proportional to $(s\mathcal{L})^{\frac{1}{4}}$; if background events are present, the limit is approximately proportional to $(s\mathcal{L})^{\frac{1}{8}}$. Changing the beam energy from 14.5 to 11 GeV necessitates an increase in $\mathcal{L}$ of a factor 1.7, just to break even. In any case, the APS

experiment expects to see a few events from $Z^0 \rightarrow \nu\overline{\nu}$ from the present run of 100 pb^{-1}, thereby entering the background regime.

In conclusion, the arguments are largely in favor of the higher beam energy. Moving the quadrupoles and lowering the beam energy reduces the flexibility of the machine, in particular to go back up to higher energy. However an upgrade with a beam energy of 11 GeV is preferable to no upgrade at all.

I.7 Comparison of High Luminosity PEP with other Facilities

In comparing B physics at PEP and CESR, the following differences are apparent. CESR runs with advantage at the $\Upsilon(4S)$, resulting in 2×10^6 B's in 1 fb^{-1}, with 33% purity; the B's being produced essentially at rest. PEP obtains 60×10^3 B's in 1 fb^{-1}, with 9% purity; and the B's move. The rate advantage of CESR over PEP is large. It is somewhat offset by the fact that one almost always knows at PEP, contrary to CESR, which tracks belong to which jet. This reduces the combinatorial background at PEP. A further advantage of 'moving' B's is that a precision lifetime measurement of B mesons is possible. Further, CESR running at the $\Upsilon(4S)$ is below threshold for $B_s\overline{B_s}$ production with important consequences for mixing. We conclude that the advantage in rate of CESR over PEP in B physics is at least partially offset by the above considerations and that the two experimental programs are complementary. To be sure, B physics is going to be hard at both PEP and CESR.

The comparison with SLC and LEP is interesting: $B\overline{B}$ production at an upgraded PEP is equal to that at SLC or LEP when they run at $\mathcal{L} = 10^{30}$ $cm^{-2}sec^{-1}$. At least initially, SLC is not expected to run at these luminosities. If and when it or LEP run at $\mathcal{L} > 10^{30}$ $cm^{-2}sec^{-1}$, PEP will cease to be competitive in hadronic physics. One should keep in mind however that average multiplicities of 20 charged and neutral each, are expected at SLC and LEP. Furthermore, the data at PEP will be simpler in that it will contain fewer multiple jet events and in this sense data from PEP will be complementary to data from SLC and LEP.

In conclusion, the consensus among the Workshop participants is that the physics program at PEP will be very worthwhile with a high luminosity upgrade and people eagerly await its implementation.

FIGURE CAPTIONS

1. Box diagram for mixing (a), Feynman diagrams for B decay (b).
2. TPC/Two-Gamma apparatus with tagging and quadrupole in mini-maxi position.
3. Deep-inelastic eγ scattering.
4. F_2 as function of Q^2.
5. Missing mass spectrum showing a 12 GeV resonance with $\Gamma_{\gamma\gamma} = 0.4$ MeV.
6. Upper limits on $\Gamma_{\gamma\gamma}$ that can be obtained with 1 fb^{-1}.
7. $\pi^+\pi^-\pi^+\pi^-$ effective mass spectrum, untagged.
8. Particle density in 3-jet events from TPC, (a) all charged particles and photons, (b) those charged particles and photons satisfying $0.3 < p_{out} < 0.5$ GeV where p_{out} is the momentum out of the event plane, and (c) a heavy particle sample of charged and neutral K, p and Λ.
9. K rapidity correlation for charged kaons.
10. The angular distribution of the $p\bar{p}$ axis with respect to the jet axis in the $p\bar{p}$ center of mass. The solid line is the Lund String Model, the dashed line is the Cluster Model, (a) before detection efficiency, (b) with detection efficiency.
11. The D* fragmentation function.
12. The F fragmentation function.
13. Λ polarization as function of p_T.
14. Correlation in like-sign pion pairs as function of Q. Q is twice the momentum of a particle in the rest system of the pion pair.

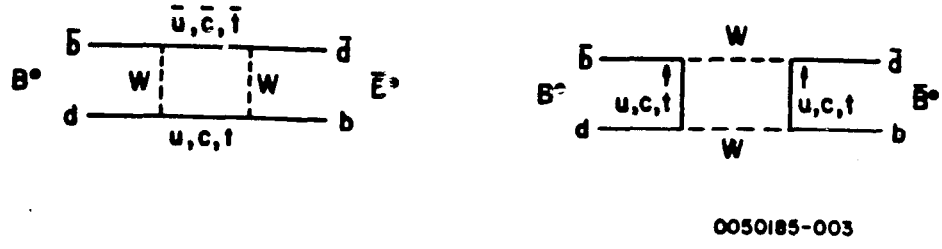
B°
b̄
ū, c̄, t̄
d̄
W
W
d
u, c, t
b
B̄°
W
b̄
d̄
u, c, t
u, c, t
d
W
b
B̄°
0050185-003

Fig. 1 (a)

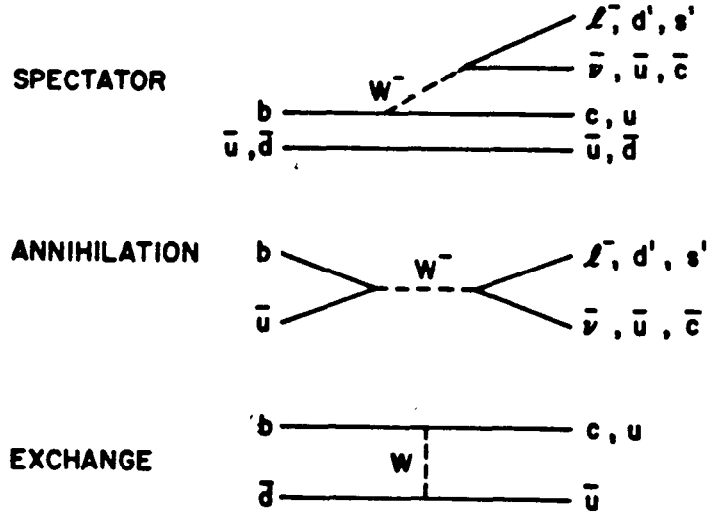
SPECTATOR
b
ū, d̄
W⁻
ℓ⁻, d', s'
ν̄, ū, c̄
c, u
ū, d̄
ANNIHILATION
b
ū
W⁻
ℓ⁻, d', s'
ν̄, ū, c̄
EXCHANGE
b
d̄
W
c, u
ū

Fig. 1 (b)

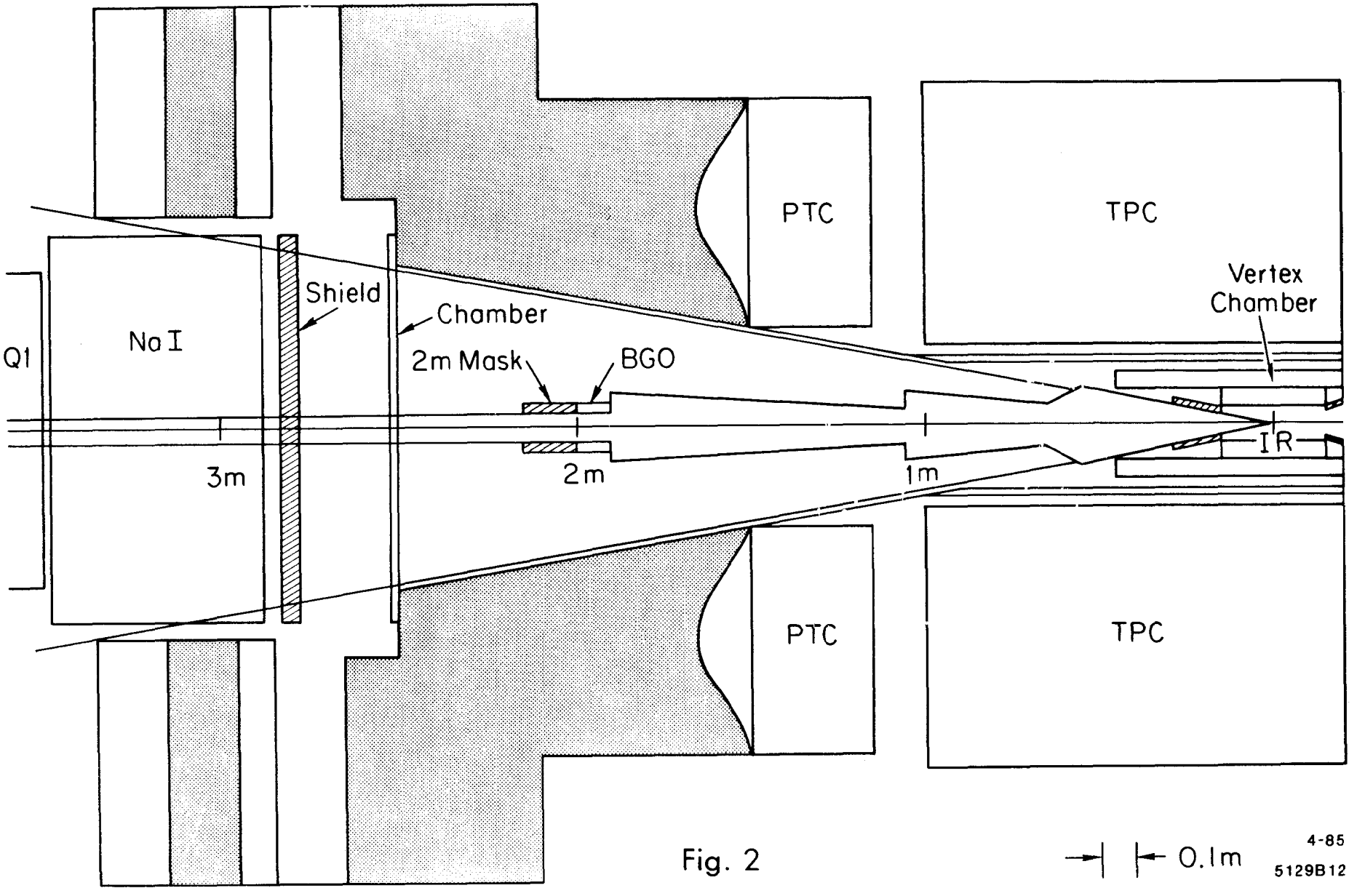
PTC
TPC
Vertex
Chamber
Shield
Chamber
Q1
NaI
2m Mask
BGO
IR
3m
2m
1m
PTC
TPC
0.1m
4-85
5129B12

Fig. 2

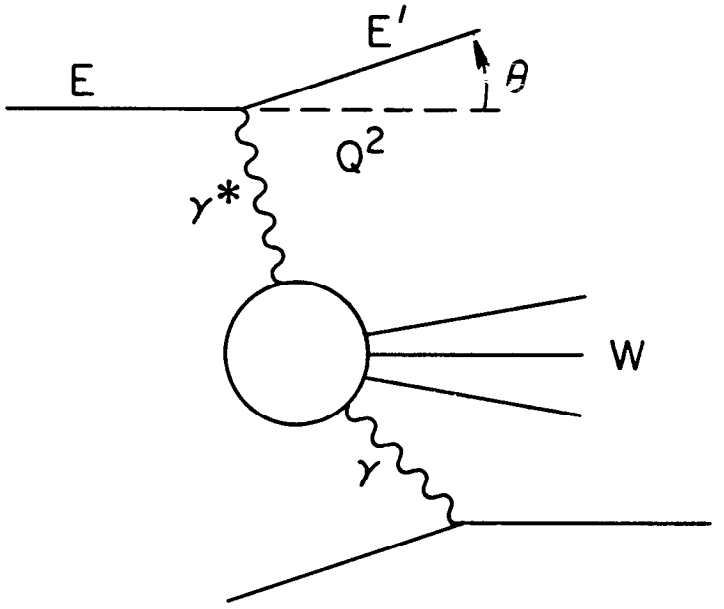

Fig. 3

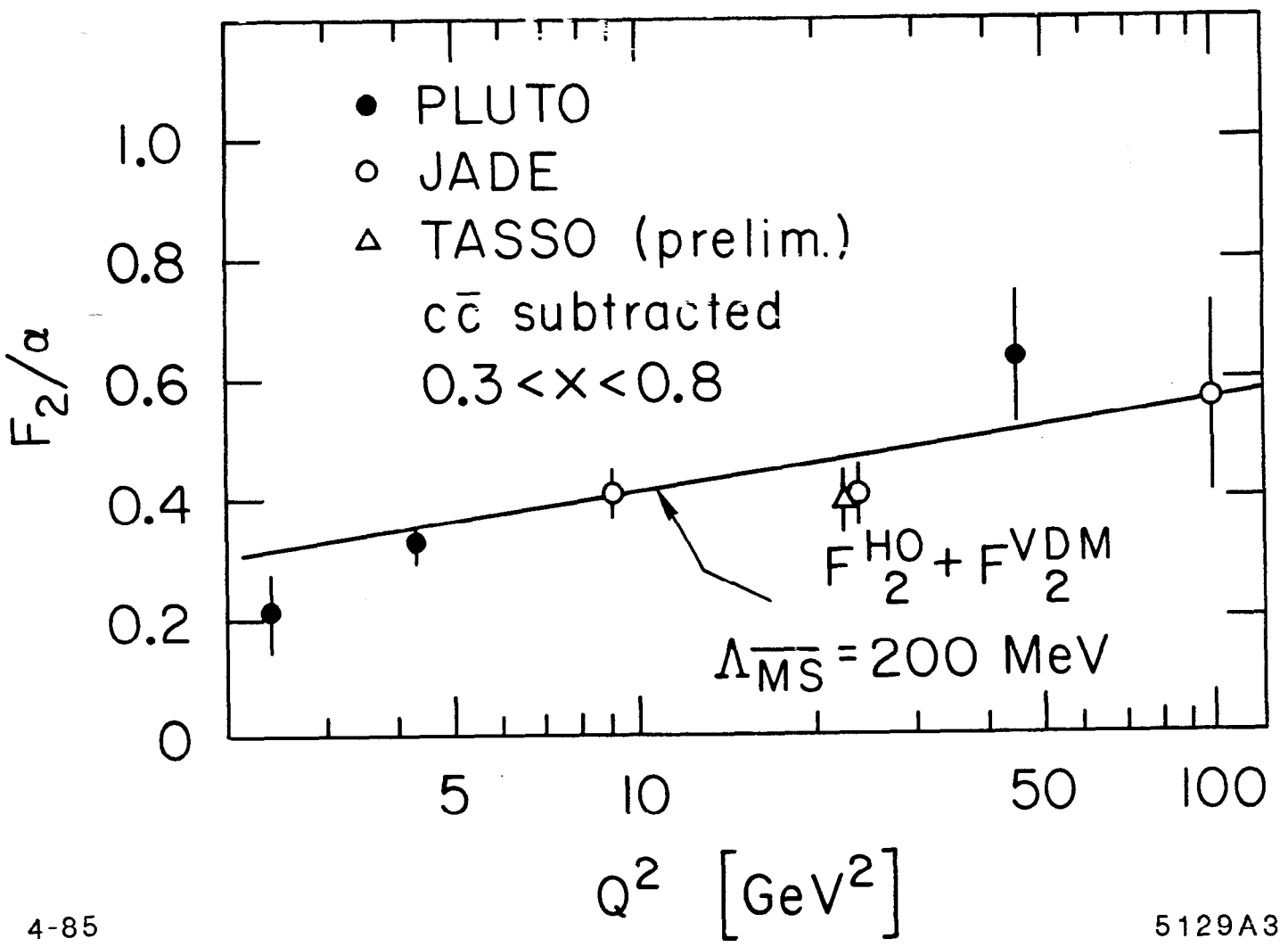

4-85

5129A3

Fig. 4

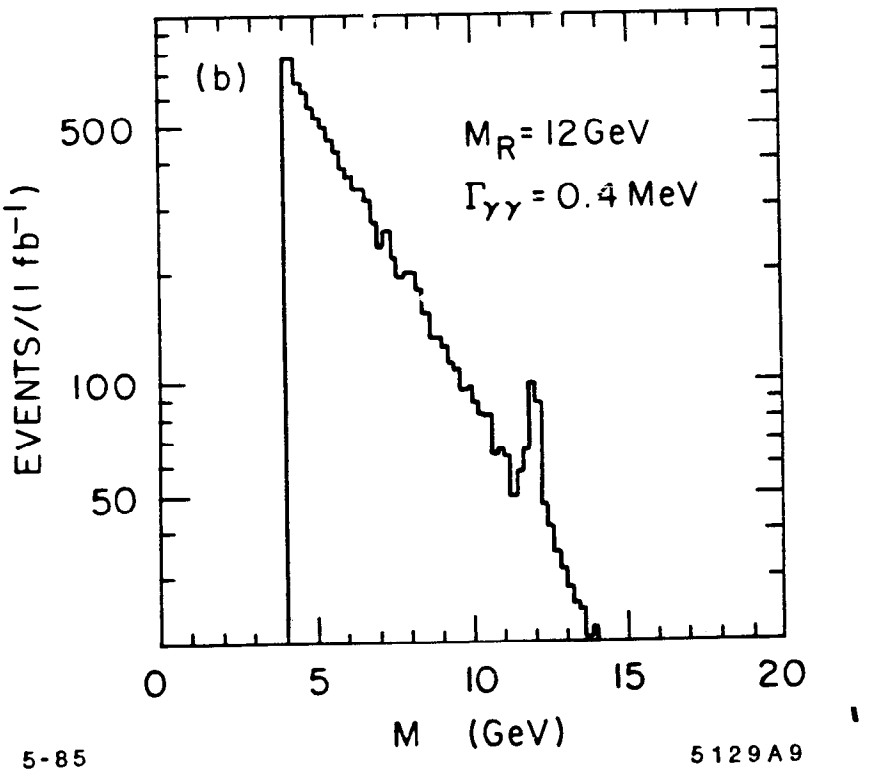
(b)
M_R = 12 GeV
$\Gamma_{\gamma\gamma}$ = 0.4 MeV
EVENTS/(1 fb^{-1})
500
100
50
0
5
10
15
20
M (GeV)
5-85
5129A9

Fig. 5

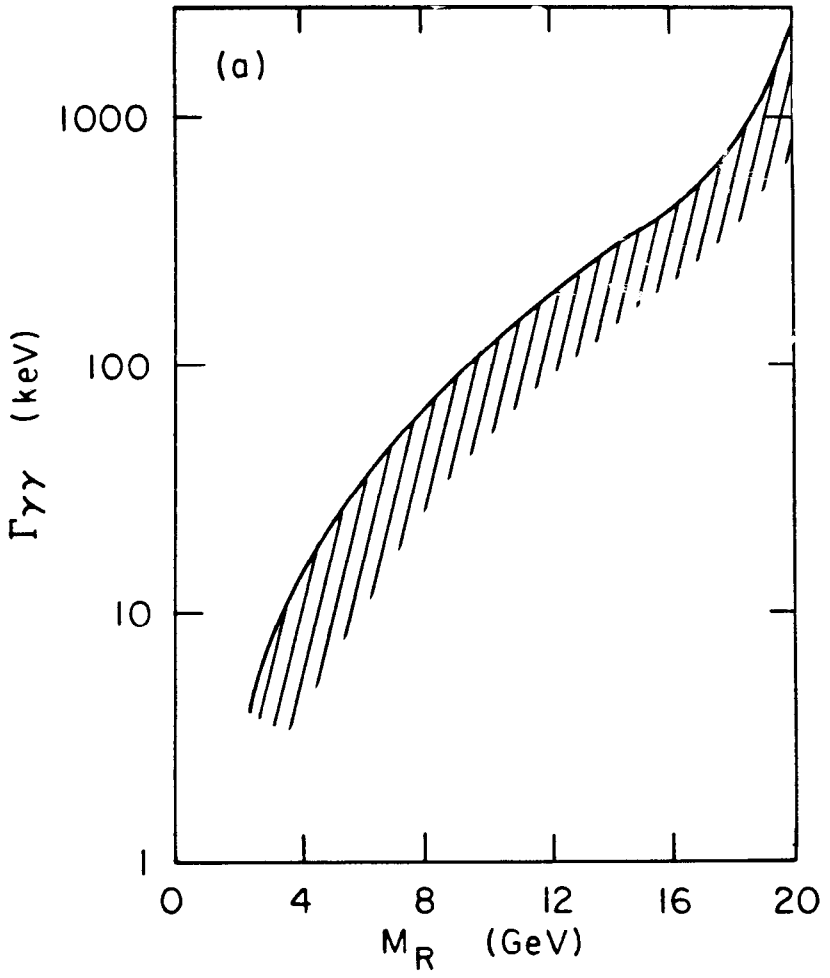

Fig 6

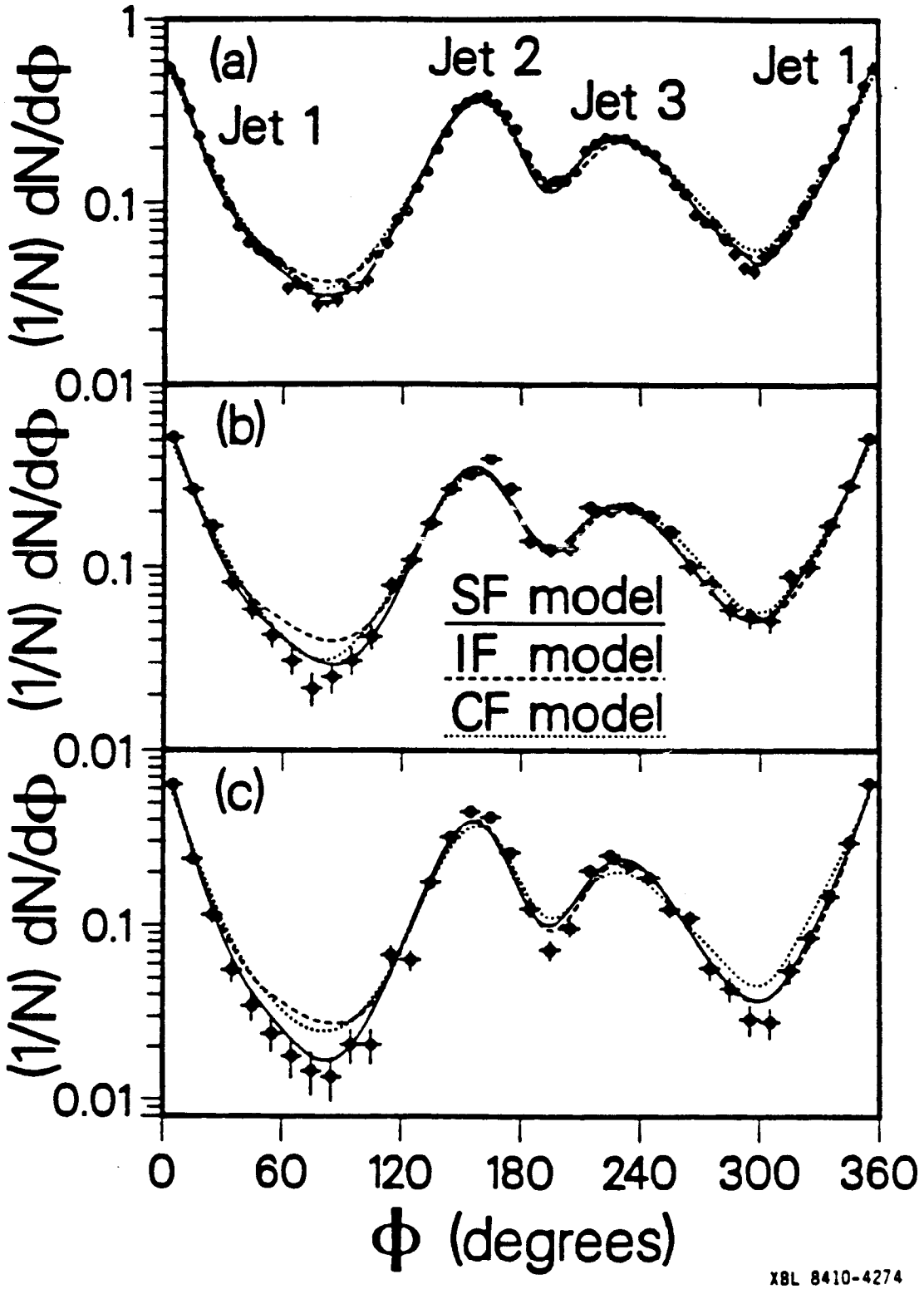
(a)
Jet 1
Jet 2
Jet 3
Jet 1
(b)
SF model
IF model
CF model
(c)
1
0.1
0.01
(1/N) dN/dΦ
0
60
120
180
240
300
360
Φ (degrees)
XBL 8410-4274

Fig. 8

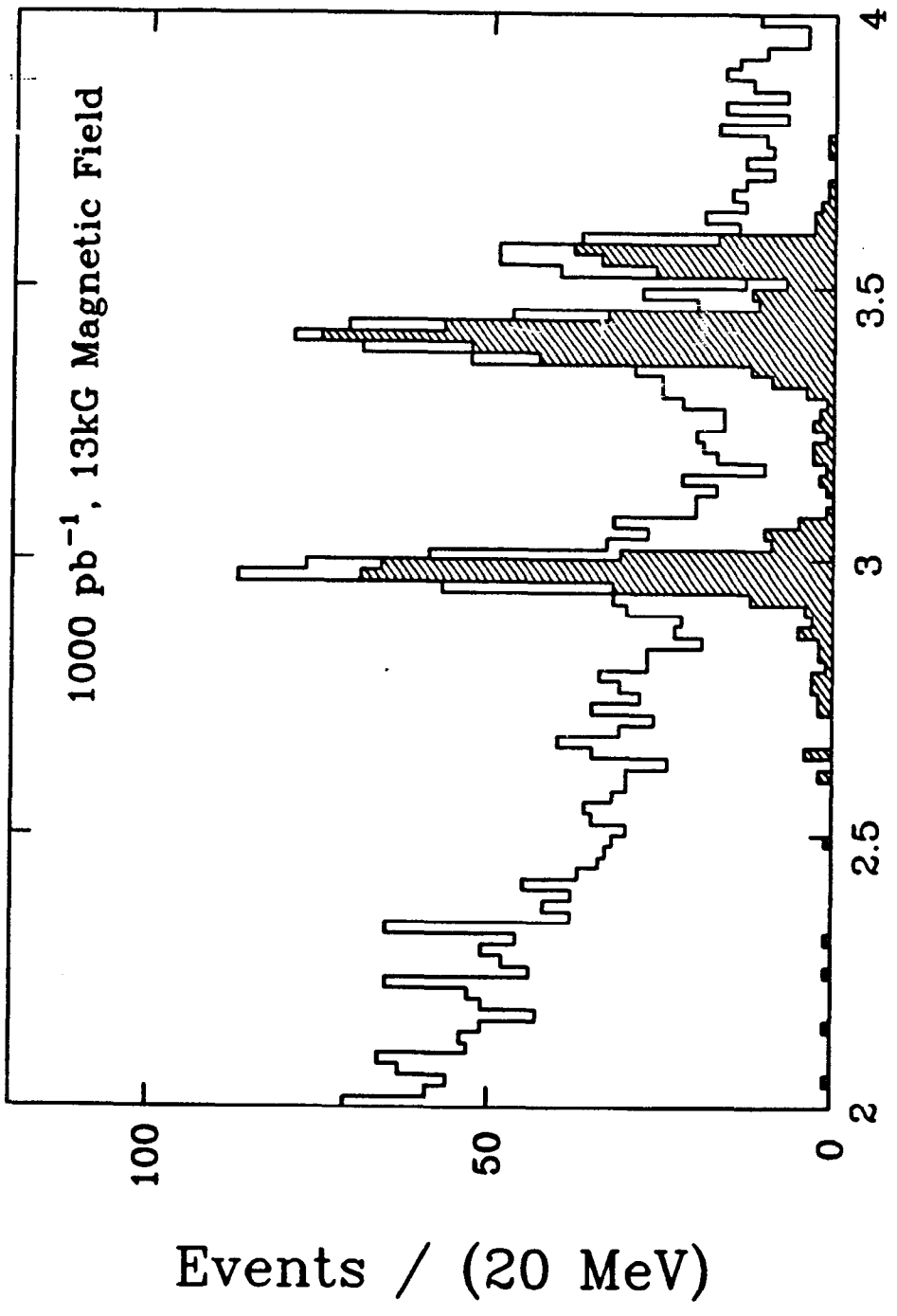
1000 pb^{-1}, 13kG Magnetic Field
Monte Carlo
Events / (20 MeV)
$M_{\pi^+\pi^-\pi^+\pi^-}$ (GeV)
0
50
100
2
2.5
3
3.5
4

Fig. 7

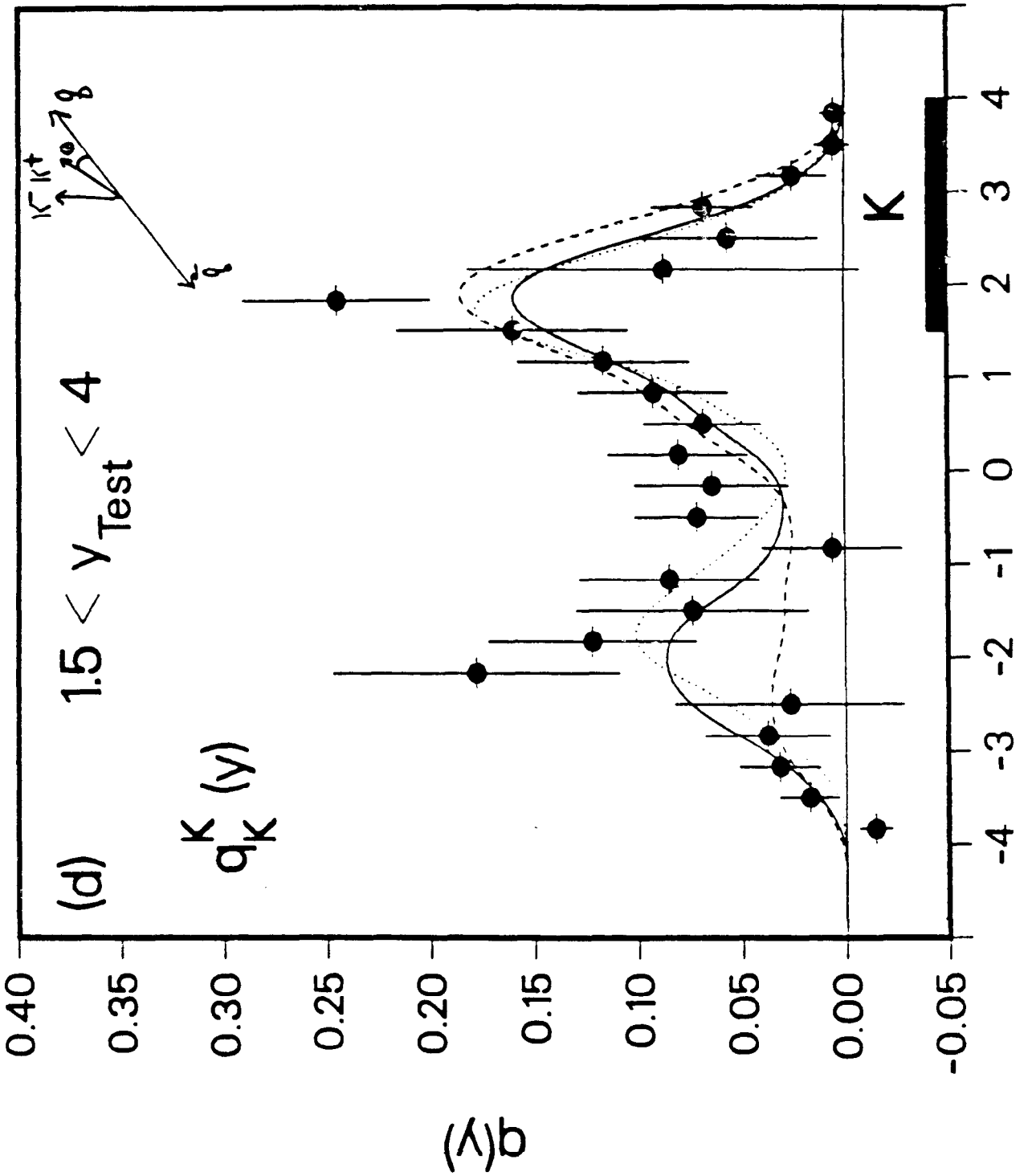
(d)
1.5 < y_Test < 4
q_K^K (y)
K
q(y)
0.40
0.35
0.30
0.25
0.20
0.15
0.10
0.05
0.00
-0.05
-4
-3
-2
-1
0
1
2
3
4

Fig. 9

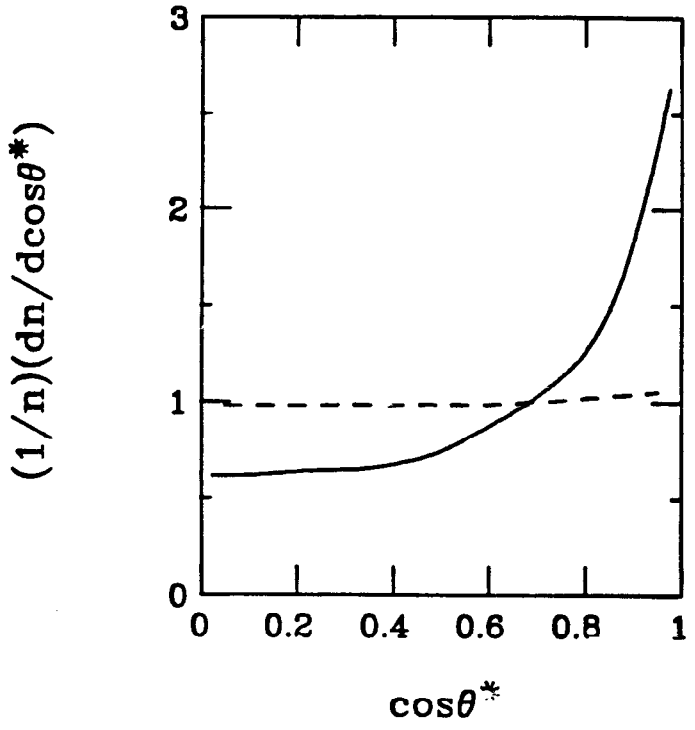
(1/n)(dn/dcosθ*)
3
2
1
0
0
0.2
0.4
0.6
0.8
1
cosθ*

Fig. 10

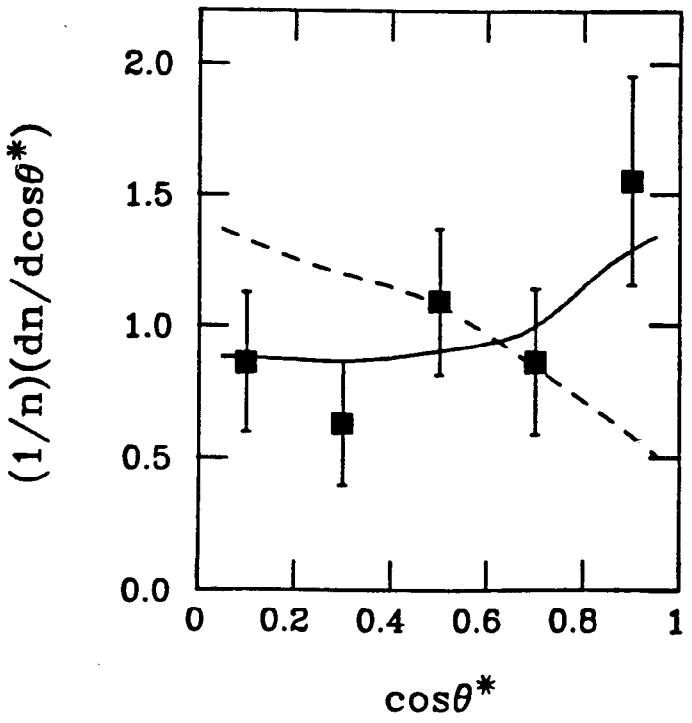
(1/n)(dn/dcosθ*)
2.0
1.5
1.0
0.5
0.0
0
0.2
0.4
0.6
0.8
1
cosθ*

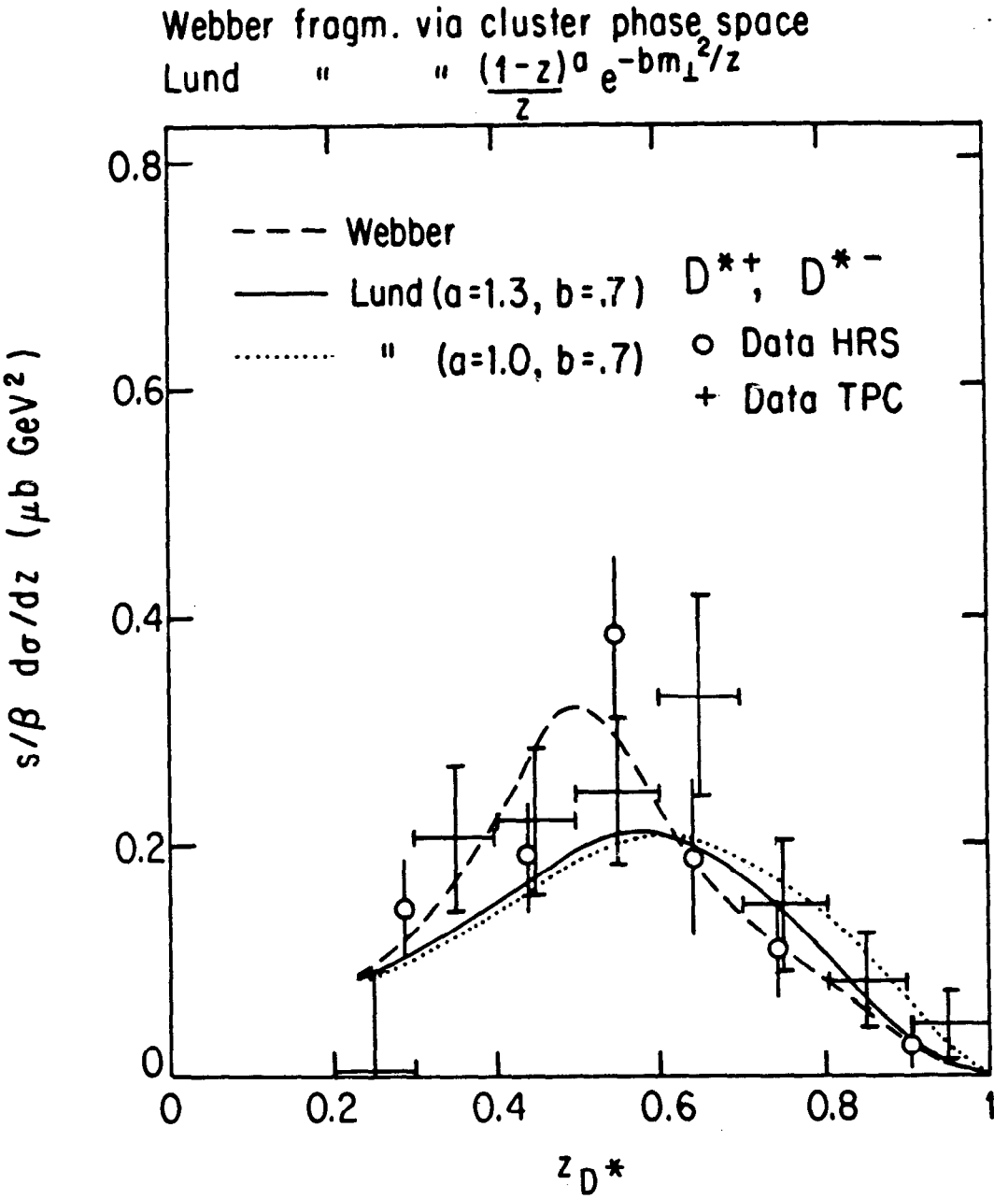
Webber fragm. via cluster phase space
Lund " " $\frac{(1-z)^a}{z} e^{-bm_\perp^2/z}$
Webber
Lund (a=1.3, b=.7)
" (a=1.0, b=.7)
D^{*+}, D^{*-}
o Data HRS
+ Data TPC
$s/\beta\ d\sigma/dz$ (μb GeV^2)
z_{D^*}
0
0.2
0.4
0.6
0.8
1

Fig. 11

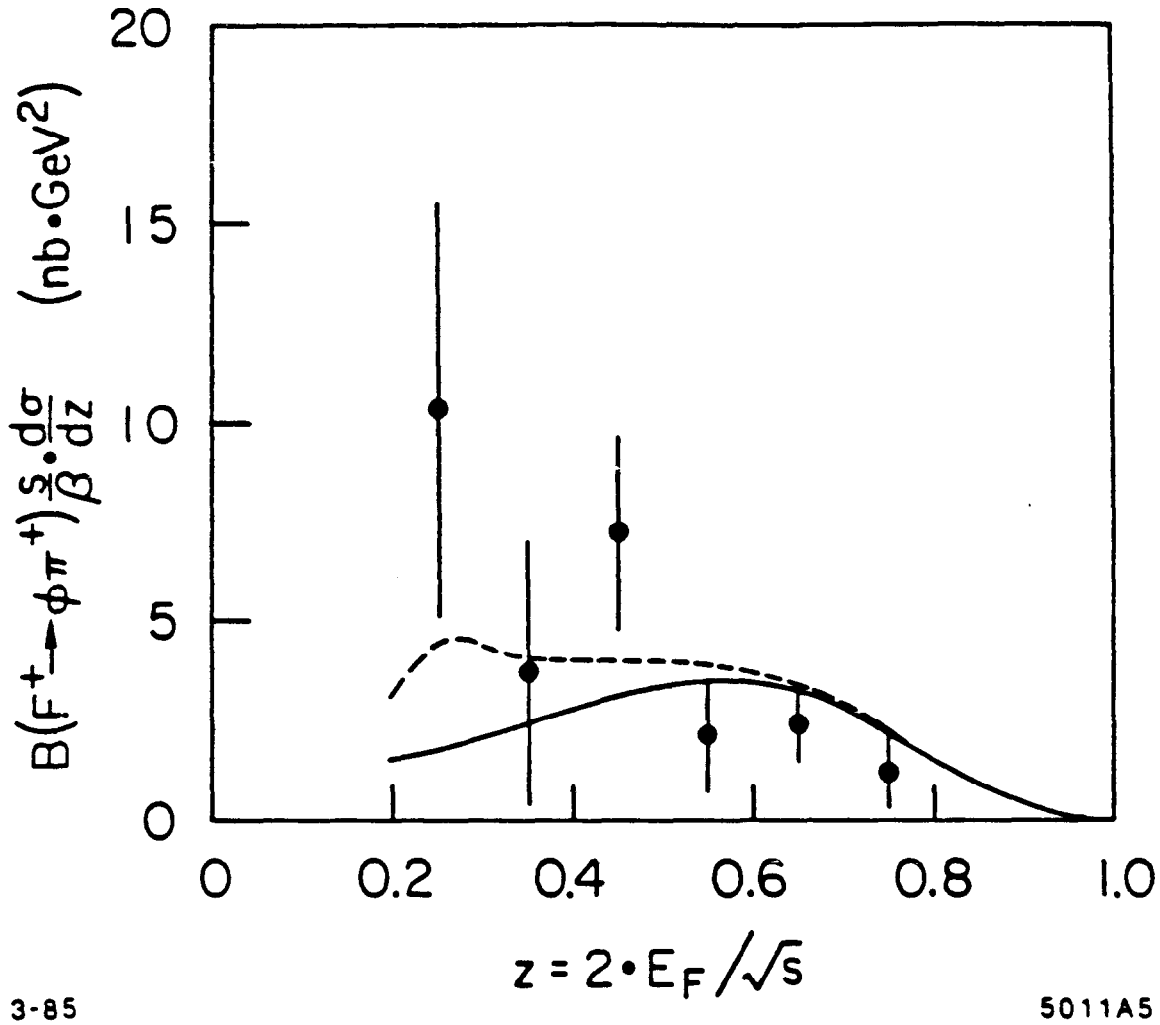
20
15
10
5
0
0
0.2
0.4
0.6
0.8
1.0
$B(F^+ \to \phi\pi^+)\frac{s}{\beta}\cdot\frac{d\sigma}{dz}$ (nb·GeV²)
$z = 2\cdot E_F/\sqrt{s}$
3-85
5011A5

Fig. 12

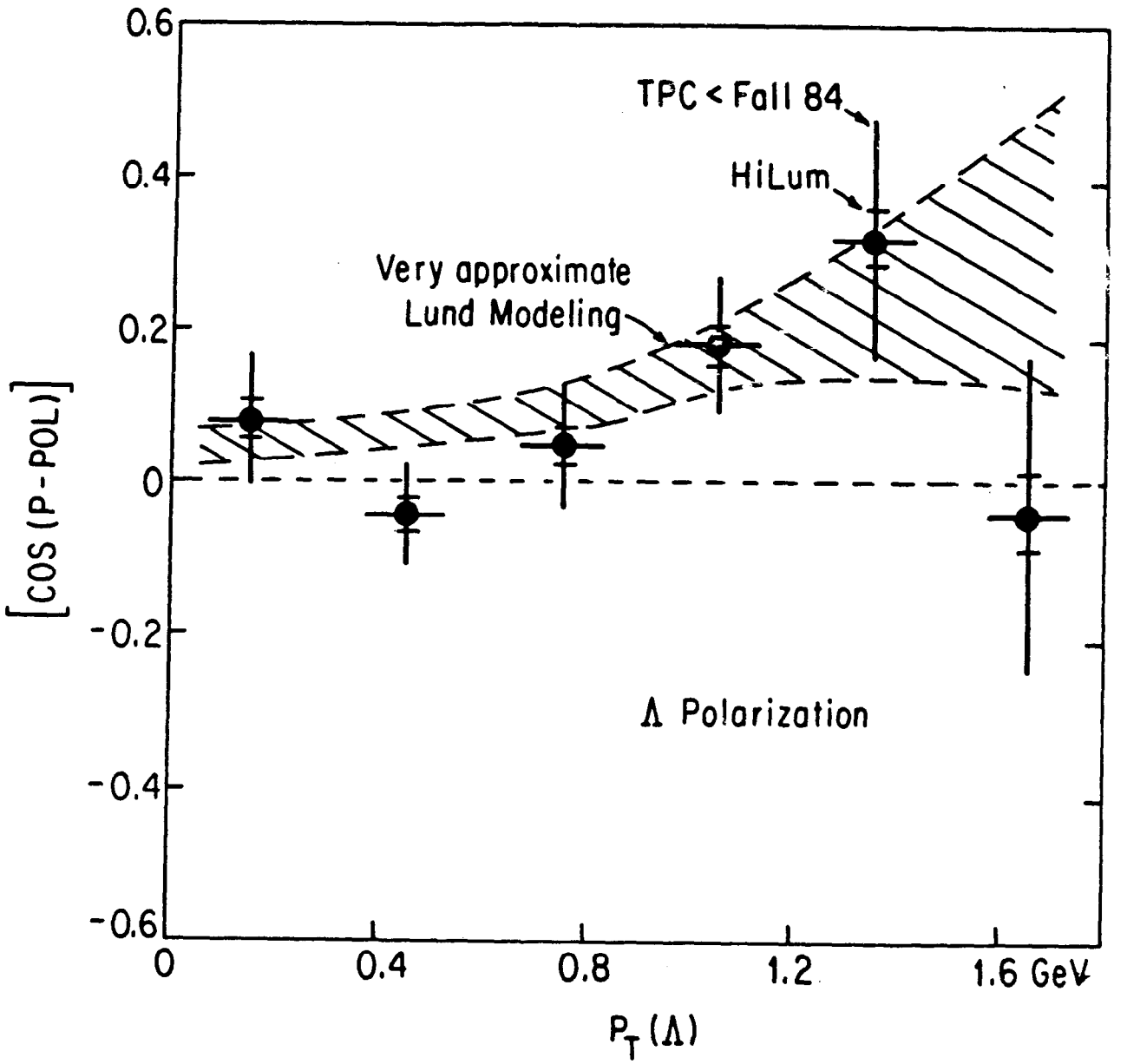
0.6
0.4
0.2
0
-0.2
-0.4
-0.6
[COS (P-POL)]
TPC < Fall 84
HiLum
Very approximate
Lund Modeling
Λ Polarization
0
0.4
0.8
1.2
1.6 GeV
P_T (Λ)

Fig. 13

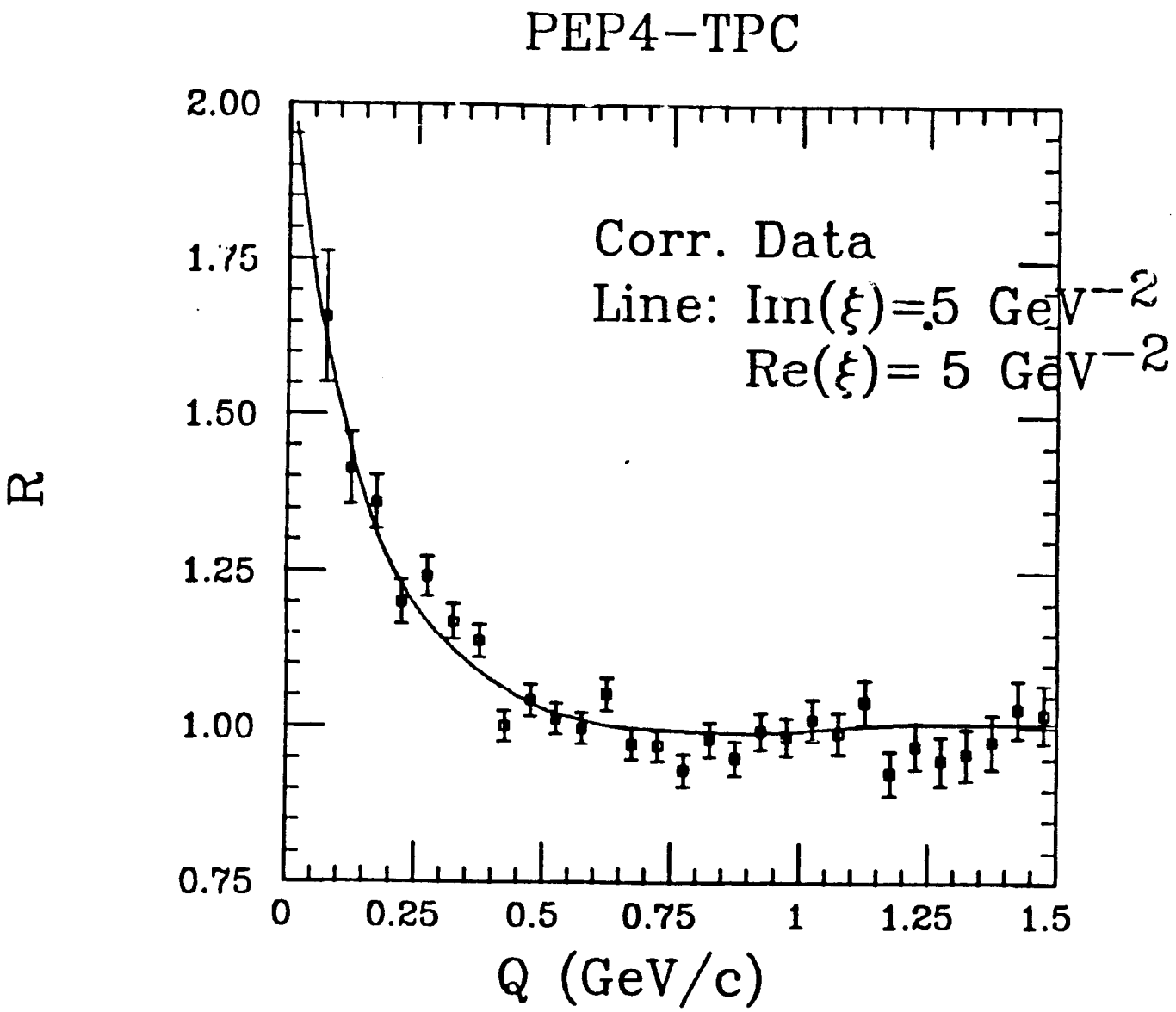
PEP4–TPC
Corr. Data
Line: Im(ξ)=.5 GeV^{-2}
Re(ξ)= 5 GeV^{-2}
R
2.00
1.75
1.50
1.25
1.00
0.75
0
0.25
0.5
0.75
1
1.25
1.5
Q (GeV/c)

Fig. 14

CHAPTER II. B PHYSICS

W. HOFMANN

and

I. I. BIGI, E. BLOOM, A. FRIDMAN, D. GROOM,
R. PANVINI, A. I. SANDA, M. D. SHAPIRO

CHAPTER II. B PHYSICS

CONTENTS

II.1 INTRODUCTION

This report is structured as follows: in the introductory part we briefly review the history of B-physics at PEP, present the assumptions concerning luminosity and event rates, and discuss the main physics goals. In the next section we introduce a variety of "tools" relevant for the study of B physics at a modified PEP. We begin by summarizing our assumptions concerning B hadron production and decay, and also regarding the detector used for the following quantitative estimates of rates, backgrounds etc. Based on this modeling, we address questions such as the optimum center of mass energy for B physics at PEP and ways to select clean samples of $b\bar{b}$ events, and we point out some of the possibilities and limitations in the reconstruction of decay vertices with a vertex detector. Finally, we present a sample of "physics benchmarks" and discuss the physics output to be expected from a high luminosity PEP.

It should be pointed out that we see as the purpose of this report to give the reader the material required to form his own opinion about the possible physics output resulting from a PEP upgrade. We feel that this goal can be achieved better by discussing the general "tools" and a few detailed examples rather than by running through the usual "shopping list."

II.1.1 The Past: B Physics at PEP

Despite its late start, PEP has accumulated a quite impressive list of contributions to the physics of b-quark production, fragmentation and decay. Among the highlights are the first measurement of the b-quark fragmentation function by the Mark II group,[1] revealing a rather hard fragmentation spectrum which confirmed theoretical speculations based on earlier measurements of charm fragmentation functions (also pioneered by the Mark II at PEP), and the recent measurement of the lifetime of hadrons containing b-quarks by the MAC[2] and Mark II[3] groups. This measurement was essential in the determination of parameters in the Kobayashi-Maskawa matrix[4] as well as for estimates of the mass

of the top quark. Numerous other investigations[5] have furthered our knowledge of leptonic branching fractions of B hadrons, the electroweak couplings of heavy quarks and the structure of events containing heavy quarks. The luminosity upgrade of PEP is a must if these successes are to be continued in the future.

II.1.2 The Future: Luminosity and Rates

We shall adopt the dogma of this workshop, namely the integrated luminosity of 1000 pb^{-1} for a first round of one or two years running. Justifications of this number will be given elsewhere in these proceedings. We note that 1000 pb^{-1} at 29 GeV center of mass energy will yield 35000 $b\bar{b}$ events, or 70000 hadrons containing b quarks (the nomenclature used here and in the following is that b denotes a b-quark, and B a hadron containing a b and a light antiquark). Including radiative corrections, event selection efficiencies and a fiducial cut requiring an angle of at least 40° between event axis and beam direction, we expect 62000 B hadrons in the detector, subdivided into 25000 charged B's, 25000 neutral B's, 8000 strange B's and 5000 B baryons (assuming that the b quark picks up u,d,s quarks from the vacuum in a ratio of 3:3:1; QCD cluster models which do not rely on this picture predict higher strange-B rates). An interesting possibility is the exclusive production of charmed B mesons;[6] although the rates are too low to be of any importance at 29 GeV center of mass energy, the process may become detectable if the energy of PEP is to be lowered significantly.

II.1.3 Physics Goals

According to the presently favored "standard model" the fundamental particles include three generations of leptons – (e,ν_e), (μ,ν_μ), (τ,ν_τ) – and three generations of quarks – (u,d), (c,s), (t,b). The interactions between these fermions are mediated by vector bosons – $\gamma, W^{\pm}, Z^0$ and the gluon. Despite the tremendous success of the standard model in explaining many phenomena, many important tests have not yet been made, and many basic parameters such as the number of

generations and the typical mass scales cannot be explained within the model. The study of particles containing the heaviest of the well-established quarks, the b-quark, provides an important testing ground for the theory.

Via the emission of charged vector bosons, the heavier quarks decay to lighter quarks and leptons. In the standard electroweak model, these transitions between generations can be parameterized in terms of the Kobayashi-Maskawa 3 $\times$ 3 matrix of amplitudes.[4] Because of unitarity constrains, the matrix elements can be expressed in terms of only three fundamental mixing angles and a phase. The decays of the lighter quarks u,d,s,c are essentially determined by one of the three angles; to study the remaining two angles, and to fully test the consistency of this description, decays of third-generation quarks have to be studied.

For example, neutral B mesons should exhibit similar mixing phenomena as observed for neutral kaons.[7,8] The mass matrix determining $B\bar{B}$ mixing is calculated by computing the box diagrams shown in Fig. 1a. Apart from the KM matrix elements, the amount of mixing depends on the t-quark mass and on properties of the meson wavefunction such as the B meson decay constant f. Although there is some uncertainty in those factors, one expects a few per cent mixing for B^0, and substantial or even complete mixing for the B_s. The reason for this difference are that in contrast to the B_s, the couplings contributing to the B^0 mixing are suppressed by small KM angles. Besides testing the standard model, measurements of the B mixing severely constrain extensions of the standard model, since many of the new particles introduced in such theories will contribute to B mixing through the box diagrams (see Appendix B for a more detailed discussion).

Given a non-vanishing phase in the KM matrix, one can "explain" the phenomenon of CP violation in the K^0 system, which is so far the only unambiguous experimental evidence for CP violation. The possibility for gaining insight into the origins of CP violation is thereby greatly limited; neutral B mesons, on the other hand, are expected[8,9,10] to violate CP symmetry to a degree governed by

the same phase parameter. CP violation in B decays manifests itself in two ways: through off-shell transitions to heavy flavors creating CP admixtures in neutral B mesons in analogy to the CP violation characterized by the parameter ϵ in the kaon system, and through on-shell B decays, corresponding to the ϵ' of the kaon system. Whereas the chances to observe CP violation in $B\bar{B}$ mixing are slim,[8,10] CP asymmetries of up to 30% are expected for exclusive on-shell decays.[10] Since the corresponding effects for the charm system should be small, on-shell B decays may be the only other process besides the kaon system where CP violation can potentially be detected.

Of interest also is the spectroscopy of B-mesons. The study of b-quark bound states makes it possible to tune the mass ratio of the two-body system over an enormous range and provides a continuous transition from non-relativistic to highly relativistic bound states. PEP offers the potential to explore bound states of b and s quarks and possibly, at reduced cms energies, of b and c quark states.

Decays of B mesons also provide a laboratory to study strong interactions. Naively, one expects that B meson decays are governed by spectator diagrams (Fig. 1b), given that the spectator decay rate is proportional to the fifth power of the quark mass, whereas the helicity-suppressed non-spectator modes go as the second power of the mass. This suppression can however be avoided by emission of a gluon, and estimates of these QCD corrections indicate that in the case of a B^0 non-spectator diagrams may contribute up to 30-40% of the decay rate.[11] The relative importance of non-spectator channels determines the semileptonic branching ratios and the lifetimes of B mesons. Data on these B decay mechanisms not only tests QCD corrections, but is also required to establish a meaningful relation between measured B-particle decay rates and the KM matrix elements.

The variety of experimental techniques used to study B's reflects the diversity of the questions outlined above. Whereas some problems are more easily accessable if B's are produced at rest, others, such as lifetime measurements,

obviously require moving B's. As discussed in the next chapter, the PEP energy range offers the advantage that decay products of B and $\bar{B}$ are kinematically well separated. At PEP strange B's and B baryons will be produced as well as charged and neutral B's. This has drastic consequences, e.g. in the search for $B\bar{B}$ mixing. It is our point of view that extensive B-physics programs both at PEP and at CESR represent complementary efforts rather than competition and will result in mutual benefit.

II.2 TOOLS

In this section we will present the "tools" required for a sensible evaluation of the physics output to be expected from a high-luminosity PEP. Among the tools required are obviously a reasonably realistic model of both the detector and the physics processes as well as techniques to select and reconstruct the events; we will also face the question of the optimum center of mass energy for this kind of physics.

II.2.1 Detector and Event Simulation

One of the major detectors at an upgraded PEP will be the TPC facility,[12] with some modifications compared to the present setup in order to make optimum use of the high luminosity. Tracking, momentum measurement and particle identification will be provided by the Time Projection Chamber in the 1.35 Tesla field of the superconducting solenoid. Combined with a vertex detector, a momentum resolution of $dp/p = 1.5\%$ at low momentum and 0.3%p at high momentum should be achievable, compared to a present resolution of 1.5% at low momentum and 1%p at high momentum (without using the vertex constraint). Particle identification will be provided by measurement of the ionization energy loss. Figure 2a demonstrates the particle separation obtained with the present setup: at low momentum, the electron, muon, pion and proton bands are well separated; at high momentum, electrons and pions are easily distinguished from heavier

hadrons, and kaons and protons are separated by 1 to 1.5 S.D. The quality of particle identification in the present TPC is summarized in Fig. 2b; a positive identification is typically possible for about 50-60% of the tracks. The improved momentum resolution provided by the vertex detector will improve the particle identification slightly; in addition, dE/dx measurements in the vertex detector (operated with a gas which exhibits little relativistic rise) will help to resolve some of the overlap regions. In the present study, we assumed a TPC operated at the usual 8.5 atm. pressure. If necessary, the momentum resolution at low momentum can be improved by a factor 2 by reducing the pressure to 4 atm., at a rather small loss in identification power.

The assumed detector differs from the present facility mainly in the replacement of the inner drift chamber by a radial drift chamber under development at LBL,[13] and in the reduction of the total amount on material in front of the main tracking chamber. The radial drift chamber occupies the space between 5 and 18 cm radius and should provide a resolution in the $r - \phi$ plane of better than 30 μ for each 5 mm track segment. Multiple tracks can be resolved if they are separated by more that 1 mm. A 1 mm Be beam pipe at 5 cm radius and a modified pressure vessel reduce the amount of multiple scattering and photon conversion. Our Monte Carlo simulations – which include the effects of track overlap, inefficiencies etc. – indicate that about half of the charged tracks at angles of more than 30° with respect to the beam line exhibit an average error in impact parameter of $20\ \mu + 65\ \mu/p$ (in GeV); for the other half the resolution is $40\ \mu + 130\ \mu/p$ (where the two terms are meant to be added in quadrature). The present track fit does not treat the multiple scattering in the material between vertex detector and TPC in a optimal way; a more sophisticated fit should improve the resolution, in particular at low momentum. Based on the experience gained with the MAC vertex detector, a likely scenario is also that beam pipe and vertex detector will be moved to a smaller radius.

Though the TPC facility emphasizes tracking and identification of charged particles, the detector will be complemented by the barrel and forward electromagnetic calorimeters and by muon chambers, as in the present setup.

In order to estimate detection efficiencies and backgrounds, annihilation events were generated using the LUND event generator, version 5.3.[14] The particles were tracked through a detailed simulation of the detector. For the purpose of this study, we assumed a conservative value of 1 ps for the lifetimes of particles containing b quarks, and the PDG values[15] for the lifetimes of charmed particles. A realistic simulation of both B particle production and decay are of course essential. We compared the predictions for inclusive π, K and p spectra and multiplicities with data from CLEO,[16] and found agreement within errors (with a slight tendency for the model to underestimate the decay multiplicities). A well-known problem of previous versions of the model – the misrepresentation of the rather hard D-meson spectrum from B decays[17] – seems to be cured meanwhile (Fig. 3). Of course, at PEP energies B-mesons are not produced exclusively. The inclusive B-meson spectrum and the number of particles produced in addition to the B's was compared with experimental data,[5,18] and no major disagreements were uncovered.

Obviously, the actual TPC facility in 1987 may differ from our model, and other detectors with different strength and weaknesses will be operating at PEP. Moreover, Nature may decide to ignore the predictions by the LUND Monte Carlo and go its own way. As a consequence, efficiencies and rates quoted in the following should not be taken too literally. We will, however, point out those predictions which are very sensitive to details in the modeling.

II.2.2 The "Best" CMS Energy for B-Physics – Is There a Cheap Solution?

Out of the many possibilities to realize increased luminosities at PEP, one attractive solution is based on the reduction of the cms energy to 22 GeV or less. In this case, use of the existing quadrupoles at the interaction regions would result in considerable savings. In this section we will address the possible losses or gains resulting from a lower cms energy. Obviously, the question of the "best" energy is a very complex one and the answer will depend on the weight attached to various physics goals, on the detector performance etc. We will concentrate on two main aspects: the measurement of lifetimes of B particles and the reconstruction of their decays. A number of relevant quantities discussed in the following are displayed in Fig. 4 for cms energies between threshold and 60 GeV. Although the Monte Carlo is not too reliable for energies above 60 GeV (it is based on 2nd order QCD), the curious reader can extrapolate the curves to SLC or LEP energies without too much trouble.

The mean flight path of a particle with a finite lifetime is given by $l = \beta\gamma c\tau$. Since the momentum distribution of B hadrons will scale in $x = p/\sqrt{s}$ at energies sufficiently above the kinematic threshold, l increases in proportion to $\sqrt{s}$, as illustrated in Fig. 4a. However, the quantities measured experimentally are impact parameters of tracks, not the decay length. The impact parameter b of a track is given by $b \cong \alpha l$, where α is the angle of the track with respect to the parent's direction of flight (assuming $\alpha \ll 1$). Since α decreases as $1/\gamma_{\text{parent}}$, the average impact parameter reaches an asymptotic value of the order $c\tau$ (Fig. 4b); hence little is gained by increasing the energy beyond the point where $\beta_{\text{parent}} \cong 1$. A more important constraint comes from the fact that the measurement of impact parameters of low-momentum tracks is severely limited by multiple scattering in the beam pipe. Adopting 1 GeV/c as a somewhat arbitrary cutoff, the number of high-momentum tracks from the decay of a B particle increases from 1.8 at 22 GeV cms energy to 2.5 at 29 GeV (Fig. 4c). At even higher energy, the advantage of having a larger number of high momentum tracks is partly offset

by the fact that those tracks are close together and the chance of track overlap in the vertex detector increases.

Another aspect is how often a high-momentum track will be misassigned to the wrong B, because it is emitted into the backward hemisphere with respect to the B direction of flight. At threshold, the probability for such a confusion is obviously 50%, decreasing to 1-2% at 22 GeV and reaching an asymptotic value of 0.3% at 30 GeV (Fig. 4d). Altogether, a higher cms energy will simplify lifetime measurements somewhat, but there is certainly no qualitative difference between 22 and 29 GeV; in particular, the higher event rate at 22 GeV (assuming a constant luminosity) will probably result in a net improvement compared to 29 GeV.

In the reconstruction of exclusive B-decays, the main problem is the combinatorial background. A typical event (Fig. 5a) will contain tracks from the primary vertex and from the second B particle in addition to the "wanted" tracks from a B decay. The number of additional tracks increases with $\sqrt{s}$ (Fig. 5b). The fact that B particles typically carry a large fraction of the beam momentum and sit at the end of the rapidity plateau however provides a powerful selection crititerion: the rapidities of decay products are similar to the rapidity of the B particle, hence a cut in rapidity will drastically reduce the combinatorics. This is evident in Fig. 6, where the rapidity distribution of decay products of a given B is superimposed to the total rapidity distribution. In particular, at 29 GeV 85% of all B's have all decay tracks in one hemisphere of the event (compared to 70% at 22 GeV). Adjusting a rapidity cut such as to typically retain all tracks from a given B, the number of tracks not associated with the given B but accepted by the cuts drops from about 5 at $B\bar{B}$ threshold to about 1.5 at 20 GeV and above (Fig. 7). It is interesting to note that with appropriate rapidity cuts the combinatorial background does not get worse as the energy is increased beyond 20 GeV; the reconstruction of B's at the SLC will most likely be not more difficult than at PEP, despite a large increase in the total hadron multiplicity in the events! As we will see later, mass resolution and reconstruction efficiencies are fairly independent

of the energy, too.

We can summarize this discussion by saying that there are certainly no strong arguments favoring 29 GeV as compared to the 22 GeV option; the "best" energy will be the one which enables us to collect the largest number of B events as soon as possible!

It is finally interesting to compare efficiency and rates of several B sources available in the near future.[10] Table I gives a comparison of the estimated rates. The quantity f_B is defined as the fraction of the total cross section leading to $B\bar{B}$ pairs, and measures the signal-to-background ratio. The assumed luminosities are 10^{30} (TEV I), 10^{32} (upgraded PEP), 10^{30} (initial SLC operation) and 10^{31} (LEP). For the fixed target experiment, a total usable rate of 10^7/sec has been assumed.

Obviously, e^+e^- machines enjoy a tremendous advantage in signal-to-background ratio over hadron machines. This, and the fact that production rates and momentum are well-known makes it likely that the decisive experiments on B physics will be done at e^+e^- machines. In the near future, until LEP and its detectors with good particle identification come into operation, PEP certainly offers a competitive environment.

II.2.3 Tagging Methods

Despite the fact that e^+e^- storage rings provide in relatively clean source of B particles, one will often have the problem to further enhance the fraction of b-events, and to select an event sample where b quarks dominate. A variety of properties of b-jets can be exploited for this purpose. We consider the following signatures for B-events (Fig. 8):

1. High p_T leptons. Because of the large B mass, leptons from semileptonic B decays typically have larger transverse momenta with respect to the jet axis than leptons from other sources such a charm decays.

Table I. Rates and Backgrounds for Various B Sources

Source	$\sqrt{s}$ (GeV)	σ_{tot}	Total Interaction rate (Hz)	f_B	$\frac{B\bar{B}}{10^7 \text{ sec}}$
TEV II (fixed target)	45	50 mb	10^7	10^{-6}	10^8
TEV I ($\bar{p}p$)	2000	100 mb	10^5	10^{-4}	10^8
CESR (e^+e^-)	10.6	5 nb	0.3	.25	7×10^5
PEP (e^+e^-)	29	.4 nb	0.04	.09	4×10^4
SLC (e^+e^-)	92	30 nb	0.03	.14	4×10^4
LEP (e^+e^-)	92	30 nb	0.3	.14	4×10^5

2. High p_T kaons. One might expect that similar to leptons, kaons can be used to tag B's.

3. Event topology. Since the heavy B particles decay isotropically, b-events will exhibit a different topology than the well-collimated, or at least planar jets resulting from the fragmentation of light quarks.

4. The finite lifetime of B-hadrons can be exploited to select events with multiple decay vertices.

The quality of any given selection criterion can be measured in terms of its efficiency ϵ defined as the fraction of true b-events retained by the selection and by the purity η of the resulting b sample. We shall often refer to the enhancement

factor g instead of the purity η. The enhancement factor is defined as the ratio between the efficiency for b-events and the average efficiency for u,d,s,c-events for a given selection criterion. Using ϵ and g has the advantage that these quantities are multiplicative if (approximately) independent selection criteria (such as the vertex tag and the topology tag) are combined. An enhancement factor g = 10 will result in about 50% b-purity; in order to obtain 70% purity, a g of 25 is required.

The Lepton Tag

Using leptons to select b-events is a standard, well-understood technique used, e.g., for the measurement of b quark fragmentation functions and in the measurement of semileptonic branching fractions and lifetimes of B hadrons.[2,3,5] Typical requirements are a minimum transverse momentum of 1 GeV/c and a minimum total momentum of 1.5 GeV/c for the lepton.[5] Backgrounds arise due to leptons from charm decays, non-prompt leptons from π and K decays, Dalitz decays of π^0's and photon conversions in the beam pipe, and finally misidentified hadrons. The TPC group has published results based on 77 pb^{-1} of data;[31] our extrapolations are based on those numbers. After cuts to enhance leptons from B's, the present samples consist of 80 (155) electrons (muons). About 69% (76%) of the leptons stem from B's (including the B $\rightarrow$ C $\rightarrow$ lepton cascade); the charm background, non-prompt leptons and misidentification account for 31% (24%) of the sample. With a vertex detector, the non-charm backgrounds in the electron sample can be reduced drastically. Figure 9 shows the momentum distribution of large-p_T electrons and the estimated backgrounds. The dotted line indicates contributions from misidentified hadrons, which are minimal because of the excellent particle identification in the TPC (here combined with the lepton-hadron separation based on the longitudinal and transverse shower shape measured in the barrel calorimeter). The dashed line indicates the background due to photon conversion in the 0.2 radiation length of material in front of the TPC. With a vertex detector and a thin beam pipe, this background is virtually non-existent, leaving only a contamination by leptons from charm decays (about

15%). Extrapolating the numbers to 1000 pb^{-1}, we expect a sample of 3000-4000 events with leptons in the b-region, a b-purity well above 70%, and a charm contamination of the order of 15%. The corresponding efficiencies are 7-9%; the enhancement factors range from 25-35.

The Kaon Tag

Somewhat to our surprise, a large p_T kaon is not a very efficient way to select B's. Given the kaon identification in the TPC (which is about 50% efficient and yields a kaon sample of more than 70% purity), the maximum enhancement factor obtained was 1.3, at a rather low selection efficiency of 10%.

The Topology Tag

A b-selection based on the event topology was used by the TASSO group in their measurement of the B lifetime;[19] the selection consists of dividing events in two hemispheres, then boosting each group of particles in the rest frame of a typical B hadron and calculating the sphericity in the boosted system. For real b-events, both hemispheres will exhibit large sphericities due to the approximately isotropic B decay. The TASSO analysis required a minimum value for the product of the two sphericities derived by this method. Other topological selection criteria based on sphericity, aplanarity and thrust values have been studied by the TPC group and others. In either case, the conclusion is that enhancement factors of 4-5 can be reached for efficiencies of about 30%. The enhancement factor cannot be raised beyond 5, even at reduced efficiency. An interesting aspect is, however, that enhancement factors of about 2 can be obtained with excellent efficiencies of the order of 60-70%. This is particulary important in that a topology tag can distinguish between b-events and c-events, as evidenced by Fig. 10.[20,21] The topology tag therefore complements e.g. a vertex tag, which offers only a limited distinction between b and c-events (at least at PEP energies), due to the finite lifetime of charmed particles.

Tagging Using Secondary Vertices

A simple method to select events with secondary vertices if to require a certain minimum number of tracks with large impact parameters with respect to the nominal interaction point (after tracks from K^0 and Λ decays are removed). Figure 11 demonstrates that a vertex detector as discussed above does indeed provide a measurement error which is small compared to the typical impact parameter for a large fraction of tracks. Unfortunately, this method is of limited use at PEP, since the size of the beamspot (which will be similar to the present beamspot of $500\mu \times 65\mu$) is of the same order as the impact parameters. Since the position of the interaction point within the beam eneveloppe is not known, this increases the effective error on the impact parameter significantly. For this reason, we considered tagging methods which do not rely on the knowledge of beam position and width.

Basically, an event is divided into two jets, and an effective vertex is calculated separately for each set of tracks (V_1, V_2 in Fig. 12a). We consider the projection D of the distance between those two vertices onto the event axis, with the sign convention that a finite decay path results in a positive D. For light quarks, the distribution in D will be centered about D = 0, whereas quarks with a finite lifetime exhibit a shift towards positive values. Figure 12b displays the pronounced difference between u,d,s events and b events; requiring a mimimum distance of 0.5 mm will greatly enhance the b fraction among the events. The width of the distribution for light quarks is dominated by the resolution of the vertex detector (Fig. 12c), the shape of the distribution for b-quarks is almost independent of the resolution and is governed by the lifetimes of B and C hadrons, and by the fraction of tracks coming from the primary vertex. Whereas light quarks are easily removed by this technique, charmed quarks constitute a serious background (Fig. 12d). Although the typical distance between the two vertices is smaller because of the larger fraction of tracks from the primary vertex, the large abundance of charmed quarks makes a sufficient rejection difficult. More sophistication than just finding an average vertex for each jet is called for.

As a first step, we calculated the most likely position of the primary vertex based on the vertices for each jet and on the beam profile (V_3 in Fig. 12a). Next, tracks are reassigned to the vertex to which they come closest, and new vertices 1 and 2 are calculated using the tracks not assigned to the primary vertex. The procedure can be iterated, if necessary. We concentrate on the vertex with the largest distance from the beam spot and calculate the invariant mass of all tracks associated with that vertex. Given a correct assignment of tracks, charm events should exhibit masses below 2 GeV. Requiring a mass greater than 2 GeV indeed enhances the fraction of b events (Fig. 13). The event topology provides additional selection criteria.

By combining the requirement of a minimum distance of the vertices 1 and 2, the mass-cut and the topology tag, we arrived at the tagging efficiencies and purities displayed in Fig. 14. The lines represent the maximum efficiency achieved for a given purity, for a vertex detector like the one discussed above with an average resolution of about 100 μ/p, and a 50 μ/p detector corresponding to a beam pipe at 2.5 cm immediately followed by a radial DC. For 70% purity, we obtain efficiencies between 10 and 20%. Further optimization of the cuts and of the tradeoffs involved will improve those numbers somewhat; based on our experience we would not count on drastic improvements, however. When trying to achieve a given purity using different combinations of cuts on distance, mass and topology, the resulting efficiencies were remarkably stable.

The results on tagging methods are summarized in Table II. It should be mentioned that any tagging method introduces a bias in the resulting b sample. Whereas this bias is obviously drastic in the case of a lepton tag, it is almost negligible for a topology tag. The vertex tag yields a sample which is biased towards larger decay lengths, and it may be questionable if such a sample can be used e.g. for lifetime measurements. Our studies showed that for the method discussed above, the bias is relatively small, since the required minimum separation of the vertices (about 0.5 mm), is small compared to the average separation of the b-vertices (1.2 mm or more, if particles from charm decays are included in

Table II. B–Tagging Methods

Tag	Cuts	g	ϵ	No. of b–Events Accepted
Lepton	$p, p_\perp$	> 25	8%	2500
Kaon	$p, p_\perp$	< 1.3	10%	3000
Topology	Sphericity Thrust	4	30%	10,000
Sec. Vertex and Topology	D, Mass	25	15–20%	6000

the effective vertex for a jet).

II.2.4 Vertex Reconstruction

A typical b-event has at least 5 vertices: the primary vertex, two B decay vertices and two charm decay vertices. Being able to reconstruct all these vertices, if only for a limited number of events, would clearly be an extremely valuable tool. Given that the resolution on impact parameters is small compared to typical impact parameters, one might hope that such a reconstruction is indeed possible. The scanning of a large sample of events however indicates the opposite. A frequent problem is displayed in Fig. 15a. Here one of the tracks from a charm decay extrapolates back to the primary vertex and cannot be assigned uniquely. Typical events shown in Fig. 15b,c,d serve to illustrate the problem further: there are either too few tracks (b), too many tracks (c) or the B and C decay vertices are too close to be separated (c),(d). Even with an ideal (but two-dimensional) vertex detector, reconstruction of all vertices is almost impossible. The reason

is easy to understand: in a two-dimensional projection, the typical 10 charged tracks form 100 intersections. Half of those can be eliminated because tracks from a charm decay e.g. will not end up in opposite hemispheres of the event. Among the remaining 50, only those vertices which have 3 or more tracks associated with them can be unambiguously reconstructed. Very often, however, a vertex has two or fewer charged tracks within the detector acceptance. Those vertices cannot be found, i.e., cannot be distinguished from intersections of unrelated tracks. Although a full reconstruction may be possible for a very minor fraction of the events, only three-dimensional tracking will improve the situation.

II.2.5 Summary on "Tools"

The main conclusions obtained so far are:

1. Center of mass energy: in the range between 20 and 30 GeV, no particular value of $\sqrt{s}$ offer major advantages or disadvantages. Whereas the lifetime measurements are slightly easier at higher energies, given a fixed luminosity one would almost certainly prefer the higher rate at the lower energies.

2. Tagging: the most useful tags for b-events are likely to be the lepton-tag and a secondary-vertex tag combined with a selection based on event topology. Either method results in sample purities of 70% or higher.

3. Vertex detector: a high-resolution vertex detector is necessary for the tagging of b-events; any improvement in resolution translates into a higher efficiency for a given purity or vice versa. It seems, however, that even a very good 2-dimensional vertex detector is of limited use as far as the vertex association on a track-by-track basis is concerned. Such an association is of course possible on a statistical basis or possibly on a track-by-track basis for a small sample of events.

4. Further tools: a very powerful tool for selecting tracks from a given B hadron is provided by the clustering in rapidity of such tracks (Fig. 6).

Furthermore, we will see later that events with reconstructed charmed particles should aide the reconstruction of the event geometry considerably. By combining the rapidity information, the data from the vertex detector and "bump hunting" a full reconstruction of a few hundred selected events should be possible.

II.3 PHYSICS "BENCHMARKS"

Based on the tools for the simulation and reconstruction of events discussed in Chapter II, we will discuss the expected performance of a TPC-like detector at a high-luminosity PEP. A few classical examples will be discussed in detail. The topics covered are: lifetime measurements, reconstruction of B decay modes, and the search for mixing and CP violation in the B system.

II.3.1 Lifetime Measurements

One of the obvious tasks at a high luminosity PEP will be the precise measurement of lifetimes of B hadrons, and the attempt to find differences in the lifetimes of charged, neutral and strange B mesons. The tools for lifetime measurements are summarized in Fig. 16: one can use the distribution of lepton impact parameters with respect to the nominal beam position, or the hadron impact parameters in tagged events or use methods based on the separation of the vertices found for each half of an event (Fig. 12a). Using lepton impact parameters – as in the original measurements by MAC[2] and Mark II[3] – minimizes the (still sizeable) systematic errors, since the lepton will in about 70% of all cases stem from the B decay vertex, whereas hadrons can come from the primary vertex, the B decay vertex or the C decay vertex. In this case, detailed knowledge about the event structure, the decays of B mesons and the spectrum and lifetimes of charmed particles from B decays is required, resulting in larger systematic errors. Lifetimes derived using the vertex separation suffer from the same problems. For events selected using the vertex tag, the distribution of decay lengths will be biased, resulting in a reduced sensitivity.

Measurements of the lifetime using lepton impact parameters suffer from the large beam size which dominates the measurement errors. This error can be reduced, if only approximately horizontal leptons are considered. As in the Mark II analysis, only leptons below a certain maximum impact parameter error are used, trading precision against statistics. Figure 17 shows the distribution of impact parameters if a maximum error of 100 μ is chosen. The number of leptons corresponds to a 1000 pb^{-1} data sample. The asymmetry due to the long-lived B particles is clearly visible. A maximum-likelihood fit to a sum of contributions from charm (with fixed charm lifetimes) and bottom gives a statistical error on the average B lifetime of ± 0.06 ps. If the cut on the vertex error is relaxed, the number of leptons increases, but the shape of the distribution is smeared out and the resulting statistical error turns out to be nearly independent of the chosen cut.

Most sources of systematic errors in lifetime measurements are related to the limited statistics available for the measurement of quantities such as the b fragmentation function, the detailed response of the detector etc. Studying these sources in detail, we believe that with a high-statistics event sample systematic errors can be reduced roughly in proportion to the statistical errors; we expect systematic uncertainties on the average B lifetime of the order of ± 0.05 ps. Measurements using hadron impact parameters in lepton tagged events or measurements of the vertex separation provide larger statistics, but are less sensitive to the B lifetime. As a result, statistical errors from those methods are similar to those for the lepton impact parameters. Based on the present experience, we expect their systematic errors to be at least twice as big as for the lepton measurement.

While measurements of average B lifetimes are relatively straightforward, the measurement of flavor-identified lifetimes, in particular of the $B^{\pm} - B^0$ lifetime difference, is difficult even with a high statistics data sample. One can try to:

1. Find evidence for a dual slope in the distribution of lepton impact parameters.

2. Compare the average lifetimes measured using leptons and hadrons. We expect that neutral and charged B's are produced at identical rates (the anomaly causing different $D^{\pm}$ and D^0 rates due to vector meson decays does not repeat itself in the B system). The hadronic lifetime will hence represent a linear average of the lifetimes. The average leptonic lifetime, on the other hand, is weighted with the leptonic branching fractions, which are proportional to the lifetimes.

3. Try to tag flavors on an event-by-event basis.

In each case we encounter severe difficulties. The distribution of lepton impact parameters shown in Fig. 17) was generated using different lifetimes – 0.6 and 1.6 ps – for charged and neutral B's. The data is certainly well described by both a single exponential smeared with the resolution (dashed curve) or by a double exponential (full curve). Based on a likelihood fit, the two-lifetime solution is preferred by slightly over two standard deviations over a single lifetime (Fig. 18). The sensitivity to lifetime differences varies strongly with the lifetimes; it is e.g. impossible to exclude a component with very short lifetime (and hence vanishing leptonic rate). It is because of this reason that the fit does not reproduce the assumed lifetimes very well – any positive fluctuation near zero impact parameter lookes like a short-lived component. Based on fit results for different lifetime combinations, we believe that this method has a resolution in the lifetime difference of about ± 0.5 ps under optimum conditions.

The second method is complementary to the first in that it has maximum sensitivity for a short-lived component. In the limit of one vanishing lifetime, the two averages differ by a factor two. Unfortunately, the method is quite insensitive to small lifetime differences (Fig. 19); a difference of 50% in the lifetimes corresponds to an only 10% change in the ratio of leptonic to hadronic lifetime, and hence to the limit of experimental sensitivity.

We investigated various techniques to directly tag charged and neutral B's. Looking at Fig. 6, an obvious idea is to simply sum up the charges of tracks with rapidities above 0.5, say. Figure 20 shows that based on the sum of charges, the composition of the B sample can indeed be varied, but only to a relatively small degree. If, for the charge-tagged samples, lifetimes are determined using one of the standard methods, we expect a statistical error on the lifetime difference which is about 10 times the error on the average lifetime. Using the vertex assignment in addition to rapidities could result in a moderate increase in sensitivity. With charge-tag techniques systematic errors will largely cancel, as far as lifetime differences are concerned.

A more promising, although somewhat speculative way is to tag B's by their charmed decay product. This is illustrated in Fig. 21. From the investigation of semileptonic $b \rightarrow c$ [22] decays we know that the invariant mass of charmed quark and spectator typically corresponds to the mass of a charmed meson, i.e. in most cases no extra particles besides the charmed meson will be produced. Since the b decays via a charged current, a charged B will dominantly decay into a neutral charmed meson, and vice versa. If we assume a similar situation for hadronic decays (i.e., if the quarks created by the W and the c-quark/spectator system fragment independently, which can be expected since each system already forms a color singlet), the charge of a D meson is related to the charge of its parent B even in hadronic decays. The correlation is weakened because of the possibility of D^* production followed by decay into a charged pion and a D, and because of the possible existence of non-spectator decay modes; in either case, however, one finds that a D^+ or D^{*+} should provide a good tag for neutral B's. This tagging scheme was found studying B decay modes predicted by the LUND model (which provides a reasonable description of the inclusive D spectrum from B's and which, by the way, includes a certain amount a decays where c quark and spectator are combined with quarks from the W, according to the relevant color factors). The exclusive B decays detected in the CLEO detector[23] do not favor such a decay scheme, but given the present statistics and backgrounds they do not contradict

it either.

Figures 22 and 25 present the flavor composition of B particles in the same jet as a high-momentum "tag-particle". Such a tag would be applied after a general b-event selection. The plots given here do not include the typical 30% contamination of the b-event sample; neither are contaminations due to misidentified tag-particles included. Figure 22 shows the frequency of different B-mesons in jets containing a $D^{*\pm}$; the LUND model predicts that over 90% of the B's are charged. Using the D^* reconstruction efficiencies obtained with the TPC for the 1982/83 data, we expect about 150 b-events with reconstructed high-momentum D^*'s ($x > 0.4$). The D^* signal has very little background (Fig. 23), and will improve further because of the higher momentum resolution obtained already with the superconducting coil and later with the vertex detector. Due to the excellent particle identification of the TPC, it will also be possible to use D^0 (Fig. 24) and F tags, resulting in enhanced samples of neutral and strange B mesons, respectively (Fig. 25).

It is likely that our present decay model overestimates the possible enhancement factors; on the other hand, the effect indicated in Fig. 21 has to be present at some level. In events tagged by charmed particles, lifetimes can be measured either by studying the impact parameter of the reconstructed charmed particle with respect to the nominal beam position, or by reconstruction of the B decay vertex. In events with a fully reconstructed charmed hadron, such a reconstruction (for the jet containing the D) should be much easier, since one vertex is known. Lifetime measurements using flavor-tagged B's should reach sensitivities comparable to present measurements of B lifetimes. In addition, measurements of the semileptonic branching fractions of charged, neutral and strange B's should be possible with approximately 30% error. We believe that the event sample with detected charmed particles will prove most valuable in other areas as well, such as in the reconstruction of exclusive B decays.

An interesting outlook is the tagging of B baryons using fast protons or lambdas; according to the LUND model 64% (87%) of b-jets containing a proton (lambda) contain a B baryon (Fig. 26). Based on present efficiencies for baryon identification, we expect about 100 events of each type, enough for a coarse measurement of lifetimes and possible semileptonic branching fractions.

Table III summarizes the expected precision for lifetime measurements; the estimates of systematic errors are obviously somewhat uncertain. Whereas a rather good precision will be reached for the measurement of average lifetimes, one will most likely not be sensitive to the expected 10-40% lifetime difference between charged and neutral B's. The limits on lifetime differences will be good enough to establish the relation between b quark lifetimes – and hence KM matrix elements – and particle lifetimes with more confidence then nowadays. It is important to point out that there are a number of rather different methods available to measure both average lifetimes and differences; the variety of measurements will help to control systematics and to further improve the precision of measurements.

II.3.2 B–Reconstruction

While PEP is unlikely to compete with CLEO in the measurement of B branching fractions into exclusive decay modes, it is important for the understanding of B spectroscopy to measure the masses of strange and (somewhat unlikely) charmed B mesons and baryons. Exclusive decays may also provide the most stringent limits/measurements of CP violation.

Consider first decays into charged particles only. According to the LUND model, typical branching fractions into charged-only modes are about 0.5%. Mass resolution and detection efficiency for these decays are shown in Fig. 27; typical efficiencies are around 40%. The mass resolution of about 45 MeV is 5 to 10 times worse than obtained at CLEO, due to the absence of a beam-energy constraint. Including the detection efficiency and cuts to reduce backgrounds, we expect

Table III. Precision of Lifetime Measurements

AVERAGE LIFETIME:

Method	Statistical Errors	System Errors
Lepton Impact Parameter	0.06 ps	0.05 ps (?)
Hadron Impact Parameter Lepton Tag	0.06 ps	0.10 ps (?)
Hadrons, Vertex Tag	0.05 ps	0.10 ps (?)

FLAVOR IDENTIFIED LIFETIMES:

Method	Sensitive to Lifetime Differences of
Lepton Impact Parameter	> 0.6 ps
Hadron/Lepton Lifetime	> 0.6 ps
Charge Tag	$> 0.5 - 0.7$ ps
Charm Tag	$> 0.3 - 0.5$ ps (?)

to see about 20 B^0, 20 $B^{\pm}$, 5 B_s, and 5 B baryons. Including decay modes with one or two π^0, those numbers will increase by factors of the order 2-5; detailed predictions are difficult since there is not yet enough experience with the performance of the TPC barrel calorimeter in conjunction with the thin superconducting coil. It is however unlikely that final states with more than two π^0's can be reconstructed. Reconstructed decay modes are dominantly low multiplicity modes, such as Dπ, D$\pi\pi\pi$, DKKπ, DKK$\pi\pi$ and ψk with a leptonic

decay of the ψ. The last mode is predicted to account for about 5-10% of the reconstructed events and is a candidate for a search for CP violation.

So far, we have not addressed the crucial question if those events can be separated from the background, given the comparatively poor mass resolution. Fortunately, the combinatorial background be reduced drastically by a few simple cuts. Since a B carries most of the momentum of a b-jet, jets containing B's with charged-only decays are characterized in that a large fraction of the jet energy is carried by charged particles. Requiring 12 to 13 GeV charged energy for a jet retains almost all events with B decay candidates and rejects about 95% of the background events. The number of particle combinations to be tried within a given event can be limited since we know that in a b-jet particles with rapidities above 1.5 will almost certainly stem from the B, and particles below y=0.3 are probably not to be associated with the B decay. This leaves for typical events only few combinations to try. For example, in over 25% of the events the region $y > 0.3$ will contain all B decay products, and no other particles. In addition, one can require a mass combination consistent with a charmed particle. Although there are no final background estimates as of the time of this writing, it seems likely that $B^{\pm}$'s and B^0's can be found without too much trouble. The situation for strange and baryonic B's is more complicated. Since typically only 50-60% of the decay particles can be identified unambiguously, reflections from non-strange B's create fake mass peaks, and strange B's with misidentified decay products result in long tails of the mass distribution. In the case of strange B's, some of these problems (but also the rate!) can be reduced by requiring an F meson. Detailed predictions are difficult because of the lack of experience and large enough Monte-Carlo event samples. As evidenced by CLEO, the search for such decays requires a certain learning process, and we will count on the ingenuity of the experimenters.

Besides fully reconstructed decays, there is a wide field of partial reconstruction, as exemplified by the measurement of two-body decays of the B mesons by the CLEO group.[24] This again will be a field that evolves once one has a

large data sample and a good deal of experience of how to deal with it. We will mention here only a possible measurement of an interesting rare decay mode, the decay $B \to \tau\nu$.

The decay $B \to \tau\nu$ provides one of the few model-independent ways to measure the $b \to u$ transition matrix element. The present limit $V_{bu}/V_{bc} < 0.14$ [25] has been derived based on the lepton spectrum in semileptonic decays and relies on plausible but yet unproven assumptions about the dynamics of B decays. Better limits can be obtained indirectly using unitarity constraints on the KM matrix.[26] The $B \to \tau\nu$ decay rate (Fig. 28) depends on the square of V_{bu}, the B meson decay constant f_B, the Fermi coupling constant and phase space factors.[27] The B meson decay constant can be derived from known light-meson decay constants by scaling arguments, or from potential models;[28] possible values range from 0.13 to 0.22 GeV, with favored values around 0.2 GeV. To estimate the branching ratio, one can either calculate a total decay width using the $b \to c$ and $b \to u$ matrix elements

$$\mathrm{Br}(B \to \tau\nu) = \frac{3107}{M_b^5} \frac{f_B^2 |V_{bu}|^2 / |V_{bc}|^2}{9.67 |V_{bu}|^2 / |V_{bc}|^2 + 3.07}$$

or use the measured B lifetime, resulting in the simple expression

$$\mathrm{Br}(B \to \tau\nu) = 96.8 \ f_B^2 |V_{bu}|^2$$

Based on these formula, one expects branching fractions of the order 10^{-4} to 5×10^{-3}. Although these values are tiny, it appears to be possible to achieve sufficient sensitivity, because these events, given that the τ decay results almost always in a single fast charged track, have a rather unique signature: an isolated, high-momentum track recoiling against a high-multiplicity b-jet (Fig. 28). The absence of such events for the given luminosity would correspond to a 90% C.L limit on the branching fraction of 3×10^{-4} at 29 GeV cms energy, or less for lower energies and comparable luminosity. First rough background estimates indicate

that at this level background contributions are non-negligible. But even the limit at some 10^{-3} possibly achievable in this case represents a valuable extension our knowledge.

II.3.3 Mixing and CP Violation

As a last example, we will address the question of the measurability of mixing and CP violation in the B system. Detection of mixing, i.e. the transistion of a neutral B meson (either B_d or B_s) into its antiparticle requires the simultaneous identification of both B hadrons in an event. A standard way is to look for like-sign leptons from B decays in opposite jets. In the standard model, the mixing rate r defined in terms of the lepton rates as

$$r = (B \to \bar{B} \to \ell^+ X)/(B \to \ell^- X)$$

is small for B_d mesons, since the Cabibbo suppressed box diagram (Fig. 1a) causing the mixing competes with the Cabibbo favored decay into a W and a C. For strange B mesons, on the other hand, the box diagram involves Cabibbo favored transitions and mixing is expected to be almost complete, making it easier to study mixing at PEP, where B_s are produced, as compared to CESR. For exclusive $B\bar{B}$ production at threshold, mixing is further suppressed since the $B\bar{B}$ pair is produced in a p-wave state, and one has to include effects due to Bose statistics. In more detail, we expect for $B\bar{B}$ systems with odd and even angular momentum:

$$R = \frac{B\bar{B} \to BB \to \ell^-\ell^- X + \text{c.c.}}{B\bar{B} \to \ell^+\ell^- X} = \begin{cases} 0.01 - 0.08 & 0.04 - 0.23 \text{ for } B_d \\ 0.10 - 0.30 & 0.30 - 1.0 \text{ for } B_s \end{cases}$$

$$\qquad\qquad\qquad\qquad\qquad\qquad\qquad\qquad \ell = 1 \qquad \text{even } \ell$$

At PEP energies this effect can be neglected, since both even and odd states will be present and since often a neutral B will be produced e.g. together with

a charged $\bar{B}$; in such a case the particles are not identical after a mixing. In the standard model, we expect that the $B\bar{B}$ mixing violates CP symmetry. For semileptonic decays, the following ratios of rates are of interest:

(1) $\frac{N^+ - N^-}{N^+ + N^-} \neq 0$ indicates CP violation

(2) $\frac{N^{++} + N^{--}}{N^{+-}} \neq 0$ indicates mixing

(3) $\frac{N^{++} - N^{--}}{N^{++} + N^{--}} \neq 0$ indicates both mixing and CP violation

Here N refers to lepton rates for a given lepton charge, or to the rate of dileptons in opposite jets. (1) and (3) are insensitive to backgrounds in the sense that misidentified hadrons or leptons not from B decays cannot fake a signal. Misidentification, leptons from charmed quarks produced either directly or in B decays have to be subtracted and can cause considerable systematic errors for the ratio (2), however. Nevertheless, the most significant signal for mixing will be expected from (2).

The observability of B-mixing in e^+e^- annihilation both at the $\Upsilon(4s)$ and at different PEP energies has been studied in detail by Fridman and Schwarz.[29] Summing over the various combinations of a B in one jet and a $B\bar{B}$ in the other jet, and weighting with the appropriate probabilities for $B \rightarrow \bar{B}$ transitions and the semileptonic branching fractions, one expects a rate R_m of like-sign dileptons from B's of 4×10^{-3} to 2×10^{-2}, depending on the frequency of B_s production, the assumed semileptonic branching fractions, the B meson decay and bag constants, the importance of non-spectator decays, the top mass and the value of the CP violating phase in the KM matrix.[29] At the $\Upsilon(4s)$, where only $B^0 - \bar{B}^0$ systems contribute, and where the mixing is suppressed because of the symmetry of the wavefunction, R_m should range between 2×10^{-5} and 6×10^{-4}.

Rates and backgrounds quoted in Ref. 29 refer to the canonical 1000 pb^{-1} data sample. A lepton detection efficiency of 90% (for $p > 1$ GeV/c) down to

angles of 25° with respect to the beam line is assumed, and backgrounds due to hadrons misidentified as leptons are neglected. Whereas the latter assumption is justified for lepton identification (see Fig. 9), it is questionable for muons, where punch-through and decays typically cause a 15% contamination. The efficiencies and solid-angle coverage are higher than reached with the TPC, but not untypical for a detector such as MAC. Leptons from B decays are enhanced by requiring a minimum lepton momentum of 1.5 GeV. The main results are summarized in Table IV which gives the expected number of b-events, the number of like-sign dileptons, the signal-to-background ratio for dileptons, the number of S. D. assuming that the background is known, and the number of S. D. assuming a 15% uncertainty in the background estimates. As emphasized by the authors, the signal-to-background ratio is a better performance measure than the straight number of S. D. based on a known background, given that the background cannot be directly measured, and that one has to rely to a large extent on calculated backgrounds. The last row of numbers represents an attempt to take the uncertainty in the background estimates into account. As mentioned before, the source of mixing at PEP is mainly B_s mixing, whereas the signal at the $\Upsilon(4s)$ is caused by B^0 mixing.

We find from Table IV that mixing should be observable at a level of several standard deviations at all PEP energies considered, with improvements at lower energies because of the higher event rate and reduced backgrounds. We feel that signal-to-background ratio and significance at the higher energies can probably be improved somewhat by applying more sophisticated, energy-dependent cuts. This is supported by a simulation based on the TPC detector. Lepton samples were selected by combined p and p_T cuts. For 29 GeV cms energy, an expected signal of about 3 S. D. (including the 15% uncertainty in the background) was obtained, despite the significantly smaller lepton detection efficiencies.

These results indicate that in the energy range of 20 to 30 GeV B-mixing should be observable, although not by a comfortable margin. Again, however, several other techniques offer similar sensitivities, with widely different sources

Table IV.

	Υ(4s)	15 GeV	22 GeV	30 GeV
Number of b-events	1000 k	128 k	60 k	32 k
Number of Like-Sign Dileptons	99	238	188	120
Signal/Background	0.4	2.4	0.8	0.4
Number of S.D.	5	13	9	6
Number of S.D., Assuming $\Delta Bg/Bg = 15\%$	3	10	5	3

of systematic uncertainties. Requiring a coincidence of a lepton and a same-sign kaon in each jet results in a low-statistics sample with reduced backgrounds.[29] Charged kaons can be used to tell if a jet contains a B or a $\bar{B}$; jets with a fast ($y > 1.5$) negative kaon e.g. contain dominantly B's. Since the efficiency of such a tag is about twice the efficiency of a lepton tag, the statistics can be considerably enhanced. A more indirect, but completely independent method to measure mixing has been proposed by Bigi[30]; for leptons from B decays, a significant amount of mixing will reduce the forward-backward asymmetry due to electroweak interference as compared to standard predictions.

The situation looks worse as far as evidence for CP violation in $B\bar{B}$ mixing is concerned. The expected asymmetry among like-sign dileptons is of the order 10^{-2}-10^{-3}, clearly undetectable given a sample of a few hundred dileptons (see Table IV). Similarly, detecting the expected 10^{-3}-10^{-4} asymmetry in inclusive lepton rates would require an increase of the data sample by two orders of

magnitude. The situation is less hopeless as far as CP asymmetries in on-shell B decays are concerned.[8] The main idea is that there are certain final states f into which both B^0 and $\bar{B}^0$ can decay – possibly after a multistep reaction; candidates for such final states are e.g. $\psi K_s, K_s + \pi$'s or $D\bar{D}K_s + \pi$'s. Mixing is invoked to provide interference of the two amplitudes exposing a possible CP violation; however, CP violation in the mixing itself is not required. One can define a CP asymmetry in $e^+e^- \rightarrow B\bar{B} + X$,

$$A = (\sigma(l^+Xf) - \sigma(l^-Xf))/(\sigma(l^+Xf) + \sigma(l^-Xf))$$

observed by detecting a lepton in one jet and the state f in the opposite jet. Asymmetries up to 30% are predicted; although the effect is probably not measureable given the small numbers of fully reconstructed decays, one comes close to the required sensitivity. In this case, studying partially reconstructed decays may provide a large enough sample to see first evidence for CP violation in B decays; the caveat is that predictions for semi-inclusive channels are extremely uncertain and model-dependent.[8]

II.4 CONCLUSION

The B system is certainly one of the more interesting topics in particle physics, equal in importance to the neutral kaon system, and offers a variety of possibilities to test and advance our knowledge of both weak and strong interactions, and to test unification schemes. Talking about the possible physics output from a high-luminosity PEP, one also has to be aware that due to the large mass and tremendous number of decay modes, exploring the physics of b quarks poses a substantial experimental challenge. Integrated luminosities of 1000 pb^{-1} and 30000 b-events sound very impressive, but those numbers should be compared with the number of K^0's "used up" in the successful study of the kaon system. A similar study of the B-system will require the combined efforts of several experimental (and theoretical) groups. In this sense, it should also be clear that

PEP will not be competing with the Cornell and DESY machines running on the $\Upsilon(4s)$ – in many cases the measurements and the physics involved are rather orthogonal and provide independent tests of the underlying dynamics.

Among the more predictable measurements to come out of a high luminosity PEP are:

1. A measurement of the average B lifetime with a precision of about 0.05 ps and a similar systematic error. The lifetime can be measured by several methods with widely different systematics, enabling checks of systematic effects.

2. Results on the lifetime difference between charged and neutral B's will most likely be phrased in terms of an upper limit in the neighborhood of 0.5 ps (90% CL), unless the difference is much larger that predicted. Again, the measurement is carried out using several independent methods, the combination of which may allow more detailed statements.

3. A few more reconstructed B^0's and $B^{\pm}$, possibly a measurement of B_s and B baryon masses.

4. A measurement or at least interesting limits on the $b \rightarrow u$ matrix element via the $B \rightarrow \tau\nu$ decay.

5. A measurement of the mixing in the B_s system at a level of several standard deviations, assuming the central values of present predictions are correct.

In a first round of 1000 pb^{-1}, a measurement of the CP violation in the B system seems unlikely, although measurements of some exclusive and semiexclusive decay channels may come close to the required sensitivity.

Besides the topics discussed explicitely, there are of course many other interesting measurements, such as improved limits on flavor changing neutral currents, precise measurements of the electroweak asymmetry for b quarks, etc. As a byproduct, the combination of vertex detector and good particle identification will allow measurements of $D^{\pm}$, D^0, and F lifetimes with errors of 0.03-0.05 ps.

It is beyond the scope of this report to try to predict the unpredictable, but obviously a sample of 10000 to 20000 tagged B's detected in a state-of-the-art vertex detector is a good place to look for surprises.

REFERENCES

1. M. E. Nelson *et al.*, Phys. Rev. Lett. 50, 1542 (1983).
2. E. Fernandez *et al.*, Phys. Rev. Lett. 51, 1022 (1983).
3. N. S. Lockyer *et al.*, Phys. Rev. Lett. 51, 1316 (1983).
4. M. Kobayashi, T. Maskawa, Prog. Theor. Phys. (Japan) 49, 652 (1975).
5. For a review see e.g. M. Sakuda, Conf. on High Energy e^+e^- Interactions, Vanderbilt (1984), AIP Conf. Proc. No. 121, 283 (1984).
6. R. R. Horgan, P. V. Landshoff, D. M. Scott, Phys. Lett. 110B, 493 (1982); S. J. Brodsky *et al.*, priv. comm.
7. J. Hagelin, Nucl. Phys. B193, 123 (1981); I. I. Bigi, A. I. Sanda, Nucl. Phys. B193, 85 (1981).
8. I. I. Bigi, A. I. Sanda, Phys. Rev. D29, 1393 (1984).
9. L. Wolfenstein, Phys. Rev. Lett. 51, 1945 (1983).
10. For a review and further refs. see J. W. Cronin *et al.*, LBL-18402 (1984).
11. A. Soni, Phys. Rev. Lett. 53, 1407 (1984).
12. H. Aihara *et al.*, Phys. Rev. Lett. 52, 577 (1984). For more details see J. E. Huth, LBL-18341 (1984) and M. D. Shapiro, LBL-18820 (1984).
13. D. R. Nygren, Talk given at this workshop.
14. T. Sjoestrand, Comm. Phys. Comm. 27, 243 (1982); 28,229 (1983). Changes in the recent versions concern mainly baryon production mechanisms, decays of heavy hadrons and the treatment of low-mass parton systems.
15. Particle Data Group, C. G. Wohl *et al.*, Rev. Mod. Phys. 56, S1 (1984).
16. M. S. Alam *et al.*, Phys. Rev. Lett. 49, 357 (1982); Phys. Rev. Lett. 53, 24 (1984); Phys. Rev. Lett. 51, 1143 (1983); A. Brody *et al.*, Phys. Rev. Lett. 48,

1070 (1982).

17. J. Green *et al.*, Phys. Rev. Lett. 51, 347 (1983).

18. P. C. Rowson *et al.*, SLAC-PUB-3557 (1985).

19. M. Althoff *et al.*, Phys. Lett. 149B, 524 (1984).

20. M. Althoff *et al.*, Phys. Lett. 135B, 243 (1984).

21. M. Sakuda *et al.*, CALT-68-1164 (1984).

22. S. Stone, Proc. Int. Symp. on Lepton and Photon Interactions, Cornell 1983, 203.

23. S. Behrends *et al.*, Phys. Rev. Lett. 50, 881 (1983).

24. R. Giles *et al.*, Phys. Rev. D30, 2279 (1984).

25. A. Chen *et al.*, Phys. Rev. Lett. 52, 1084 (1984).

26. F. J. Gilman, Rev. Mod. Phys. 56, S296 (1984).

27. A. Ali and C. Jarlskog, Phys. Lett. 144B, 266 (1984).

28. V. Barger *et al.*, Phys. Rev. Lett. 45, 83 (1980).

29. A. Fridman and A. Schwarz, SLAC-PUB-3595 (1984).

30. I. I. Bigi, PITHA 84/41 (1984).

31. A. Aihara *et al.*, LBL-17545 (1984); JHU 8501 (1985).

FIGURE CAPTIONS

1. a) Diagrams of amplitudes involved in $B\bar{B}$ mixing.

   b) Diagrams of B decay mechanisms.

2. a) Distribution of the dE/dx energy loss (defined as the 65% truncated mean) versus momentum for tracks with a least 80 wire-hits (from the TPC detector).

   b) dE/dx separation between species as a function of momentum.

3. Momentum spectrum of D*'s from B decays at rest.

   a) Points represent data from CLEO. The full line shows the charmed-quark spectrum expected for semileptonic decays governed by a V-A matrix element; the dashed line is a prediction by early versions of the LUND model.

   b) The D* spectrum as obtained from the recent version of the LUND model.

4. As a function of center of mass energy:

   a) Average $\beta\gamma$ for B hadrons in b-jets.

   b) Average impact parameter of hadrons with at least 1 GeV/c momentum.

   c) Average number of tracks with at least 1 GeV/c momentum per B decay.

   d) Probability that a track with more than 1 GeV/c momentum is emitted into the hemisphere of the event opposite to the decaying B.

5. a) b-event with tracks from the B and $\bar{B}$ decay and from the primary vertex.

   b) Number of charged particles produced in addition to particles from a given B (i.e., number of tracks associated with the $\bar{B}$ decay and with the primary vertex).

6. Distribution in rapidity with respect to the sphericity axis, for all charged particles (full line) and for decay products of the B hadrons moving in the +y direction (dashed line).

7. Mean number of charged particles not associated with the decay of a given B hadron found within the rapidity region populated by decay products of the B.

8. Schematic representation of b tagging methods.

9. Momentum distribution of prompt-electron candidates, as measured by the TPC detector. The low p_T sample is charm-enriched; the high p_T sample if B-enriched. Dashed line: background due to photon conversion. Dotted line: misidentified hadrons.

10. Sphericity distribution for $c\bar{c}$ events (a) [20] and $b\bar{b}$ events (b) [21] compared to the distribution for average events (full lines).

11. Average impact parameter of B decay products as a function of particle momentum (full line). Also shown: typical impact parameter resolution (dotted line) and fraction of tracks with momentum greater than a given momentum (dashed line).

12. a) Separation D of the vertices V_1, V_2 reconstructed using the two jets in an event. D is the projection of the distance between V_1 and V_2 onto the event axis; the sign is defined such that a finite lifetime of the particle creating the jet results in a positive D. The estimate for the primary vertex V_3 is defined as the point of maximum beam intensity along the line joining V_1 and V_2.

    b) Distribution in D. Full line: $u\bar{u}$, $d\bar{d}$ and $s\bar{s}$ events. Points: $b\bar{b}$ events. The relative normalization of the curves is arbitrary.

    c) Influence of the vertex detector resolution (for $u\bar{u}$, $d\bar{d}$ and $s\bar{s}$ events). Dotted line: configuration as described in Section II.2. Dashed line: vertex detector and beam pipe at 2.5 cm radius. Full line: ideal vertex detector

with infinite resolution, showing that the removal of long-lived particles such as K^0 poses no problems.

d) as b), but for $c\bar{c}$ events.

13. Reconstructed invariant mass of the decay vertex best separated from the beam line, after requiring a minimum D of 0.5 mm. Full line: $c\bar{c}$ events (plus the few $u\bar{u}$, $d\bar{d}$ and $s\bar{s}$ events surviving the cut in D). Points: $b\bar{b}$ events.

14. Maximum b-event selection efficiencies obtained for a given sample purity, using combined vertex and topology tags, for vertex detectors providing typical resolutions of 100 μ/p and 50 μ/p. The first value corresponds to a vertex detector and beam pipe at 5 cm radius, the second to 2.5 cm radius.

15. a) A 5-vertex $b\bar{b}$ event indicating the possibilities of confusion in the vertex finding.

    b)–d) Simulated $b\bar{b}$ events as measured using the vertex detector. The dashed line indicates the direction of the jet axis. The dashed circle corresponds to the primary vertex, the full circles to charm and bottom decay vertices. The radius of the circles is 2000 μ.

16. Schematic representation of methods to measure B lifetimes. The ratio of charged and neutral B's contributing to the signal differs for methods based on lepton and hadron impact parameters.

17. Distribution in impact parameter for leptons with at least 1.5 GeV total momentum and 1 GeV transverse momentum, and with an impact parameter error (including the beam size) of less than 100 μ. Dashed line: fit using one variable B lifetime and a fixed background due to leptons from charm. Full line: fit using two variable B lifetimes, assuming that the corresponding leptonic branching fractions scale with the lifetimes.

18. Contours corresponding to 1, 2, and 3 standard deviations of the two-lifetime fit shown in the previous figure.

19. Ratio of lifetimes measured using semileptonic and hadronic decays, as a function of the $B^0/B^{\pm}$ lifetime ratio.

20. Relative frequency of charged, neutral and strange B's in jets with a charge sum for particles with y > 0.5 of 0, ± 1 and $> \pm 2$. About 35% of all events fall into the charge-0 category, 47% have charge ± 1 and 18% have charges of 2 or more.

21. Diagrams for B decay modes.

22. Relative frequency of charged, neutral and strange B's in b-jets containing a $D^{*\pm}$ with rapidity y > 0.5.

23. D^* signal in the 1982/83 data from the TPC detector; shown is the distribution of the $D^* - D$ mass difference for several decay modes of the D.

24. Preliminary D^0 signal in a 20 pb^{-1} sample of '85 TPC data.

25. As Fig. 22, but requiring a D^0 or F tag at y > 0.5.

26. Relative frequency of charged, neutral, strange and baryonic B's in b-jets containing a proton or lambda with rapidity y > 1.

27. As a function of center of mass energy:

    a) Mass resolution for charged decay modes of B's. At threshold, the resolution is drastically improved because the B energy is known exactly.

    b) Probability to detect all decay products for charged-only decay modes of B's.

28. $B \rightarrow \tau\nu$ decay and its experimental signature.

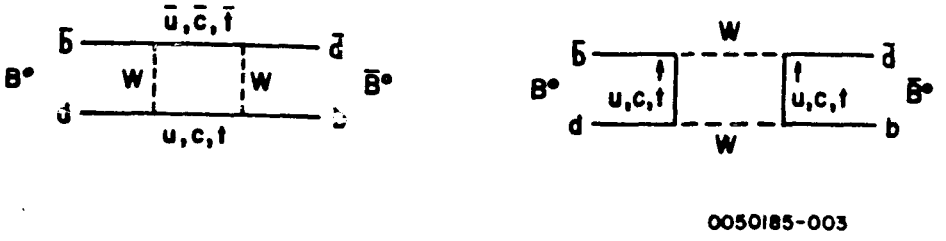
B°
b
ū, c̄, t̄
W
W
d̄
B̄°
d
u, c, t
b
W
B°
b
u, c, t
W
d̄
B̄°
d
u, c, t
b
0050185-003

Fig. 1 (a)

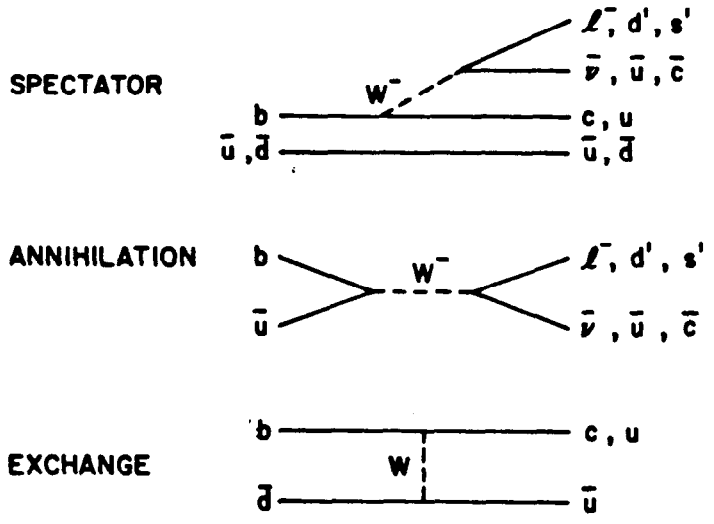
SPECTATOR
b
ū, d̄
W⁻
ℓ⁻, d', s'
ν̄, ū, c̄
c, u
ū, d̄
ANNIHILATION
b
ū
W⁻
ℓ⁻, d', s'
ν̄, ū, c̄
EXCHANGE
b
d̄
W
c, u
ū

Fig. 1 (b)

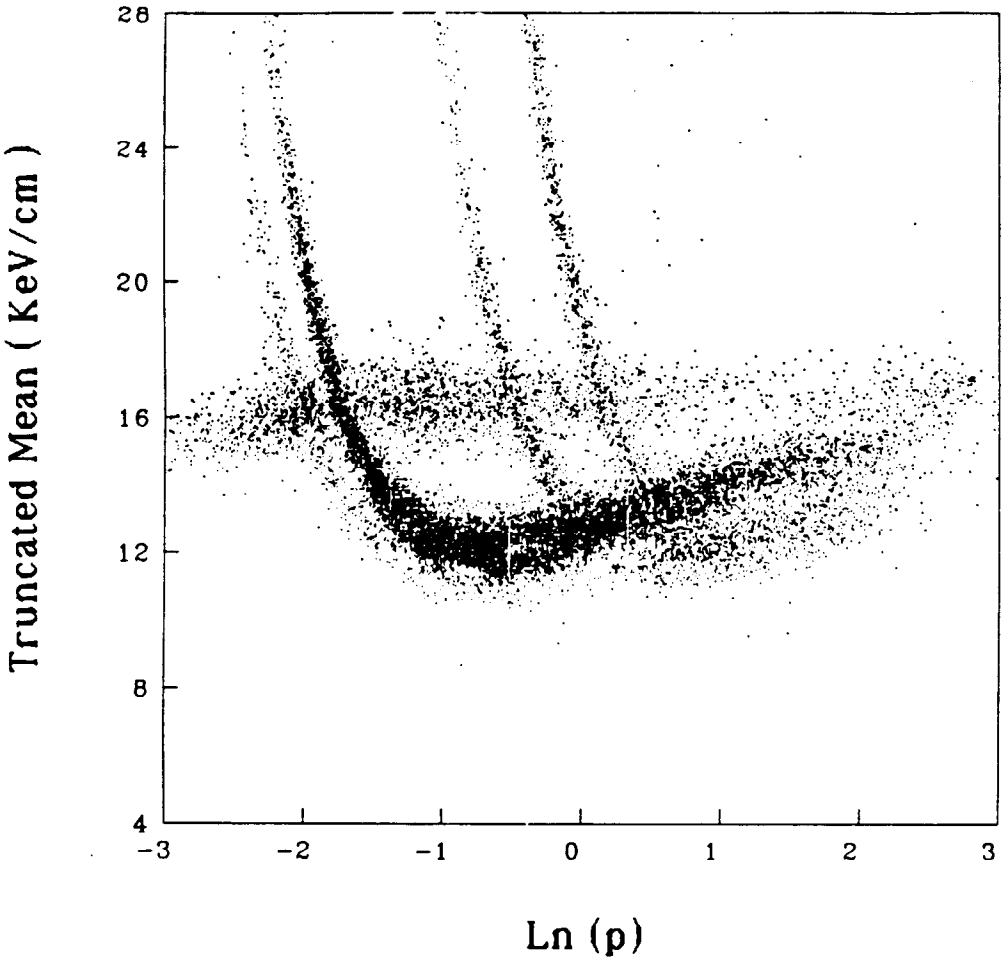

Fig. 2 (a)

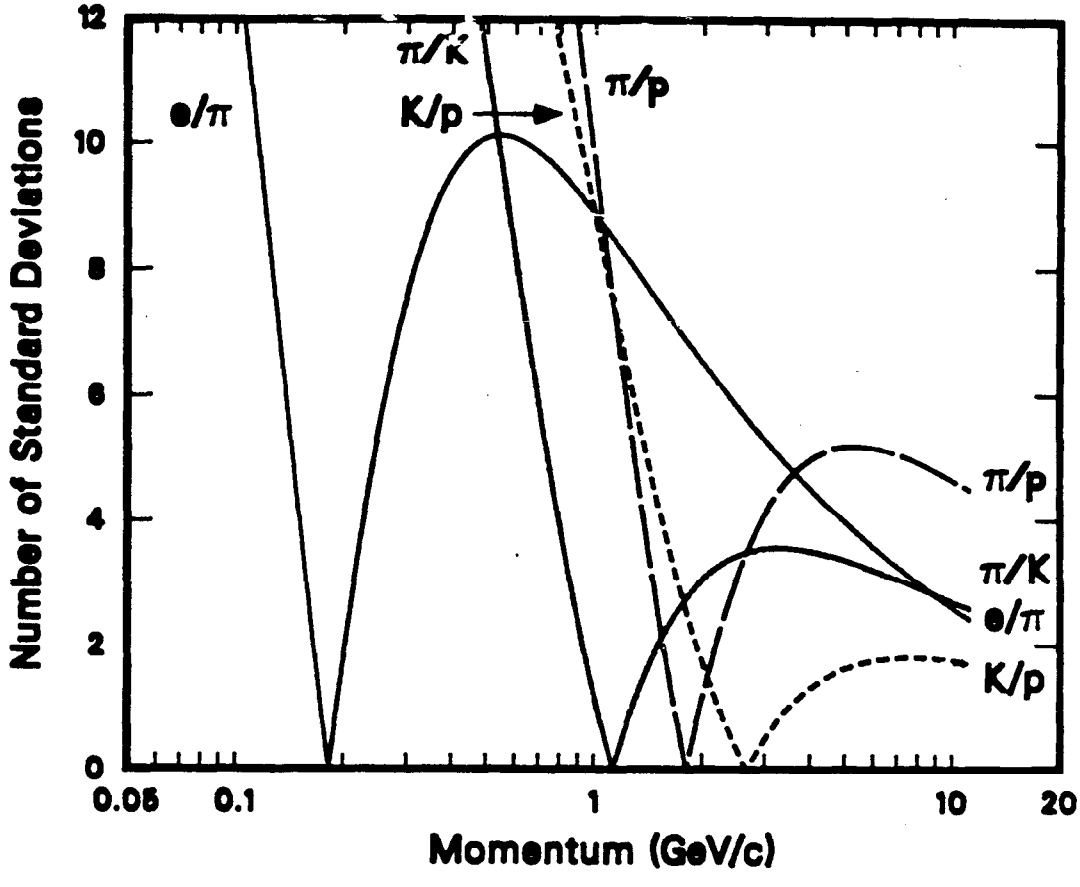
Number of Standard Deviations
Momentum (GeV/c)
e/π
π/K
K/p
π/p
π/p
π/K
e/π
K/p
0
2
4
6
8
10
12
0.05
0.1
1
10
20

Fig. 2(b)

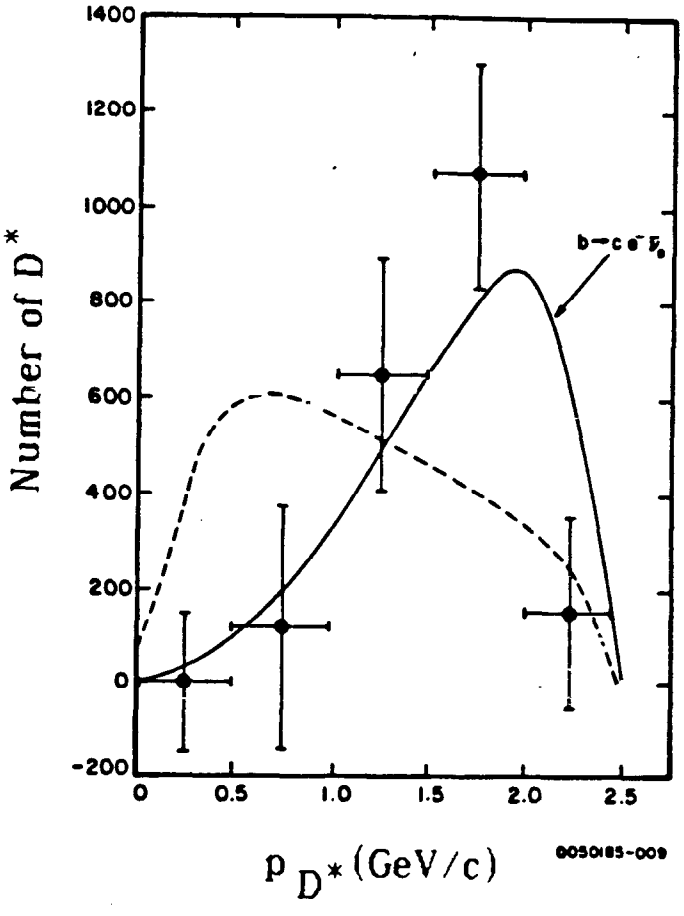
Number of D*
1400
1200
1000
800
600
400
200
0
-200
0
0.5
1.0
1.5
2.0
2.5
p D* (GeV/c)
0050185-009

Fig. 3 (a)

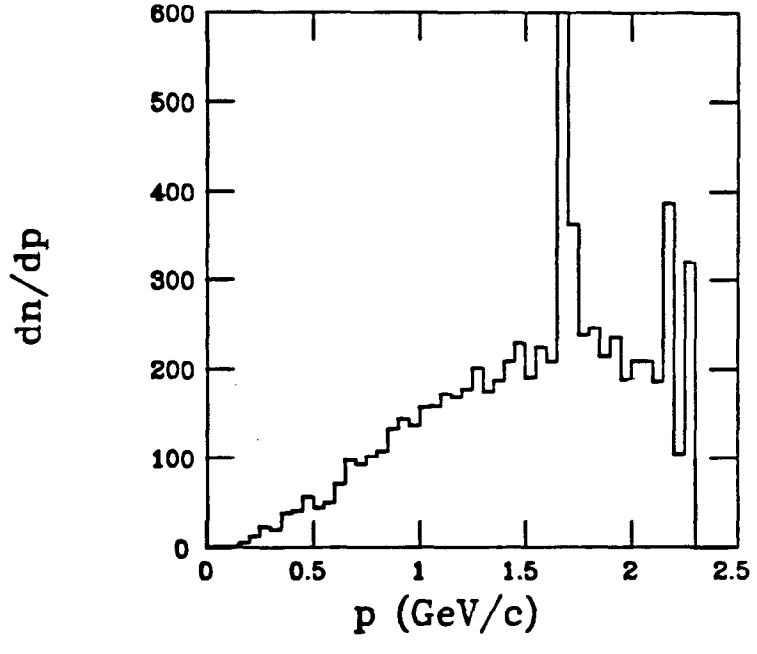
dn/dp
600
500
400
300
200
100
0
0
0.5
1
1.5
2
2.5
p (GeV/c)

Fig. 3 (b)

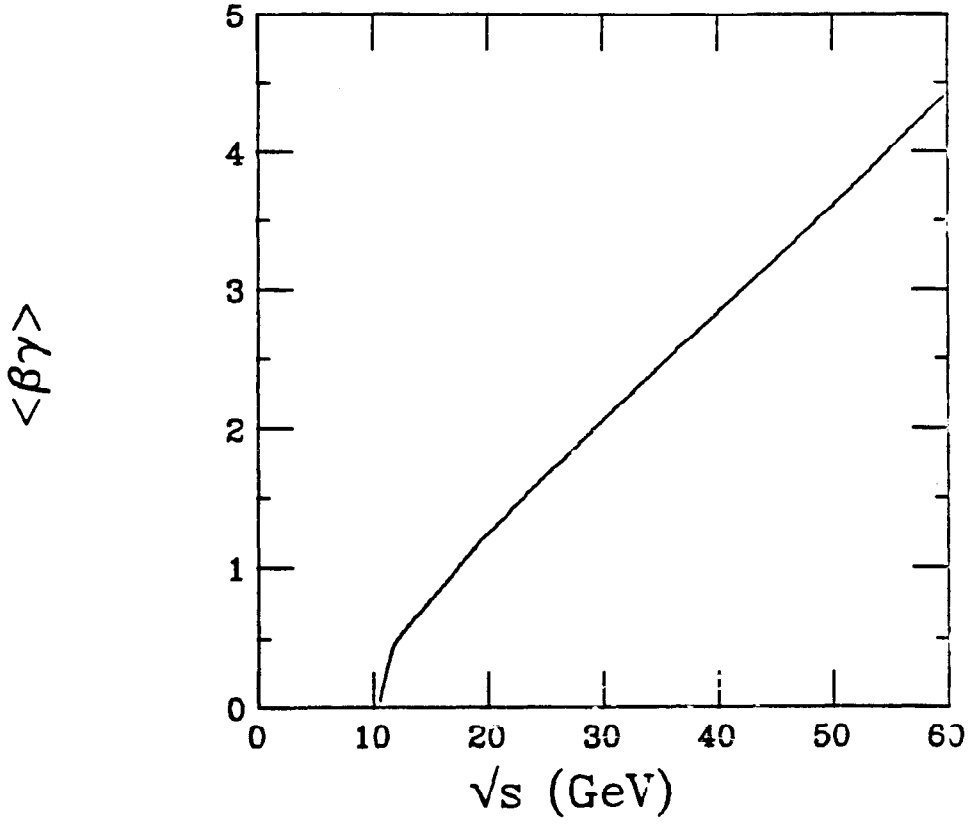
$<\beta\gamma>$
5
4
3
2
1
0
0
10
20
30
40
50
60
$\sqrt{s}$ (GeV)

Fig. 4 (a)

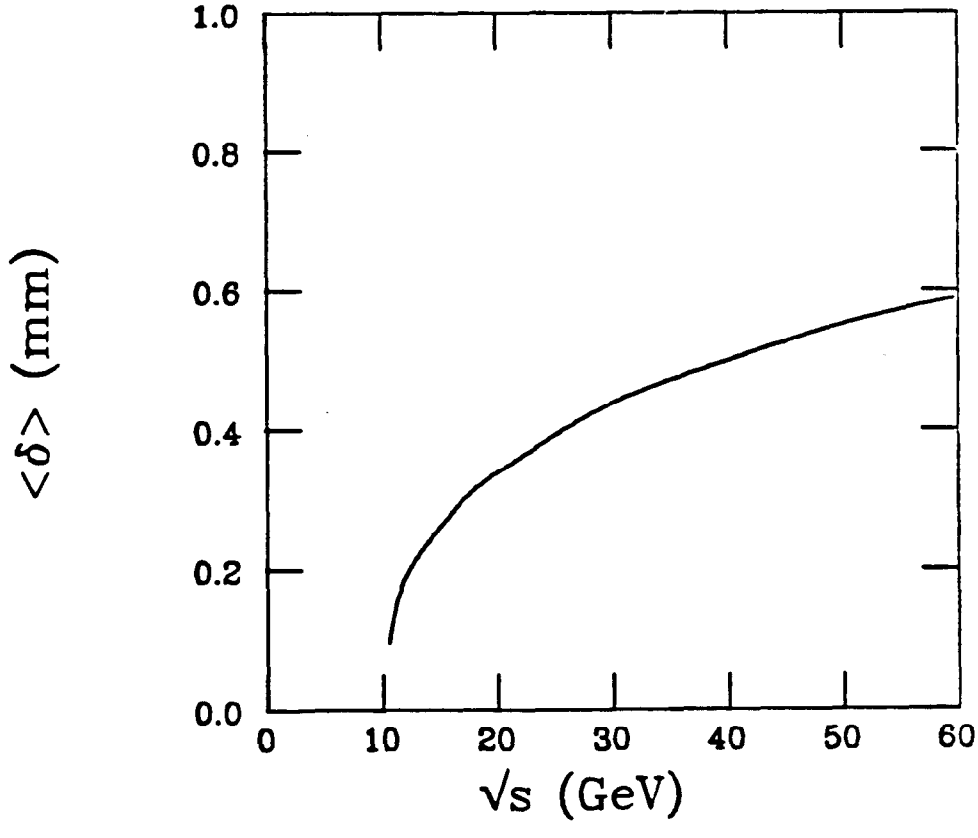
$<\delta>$ (mm)
1.0
0.8
0.6
0.4
0.2
0.0
0
10
20
30
40
50
60
$\sqrt{s}$ (GeV)

Fig. 4(b)

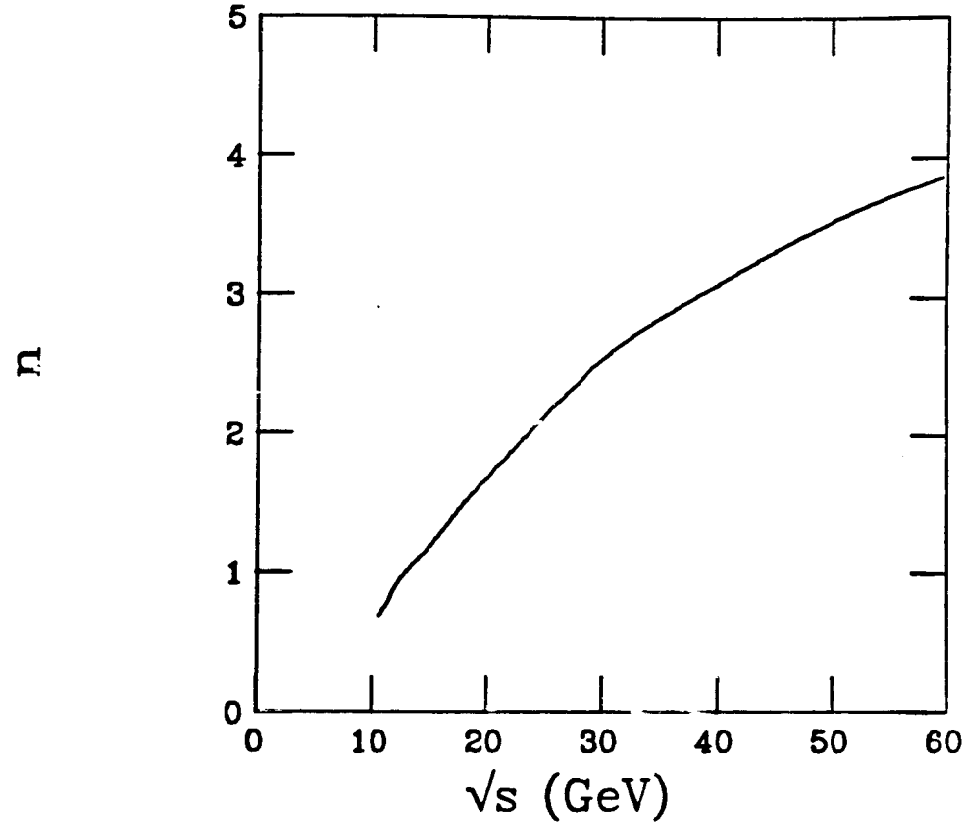
n
5
4
3
2
1
0
0
10
20
30
40
50
60
√s (GeV)

Fig. 4 (c)

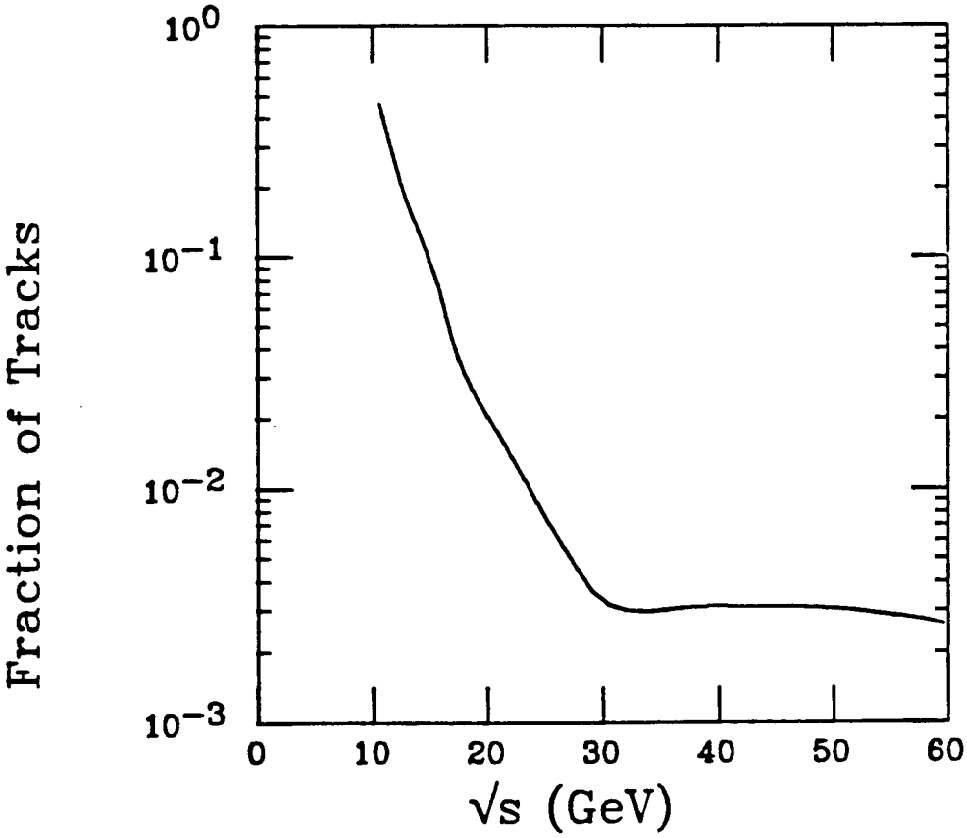
Fraction of Tracks
10^0
10^-1
10^-2
10^-3
0
10
20
30
40
50
60
√s (GeV)

Fig. 4 (d)

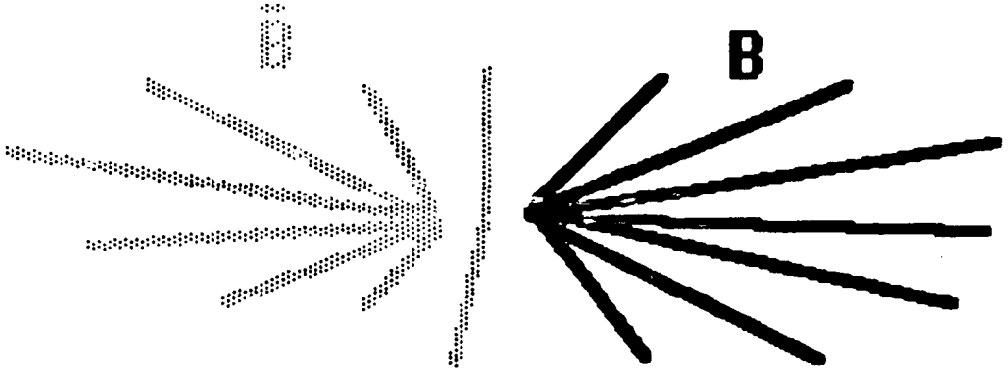

Fig. 5 (a)

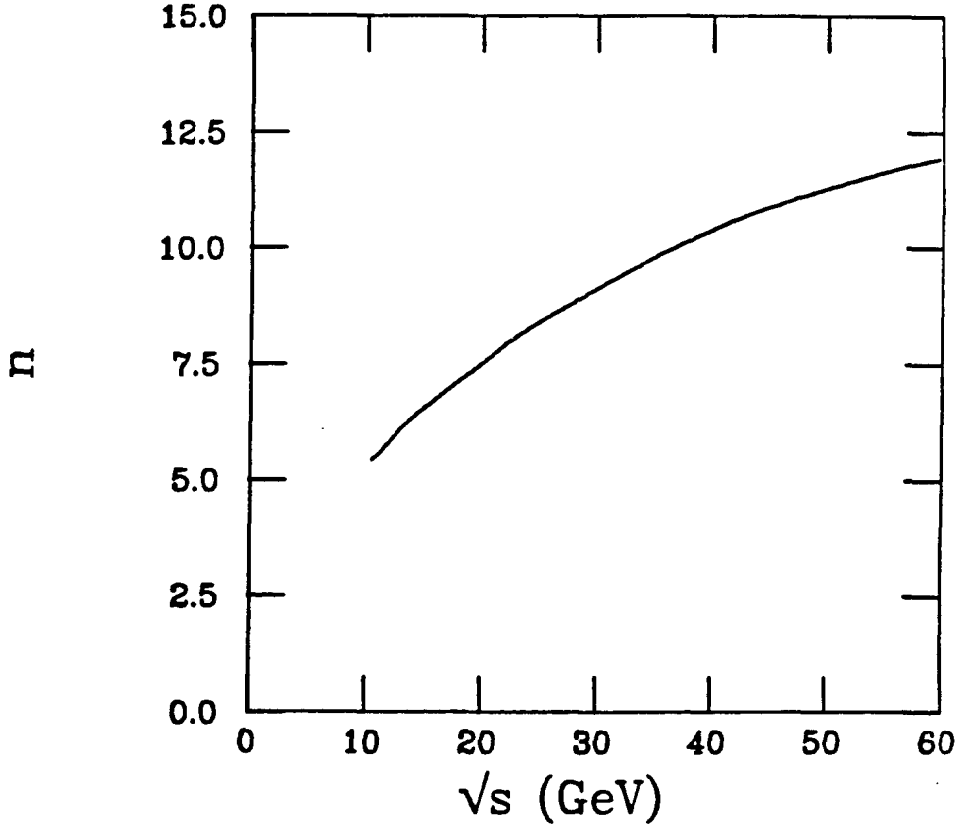

Fig. 5 (b)

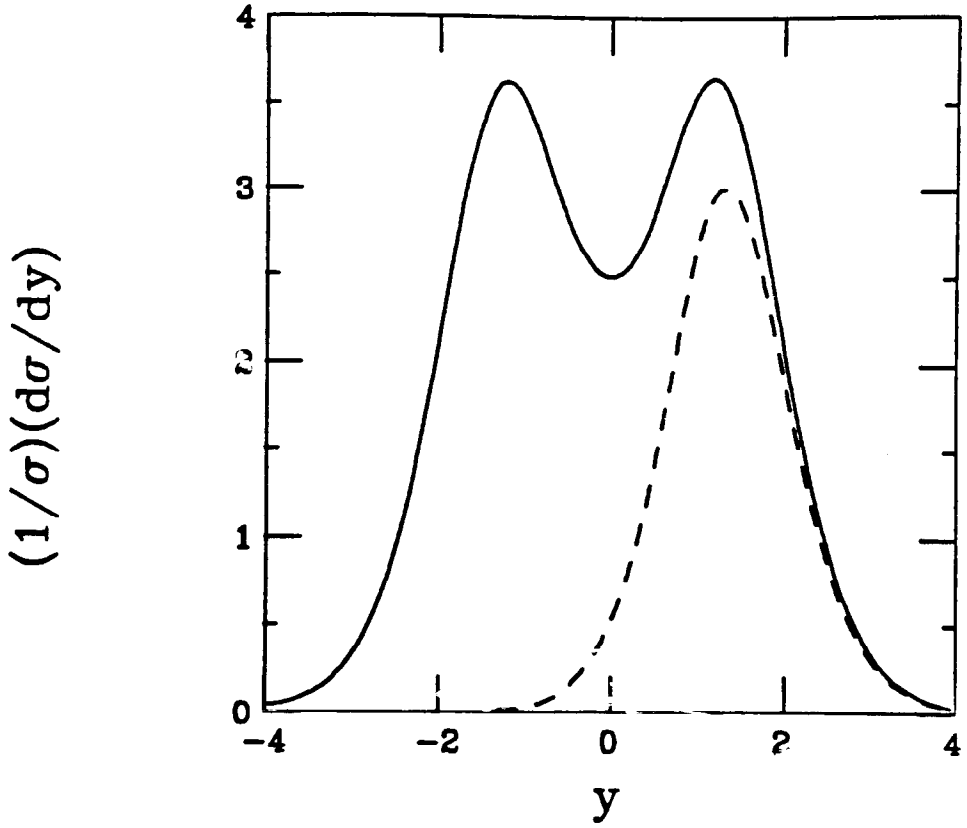

Fig. (6)

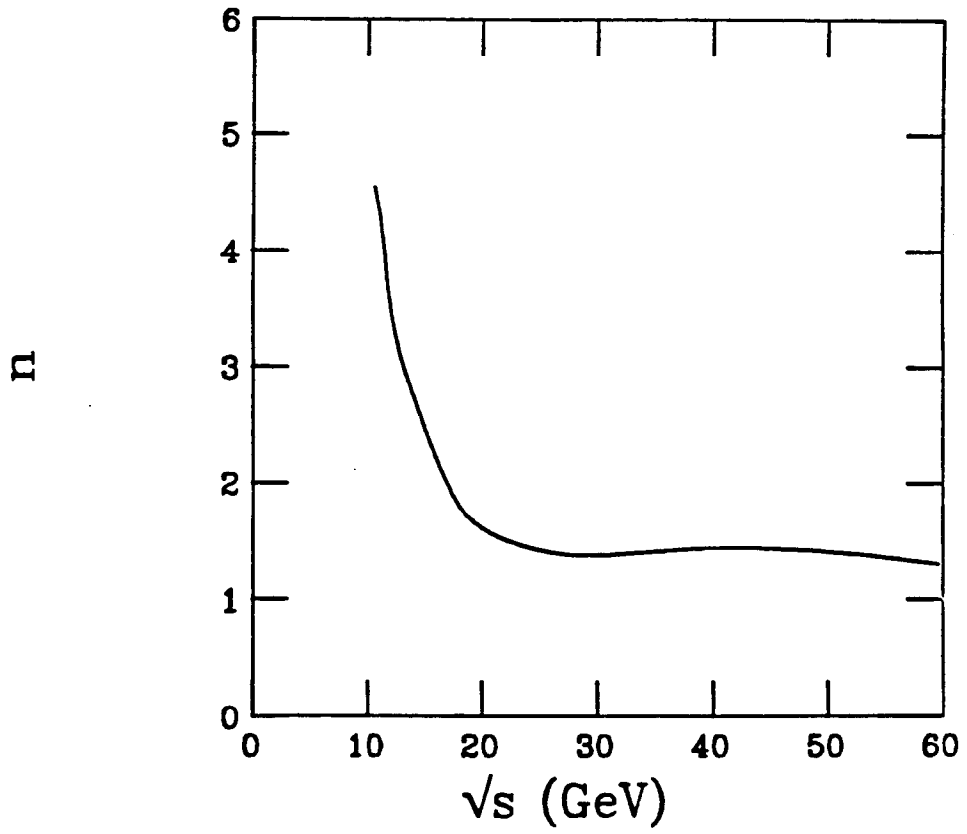

Fig. (7)

B-Tagging Methods

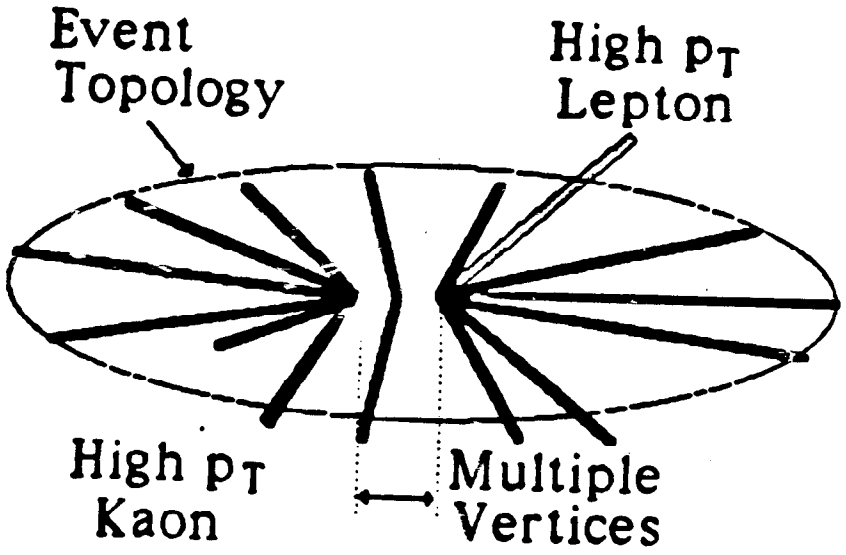

Fig. 8

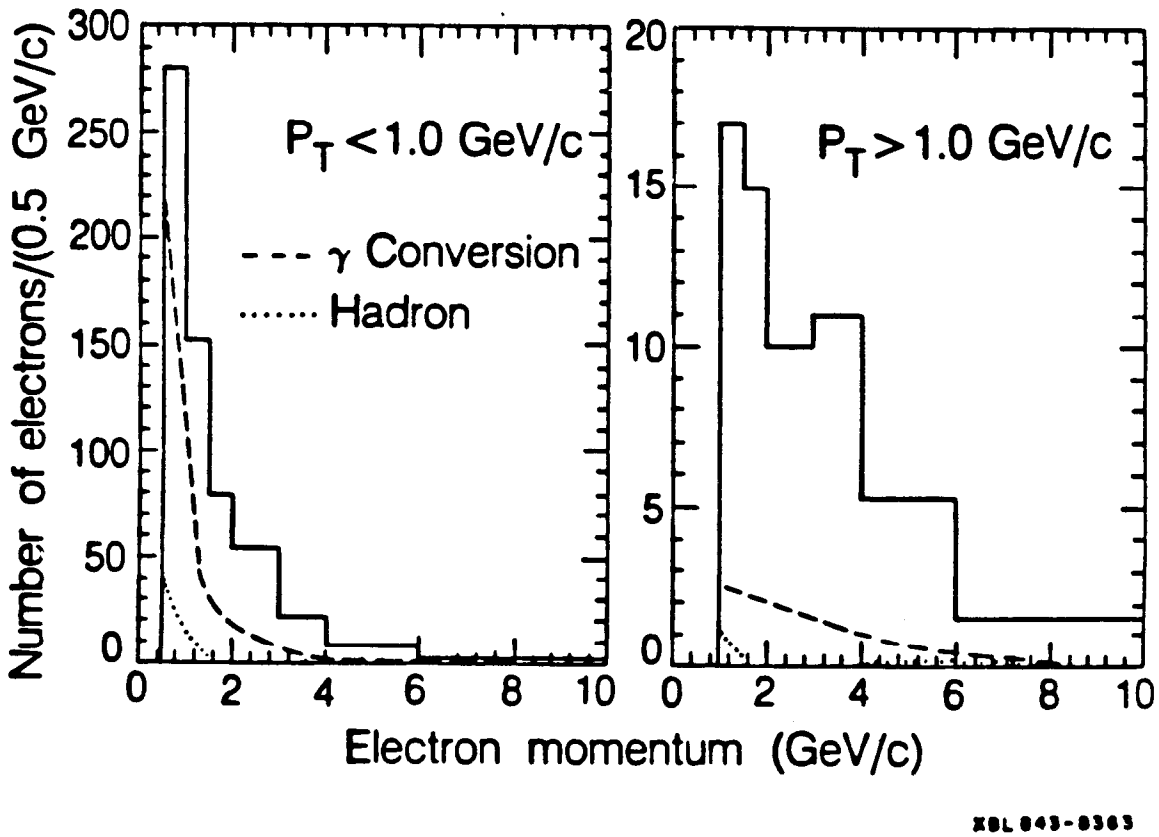

Fig. 9

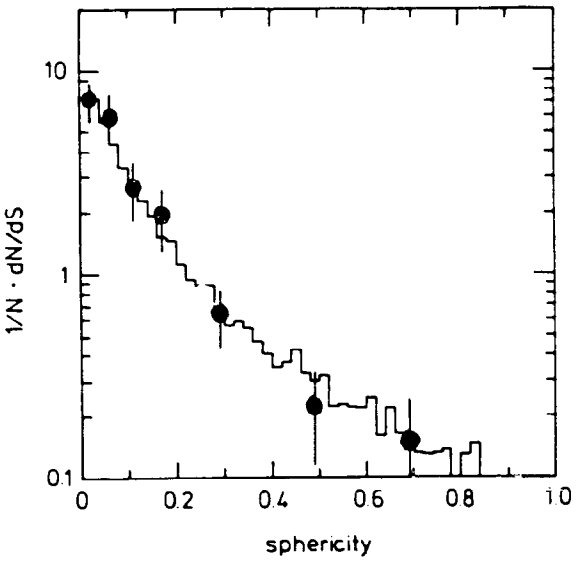

Fig. 10 (a)

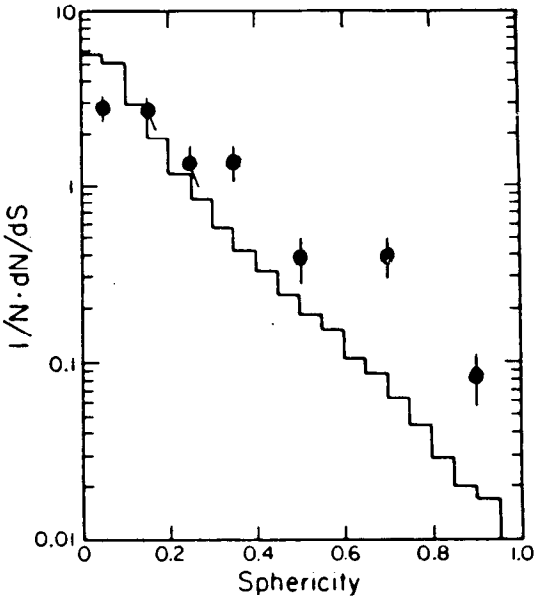

Fig. 10 (b)

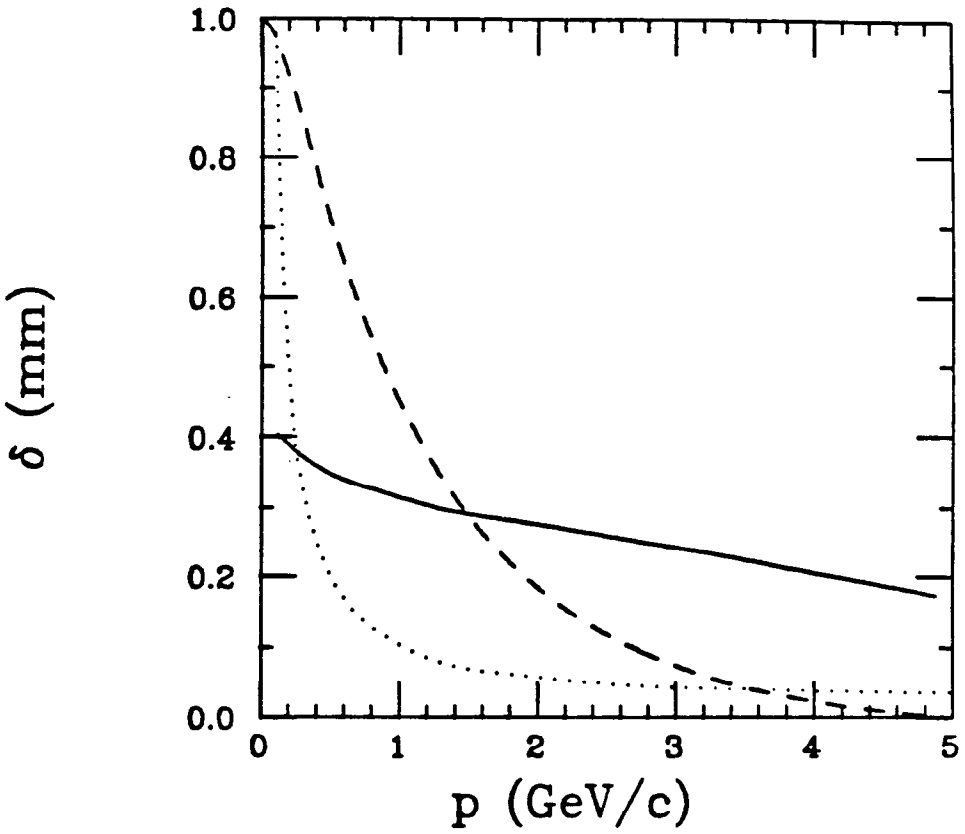

Fig. 11

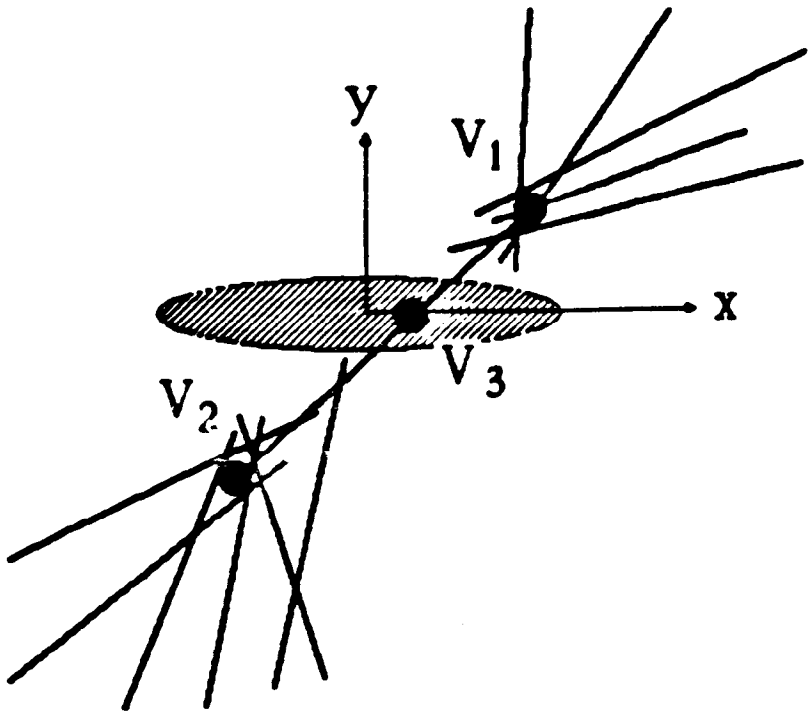

Fig. 12 (a)

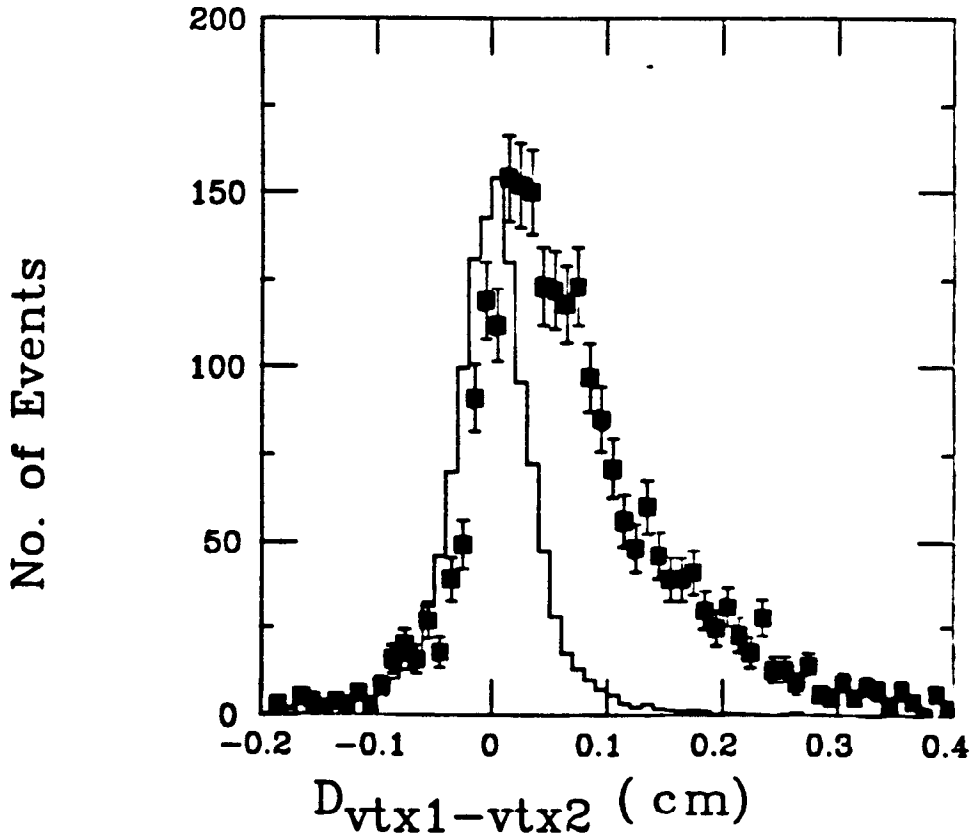

Fig. 12 (b)

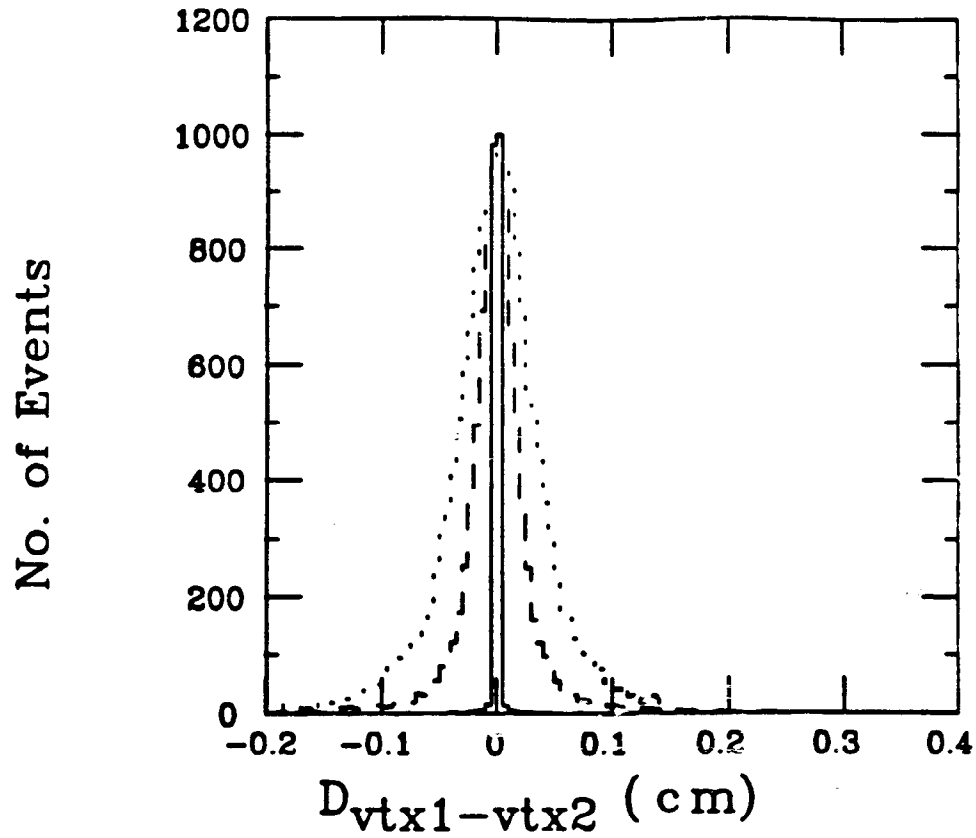

Fig. 12 (c)

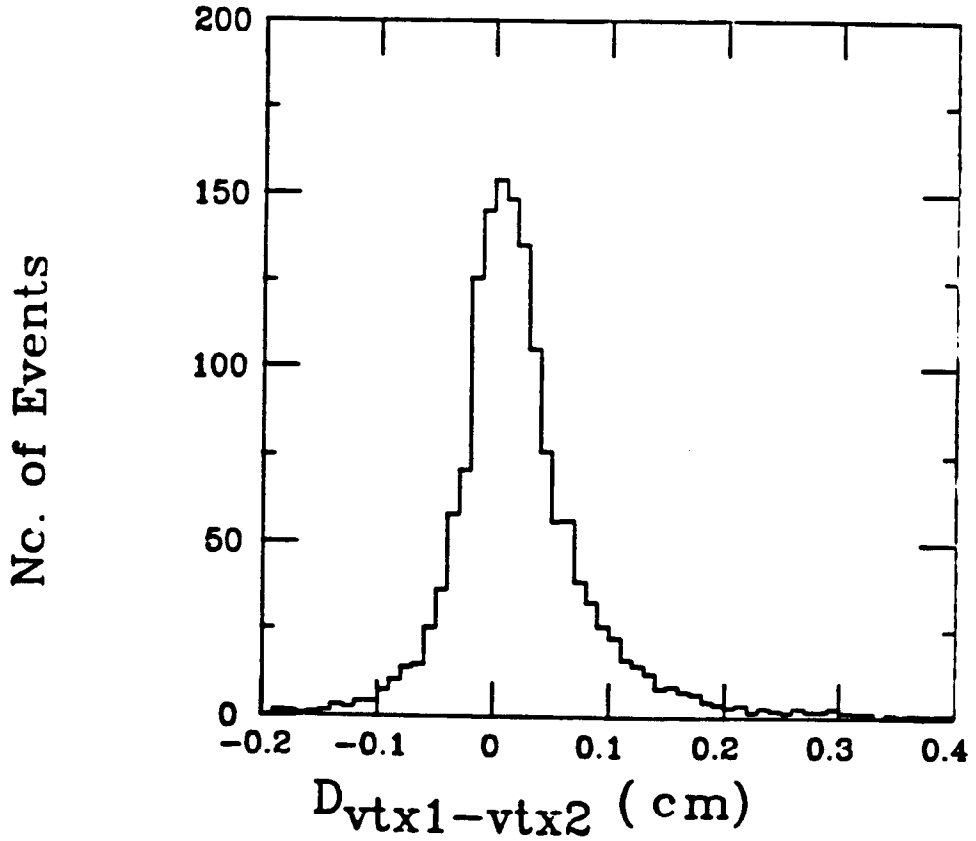

Fig. 12(d)

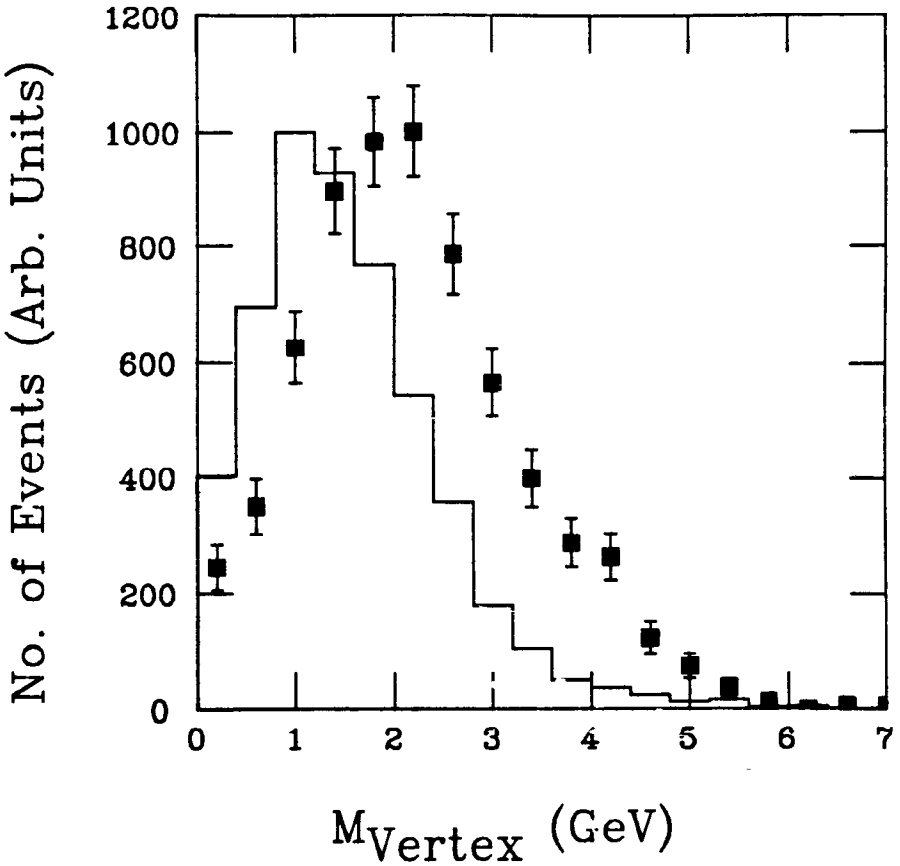
No. of Events (Arb. Units)
1200
1000
800
600
400
200
0
0
1
2
3
4
5
6
7
M_{Vertex} (GeV)

Fig. 13

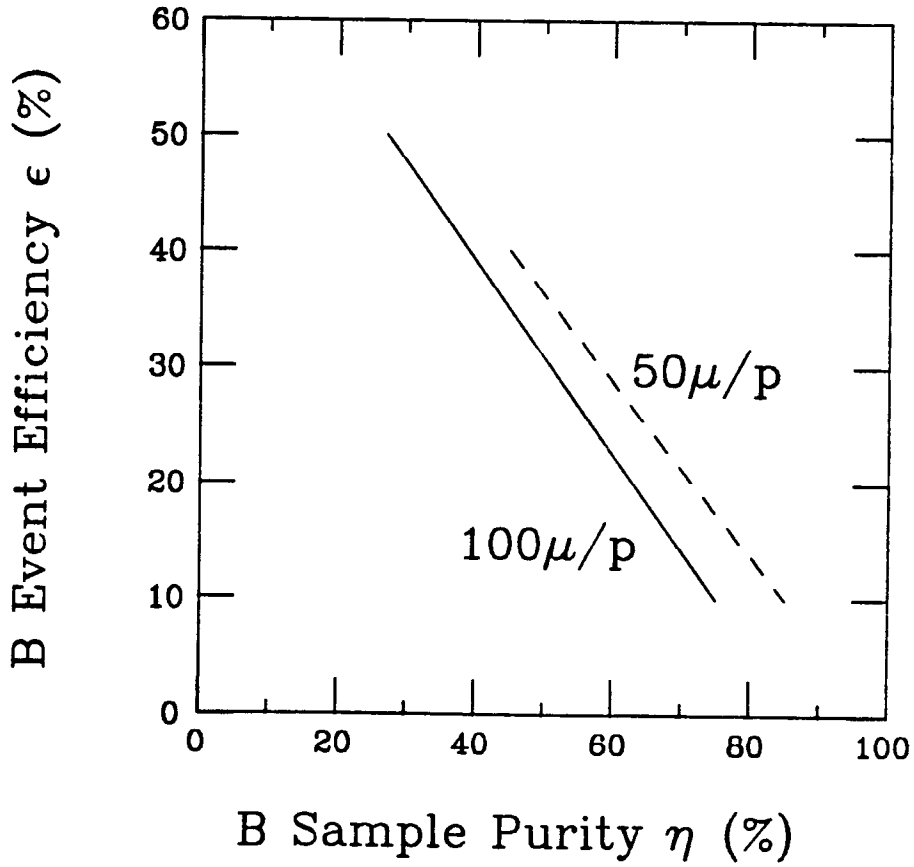
B Event Efficiency ϵ (%)
60
50
40
30
20
10
0
0
20
40
60
80
100
50μ/p
100μ/p
B Sample Purity η (%)

Fig. 14

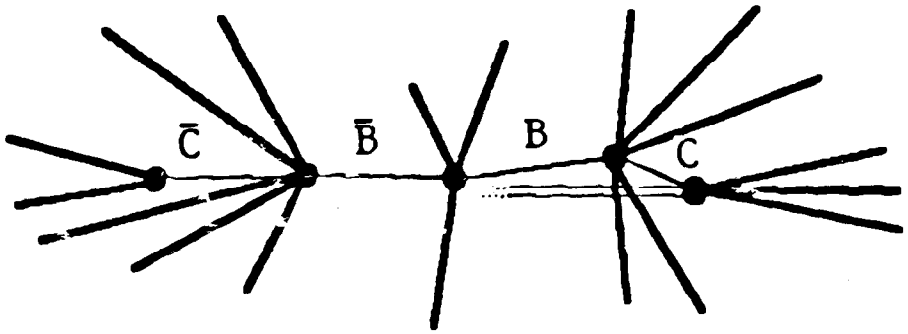

Fig. 15 (a)

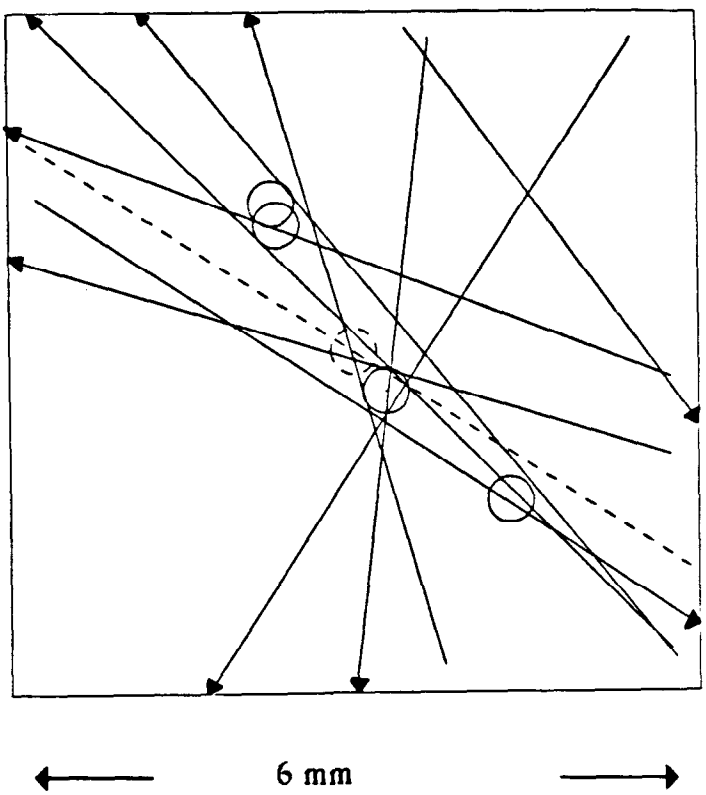

Fig. 15 (b)

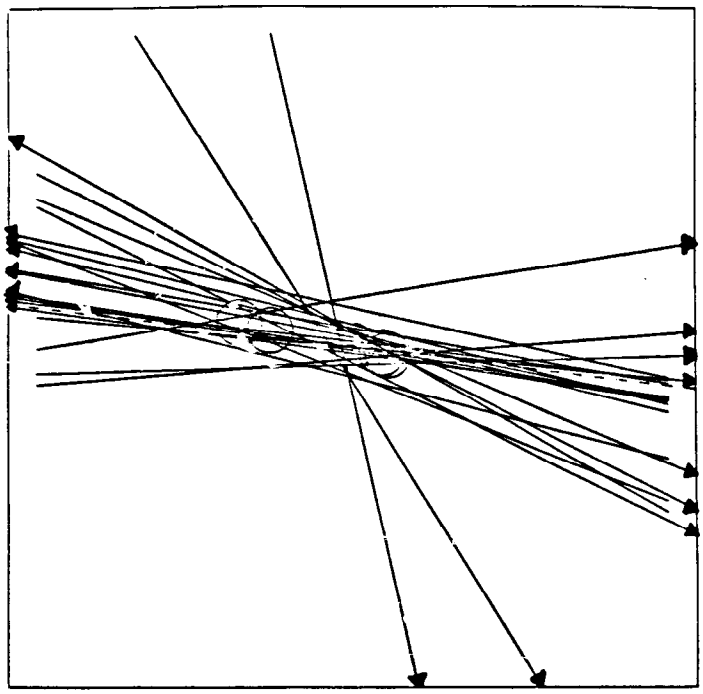

Fig. 15 (c)

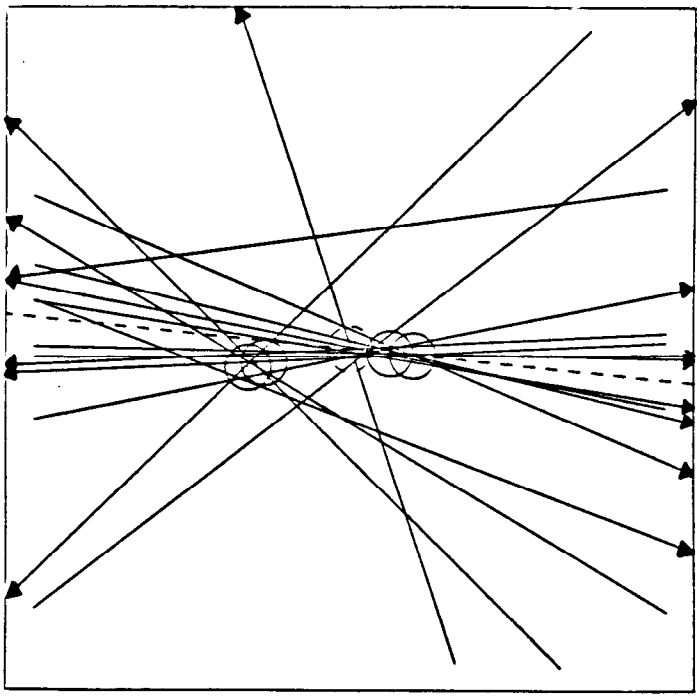

Fig. 15 (d)

Lifetime Measurement

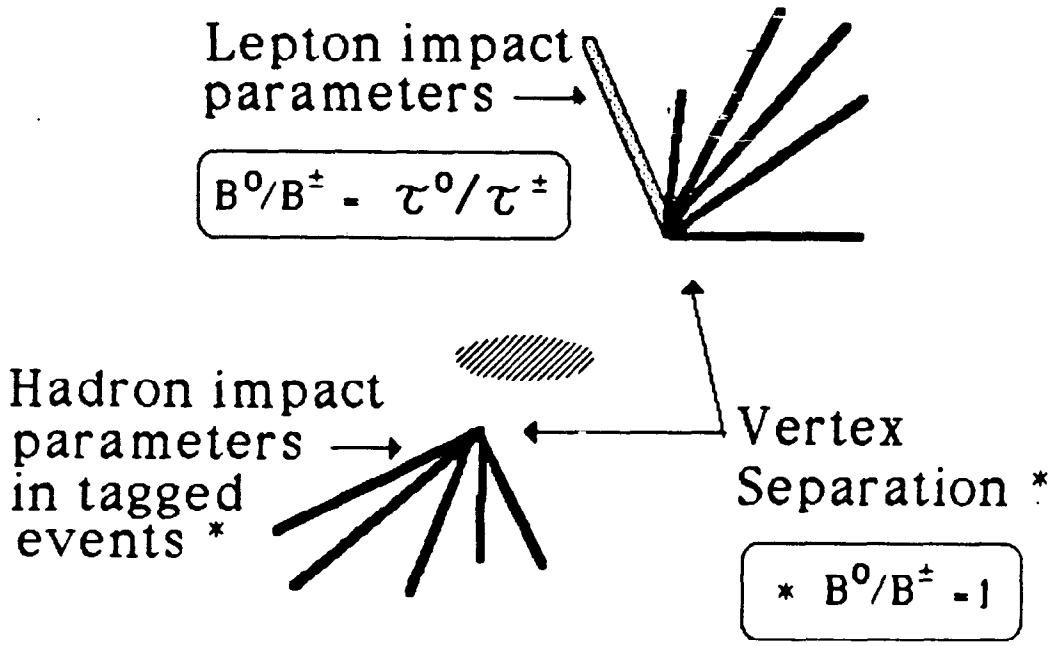

Fig. (16)

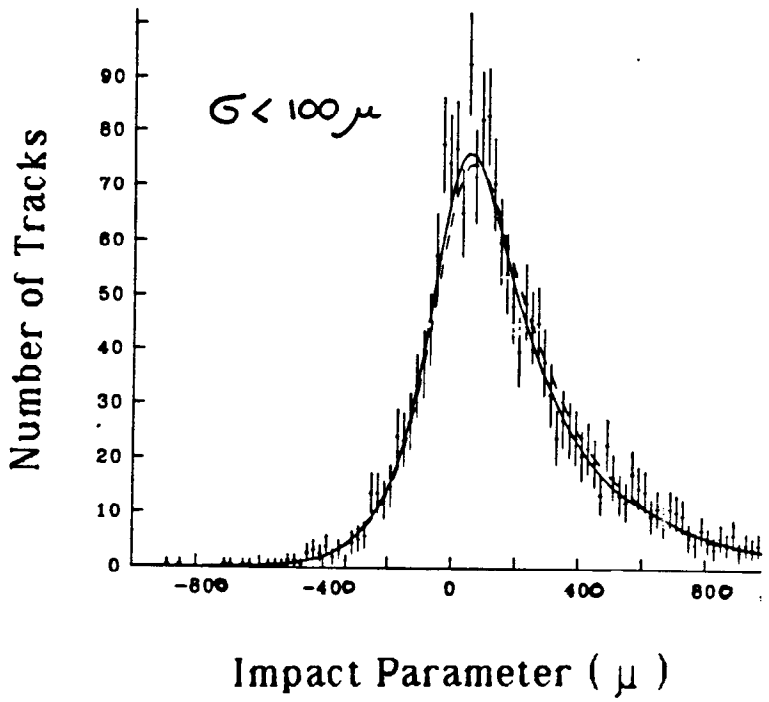
σ < 100μ
Number of Tracks
90
80
70
60
50
40
30
20
10
0
-800
-400
0
400
800
Impact Parameter (μ)

Fig. 17

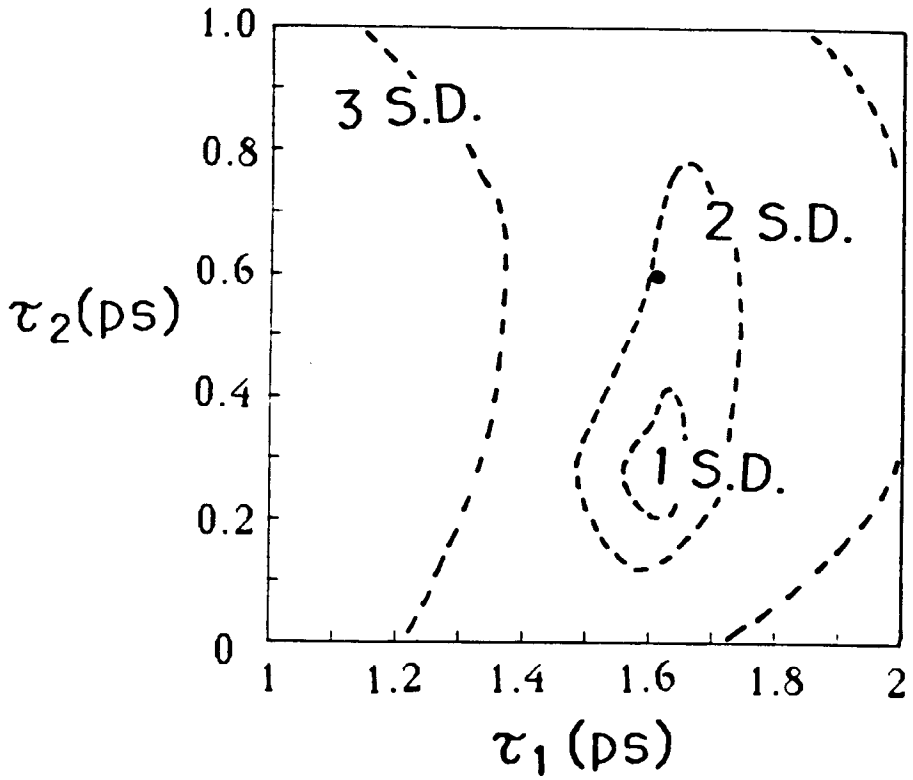
1.0
0.8
0.6
0.4
0.2
0
3 S.D.
2 S.D.
1 S.D.
τ2(ps)
1
1.2
1.4
1.6
1.8
2
τ1 (ps)

Fig. 18

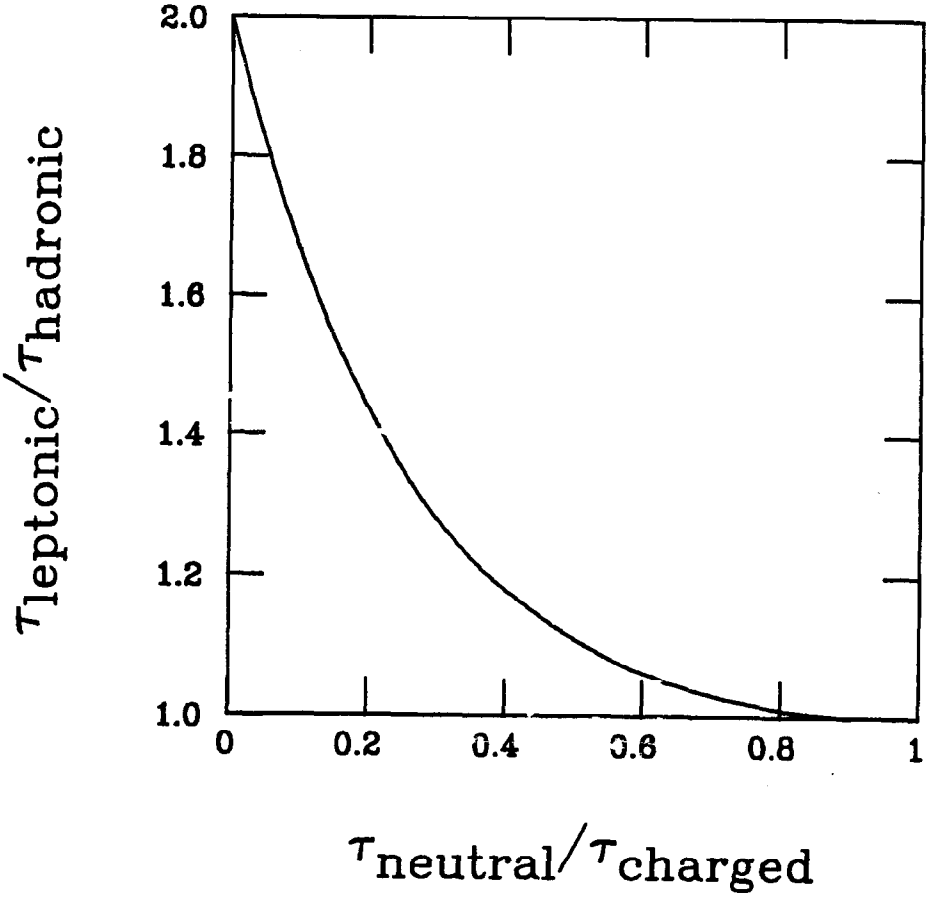
2.0
1.8
1.6
1.4
1.2
1.0
0
0.2
0.4
0.6
0.8
1
$\tau_{leptonic}/\tau_{hadronic}$
$\tau_{neutral}/\tau_{charged}$

Fig. 19

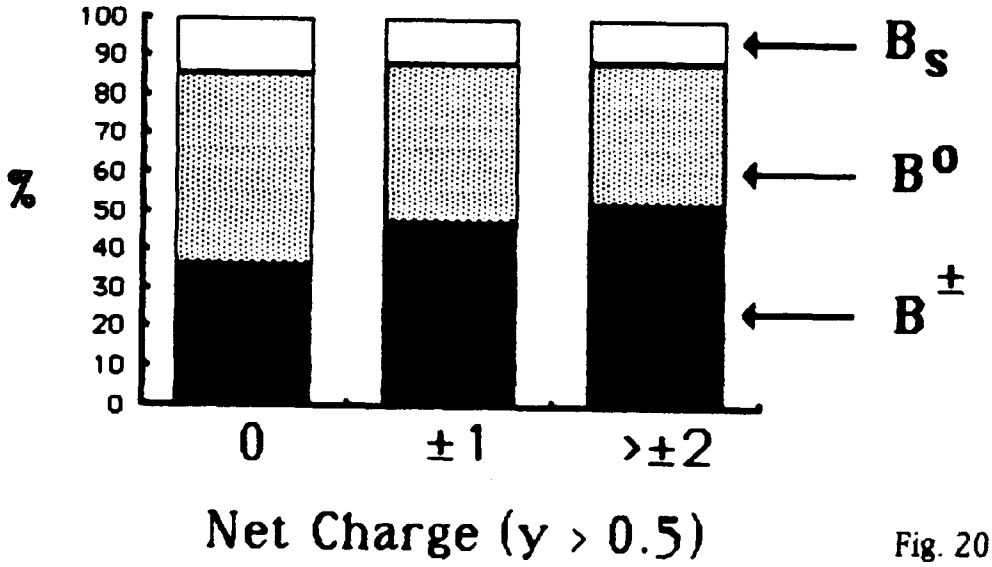
100
90
80
70
60
50
40
30
20
10
0
%
0
±1
>±2
Net Charge (y > 0.5)
B_s
B^0
$B^{\pm}$

Fig. 20

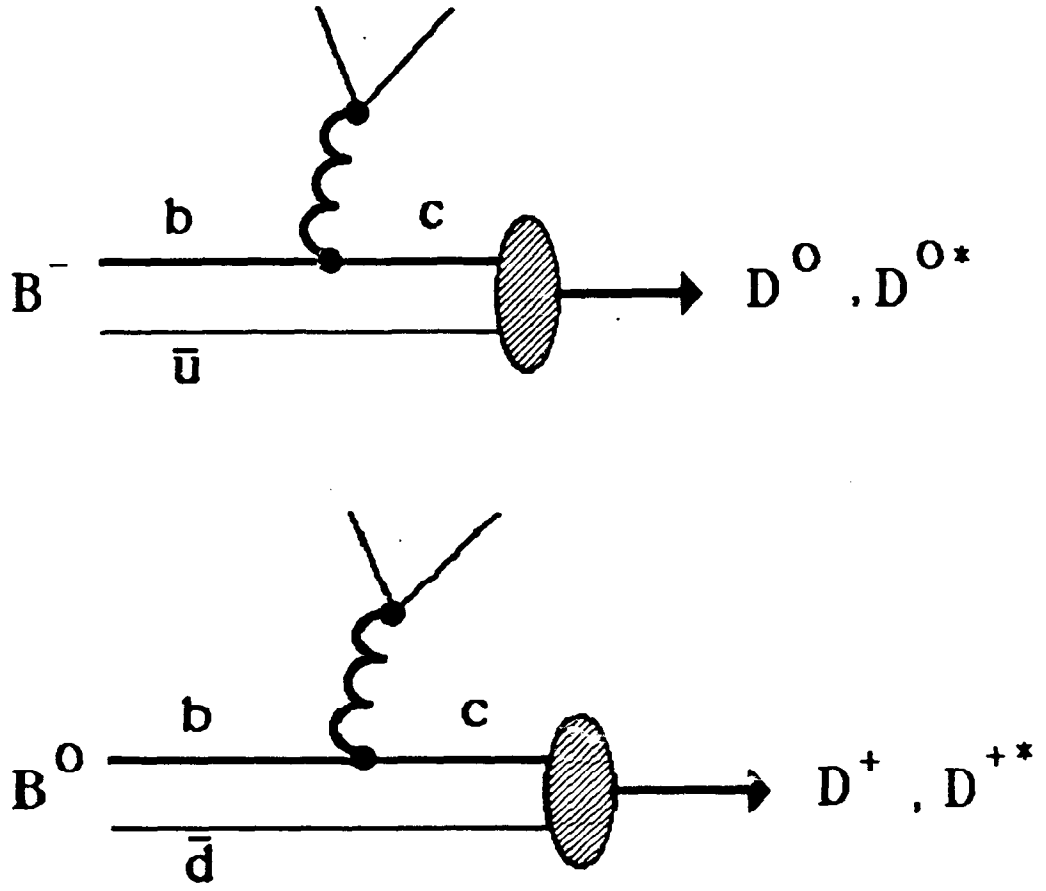
b
c
B⁻
ū
D⁰ , D⁰*
b
c
B⁰
d̄
D⁺ , D⁺*

Fig. 21

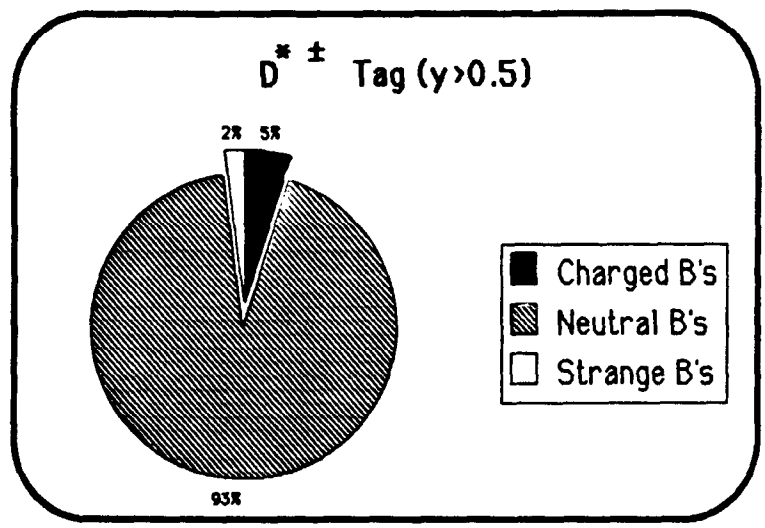
D* ± Tag (y>0.5)
2%
5%
93%
Charged B's
Neutral B's
Strange B's

Fig. 22

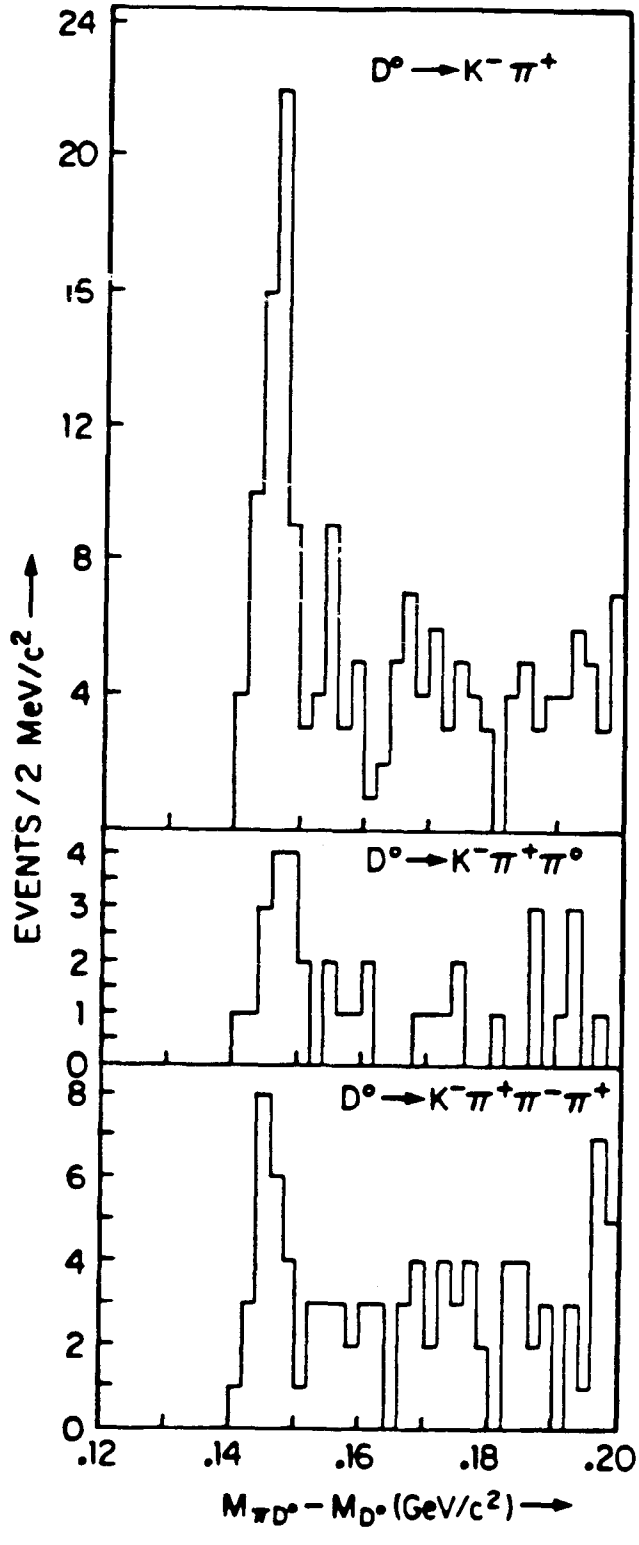
D° → K⁻ π⁺
D° → K⁻ π⁺ π°
D° → K⁻ π⁺ π⁻ π⁺
EVENTS / 2 MeV/c² →
M_πD° − M_D° (GeV/c²) →
24
20
15
12
8
4
4
3
2
1
0
8
6
4
2
0
.12
.14
.16
.18
.20

Fig. 23

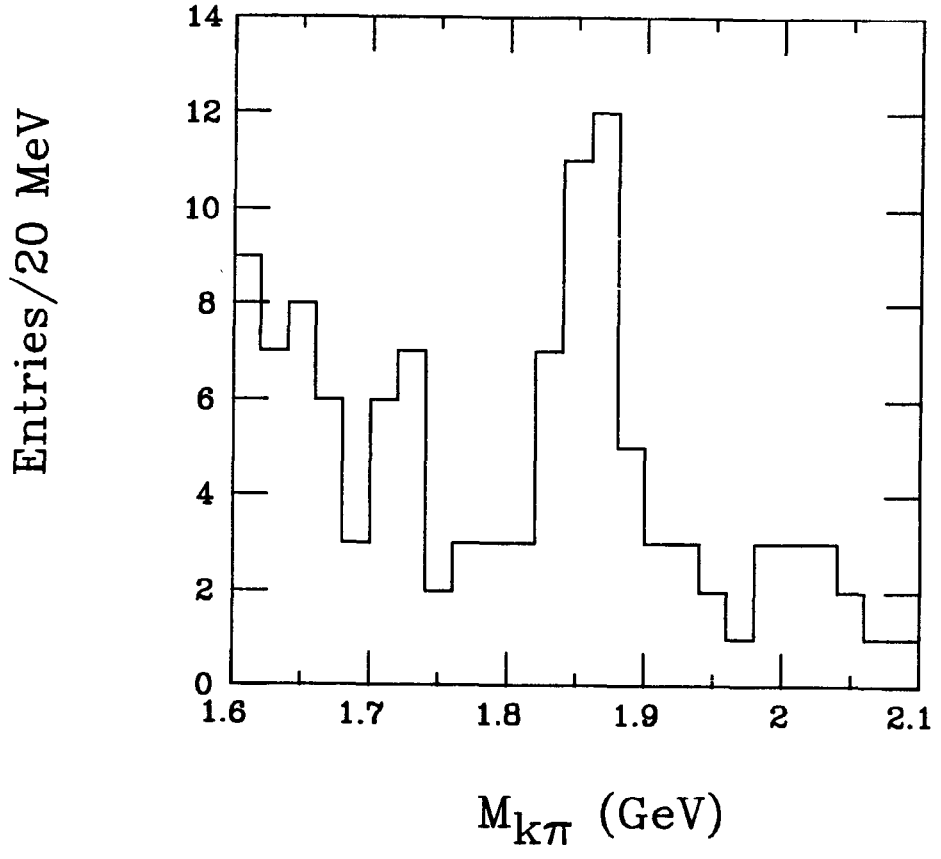

Fig. 24

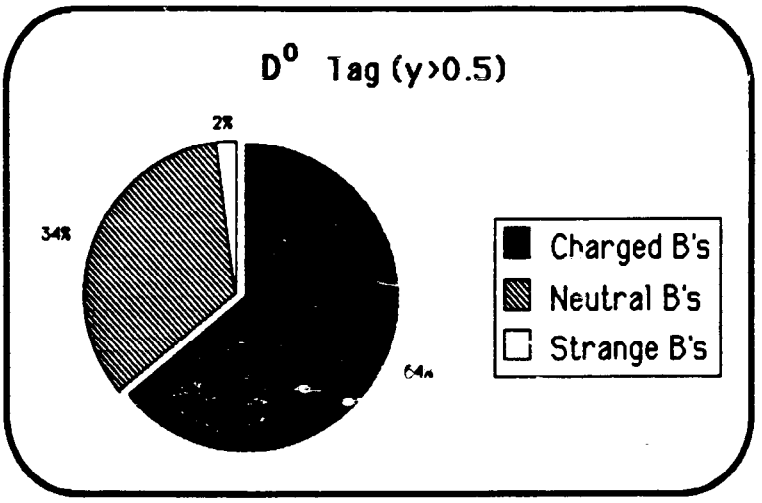
D⁰ Tag (y>0.5)
2%
34%
64%
Charged B's
Neutral B's
Strange B's

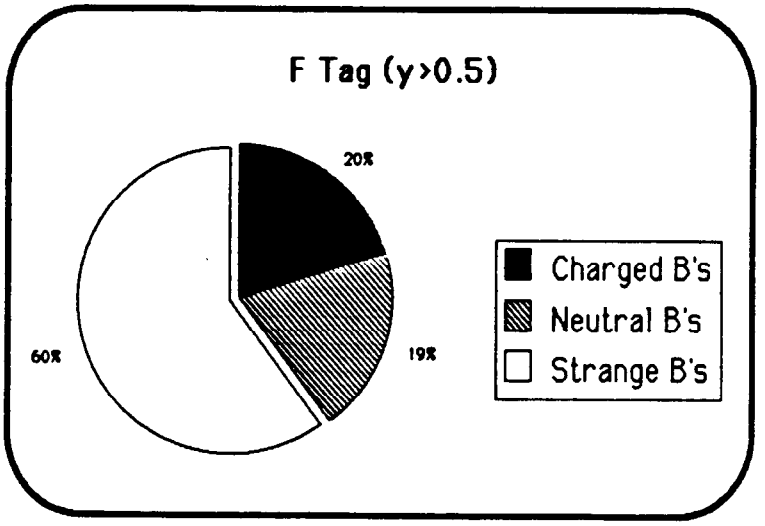
F Tag (y>0.5)
20%
60%
19%
Charged B's
Neutral B's
Strange B's

Fig. 25

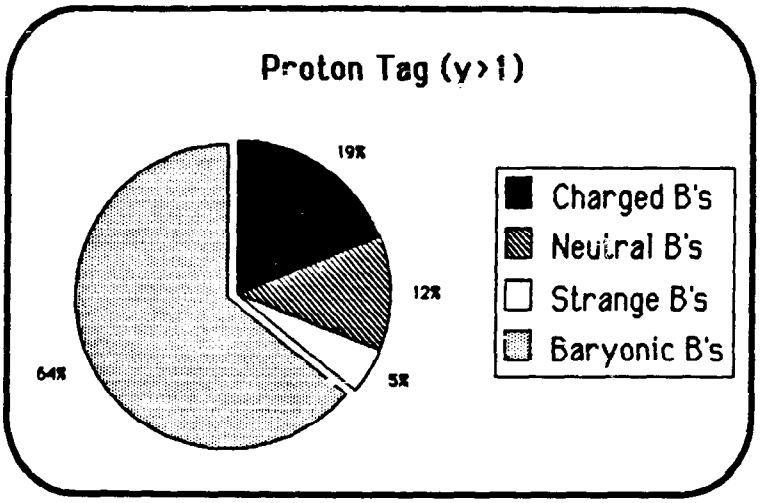
Proton Tag (y>1)
19%
12%
5%
64%
Charged B's
Neutral B's
Strange B's
Baryonic B's

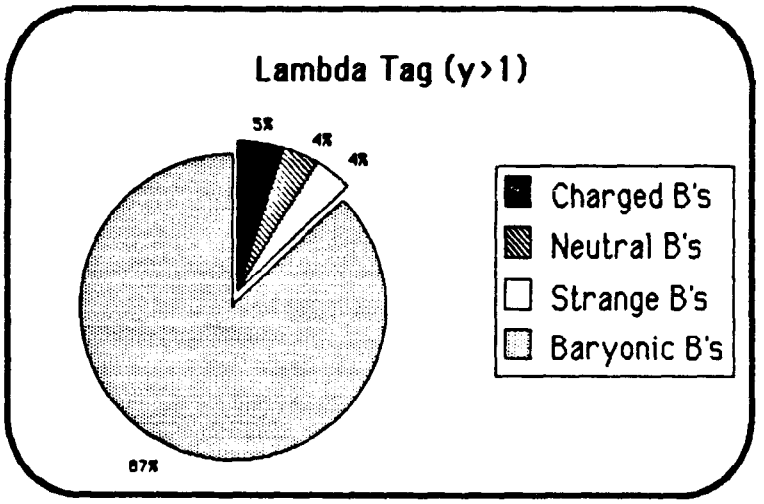
Lambda Tag (y>1)
5%
4%
4%
87%
Charged B's
Neutral B's
Strange B's
Baryonic B's

Fig. 26

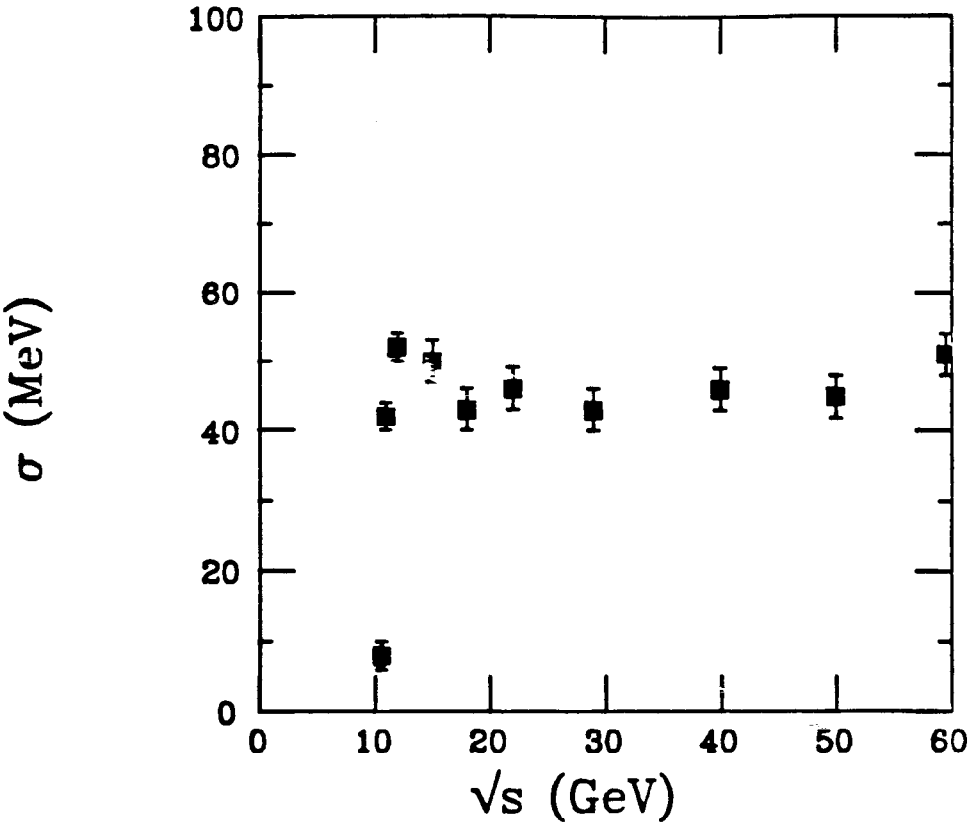

Fig. 27 (a)

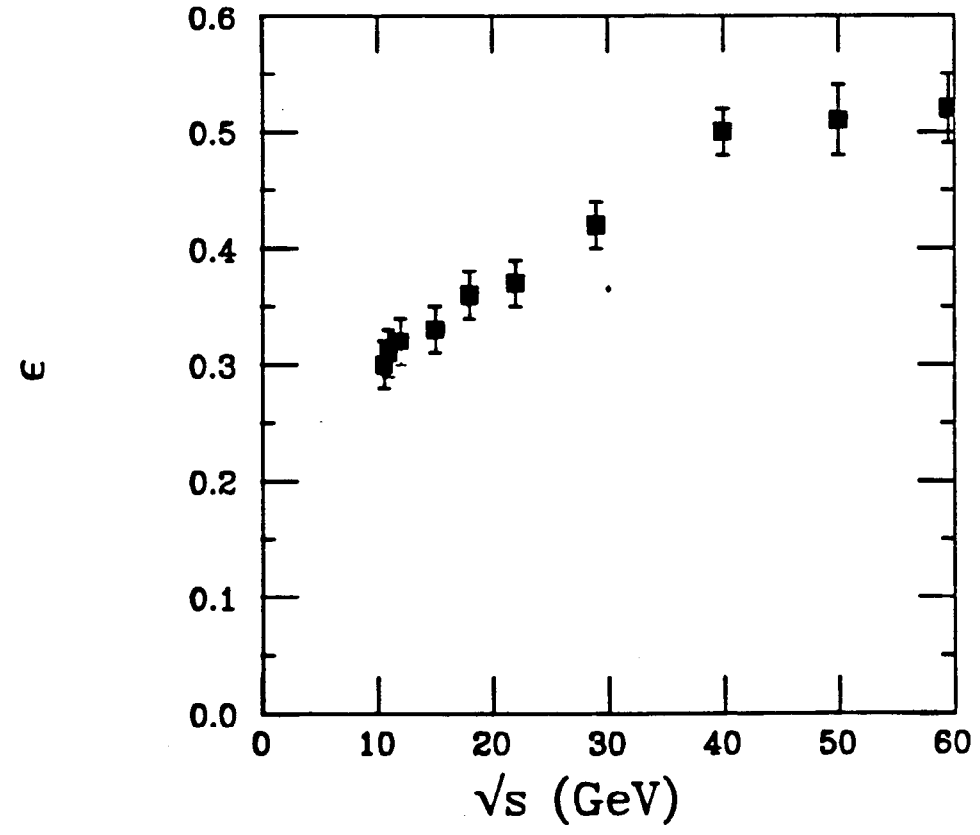

Fig. 27 (b)

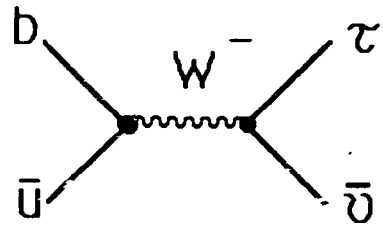

$$\Gamma(B^- \to \tau \bar{\upsilon}) = \frac{G_F^2}{8\pi} m_B m_\tau^2 \left[1 - \frac{m_\tau^2}{m_B^2}\right]^2 |V_{bu}|^2 f_B^2$$

Fig. 28 (a)

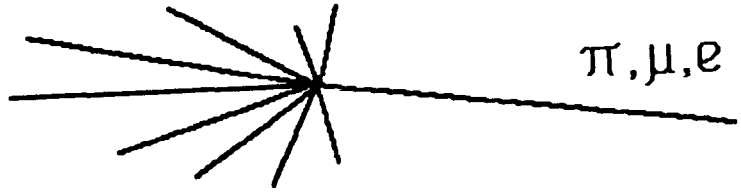

Fig. 28 (b)

CHAPTER III. $\gamma\gamma$ PHYSICS

J. G. LAYTER

and

I. ANTONIADIS, A. BUIJS, A. M. EISNER, F. C. ERNÉ,
S. J. MAXFIELD, R. R. MCNEIL, H. P. PAAR, J. L. ROSNER,
J. R. SMITH, J. E. SPENCER, D. H. STORK, M. K. SULLIVAN,
W. VERNON, W. WAGNER, P. M. ZERWAS

CHAPTER III. $\gamma\gamma$ PHYSICS

CONTENTS

The past five years have seen the field of two-photon physics progress from the status of conjecture to relative maturity. A large body of high quality data now exists on the $\gamma\gamma$ widths of the pseudoscalar and tensor mesons.[1] The observation[2] of an unexpectedly large enhancement in $\gamma\gamma \rightarrow \rho^0\rho^0$ may be an indication of the presence of four-quark states.[3] The existence of hard scattering processes is evident both in jet production[4] and in high mass exclusive channels.[5] The general expectations for the behavior of the F_2^γ structure function have been borne out by the data.[6]

Although cross sections for two-photon processes are comparable to annihilation cross sections in the PEP energy range, the available $\gamma\gamma$ luminosity severely limits rates, particularly if one of the photons is tagged by detection of its parent beam electron. Data obtained from a wide variety of two-photon processes tend to agree with QCD predictions for these processes, but for the most part they lack the statistical power to clearly support or disprove them. High luminosity running at presently available energies and with existing detectors will enable two-photon physics to achieve its promise of becoming a testing laboratory for perturbative and non–perturbative quantum chromodynamics.

In this section we will look at a number of two-photon processes to see in detail what would be achieved if the integrated luminosity were 1 inverse femtobarn. We will consider the following areas:

1. Deep Inelastic $e\gamma$ Scattering
2. 2-Body Production Processes
3. Charmonium
4. Double Tag Missing Mass
5. Gluonia

For the sake of the discussion we assume these processes will be studied in the TPC/2γ detector as it might appear in one of the versions of the high luminosity PEP ring under consideration. This is sketched in Fig. 1. The

tagging devices are the NaI arrays, at ±2.8 m from the beam crossover point, covering the angular region from 40 to 180 mrad. BGO crystals could be installed around the beampipe after the Q1 quadrupole or before the 2-meter mask, as shown in the figure, to extend the tagging coverage to 20 mrad. A thin layer of presampler chambers could be installed in the pole face recess currently occupied by drift chambers of the forward arm spectrometers.

A new vertex detector at the inner radius of the TPC, from 5 to 16 cm, would provide spatial resolution approaching 30μ and 1 mm two-track separation. This device would extend the tracking coverage of the central detector to approximately 14° from the beam line, nearly compensating for the solid angle coverage lost by the removal of the forward arm chambers. Preliminary studies show that adequate masking for the vertex detector would be provided by masks around the beam pipe at ±2 m and by conical masks at each end of the detector at the inner radius.

III.1 Deep Inelastic eγ Scattering

Deep inelastic eγ scattering (Fig. 2) probes the hadronic quantum fluctuations of the target photon. For low momentum transfer to the target, Q^2, the photon will behave hadronically as a vector meson. At higher Q^2, the photon will appear pointlike. The cross section is specified by three structure functions:

$$\frac{d\sigma}{dxdyd\phi} = \frac{8\alpha^2 EE_\gamma}{Q^4}\left[(1-y)F_2^\gamma + xy^2F_1^\gamma + (1-y)\varepsilon(\xi)F_3^\gamma \cos 2\phi\right]N_\gamma$$

with

$$Q^2 = 2EE'(1-\cos\theta)$$
$$x = \frac{Q^2}{Q^2+W^2}$$
$$W^2 = (\Sigma p_i)^2$$
$$y = 1 - \frac{E'}{E}\cos^2\frac{\theta}{2}$$

The measured quantities are the energy of the tagging electron E′ and its angle

with the beam line θ, and the energy of the final state particles W. Since the detector is unable to measure all the final state particles due to its finite acceptance, the true invariant mass W_{true} must be inferred from the measured W_{vis} by an unfolding procedure. Maintaining good angular coverage is essential to ensure that the unfolding operation is well-behaved and preserves the statistical power of the data. In the experimental situation under discussion y is small and F_1^γ can be ignored.

The F_2^γ structure function was evaluated more than ten years ago in the framework of the Quark Parton Model in which the quarks are pictured as free particles.[7] In recent years F_2^γ has been calculated in QCD taking into account the dynamical interactions of the quarks.[8] Both QPM and QCD predict the structure function F_2^γ to rise with x in contrast to hadronic structure function behavior, and this has been amply confirmed.[9] They also both predict a linear rise in $\ln Q^2$ with a well defined slope (Fig. 3) that is a function of x (Fig. 4).[10] Existing data confirm a rise with $\ln Q^2$ but lack the statistics to determine the slope, even when averaged over a large region of x, as is shown in Fig. 5.[11] The first objective of a large luminosity investigation of F_2^γ should be to determine the slope at a fixed value of x.

However, since F_2^γ rises almost linearly with $\ln Q^2$ at all levels of approximation, only a failure to confirm the predicted rise would be surprising. But the higher order QCD calculation of the structure function provides an absolute normalization which depends only on the QCD scale parameter $\Lambda_{\overline{MS}}$. Hence the measurement of F_2^γ has been looked to to provide a high precision measurement of $\Lambda_{\overline{MS}}$, depending on the absolute normalization and not on the Q^2 evolution of the structure function as is the case for the leptonic structure functions. And in fact the $\Lambda_{\overline{MS}}$ measurement that has been obtained from F_2^γ, 230 ± 40 MeV, is comparable to the best determinations made by other methods.[11]

For this measurement to be reliable however, a deeper theoretical understanding must be reached regarding two assumptions that are implicit in the cal-

culations: first, that uncertainties in the regularization of spurious singularities in the operator product expansion of F_2^γ can be confined to the small-x region;[12] and second, that the uncalculable hadronic parts of the structure function can be adequately supplied from measurements of the pion structure function.[13] Confidence in the reliability of these two assumptions could be gained by obtaining good agreement between the data and the predictions of the higher order theory throughout the accessible regions of the (x,Q^2) plane, a project that would require a ten– to fifteen–fold increment in luminosity. Figure 6a shows existing data in two Q^2 ranges to be compared with the error bars expected if 1 fb^{-1} of data were available, shown in Fig. 6b.

The virtual photons in two-photon e^+e^- scattering are typically strongly plane-polarized in the lepton scattering planes. The third structure function, F_3^γ, measures the polarization dependence of $e\gamma$ scattering.[14] In hadronic models of the target photon, where the p_T of the constituent quarks is limited, F_3 is expected to be small relative to F_2. For $p_T \to 0$, F_3 must vanish because of rotational invariance:

$$F_3^{had} \sim \frac{< p_T^2 >}{Q^2} F_2^{had}$$

In the case of point-like coupling of quarks to the target photon, however, the transverse momenta squared of the quarks can be of order Q^2, and F_3^γ approaches F_2^γ in magnitude. QCD predicts that the structure function F_3^γ should scale in leading order. It exhibits a striking x^3 dependence and is negative:

$$F_3^\gamma = -\frac{\alpha}{\pi} \sum_{\text{flavors}} 3e_q^4 x^3$$

F_3^γ can be determined by measuring the distribution of ϕ, the angle between the scattering planes of the electron and positron. Consequently the scattered leptons must both be detected: one at large angles associated with the high Q^2 probe and one at small angles associated with the low Q^2 target photon. The rate for such double-tagged events is $\sim$ 10 times smaller than the corresponding

single-tag rate, Nevertheless, a determination of F_3^γ, including its x-dependence, should be possible with high luminosity running at PEP.

III.2 2-Body Production Processes

A second area in which clear-cut QCD predictions exist is that of large momentum transfer exclusive processes. The factorization scheme worked out by Brodsky and Lepage[15] provides detailed predictions for photon-photon annihilation into two mesons $H\bar{H}$ of large invariant mass $W_{\gamma\gamma}$. The cross section is expressed in terms of helicity amplitudes $M_{\lambda\lambda'}$

$$M_{\lambda\lambda'}(W_{\gamma\gamma},\theta_{c.m.}) = \int_0^1 dx_i\ dy_i\ \phi^*_H(x_i,Q)\ \phi_{\bar{H}}(y_i,Q)\ T_{\lambda\lambda'}(x,y;W_{\gamma\gamma},\theta_{c.m.})$$

$T_{\lambda\lambda'}$ is the amplitude for scattering clusters of valence quarks in each produced meson and is calculable in QCD and scales according to dimensional counting rules. The quark distribution functions $\phi_H(x_i,Q)$, probability amplitudes for finding valence quarks with a given fraction x of the meson's momentum, require non-perturbative inputs, but their dependence on $\ln Q^2$ can be determined by evolution equations. The predictions are not sensitive to the precise form of the distributions. The functions are normalized to the meson's leptonic decay constant

$$\int_0^1 dx\ \phi_H(x,Q) = f_M/2\sqrt{3}.$$

This formalism gives very good agreement, both in shape and normalization, with the high mass dimeson continuum measured by the Mark II collaboration (Fig. 7).[5] However a number of questions remain to be answered before the extension of the factorization approach to the two-photon area can be relied upon:

- The QCD model predicts a Q^2 dependence similar to QED, i.e., $1/(1+Q^2/s)$, in contrast to the much faster falloff of resonance channels behaving according to the vector dominance model. The Q^2 dependence of identified dipions has been looked at by TPC/2γ, but the data are statistically insignificant — there are 29 events with non-zero Q^2 for 70 pb^{-1}.
- Precise predictions on angular distributions are provided by the theory but again have not been checked for lack of statistics. For neutral mesons, these predictions are highly sensitive to the shape of the distribution amplitudes.
- The K/π ratio predicted by the theory could be tested using the dE/dx capabilities of the TPC. However, the bulk of the data lie at the K/π crossover point in the dE/dx vs momentum plane, and there are few events in unambiguous regions.

In the case of baryons, there are at the outset theoretical inconsistencies to be overcome since two available predictions differ by several orders of magnitude in the cross sections.[16,17] In the meantime event samples of a few tens of $p\bar{p}$ events are available both at PEP (Fig. 8a) and PETRA, and a small sample of $\Delta^{++}\overline{\Delta^{++}}$ events has been isolated by TPC/2γ (Fig. 8b).

For both mesons and baryons, current data samples clearly show that large momentum transfer processes exist, but they do little more than that. Thorough tests of the theory need a signficant increase in statistics.

III.3 CHARMONIUM

A measurement of the $\gamma\gamma$ widths of the charmonium S– and P–wave states can provide information on the wavefunctions of these states. In lowest order $\Gamma_{\gamma\gamma}$ for η_c is given by[18]

$$\Gamma(\eta_c \to \gamma\gamma) = \frac{12\alpha^2 e_q^4}{M^2}|R_S(0)|^2$$

where $R_S(0)$ is the radial radial wavefunction at the origin. ψ, also an S state, will be described by the same wavefunction; thus its width for decay to muons is

Charmonium States			
State	Mass (GeV)	$I^G(J^P)C$	Spectroscopic Notation
η_c	2.980	$0^+(0^-)+$	$^1S_0$
χ_0	3.415	$0^+(0^+)+$	$^3P_0$
χ_2	3.555	$0^+(2^+)+$	$^3P_2$
η_c'	3.592	$0^+(0^-)+$	$^2S_0$

given by

$$\Gamma(\psi \to \mu\mu) = \frac{4\alpha^2 e_q^2}{M^2}|R_S(0)|^2$$

The decay of η_c to hadrons proceeds via a two-gluon intermediate state, and the calculation of this width again involves $R_S(0)$:

$$\Gamma(\eta_c \to gg) = \frac{8}{3}\frac{\alpha_S^2(m^2)}{M^2}|R_S(0)|^2$$

A measurement of $\Gamma_{\gamma\gamma}$ for η_c provides a useful crosscheck of the understanding of the wavefunction, and – assuming the gluons turn into hadrons with unit probability – a prediction of the hadronic width of η_c. Similar arguments can be made for the χ states.

An attempt has been made to find charmonium states in the TPC using dE/dx identification to select $\pi\pi\pi\pi$ and $\pi\pi KK$ final states, which have large branching ratios. An additional handle is provided by the Q^2 dependence, which is expected to follow the ψ.[19] A final sample of perhaps ten events was obtained from 70 pb^{-1} of running, but could not be resolved into distinguishable mass states with the low–field mass resolution of the TPC. A similar analysis with the improved mass resolution provided by the superconducting coil and with statistics of 1 fb^{-1} should give a recognizable signal, as is demonstrated in Fig. 9.

III.4 Double Tag Missing Mass

The NaI taggers of the TPC/2γ forward detector have achieved an energy resolution of 1.2% at 14.5 GeV. With their good angular resolution they constitute a powerful missing mass spectrometer for double tagged events. A study has been made to evaluate this resolution, assuming as a background the hadronic cross section measured previously by PEP-9.[20] Requiring a 5σ separation of the signal from background, one could detect a narrow resonance coupling to two photons with a $\gamma\gamma$ width varying from 10 keV at a mass of 4 GeV to 1 MeV at a mass of 16 GeV. This is indicated in Fig. 10a. The signal one would observe from a hypothetical particle of mass 12 GeV and $\Gamma_{\gamma\gamma}$ of 0.4 MeV is shown in Fig. 10b, assuming 1 fb^{-1} of running.

One possible candidate to produce such a signal is a (pseudo)scalar resonance R produced in the radiative decay of the Z^0 and subsequently decaying into a lepton pair (Fig. 11a). Such a particle has been postulated to explain the large rate from radiative Z^0 decays. Most models envisage large couplings to e^+e^- for such a resonance, but no signal has been observed so far up to an energy of 45.52.[21] However, chiral invariance could require that the coupling $Rf\bar{f}$ be proportional to m_f, the fermion mass, so that this state would not have been observed in e^+e^- collisions.[22] It could still have a large $\gamma\gamma$ width, given for example by

$$\Gamma(R \rightarrow \gamma\gamma) = \frac{1}{2}\pi\alpha^2 \frac{f_R^2}{m_R}$$

with $f_R \approx 100$ GeV.[23] This gives a width of 40 MeV at a mass of 20 GeV.

A composite Higgs boson could have a large coupling to $\gamma\gamma$ in the context of W-dominance models (Fig. 11b).[24] The coupling $H\gamma\gamma$ would be of order e^2/Λ_{eff} with Λ_{eff} having the value M_W. A 10 GeV Higgs would then have a $\gamma\gamma$ width of 14 MeV. Although these estimates are highly speculative, they indicate that the double tag spectrometer could encounter some surprises.

III.5 GLUONIA

A striking consequence of the non-abelian character of QCD is the implied existence of gluonic bound states. These states would be both color and flavor singlets and would therefore possess flavor-independent couplings, decaying with equal probability into $u\bar{u}$ or $s\bar{s}$ pairs. It is unlikely that pure glueball states would remain unmixed with ordinary mesons, so one would expect physical states to contain both quark and gluonic components. For this reason the search for mesons having gluonic content has proceeded by considering the physical states to be represented as[25]

$$|\psi\rangle = \frac{x}{\sqrt{2}}(|u\rangle + |d\rangle) + y\,|s\rangle + z\,|G\rangle$$

The amplitudes x and y can be evaluated using SU(3) relations in comparing various decays widths. If $x^2 + y^2 < 1$, the state is presumed to have a gluonic component. A likely candidate is the η'. Since the branching ratios of η' to $\gamma\gamma$ and $\rho\gamma$ are known, the published value[26] of $\Gamma(\eta' \to \gamma\gamma)$ can used to obtain $\Gamma(\eta' \to \rho\gamma)$, which with $\Gamma(\omega \to \pi^0\gamma)$ determines $x_{\eta'}$. This is shown as a vertical band in Fig. 12. (Also shown in the figure are y values that would be obtained from a measurement of the branching ratio of $\phi \to \eta'\gamma$. This would make the estimate of the gluonic content of η' independent of the assumption of nonet symmetry.[27] However the measurement has not yet been made.)

With the assumption of nonet symmetry, one can compare $\Gamma(\eta' \to \gamma\gamma)$ with $\Gamma(\pi^0 \to \gamma\gamma)$ to obtain a constraint on the quantity $|x + \frac{\sqrt{2}}{5}y|$. This results in the inclined band in the figure. The resulting value for $x^2 + y^2$ is 0.85 ± 0.14, which indicates that η' may have some amount of gluonic content.

The current measurements of $\Gamma_{\gamma\gamma}$ are systematics limited, so there would seem to be little benefit in obtaining large increases in luminosity. This is not the case however, since improved statistics can be used to obtain better control of systematic effects. The gluonium problem is typical of the general states of

resonance studies in two–photon physics: higher luminosities would result in substantial reduction in the overall errors.

An alternative approach to the identification of gluonium candidates is the nonobservation in $\gamma\gamma$ production of states seen in radiative J/ψ decay. The radiative J/ψ decay leads naturally to gluonic intermediate states and is only slightly suppressed relative to hadronic decays. However $\gamma\gamma$ production of gluonic states should be strongly suppressed. Figure 13a shows the signal of the candidate gluonic states θ and ξ observed in radiative J/ψ decay to K^+K^- by Mark III.[28] Fig. 13b presents the $K^0\bar{K}^0$ mass distribution obtained by the TASSO Collaboration.[29] The reported upper limits are

$$\Gamma_{\gamma\gamma}(\theta)\mathrm{Br}(\theta \to K^0\bar{K}^0) < 1.2 \text{ keV}$$

and

$$\Gamma_{\gamma\gamma}(\xi)\mathrm{Br}(\xi \to K^0\bar{K}^0) < 0.5 \text{ keV} ,$$

both at 95% confidence level. More stringent limits will clearly come from higher luminosity running; the question of what limits are stringent enough must come from the theory.

The areas discussed, and many others not considered, underline the salient point of two-photon physics: much higher e^+e^- luminosities are required to offset the intrinsic limitation of low $\gamma\gamma$ luminosity. Existing luminosities on the present machines, and expected luminosities on future machines, will not overcome this obstacle to the realization of the potential of two-photon physics which is clearly visible in the current data.

REFERENCES

1. H. Kolanoski, *Two-Photon Physics at* e^+e^- *Storage Rings*, Tracts in Modern Physics, Vol. 105, Springer Verlag (1985).

2. R. Brandelik *et al.*, *Phys. Lett.* **97B**, 448 (1980),
   M. Althoff *et al.*, *Z. Phys.* **C16**, 13 (1982),
   D.L. Burke *et al.*, *Phys. Lett.* **103B**, 153 (1981),
   H.–J. Behrend *et al.*, *Z. Phys.* **C21**, 205 (1984).

3. B.A. Li and K.F. Liu, *Phys. Rev. D30*, 613 (1984),
   Phys. Lett. **30B**, 435 (1982).

4. N. Wermes, *Proceedings of the Fifth International Workshop on Photon-Photon Collisions*, Aachen; ed. Ch. Berger, Lecture Notes in Physics, Vol. 191, Springer Verlag (1983).

5. J.R. Smith *et al.*, (Mark II Collaboration), *Phys. Rev.* **D30**, 851 (1984).

6. P.M. Zerwas, XV Symposium on Multiparticle Dynamics, Lund, 1984; PITHA 84/24.

7. T.F. Walsh and P.M. Zerwas, *Phys. Lett.* **44B**, 195 (1973).

8. E. Witten, *Nucl. Phys.* **B120** 189 (1977),
   R.J. DeWitt *et al.*, *Phys. Rev.* **D19**, 2046 (1979); **D20**, 1751 (E) (1979).
   W.A. Bardeen and A.J. Buras, *Phys. Rev.* **D20**, 166 (1979)
   D.W. Duke and J.F. Owens, *Phys. Rev.* **D22**, 2280 (1980).

9. Ch. Berger *et al.*, (PLUTO Collaboration), *Phys. Lett.* **107B**, 168 (1981).

10. M. Glück, K. Grassie, and E. Reya, *Phys. Rev.* **D30**, 1447 (1984).

11. W. Wagner, Sixth International Workshop on Photon-Photon Collisions, Lake Tahoe, 1984; UCD–850220.

12. I. Antoniadis and G. Grunberg, *Nucl. Phys.* **B213**, 445, (1983).

13. C.B. Newman *et al.*, *Phys. Rev. Lett.* **42**, 951 (1979).

14. W.R. Frazer and G. Rossi, *Phys. Rev.* **D21**, 2710 (1980).

15. S.J. Brodsky and G.P. Lepage, *Phys. Rev.* **D24**, 1808 (1981).

16. G.R. Farrar, E. Maina, and F. Neri, Rutgers preprints RU–83–33 and RU–84–13. Also Sixth International Workshop on Photon-Photon Collisions, Lake Tahoe, 1984.

17. P.H. Damgaard, *Nucl. Phys.* **B211**, 435 (1983).

18. F. Close, *An Introduction to Quarks and Partons*, Academic Press, London, 1979.

19. R. Kirschner and A. Schiller, *Z. Physik* **C16**, 141 (1982).

20. D. Bintinger *et al.*, *Phys. Rev. Lett.* **54**, 763 (1985).

21. B. Adeva *et al.*, (Mark J Collaboration), *Phys. Rev. Lett.* **53**, 134 (1984).

22. J.H. Kühn and P.M. Zerwas, *Phys. Lett.* **142B**, 221 (1984).

23. U. Baer, H. Fritzsch, and H. Faissner, *Phys. Lett.* **135B**, 313 (1984).

24. F.M. Renard, *Phys. Lett.* **126B**, 59 (1983).

25. J.L. Rosner, *Phys. Rev.* **D27**, 1101 (1983).

26. Ch. Berger *et al.*, *Phys. Lett.* **142B**, 125 (1984).

27. J.L. Rosner, Private Communication.

28. K. Einsweiler, Ph. D. Thesis, SLAC–272 (Unpublished).

29. H. Kolanoski (TASSO Collaboration), XXII International Conference on HIgh Energy Physics, Leipzig, 1984.

FIGURE CAPTIONS

1. Schematic view of the TPC/2γ detector in a high luminosity version of the PEP ring. The vertex detector, BGO, and presampler are proposed new elements.

2. Deep inelastic eγ scattering

3. Linear rise of F_2^γ with $\ln Q^2$ estimated from several models. (This and the following figure are adapted from Ref. 10.)

4. Dependence of the slope of F_2^γ on x.

5. Existing data, F_2^γ/α vs Q^2. (Note that the points are averaged over a large x interval.)

6. a) Existing data on F_2^γ/α vs x.
   b) Estimated errors on F_2^γ/α for 1 fb^{-1}.

7. High mass dimeson continuum measured by Mark II.

8. a) Preliminary mass distribution of $p\bar{p}$ events found by the TPC/2γ collaboration.
   b) Scatterplot of doubly charged pπ events showing concentration in the $\Delta^{++}\overline{\Delta^{++}}$ region. (TPC/2γ Preliminary).

9. Estimated signals from charmonium in the TPC for 1 fb^{-1}.

10. a) Minimum width observable with 5σ separation from background, as a function of mass of a narrow resonance.
    b) Particle of mass 12 GeV and $\gamma\gamma$ width 0.4 MeV seen in 1 fb^{-1} of running with the Double Tag spectrometer.

11. a) Radiative decay of Z^0 to a (pseudo)scalar resonance R which subsequently decays into a lepton pair.
    b) $\gamma\gamma$ decay of composite Higgs.

12. Evidence for the gluonic content of η'.

13. a) Invariant mass of K^+K^- in the decay $\psi \to \gamma K^+K^-$ showing f′, θ, and ξ peaks (Mark III).

    b) Mass spectrum of $\gamma\gamma \to K^0\bar{K}^0$ showing the absence of θ and ξ signals (TASSO).

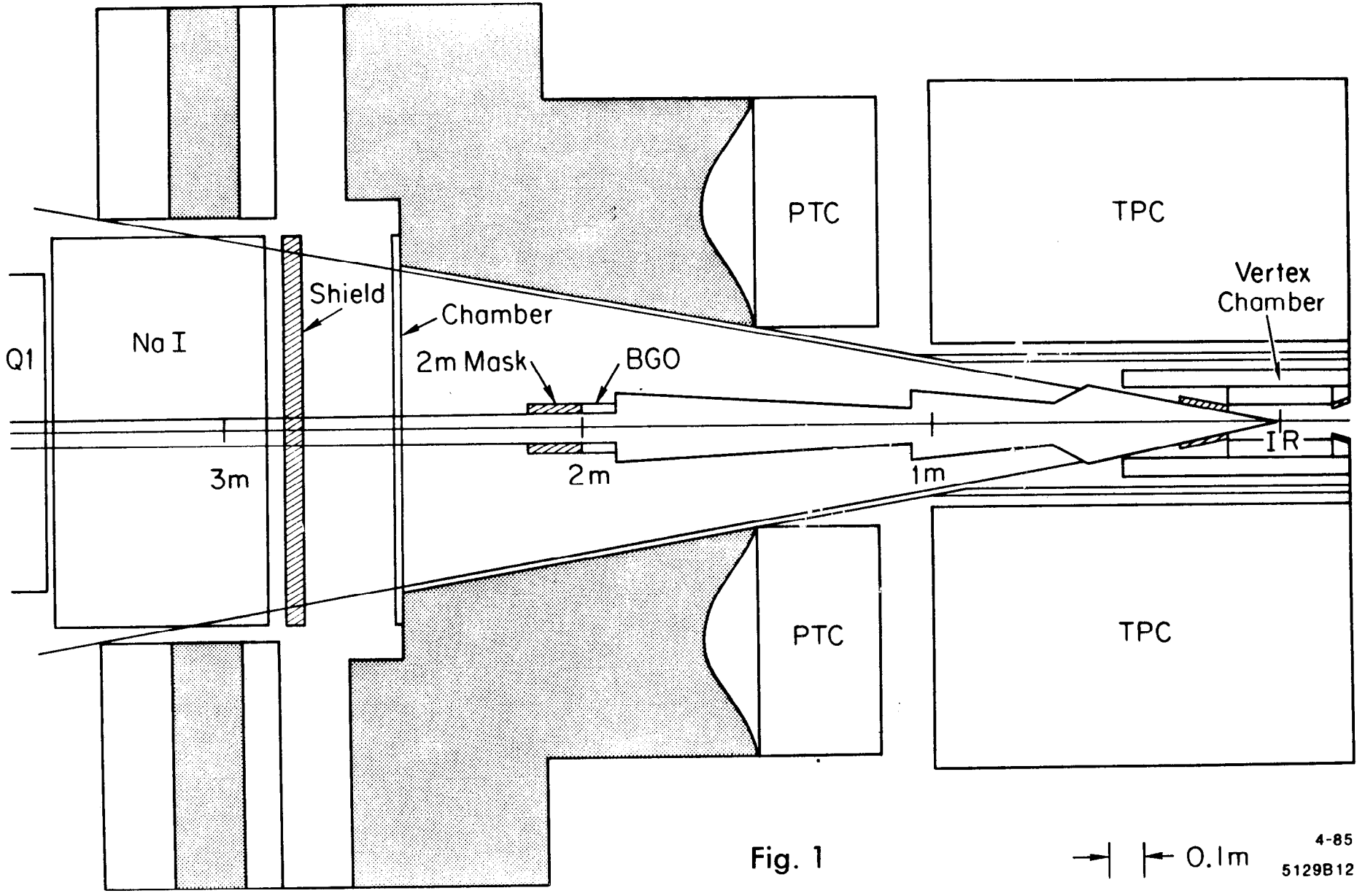
PTC
TPC
Vertex
Chamber
Shield
Chamber
Q1
Na I
2m Mask
BGO
IR
3m
2m
1m
PTC
TPC
0.1m
4-85
5129B12

Fig. 1

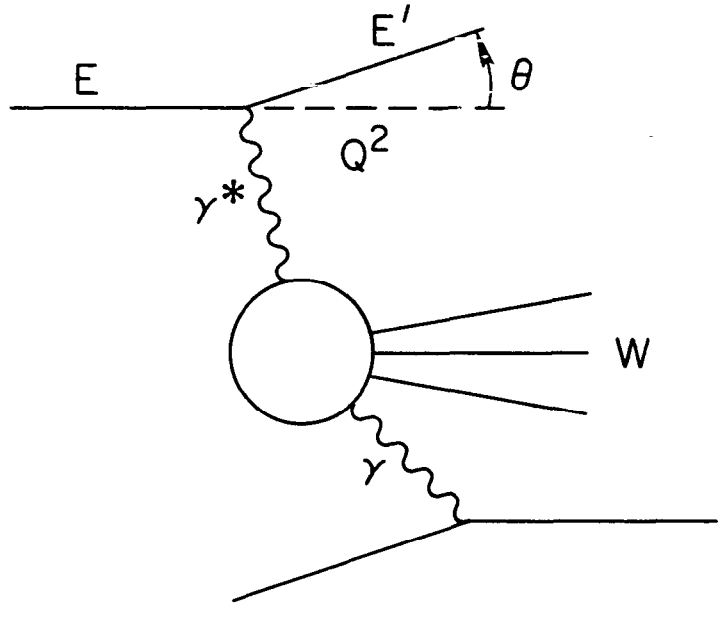

Fig. 2

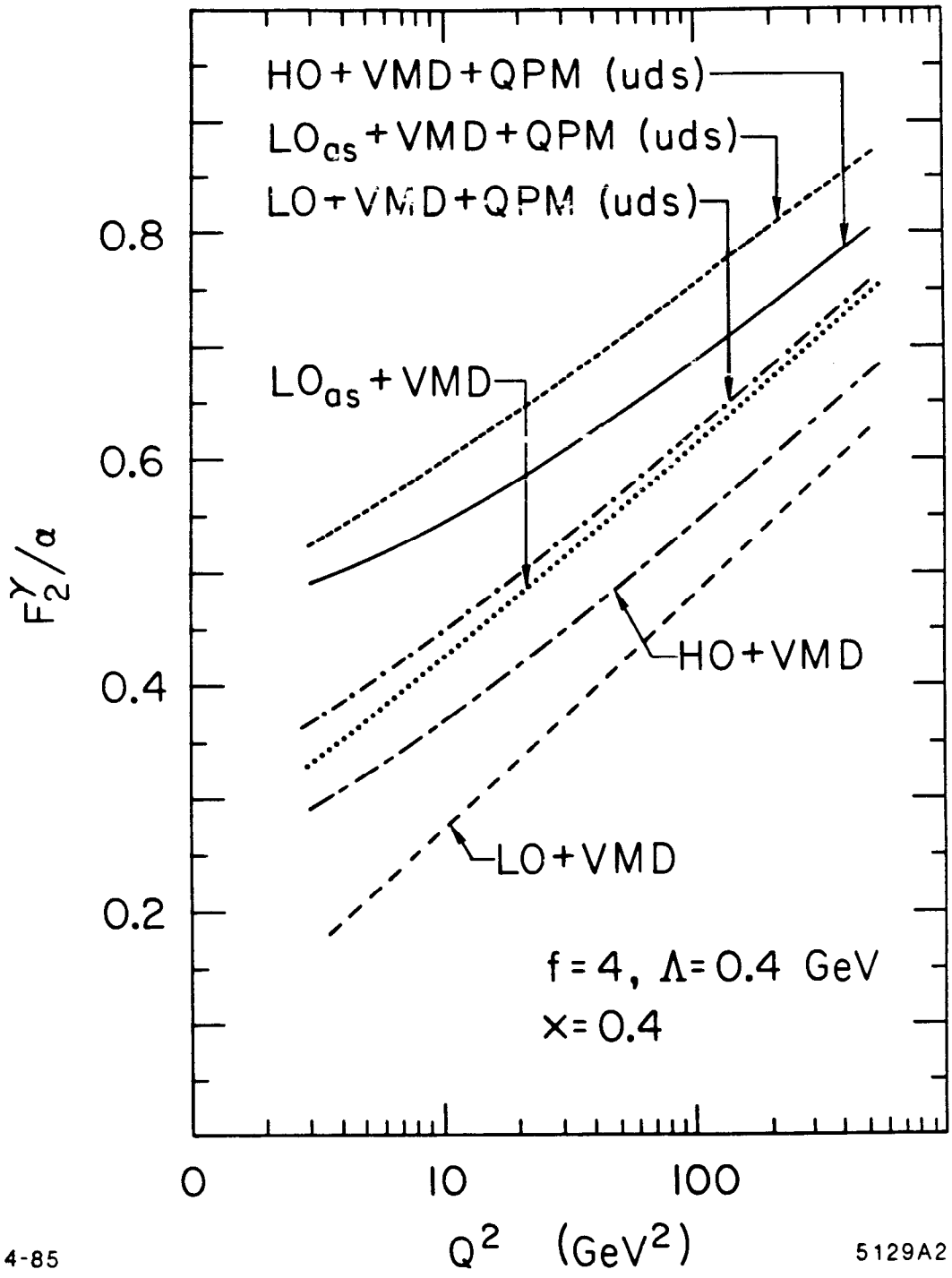
HO+VMD+QPM (uds)
LO$_{as}$+VMD+QPM (uds)
LO+VMD+QPM (uds)
LO$_{as}$+VMD
HO+VMD
LO+VMD
f=4, Λ=0.4 GeV
x=0.4
F_2^γ/α
0.8
0.6
0.4
0.2
0
10
100
Q^2 (GeV^2)
4-85
5129A2

Fig. 3

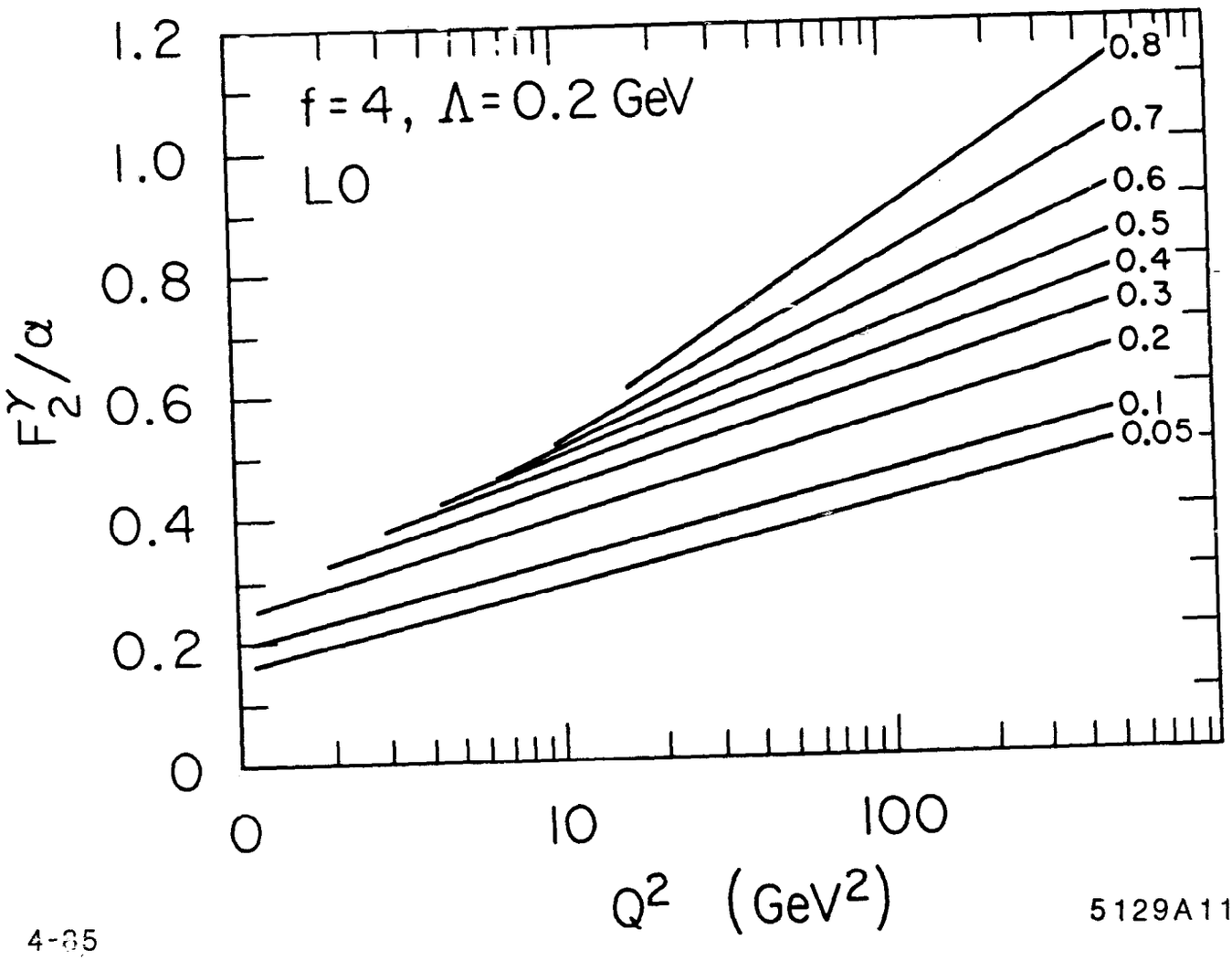
f = 4, Λ = 0.2 GeV
LO
0.8
0.7
0.6
0.5
0.4
0.3
0.2
0.1
0.05
1.2
1.0
0.8
0.6
0.4
0.2
0
F_2^γ/α
0
10
100
Q^2 (GeV^2)
5129A11
4-85

Fig. 4

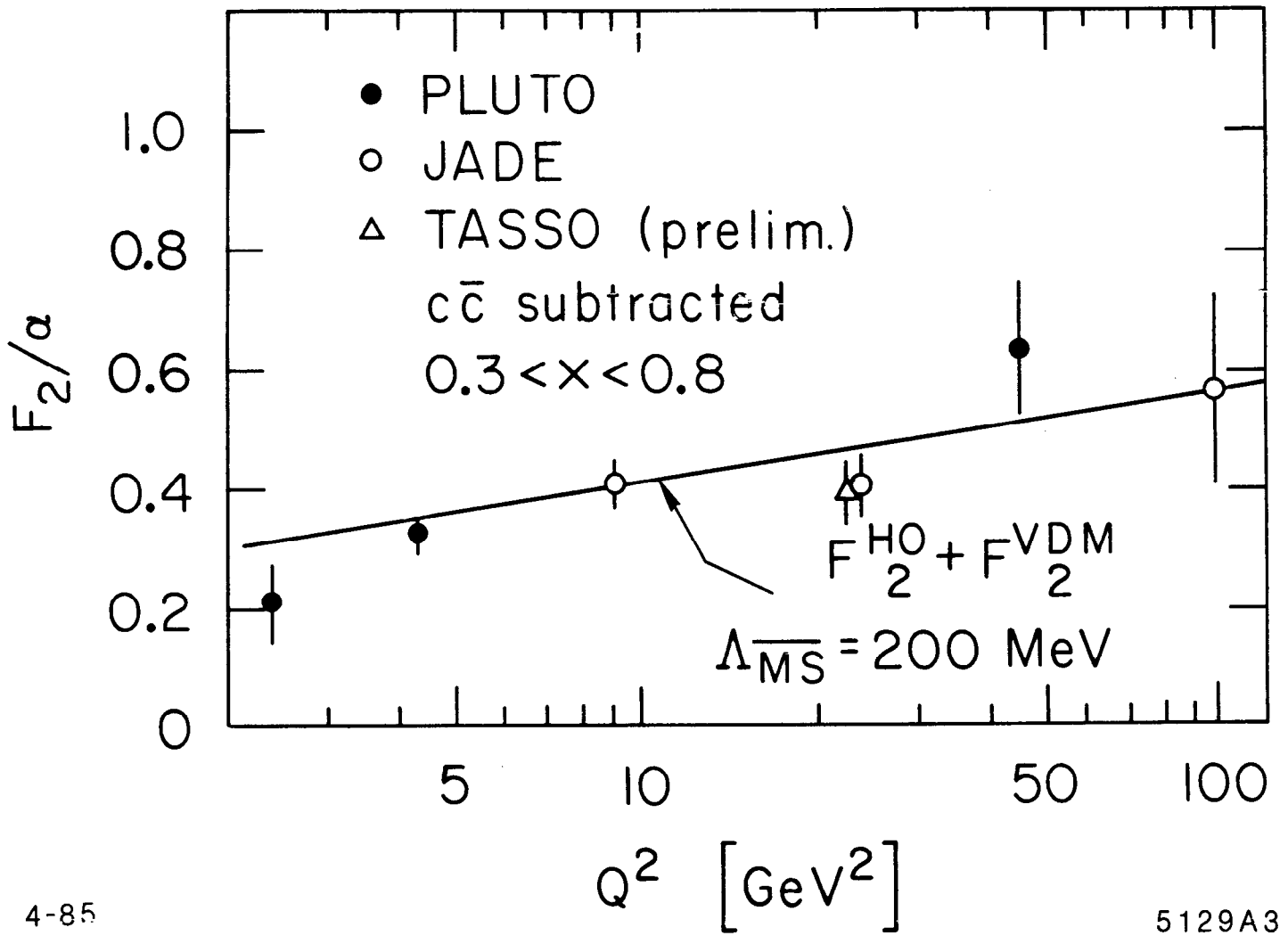
PLUTO
JADE
TASSO (prelim.)
$c\bar{c}$ subtracted
$0.3 < x < 0.8$
$F_2^{HO} + F_2^{VDM}$
$\Lambda_{\overline{MS}} = 200$ MeV
F_2/α
1.0
0.8
0.6
0.4
0.2
0
5
10
50
100
Q^2 [GeV^2]
4-85
5129A3

Fig. 5

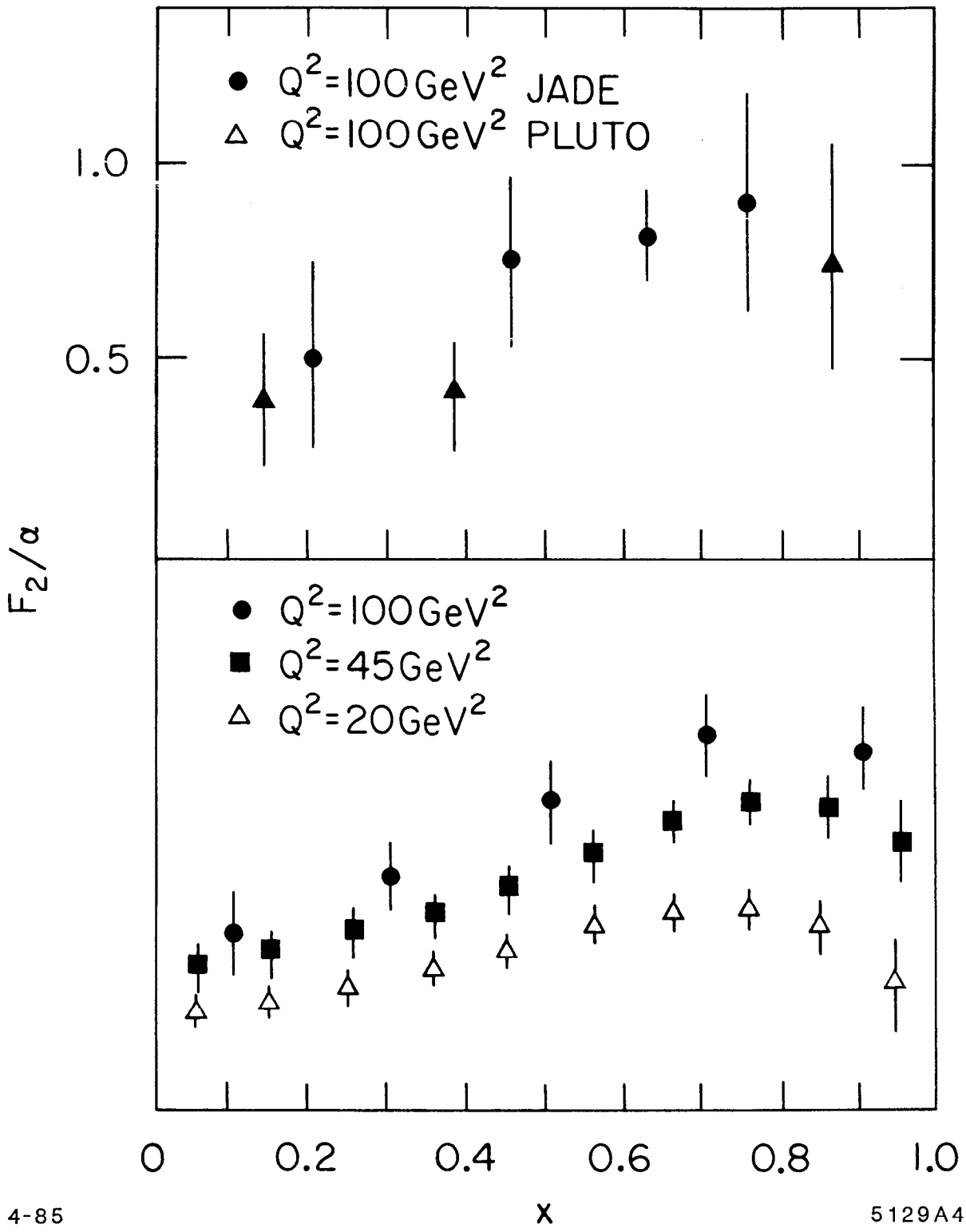
Q^2=100GeV^2 JADE
Q^2=100GeV^2 PLUTO
1.0
0.5
F_2/α
Q^2=100GeV^2
Q^2=45GeV^2
Q^2=20GeV^2
0
0.2
0.4
0.6
0.8
1.0
X
4-85
5129A4

Fig. 6

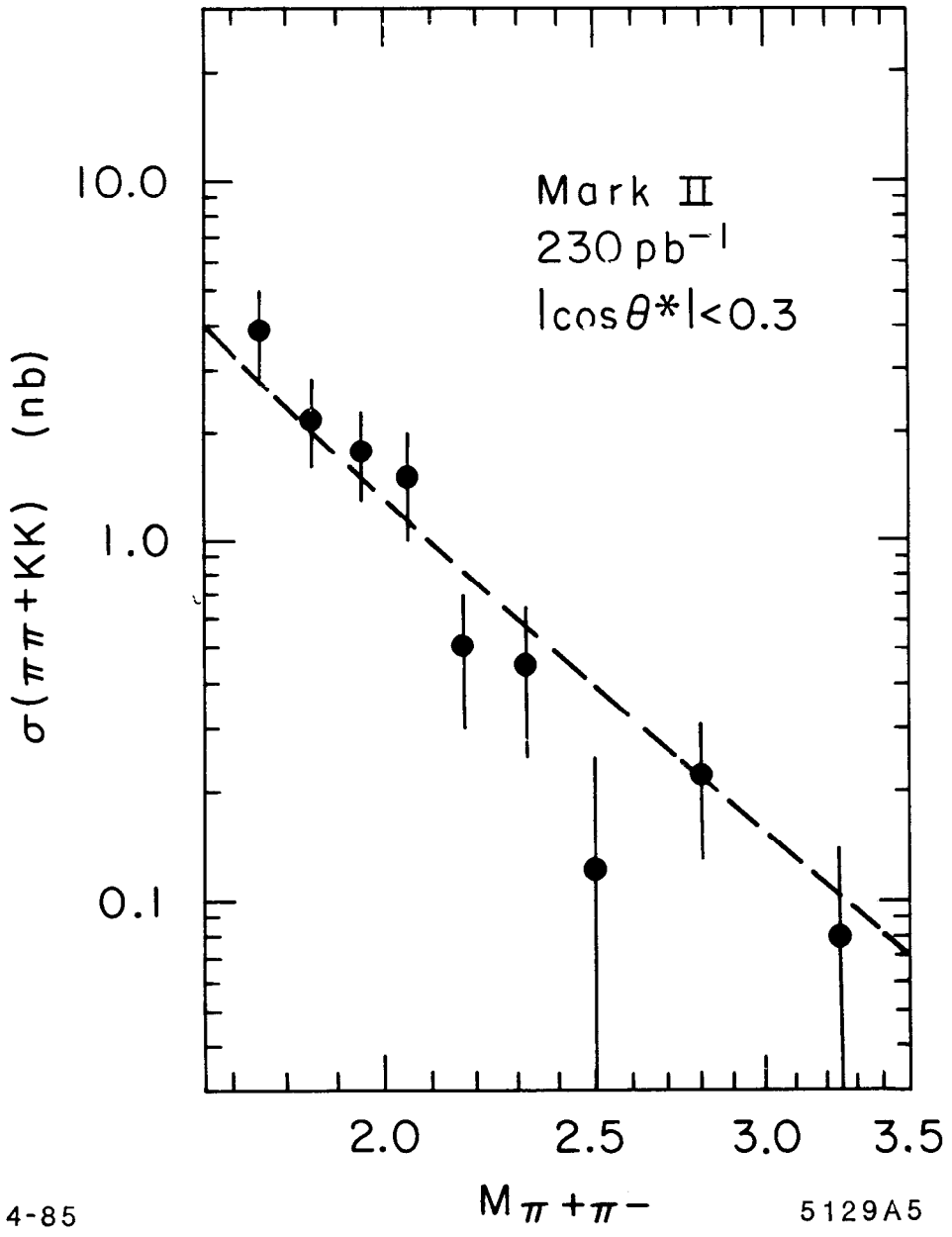
Mark II
230 pb⁻¹
|cosθ*|<0.3
10.0
1.0
0.1
σ(ππ+KK) (nb)
2.0
2.5
3.0
3.5
Mπ+π−
4-85
5129A5

Fig. 7

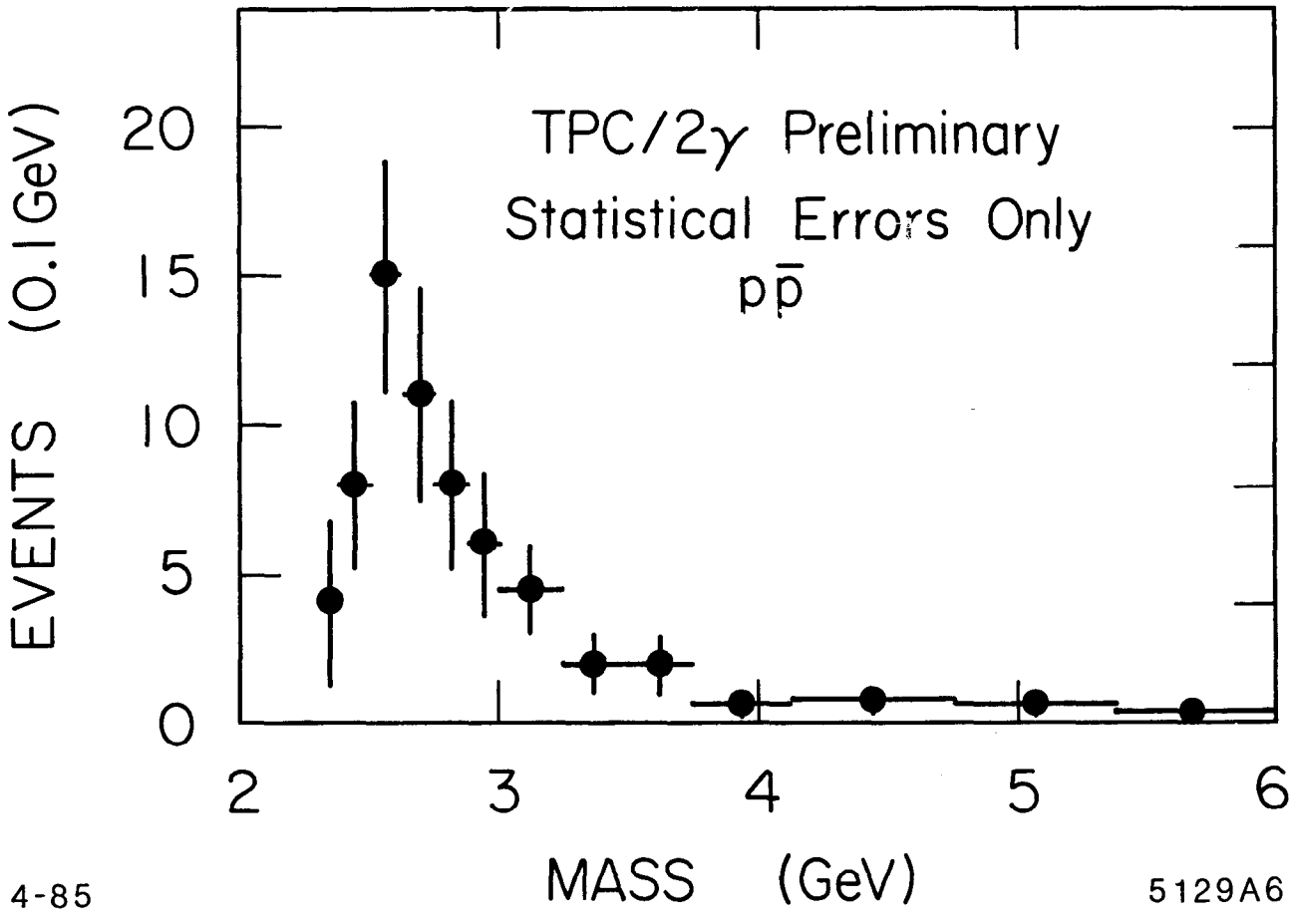
TPC/2γ Preliminary
Statistical Errors Only
pp̄
EVENTS (0.1GeV)
20
15
10
5
0
2
3
4
5
6
MASS (GeV)
4-85
5129A6

Fig. 8a

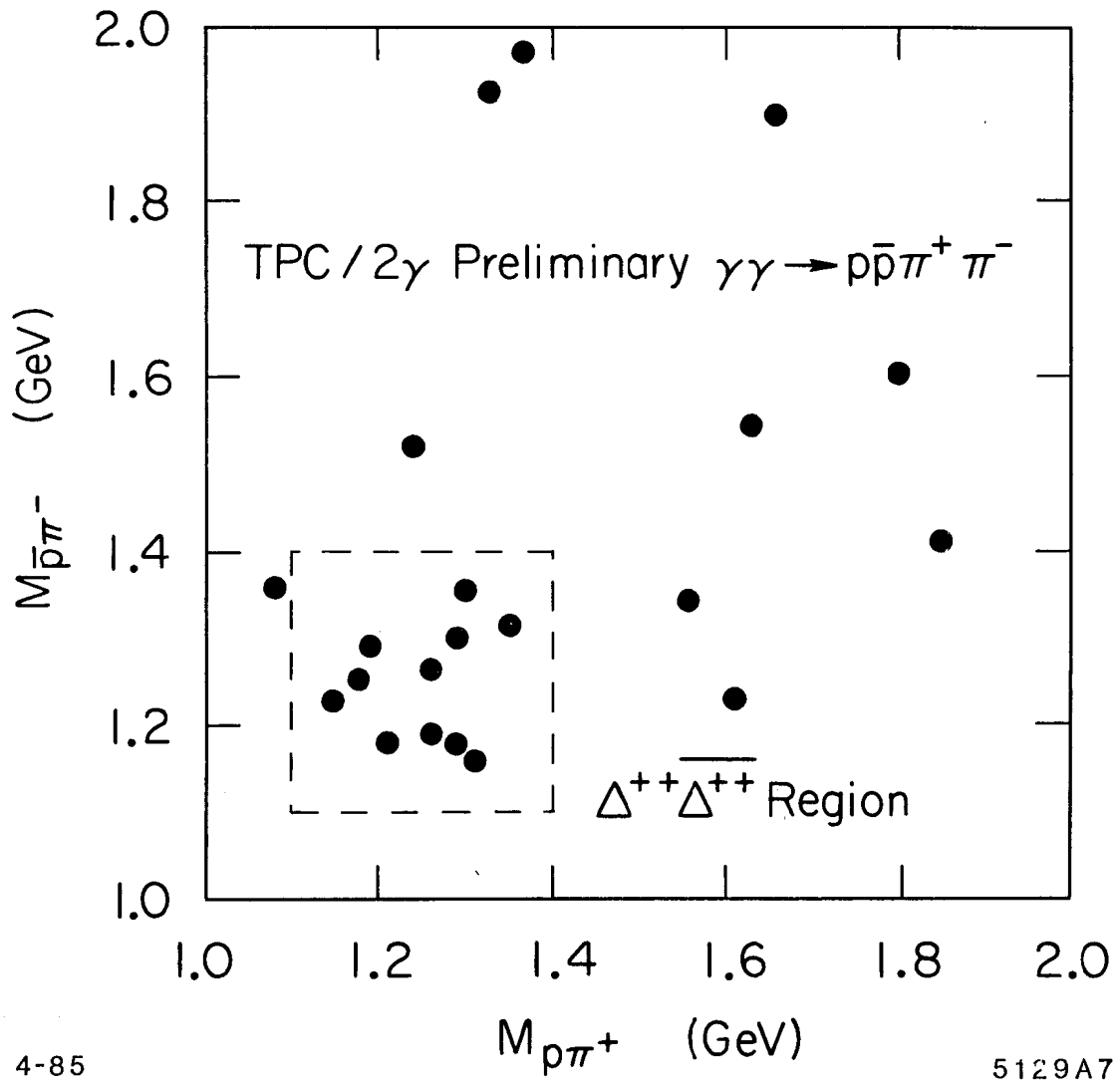
TPC / 2γ Preliminary γγ → pp̄π⁺π⁻
Δ⁺⁺Δ̄⁺⁺ Region
M p̄π⁻ (GeV)
M pπ⁺ (GeV)
2.0
1.8
1.6
1.4
1.2
1.0
1.0
1.2
1.4
1.6
1.8
2.0
4-85
5129A7

Fig 8b

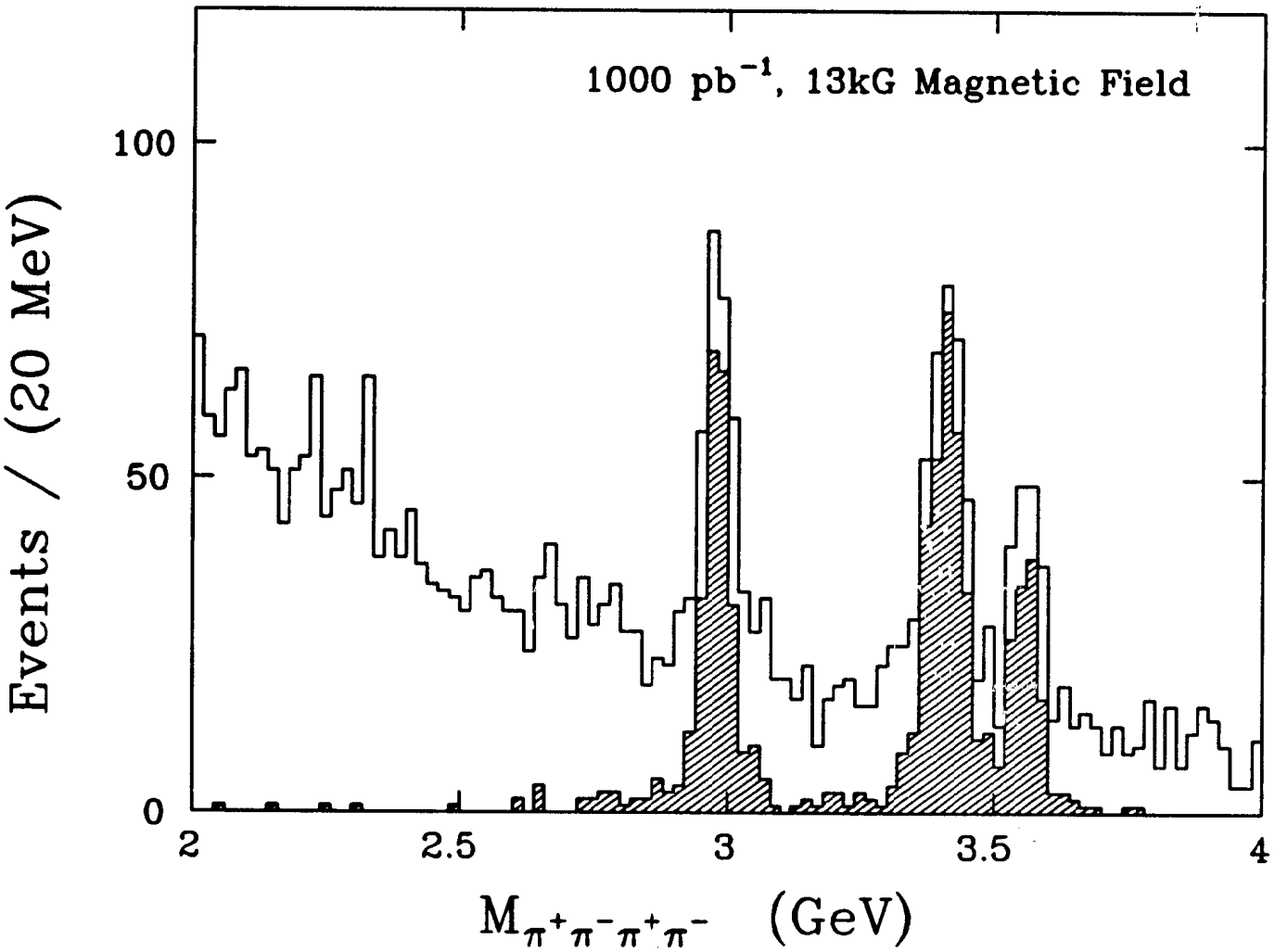

Monte Carlo

Fig. 9

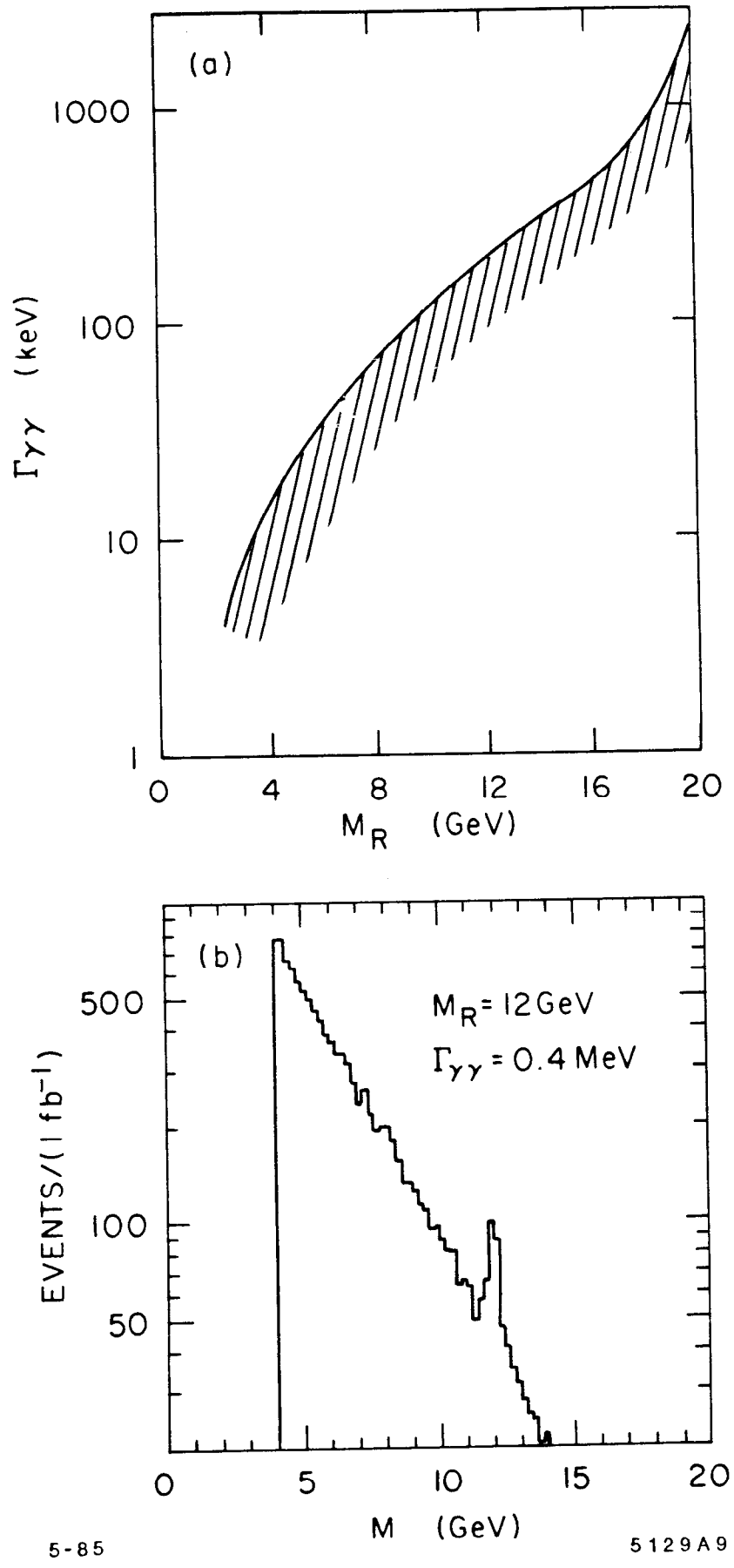
(a)
1000
100
10
1
$\Gamma_{\gamma\gamma}$ (keV)
0
4
8
12
16
20
M_R (GeV)
(b)
M_R = 12 GeV
$\Gamma_{\gamma\gamma}$ = 0.4 MeV
500
100
50
EVENTS/(1 fb^{-1})
0
5
10
15
20
M (GeV)
5-85
5129A9

Fig. 10

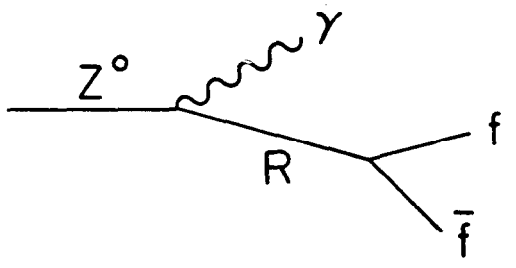

$$\Gamma(R \rightarrow \gamma\gamma) = \frac{\pi\alpha^2}{2}\frac{f_R^2}{M_R}$$

4-85 (a)

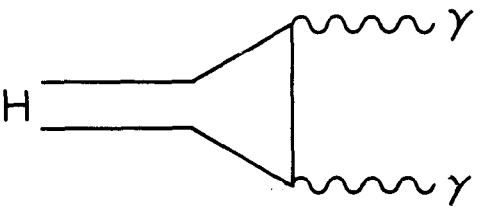

$$\Gamma(H \rightarrow \gamma\gamma) = \alpha M_H \sin^2\theta_W$$

(b) 5129A10

Fig. 11

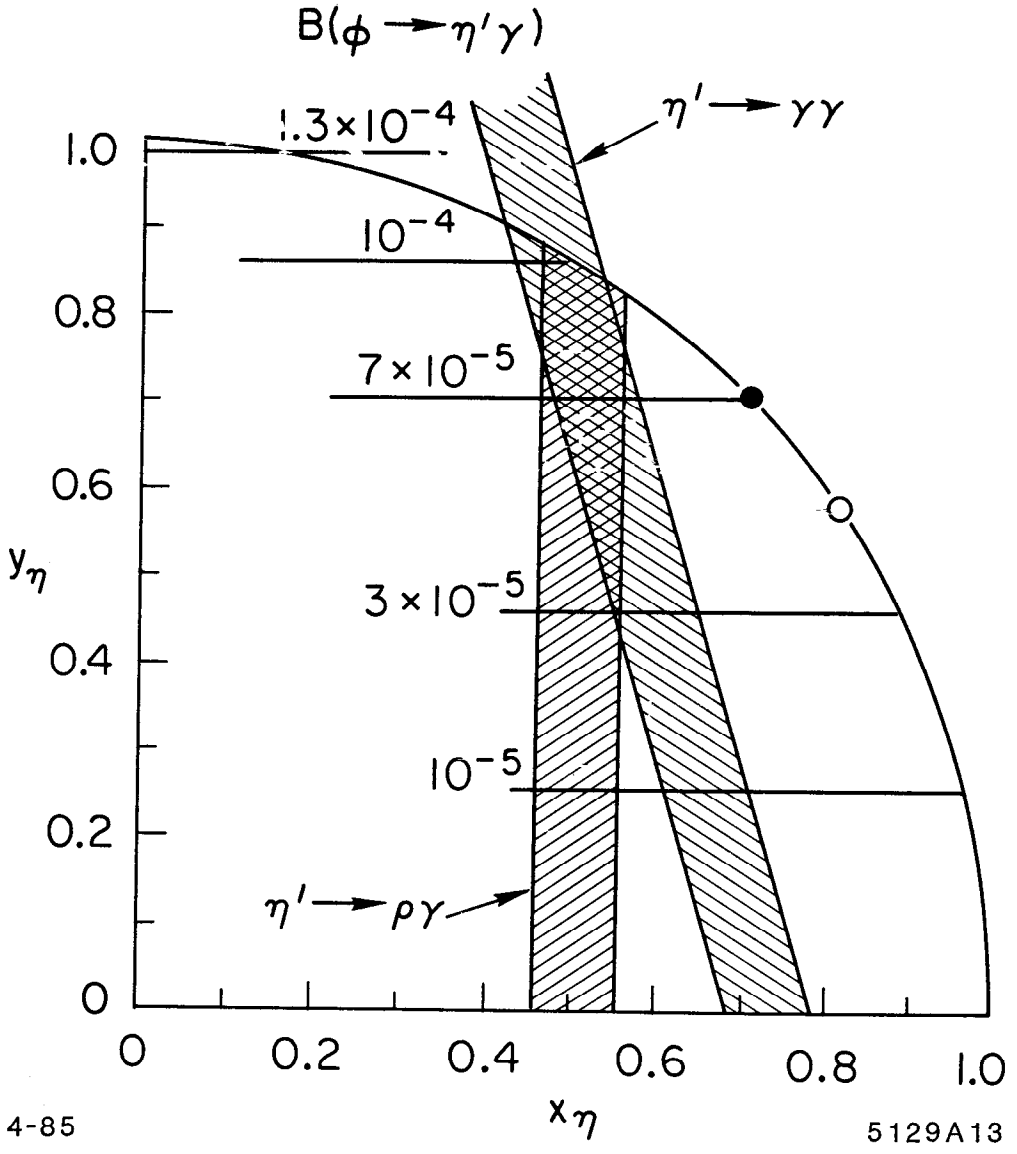
B(φ → η′γ)
1.3×10⁻⁴
η′ → γγ
10⁻⁴
7×10⁻⁵
3×10⁻⁵
10⁻⁵
η′ → ργ
1.0
0.8
0.6
0.4
0.2
0
yη
0
0.2
0.4
0.6
0.8
1.0
xη
4-85
5129A13

Fig. 12

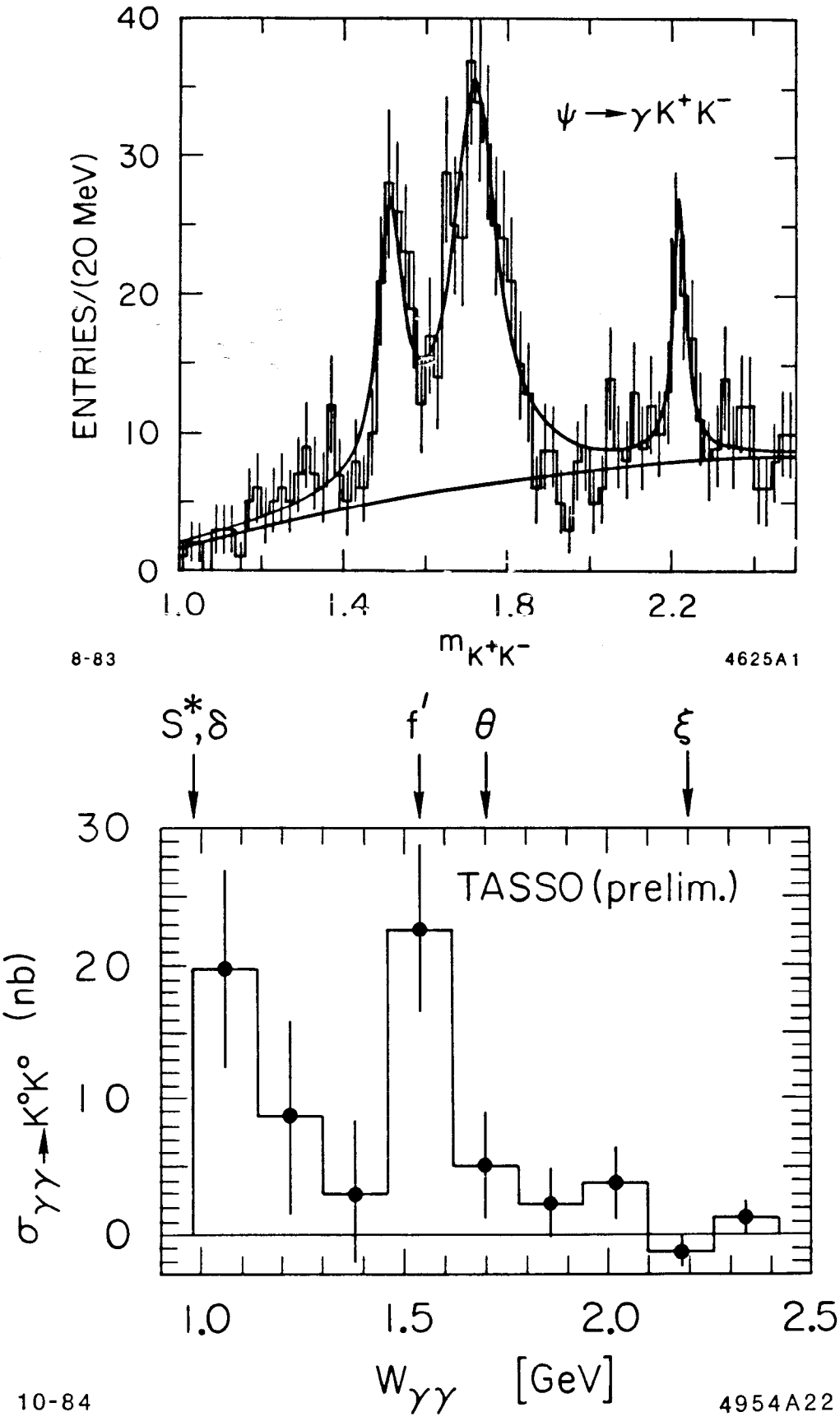
ψ → γK⁺K⁻
ENTRIES/(20 MeV)
40
30
20
10
0
1.0
1.4
1.8
2.2
m K⁺K⁻
8-83
4625A1
S*,δ
f′
θ
ξ
TASSO (prelim.)
σγγ→K°K° (nb)
30
20
10
0
1.0
1.5
2.0
2.5
Wγγ [GeV]
10-84
4954A22

Fig. 13

CHAPTER IV
HADRONIZATION DYNAMICS AT HILUM PEP: STUDIES OF THE BEHAVIOR OF THE FIELDS BETWEEN PARTONS

C. BUCHANAN

and

B. ANDERSSON, P. BARINGER, H.-U. BENGTSSON, M. DERRICK, J. W. GARY, J. HAUPTMAN, W. HOFMANN, P. KOOIJMAN, P. ODDONE, M. SHAPIRO, K. SUGANO, H. YAMAMOTO

CHAPTER IV.
HADRONIZATION DYNAMICS AT HILUM PEP: STUDIES OF THE BEHAVIOR OF THE FIELDS BETWEEN PARTONS

CONTENTS

I.1 INTRODUCTION

Thesis 1: Hadronization Dynamics, that is, the process as quark-gluon systems evolve into observed hadrons, is a very rich area to be probed. It is rapidly evolving into the study of the behavior of the fields between partons, what would be called "ColorField Dynamics" if in fact the hadronization process is a manifestation of non-perturbative QCD. There are many phenomena to be explored experimentally.

Thesis 2: Probing this infant field requires:

- Large data samples
- Powerful sensitive detectors (for particle identification and correlations amongst identified particles)
- Simple quark-parton-colorfield systems (e.g., created by electron-positron collisions with the center-of-mass energy appropriate for 0-2 major gluons)

HiLum PEP provides these.

Thesis 3: If HiLum PEP occurs (defined as 1.0 fb^{-1} per 2 years), five years from now our understanding of how non-perturbative QCD works will be much more detailed than it is now.

Thesis 4: If HiLum PEP does not occur, we may never gain this understanding. At best, about 1990, SLC and LEP with detectors with good particle identification will provide some such information. But that $E_{c.m.}$ may be too high for simple systems.

If we presume that QCD is in fact valid (and certainly something like it—with strongly confined and confining fields—is true), then Fig. 1 illustrates the paradigm in the area, with analogy made to the classical "scientific-method relationship" of Brahe, Kepler, and Newton. HiLum PEP will provide the detailed

information (Brahe) from which, in conjunction with the present models such as strings and QCD clusters, will emerge a detailed empirical picture of how colorfields behave (Kepler's Laws). This will provide the testing ground for theoretical attempts to develop techniques for calculating in the non-perturbative QCD regime (Newton).

In addition, understanding simple quark-gluon-colorfield systems in electron-positron interactions will also shape our understanding of lepton-hadron and hadron-hadron systems and will prepare us to understand interactions at higher energies.

Optimal center-of-mass energies range from approximately 20 to 50 GeV. At $E_{c.m.} = 29$ GeV, $\sim$ 12% of events are 3-jet; at 22 GeV, $\sim$ 6%. Below 20 GeV, there are very few 3-jet events and even the 2-jet events begin to lose their obvious axes. Above $\sim$ 50 GeV, the fraction of 4-jet events begins to complicate the samples.

Figures 2 and 3 illustrate pictorial aspects of "3-jet events" (involving one substantial radiated gluon) and "2-jet events" (the simplest system involving only a quark and an antiquark), respectively. Figures 2a, 2b, and 2c, respectively, depict a 3-jet event as described by: Independent Fragmentation, where each parton fragments independently of the others; String Fragmentation, where the final state hadrons emerge from the fragmentation of a narrow colorfield which passes from the quark through the gluon to the antiquark; and Cluster Fragmentation, where soft gluons are emitted which lead to clusters which fragment to the hadrons. As we will discuss later, experimental data in the regions between the jets favor the String or Cluster modeling.

Figure 3 is a naive space-time depiction of a "very simple" 2-jet event which attempts to illustrate some of the features which are presently accepted and some of those which we would like to learn about through HiLum PEP. It represents a "snapshot" of a quark-antiquark system, created by an electron-positron collision at $E_{c.m.}$ of 20-30 GeV, when the quark and antiquark are separated by about

1.0 fm: There is some sort of field stretched between the quark and antiquark which has a transverse dimension of about 0.2 fm, since $p_\perp$ is typically about 300-400 MeV/c, and a tension of about 1 GeV/fm. As the quark and antiquark have separated, they have radiated a series of semi-soft gluons, reasonably well calculated by leading log QCD. Then, via some mechanism, the energy density in the field is converted into quark-antiquark pairs, or sometimes somehow into diquark-antidiquark pairs, which form color-neutral systems which in turn ultimately evolve into the final state mesons and baryons. This much most people in the field would agree to.

A Cluster model[1,2,3] would then split the gluons into quark-antiquark pairs, combine them into color-neutral clusters, and fragment the clusters into hadrons via some prescription. A String model[4] would simply stretch a narrow color field from the quark to the antiquark, or in a more sophisticated version perhaps from gluon to gluon in the intermediate region, and then fragment the colorfield into hadrons, again via some prescription. We note also though that there is the possibility of significant energy density in the field away from the "central core" of the colorfield, which of course can lead to events that are more "dis-ordered" than in the simple models. Figure 3 also depicts baryon formation where diquarks are treated as "fundamental" objects (on the left) and where diquarks are formed in a two step process (on the right) with, in this case, a meson formed between the baryon and antibaryon.

There is much that can be learned empirically about the behavior of such systems: how orderly the fragmentation is, how are diquarks formed, how the field energy converts to quark-antiquark pairs, whether all production is from the central core of the field, etc. The Table on the following page provides a series of such questions, indicating where we have begun to learn answers and where HiLum PEP potentially will provide answers.

Questions Involving Fields Between Partons

Question	Already Known	Sources of Information with HiLum PEP
• Does core of colorfield follow major partons?	Yes, from 3-jet boosts	
• How often are various quark pairs ($u\bar{u}, d\bar{d}, s\bar{s}; c\bar{c}$?) formed in the field?	$u\bar{u} = d\bar{d} \simeq 4s\bar{s}$, from general rates	
• How are particles "pulled" in the colorfield?	Along colorfield, from $p\bar{p}$ $\theta^{jet}_{c.m.}$ study	
• Are diquarks formed directly, or in a 2-step process?	$p\bar{p}$ p_T correlations suggest 2-step process	
• When some particle is formed, what forms nearby?		Correlations amongst identified heavy particles
• How does field fragment longitudinally?		Very high z and D^*, F fragmentation functions
• How often are diquarks of various flavors and spins formed?		Strange baryon rates
• How do quark spins work?		Baryon spin correlations
• How ordered are events?		Baryon-baryon "repulsion" Λ polarization
• Are there mass/energy concentrations? Is p_T locally conserved? Is angular momentum locally conserved?		Λ polarization
• Are there non-nearest neighbor interactions?		Baryon-baryon "repulsion" $\Lambda\bar{\Lambda}/\Lambda$ rate, merging jets
• How do colorfields work when two major partons are nearby?		Merging jets

In order to derive these kinds of information, it is necessary to have large samples of data and good particle identification of heavy particles. Relatively heavy particles are needed because they preserve the momentum information of the fragmentation process better than light particles: heavy particles less frequently originate from the decays of resonances and even when they are from resonance decay they preserve the original momentum information of the resonance better than light particles. In this regard, pions are almost useless, kaons are marginal, vector mesons and baryons are reasonable. Further, in the studies involving correlations, high signal to noise (4/1) is needed in identifying the states used in order to avoid signal-background correlations. For these studies, weakly decaying baryons and ϕ mesons are useful but many vector mesons (e.g., K*'s and ρ's) have poor signal to noise and are not very useful. Overall, large sample sizes are needed both to provide rarer heavier particles and to provide correlation studies.

In Figs. 4-8, we provide some of the dE/dx, Λ, D and F meson signals from TPC and HRS to indicate the quality of the data which will be available. In particular, we note that the improved TPC detector now identifies Λ's with an efficiency of 15-20% and S/N of 4/1 which opens up a large range of strange baryon distribution and correlation studies. The improved TPC also now sees appropriate signals at the D and F masses, whereas HRS already had seen these signals.

I.2 Present Probes of Colorfield Dynamics (Track Record So Far)

In this section we review areas where we have already begun to form conclusions concerning some aspects of the behavior of the fields between partons, features which are more detailed than previous general information on hadronization processes. In the following section we will discuss other areas either (a) where we are beginning to gather information, but our understanding has not yet really

crystalized or (b) where we don't yet have relevant data samples, but anticipate that HiLum PEP will provide them.

The topics covered in this section are: (A) Topological studies of the particles between jets in 3-jet events, (B) Short range rapidity correlations between charged kaons, (C) Proton-antiproton distributions in the $p\bar{p}$ center-of-mass angle between the $p\bar{p}$ axis and the jet axis, and also proton-antiproton p_T correlations.

I.2.1 Topological Studies of 3-Jet Events

Figure 2 displays pictorially the behavior of the hadrons from the interparton field as described in "Independent Fragmentation".[5,6] Figure 2a illustrates a 3-jet event as described by an "Independent Fragmentation" model such as the original Field-Feynman description[7] in which each parton fragments into a jet of hadrons independent of the other partons. In this type of model, each of the three regions between the major partons is similar, exhibiting possible kinematic, but no dynamic differences. Figure 2b illustrates String Fragmentation (as in the Lund model) where a color string stretches from the SU3-triplet quark through the SU3-octet gluon to the SU3-antitriplet antiquark. In this very ordered model, the fragmentation of the color string directly populates the regions between the quark and the gluon and the gluon and the antiquark, but the quark-antiquark region can only be populated by hadrons with enough $p_\perp$ from the fragmentation process or from resonance decay to move from one of the other regions into it. Figure 2c illustrates a QCD Cluster model in which a shower of gluons is generated via perturbative and/or leading log QCD, the gluons then virtually fragment into quark-antiquark pairs, and color-singlet clusters are formed which fragment into the observed hadrons. Cluster modeling can vary in the degree of coherence or "orderliness"; Fig. 2c shows a model such as Webber's in which the ordering is almost as high as in the String model.

This type of study was pioneered by JADE[8] and elaborated by the TPC. Figure 9 shows the results of the present TPC study.[9] The most crucial part

of the result is that particles in the "1-3 region" – the region between jet 1 (the most energetic jet) and jet 3 (the least energetic of the 3 jets, typically the gluon jet) – have a higher population than region 1-2, even after taking their small kinematic differences into account. The only obvious interpretation for this is that the soft hadrons originate from sources which are Lorentz-boosted toward regions 1-3 and 2-3 and away from 1 2. There is no way in which Independent Fragmentation[5–7] can be varied to reproduce this. The Lund string model fits well.[4] Rather highly ordered cluster models such as Webber's[2] which build in a large amount of correlation between the clusters can also simulate the data.

I.2.2 Short Range Correlations Between Charged Kaons

In a highly ordered event, there is a short range correlation (SRC) between a produced particle and its neighbor. Pions exhibit such a correlation, but unfortunately their correlations are dominated by resonance decays (ρ's, ω's, ...). To look for SRC from the actual fragmentation process, we must use heavier particles.

Figure 10, from the TPC,[10] displays the SRC in rapidity for charged kaons, selected with rapidity between 1.5 and 4.0. Then the density of opposite-charged kaons minus the density of same-charged kaons is plotted. Figure 10 shows a long range correlation due to primary charm and strange quark production and also a short range correlation. Calculations indicate that about 20% of the SRC comes from ϕ and F meson decay, the rest coming from the fragmentation or hadronization process. This primary probe yields the information that the fragmentation SRC length is about 1.0 units of rapidity. Though this study provides fundamental information on the hadronization process, it does not discriminate amongst sensible models: The dotted line is the Webber cluster model, the solid line is the Lund string model, and the dashed line, added for contrast, is the Lund string model with charmed primary quarks turned off. Both the Webber model and the normal Lund model are compatible with the data at its present level.

I.2.3 Proton-Antiproton Correlations

Baryon-baryon correlations are a potentially very rich field of information on colorfield behavior, which in fact appears to discriminate between string modeling and simple cluster modeling Figure 11 depicts three different models of baryon-antibaryon production. Figure 11a shows Lund-string-type structure incorporating fundamental diquark-antidiquark production. Figure 11b also represents string modeling but with the diquark and antidiquark each formed in a two-step process yielding, in the case shown, a meson formed in between. Figure 11c shows cluster modeling in which a baryon-neutral cluster is formed which then decays to a baryon-antibaryon pair.

In present cluster models, each cluster is decayed isotropically in its own rest frame. Thus in the proton-antiproton center-of-mass system, the angle between the proton-antiproton axis and the jet axis would be isotropic (dashed line of Fig. 12a). By contrast, in the Lund string model, the diquark and antidiquark are pulled apart by the string tension, thereby causing a peaking of the proton-antiproton axis along the jet (colorfield) axis (solid line of Fig. 12a). When these models are corrected for acceptance effects associated with the TPC detector, the behavior predicted in Fig. 12b are obtained.[11] The data agree nicely with the string model and disagree with the isotropically decaying baryon-neutral cluster model at the 98% confidence level. Thus there seems to be some mechanism which pulls the hadrons along the jet-axis.

The correlation between proton and antiproton in p_T relative to the jet axis has also been studied. The results are less "ordered" than the simple string modeling of Fig. 11a in which the p_T of the baryon is largely compensated locally by the p_T of the antibaryon. This correlation would be most pronounced analyzing p_T out of the event plane since the p_T correlation effect in the plane would be mixed up with the Lorentz boosts of the strings. In Fig. 13, the

correlation coefficient

$$\alpha_{out} \equiv \frac{\langle p_{out,\bar{p}} \cdot p_{out,p} \rangle}{\langle p_{out}^2 \rangle}$$

and the analogously defined α_{in} are displayed.[11] The most striking result is that for α_{out} there is a slightly positive correlation, not the negative result expected if the events are highly ordered with local p_T compensation and simple direct diquark- antidiquark formation (Fig. 11a). In Fig. 13a the value of α_{out} predicted by the Lund model is plotted against the fraction of time that a meson is created between the baryon and antibaryon if the diquarks are formed in a two-step process. The results are compatible with the data if an intermediate meson is created in more than about 50% of the cases.

Summary of Present Probes of Colorfield Behavior

- We have learned that the soft hadrons between jets in 3-jet events originate from sources that are Lorentz-boosted toward the quark-gluon and antiquark-gluon regions and away from the quark-antiquark region. This behavior is incompatible with Independent Fragmentation models but it agrees nicely with string modeling and the more correlated versions of cluster modeling.

- From correlations amongst charged kaons, we have learned that the short range correlation length for the fragmentation process is about one unit in rapidity.

- From studies of the proton-antiproton center-of-mass angle between the baryon-antibaryon system and the jet axis, we have learned that the hadrons are somehow pulled along the jet (colorfield) axis in a manner compatible with the tension of a string-like model and incompatible with the istropic decay of baryon-neutral cluster models.

- These present studies, interesting and informative as they are, barely scratch the surface of what can be done and learned. Also, we are just beginning

to learn how to ask detailed questions of how the fields between partons behave. The reader is invited to speculate on the types of interesting information which can be learned concerning boosted hadron sources, the "orderliness" of events, diquark formation, local p_T compensation, etc., from an order of magnitude increase in sample size in these present studies plus similar large sample correlation studies in rapidity, p_T, center-of-mass-angle, etc. amongst $\Lambda\bar{\Lambda}$, $\Lambda\bar{p}$, ΛK, etc!

I.3 Selected Emerging Areas of Hadronization Studies for HiLum PEP

I.3.1 Bose-Einstein Correlations

A very interesting probe of small distance behavior is the "Bose-Einstein effect" in which symmetrization of the wave-functions for identical bosons results in an enhancement in the number of boson pairs when the two bosons have very similar momenta. Fig. 14 demonstrates that such an effect occurs for pions in the TPC data.

The "classical tradition" in the field has been to interpret these sorts of data in terms of a size of the source emitting the pions.[12] Interpreted in this way, we find the emitting source to be about 0.65 fm with some suggestion (Fig. 15) that the source is longer along the direction of the jet axis.[13]

Recently a very interesting new interpretation of the effect has emerged using the Lund string model.[14] In this approach, it is recognized that the space-time picture for emitting two idential pions in one configuration and in the particle-interchanged configuration are different (Fig. 16). When these configurations are incorporated into a properly symmetrized matrix element, a correlation dependence on the difference in area of the two configurations emerges, yielding a

symmetrized matrix element of

$$M = \frac{1}{\sqrt{2}}\left(e^{i\xi A_{12}} + e^{i\xi A_{21}}\right) \qquad \text{or}$$

$$|M^2| = \frac{1}{2}\left[e^{-2Im\xi A_{12}} + e^{-2Im\xi A_{21}} + 2\cos\{Re\xi(A_{12} - A_{21})\}e^{-Im\xi(A_{12}+A_{21})}\right]$$

Since the Lund string model has a constant tension of about 1 GeV/fm and therefore a linearly rising confining potential between the separating quark and antiquark, in this model this area difference corresponds to a Wilson loop integral. This in turn leads to the identifications of

$$Re\ \xi = \frac{1}{K} \quad \text{where K is the string tension} \sim 1\ \text{GeV/fm} \sim .2\ \text{GeV}^2$$

$$Im\ \xi = \frac{b}{2} \quad \text{where b describes the Lund symmetrized fragmentation and is} \sim 1.0\ \text{GeV}^{-2}\ .$$

Then, within the assumption that pion-pion correlations arising from resonance decay are approximately properly treated by phase-space, this approach makes a parameter-free prediction of the Bose-Einstein correlation. The result is shown in Fig. 17 and agrees remarkably with the data.

Summary of Bose-Einstein Correlations

This clearly is an area calling for more theoretical consideration and for larger, more sensitive data samples in order to study the correlation behavior in more detail for low momentum differences between the pions.

I.3.2 Light and Heavy Quark Fragmentation and Jet-Tagging

Longitudinal fragmentation (e.g., in an e^+e^- interaction, the fraction of the momentum or energy of a primary quark that goes into the meson containing that quark) and how it depends on the mass of the quark provides very important information on the hadronization process. However, to avoid resonance decays and non-primary fragmentation effects, we need either to look at very energetic particles at high $z = E_{hadron}/E_{beam}$ or at a fundamental particle such as the D^* which will almost always come directly from a primary charm quark for $z \geq .4$. At very high z, simple dimensional counting would yield a fragmentation function of the form

$$F(z) \sim (1-z)^2$$

Each model (strings, clusters) would potentially modify this somewhat. Also, the higher twist effect of direct meson production at the virtual photon vertex would add a term of μ^2/Q^2 to the fragmentation function where μ^2 is expected to be about 0.1 to 1.0 GeV^2.

In addition, the expected form for the mean fragmentation differs with different types of models:

$$\langle z \rangle \sim \left(1 - \frac{m_0}{m_q}\right)^2 \left\{ \begin{array}{l} \text{for the string model using the Lund} \\ \text{symmetric fragmentation function.} \end{array} \right.$$

versus

$$\langle z \rangle \sim \left(1 - \frac{m_0'}{m_q}\right) \left\{ \begin{array}{l} \text{where, roughly, the cluster} \\ \text{mass controls } m_0'. \end{array} \right.$$

The present status is displayed in Figs. 18 and 19. Figure 18 shows the very high z data from HRS[15] where its extremely good momentum resolution ($\delta p/p^2 \sim .1\%$ GeV/c) is very useful. Indeed the data approximately follow $(1-z)^2$ from $z \sim .6$ to $z \sim .9$ to .95 where the statistics in the present sample drop toward zero. For $z < .6$, the dependence is $\sim (1-z)^3$ reflecting effects of resonance decay and non-primary fragmentation. Within present statistics,

the Lund model follows the data rather well.[16] However, cluster models drop tend to somewhat below the data at very high z; this is possibly related to the non-isotropy result of the proton-antiproton axis (see Section IV.2.3) relative to the jet-axis, presumably implying the need to include a non-isotropic mechanism favoring greater longitudinal momentum in cluster decay models.

Figure 19 shows the data for D^* fragmentation from HRS and TPC[17,18] (there are similar results results from TASSO, JADE, and ARGUS), along with the present modeling of Webber[2] and Lund.[16] In each case, the models have been tuned to fit low z data on pions, kaons, etc. (with of course additional parameters to handle secondary processes), and then used to predict the D^* spectrum. There are differences between the model predictions, but the present level of data cannot discriminate between them or, alternatively, force modifications in either of them.

We also display in Fig. 20 the spectrum of F mesons as measured by HRS.[19] It resembles that of the D^*-meson, with the exception that at low $z \sim .2$ to .3 there appears to be more F production than present modeling of primary charm production plus "feed-down" from primary b-quarks would provide (dashed line).

An area pioneered by HRS which is related to high z and D^* fragmentation studies is that of "jet-tagging".[15] The HRS group has used its high z particles to tag events with primary light quarks (u,d,s) and the reconstructed D^*'s to tag primary charm quarks. They obtain 200-300 events of each with purities of about 90%. This allows, presently with low statistics, the study of the composition of the partner jet in each case.

Summary of Light and Heavy Quark Fragmentation and Jet-Tagging Studies

All four of the studies discussed (high z behavior, fragmentation into D^*'s, F production, and jet-tagging) are in the regime where an order of magnitude in data (that is, statistical uncertainties a factor of 3 smaller than at present) would provide additional information on the hadronization process and constrain the form and/or parameters of models as they are tuned to agree with the data.

I.3.3 General Comments on Lambda Production

Perhaps the most useful particle in studying the behavior of the fields between partons is the lambda.* This is because:

- It is heavy and therefore reflects fairly accurately the initial fragmentation momentum.
- It is strange and it is a baryon, allowing the study (simultaneously?) of strangeness and baryon correlation effects.
- It is polarizable and the polarization is measurable in its abundant proton-pion decay mode.
- It has relatively good detection efficiency over a wide kinematic range and high signal-to-noise which is required for useful correlation studies.
- It is produced fairly copiously both from primary charm quarks and also from the fragmentation of the field between the primary quarks. Fairly high purity samples from these sources can be separate by, for example, a rapidity cut.

Approximately 0.2 Λ or $\bar{\Lambda}$ occur per multi-hadronic event at PEP. (We will henceforth use the terminology of "Λ" to include both Λ and $\bar{\Lambda}$.) The HRS detector, without using proton identification, reconstructs 8% of these (including the branching fraction to $p\pi^-$), with a width of $\sim$ 1.5 MeV and a signal to noise S/N of $\sim$ 2/1. The TPC detector, which uses some loose dE/dx information on the protons, in its pre-1984 sample reconstructed 6% with a width of $\sim$ 6 MeV and S/N $\sim$ 4/1. The TPC's new data beginning in Fall 1984 is strikingly better: tuning the cuts to give the same S/N $\sim$ 4/1, it now reconstructs 17% of the Λ's (almost a factor of 3 more!) with width of $\leq$ 3 MeV. Thus, in a canonical HiLum PEP sample of 1000 pb^{-1} or 400,000 detected multihadronic events, HRS will reconstruct $\sim$ 6000Λ's (including $\bar{\Lambda}$'s) and TPC $\sim$ 14,000.

---

* B. Andersson of Lund has referred to the lambda as "God's gift to humanity." This may be a little too sweeping in its scope, but it does capture some of the feeling of the workers in the field.

Figure 21 displays a Monte Carlo distribution (from the Lund model) of Λ's from various sources versus rapidity relative to the event jet axis. By naively making a simple cut at rapidity of 1.7, the Λ's divide into two samples:

Rapidity < 1.7 "Color Field Fragmentation"		Rapidity > 1.7 "Charm Enriched"
70% of Λ's		30% of Λ's
50%	Direct from Colorfield Fragmentation	35%
$\lesssim$ 10%	From Primary Charmed Quarks	40%

In the following two sections, we will focus on two of the most important probes using Λ's: Λ polarization as a probe of interparton field behavior and the number and uses of reconstructed strange baryons to which identified Λ production provides an entree. Uses of lambda production will also be touched on in our discussions of baryon-baryon correlations, charmed baryon studies and in the comparison of gluon fragmentation with quark fragmentation.

I.3.4 Lambda Polarization

A very interesting probe of the behavior of the field between partons which requires highly ordered events is the polarization of lambdas when the lambda has a significant p_T relative to the jet axis.

The model which produces Λ polarization is shown in Fig. 22.[4] The argument is as follows: The mass of a quark-antiquark pair made from the colorfield must come from a length of string of comparable energy. Thus for 300 MeV mass strange quarks and a string tension of 1 GeV/fm, the s and $\bar{s}$ are actually created with a separation of $\sim$ 0.6 fm and in a definite direction relative to the colorfield direction from the primary antiquark to the primary quark. If the s and $\bar{s}$ have equal and opposite p_T of 500 MeV relative to the jet axis, then they have a total

orbital angular momentum of $\simeq 1.5\ \hbar$. If angular momentum is locally conserved, then the spins of the s and $\bar{s}$ will oppose the orbital angular momentum.

If, as is shown, the s-quark then combines with a ud spin-zero diquark to form a Λ, then the s-quark spin determines the Λ spin and the Λ tends to have a p_T correlated with the p_T of the s-quark. Thus, Λ's made in this manner at $p_T \sim 0.5$ to 1.0 GeV/c should exhibit a measurable polarization in their decay to $p\pi^-$.

Note that this effect requires at some level several forms of order in the event:

- An ordered colorfield direction.
- No local mass/energy concentrations.
- Local angular momentum compensation.
- Local p_T compensation.
- The spin of the s-quark determines the spin of the Λ.
- The p_T of the s-quark determines the p_T of the Λ.

The result from a 400 Λ sample of the TPC in pre-1984 data[20] is shown in Fig. 23. A very approximate modeling of the expectation from the Lund string model is also shown. From $p_T = 0.6$ to 1.5 GeV, there is a 2.0 standard deviation effect in the proper direction.

Summary of Lambda Polarization

- If the present suggestion of an effect is true, HiLum PEP will produce greater than a 10 σ effect, with some p_T bin-to-bin discrimination.
- If polarization is confirmed, cluster models would have to find a mechanism.
- If no polarization is found, then one (or more) of the Lund string mechanism requirements must be untrue.
- Either way, something interesting has been learned about the behavior of the field between partons.

I.3.5 Strange Baryon Production

Lambda reconstruction of high efficiency and high signal-to-noise opens up a large and very fertile area of study of strange baryon production dynamics. Figure 24a displays strange baryon production in an event which is highly ordered in the colorfield and presumes fundamental diquarks. Figure 24b shows a more disordered event (see Section IV.3.6 on baryon-antibaryon correlations) in which diquarks are made in a two step process, which leads to effects such as a meson being created between the baryon and antibaryon and also to the possibility of the diquark spin being different from the antidiquark spin.

The expected rates and signal-to-noise for various strange baryons for the TPC at HiLum PEP are given in Table I. Note that the strange baryon samples, which couple to the high lambda efficiency, are a factor of $\sim$ 40 greater than the present pre-1984 data. Figure 25 displays some of the expected signals from Monte Carlo simulation of HiLum PEP.[20]

Table II displays the diquark and quark content of various strange baryons, presuming that diquarks are fundamental objects as shown in Figure 24a. Thus, measurement of the rates of various strange baryons probes the probability for diquarks of various flavors and spins, or shows that such a parametrization is too simple. This in turn provides information on the suppression of various kinds of diquarks and thereby, presumably, on how they are formed. We might note, for example, that the 5 Ω^- mesons presently detected indicate that the (partially theoretically derived) value of $(ss)_1$ presently used in the Lund model is at least an order of magnitude to low.

Table I. Strange Baryons with TPC at PEP

		< Fall 1984 77 pb^{-1} 30,000 events			HiLum 1000 pb^{-1} 400,000 events		
Particle	# Occurring Per Event	Acceptance (Including Decay)	# Seen (Real)	S/N	Acceptance (Including Decay)	# Seen (Real)	S/N
$p^{\pm}$	.6	.12	2100	20/1	.12	28,000	20/1
$\Lambda/\bar{\Lambda} \rightarrow p\pi$	.2	.06	360	4/1	.17	14,000	4/1
$\Xi^- \rightarrow \Lambda\pi$	.025	.022	17	1/1	.06	600	3/1
$\Sigma^{*\pm} \rightarrow \Lambda\pi$	.07	.018	40	.16/1	.05	1500	.16/1
$\Xi^{*o} \rightarrow \Xi\pi$	?.01?	.025	–	–	.07	280	3/1
$\Omega^- \rightarrow \Lambda K$	.01	.016	5	10/1	.045	180	20/1

Note: Because of the increased Λ efficiency, the HiLum strange baryons are ~ 40 times larger than the present samples.

Table II. Di-Quark Probabilities

Parameter	Approx. Lund Value	Cluster Value	Relevant Particle
s/u	$-.3$ ($\Rightarrow$ s/all = .13)		$K^{\pm}$
$(qq)_0/q = (ud)_0/q$	$-.09$	**Set by**	p, Λ
$(us)_0/(ud)_0$	$-.06$	**Phase-Space**	Ξ^-, Σ
$(ud)_1/(ud)_0$	$-.15$	**of**	$\Delta, \Sigma^{*\pm}$
$(us)_1/(ud)_0$	$-.01$	**Cluster Mass**	Ξ^{*o}
$(ss)_1/(ud)_0$	$-.0005$		Ω^-

p	$(uud)_{1/2}$	$(ud)_0 u + (ud)_1 u$	$\simeq$	$(ud)_0 + u$
Λ	$(uds)_{1/2}$	$\frac{2}{3}(ud)_0 s + \frac{1}{3}(us)_0 d + (us)_1 d$	$\simeq$	$(ud)_0 + s$
Ξ^-	$(dss)_{1/2}$	$(ds)_0 s + \frac{1}{3}(ds)_1 s + \frac{2}{3}(ss)_1 d$	$\simeq$	$(ds)_0 + s$
$\Sigma^{*\pm}$	$(qqs)_{3/2}$	$\frac{8}{3}(qq)_1 s + \frac{16}{3}(qs)_1 q$	$\simeq$	$(qq)_1 + s$
Ξ^{*o}	$(uss)_{3/2}$	$\frac{8}{3}(us)_1 s + \frac{4}{3}(ss)_1 u$	$\simeq$	$(us)_1 + s$
Ω^-	$(sss)_{3/2}$	$\frac{4}{3}(ss)_1 s$	$\simeq$	$(ss)_1 + s$

Note: Lund Values may be 3-10 $\times$ low for $(us)_1/(ud)_0$ and $(ss)_1/(ud)_0$.

Summary of Strange Baryon Production

The samples with HiLum PEP of the various identifiable strange baryons ($\Lambda, \Xi^-, \Xi^{0*}, \Omega^-$ with high S/N; possibly $\Delta^{++}, \Sigma^0, \Sigma^{\pm}, \Sigma^{*\pm}$ with low S/N) will establish the relative probabilities for diquarks of various flavors and spins, or show that such a parametrization is too simple.

I.3.6 Baryon (Anti)Baryon Correlations

Perhaps the most interesting probes of interparton field behavior will come from baryon-baryon correlations,[11,21,22] especially involving strange baryons. Baryons are potentially useful because they are heavy and therefore preserve fragmentation momentum information; they also allow studies which probe diquark formation and the "orderliness" of events. Table III gives the rates, S/N, and number of events detected for various combinations.

Note in particular:

- HiLum PEP will provide $\sim$ 1000 detected events <u>each</u> of $p\bar{p}$, $\Lambda\bar{p}$, $\Lambda\Lambda$. (Because of increased Λ identification efficiency, the HiLum $\Lambda\bar{\Lambda}$ sample will be $\sim$ 100 times the present sample!)
- The correlation samples of Λ plus another strange baryon will be $\sim$ 10-100 events.
- Three-body correlation data such as $\Lambda\bar{p}K^+$ will be $\sim$ 100 events.

The types of correlation studies pursued thus far include

- Two-particle rates.
- Rapidity.
- θ^* (the angle in the baryon-baryon center-of-mass between the baryon-baryon axis and the jet axis).
- p_T
- Other?

Table III. Baryon-(Anti)Baryon Correlation Samples with TPC

		< Fall 1984 77 pb^{-1} 30,000 events			HiLum 1000 pb^{-1} 400,000 events		
Particle	# Occurring Per Event	Acceptance (Including Decay)	# Real Seen	S/N	Acceptance (Including Decay)	# Real Seen	S/N
$p\bar{p}$	.15	.022	100	10/1	.022	1,300	10/1
$\Lambda/\bar{p}$	?.10?	.013	?~40?	?~8/1?	.03	?1,200?	10/1
$\Lambda\bar{\Lambda}$	.04	.008	10	6/1	.06	1,000	10/1
$\Lambda\overline{\Xi^-}$	?.005?	–	–	–	.02	?40?	–
$\Lambda\overline{\Xi^{*o}}$	?.002?	–	–	–	.02	?10?	–
$\Lambda\bar{p}K^+$	?.01?	–	–	–	.02	?100?	–

Note: Because of the increased Λ efficiency, the HiLum strange baryons-strange baryon samples ($\Lambda\bar{\Lambda}, \Lambda\Xi^-, \Lambda\Xi^{*o}$) are $\sim$ 100 times larger than the present samples.

From the present correlation studies (see Section IV.2), we have learned:

From K^+K^- rapidity correlations	The fragmentation correlation length is about 1.0 units of rapidity
From $p\bar{p}$ θ^* distribution	Particles are "pulled" along the jet axis.
From $p\bar{p}$ p_T correlation	There is *not* a strong local p_T compensation for the proton-antiproton case. This may indicate a two-step diquark formation process.

All these studies will of course be performed on all the various 2-baryon combinations. Of especial interest are the $p\bar{p}$, $\Lambda\bar{p}$, and $\Lambda\bar{\Lambda}$ samples which are all large and allow comparable studies of nonstrange-nonstrange, strange-nonstrange, and

strange-strange baryon correlations.

Figure 26 displays a Monte Carlo HiLum study for $\Lambda\bar{p}$ and Λp rapidity correlations using the Lund string model. In this simulation, we have demanded either a proton or antiproton with rapidity between -1.0 and -0.2 and then plotted the rapidity of the Λ's (not $\bar{\Lambda}$'s) for each test particle. We note that the presence of an antiproton enhances the probability of a Λ whereas a proton reduces the Λ probability.

We find that the $\Lambda\bar{p}$ correlation is somewhat broadened by allowing a looser 2-step diquark formation rather than forming "fundamental" diquarks. This is approximately a 3 standard deviation effect in the maximal bin. This, however, is a difficult study since there is not a "known distribution" to which to normalize.

The Λp distribution demonstrates a baryon-baryon "repulsion effect" characteristic of a highly ordered structure. For example, if a string forms a baryon at one "break", the next nearest baryon must be two "breaks" away. As depicted, this is a 3-4 standard deviation effect. Less-ordered models, of course, would show less of an effect.

Correlations of Λ's with other spin-1/2 and spin-3/2 strange baryons (detected samples of 10-100) provide information on whether a spin-1 diquark can be correlated with a spin-0 diquark (a dis-ordered phenomenon). (See Fig. 24b.)

Summary of Baryon-Baryon Correlations

The high-statistics samples of HiLum PEP ($\sim$ 1000 each of $p\bar{p}$, $\Lambda\bar{p}$, and $\Lambda\Lambda$; 10-100 of Λ with a higher mass strange baryon; 3-particle correlation data such as $\sim$ 100 events of $\Lambda\bar{p}K^+$) provide very delicate probes for studying fragmentation lengths, "pulling" of particles in the colorfield, studies of order or disorder, etc.

I.3.7 Charmed Baryon Studies

A HiLum sample of 400,000 $q\bar{q}$ events will produce $\sim$ 140,000 $c\bar{c}$ events in which essentially all the charmed hadrons produced will contain the primary c or $\bar{c}$ and therefore have relatively high rapidity or momentum. If 15% of the charmed hadrons are baryons, then there would be $\sim$ 40,000 charmed baryons, most of them ($\sim$ 30,000?) at high rapidity. This presents a great potential not only for studying "normal" charmed baryons, but also singly and doubly strange baryons, e.g., csd and css. However, the branching fraction into any particular exclusive decay mode is small ($\sim$ 1-2%?), which represents a formidable challenge in attempting actually to reconstruct the original state. For example, 5000 of the 14,000 Λ's reconstructed in a sample of 400,000 events will have rapidity greater than 1.7; of the 5000, 2000 will be from primary charmed quark states. However, linking these to the 30,000 high rapidity charmed baryons is not easy.

Several indirect or inclusive approaches are available to monitor charmed baryon rates. Examples are:

- The $\Sigma^{*+} - \Sigma^{*-}$ rate difference, displayed in Fig. 27 for a HiLum sample, monitors Λ_c production via the decay diagram shown in the same figure. There is a measureable effect of several standard deviations.
- $\Lambda\bar{\Lambda}$ production with high rapidity difference ($\Delta y > 4$) monitors $c\bar{c}$ events where both the c and the $\bar{c}$ have fragmented into charmed baryons.
- The high rapidity Ξ^- rate monitors the singly strange charmed baryon production (in the present Lund model, csd-spin 1/2 decays to Ξ^- 40% of the time) and similarly with Ω^- for doubly strange charmed baryons (css-spin 3/2 decays to Ω^- 60% of the time). The present TPC samples of 17 Ξ^- and 5 Ω^- suggest rather high production rates for these strange charmed baryons. See Section IV.3.8 for more comments on the last two topics.

It is probable, but not certain, that the TPC will be able to see a Λ_c signal

in its HiLum sample.[20] Figure 28 displays the Lund modeling for $\Lambda_c \rightarrow pK^-\pi^+$ with $p(pK\pi) > 8$ GeV and $p_p > p_K > p_\pi$. There is a signal above background of 100 $\pm$ 16 events. However, two modification which tend to cancel should also be incorporated: (a) The modeling uses a branching fraction for $\Lambda_c \rightarrow pK\pi$ of 7.5% compared with the Particle Data Table value of $2.2 \pm 1.0\%$. (b) The Lund modeling is probably low by a factor of 2 or more on charmed baryon production rate. Reconstructing Λ_c's would establish the charmed baryon rate, yield information on whether the $(ud)_0$ diquark probability depends on the mass of the baryon created, and provide an entree into Σ_c's.

It seems very unlikely that the HiLum PEP sample size would allow identifiable reconstruction of any of the strange charmed baryon states. E.g., if there were 4000 csd-baryons with a 1% branching fraction to $\Xi^-\pi^+$ and a 2% Ξ^- reconstruction efficiency, then only one event of csd would be reconstructed.

Summary of Charmed Baryon Studies

An intriquing, but somewhat slippery area. HiLum PEP will provide tens of thousands of charmed baryons, typically at high rapidity and/or momentum.

There is a fairly good chance of reconstructing $\Lambda_c \rightarrow pK^-\pi^+$, but it seems unlikely that strange charmed baryon states will be reconstructed exclusively.

The production rates for non-strange, singly-strange, and doubly-strange baryons can be monitored, respectively, through the $\Sigma*^+ - \Sigma*^-$ difference and/or high rapidity difference $\Lambda\bar{\Lambda}$ pairs, high rapidity Ξ^- production, and high rapidity Ω^- production.

I.3.8 Three Unusual Low-Statistics Strange Baryon Effects

To emphasize the kinds of questions which can be answered with high statistics samples, we select three areas where the present low-statistics samples suggest possibly interesting effects (not necessarily true!) which will be answered by high luminosity running at PEP.

$\Lambda\bar{\Lambda}$ Rate vs. Λ Rate

The TPC[21] and TASSO[22] each with detected $\Lambda\bar{\Lambda}$ samples of about 10 events, each find that if an event has a Λ in it, then the probability of there being a $\bar{\Lambda}$ also in the event is $40\% \pm 20\%$. Figure 29 shows the measured $\Lambda\bar{\Lambda}$ rate vs. Λ rate compared with the Lund prediction, which of course includes various "feed-downs" into Λ's. If the present value remained in the HiLum running, the result would be 3-4 standard deviations above the Lund prediction.

Figure 30 demonstrates that in the simplest string type of modeling and ignoring feed-down, the conditional $\bar{\Lambda}$ probability is $\sim 13\%$, corresponding to s/u = 0.3. Figure 30 also depicts some "non-standard" possibilities:

i) If the Λ is made from a $(us)_0$ diquark, then the $\bar{\Lambda}$ probability is $\sim 43\%$.

ii) In cluster modeling, the $g \rightarrow s\bar{s}/g \rightarrow u\bar{u}$ ratio is probably somewhat higher than the s/u string breaking ratio. This could lead to conditional $\bar{\Lambda}$ probabilities of $\sim 20\%$.

iii) This the most radical possibility, in which the transverse energy density of the colorfield allows the Λ and $\bar{\Lambda}$ to be formed from the same $s\bar{s}$ and diquark-antiquark pairs. In this mechanism, a $\bar{\Lambda}$ is created with every Λ.

We note that the "standard" model and the second "non-standard" model have extra production of strange particles, whereas the first and third "non-standard" models do not. Thus, these classes of models in principle are expermentally distinquishable.

$\Lambda\bar{\Lambda}$ Events with Large Rapidity Differences

As shown in Fig. 31, of all 11 TPC $\Lambda\bar{\Lambda}$ events, two have rapidity differences of > 4.5. (It might be noted that TASSO[22] has 10 $\Lambda\bar{\Lambda}$ events and Mark II[23] has 27, and none of them have rapidity differences this large.) The present Lund modeling predicts ~ 0.1 such events for the TPC. Such $\Lambda\bar{\Lambda}$ events would indicate a large rate of charmed baryon production.

Ω^- Production

The 5 Ω^- events seen by the TPC (with $< .5$ event background) are more than an order of magnitude larger than the present Lund modeling predicts. If their rate is confirmed in high luminosity running, it could be explained by a large $(ss)_1$ diquark probability and/or large charmed baryon production.

Summary of Unusual-Statistics Strange Baryon Effects

Fun. Not necessarily true. We will find out the answers from HiLum running. These effects demonstrate the kinds of questions which can be contemplated.

I.3.9 Gluon Fragmentation Studies

The PEP center-of-mass energy region is an ideal one for making detailed studies of the properties of events containing hard gluon radiation. The energy is high enough that a third jet can be easily resolved in 3 to 10% of the hadronic events (depending on cuts), yet low enough to allow detailed reconstruction of the individual particles within jets.

Using a very clean sample, detailed studies of the properties of gluon jets could be made as a function of the gluon jet energy (typically 4-12 GeV). Properties such as the multiplicity distribution, the KNO scaling distribution, particle rapidity, and transverse momentum spectra could be well and unambiguously measured. Based on current measurements, we would expect to reconstruct 200-300 Λ's and 300-400 K°'s in such a clean sample.

The topological studies described in Section IV.2.1, will become much more detailed. In particular, the flow of particles such as the Λ's and K°'s mentioned above can be studied. There even will be available for study a few tens of 3-jet events with correlated pairs of identified heavy particles.

The characteristics of events with gluon radiation can also be studied without specifically identifying a 3-jet topology by looking instead at multiplicity, inclusive particle distributions, etc., as a function of event shape variables such

as sphericity and jet mass. While this technique does not unambiguously single out properties of gluon jets, it does provide interesting qualitative constraints on fragmentation schemes and reflects properties of the underlying QCD structure. For example, a recent HRS result[24] shows a clear rise in charged particle multiplicity as sphericity rises. Without medium-soft gluon radiation properly accounted for, the Lund model cannot reproduce this rise. The K° and Λ multiplicities were also measured as a function of sphericity (Fig. 32) and the Lund model did not reproduce these shapes particularly well. The improvement in these measurements obtainable with HiLum PEP would provide the answers to some interesting questions such as whether baryon and strange particle content increase with sphericity at the same rate as the general multiplicity.

Another question that could be answered with high luminosity is whether the width of the KNO scaling distribution changes with increasing gluon content. One might expect the shapes to be different due to the presence of a third generator in the gluon events; however, current HRS data[24] show the distribution at low and high sphericity to be quite similar.

I.3.10 The Merging of Nearby Jets

A very interesting and as yet not well understood area is what happens to the colorfield and its product hadrons when two relatively major color-connected partons (e.g., a quark and a gluon) are fairly near each other in phase space; that is, not separate enough to make experimentally separable jets and not close enough to be merged into a normal jet with normal p_T distributions.[25] Such an event is depicted in Fig. 33 Presumably the field will exhibit different properties involving order/disorder, coherent effects, non-nearest-neighbor interactions, etc. compared with "simple" 2-jet or 3-jet events. (This phenomenon involving two major overlapping partons is closely related to the second half of the previous section on Gluon Fragmentation Studies in which events generally broadened by above-average soft gluon emission are discussed.) It is a relatively undeveloped

area of considerable information on how interparton fields behave, but will require large data samples of detailed particle information to unravel.

Summary of "Gluon Fragmentation Studies" and "The Merging of Nearby Jets"

There is a great deal to learn concerning the colorfield behavior involved (a) when there is one major separated gluon (3-jet events), (b) multiple emission of fairly soft gluons leading to a high sphericity event, and (c) when a major gluon is somewhat nearby in phase space to a quark (merging jets). Understanding these phenomena will require large data samples with identified heavy particles in order to study the details of the colorfield behavior.

I.3.11 Other Physics Areas

The hadronization study area is a very broad one. Above, we have discussed selected topics. We here mention some other areas of potential study.

A polarization argument similar to that developed for the Λ can also be applied to the ϕ meson at high p_T. The decay density matrix then leads to K^+K^- emission out of the plane defined by the jet axis and the p_T of the ϕ, independent of the direction of the colorfield. This probes many of the same "orderliness" questions as the Λ polarization.

Possible $c\bar{c}$ production from the colorfield (i.e., string-breaking or cluster-decay) is a very interesting property, but unfortunately very difficult to identify. Cluster models would suggest $c\bar{c}/u\bar{u} \sim 10^{-3}$ or so. Simple string tunneling suggest $c\bar{c}/u\bar{u} \sim 10^{-11}$; however modified string modeling allowing energy concentrations or multiple medium-soft gluon emission will raise this. Unfortunately, we have not yet found an adequate way to look for this at less than about 10^{-1} or 10^{-2}. Looking for soft D-mesons ($z \leq .2$) is obscured by combinatorics and also by bottom decay. The acceptance is not high enough to look for events with 3 D's (primary $c\bar{c}$, plus $c\bar{c}$ from the colorfield). This remains an open question.

We have only touched in passing on the information to be learned from the rich area of p_T studies: in 3-jet events, studies of p_T relative to the "jet-axes" and

relative to presumed strings connecting partons; how p_T depends on the mass of the hadron; whether the p_T of a baryon (3 quarks) is statistically larger than expected; whether gluon jets have appreciably higher p_T than quark jets.

As the area moves into the high luminosity era, many more questions will of course be posed and hopefully answered.

I.4 CONCLUSIONS

There are many interesting areas involving interparton field behavior to be developed with high luminosity samples of $\sim 1000\ pb^{-1}$ and sensitive powerful detectors at PEP. These include:

- Bose-Einstein correlation studies which potentially probe confinement and determine the tension in the interparton field.
- Detailed fragmentation studies, in particular at high z and of D*'s (high mass) where the results avoid the ambiguities caused by resonance decay.
- A definitive measurement of Λ polarization, which simultaneously probes many aspects of the "orderliness" of the field behavior.
- Strange Baryon production and their correlations, which is basically a *new field* with potentially much interesting information and, already, a few enticing low statistics effects.
- Determination of the formation probabilities for various diquark flavors and spins.
- Probes of many aspects of the "orderliness" of interparton field behavior such as Λ polarization and "baryon-baryon rapidity repulsion" and also many "ordered" effects which relate to how diquarks and baryons are formed including baryon-antibaryon p_T and rapidity correlations, spin 1/2-spin 3/2 correlations, and $\Lambda\bar{\Lambda}$ rate vs. Λ rate.
- Monitoring of non-strange, strange, and doubly-strange charmed baryon production rates and probably reconstruction of a Λ_c signal.

- Measuring of short range fragmentation rapidity correlations for various species of heavy particle pairs.
- Detailed studies of how produced particles are "pulled" in the interparton field.
- Detailed study of 3-jet events, in particular focusing on the behavior of identified heavy particles.
- Studies of gluon fragmentation compared with quark fragmentation.
- Merging jet studies of the effects which occur when the fields of two major partons overlap.

Sample sizes will be 10 times larger than present samples for light quarks, and 30-40 times larger for strange quark samples (thousands of Λ's, hundreds of Ξ^- and Ω^-'s). There will be roughly $\sim$ 1000 each of $p\bar{p}$, $\Lambda\bar{p}$, and $\Lambda\bar{\Lambda}$ correlation samples.

There is much that <u>can</u> be experimentally learned with HiLum PEP on how the fields between partons actually behave as they evolve toward the hadrons which we observe.

REFERENCES

1. G. C. Fox and S. Wolfram, Nucl. Phys. B168, 285 (1980); R. D. Field and S. Wolfram, Nucl. Phys. B213, 65 (1983).

2. B. R. Webber, Nucl. Phys. B238, 492 (1984).

3. T. D. Gottschalk, Nucl. Phys. B214, 201 (1983); B239, 325 (1984); B239, 349 (1984).

4. B. Andersson *et al.*, Phys. Report 97, 31 (1983); B. Andersson, G. Gustafson and B. Söderberg, Z. Phys. C20, 317 (1983); T. Sjöstrand, Comput. Phys. Commun. 27, 243 (1982); 28, 229 (1983).

5. A. Ali *et al.*, Phys. Lett. B93, 155 (1980).

6. P. Hoyer *et al.*, Nucl. Phys. B161, 349 (1979).

7. R. D. Field and R. P. Feynman, Nucl. Phys. B136, 1 (1978).

8. W. Bartel *et al.* (JADE), Phys. Lett. B134, 275 (1984); A. Petersen, "Further Studies of Quark and Gluon Fragmentations," Proceedings of the XV Symposium on Multiparticle Dynamics, Lund, Sweden, June 10-16, 1984.

9. H. Aihara *et al.* (TPC), Phys. Rev. Lett. 54, 270 (1985); H. Aihara *et al.* (TPC), "Tests of Models for Quark and Gluon Fragmentation in e^+e^- Collision at $\sqrt{s} = 29$ GeV," LBL-18408, to be published in Z. Physik.

10. H. Aihara *et al.* (TPC), Phys. Rev. Lett. 53, 2199 (1984).

11. H. Aihara *et al.* (TPC), "Baryon Production in e^+e^- Annihilation at $\sqrt{s} =$ 29 GeV: Cluster, Diquarks, Popcorn?," to be submitted to Phys. Rev. Lett.

12. G . Goldhaber *et al.*, Phys. Rev. 120, 300 (1960); G. Kopylev and M. Podgoretzki, Sov. Nucl. Phys. 18, 336 (1974); 19, 215 (1974); G. Cocconi, Phys. Lett. 49B, 454 (1974).

13. H. Aihara *et al.* (TPC), Phys. Rev. D31, 996 (1985).

14. B. Andersson (Lund) and W. Hofmann (TPC), private communication.

15. D. Bender, *el al.* (HRS), Phys. Rev. D31, 1 (1985); M. Derrick. *el al.* (HRS), "Some Aspects of Quark Fragmentation: Comparison of Heavy (c) and Light (u,d,s) Quarks," Proceedings of the XV Symposium on Multiparticle Dynamics, Lund, Sweden, June 1984.

16. H. U. Bengtsson (Lund, TPC), private communication.

17. M. Derrick, *et al.* (HRS), Phys. Rev. Lett. 53, 1971 (1984).

18. TPC Collaboration, To be published.

19. M. Derrick, *el al.* (HRS), ANL-HEP-PR-85-02.

20. H. Yamamoto *et al.* (TPC), private communication.

21. H. Aihara *et al.* (TPC), Phys. Rev. Lett. 54, 274 (1985).

22. M. Althoff *et al.* (TASSO), DESY Report No. DESY 84-065 (1984); to be submitted to Z. Phys. C.

23. C. de la Vaissierre, *el al.* (Mark II), Submitted to Phys. Rev. Lett.

24. P. Baringer and K. Sugano, (HRS) Private communication.

25. T. Sjöstrand, "Jet Fragmentation of Nearby Partons," DESY 84-01 (1984); "The Merging of Jets," DESY 84-019 (1984).

FIGURE CAPTIONS

1. Paradigm of HiLum PEP data, phenomenological understanding of color-field dynamics, and non-perturbative QCD calculations.

2. Three-jet events for (a) Independent Fragmentation, (b) String Fragmentation, and (c) Cluster Fragmentation.

3. Naive space-time depiction of a 2-jet event to illustrate some of the features and questions involving the behavior of fields between partons.

4. The dE/dx plot with the newly upgraded TPC.

5. Lambda mass from HRS.

6. Lambda mass from the upgraded TPC.

7. (a) HRS results (i) $D^\circ \to K^-\pi^+$ and (ii) $D^+ \to K^-\pi^+\pi^+$.

   (b) HRS results for $F \to \phi\pi^+$ with (above) $0.2 < z(\phi - \pi) < 0.4$ and (below) $z(\phi - \pi) > 0.4$. The lower histograms are selected at particular decay angles.

8. Upgraded TPC results: (a) $D^\circ \to K^-\pi^+$, (b) $D^\circ \to K^-\pi^+\pi^-\pi^+$, (c) $D^* \to D^\circ$, and (d) $F \to K^+K^-\pi^+$.

9. Angular distribution of particles in the event plane for 3-jet events for (a) all charged particles and photons, (b) for charged particles and photons with $0.3 < p_{out} < 0.5$ GeV/c, and (c) for heavy particles (K,p,Λ).

10. K – K rapidity correlation for charged kaons from TPC.

11. Baryon formation models.

    (a) Lund string model with "fundamental" diquarks.

    (b) Lund string model with diquarks formed in a two-step process.

    (c) Cluster decay to baryon-antibaryon.

12. The angular distribution between the $p\bar{p}$ axis and the jet axis in the $p\bar{p}$ center of mass. The dashed line is the Webber cluster model. The solid line is the Lund string model. (a) Before detection efficiency. (b) After detection efficiency.

13. The p_T correlation (see text) for proton and antiproton.

    (a) Out of the event plane. (b) In the event plane.

14. The Bose-Einstein correlation between like-sign pions from TPC.

    (a) Uncorrected data.

    (b) Data corrected for particle misidentification and Coulomb effects.

    (c) Monte Carlo results based on an uncorrelated jet model generator.

    (d) Monte Carlo results from the Lund model generator without any Bose-Einstein correlations built in.

15. The size of the like-sign dipion emitting source as a function of angle, from the TPC Bose-Einstein study.

16. Space-time diagram for identical boson emission in Lund string model.

17. Bose-Einstein correlation from Lund string model with identical particle symmetrization correlation built in, compared with TPC data.

18. High z fragmentation function from HRS. Also displayed are a $(1-z)^2$ curve, the result of the most recent Lund parametrization from TPC, and the effect of a higher twist term at the virtual gamma vertex.

19. D^* fragmentation function.

20. F^+ fragmentation function from HRS. The solid curve is the Peterson fit to the HRS data for $z(D^*) > 0.4$. The dashed curve also includes estimated B decays.

21. Rapidity plot of lambda production from Lund string model.

22. Lund string model of lambda polarization.

23. Lambda polarization versus p_T from TPC.

24. Multi-purpose strange baryon event

    (a) highly ordered, (b) somewhat disordered.

25. Monte Carlo results of expected strange baryon signal with HiLum PEP.

26. Monte Carlo result of $\Lambda\bar{p}$ and $\bar{\Lambda}p$ rapidity correlation for HiLum PEP.

27. Monte Carlo result of $\Sigma^{*+} - \Sigma^{*-}$ momentum distribution with HiLum PEP. Also shown is the cud decay leading to an excess of Σ^{*+}.

28. Monte Carlo result for reconstruction of $\bar{\Lambda}_c$ for HiLum PEP (See text for comments on production rate and branching fraction used.)

29. Plot of $\Lambda\bar{\Lambda}$ rate versus Λ rate from TPC.

    In band (1), the Λ and $\bar{\Lambda}$ are uncorrelated.

    In band (2), they are always pair-produced. The solid line shows the Lund prediction as a function of (us/ud)/(s/u).

30. Models for $\Lambda\bar{\Lambda}$ formations.

31. Rapidity difference for Λ and $\bar{\Lambda}$ from TPC.

32. Lambda and K° production versus sphericity from HRS.

33. Space-time depiction of a "merging-jet" event.

PARADIGM

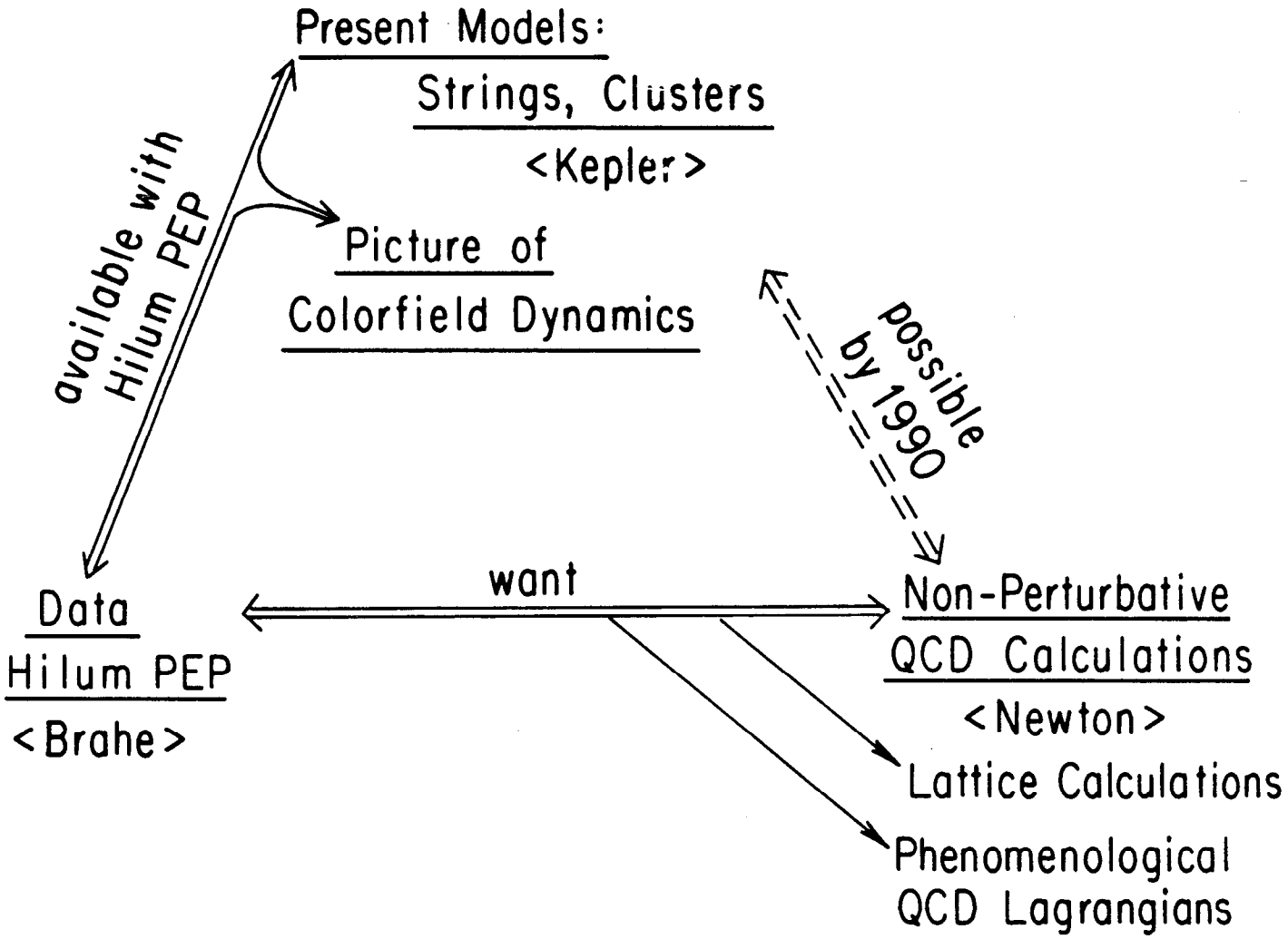

Fig. 1

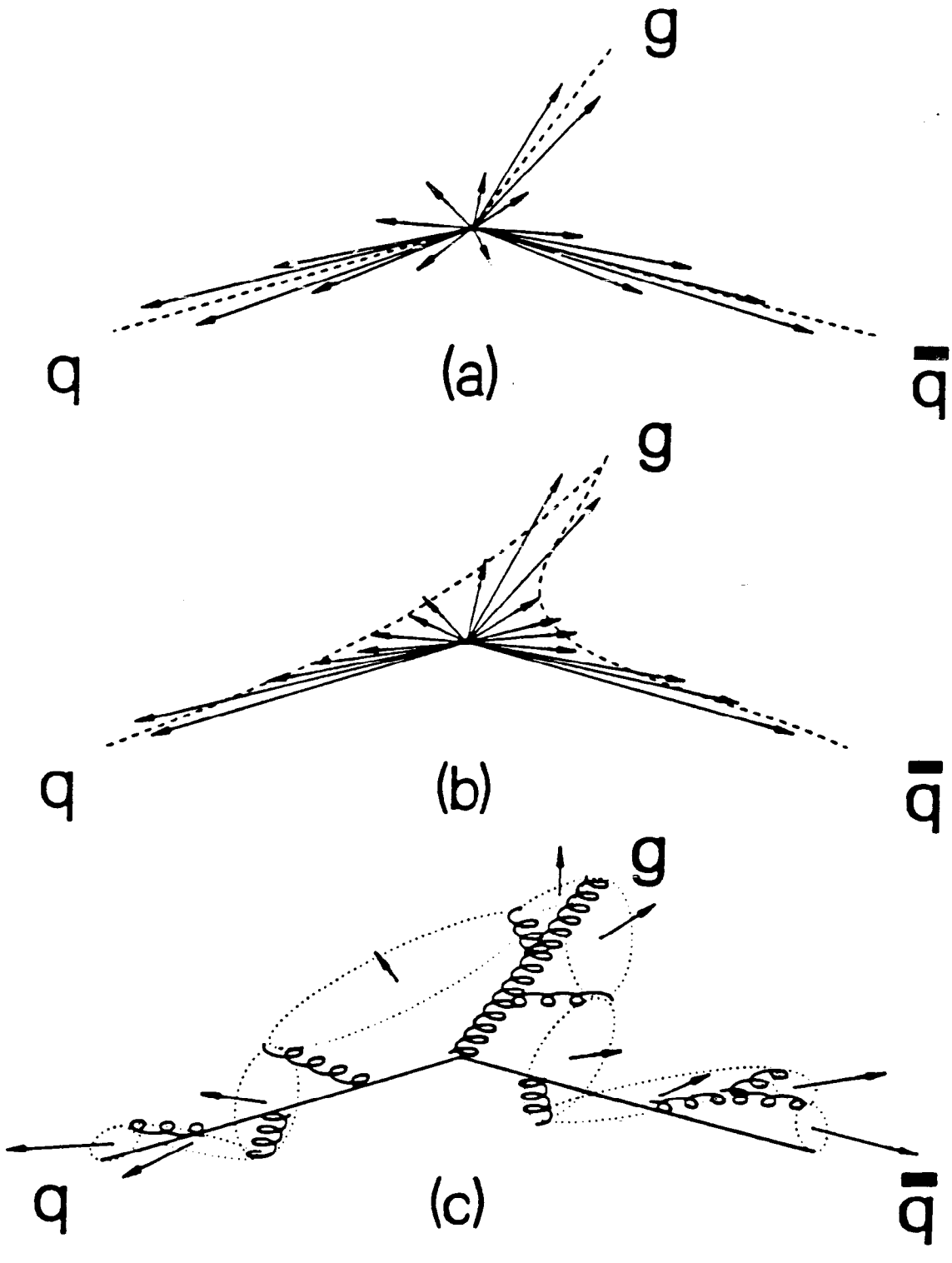

Fig. 2

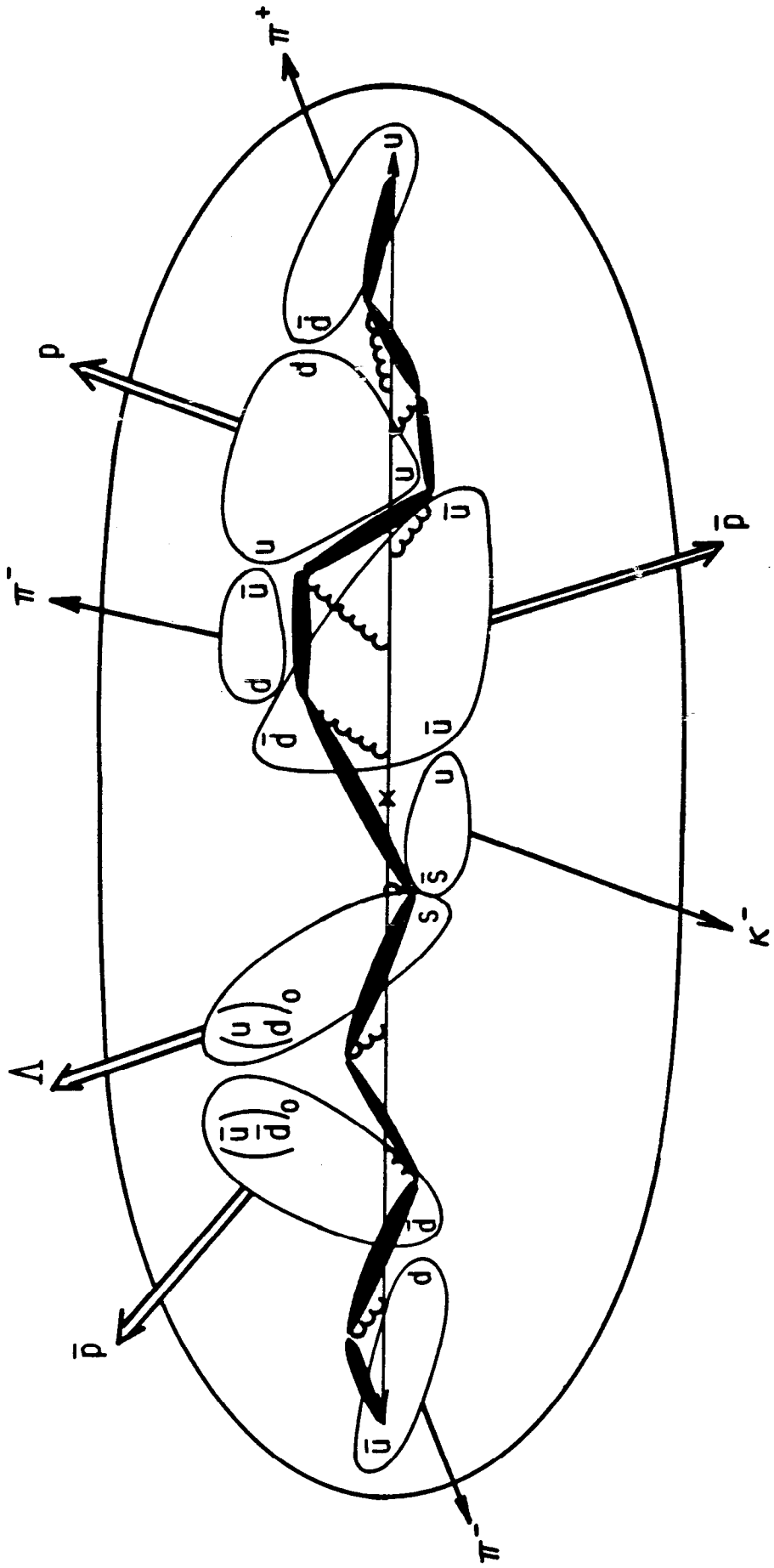

Fig. 3

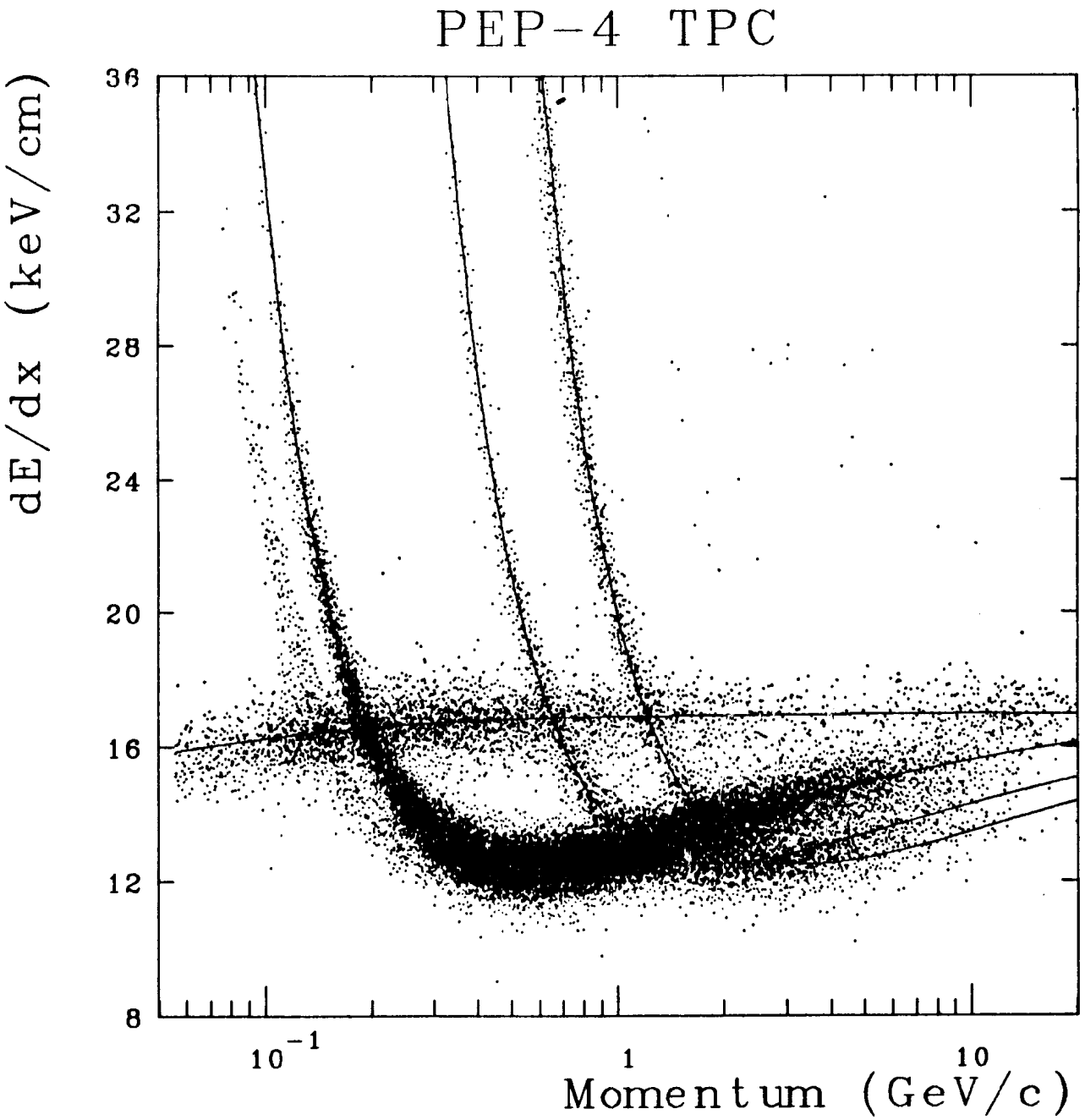

Fig. 4

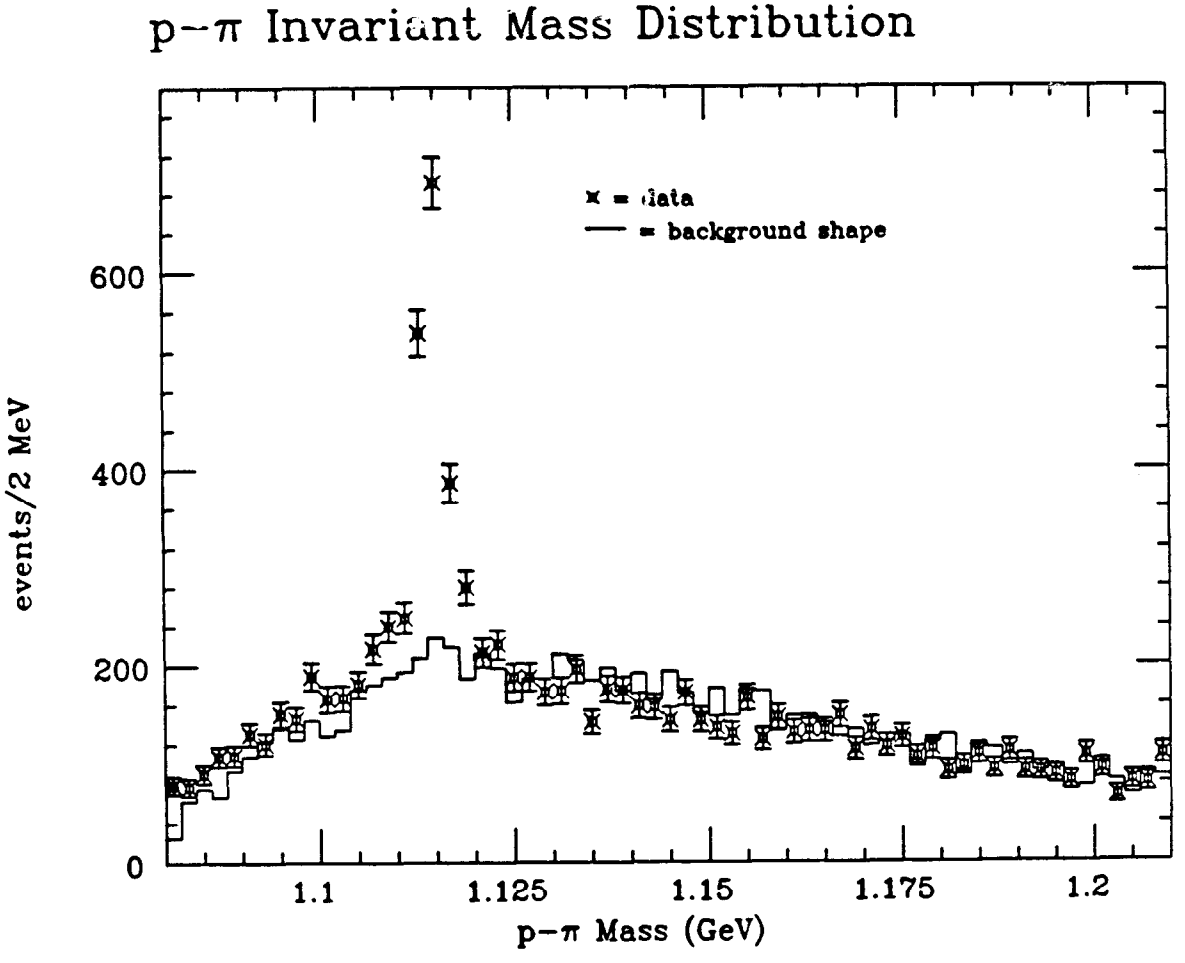
p−π Invariant Mass Distribution
× = data
— = background shape
events/2 MeV
600
400
200
0
1.1
1.125
1.15
1.175
1.2
p−π Mass (GeV)

Fig. 5

Run 10-11

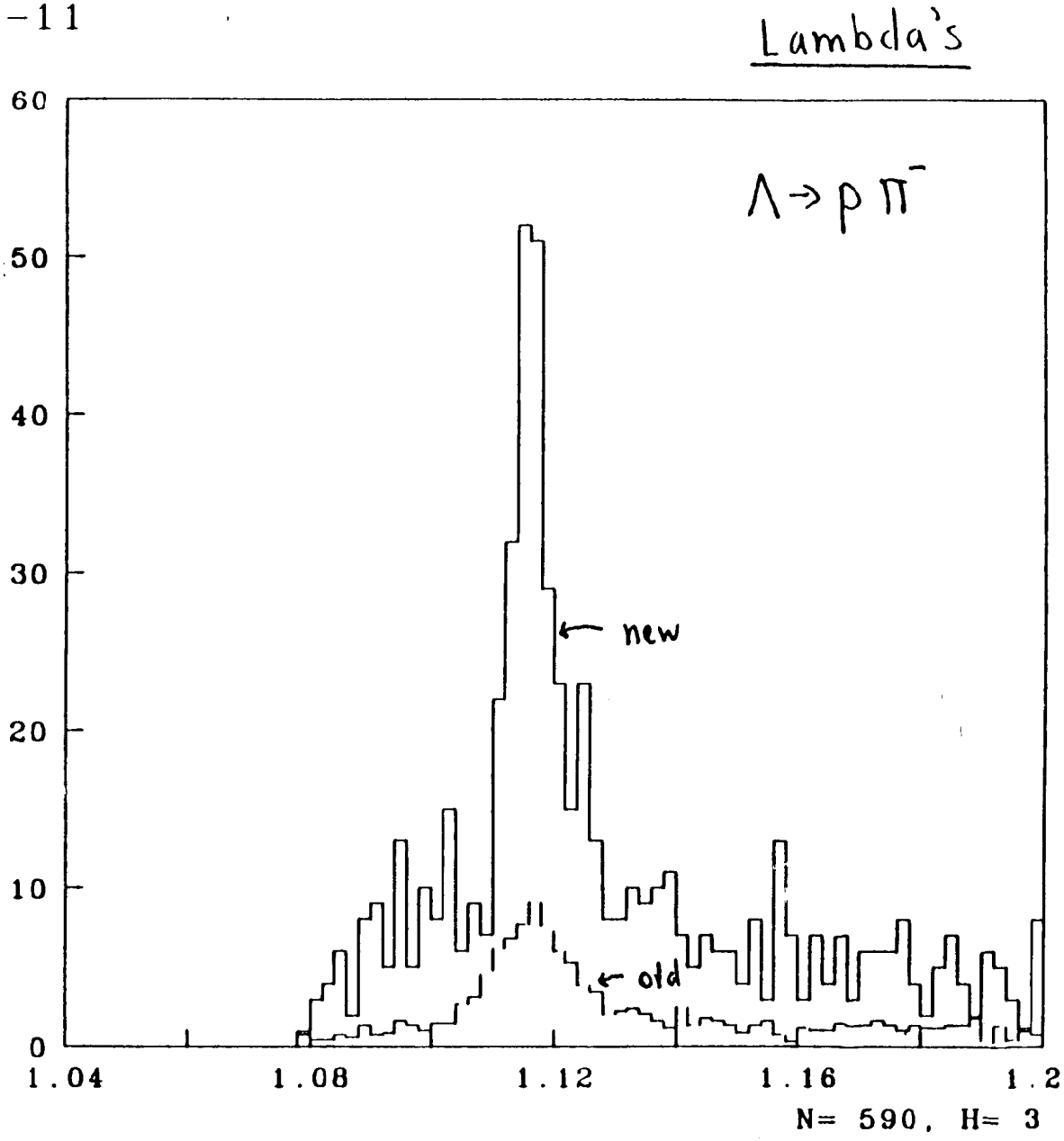

Fig. 6

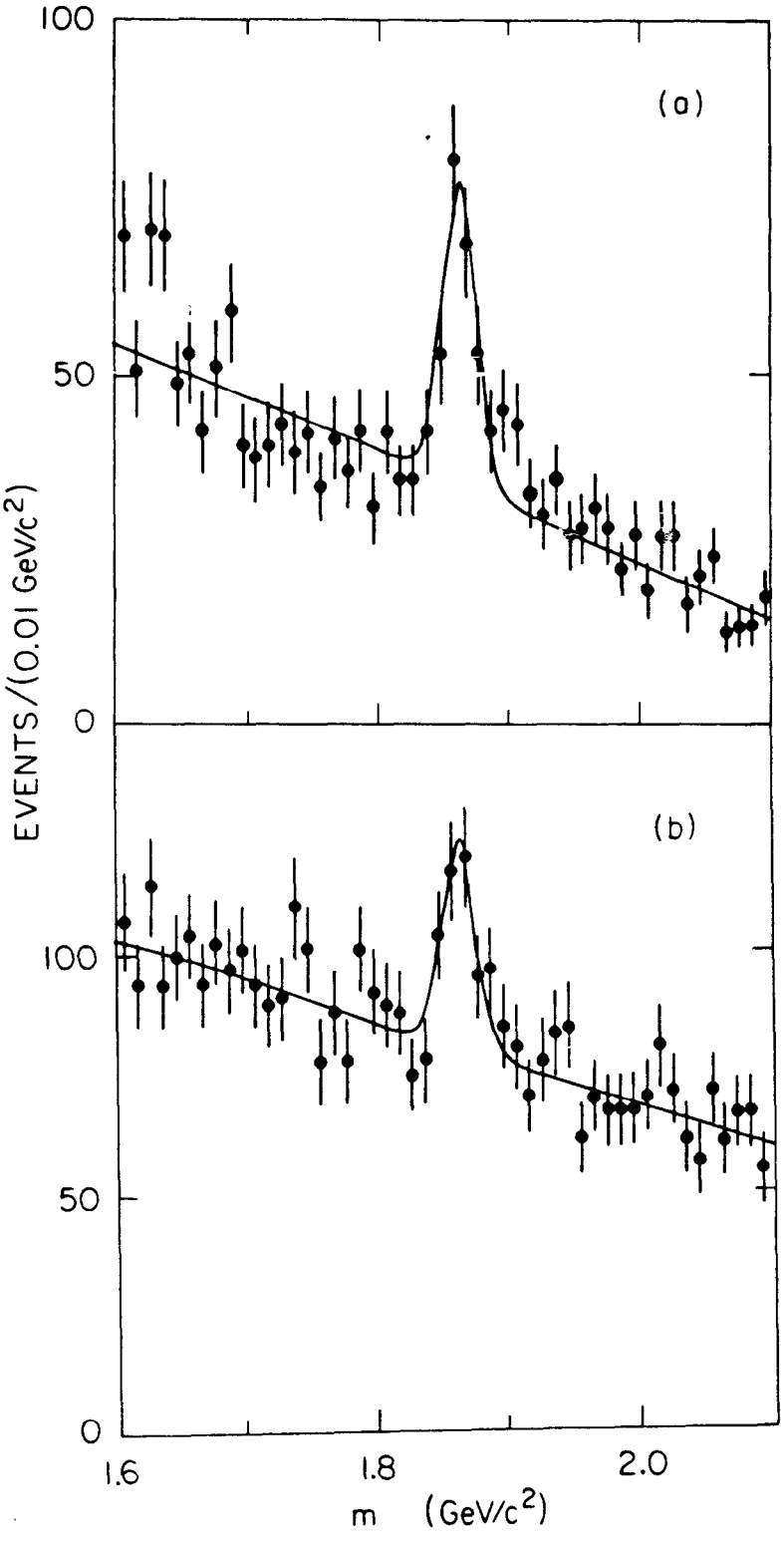

Fig. 7 a

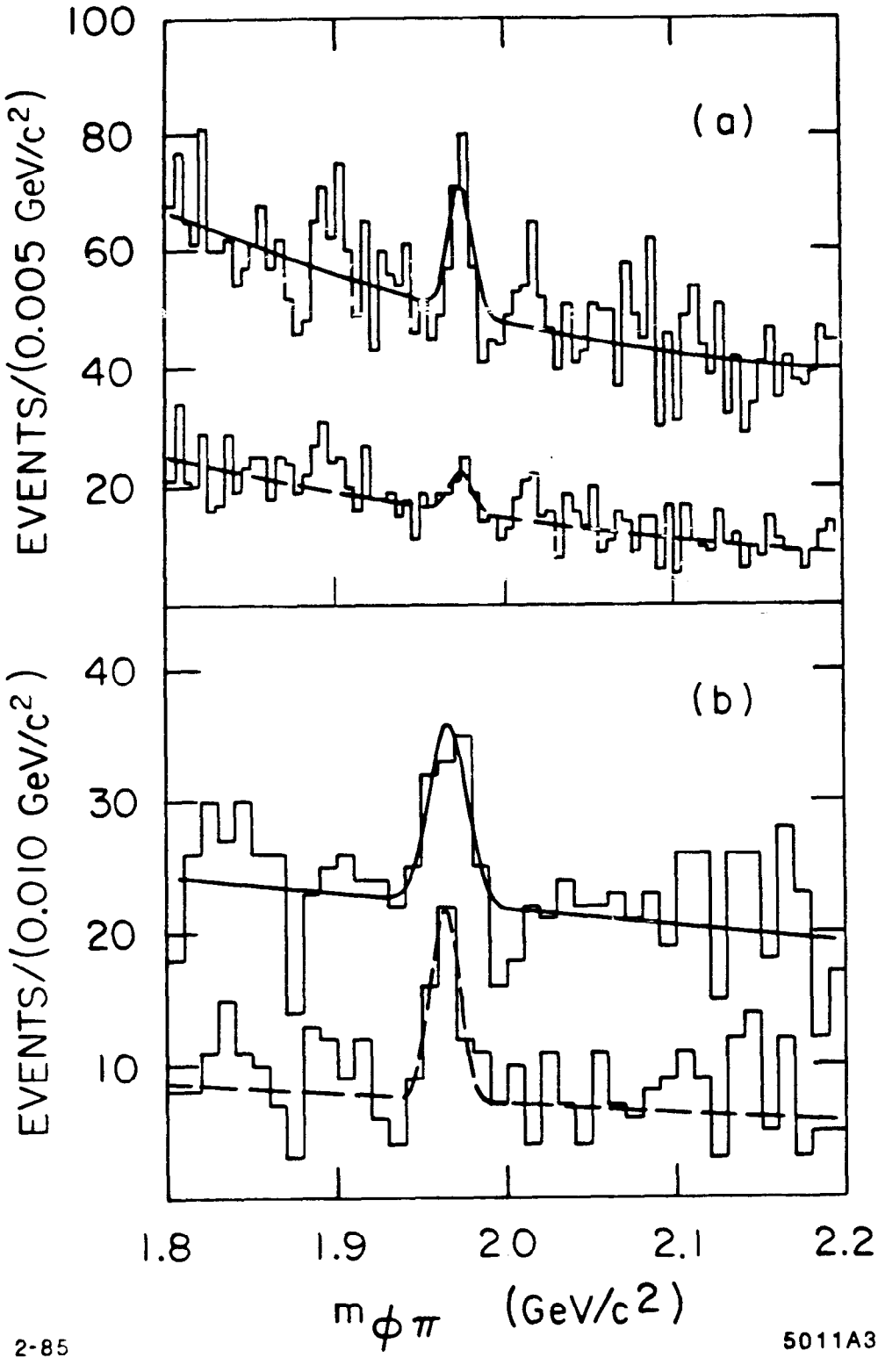
100
80
60
40
20
EVENTS/(0.005 GeV/c²)
(a)
40
30
20
10
EVENTS/(0.010 GeV/c²)
(b)
1.8
1.9
2.0
2.1
2.2
$m_{\phi\pi}$ (GeV/c²)
2-85
5011A3

Fig. 7 b

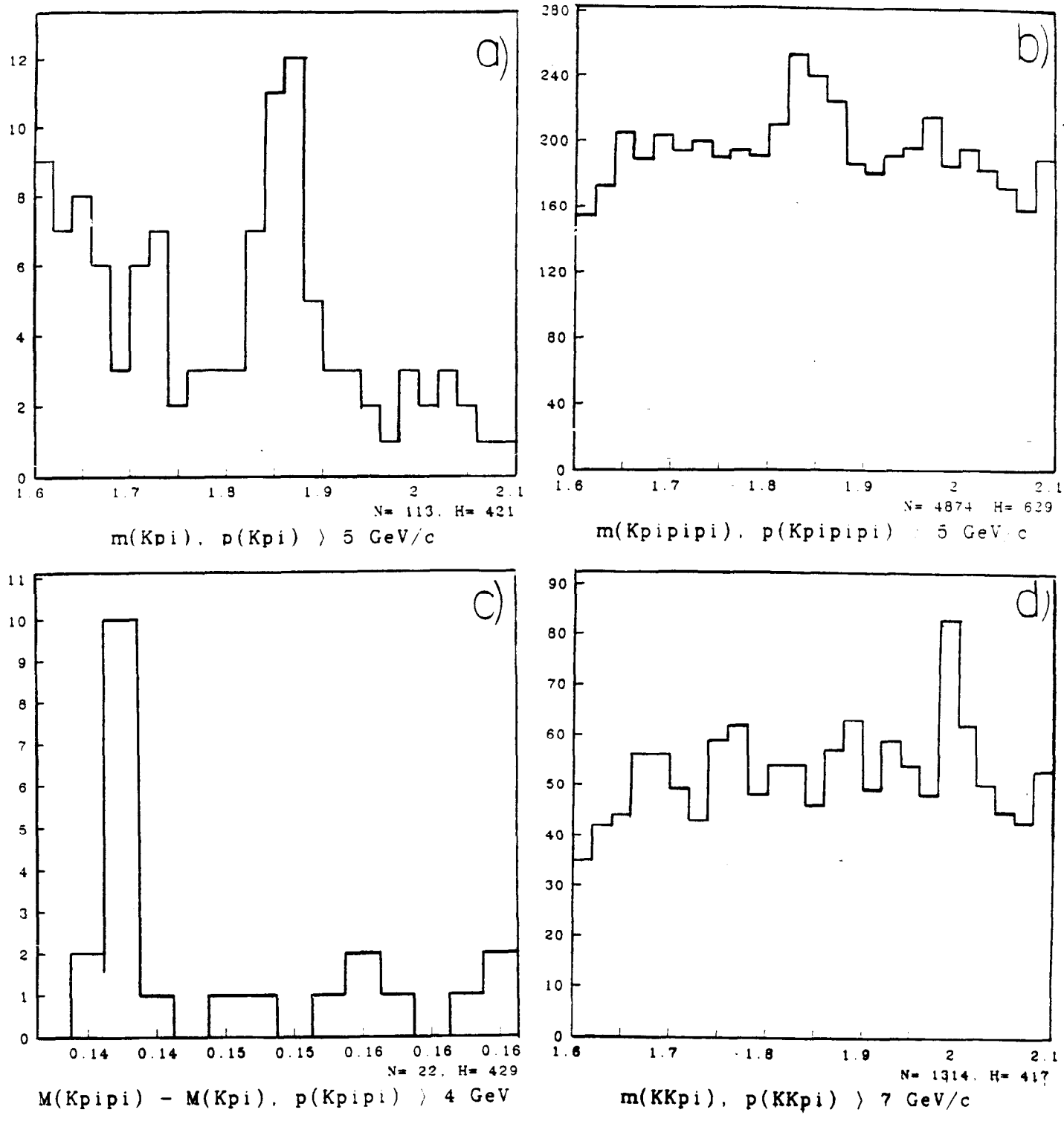
a)
N= 113. H= 421
m(Kpi), p(Kpi) > 5 GeV/c
b)
N= 4874 H= 629
m(Kpipipi), p(Kpipipi) > 5 GeV/c
c)
N= 22. H= 429
M(Kpipi) - M(Kpi), p(Kpipi) > 4 GeV
d)
N= 1314. H= 417
m(KKpi), p(KKpi) > 7 GeV/c

Fig. 8

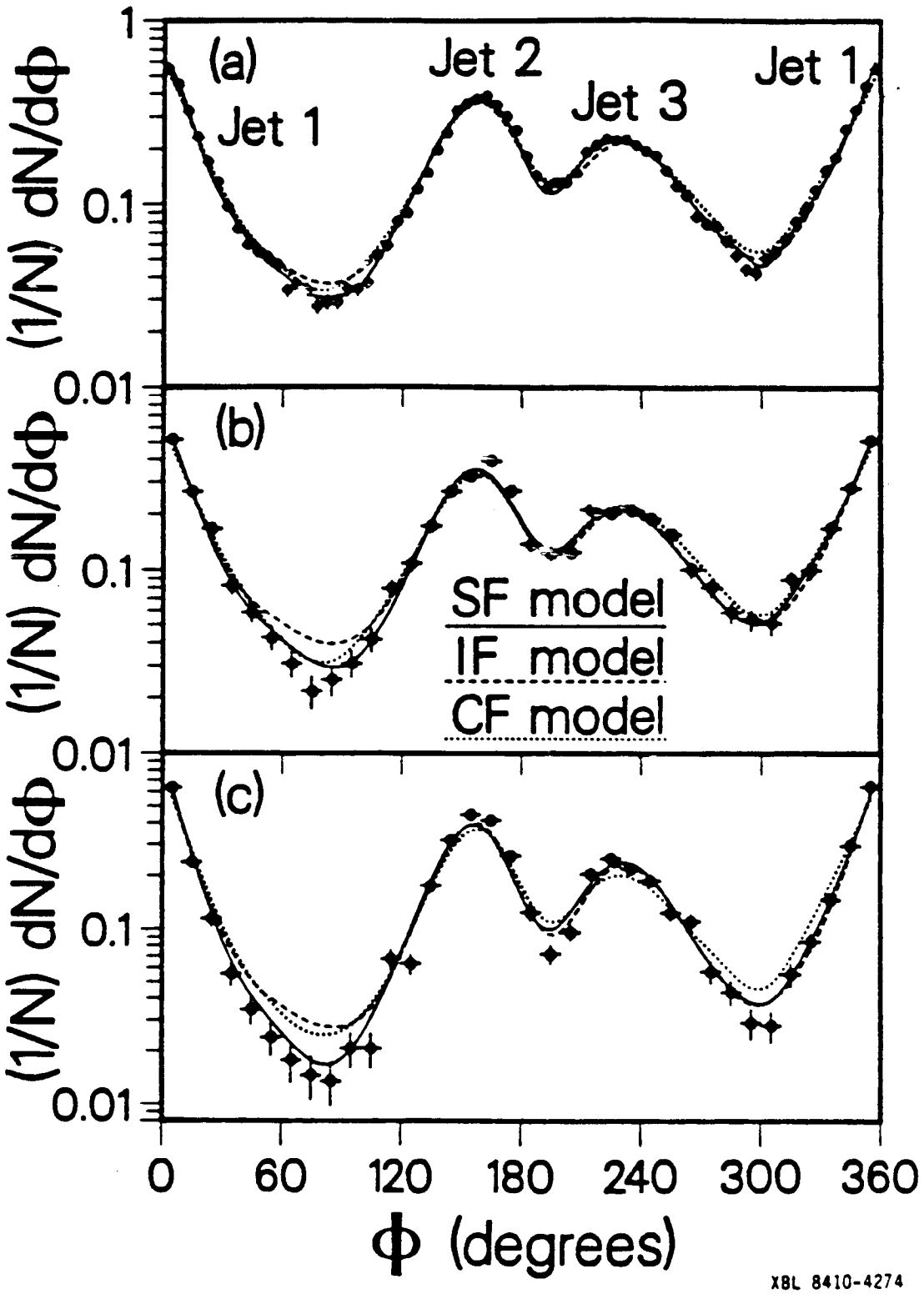
(a)
Jet 1
Jet 2
Jet 3
Jet 1
(b)
SF model
IF model
CF model
(c)
(1/N) dN/dΦ
1
0.1
0.01
0
60
120
180
240
300
360
Φ (degrees)
XBL 8410-4274

Fig. 9

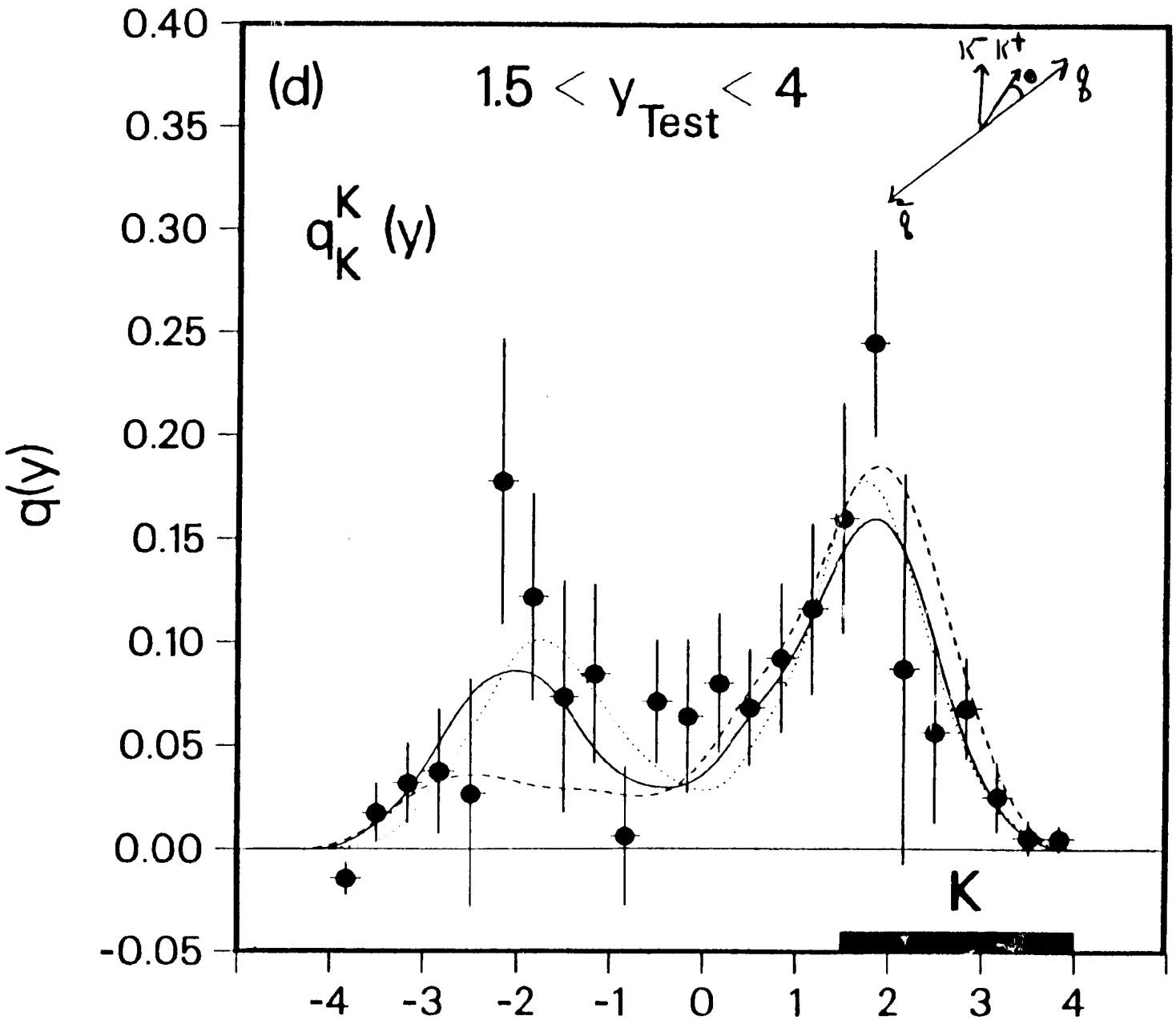
(d)
1.5 < y_Test < 4
q_K^K (y)
q(y)
K⁻ K⁺
q
q̄
K
0.40
0.35
0.30
0.25
0.20
0.15
0.10
0.05
0.00
-0.05
-4
-3
-2
-1
0
1
2
3
4

Fig. 10

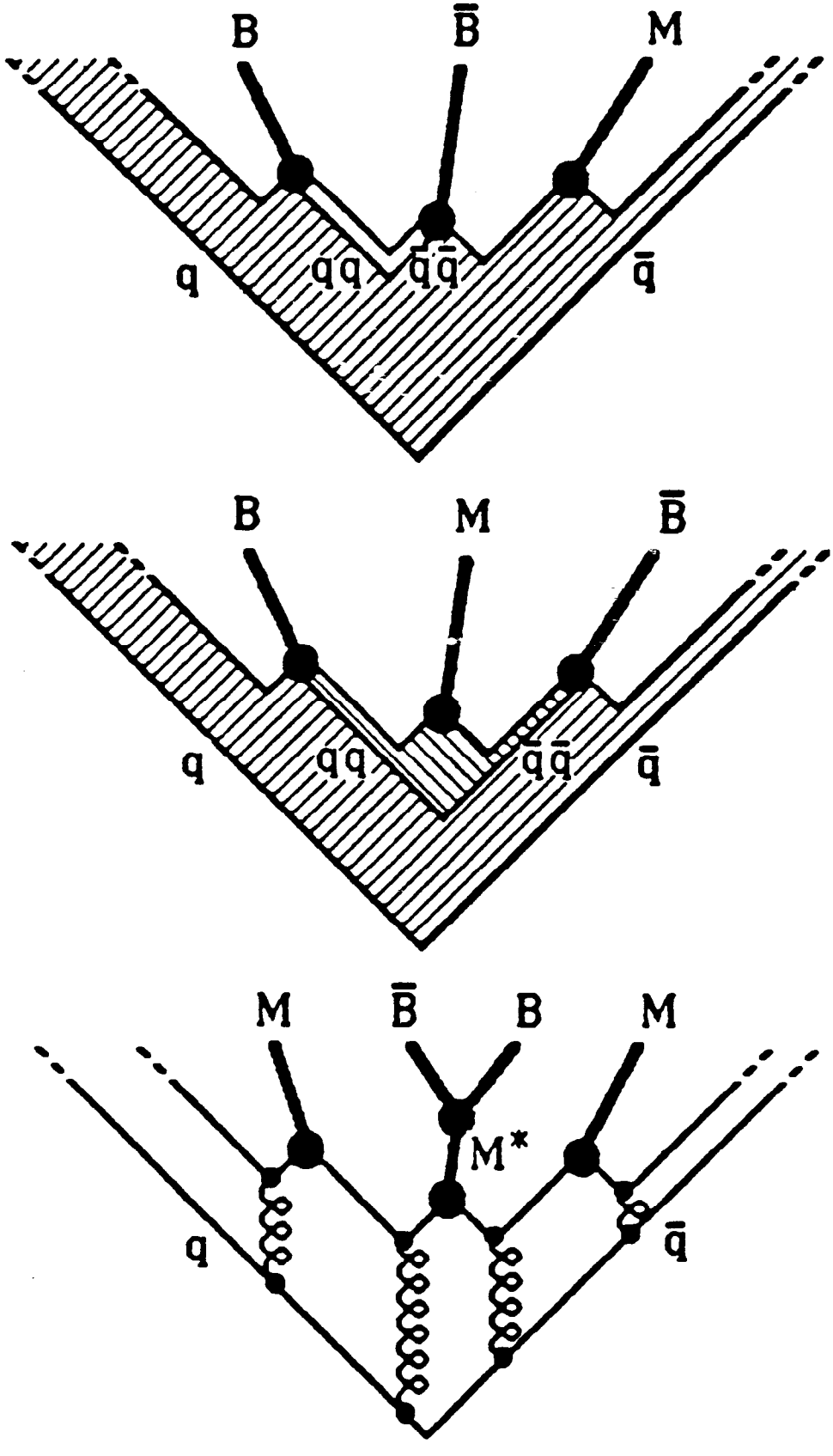

Fig. 11

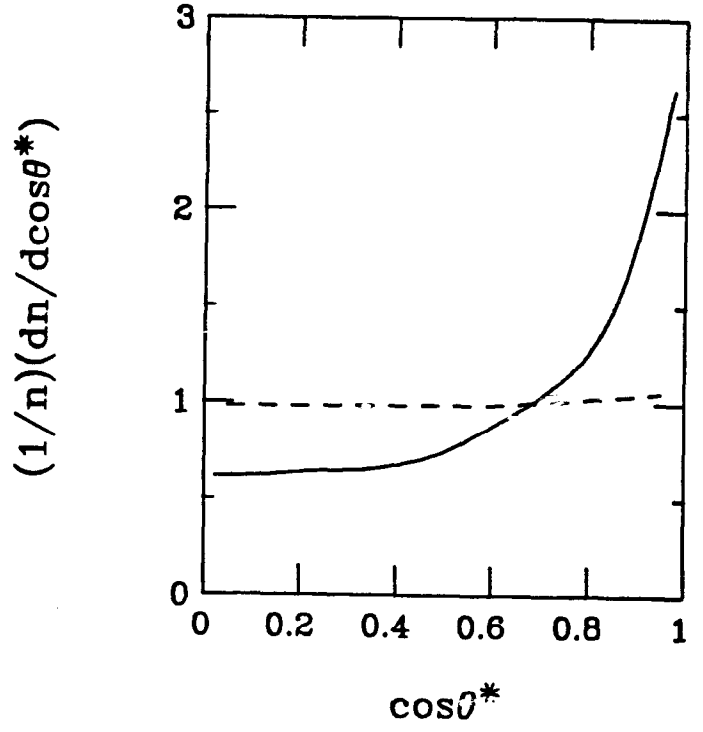
3
2
1
0
0
0.2
0.4
0.6
0.8
1
(1/n)(dn/dcosθ*)
cosθ*

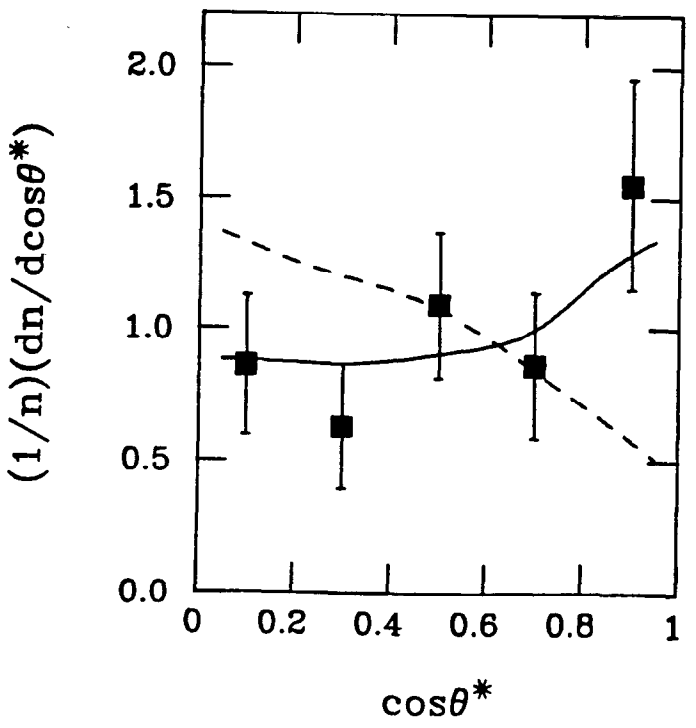
2.0
1.5
1.0
0.5
0.0
0
0.2
0.4
0.6
0.8
1
(1/n)(dn/dcosθ*)
cosθ*

Fig. 12

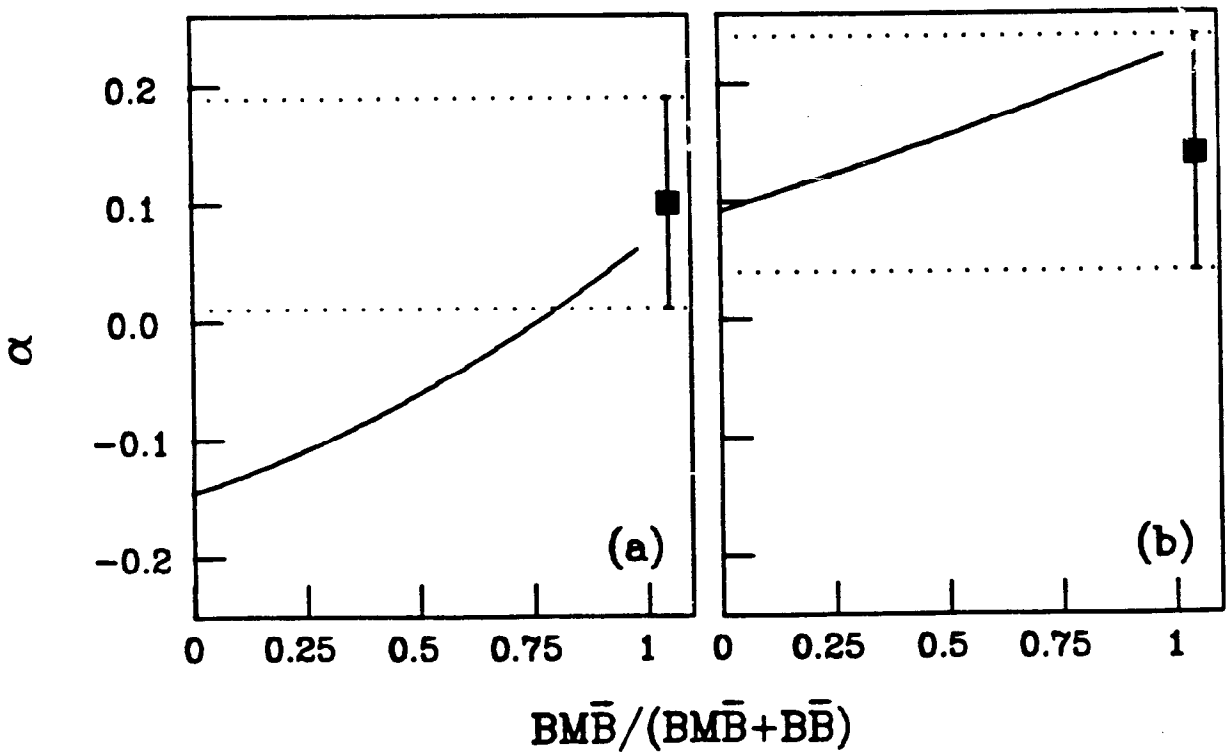

Fig. 13

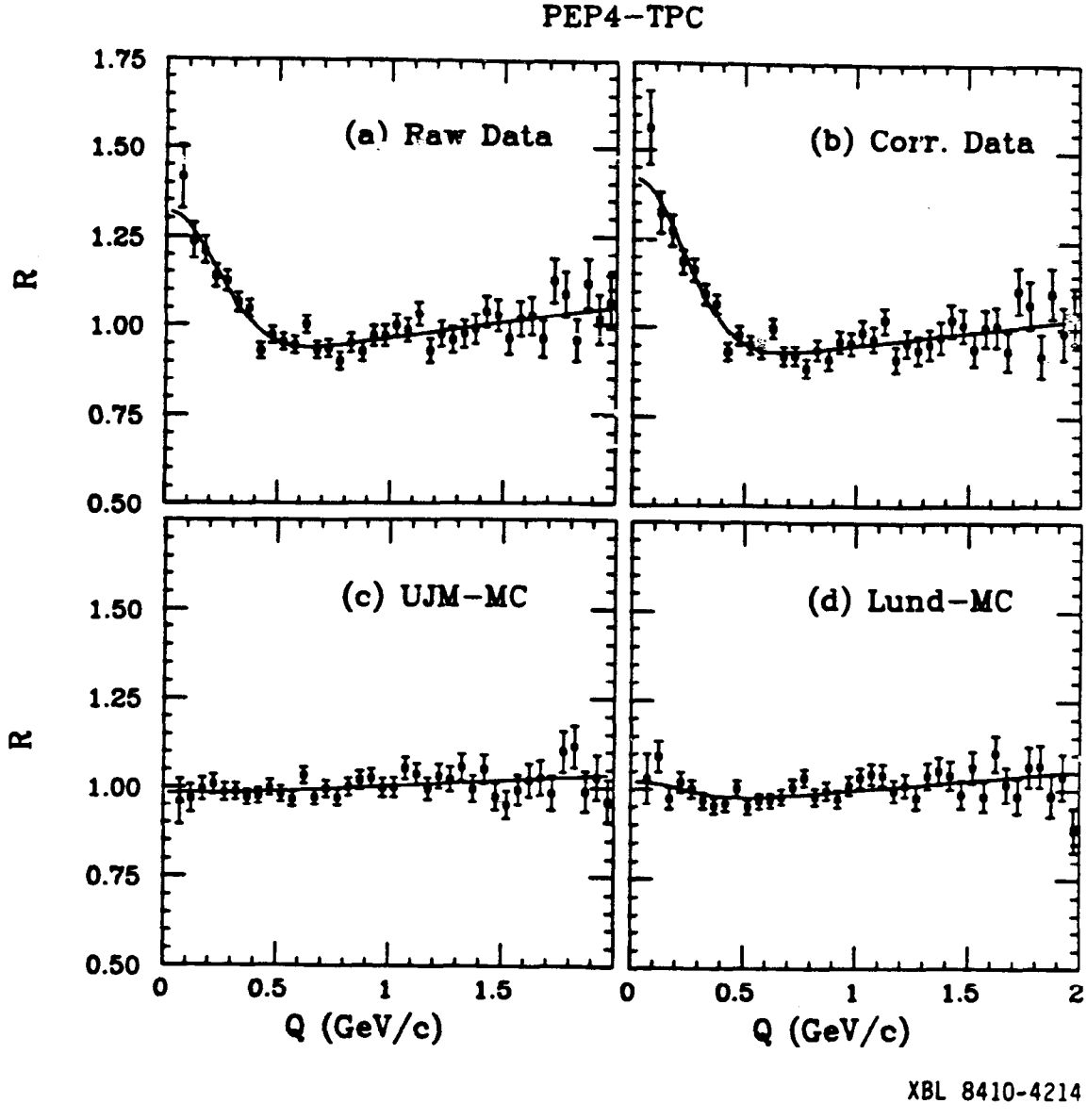
PEP4-TPC
(a) Raw Data
(b) Corr. Data
(c) UJM-MC
(d) Lund-MC
R
R
1.75
1.50
1.25
1.00
0.75
0.50
0
0.5
1
1.5
2
Q (GeV/c)
Q (GeV/c)
XBL 8410-4214

Fig. 14

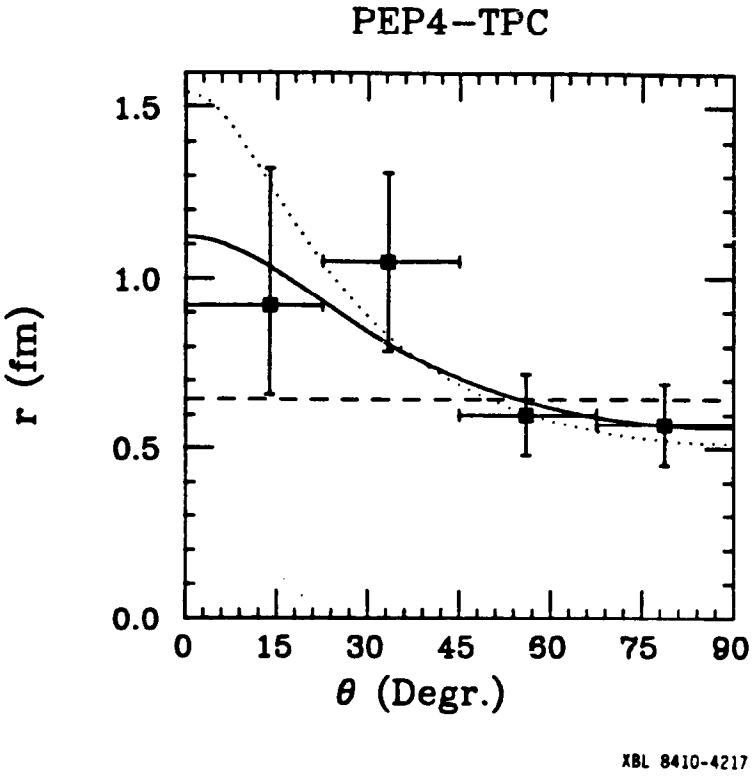

Fig. 15

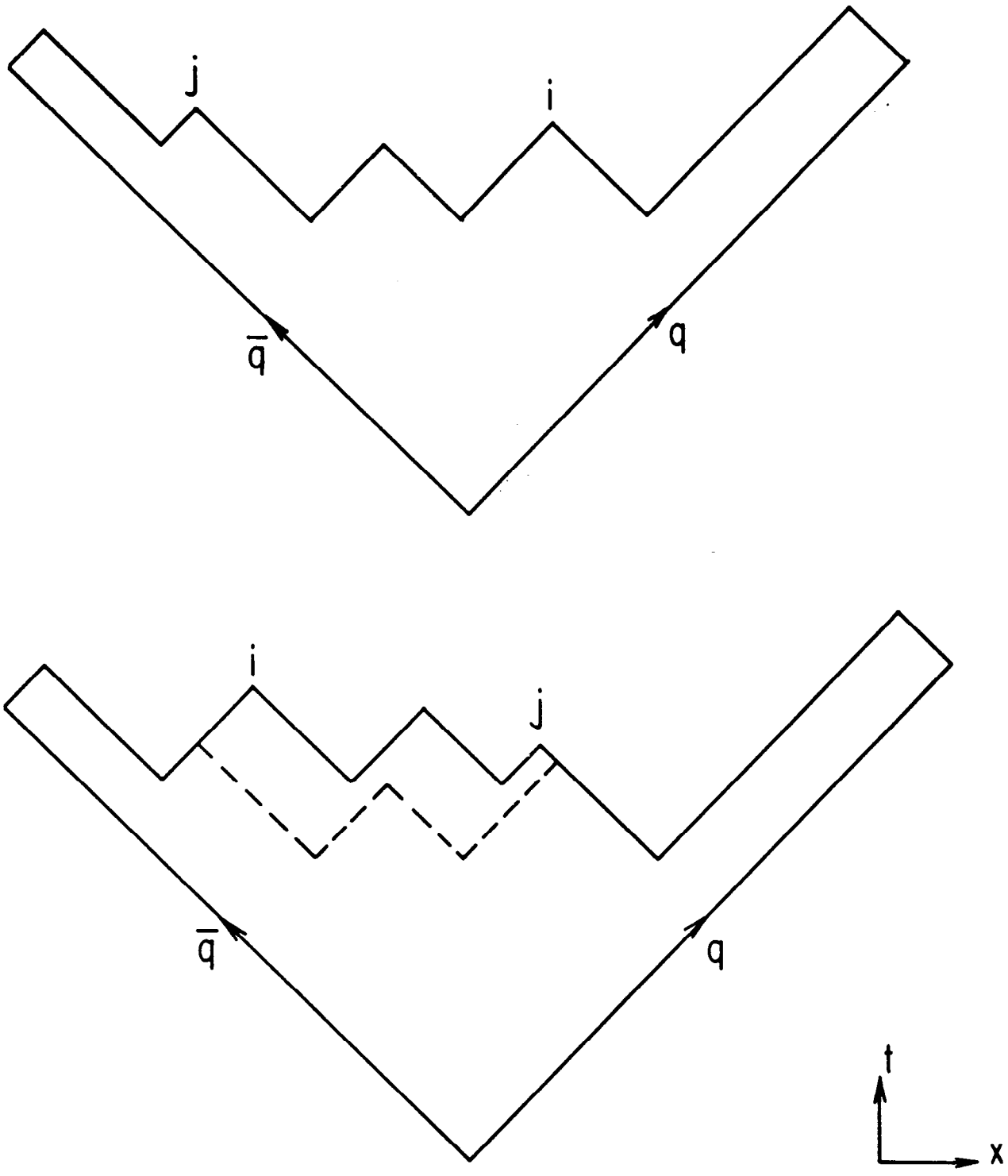

SPACE-TIME DIAGRAM FOR IDENTICAL BOSON EMISSION

Fig. 16

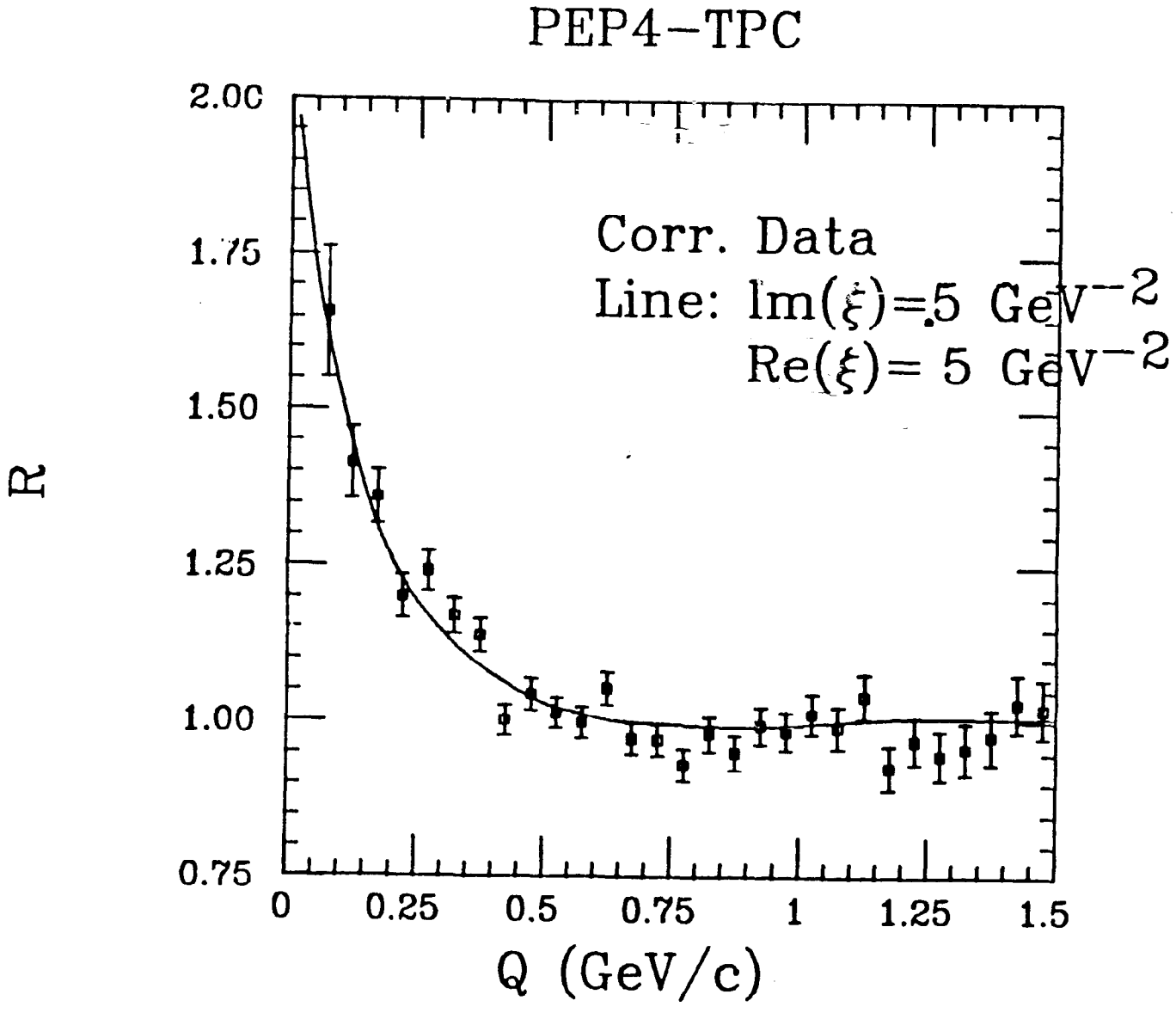
PEP4–TPC
Corr. Data
Line: Im(ξ)=.5 GeV^{-2}
Re(ξ)= 5 GeV^{-2}
R
Q (GeV/c)
2.00
1.75
1.50
1.25
1.00
0.75
0
0.25
0.5
0.75
1
1.25
1.5

Fig. 17

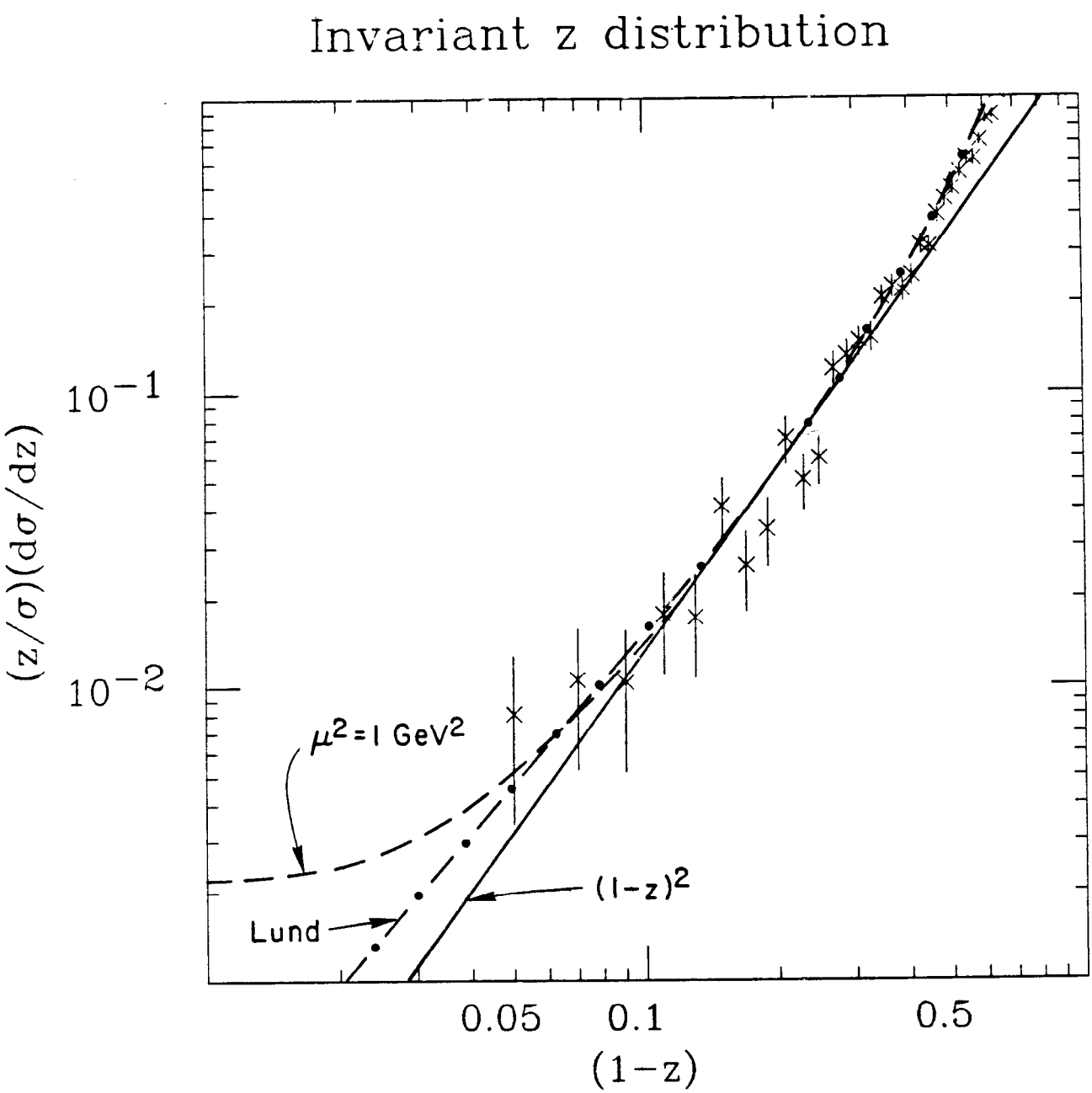
Invariant z distribution
$(z/\sigma)(d\sigma/dz)$
10^{-1}
10^{-2}
$\mu^2 = 1$ GeV^2
$(1-z)^2$
Lund
0.05
0.1
0.5
$(1-z)$

Fig. 18

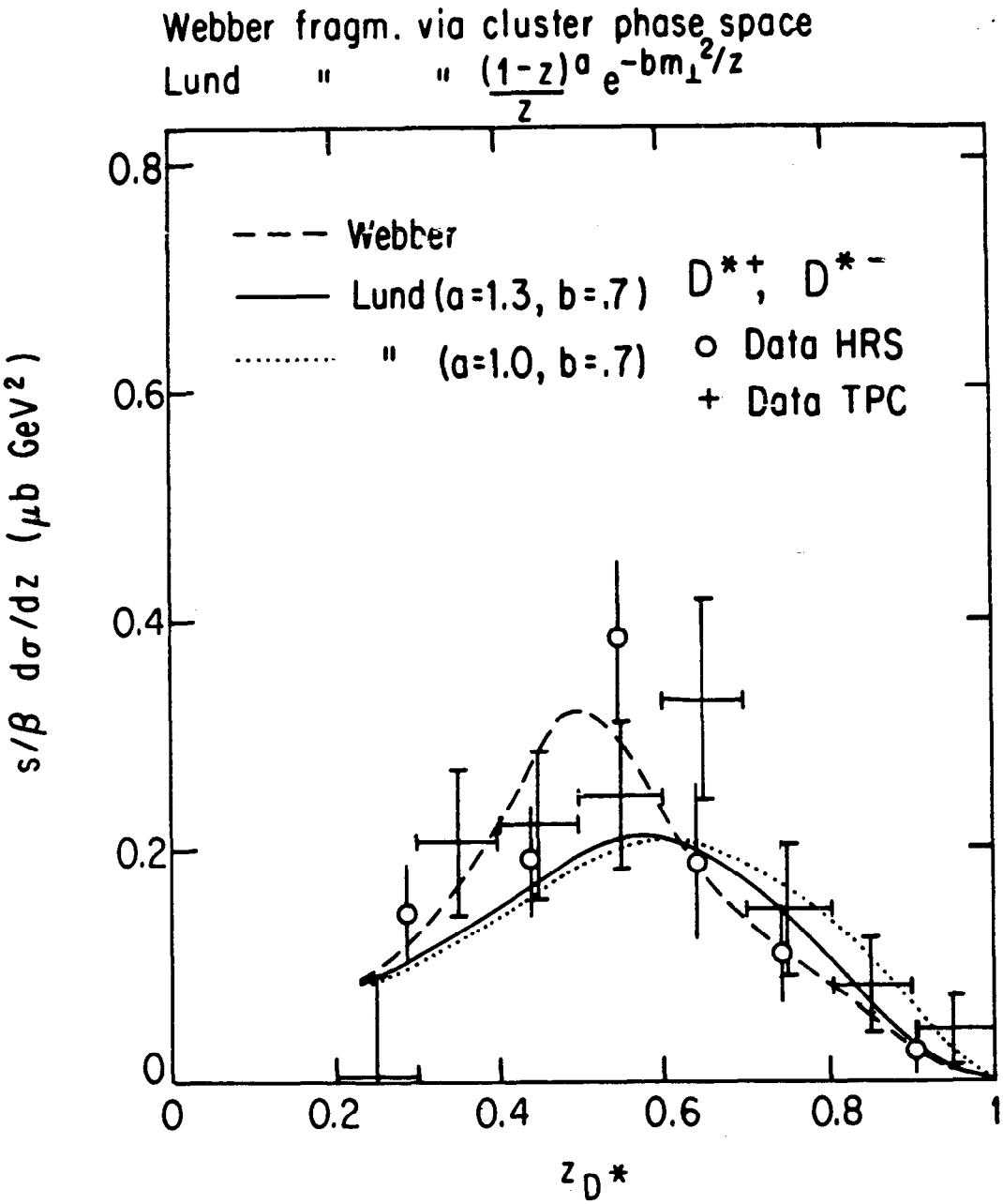
Webber fragm. via cluster phase space
Lund " " $\frac{(1-z)^a}{z} e^{-bm_\perp^2/z}$
Webber
Lund (a=1.3, b=.7)
" (a=1.0, b=.7)
D^{*+}, D^{*-}
o Data HRS
+ Data TPC
$s/\beta\ d\sigma/dz\ (\mu b\ GeV^2)$
z_{D^*}
0
0.2
0.4
0.6
0.8
1

Fig. 19

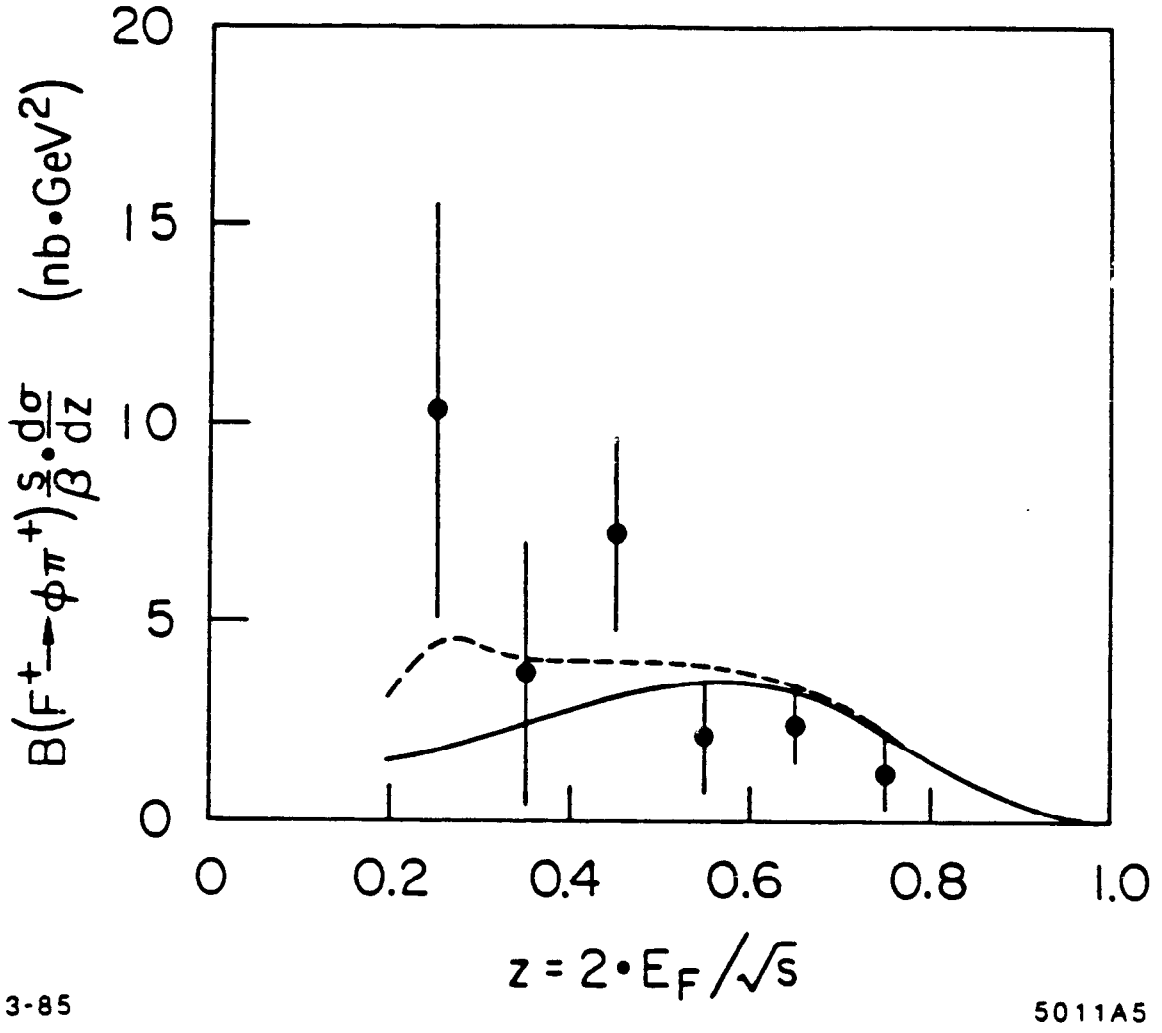
20
15
10
5
0
0
0.2
0.4
0.6
0.8
1.0
$B(F^+ \to \phi\pi^+)\frac{s}{\beta}\cdot\frac{d\sigma}{dz}$ (nb·GeV²)
$z = 2 \cdot E_F/\sqrt{s}$
3-85
5011A5

Fig. 20

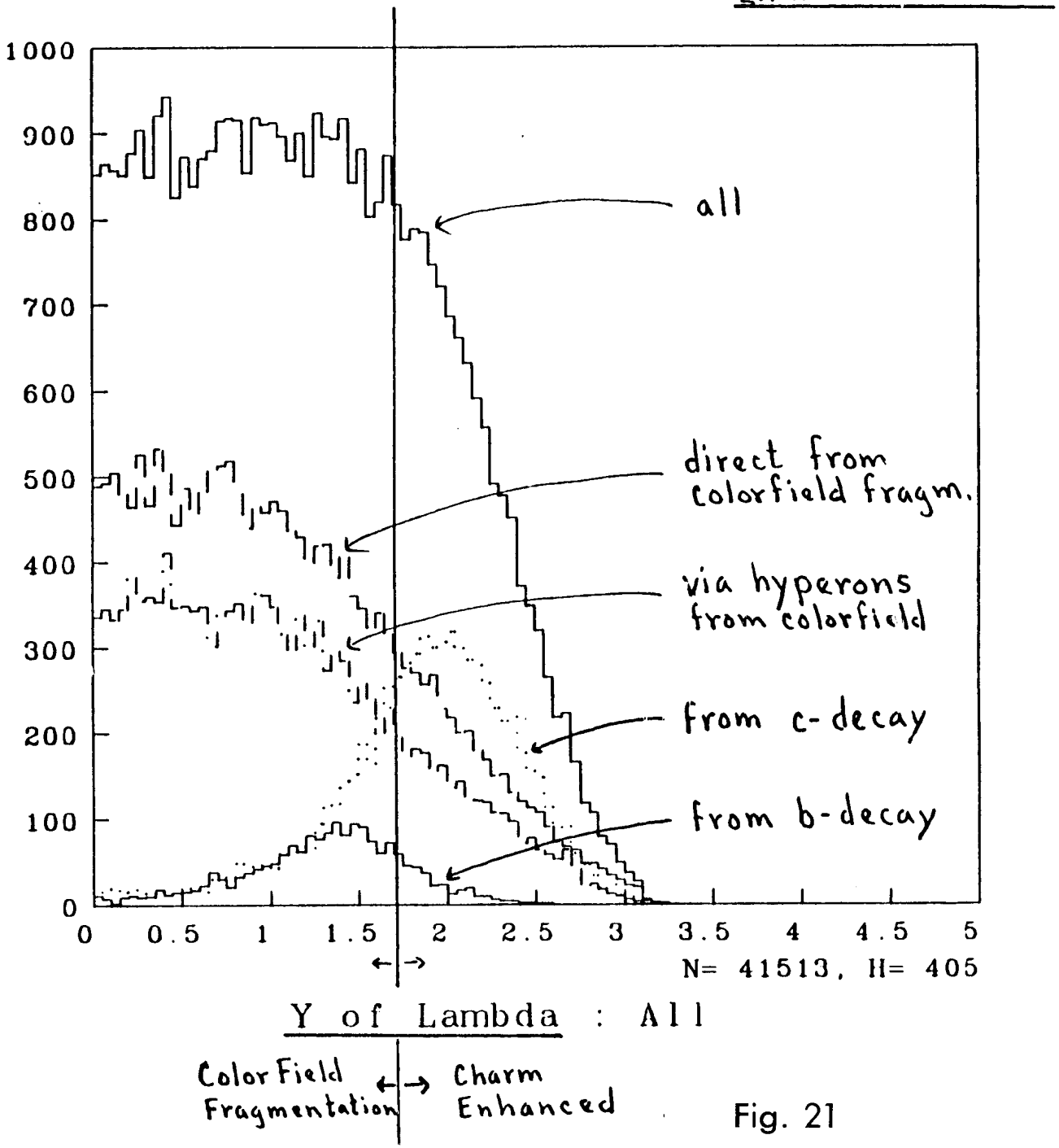
Run 62-301 02-Aug-84 09:08
LAMDA's VS. RAPIDITY
1000
900
800
700
600
500
400
300
200
100
0
0 0.5 1 1.5 2 2.5 3 3.5 4 4.5 5
all
direct from colorfield fragm.
via hyperons from colorfield
from c-decay
from b-decay
N= 41513, H= 405
Y of Lambda : All
ColorField Fragmentation
Charm Enhanced

Fig. 21

LAMBDA POLARIZATION

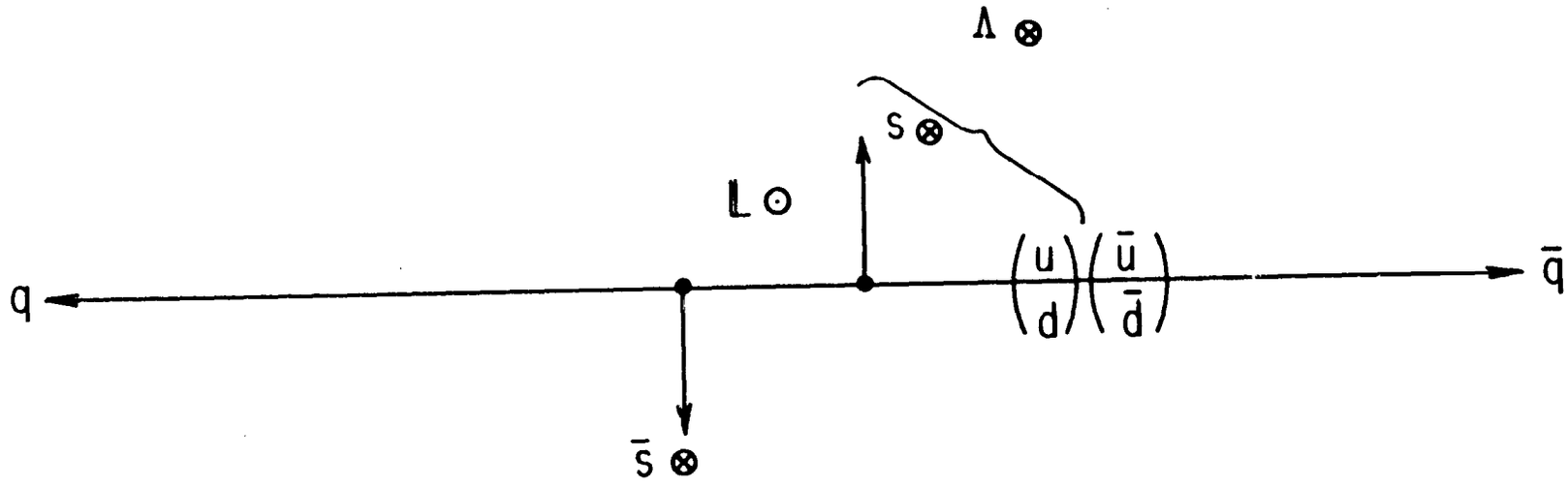

Fig. 22

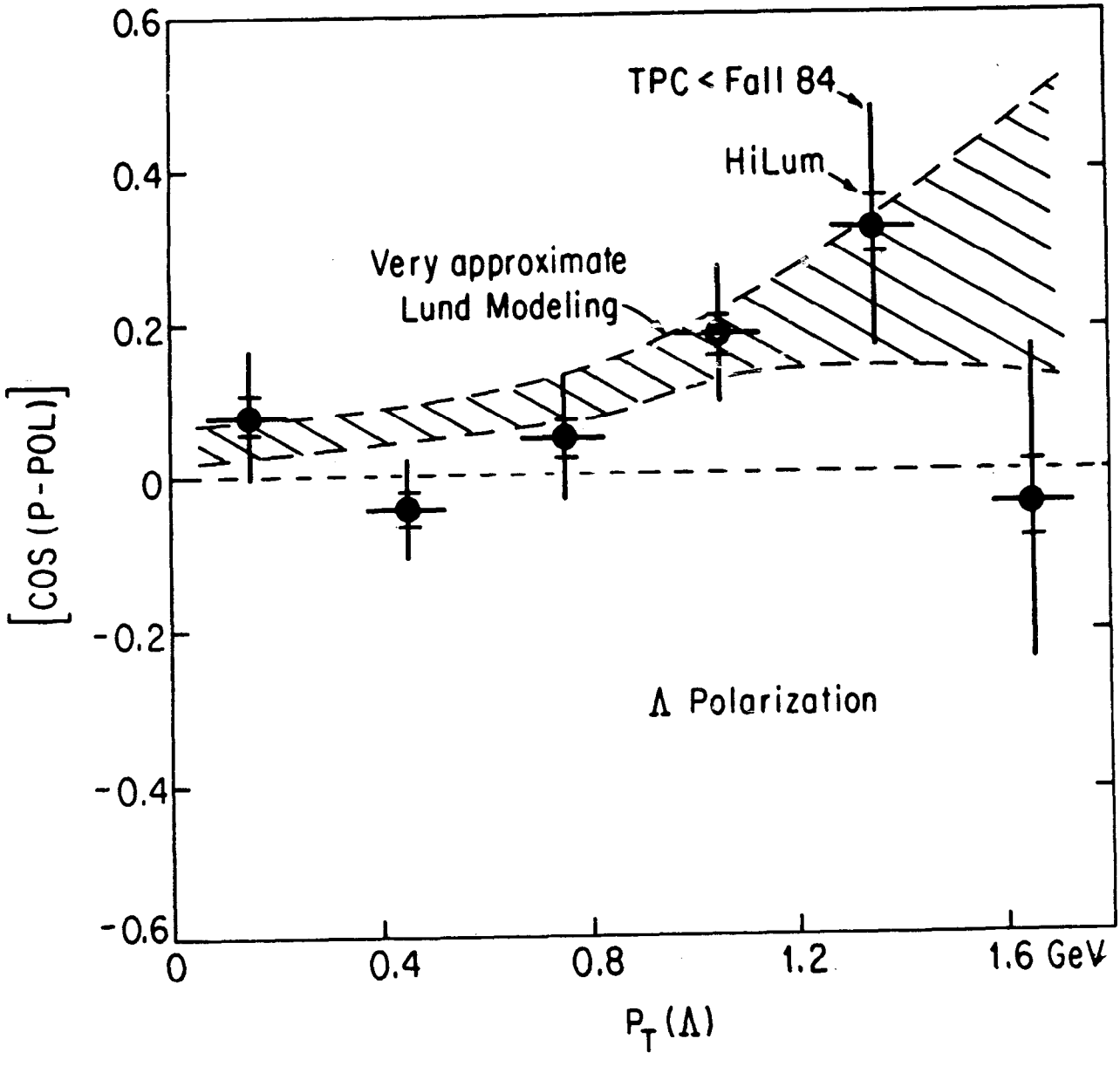
0.6
0.4
0.2
0
-0.2
-0.4
-0.6
[COS (P-POL)]
TPC < Fall 84
HiLum
Very approximate
Lund Modeling
Λ Polarization
0
0.4
0.8
1.2
1.6 GeV
P_T (Λ)

Fig. 23

Multi-Purpose Strange Baryon Event
(assumed: Ordered, 1-Step Di-Quarks)

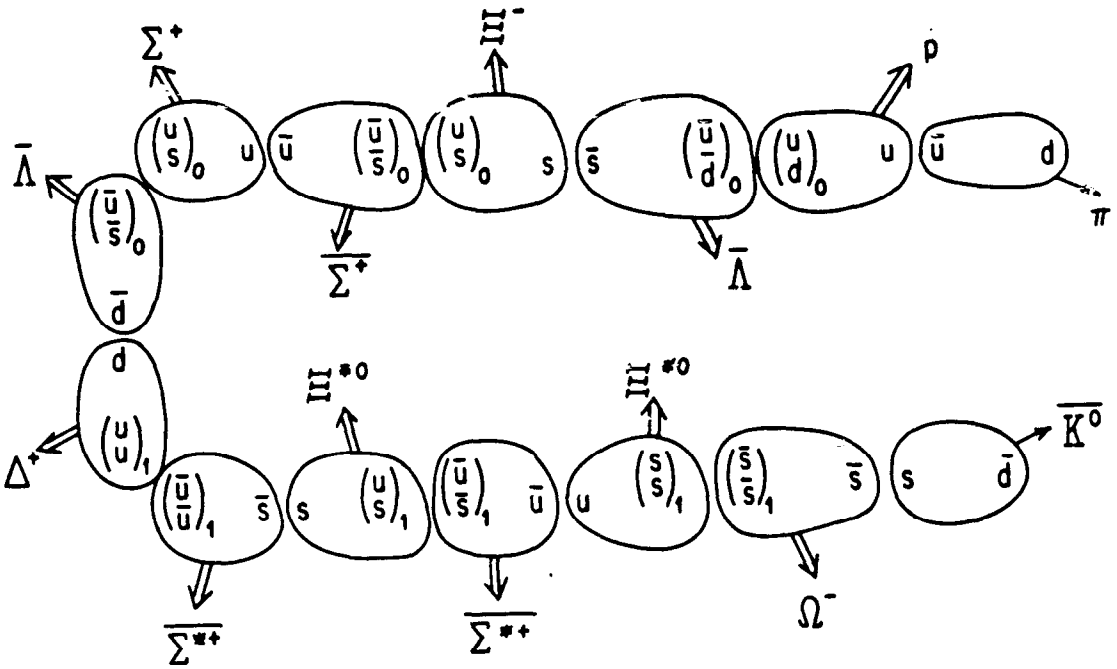

(or: Dis-ordered)

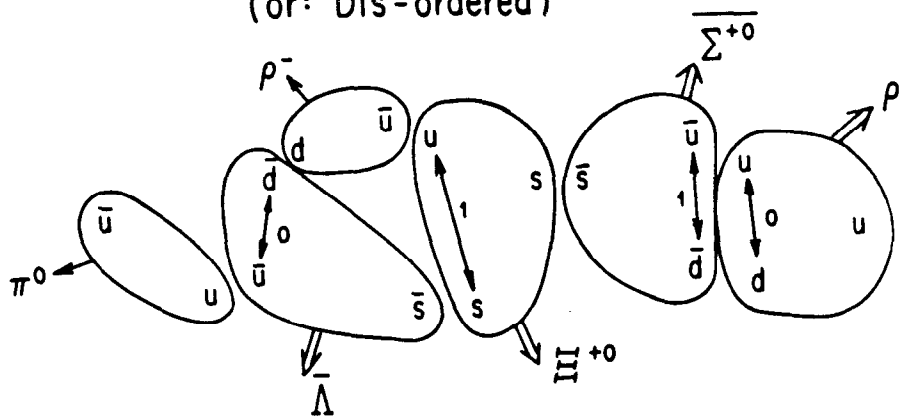

Fig. 24

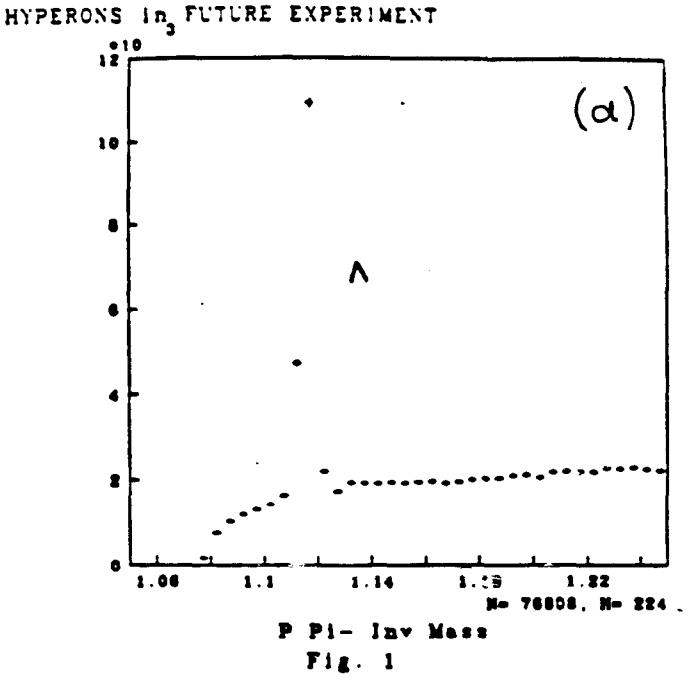
HYPERONS In$_3$ FUTURE EXPERIMENT
(a)
Λ
P Pi- Inv Mass
Fig. 1

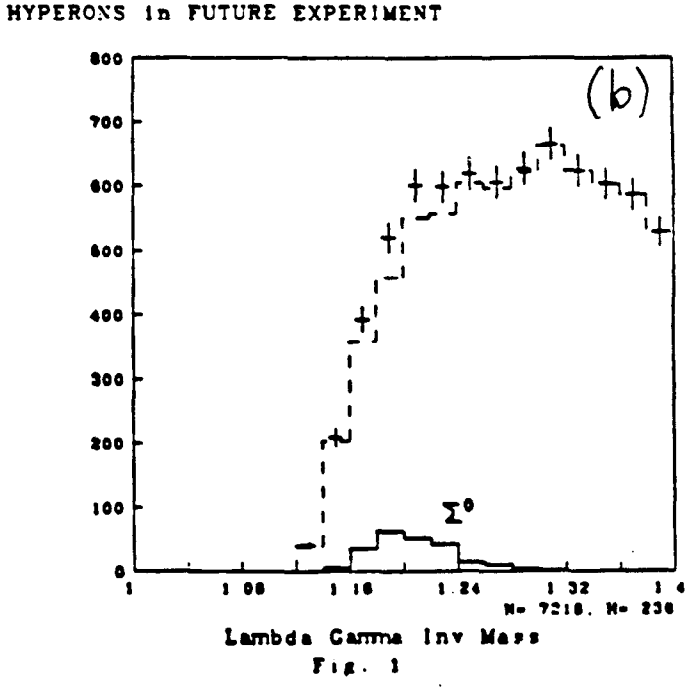
HYPERONS In FUTURE EXPERIMENT
(b)
Σ0
Lambda Gamma Inv Mass
Fig. 1

Fig. 25

HYPERONS in FUTURE EXPERIMENT

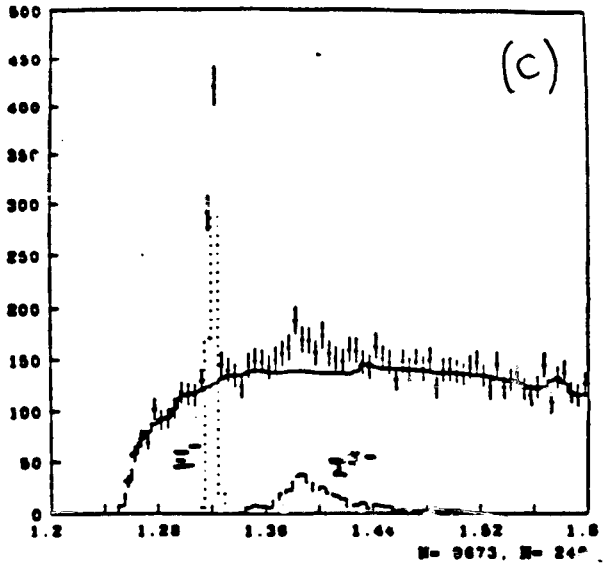

Lambda Pi- Inv Mass

Fig. 1

HYPERONS in FUTURE EXPERIMENT

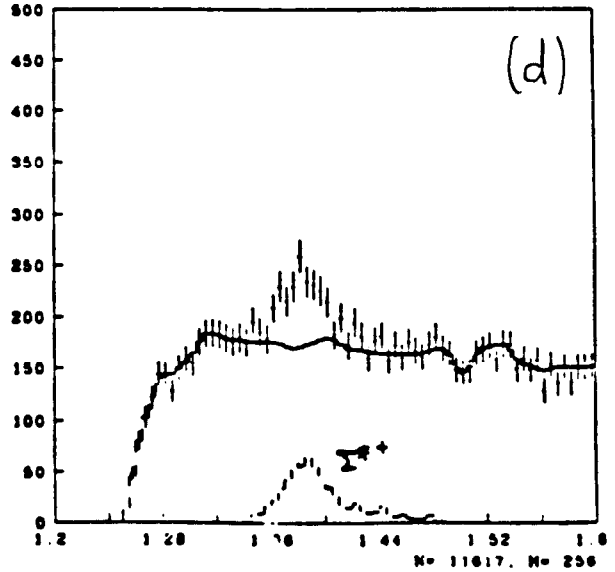

Lambda Pi+ Inv Mass

Fig. 1

Fig. 25

HYPERONS in FUTURE EXPERIMENT

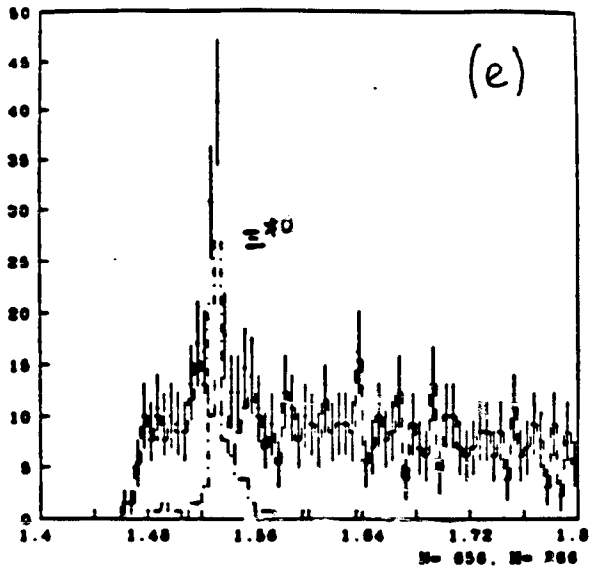

Xi- Pi+ Inv Mass
Fig. 1

HYPERONS in FUTURE EXPERIMENT

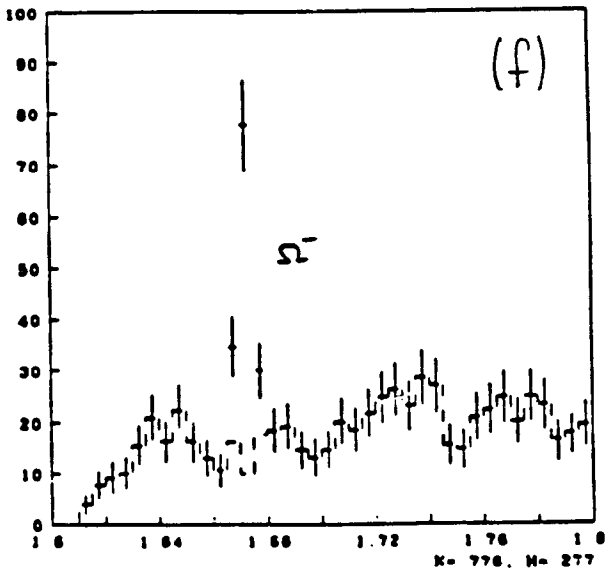

Lambda K- Inv Mass
Fig. 1

Fig. 25

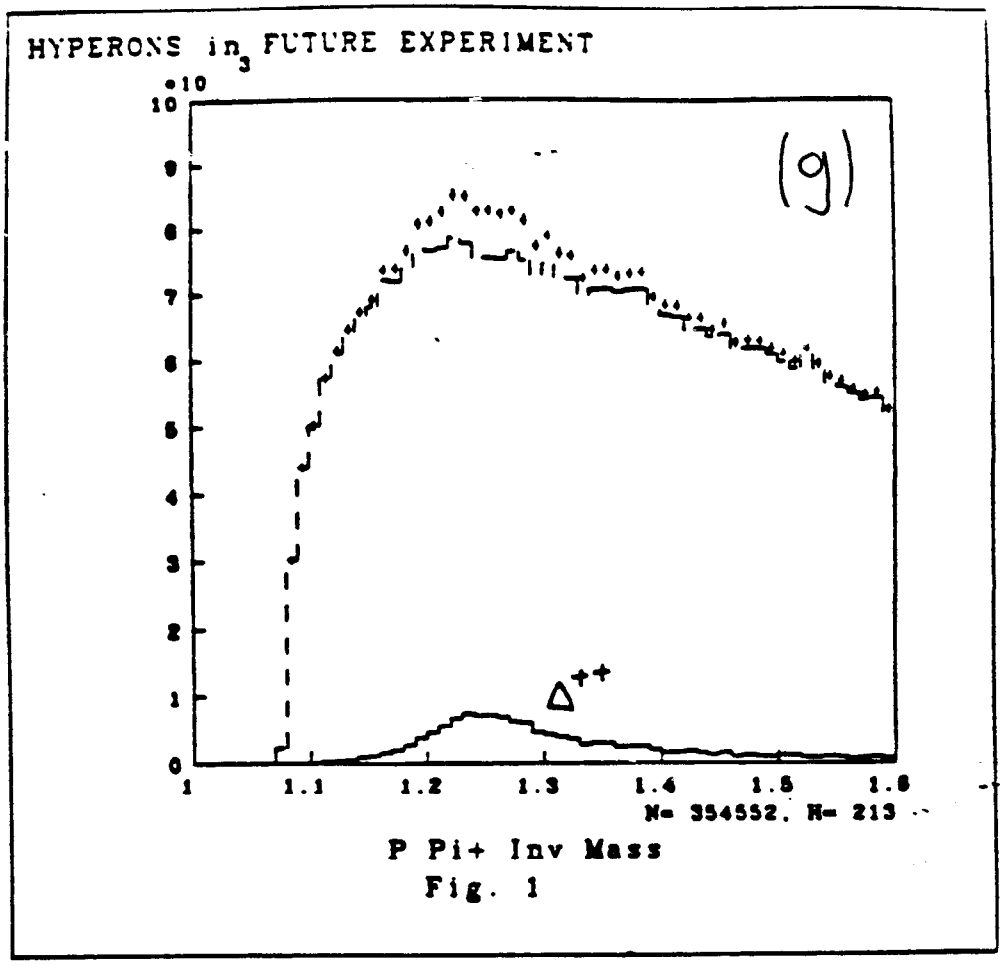
HYPERONS in FUTURE EXPERIMENT
3
•10
10
9
8
7
6
5
4
3
2
1
0
1
1.1
1.2
1.3
1.4
1.5
1.6
(g)
Δ++
N= 354552. M= 213
P Pi+ Inv Mass
Fig. 1

Fig. 25

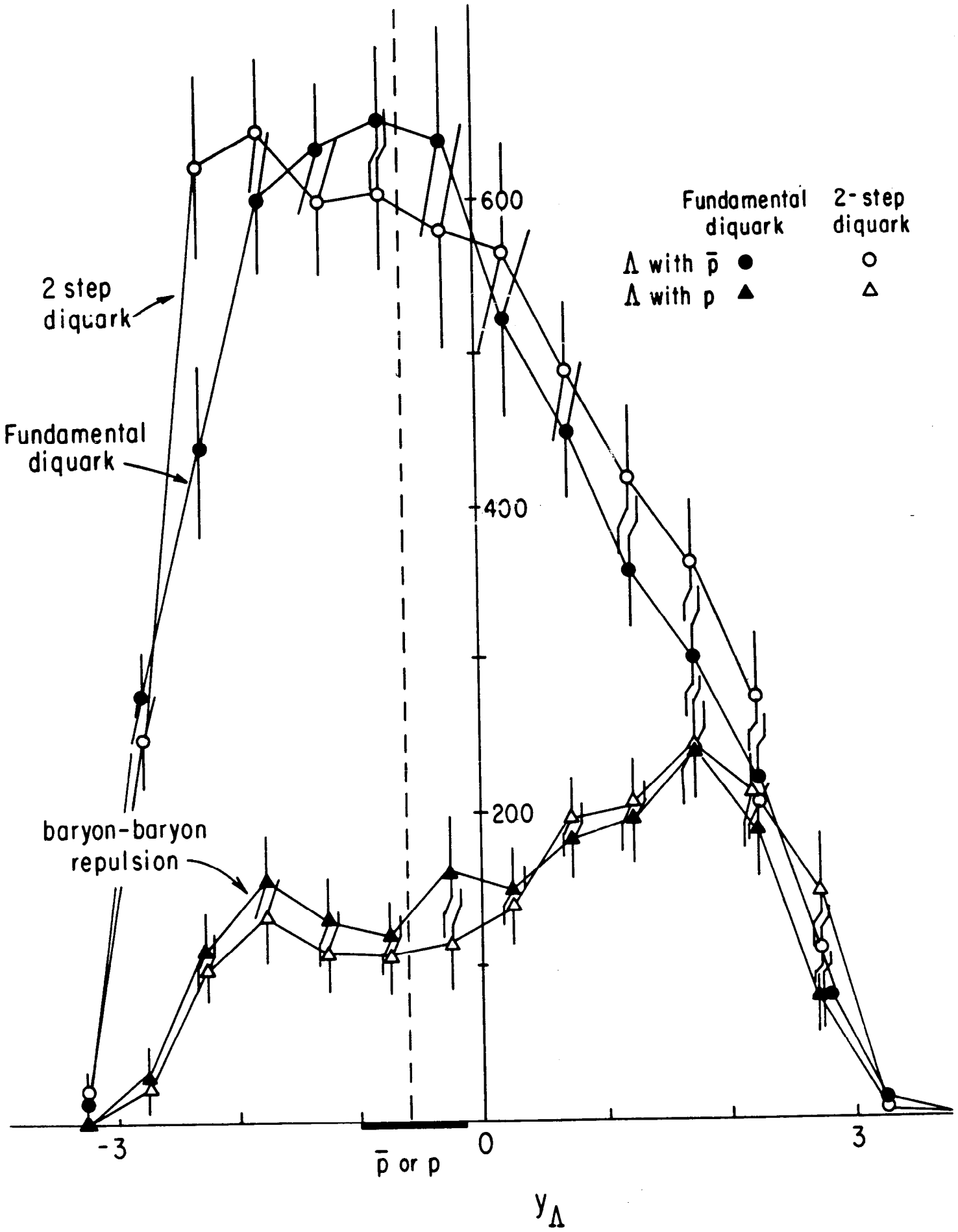
Fundamental diquark
2-step diquark
Λ with p̄
Λ with p
2 step diquark
Fundamental diquark
baryon-baryon repulsion
600
400
200
-3
0
3
p̄ or p
y_Λ

Fig. 26

HYPERONS in FUTURE EXPERIMENT

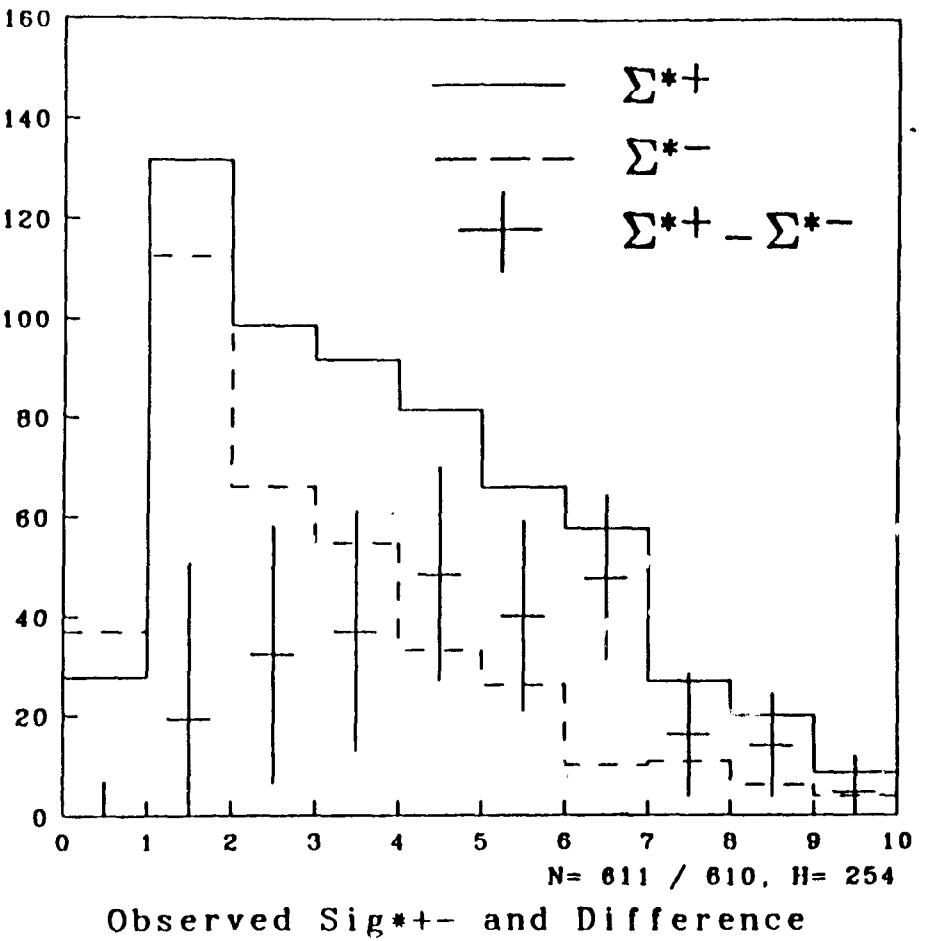

Momentum distributions of Σ^{*+} and Σ^{*-}

Fig. 27

Run 51-1 31-Mar-85 17:58

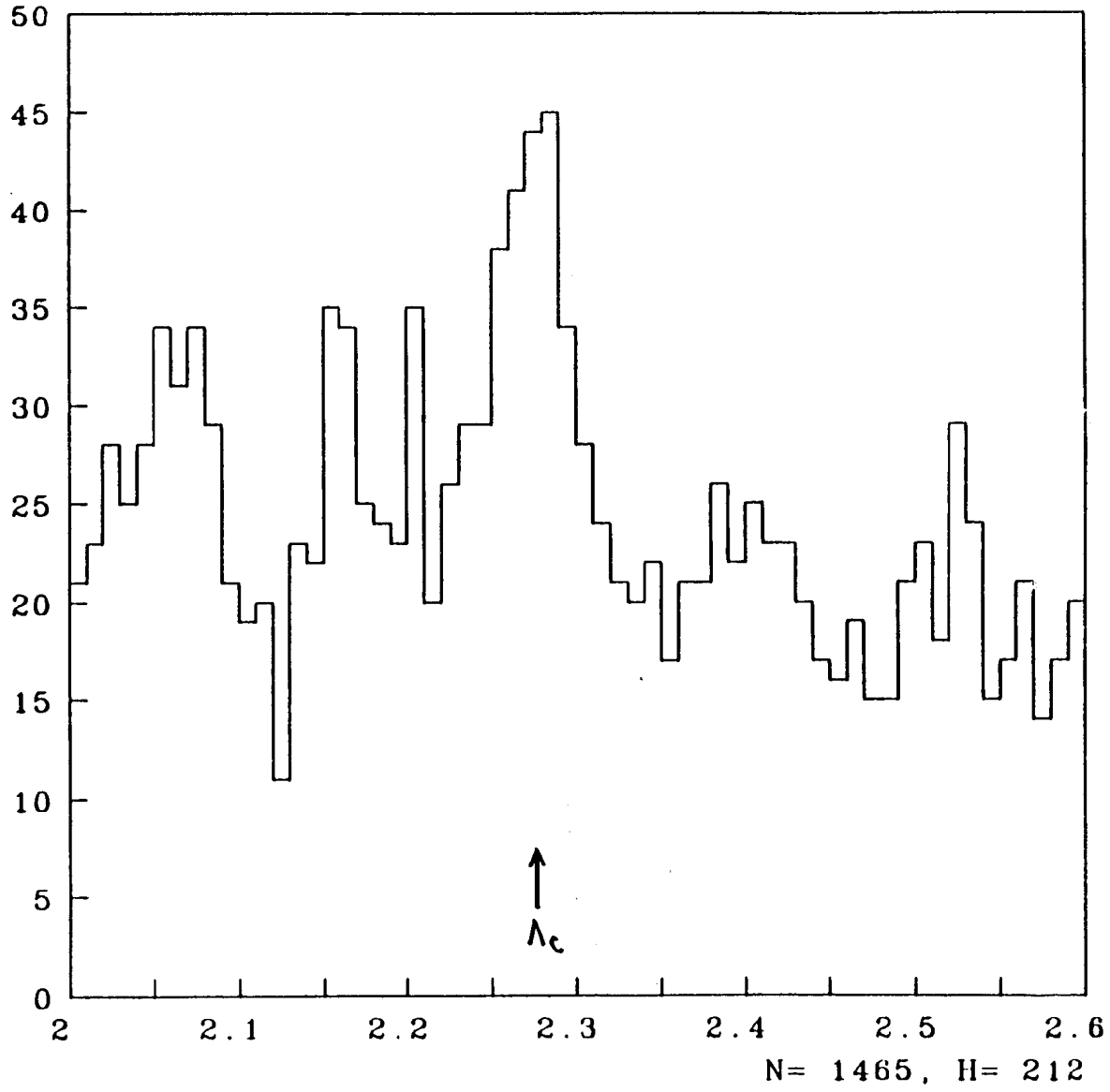

LaC--⟩PKPi : P(LaC) ⟩ 8GeV : P⟩K⟩Pi

LaC --⟩ La + Pi+

Fig. 28

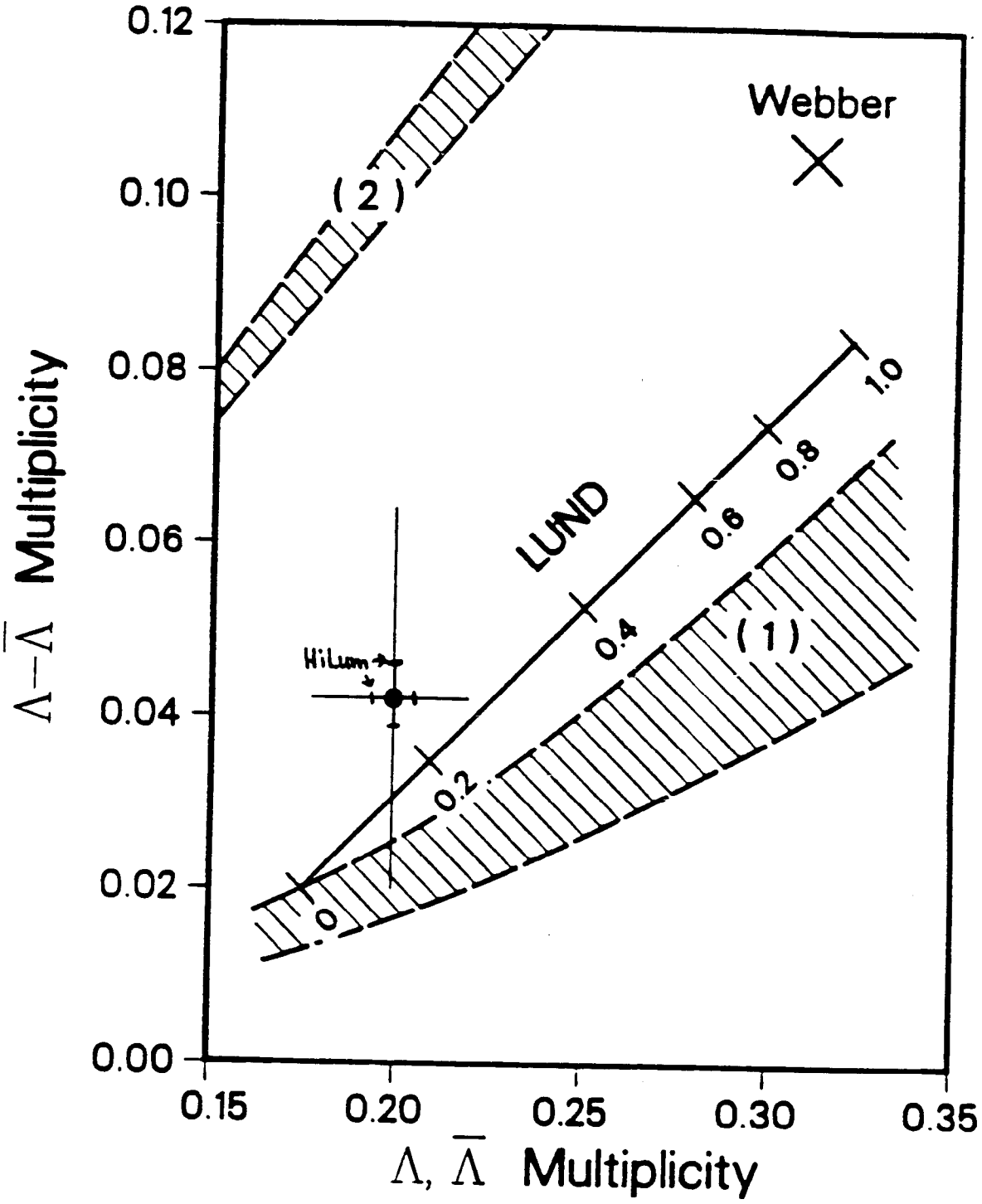
0.12
0.10
0.08
0.06
0.04
0.02
0.00
0.15
0.20
0.25
0.30
0.35
$\Lambda - \bar{\Lambda}$ Multiplicity
$\Lambda, \bar{\Lambda}$ Multiplicity
Webber
(2)
(1)
LUND
0
0.2
0.4
0.6
0.8
1.0
Hilum
XCG 849-13256 B

Fig. 29

Λ Formation from
Standard, Ordered
Fundamental DiQuarks

$\bar{\Lambda}\Lambda/\Lambda \sim 13\%$

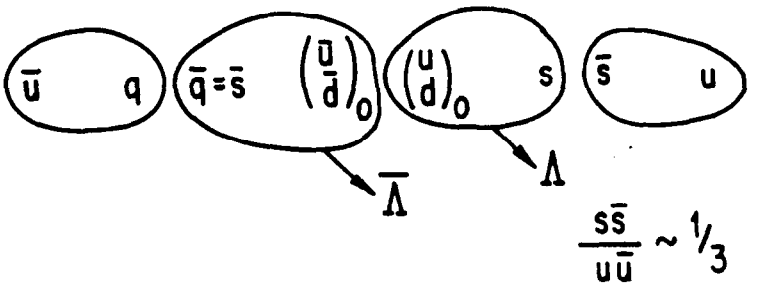

$\frac{s\bar{s}}{u\bar{u}} \sim 1/3$

NON-STANDARD POSSIBILITIES

Ordered String with
Large $(us)_0$ Probability

$\Lambda\bar{\Lambda}/\Lambda \sim 43\%$

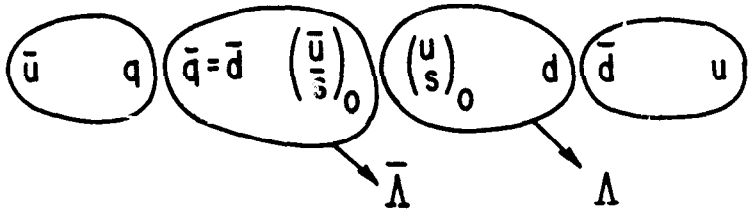

Ordered Cluster Model

$\Lambda\bar{\Lambda}/\Lambda \sim 20\%$

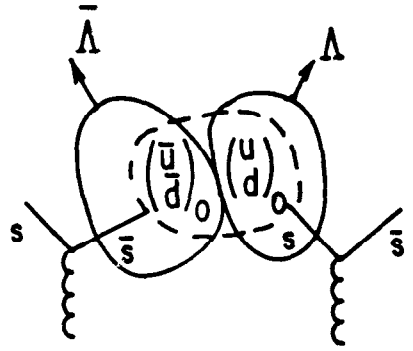

$\frac{g\to s\bar{s}}{g\to u\bar{u}} \sim 1/2$

Non-Nearest Neighbor

$\Lambda\bar{\Lambda}/\Lambda \sim 100\%$

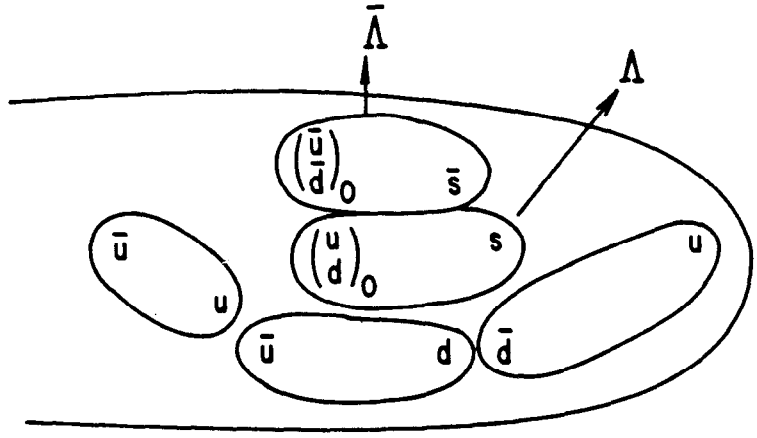

(Note: Colors match correctly.)

Fig. 30

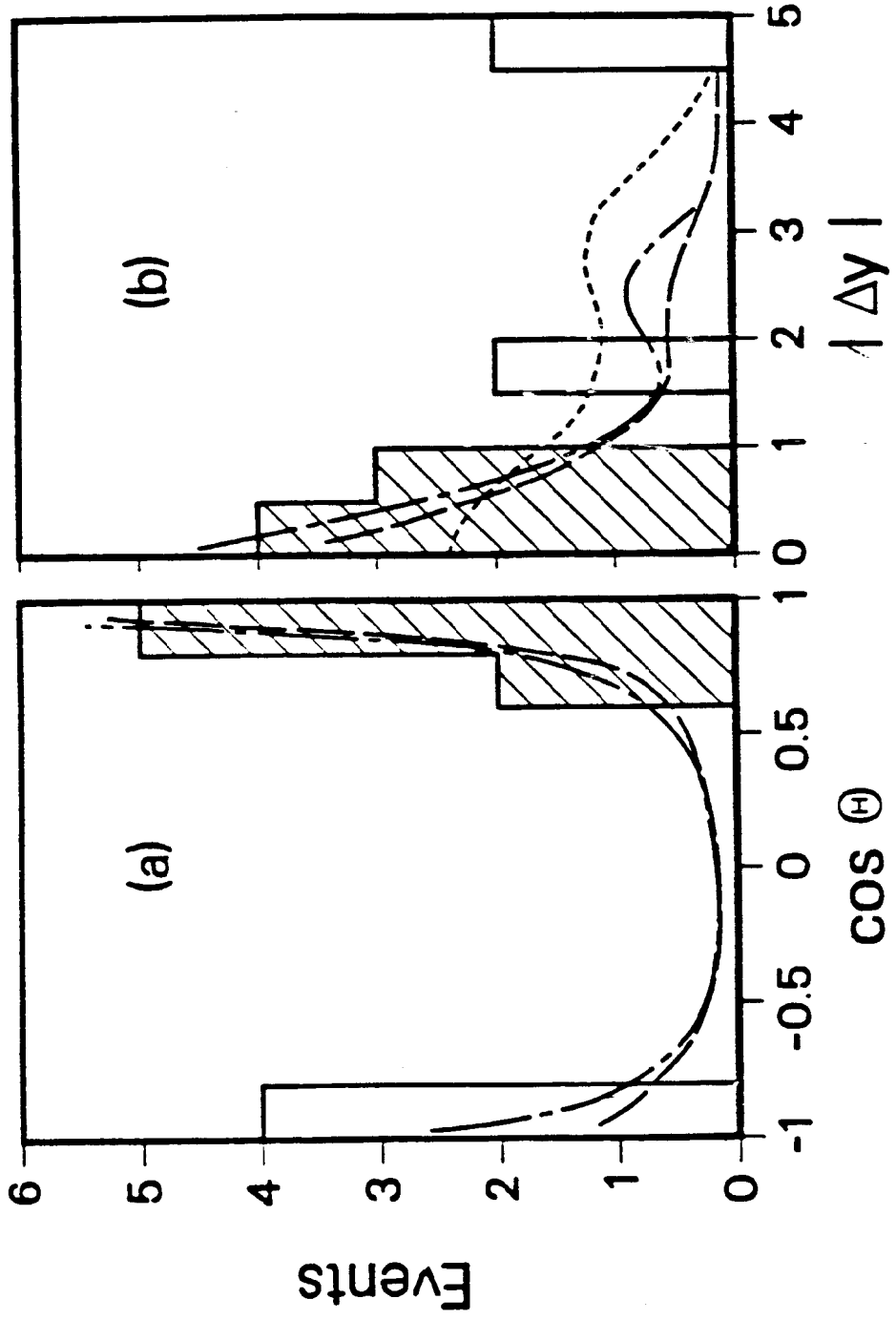

Fig. 31

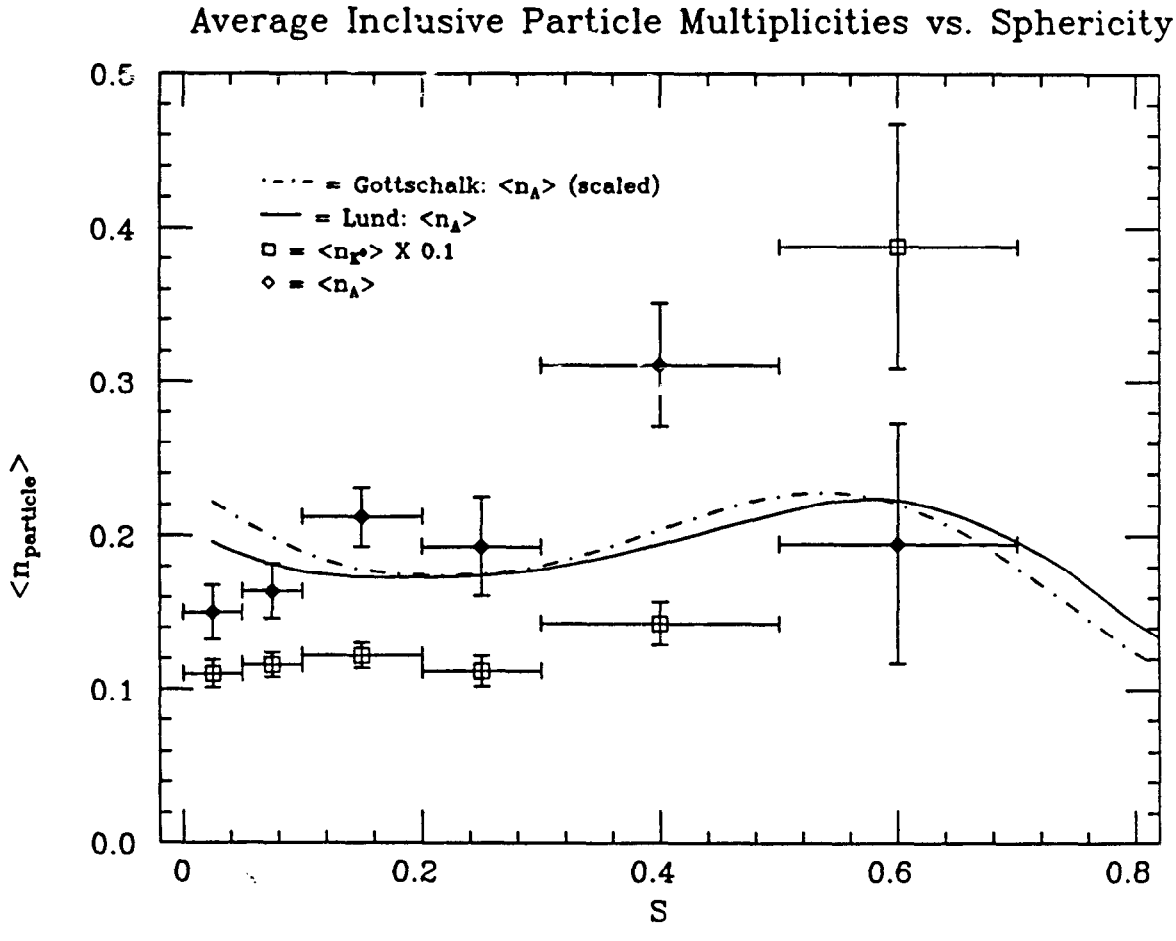
Average Inclusive Particle Multiplicities vs. Sphericity
= Gottschalk: <n_A> (scaled)
= Lund: <n_A>
= <n_K0> X 0.1
= <n_A>
<n_particle>
S
0.0
0.1
0.2
0.3
0.4
0.5
0
0.2
0.4
0.6
0.8

Fig. 32

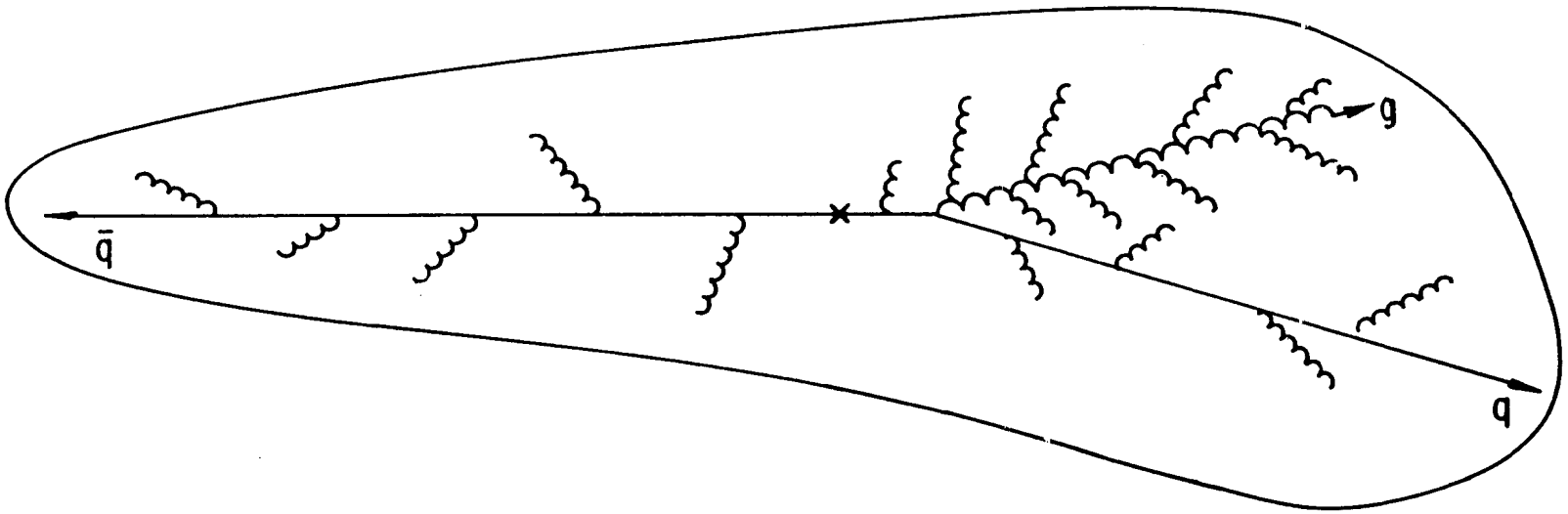

Merging Jets
from Nearby Partons

Fig. 33

CHAPTER V. ON NEW PARTICLE SEARCHES

M. DERRICK

and

D. BURKE, K. K. GAN, F. GILMAN, R. HOLLEBEEK, J. JAROS,
D. KOLTICK, P. KOOIJMAN, M. PERL, R. PREPOST,
R. THUN, P. TSAI, M. WILLUTZKY, R. WILSON

CHAPTER V. ON NEW PARTICLE SEARCHES

CONTENTS

V.1 INTRODUCTION

The Standard Model is a remarkable result of decades of work in particle physics, but it is clearly an incomplete representation of the world. Exploring possibilities beyond the Standard Model is a major preoccupation of both theorists and experimentalists. Despite the many suggestions that are extant about the missing links within the Standard Model as well as extensions beyond it, no hard experimental evidence exists. In particular, in more than five years of experimentation both at PETRA and PEP no new particles have been found that would indicate new physics. Several reasons are possible for these negative results: the particles may be too heavy; the experiments may not be looking in the proper way; the cross sections may be too small or finally the particles may not exist.

A continuing PEP program, at high luminosity will ensure that the second and third reason continue to be addressed. The higher energy e^+e^- storage rings such as TRISTAN and LEP will extend the mass limits. High mass particles can also be produced at the CERN collider and soon with the Tevatron collider.

A concise summary of the mass limits from the PETRA experiments has been given in a recent Mark J publication.[1] The results, shown in Table I, provide a convenient yardstick against which to measure future search experiments.

V.2 CHARGED PARTICLE SEARCHES

The TPC has placed the best limits[2] on stable fractionally charged particles by measuring the momentum and dE/dx. The limits are somewhat model dependent but are typically $R_q \lesssim 10^{-3}$ for $\frac{1}{3}, \frac{2}{3}$ and $\frac{4}{3}$ charged particles.

Unstable charged particles such as technipions or charged Higgs would be revealed by an increase in the R value, the ratio of hadronic to the $\mu^+\mu^-$ pair cross sections. Figure 1 shows a compilation of such measurements. The most

Table I. Lower mass limits (95% CL) for new particles

Particles	Mark J Lower Mass Limit (GeV)	Mark J Remarks	CELLO Lower Mass Limit (GeV)	JADE Lower Mass Limit (GeV)	TASSO Lower Mass Limit (GeV)
A. QED					
e^*	72	$\lambda = 1$	59	61	61
μ^*	25	$\lambda = 1$	–	22	–
B. Standard Theory					
$L^{\pm}$	22.5	Lifetime < 10 ns	–	18	15.5
Toponium	46.6	$\Gamma_{ee}\, B_h < 3$ keV	46.6	–	45.2
Open Top	46.6	–	46.6	35	44
C. Extended Theory					
$H^{\pm}$ and Technipions	17	$B_r(\tau\nu) > 1/4$	–	14	13
D. SUSY					
$\tilde{\gamma}$	20.5	decay path < 5 cm, $M_{\tilde{e}} = 50$ GeV	13	18	6
$\tilde{e}$	22	–	16.8	25.2	16.6
$\tilde{\mu}$	20	–	16	20.9	16.4
$\tilde{\tau}$	17	–	15.3	–	–
$\tilde{H}^{\pm}$	22.5	$M_{\tilde{\gamma}} = 4$ GeV	–	–	–
$\tilde{Z}^{\circ}$	35	$M_{\tilde{\gamma}} < 2$ GeV	–	30	–
		$M_{\tilde{e}} < 40$ GeV	–	–	–
$\tilde{W}^{\pm}$	25	$M_{\tilde{\gamma}}, M_{\tilde{\nu}} \ll M_{\tilde{W}^{\pm}}$	–	–	–
E. Scalar					
X	46.6	$\gamma\gamma, \mu\mu$,hh	$\simeq 45$	–	–
	48	$e\bar{e}$	–	–	–

precise results at high energy are:

$$R = 3.96 \pm 0.09 \text{ at } \sqrt{s} = 29 \text{ GeV from MAC}^{[3]}$$

$$\text{and} \quad R = 3.97 \pm 0.05 \pm 0.10 \text{ in the } \sqrt{s} = 12 - 36 \text{ GeV}$$

energy range from JADE.[4] These values may be compared to the expectation of $R = \frac{11}{3}(1 + \frac{\alpha_s}{\pi} + ...) = 3.88$.

The production of a scalar charged particle would increase R by 0.25 units which seems unlikely compared to the difference of 0.08 ± 0.07 between the experiment and theory. However the β^3 threshold factor rises very slowly as seen in Fig. 2 and so the production of a pair of charged scalars with mass as low as 10 GeV would still be possible. A pair of spin $\frac{1}{2}$ particles have a much sharper cross section increase above threshold as well as $\Delta R = 1$ and so would have been seen.

A more sensitive technique is to look for specific decay modes. A Higgs particle that preferentially couples to mass would decay to $\tau\nu_\tau$ and to $c\bar{s}$, or $c\bar{b}$ depending on the Higgs mass. A series of experiments at PETRA[5] looking for both leptonic and hadronic decays excludes such a charged Higgs below a mass in the range (14-17) GeV as seen in Fig. 3. Very little else can be said and it is an open question if scalars whose decay modes are not so determined might exist.

The classic search technique is to scan the energy range and look for the appearance of a class of isotropic events as the threshold is passed. This has been done by PETRA at the higher energies in the top quark search but not in the energy range between CESR and PEP. As seen in Fig. 1, essentially no data exists from $\sqrt{s} \simeq 12$ to $\sqrt{s} \simeq 25$ GeV. Here is some unfinished business, although it is clearly a long shot in looking for new phenomena.

A number of searches have been made for excited leptons. These can be produced either directly or as a propagator as in the diagrams of Fig. 4. The direct search looks for an effective mass peak in the lepton-photon system above

a continuum coming from radiative events. The MAC result[6] is shown in Fig. 5. The PETRA mass limit[1] for a μ^* is 25 GeV.

For the electron, a better limit comes from the $e^+e^- \rightarrow \gamma\gamma$ reaction. The cross section can be written[7] as:

$$\frac{d\sigma}{d\Omega} = \frac{\alpha^2}{s} \frac{1+\cos^2\theta}{\sin^2\theta} \left\{1 \pm \frac{s^2}{2\lambda_\pm^4} \sin^2\theta\right\} \qquad (1)$$

where the first term is the simple QED contribution and the parameter λ is essentially the mass of the hypothesised excited electron e^*. The cross section is large, as seen in Fig. 6, and so most PEP detectors have collected $\sim$ 20 K events. In the central region the modified angular dependance coming from the propagator is small (Fig. 7) so the sensitivity of the experiment depends on how well the systematic errors on the luminosity can be controlled. A cross section comparison between the e^+e^- and $\gamma\gamma$ final states is needed.

The current PEP limits on λ, now the 40–50 GeV range,[8] can be pushed to perhaps 70 GeV with the large data samples now available. This is in the same mass range limit as the Mark J result given in Table I. So in this case the higher energy at PETRA will just be balanced by the higher event rate at PEP. The relative sensitivity goes as $s^{\frac{1}{2}}N^{\frac{1}{8}}$, where N is the number of events.

Data on this reaction were used to limit possible explanations[9] of the few radiative Z° decays seen at the CERN collider assuming that the radiative decay went through a new spin zero boson (X) as $Z^\circ \rightarrow X\gamma$ followed by $X \rightarrow e^+e^-$. Such a particle would contribute an isotropic term to the $e^+e^- \rightarrow \gamma\gamma$ cross section. The MAC results shown in Fig. 8 agree with QED and give a limit on the isotropic cross section of < 1.56 pb/sr at 95% C.L. This result plus similar data from PETRA were used to limit the $\gamma\gamma$ width of X as a function of its mass.

V.3 SEARCH FOR SUSY PARTICLES

This popular extension of the standard model predicts partners of all the known particles with spin differing by one half. In the limit of exact supersymmetry the masses of the particles and their SUSY partners are equal. At what scale the symmetry is broken, and so the masses of the SUSY particles themselves, is unknown. Such particles, if charged, will be produced in e^+e^- collisions at the same rate as the known particles. A simple search can then be made, for example, for $e^+e^- \rightarrow \tilde{e}^+\tilde{e}^-$ followed by the decays $\tilde{e} \rightarrow e\tilde{\gamma}$ where the photino $\tilde{\gamma}$ escapes from the detector. The experiment then consists of looking for acolinear e^+e^-, $\mu^+\mu^-$ or $\tau^+\tau^-$ pairs with no accompanying photons as seen in Fig. 9a. The predominant background comes from radiative events. Such experiments are limited to SUSY particle masses below the beam energy and although PEP experiments[10] quickly ruled out scalar electrons $\tilde{e}$ up to 14.5 GeV as seen in Fig. 10 the higher beam energy at PETRA provided a more stringent limit-in the 20-25 GeV range.

The limit can be pushed beyond the beam energy by searching for single $\tilde{e}$ production via the diagram of Fig. 9b. In this case the scalar electron can be produced almost at rest in the laboratory and the decay gives a single electron of energy $\simeq M_{\tilde{e}}/2$. The result from the Mark II and MAC collaborations are similar.[11] The MAC limit is $M_{\tilde{e}} > 23.4$ GeV. More luminosity would not give significantly better values, higher beam energies are needed. It is a good early experiment for TRISTAN.

A more promising immediate avenue for SUSY searching is to look for the photino. As we have discussed the $e^+e^- \rightarrow \gamma\gamma$ reaction has a large cross section as does the SUSY equivalent $e^+e^- \rightarrow \tilde{\gamma}\tilde{\gamma}$ shown in Fig. 9c. In this case the $\tilde{e}$ appears in the propagator and so one could hope to approach $\tilde{e}$ masses near the 70 GeV limit for the e^* previously discussed. Although many thousands of such events may have been made at PEP they are difficult to observe as a low mass photino is sterile. The signature is to look for a radiative event, such as in Fig.

11a, with no other particles in the final state.

This search puts a premium on detecting photons at low transverse momentum, i.e., at small angles to the beam. The background process which presumably does occur is $e^+e^- \rightarrow Z^\circ \rightarrow \nu\bar{\nu}$ and the equivalent W exchange diagram also shown in Fig. 11b. The neutrino pair production rises rapidly with $\sqrt{s}$ and should be simple to observe at TRISTAN as seen in Fig. 12 which is calculated for the conditions of the MAC search. The results from the latter experiment are shown in Fig. 13: one candidate event is found with $E_\perp^\gamma > 3$ GeV which leads to the contours shown in Fig. 14 in the $M_{\tilde{\gamma}}$: $M_{\tilde{e}}$ space. For $m_{\tilde{\gamma}}$ small and $m_{\tilde{e}_L} = M_{\tilde{e}_R}$ a limit of 37 GeV is found for the scalar electron mass.

A more sensitive experiment (ASP)[12] designed specifically for this search came into operation at PEP this fiscal year and will soon be able to improve this limit. With the good current operation of the storage ring, ASP could place a limit close to 60 GeV as shown in Fig. 15 or indeed discover the photino if it exists and is in this mass range.

As we have discussed, the sensitivity of such an experiment goes as the fourth root of the integrated luminosity so an experiment with ten times the integrated luminosity could push the limit 1.8× higher. Taking data at a higher rate is good for such experiments, assuming that the beam gas backgrounds do not dominate, as the cosmic ray background is relatively supressed and the apparatus needs to be kept in fully calibrated condition for fewer years.

When the neutrino signal is observed, which should occur for an $M_{\tilde{e}}$ limit about 70 GeV, the SUSY experiment loses sensitivity as now a background subtraction will be needed. However the detection of the $\gamma\nu\bar{\nu}$ final state at about the expected level would in itself be an experimental feat and would validate the SUSY search. A major difficulty of all negative results from search experiments is proving that the expected signal would in fact have been seen, if present. The expected limit on the number of light neutrino generations from ASP is ~ 8.

The extension of such experiments into the early 1990s when the width of the Z° will have been measured could be interesting and justified since the two experiments measure somewhat different things. For example both experiments measure the number of light neutrinos but only the lower energy experiment is sensitive to the existence of the photino. By contrast the Z° can decay to $\tilde{H}°$ the SUSY Higgs partner. Scalar neutrino pairs could be produced by both processes depending on the mass of the $\tilde{\nu}$. The cross section ratio $(e^+e^- \rightarrow \tilde{\nu}\tilde{\bar{\nu}})/(e^+e^- \rightarrow \nu\bar{\nu})$ will be 0.25 times a threshold factor depending on $M_{\tilde{\nu}}$. If the $\tilde{W}$ were much lighter than 83 GeV the scalar neutrino pair production could dominate.

One should not take the SUSY discussion too literally as there is no experimental evidence that the current models have anything to do with the world as seen at present energies. However such complementarity and interplay of results from a lower energy and a higher energy facility has been important in the past, and would justify continuing a PEP physics program even into the SLC/LEP era. In general any particle that couples not to the Z° but to the photon would be much more strongly produced at PEP.

A recent example of such complementary, this time between PEP and the CERN Collider, is provided by the monojet experiments. The results can also be interpreted in SUSY models. Three experiments from PEP[13] and one from PETRA[14] have recently reported similar limits on the production of monojets in e^+e^- annihilation. Table II summarizes the results of the PEP experiments. A monojet is defined as a cluster of energetic particles with unbalanced p_T. Figure 16 shows such an event candidate seen in the HRS. The background comes primarily from annihilations following a catastrophic bremsstrahlung of one of the beam electrons so that the jet resulting from the fragmentation of the $q\bar{q}$ system is balanced by a single photon. If the photon escapes in the small cracks in the shower counters then an apparent monojet will result.

For the MAC experiment the main background comes from $\tau^+\tau^-$ pair production in which one tau decays into a single charged particle going in the backward

Table II. PEP magnet Searches

Group	$\int \mathcal{L}\,dt$	Experimental Cuts			Candidates	Background	Z° B.R.
	pb^{-1}	$\cos\theta^*$	p_T GeV/c	n_{ch}			limit %
HRS	176	0.5	7.2	4	1	3.3 ± 1.5	1.5
Mark II	222	0.67	8.0	2	2	consistent with 2	0.7
MAC	238	0.8	3.0	2	11	13.2	0.5

hemisphere. Such background events are 4 prongs as are all the candidates for this detector. All experiments require more than 2 prongs in the monojet.

The cross section for the reaction $e^+e^- \rightarrow Z^\circ \rightarrow$ any is given by:

$$\sigma = \frac{G_F M_Z^2 \Gamma_z}{\sqrt{2}(M_Z^2 - s)^2}(1 - 2\sin^2\theta_w + \sin^4\theta_w) \qquad (2)$$

$$= 6 \text{ pb at } \sqrt{s} = 29 \text{ GeV}$$

Hence each PEP experiment has collected more than 1000 such events – more than the detectors at the CERN collider. The monojets from UA1 are about as frequent as $Z^\circ \rightarrow e^+e^-$ decays[15] and so would correspond to Z° decaying to monojets with a branching ratio of several percent. Therefore if the monojets reported by the UA1 experiment come from anomalous Z° decay each PEP experiment should have seen 10-20 events in clear contradiction to the observation.

A quantitative comparison for the Mark II and MAC experiments is shown in Fig. 17 from which one sees that monojets in the jet mass range from 2 to 10 GeV coming from Z° decay are excluded. This result assumes the reaction $e^+e^- \rightarrow Z^\circ \rightarrow \chi_1\chi_2$ leads to a final state of two spin zero particles with the corresponding $\sin^2\theta$ angular distribution. If the χ particles are spin $\frac{1}{2}$ heavy leptons with a $(1 + \cos^2\theta)$ angular distribution then the sensitivity is somewhat reduced as shown by the lower curve in Fig. 17a. If χ_1 decays to 3ν with a 10%

branching ratio[16] then such a reaction is also excluded for χ_2 masses between 2 and 10 GeV.

The HRS group has also compared their limits to the expectation of a SUSY model. The $\tilde{e}$ exchange diagram of Fig. 18 leads to a cross section, estimated by Haber,[17] of

$$\sigma = 0.61(1 - R^2)(1 + R/2)\lambda^2/r^4 \text{ pb}$$

where $R = M^2_{\chi 2}/s$, λ^2 is the zino fraction in the $\tilde{H}, \tilde{Z}$ mixing and r is the mass ratio $M_{\tilde{e}}/M_w$. The production angular distribution goes as:

$$\frac{d\sigma}{d\Omega} \sim (1 + R) + (1 - R)\cos^2\theta \ .$$

The decay of χ_2 could go via $l^+l^-\tilde{\gamma}, q\bar{q}\tilde{g}$ or $q\bar{q}\tilde{\gamma}$. The latter would dominate if the gluino mass is larger than a few GeV and if $M_{\tilde{q}} \sim M_{\tilde{e}}$. If B is the branching ratio of χ_2 to $q\bar{q}\tilde{\gamma}$ then the HRS experiment leads to the contours shown in Fig. 19. Regions to the left of the curves are excluded. This result is more model dependent than the case where $\chi_1 = \chi_2 = \tilde{\gamma}$ discussed previously but gives somewhat higher limits on $M_{\tilde{e}}$ for $\lambda^2 B$ values greater than ~ 0.1.

V.4 Other New Particles From Z Decay

The previous discussion of monojets illustrates the capability of an e^+e^- machine that operates well below the Z° mass to study effects that could come from such decays. Although the PETRA measurements show that the charged lepton and the quarks from the fourth generation are above the PEP energy range this may not be the case for the associated neutrino.[18] The ASP experiment may see a few events of $e^+e^- \to \gamma N\bar{N}$ where N is the fourth generation neutrino, but the precision will be insufficient to definitely ascribe the few events expected to generations beyond three.

If the neutrino were to decay then it could be observed as:

a) A jet, perhaps a monojet if the second neutrino escaped the detector,

b) an isolated lX pair from a diagram such as shown in Fig. 20,

c) a group of particles with a vertex well separated from the main vertex, if the lifetime is long.

We have discussed the results of the monojet search. The second kind of event was looked for in the HRS[19] with again a negative result. Six candidates were found, consistent with known backgrounds, and giving limits on σB of 0.08 to 0.2 pb for neutrino masses ranging from 1 to 7 GeV.

The Mark II group has recently reported on a negative search for events with separated vertices.[20] These results are compared with other limits in Fig. 21[21] where the mixing between the fourth and first generations, $|U_{41}|^2$ is plotted against the mass of the fourth generation neutrino, M_N.

The dashed line in Fig. 21 corresponds to $\gamma c\tau$ of 1 m whereas the right hand edge of the region (8), excluded by the Mark II experiment, is $\gamma c\tau$ of a few mm set by the vertex resolution.

The line (7) is the sum of all of the three PEP monojet experiments interpreted in terms of single N production via the reaction $e^+e^- \rightarrow N\bar{\nu}_e$ which proceeds by W boson exchange. The cross section is:

$$\sigma(e^+e^- \rightarrow N\bar{\nu}_e) = |U_{14}|^2 \frac{G_F s}{6\pi}\left(1 - \frac{M_N^2}{s}\right)^2\left(1 + \frac{M_N^2}{2s}\right)$$

$$\simeq 4.7|U_{14}|^2 \text{ pb}$$

This limit would fall by perhaps an order of magnitude with a high luminosity PEP. It should also be possible to extend the boundary of the detached vertex search experiment to somewhat higher masses with an optimal vertex chamber.

An experiment with more events or one that searches to greater distances could also fill in the region between contour (5) which comes from the CERN CHARM experiment and the Mark II result.

The cross section (2) for the reaction $e^+e^- \rightarrow Z^\circ \rightarrow$ any is shown in Fig. 22. Since at PEP energies we are working far out on the tail of the resonance the cross section varies only slowly with $\sqrt{s}$. The signal to noise is poor and decreases somewhat faster than s^{-1}. At $\sqrt{s} = 29$ GeV the 6 pb Z° cross section may be compared to a total hadronic cross of $\sim$ 380 pb. With a luminosity upgrade, even if operating at $\sqrt{s} = 24$ GeV, each experiment could collect 1500-2000 Z° events per year. Such rates will be interesting until the new e^+e^- machines, operating at the Z° pole come into operation. A possible scenario is shown in Fig. 23 from which it is clear that a limited window of opportunity exists. The PEP upgrade is overdue if the program is to contribute to Z° physics.

V.5 Physics Within The Standard Model

Although those of us brought up on the V-A, two component theory know that neutrinos are massless this is not the case in many other theories. How it is in nature is an open and important experimental question. A report[22] of a finite result of $M_{\nu_e} \sim 30$ eV from the end point of the $H^3\beta$ decay spectrum gives an added edge to such searches. The current best limit[23] for M_{ν_μ} is 250 keV at 90% C.L., below the electron mass. The old problem with the rate of neutrino interactions from the sun also stimulated a major experimental activity in searching for neutrino oscillations. Despite a number of false alarms no convincing evidence exists for such effects.[24] The experiments continue. PEP can address such issues through measurements that limit tau neutrino mass. Two recent results[25] from Mark II of 143 MeV from the $\rho' \rightarrow 3\pi^+\pi^\circ$ decay and 157 MeV from the DELCO study of events of the ρ' decay to $KK\pi$, represent the best published values.

Left-right symmetric models[26] such as $SU(2)_L \times SU(2)_R \times U(1)$ give a natural scaling between generations as M_ν/M_l^2 so a 100 MeV tau neutrino mass would correspond to $\sim$ 8 MeV for the electron neutrino which is already much less than the 30 eV measurement.

There are some important constraints coming from astrophysics.[27] The expansion rate of the universe limits the mass of a stable neutrino to $\lesssim$ 100 eV.

However neutrinos must then decay with the favored process shown in Fig. 24. The matrix U_{el} connects the flavor eigenstates ν_e with the mass eigenstates ν_i

$$N_l = \sum U_{li}\nu_i \ .$$

The lifetime is given by:

$$\tau \simeq \frac{2.9 \times 10^4}{M_N^5 |U_{li}|^2} \qquad \text{(phase space)}$$

The radiative decays such as $\nu_\mu \rightarrow \nu_e\gamma$ are much slower.

The current density of deuterium and helium in the universe limits the possible neutrino lifetimes as decays such as $\nu_\tau \rightarrow e^+e^-\bar{\nu}_e$ occurring during nucleosynthesis would give γ rays which in turn would photo-disintegrate the D_2 and He.

These considerations combined with decay and neutrino beam dump experiments rule out the electron decay of the tau neutrino.[27] However a region in the $U_{32} : M_{\nu_\tau}$ space is still allowed. It is therefore important to push the tau neutrino mass limit below the muon mass and so forbid the $\nu_\tau \rightarrow \mu e \nu_e$ decay.

The recent observation by the HRS group of the $\tau \rightarrow 5\nu^{\pm}\pi^{\circ}\nu_\tau$ decays allows this to be done. The mass spectrum of the 5π and 6π final states is shown in Fig. 25. Fits to these spectra with a number of different models for the final state hadronic system give a 95% C.L. upper limit of the tau neutrino of 89 MeV.[28]

Since the charged particle effective mass resolution for the $5\pi^{\pm}\nu_\tau$ final state is 10-15 MeV in the HRS, the observation of a few events at the kinematic limit of 1784 MeV will limit the tau neutrino mass to the 10-20 MeV range. This can be done with a high luminosity PEP upgrade. The rate of this decay is one observed event every 37 pb^{-1} so 1000 pb^{-1} would give 27 events.

A second, important but very difficult experiment requires a precision check of μe universality in τ decay.[29] The ratio should be given by:

$$R = \frac{BR(\tau \rightarrow \mu\nu\nu)}{BR(\tau \rightarrow e\nu\nu)} = 1 - 0.027$$

where the 2.7% lower μ decay branching ratio comes from phase space. The current measurements of both the $\mu\nu\nu$ and $e\nu\nu$ final states have errors that are typically 3%.[30] Apart from the general interest in measuring such a fundamental calculable quantity as accurately as possible, a breakdown of μ,e universality could indicate new physics.

A calculation[29] assuming a contribution from a charged Higgs as shown by the diagram of Fig. 26 gives:

$$R = 1 - 0.027 + 0.243\frac{M_\mu^2 M_\tau^2}{M_H^4}\ \cot^4\alpha$$

where α is the vacuum expectation value of the Higgs field. In GeV units this is:

$$R = 1 - 0.017 + \frac{0.0086}{M_H^4}\ \cot^4\alpha$$

This is a very small effect unless cot α happens to be large. If M_H = cot α then an experiment at the 0.5% level is required. As discussed earlier the PETRA limit on M_H is 17 GeV.

Scaling from the present PEP experiments a 1000 pb^{-1} experiments, would yield about 8000 events in each of the e and μ decay modes so the statistical errors could approach 1%. Since one measure a ratio most of the systematic errors would cancel; however, a 1% measurement in a typical e^+e^- spectrometer is difficult.

V.6 CONCLUSIONS

Although no qualitatively new phenomena have been seen at PEP several search experiments have been done and several more are underway that are as interesting and have as much promise as those of any competitive program.

Whether the CERN and Fermilab colliders will show qualitatively new things beyond the Standard Model is as yet an open question. In any case the advantage of the known electroweak couplings means that search experiments in e^+e^- annihilation are easy to interpret and so can be definitive. By exploring reactions in which new states can appear in the propagator high masses, approaching 100 GeV, can be probed. A window of opportunity exists before the Z° factories come into full operation but the existence of the SLC and LEP projects means that a timely increase of luminosity of PEP is essential. Even after these machines are operating, a lower energy faculty can provide complementary information although operation at energies below 29 GeV is not favored for the search experiments. To fully exploit this physics the detectors should be made hermetic.

REFERENCES

1. B. Adeva *et al.*, "New Particle Searches," MIT Report 141 (1984).
2. H. Aihara *et al.*, Phys. Rev. Lett. 52, 168 (1984); ibid. 52, 2332 (1984).
3. E. Fernandez *et al.*, SLAC-PUB-3479 (1984), Phys. Rev. D.
4. W. Bartel *et al.*, Phys. Lett. 129B, 145 (1983).
5. S. L. Wu, Phys. Report 107, 59 (1984);
6. W. T. Ford *et al*, Phys. Rev. Lett. 51, 257 (1983).
7. A. Litlee, Harvard University Thesis (1978). The complete differential cross section for polarized beams is given by J. M. Kühn, H. D. Tholl and P. Zerwas, CERN TH 4131/85.
8. D. Wood (HRS Collaboration), Purdue University Thesis (1984).
9. R. L. Messner, "Recent Particle Searches at PEP," Proceedings of Vanderbilt Conference (1984).
10. D. Bender *et al.*, Phys. Rev. D30, 515 (1984); E. Fernandez *et al.*, Phys. Rev. Lett. 52, 22 (1984); L. Gladney *et al.*, ibid 51, 2253 (1984).
11. E. Fernandez *et al.*, Phys. Rev. Lett. 54, 1118 (1985).
12. R. Hollebeek, Talk given at 1985 Moriond Conference.
13. C. Akerlof *et al.*, Phys. Lett. (to be published); G. J. Feldman *et al.*, SLAC-PUB-3581, Phys. Rev. Lett.; W. W. Ash *et al.*, SLAC-PUB-3591, Phys. Rev. Lett.
14. W. Bartel *et al.*, Phys. Lett. 146B, 126 (1984); DESY 85/022.
15. G. Arnison *et al.*, Phys. Lett. 139B, 115 (1984).
16. J. L. Rosner, CERN TH 4086/85.
17. H. E. Haber and G. L. Kane, Phys. Report 117, 75 (1985); H. E. Haber, private communication.

18. M. Perl, reviews all such experiments in a talk given at the DPF Meeting in Santa Fe; "The Search for Neutral Leptons," SLAC-PUB-3526 (1984).

19. D. Errede *et al.*, Phys. Lett. 51, 519 (1984).

20. G. J. Feldman, Talk given at the 1985 Moriond Conference.

21. F. Gilman and S. H. Rhie, SLAC-PUB-3657 (1985).

22. V. A. Lyubimov, Phys. Lett. 94B, 266 (1980); Talk given at Leipzig Conference.

23. R. Abela *et al.*, Phys. Lett. 146B, 431 (1984).

24. F. Bohm and P. Vogel, Ann. Rev. Nucl. Part. Sci. 34, 125 (1984).

25. C. Matuzzi *et al.*, Phys. Rev. Lett. 52, 1869 (1984); SLAC-PUB-3560 (1985); G. B. Mills *et al.*, Phys. Rev. Lett. 54, 624 (1985).

26. See for example, R. N. Mohapatra and G. Senjanovic, Phys. Rev. Lett. 44, 912 (1980).

27. L. M. Krauss, Phys. Lett. 128B, 37 (1983); Harvard Preprint HUTP 84/A050; S. Sarlew and A. M. Cooper, CERN TH 3976.

28. D. Koltick, Talk given at Washington, APS Meeting (1985).

29. P. Tsai, private communication.

30. See the review by W. Ruckstuhl, Proceedings of the 1984 SLAC Summer Institute.

FIGURE CAPTIONS

1. Energy dependence of $R = \sigma(e^+e^- \to \text{hadrons})/\sigma_{\mu\mu}$.
2. Threshold factors.
3. PETRA limits on mass of charged Higgs as a function of leptonic and hadronic branching ratios.
4. Excited lepton production diagrams.
5. $\mu\gamma$ effective mass spectra compared to QED.
6. Cross section for $e^+e^- \to \gamma\gamma$.
7. Differential cross section for $e^+e^- \to \gamma\gamma$.
8. Measured cross section for $e^+e^- \to \gamma\gamma$ compared to QED predictions.
9. (a) Scalar electron pair production.

   (b) Single scalar electron production.

   (c) Photino pair production.
10. Mass limit for $\tilde{e}^+\tilde{e}^-$ pair production.
11. (a) Radiative photino pair production.

    (b) Neutrino pair production.
12. Cross section for radiative $\tilde{\gamma}\tilde{\gamma}$ and $\nu\bar{\nu}$ production.
13. Transverse energy distribution for MAC experiment.

    (a) 10° veto and (b) 5° veto.
14. Contours of excluded region in $m_{\tilde{\gamma}}$: $m_{\tilde{e}}$ space. The full line assume $m_{\tilde{e}_R} = m_{\tilde{e}_L}$, the dashed line that $m_{\tilde{e}_R} \gg m_{\tilde{e}_L}$.
15. Expected limit from ASP experiment. The dotted line shows the PETRA limit.
16. HRS monojet candidate.

17. (a) MAC limit on scalar pair production ($\chi^\circ\lambda^\circ$) and fermion pair production ($N\bar{N}$).

    (b) Mark II limit on scalar pair production (SP).

18. SUSY production of $\tilde{\gamma}$ and $\tilde{H}^\circ$, $\tilde{Z}^\circ$ mixture.

19. Limits on scalar electron mass from HRS monojet experiment.

20. Prompt heavy fermion pair production.

21. Excluded regions in mixing angle $|U_{14}|$: heavy neutrino mass (M_N) space:

    (1),(2) $\pi \rightarrow e\nu$, (3) $K \rightarrow e\nu$, (4),(5) Charm neutrino experiment, (6) universality (7) PEP monojet experiments, (8) Mark II secondary vertex search.

22. Cross section for $e^+e^- \rightarrow Z^\circ$.

23. Z° production rates from different storage rings.

24. Heavy neutrino decay diagram.

25. Hadronic system mass from 5π and 6π decay of tau.

26. Tau decay via charged Higgs.

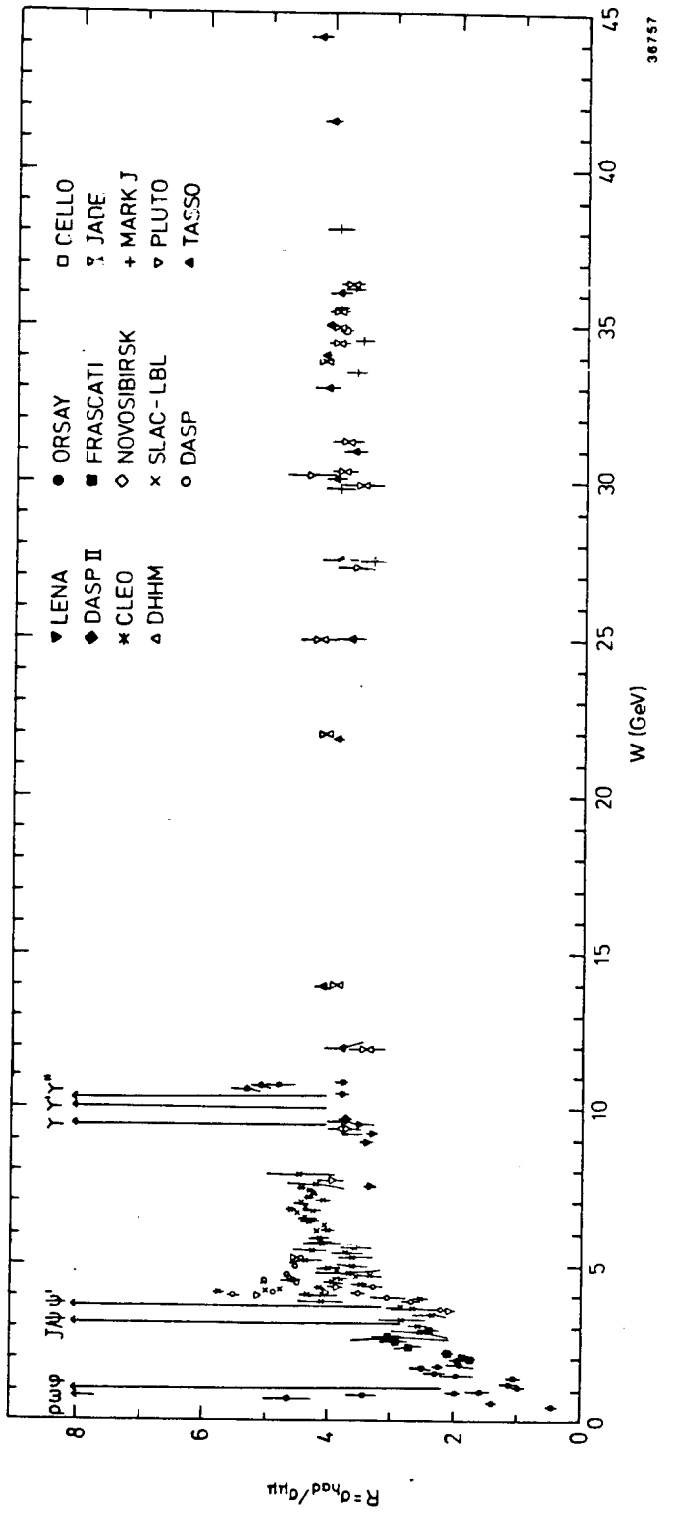
R=σhad/σμμ
W (GeV)
ρωφ
J/ψ ψ'
γγγ*
LENA
DASP II
CLEO
DHHM
ORSAY
FRASCATI
NOVOSIBIRSK
SLAC-LBL
DASP
CELLO
JADE
MARK J
PLUTO
TASSO
36757

Fig. 1

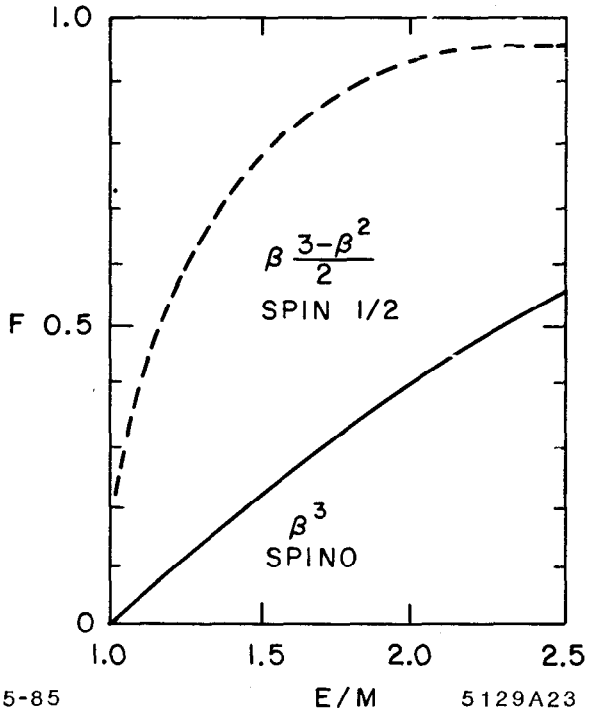
1.0
F 0.5
0
$\beta \frac{3-\beta^2}{2}$
SPIN 1/2
β^3
SPINO
1.0
1.5
2.0
2.5
E/M
5-85
5129A23

Fig. 2

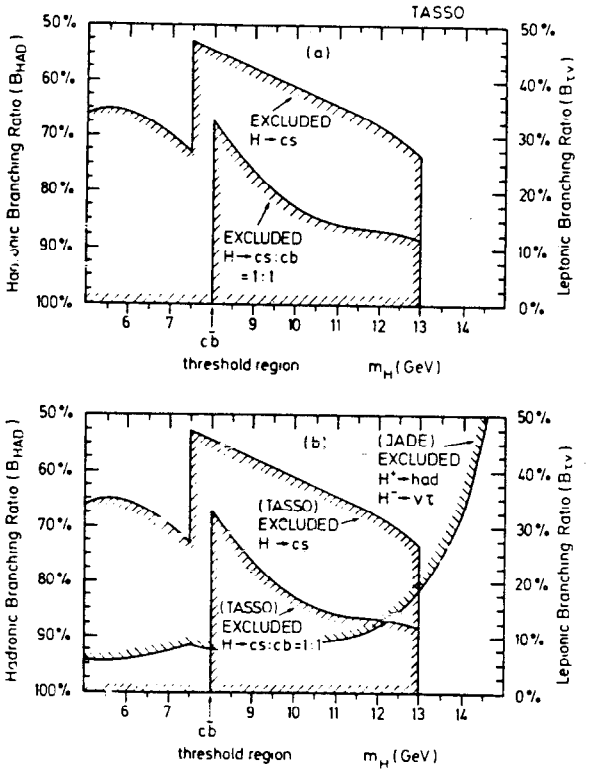
TASSO
(a)
EXCLUDED
H→cs
EXCLUDED
H→cs:cb
=1:1
Hadronic Branching Ratio (B_{HAD})
Leptonic Branching Ratio ($B_{\tau\nu}$)
50%
60%
70%
80%
90%
100%
40%
30%
20%
10%
0%
6
7
9
10
11
12
13
14
$c\bar{b}$
threshold region
m_H (GeV)
(b)
(JADE)
EXCLUDED
H^+→had
H^-→$\nu\tau$
(TASSO)
EXCLUDED
H→cs
(TASSO)
EXCLUDED
H→cs:cb=1:1
Hadronic Branching Ratio (B_{HAD})
Leponic Branching Ratio ($B_{\tau\nu}$)
$c\bar{b}$
threshold region
m_H (GeV)

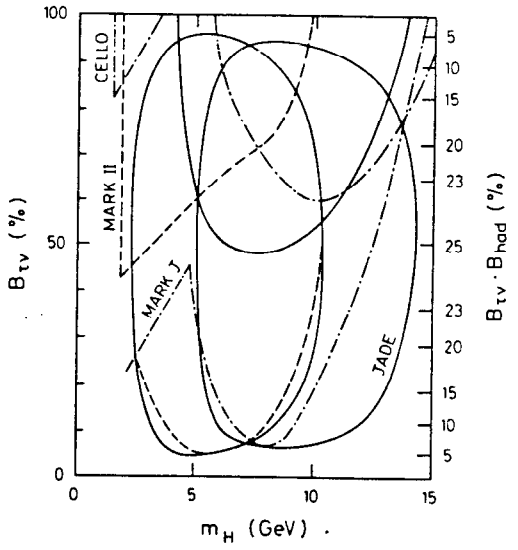
CELLO
MARK II
MARK J
JADE
$B_{\tau\nu}$ (%)
$B_{\tau\nu} \cdot B_{had}$ (%)
100
50
0
5
10
15
20
23
25
m_H (GeV)

Fig. 3

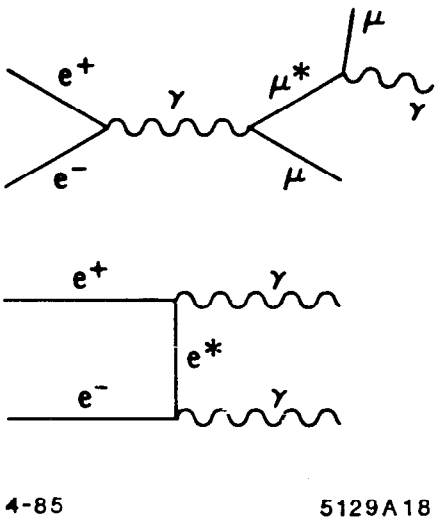
e+
e−
γ
μ*
μ
γ
e+
e−
e*
γ
γ
4-85
5129A18

Fig. 4

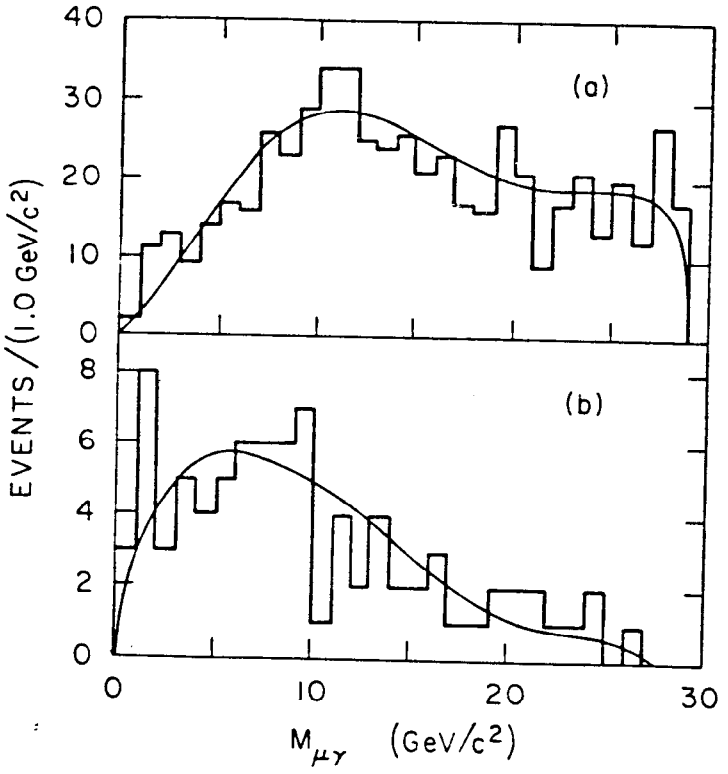
EVENTS/(1.0 GeV/c²)
(a)
(b)
0
10
20
30
40
0
2
4
6
8
0
10
20
30
Mμγ (GeV/c²)

Fig. 5

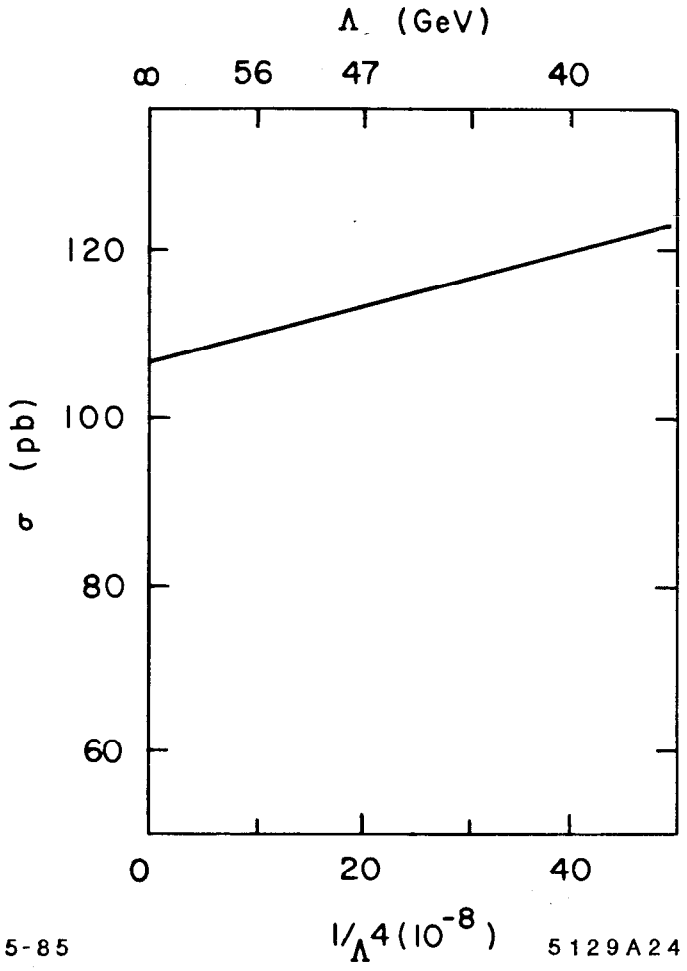

Fig. 6

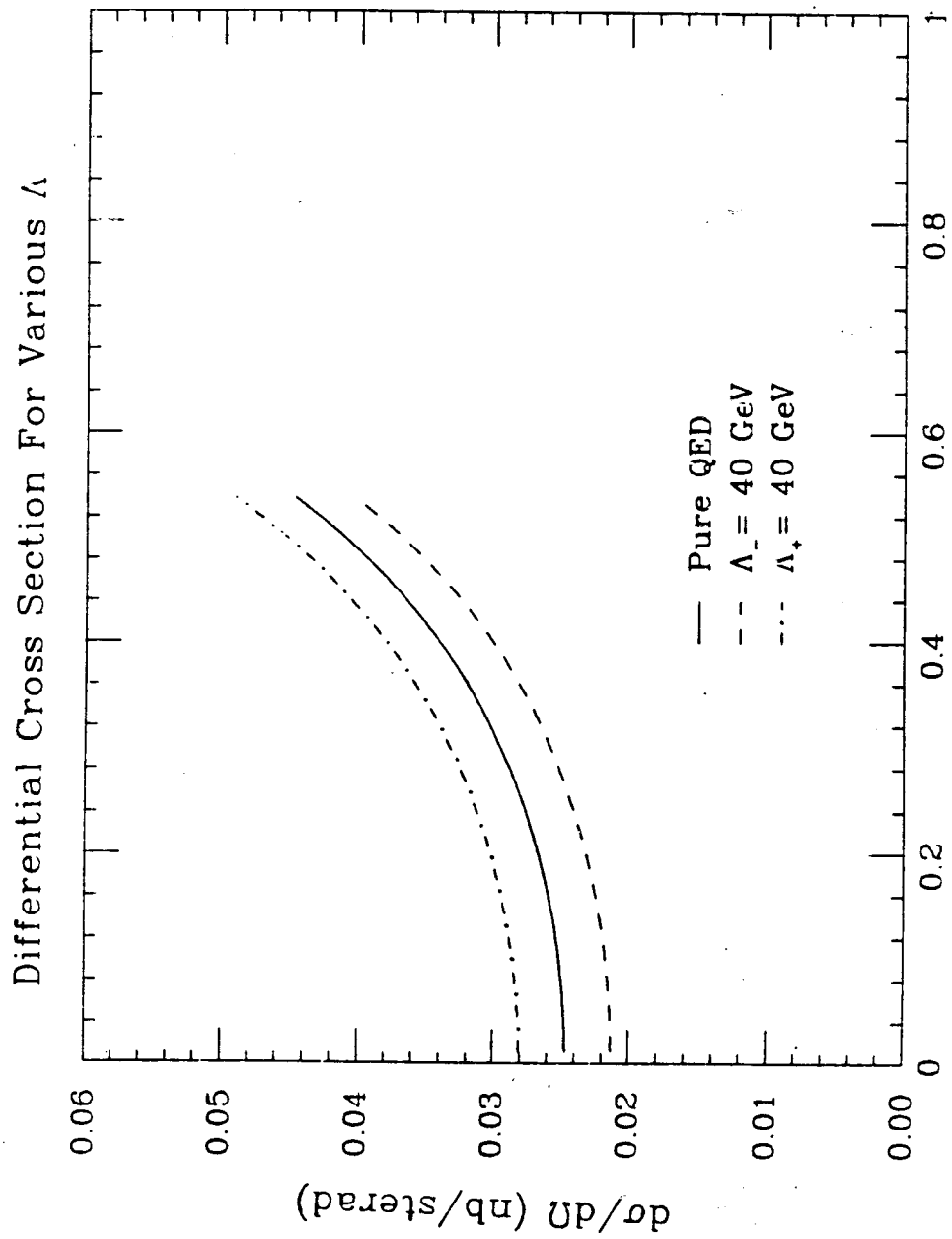
Differential Cross Section For Various Λ
dσ/dΩ (nb/sterad)
|COS θ|
Pure QED
Λ_ = 40 GeV
Λ+ = 40 GeV
0.06
0.05
0.04
0.03
0.02
0.01
0.00
0
0.2
0.4
0.6
0.8
1

Fig. 7

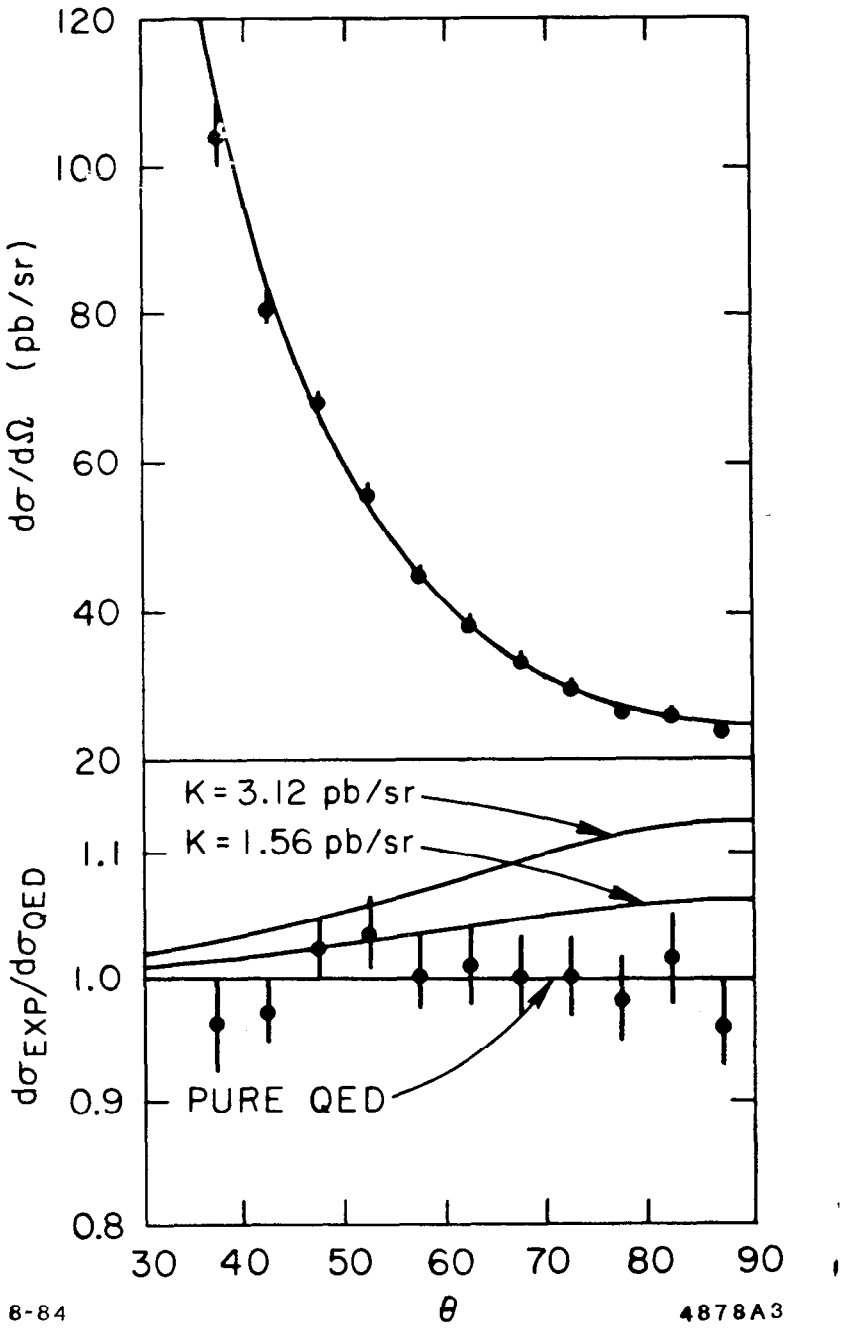
120
100
80
60
40
20
dσ/dΩ (pb/sr)
K = 3.12 pb/sr
K = 1.56 pb/sr
1.1
1.0
0.9
0.8
dσEXP/dσQED
PURE QED
30
40
50
60
70
80
90
θ
8-84
4878A3

Fig. 8

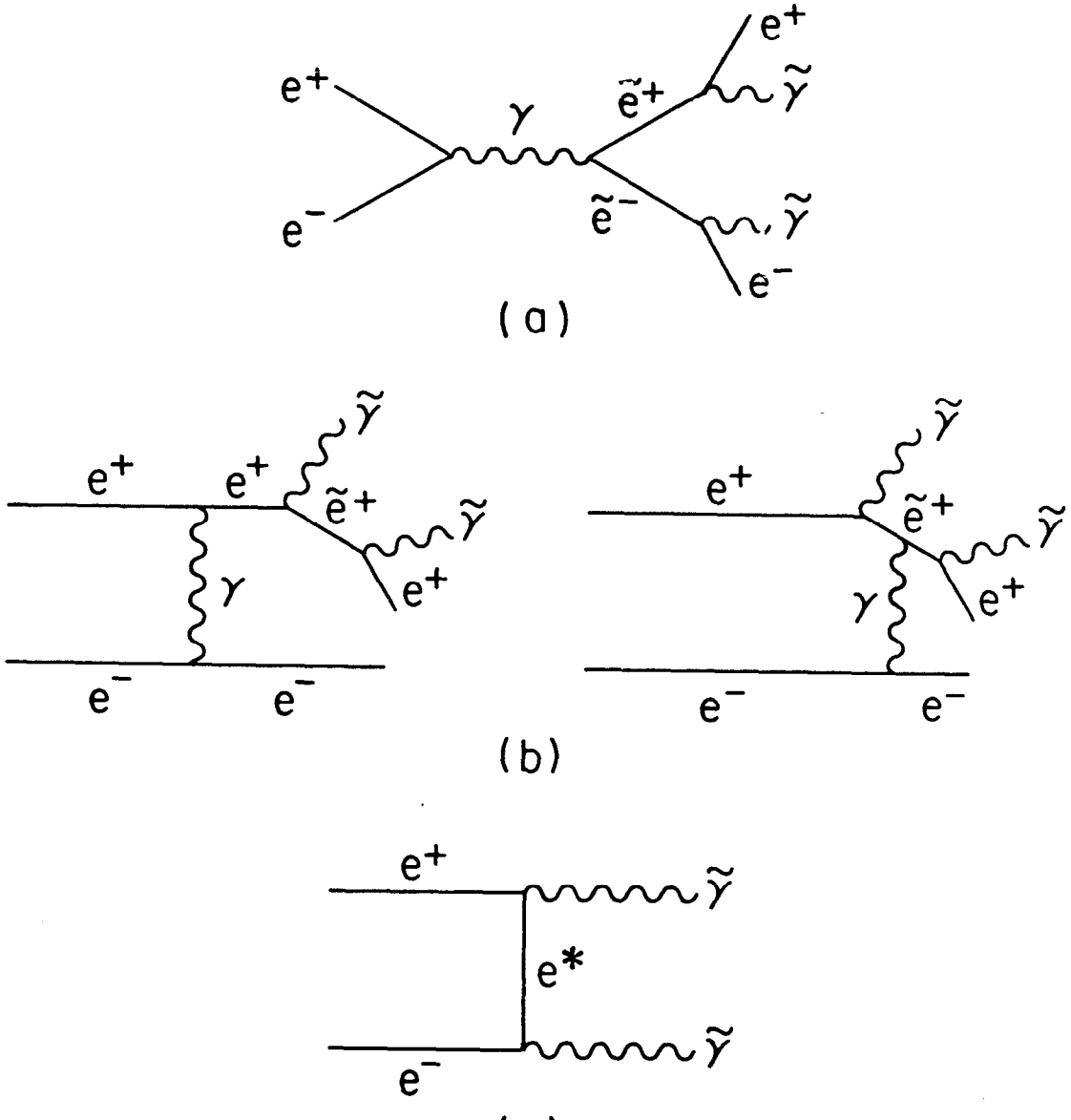

Fig. 9

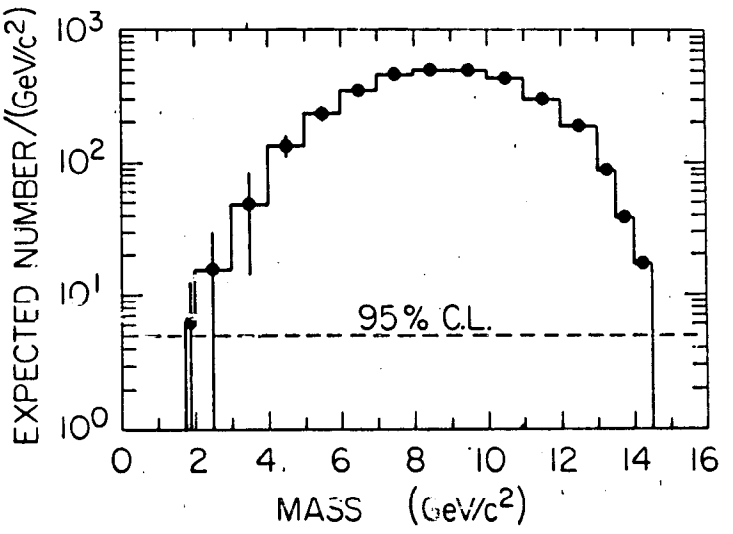
EXPECTED NUMBER/(GeV/c²)
10³
10²
10¹
10⁰
95% C.L.
0
2
4
6
8
10
12
14
16
MASS (GeV/c²)

Fig. 10

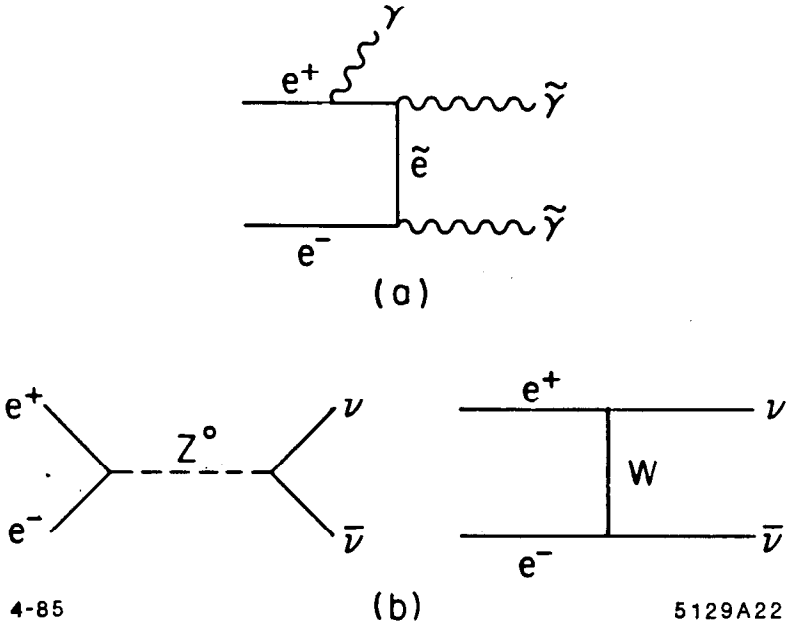
e⁺
γ
γ̃
ẽ
γ̃
e⁻
(a)
e⁺
Z°
ν
e⁻
ν̄
e⁺
ν
W
e⁻
ν̄
4-85
(b)
5129A22

Fig. 11

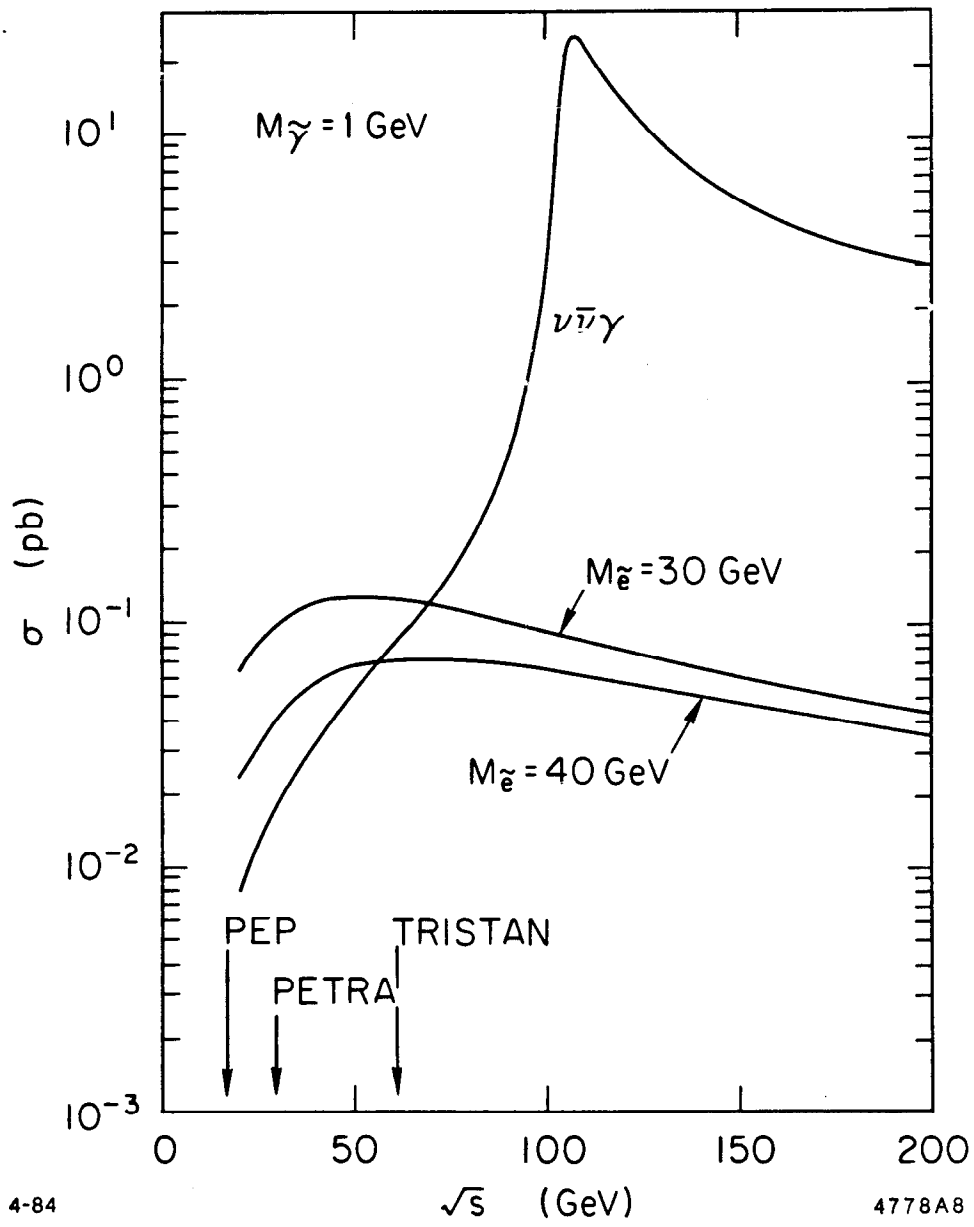
$M_{\tilde{\gamma}}$ = 1 GeV
$\nu\bar{\nu}\gamma$
$M_{\tilde{e}}$ = 30 GeV
$M_{\tilde{e}}$ = 40 GeV
PEP
PETRA
TRISTAN
10^{1}
10^{0}
10^{-1}
10^{-2}
10^{-3}
σ (pb)
0
50
100
150
200
$\sqrt{s}$ (GeV)
4-84
4778A8

Fig. 12

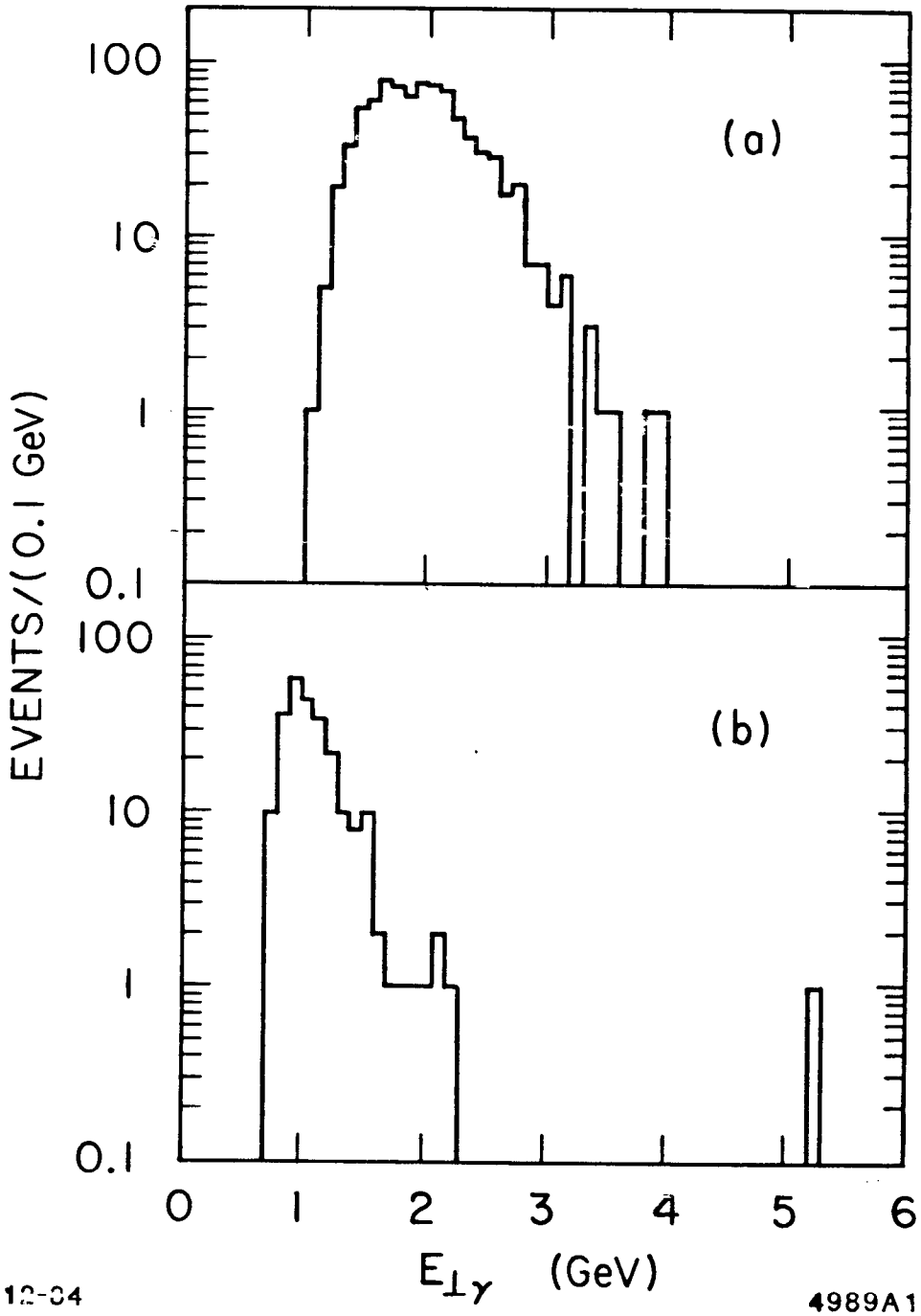
100
10
1
0.1
(a)
EVENTS/(0.1 GeV)
100
10
1
0.1
(b)
0
1
2
3
4
5
6
$E_{\perp\gamma}$ (GeV)
12-84
4989A1

Fig. 13

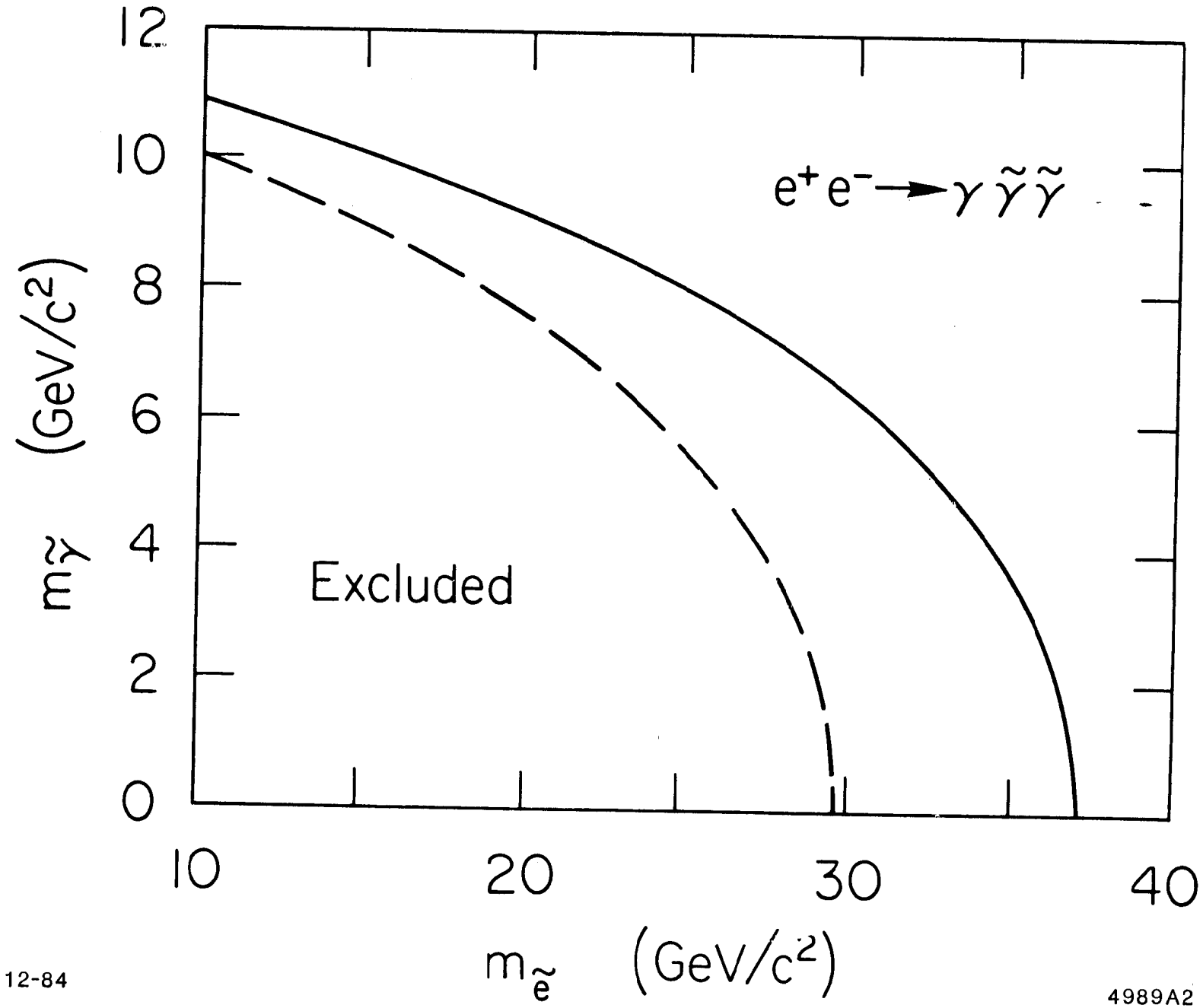
12
10
8
6
4
2
0
$m_{\tilde{\gamma}}$ (GeV/c^2)
$e^+e^- \rightarrow \gamma\tilde{\gamma}\tilde{\gamma}$
Excluded
10
20
30
40
$m_{\tilde{e}}$ (GeV/c^2)
12-84
4989A2

Fig. 14

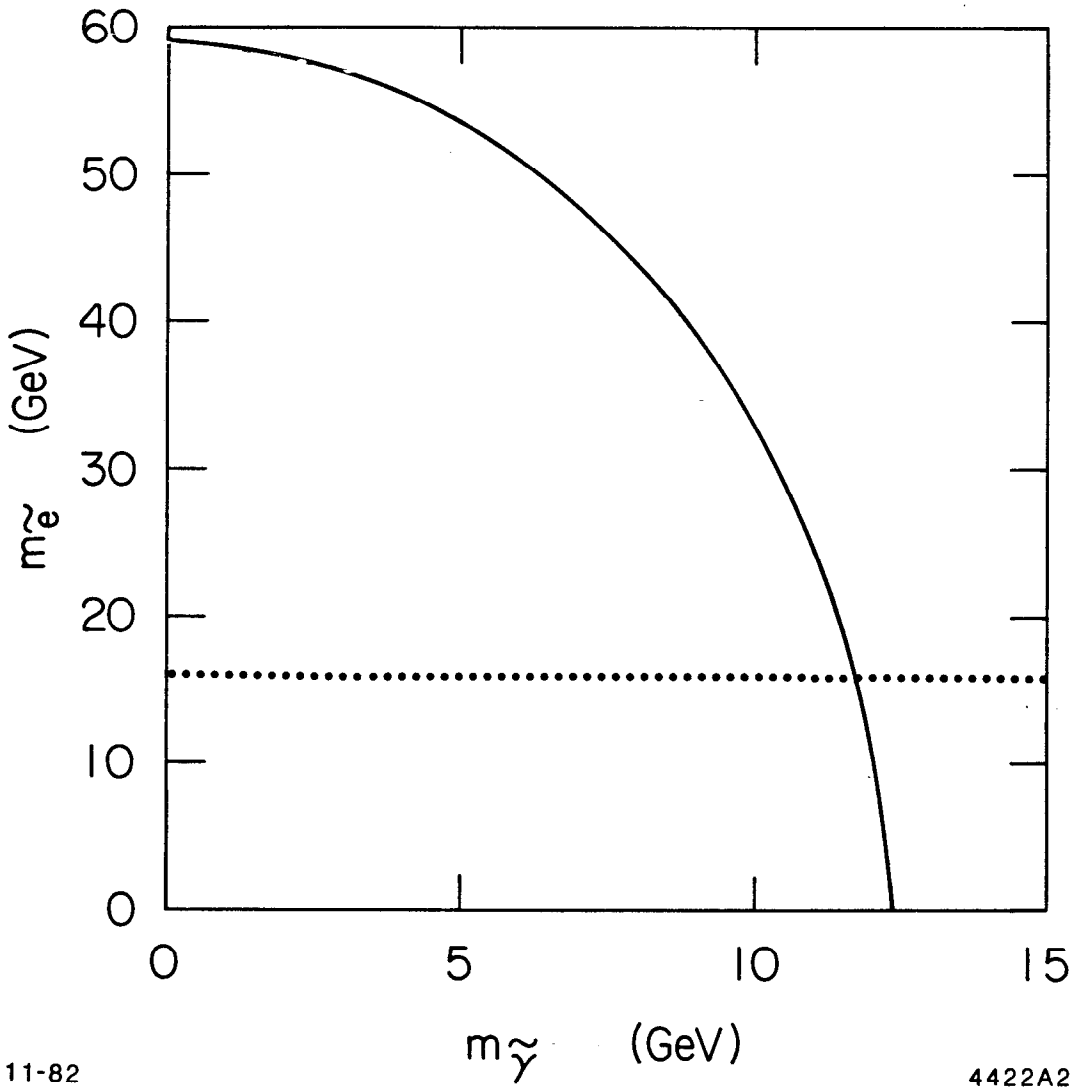
60
50
40
30
20
10
0
$m_{\tilde{e}}$ (GeV)
0
5
10
15
$m_{\tilde{\gamma}}$ (GeV)
11-82
4422A2

Fig. 15

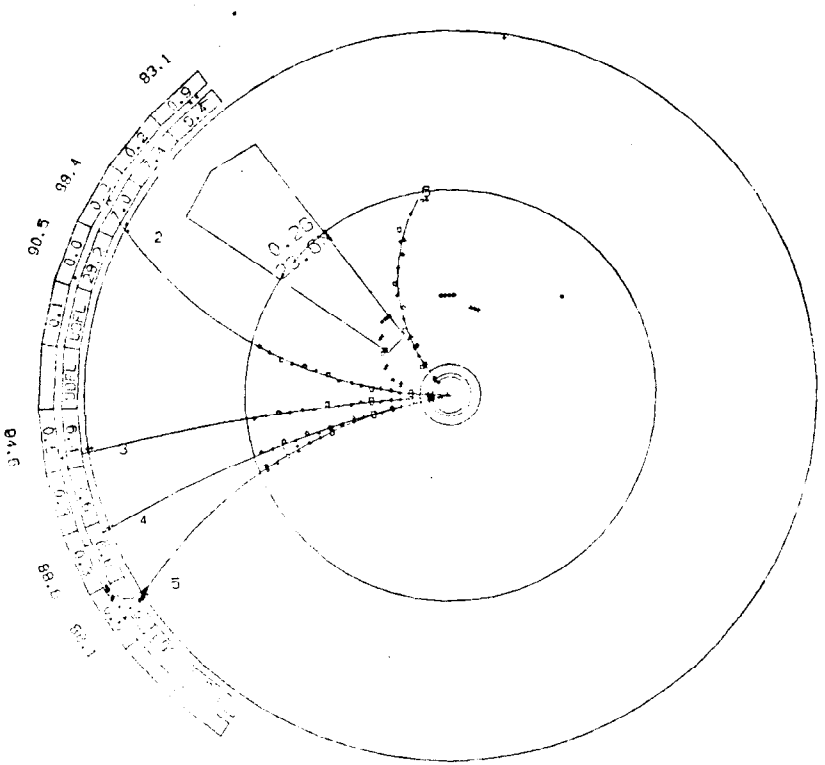

H [illegible] FUN=6106

EVENT= 3692
DCHITS = 138
NPRNG = 6
SH SUM= 3.1 · 0.2

TRACK	MOMENTUM	THETA
2	1.0	85.9
3	-5.0	94.9
4	-2.8	87.9
5	-1.1	89.3
6	0.5	59.0

TRIG.= F2 F3 S6 A2 D1 D2.

Fig. 16

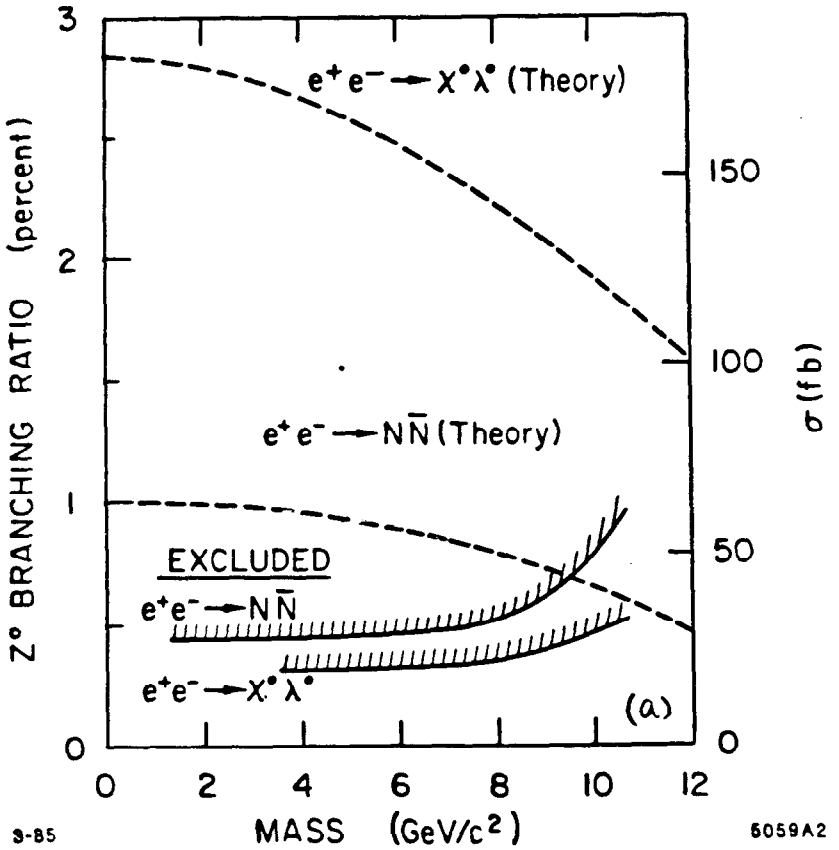
Z° BRANCHING RATIO (percent)
σ (fb)
e⁺e⁻ → X°λ° (Theory)
e⁺e⁻ → NN̄ (Theory)
EXCLUDED
e⁺e⁻ → NN̄
e⁺e⁻ → X°λ°
(a)
MASS (GeV/c²)
3-85
5059A2

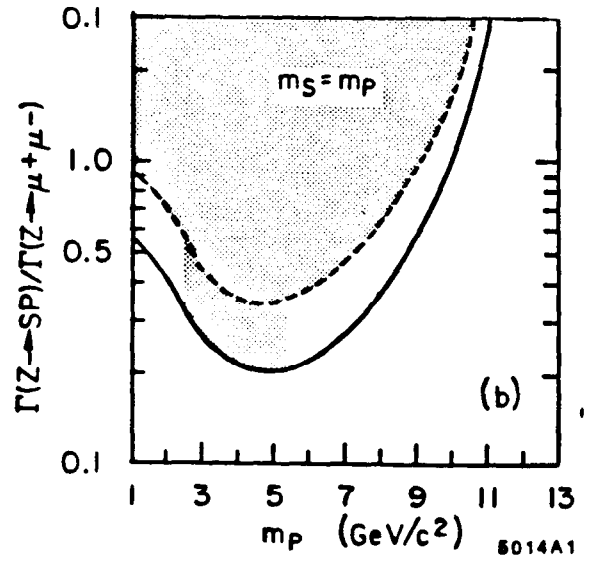
Γ(Z→SP)/Γ(Z→μ⁺μ⁻)
m_S = m_P
(b)
m_P (GeV/c²)
5014A1

Fig. 17

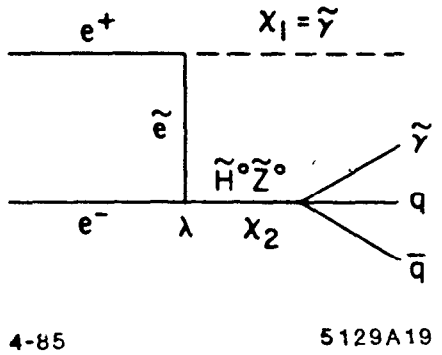
e+
X1 = γ̃
ẽ
H̃°Z̃°
γ̃
q
e−
λ
X2
q̄
4-85
5129A19

Fig. 18

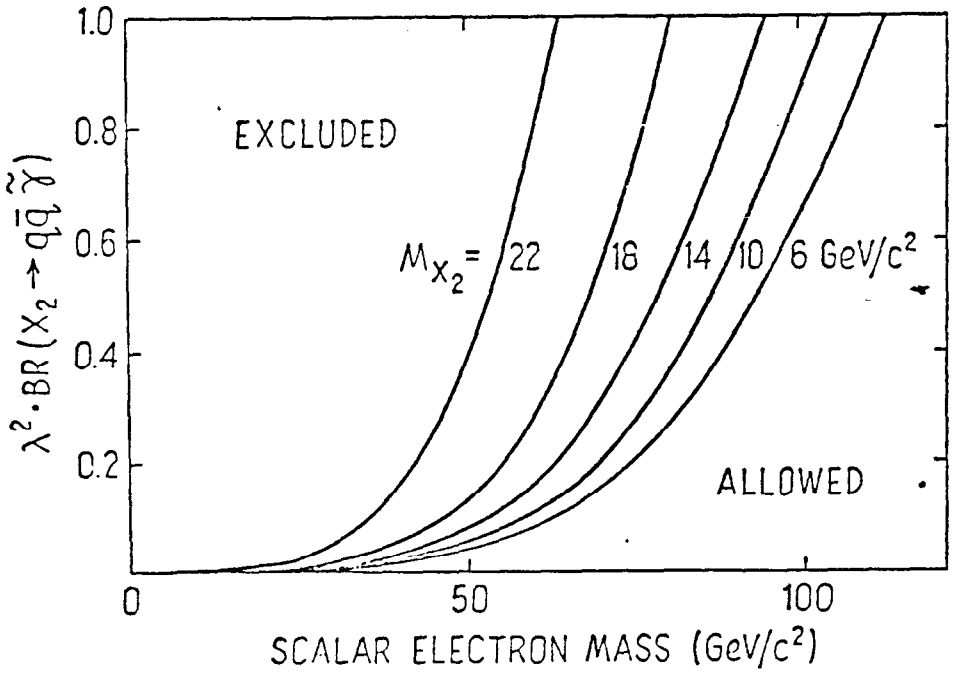
1.0
0.8
0.6
0.4
0.2
EXCLUDED
ALLOWED
M_{X_2} = 22 18 14 10 6 GeV/c²
$\lambda^2 \cdot BR(X_2 \to q\bar{q}\tilde{\gamma})$
0
50
100
SCALAR ELECTRON MASS (GeV/c²)

Fig. 19

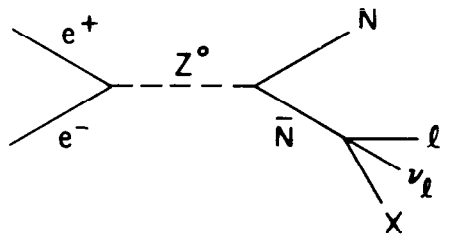

Fig. 20

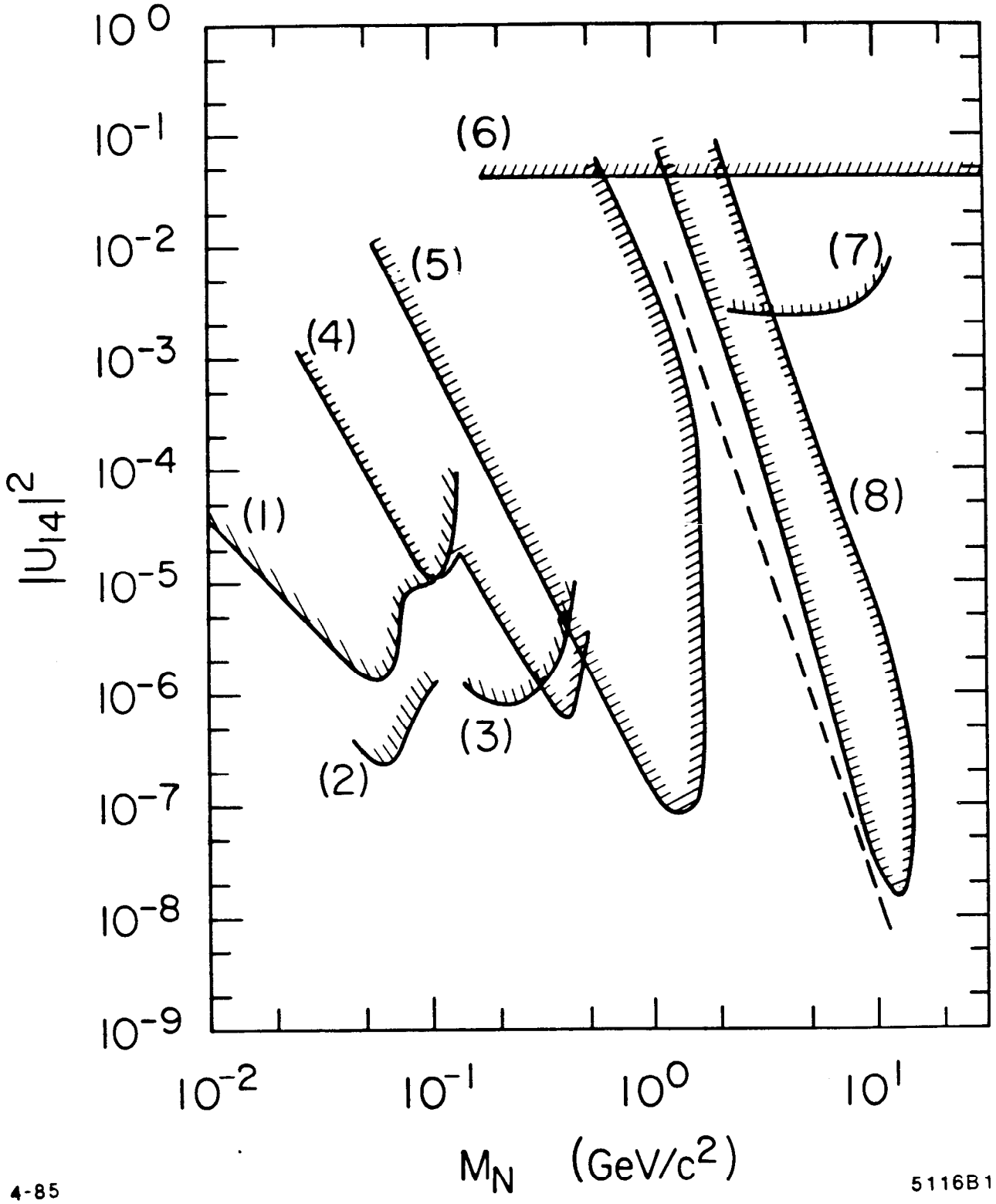
10^0
10^{-1}
10^{-2}
10^{-3}
10^{-4}
10^{-5}
10^{-6}
10^{-7}
10^{-8}
10^{-9}
$|U_{14}|^2$
(1)
(2)
(3)
(4)
(5)
(6)
(7)
(8)
10^{-2}
10^{-1}
10^0
10^1
M_N (GeV/c^2)
4-85
5116B1

Fig. 21

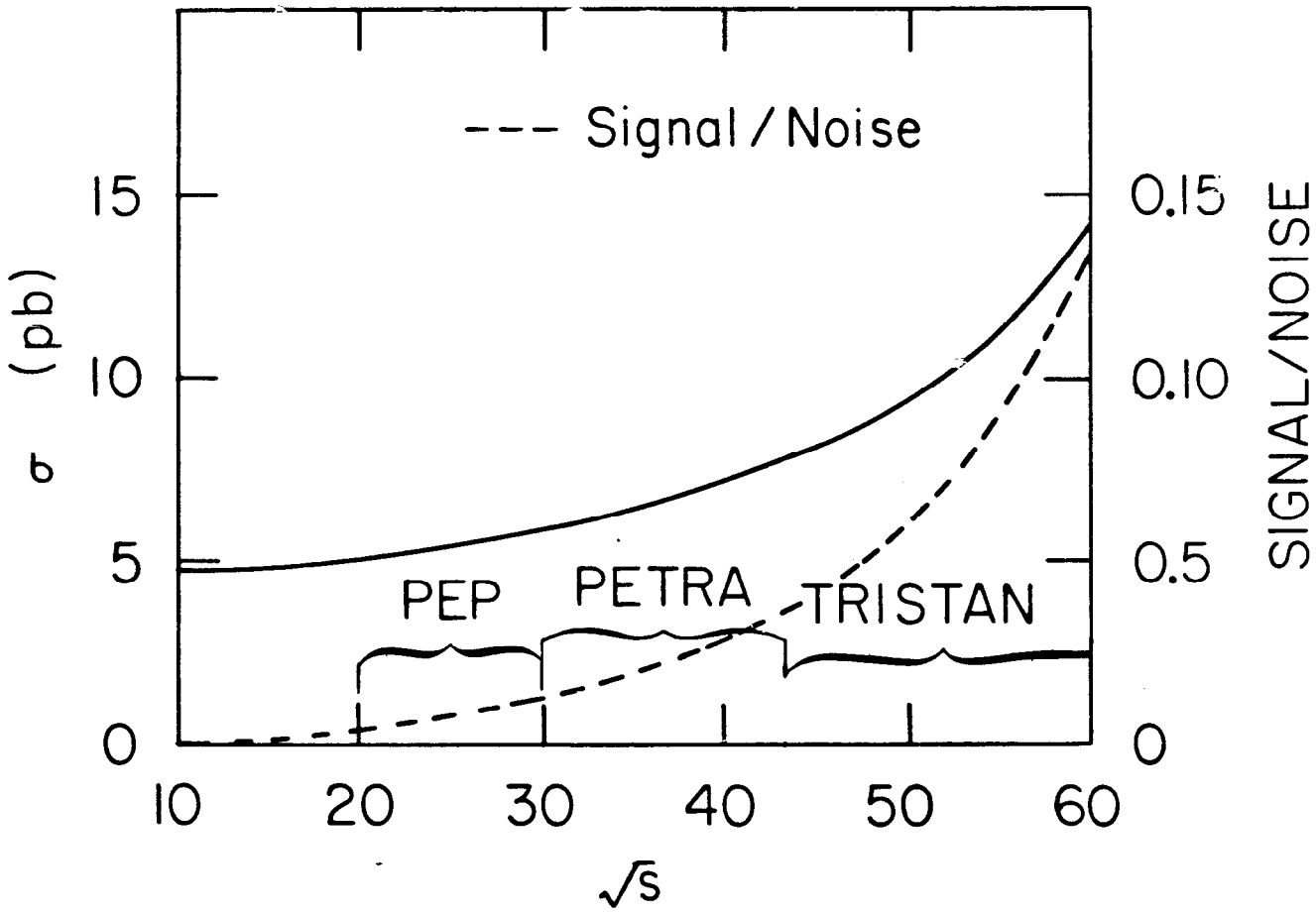
--- Signal / Noise
15
10
5
0
σ (pb)
0.15
0.10
0.5
0
SIGNAL/NOISE
PEP
PETRA
TRISTAN
10
20
30
40
50
60
√s

Fig. 22

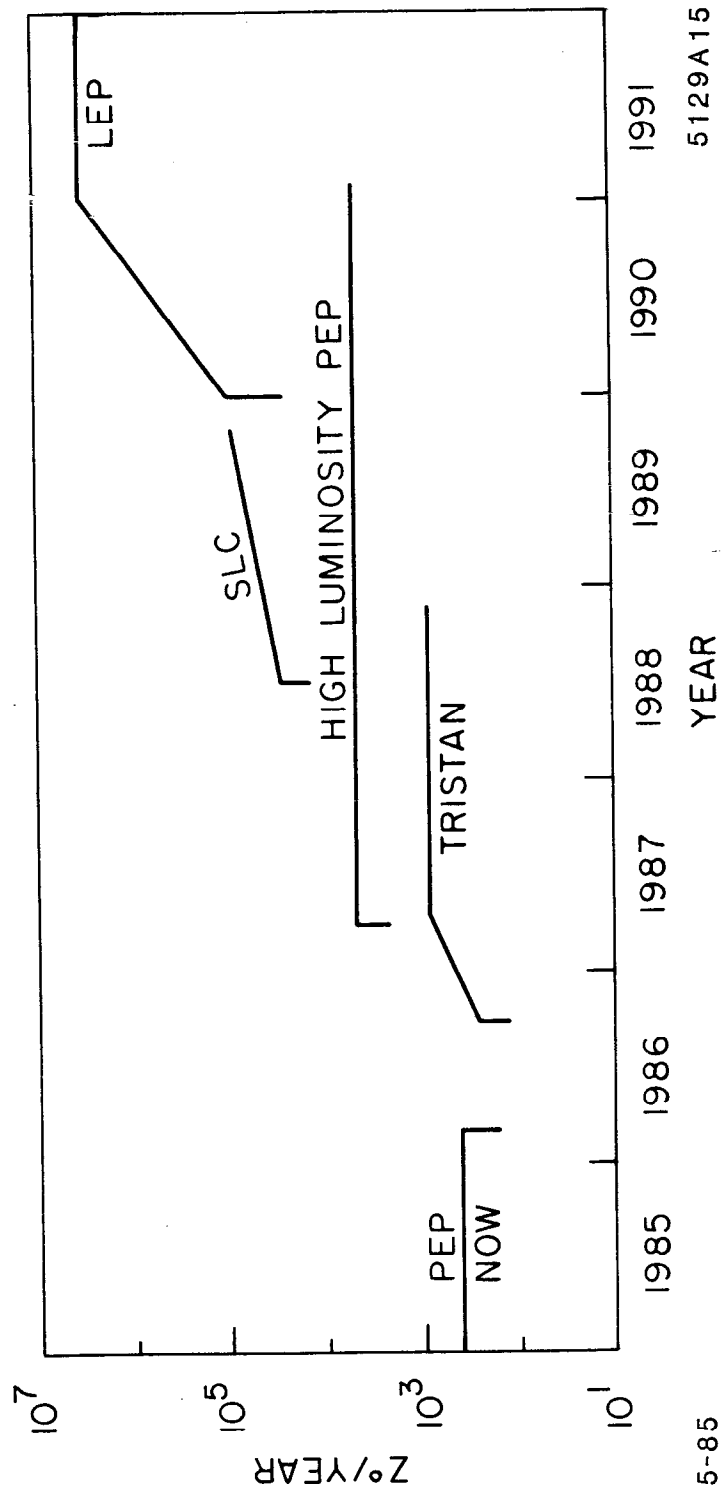
LEP
SLC
HIGH LUMINOSITY PEP
TRISTAN
PEP
NOW
1985
1986
1987
1988
1989
1990
1991
YEAR
Z°/YEAR
10^7
10^5
10^3
10^1
5-85
5129A15

Fig. 23

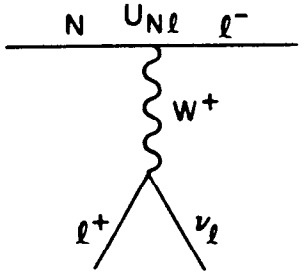

4-85 5129A17

Fig. 24

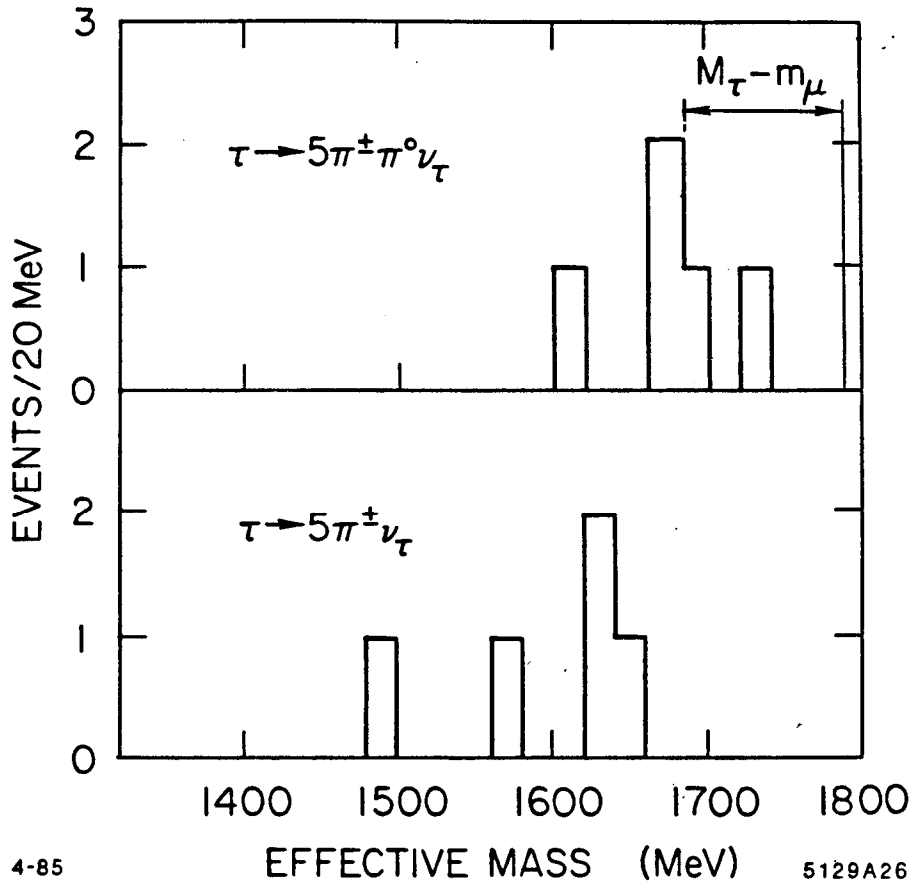

4-85 5129A26

Fig. 25

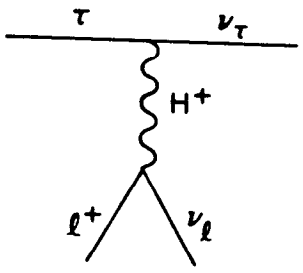

4-85 5129A16

Fig. 26

CHAPTER VI. LUMINOSITY UPGRADES ON PEP

J. M. PATERSON

and

M. DONALD, R. HELM, L. KARVONEN

CHAPTER VI. LUMINOSITY UPGRADES ON PEP

CONTENTS

I.1 INTRODUCTION

Over the past two years we have explored several ideas for Luminosity Upgrades on PEP. This followed the recommendation of the Goldhaber Committee which concluded that "unless PETRA uncovered new physics at higher energies then PEP should concentrate on higher luminosity at its present energy." These studies explored many schemes which involved lowering the "β functions" (stronger focussing) at the interaction points, as it has been employed at CESR, PETRA, DORIS II and in PEP.

The first round of studies assumed that all six interaction regions would be required and that the overall chromatic aberrations which could be tolerated and corrected should not exceed their present value. This led to designs which incorporated quadrupoles for the low-β insertions which were placed inside the magnetic field region of the detectors. Because of the high fields in some of the detectors, these quadrupoles would have to be either superconducting iron-free, or permanent magnet (samarium-cobalt) designs. Although machine lattice designs were readily achievable using these techniques, the engineering complexity and the impact on detectors made these schemes rather unattractive. This forced a review of the above assumptions and led to the studies of the Mini-Maxi Beta and the Six-Fold Mini Beta schemes described below.

Other approaches to higher luminosity which were explored and shelved were "Increased Number of Bunches" and "Lower Tune Operation." Both of these techniques require more physical (and dynamic) aperture in the storage ring vacuum and magnet systems than is available when operating at 29 GeV in the center of mass. At lower energy more aperture is available as the beam size, in a constant lattice, is a linear function of energy. However, even at much lower energies, no solutions were found that looked like interesting and competitive approaches for continued study.

The work summarized below involved many people in the Accelerator Department and many interactions with other SLAC groups and with PEP users,

however, the majority of the effort came from R. Helm, M. Donald, and L. Karvonen.

I.2 MINI-MAXI BETA

In continuing studies of mini-beta schemes on PEP, we first reviewed the assumptions discussed above and set the following criteria:

1. There would be fewer than six interaction regions needed for high energy physics in the long range program.
2. Quadrupoles should not be placed inside the detectors to reduce the physics impact and engineering complexity.
3. The overall chromaticity should not exceed present values and the lattice should be flexible to allow exploration of new ideas.

We took as typical general purpose large detectors the TPC and the HRS. This set the distance from the interaction point to the beginning of the first quadrupole at approximately 3.5 meters and their location in IR2 and IR6 suggested the three-fold Mini-Maxi design. In this design PEP is modified from its present six-fold symmetric lattice to one where there are three symmetric low-β insertions (2, 6, 10) and three insertions where the β functions are increased to higher values than presently used. This allows a design, whose characteristics are summarized in Fig. 1 and Table 1, where the chromatic aberrations are similar to present values and the β functions in the active interaction regions are reduced by a factor of three. The beams would be separated at the high-β crossing points, so that they do not contribute in limiting performance.

Table 1

		Mini-Beta	Maxi-Beta
	Present	*Regions*	*Regions*
Free Space Between Quads	12.7 m	7 m	20 m
Vertical Beta at IP	0.12 m	0.04 m	0.6 m
Horizontal Beta at IP	3.0 m	1.0 m	15 m
Maximum Beta in Quads	400 m	360 m	180 m
Uncorrected Chromaticity Horiz./Vert.	$-34/-92$	$-33/-82$	
Average Beta in the RF System	60 m	30 m	

To implement this design, one needs twelve new high gradient, high quality quadrupoles in the Mini-Beta IR's, comparable and in addition to the existing quads. In the High Beta IR's, the existing quads are moved outwards and overall four new power supplies and high current busses are required to power this three by three fold symmetric lattice. This lattice is flexible and one could operate with a wide variety of IP parameters. An additional benefit of this approach is the separation of the IR's used for physics from those containing the RF accelerating system, namely 12, 4 and 8. This would allow future tests with lattices where higher operating currents could be required and where independent tuning of the optics in the accelerating cavities (the major instability driving impedance in PEP) and in the active IR's is possible. In addition to the magnet system and power supply system modifications mentioned above, there is by necessity much vacuum system and instrumentation and control system modification required to implement this design. The total effort is somewhat dependent on the assumed physics program and operating detectors, but both the technical implementation and impact on resources are very dependent on assumptions of the availability of experienced engineering personnel during the completion and commissioning of the SLC.

This leads us to the obvious questions: What mini-beta program is possible using existing hardware? – Can we devise a program of upgrades which satisfy the real world limitations of available resources? – A phased program? – What are the physics program tradeoffs?

I.3 SIX-FOLD MINI-BETA

In an attempt to answer some of these questions, we have studied a six-fold symmetric mini-beta scheme which uses the existing magnets and power supplies. We assumed that as in the Mini-Maxi Beta, the minimum distance from the IP to the beginning of Q_1 would be 3.5 m. As Q_1 and Q_2 are moved towards this position, we find the following effects in the resulting lattices.

1. The range of beta values at the IP over which the lattice can be adjusted rapidly diminishes.
2. The total chromaticity must be allowed to increase in order to achieve the desired beta values.
3. The strength of Q_1 increases significantly as shown in Fig. 2.

The tunability of the lattice was increased by repositioning Q_3, the quadrupole at the beginning of the arc, improving the optics match between the long insertions and the arcs. In lowering the β functions, the total chromaticity increased by 30%, however, we found that the residual aberrations after correction with the sextupole system, were no worse than with the Mini-Maxi scheme. This appears to be due to the higher degree of symmetry, i.e. six-fold, which of course matches the geometrical distribution of sextupoles. Two out of the seven families of sextupoles would be required to operate above the power supply and magnet limits at 29 GeV but would be satisfactory at 22 GeV. Alternatively, the 48 sextupoles affected could be replaced by stronger units which have been designed.

The variation in required strength of the insertion quads is shown in Fig. 2. The Q_1 quadrupoles were designed to operate at these levels but the installed

power supply and cable plant would need to be upgraded. Again, operating PEP at the reduced energy of 22 GeV, one would use the existing equipment.

The projected performance figures of these two different approaches to mini-beta are very comparable. In the Mini-Maxi scheme, any uncertainty lies in the three-fold symmetry and chromatic correction; while in the six-fold, the chromatic correction required is stronger but more symmetric. At 29 GeV both require many additions to the ring systems, magnets, power supplies, busses; however, the six-fold can be tested and operated at 22 GeV with existing equipment.

I.4 ALTERNATE SCHEMES

There are many alternate variations of Mini-Beta which incorporate some of the concepts from the above schemes. One can combine both ideas and have a Mini-Maxi lattice with no new insertion quads (but six power supplies) and lower total chromaticity. Unfortunately, this lattice has proved to be very difficult to chromatically correct. At the present, this is not well understood and studies are continuing.

One can also consider one or two fold schemes which could be tailored to the physics program. For example if we look at a one-fold scheme, we have a choice of adding additional quads and power supplies or no new quads but even more power supplies. The choice would be made balancing cost versus flexibility and conservatism. The possible effects of one-fold symmetry on chromatic corrections and beam-beam performance are impossible to predict and the total project costs are way below being a linear function of the number of IR's.

In summary, there are several choices of PEP luminosity Upgrades which look interesting. They could have from one to six active IR's so we need a better fix on the future physics program in order to optimize performance versus effort and risk.

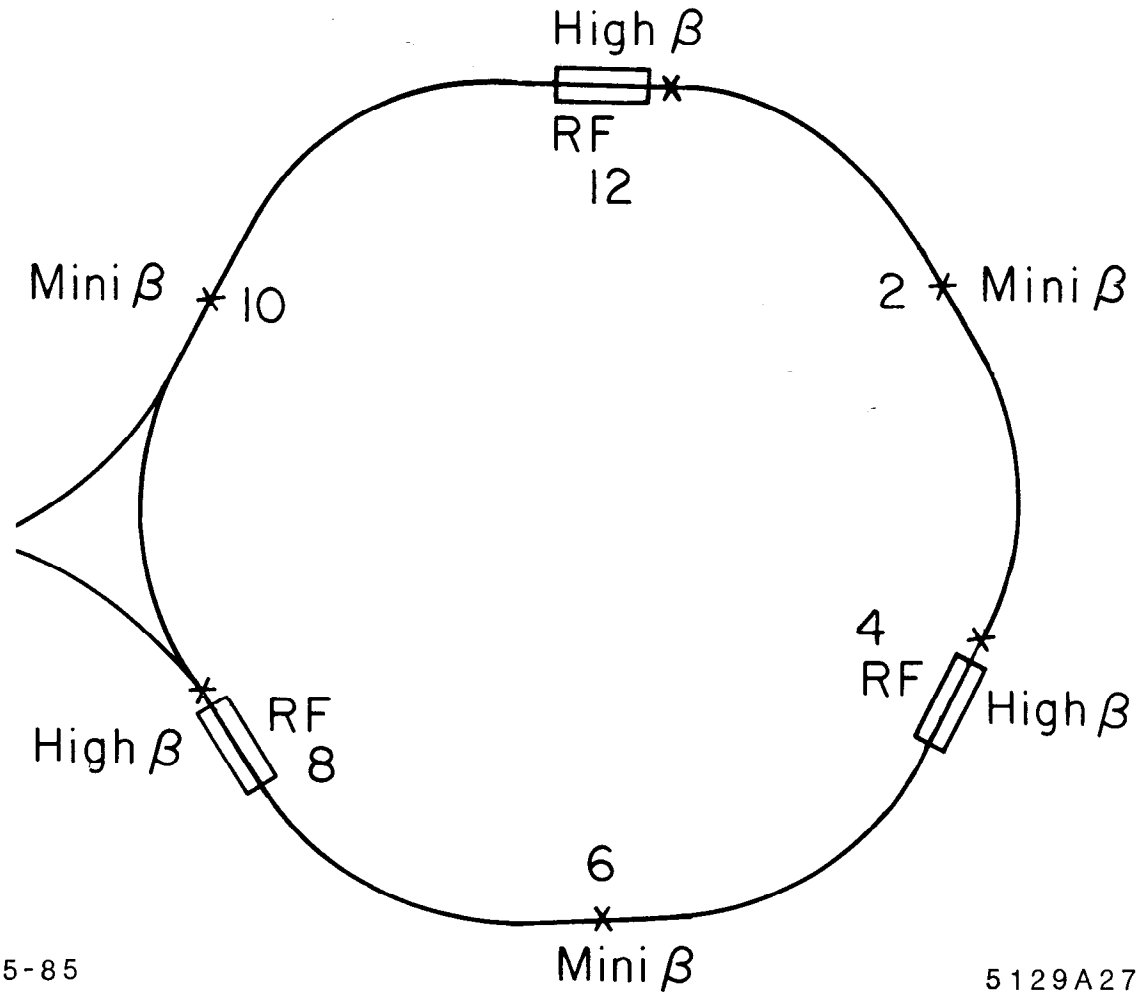
High β
RF
12
Mini β
10
2
Mini β
4
RF
High β
High β
RF
8
6
Mini β
5-85
5129A27

Fig. 1

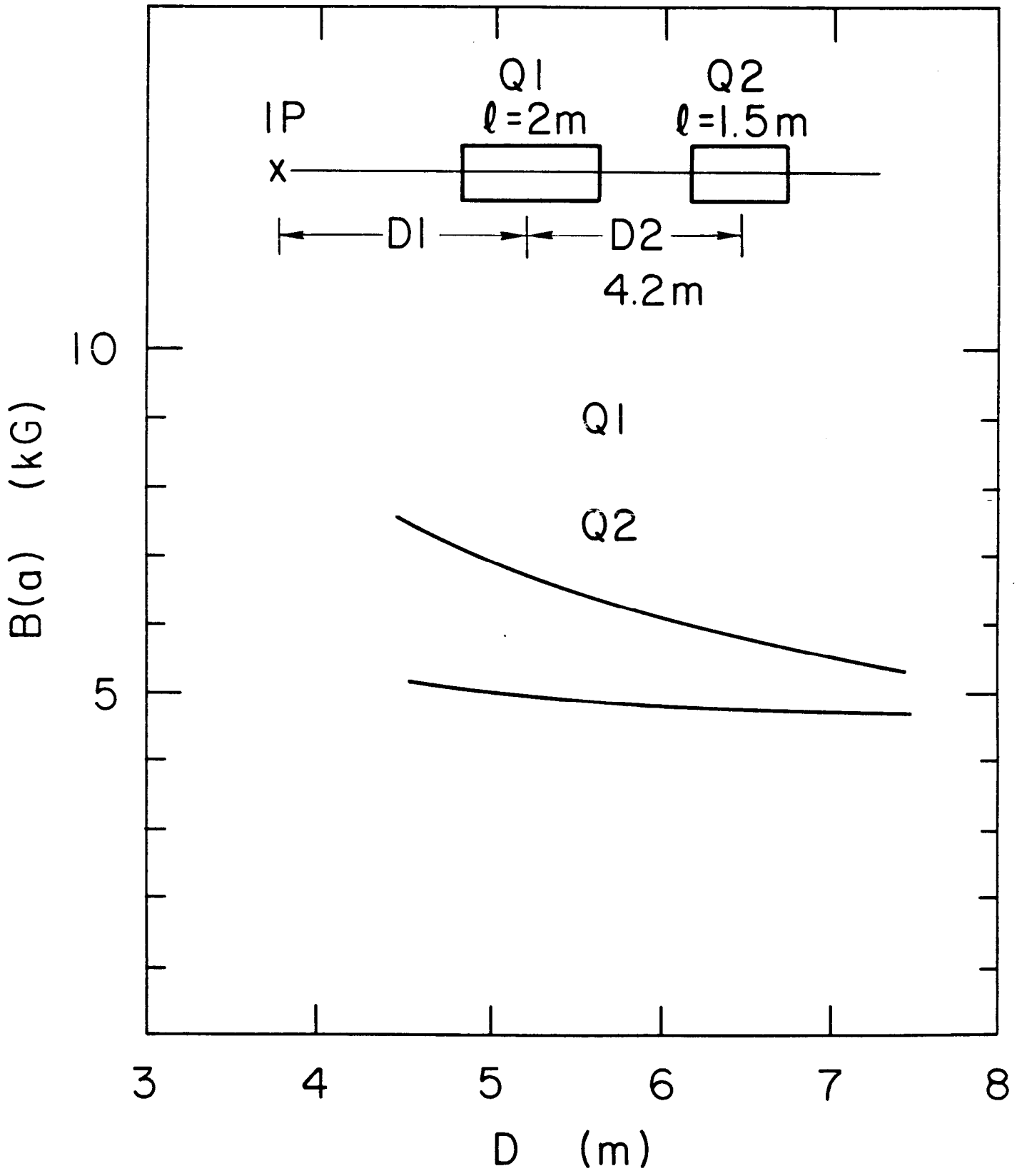

Fig. 2

CHAPTER VII.
THE CAPABILITIES OF THE TPC IN THE HIGH LUMINOSITY ERA

CONTENTS

VII.1 Description of the Present Hardware

The TPC hardware has operated in two configurations: a) in the 1982/83 running cycle with a 3.9 kG conventional coil, and b) in the 84/85 running cycle with a 13.25 kG superconducting coil. During the period between these two cycles, the TPC was upgraded with modifications of the electrostatic field cages, a new thin inner insulator and the addition of gating grids to the TPC sectors. Figure 1 shows a cross section of the hardware along the beam, and Fig. 2 shows a cross section transverse to the beam. Figure 3 shows a perspective slice through the detector, including one of the forward spectrometser of the PEP-9 2γ detector. The status of each component of the present hardware is described in the following paragraphs, with emphasis on the central detector.

VII.1.1 Superconducting Magnet

The thin (0.86 r.l. package) superconducting coil operates at 1900 A. The magnet provides a very uniform magnetic field of 13.25 kG throughout a volume 2.15 m in diameter and 3.0 m in length. The coil is protected by a quench detection circuit which is capable of detecting a voltage drop of 80 mV across the coil. Within a few milliseconds of the coil beginning to turn normal, a center tap quench protection system dumps about 12 kJ of energy into the coil to turn the entire coil normal.[1]

After the final tests of the coil in the PEP-4 iron yoke, the field was carefully mapped with NMR probes. The field was found to be uniform to within 10 G over most of the TPC drift volume. The pole tip Iron saturates at high field and 1900 A was chosen to optimize the field uniformity. The field maps will be used to generate correction algorithms for track reconstruction and vertex fitting with the new 84/85 data.

VII.1.2 Time Projection Chamber (TPC)[2]

The TPC detector was modified during the Fall of 1983. Each of the 12 endcap sectors was fitted with an additional gated grid. This 1 mm spacing grid is operated with a ±100 V difference from wire to wire. The field across the gaps prevents primary ionization from drifting to the sense wires and being amplified (gated grid shut). When a pretrigger decision is made, the opposing voltage is removed, making the grid transparent (gated grid open). The use of the new gating grid has eliminated the large space charge distortions seen in the 82/83 data.

A new thin inner insulator made of high density polyethylene has been installed to reduce the amount of material between the interaction point and the detector volume. The electrostatic field cage has been coated with resistive polyurathane paint to provide a more uniform field gradient and to further reduce drift distortions. At this point in the analysis, the remaining distortions are small and are not being corrected.

The TPC is operating with a 50 kV/m drift field instead of the previous 75 kV/m. The corresponding reduction in the drift velocity minimizes the amount of information lost near the endcaps due to the electronic noise induced by the switching of the gated grid. The longer (30 μsec) drift time increases diffusion somewhat but the overall TPC performance is excellent. We are now obtaining a dE/dx resolution of 3.5 percent for hadrons within a jet environment. The momentum resolution is now approximately given by:

$$\sigma_p/p = 1.5 \text{ percent} + 1.0 \text{ percent } p \text{ (p in GeV/c)}$$

The momentum dependent term will be gradually reduced towards the theoretically possible 0.5 percent · p as the remaining distortions are corrected.

VII.1.3 Inner Drift Chamber (IDC)/Outer Drift Chamber (ODC)[3]

The 1.2 m long, inner drift chamber is sensitive from 13 to 19 cm in radius and has four axial layers. The IDC is operated in the same 8.5 atmosphere Ar-CH_4 (80-20 percent) gas volume as the TPC. At present the IDC is only used for triggering.

The 3 m long, outer drift chamber has three axial layers at 1.2 m in radius. It is operated in Ar-CH_4 (80-20 percent) at 1 atm. The ODC is used in generating the Trigger and is being used to correct for photon conversions in the magnet coil package.

VII.1.4 Hexagonal Calorimeter (HEX)[4]

The Hexagonal calorimeter is a gas-sampling calorimeter operating in the limited Geiger mode. The calorimeter is 4.2 m long and is situated at 1.2 m radius. Lead laminates have been stacked to a total of 10.6 r.l. with 40 sampling gaps. The three 60 degree stereo views are measured in the same gap, thus providing a strong correlation of the signal size in different views. The sense wires of the chamber provide one azimuthal view and the projective strip geometry with 9 milliradian angular segmentation provides the two other views. The energy resolution obtained to date is:

$$\sigma_E/E = 16 \text{ percent}/\sqrt{E} \text{ , below 1 GeV}$$

$$= 14 \text{ percent for Bhabhas at 14.5 GeV}$$

Two of the six modules were unstacked and cleaned after our early experience with ethyl bromide. A replacement gas, composed of argon, methylal and N_2O, has been found to provide comparable but slightly inferior performance.

VII.1.5 Pole Tip Calorimeter (PTC)

The Pole Tip Calorimeter is a proportional mode, gas-sampling lead laminate calorimeter consisting of two modules (one on each polebase). The calorimeter shares the same argon-methane (80-20 percent) gas volume as the TPC. There are a total of 51 samples (13.5 r.l.), which are read out in three 60° stereo views. The cathode strips are arranged in a projective strip geometry with 8 mrad angular segmentation. The energy resolution obtained is

$$\sigma_E/E = 11 \text{ percent}/\sqrt{E} \text{ , below 10 GeV}$$

$$= 6.0 \text{ percent for Bhabhas at 14.5 GeV}$$

VII.1.6 Muon Detection System[5]

The magnet flux return and two layers of iron in the Muon detector system provide a total of 810 gm/cm^2. The detectors are triangular, double layer, extruded Al proportional tubes operating with argon-methane (80-20 percent) at 1 atm. The barrel chambers are arranged in three layers with axial wires and a fourth layer at 90 degrees. The endcap region is covered with three layers, providing a complete coverage of 98 percent of 4π sr.

VII.1.7 Trigger[6]

During the past year the trigger has been modified to make decisions at three levels: the gating grid, pretrigger and trigger levels. The addition of the third level was necessary in order to switch the TPC gating grid to the transparent mode and then to use TPC wire information in the charged pretrigger decision. The neutral triggers were modified to take advantage of the three level decision making.

For the Spring 1985 data runs with luminosities of the order of 20×10^{30} $cm^{-2}sec^{-1}$, the trigger rates have been averaging:

Gating Grid	1000 per sec ,
Pretrigger	100 per sec ,
Trigger	1 per sec ,

where the Trigger decision allows us to accept $q\bar{q}$ events with essentially no bias and to record No Tag 2γ events with some biases. At these rates the deadtime for triggering and readout has been averaging about 10 percent. The deadtime per event is dominated by the time required to digitize the data stored in the CCDs and the readout of the large volume of data (6 K words/event on average) into the VAX computer memory.

VII.1.8 Online/Offline Analysis

The Online computer has been upgraded to a VAX 11/782 to allow us to reconstruct a large fraction of the events. This Online analysis allows us to better monitor the detector, to eliminate one pass through the data to determine constants and to reduce the Offline load. The Offline data reconstruction has been automated and is currently running a few days behind the data acquisition.

VII.2 Performance of the Detector in the 84/85 Running Cycle

Several improvements were incorporated prior to this cycle. In particular:

1. The field cages were coated with a resistive paint to insure a uniform field at the cage surface.
2. The gated grid was added in order to reduce the positive ion feedback into the main volume of the TPC.

3. The magnetic field was increased from 3.9 kG to 13.25 kG by operating the thin superconducting coil.

4. A new calorimeter gas was developed for operating the modules safely.

5. A new thin inner insulator was built for the TPC to decrease the amount of material between the beam collision point and the TPC.

The TPC proper has operated very well. The new thin inner insulator has been trouble free, the gated grid has operated even better than expected, and the electrostatic distortions are largely gone. Figure 4 shows the new dE/dx vs. p curves. The improved momentum resolution dramatically sharpens the particle bands in the horizontal direction. For instance, the low momentum muon band is now distinct, whereas in the 'old' data this band could not be seen. In fact the high dE/dx data can be used to determine a mass spectrum as illustrated in Fig. 5 for positive and negative tracks. These dE/dx curves did not require any corrections for the gated grid operation since the baseline is restored before we start to collect data. The net spatial loss introduced by the delay due to the gated grid operation has been 8 cm.

The momentum resolution is greatly improved. The improvement factor is about 3 at low momentum where errors are dominated by multiple scattering, and about 5 at the highest momenta. Mass resolutions have correspondingly improved. In some instances, especially at low momenta, they have become limited by the measurement of angles, where the material in front of the TPC still plays the dominant role. Many resonances which were not directly observable in the previous running at 4 kG, have become quite visible. This is especially true for charm mesons which are fast. For some particles, like Λs, the improvement leads to much better signal to noise, or correspondingly, a greater acceptance for a fixed signal to noise. Some of these points are illustrated in the following paragraphs, using data from less than 20 pb^{-1} of running under the new conditions.

Kaon identification greatly improves the ability of the TPC to detect the decays of charmed particles. Figure 6a shows the mass spectrum for $K^-\pi^+$ (+

charged conjugate) combinations whose total momentum is above 5 GeV/c. The D^0 signal is clearly visible and has a very low background. A highly pure D^0 signal can thus be obtained for lifetime, forward-backward asymmetry, mixing, and B meson decay measurements. Other D meson decays are shown in Fig. 6b ($D^0 \rightarrow K^-\pi^+\pi^+\pi^-$) and Fig. 6c ($D^+ \rightarrow K^-\pi^+\pi^+$). The background level is much higher for these signals because of combinatorics. A very pure D^{*+} signal is shown in Fig. 6d, in which the $K^-\pi^+$ combinations that form D^0 candidates have been combined with an additional pion and the mass difference ($m(D^{*+}) - m(D^0)$) is taken.

When two charged kaons are present in a decay, even greater background rejection can be obtained. Figure 7 shows the mass spectrum of $K^+K^-\pi^+$ combinations with total momentum greater than 7 GeV/c. An $F^\mp$ signal is seen – the first measurement of $F^\mp \rightarrow K^+K^-\pi^\mp$ without the requirement of $\phi \rightarrow K^+K^-$ or the requirement of a γ from the decay $F^* \rightarrow \gamma F$.

Figure 8 shows a comparison of the new and old data samples for Λs, for two momentum ranges: 1-2 GeV/c and 5-10 GeV/c. The improvement is dramatic, especially in the higher momentum data. A similar comparison is shown for ϕs in Fig. 9. Figure 10 illustrates how these gains in resolution can translate into gains in efficiency for a given signal to noise ratio. In the case of Λs a factor of about 2.5 in acceptance can be achieved. This is especially important for correlation studies where such a gain translates to a gain greater than a factor of 6 for $\Lambda\Lambda$ pairs. In the case of Ξ^-, $\overline{\Xi}^+$ reconstruction efficiency this translates into a gain of a factor 2.8 as illustrated in Fig. 11.

In all the results described above, no distortion corrections have been made. We expect some improvement after making corrections for the small remaining distortions.

The other systems in the facility are operating well. The Hexagonal Calorimeter is operating with its six modules and has reached a performance with the 'New Gas' comparable, although slightly inferior, to the performance achieved

with ethyl bromide. A π^0 peak is shown in Fig. 12a for the new data, compared with a π^0 peak in Fig. 12b for the old data.

Our data analysis system is now able to keep up with 1 pb^{-1} of data per day. We typically have data summary tapes for annihilation events (really an updated data summary disk) from one to a few days after the data is collected.

VII.3 FUTURE DETECTOR UPGRADES, CHANGES

In the high luminosity era the interaction region quadrupoles move forward towards the interaction point. This motion is incompatible with the present 2γ forward spectrometers. Thus the spectrometers will be dismantled and only the central detector will be used. In order to preserve tagging, the NaI shower counters will be moved to a position adjacent to the detector as shown in Fig. 13.

The only new device to be added for the high luminosity running will be the vertex chamber. This addition will be done in the place presently occupied by the inner drift chamber (IDC). The leading candidate for a vertex detector is the radial drift chamber (RDC) which we describe below. It would occupy the space between 5 cm and 15 cm from the beam and would provide the following capabilities:

1. Maximum information for tracking: approximately 20 measurements per centimeter would be obtained for a total of over 200 measurements per track.

2. Each of the 200 measurements would have, on average, 40μ point setting error (at 1.5 atm).

3. Each point would also provide ionization information which would resolve some of the dE/dx ambiguities in the TPC (since DME has nearly no relativistic rise, its dE/dx vs. p curves are different from those for Argon-CH_4).

The installation of the radial drift chamber is motivated primarily by the desire to study the properties of "third generation" leptons and quarks, namely the b quark and the τ lepton. In addition to a measurement of the lifetimes of these particles, more difficult goals such as b tagging, $B - \overline{B}$ mixing and even $b \rightarrow u$ studies may be realizable with the addition of a high resolution tracking chamber near the vertex. The radial drift chamber (RDC) is designed to provide not only a high tracking accuracy (200 measurements, each with 40 μm resolution), but also can function as a fast, momentum dependent trigger, and can give $\langle dE/dx \rangle$ information which is complementary to the information from the TPC.

VII.3.1 Conceptual Design of the Radial Drift Chamber

Most current strategies in the design of vertex detectors focus on a straightforward extrapolation of drift chamber technology. This includes packing the chamber with a large number of small drift cells, and the use of slow velocity gas mixtures. In such chambers, although there may be as many as 100 ionization electrons in a single cell, only the information from the first electron arriving at the sense wire is used in determining tracking coordinates. The radial drift chamber, in contrast, is designed to use the maximum amount of information available from the track ionization. The design of this device takes advantage of a number of recent innovations in gaseous tracking chambers; the use of pickup wires near the sense wire to localize avalanche coordinates,[7] the use of waveform sampling rather than leading edge discrimination, and the use of slow, cool organic gases with limited diffusion.[8]

The chamber itself (Fig. 14) consists of five cylindrical shells. The innermost shell is formed by the beam pipe followed (moving out in radius) by an instrumented layer of wires, a central cathode, an outer layer of wires and an outer pressure wall. With the central cathode held at negative high voltage, the ionization formed in the inner half of the chamber drifts to the inner layer of wires, and the ionization formed outside the central cathode will drift out to the outer layer of wires. The instrumented sets of wires (Fig. 15) consist of a sense

wire strung between a pair of pickup wires, these are designated as "triplets". In addition, field shaping wires are strung between wire triplets to enhance the field in the amplification region.

Once a start time has been defined by a fast trigger in conjunction with a beam crossing, the signals on the sense and pickup wires are continuously sampled until the entire drift volume has been read out. The radial coordinate of an ionization cluster is determined by its arrival time at the anode wire, relative to some common start time. Within one cell, defined by the field lines mapped onto a single anode wire, the azimuthal coordinate is determined from the position of the avalanche around the sense wire. The position of the avalanche is deduced from the asymmetry in the response of the pickup wires as a function of the avalanche angle, α (see Fig. 15) Our studies, described below, indicate that if the pickup wires are placed close to the sense wire, and if one uses a gas with limited transverse avalanche spread, that this asymmetry can be quite sizable, and can be used as a reliable measure of the angle, α. With a knowledge of the electrostatics of the chamber, it is relatively simple to deduce the field line an ionization cluster followed from a measurement of α.

The use of pickup wires to determine avalanche coordinates was first investigated by Walenta[7] for use in the time expansion chamber (TEC). The radial drift chamber differs from the TEC in two significant aspects. First, there is no grid structure separating the drift region from the amplification region which will distort the ionization from a track. Secondly, the angle a track typically forms with respect to the plane of the wire triplets, θ, is approximately 90° in the RDC, whereas $\theta \approx 0°$ in the TEC. This allows a much slower collection time in the PDC, coupled with a reduction in possible systematic errors associated with tracks with varying values of θ.

We intend to use dimethyl ether (Ref. [8]) at 1.5 atm as the chamber gas. Dimethyl ether has a number of desirable properties, it has a slow drift velocity ($\approx$ 1 cm/μsec), a limited transverse diffusion (40-50 μm/cm$^{1/2}$), and, as we have

found, a limited transverse avalanche growth. In DME at 1.5 atm, a minimum ionizing particle will deposit 180 electrons on average per centimeter of track length. If we sample the sense and pickup wires at a rate of 50 MHz, then each sample will contain information from $\approx$ 8 electrons. With 200 samples over the track length, each with an accuracy of 40 μm per sample, a tracking resolution of $\approx$ 5 μm may be ultimately achievable.

Aside from the inherent tracking accuracy of the RDC, prompt ionization information collected from tracks piercing both wire layers can be used to form a momentum dependent trigger for the TPC. Track ionization near the sense wires can be collected within 50 nsec. By simply defining whether or not a triplet has a charged particle passing through the cell, a coincidence between the inner and outer layers can be formed.

VII.3.2 Test of the RDC Concept: Avalanche Localization

In practice, we use the asymmetry:

$$\frac{L - R}{A} \tag{VII.1}$$

where

L is the signal induced on the left sense wire.

R is the signal induced on the right sense wire.

as a measure of the angle α. To a first approximation, we can write the asymmetry, $(L - R)/A$, in terms of α as:[9]

$$\frac{L - R}{A} = a_1 \sin a_2\alpha \tag{VII.2}$$

where a_1 and a_2 are arbitrary constants, which depend on the geometry and the relative signal strengths seen on the anode and the pickup wires. If we make the

assumption that there is a linear mapping of the angle α to the position, x, of the cluster in the linear region,[10] then we can write,

$$\frac{L-R}{A} = b_1 \sin b_2 x \qquad \text{(VII.3)}$$

In order to study this response, we built a test chamber which we operated at 1 atm in DME, and also in Ar-CH_4 to establish a baseline. The test chamber consisted of a planar array of 34 wire triplets. The anode-anode distance was 1.5 mm the anode-pickup distance was 250 μm. Anode wires were 20 μm gold coated tungsten, strung at 50 gm, the pickup wires were 75 μm gold coated Cu-Be alloy, strung at 100 gm. Because of spatial limitations, we instrumented only 4 triplets. The wire plane was placed midway between two Cu cathode planes, separated by 12 mm. Through a hole in one of the cathode planes, a pointlike source of thermal electrons could inject a known number of electrons into the drift region. By examining the response of the pickup and anode wires as a function of the location of the electron source, asymmetry maps of $(L-R)/A$ as a function of x could be made.

A parallel chain of electronics was used to establish on a pulse by pulse basis, the ratio, $(L-R)/A$ for the wire triplets. By scanning the thermal electron source at well determined intervals (using a micrometer), detailed maps of $(L-R)/A$ could be made. Figure 16 shows a spectrum of peaks, from such a scan. Here each peak represents $\approx$ 500 values of $(L-R)/A$ for a single gun position. In the figure, adjacent peaks are separated by 300 μm. Using the peak separation to set the distance scale, an equivalent spatial resolution can be derived from the widths of the peaks.

Figure 17 shows a plot of the measured response, $(L-R)/A$ as a function of the gun location, along with a best fit to the sinusoidal parameterization described above. In this figure, there is $\approx$ 5 μm RMS deviation of the data from the fit to the sinusoid.

By varying the number of electrons ejected by the thermal source, the resolution as a function of the number of electrons can be measured, and serves as a basis for our estimates of the spatial resolution for the RDC. From these measurements, we have found that there is ≈ 40 μm accuracy for clusters with 8 electrons; the yield per sample expected in the RDC.[9]

REFERENCES

1. R. G. Smits *et al.*, Journal de Physics, **45**, C1-653 (1984).
2. H. Aihara *et al.*, IEEE Trans. NS-30, (1983) 63, 76, 162; Nucl. Instrum. Methods **223**, 40 (1984).
3. W. Gorn *et al.*, IEEE Trans. NS-26, 67 (1979); IEEE Trans. NS-30, 153 (1983).
4. H. Aihara *et al.*, IEEE Trans. NS-30 117 (1983); Nucl. Instrum. Methods **217**, 259 (1983).
5. J. Bakken *et al.*, IEEE Trans. NS-30, 67 (1983).
6. M. Ronan *et al.*, IEEE Trans. NS-29, 427 (1982).
7. A. H. Walenta *et al.*, Proc. Intl. conf. on Instrumentation for Colliding Beams, SLAC, Stanford, CA, February 17-23, 1982.
8. F. Villa, Nucl. Instrum. Methods **217**, 273 (1983).
9. J. Huth and D. Nygren, LBL-19462 (1985).
10. G. A. Erskine, Nucl. Instrum. Methods **105**, 565 (1972).

FIGURE CAPTIONS

1. The PEP-4 facility. A vertical section through the colliding beam line.
2. The PEP-4 facility. A vertical section perpendicular to the colliding beam line.
3. The PEP-4 facility with the PEP-9 forward spectrometer shown on one end.
4. A scatter plot of events based on the measured value of dE/dx (vertical axis) and the ln p (horizontal axis). The rising bands are clearly seen from left to right for μ, π,K,p,d.
5. Number of events as a function of ln mass for tracks with dE/dx $>$ 1.67 times minimum. For positive tracks (top) and negative tracks (bottom).
6. D mesons in the new sample. a) $D^0 \rightarrow K^-\pi^+ + cc$; b) $D^0 \rightarrow K^-\pi + \pi^+\pi^-$; c) $D^+ \rightarrow K^-\pi^+\pi^+$; d) $M(K\pi\pi) - M(K\pi)$ showing $D^{*+} \rightarrow D^0\pi^+$ peak.
7. $F^{\mp}$ events decaying via $F^{\mp} \rightarrow K^+K^-\pi^{\mp}$. Selection of events with K^+, K^- and $P(K\pi\pi) > 7$ GeV/c.
8. The Λs in the new data sample (upper two plots) compared to the Λs in the old data sample (lower two plots).
9. The ϕs in the old data sample (upper plot) compared to the ϕs in the new data sample (lower plot).
10. Efficiency vs. signal to noise ratio for Λs in the old and new data samples.
11. The $\Xi^- + \overline{\Xi}^+$ in the new data (upper plot) compared to the old data (lower plot).
12. The π^0 mass spectrum in the new data (a) and in the old sample (b).
13. Drawing shows the proposed new location of the NaI detectors relative to the TPC and the iron pole tip of the magnet.

14. Transverse cross section of the radial drift chamber. A central cathode divides the chamber into two drift regions. Inside the cathode, tracks drift to a set of wires at the inner radius. Outside the cathode, tracks drift out to a set of wires on the outer radius. The radial coordinate of the track is found from the arrival time of the ionization clusters at the wires. The azimuthal coordinates of the track are determined from the signals induced on pickup wires which localize the avalanche position on nearby anode wires.

15. View of one wire triplet, consisting of a pair of pickup wires and one sense wire. In addition, field shaping wires are used to enhance the electric field around the sense wire.

16. Oscilloscope trace showing a spectrum of measurements taken of $(L - R)/A$ on a pulse by pulse basis. The spacing between peaks in the figure is 300 μm. The 3 plots correspond to different number of electrons from the source.

17. Values of $(L - R)/A$ taken on a pulse by pulse basis as a function of the position of the electron source. Also plotted is the result of the best fit to a sinusoid (see text for parameterization).

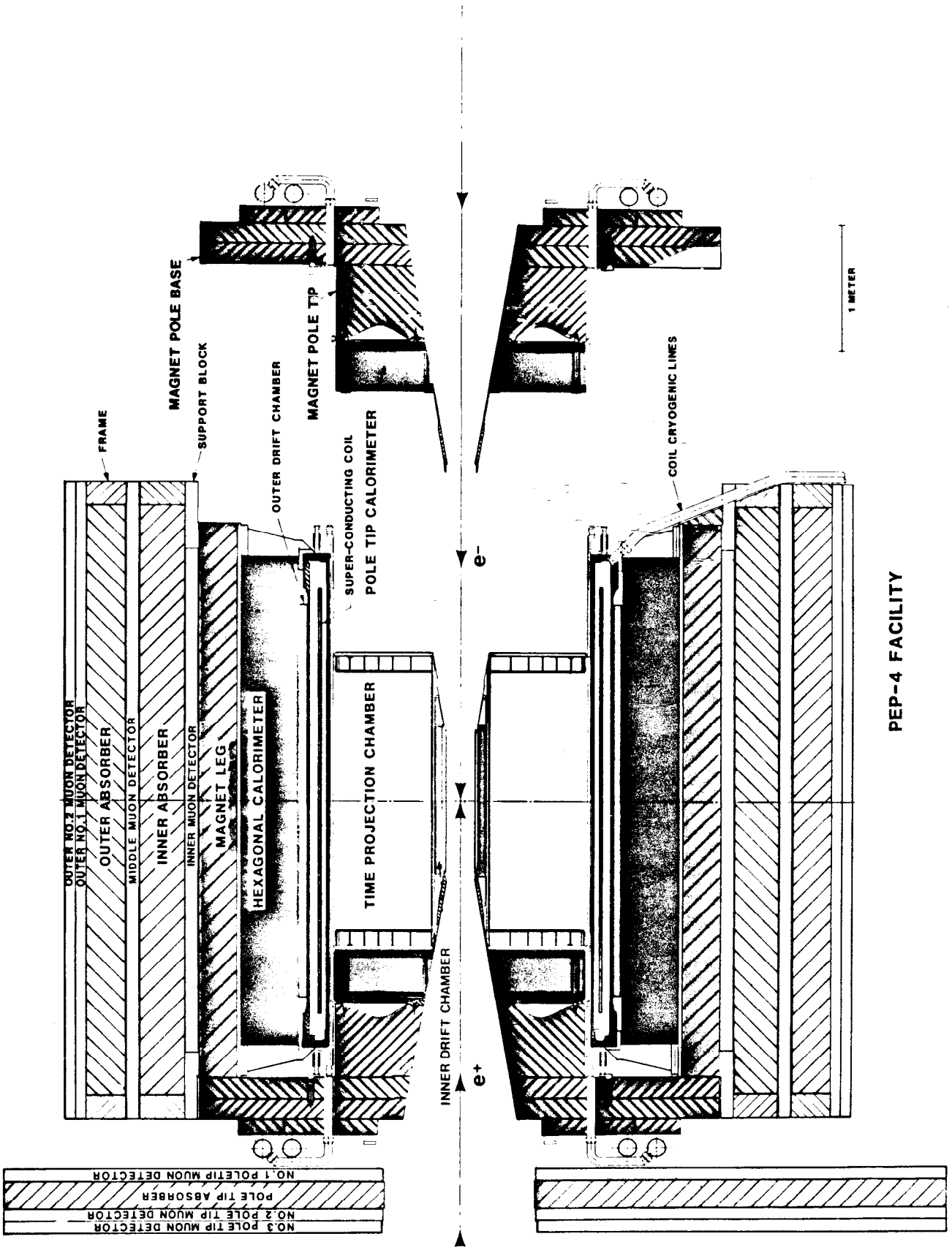
MAGNET POLE BASE
SUPPORT BLOCK
FRAME
OUTER DRIFT CHAMBER
MAGNET POLE TIP
SUPER-CONDUCTING COIL
POLE TIP CALORIMETER
COIL CRYOGENIC LINES
1 METER
OUTER NO.2 MUON DETECTOR
OUTER NO.1 MUON DETECTOR
OUTER ABSORBER
MIDDLE MUON DETECTOR
INNER ABSORBER
INNER MUON DETECTOR
MAGNET LEG
HEXAGONAL CALORIMETER
TIME PROJECTION CHAMBER
INNER DRIFT CHAMBER
e-
e+
NO.1 POLE TIP MUON DETECTOR
POLE TIP ABSORBER
NO.2 POLE TIP MUON DETECTOR
NO.3 POLE TIP MUON DETECTOR
PEP-4 FACILITY

Fig. 1

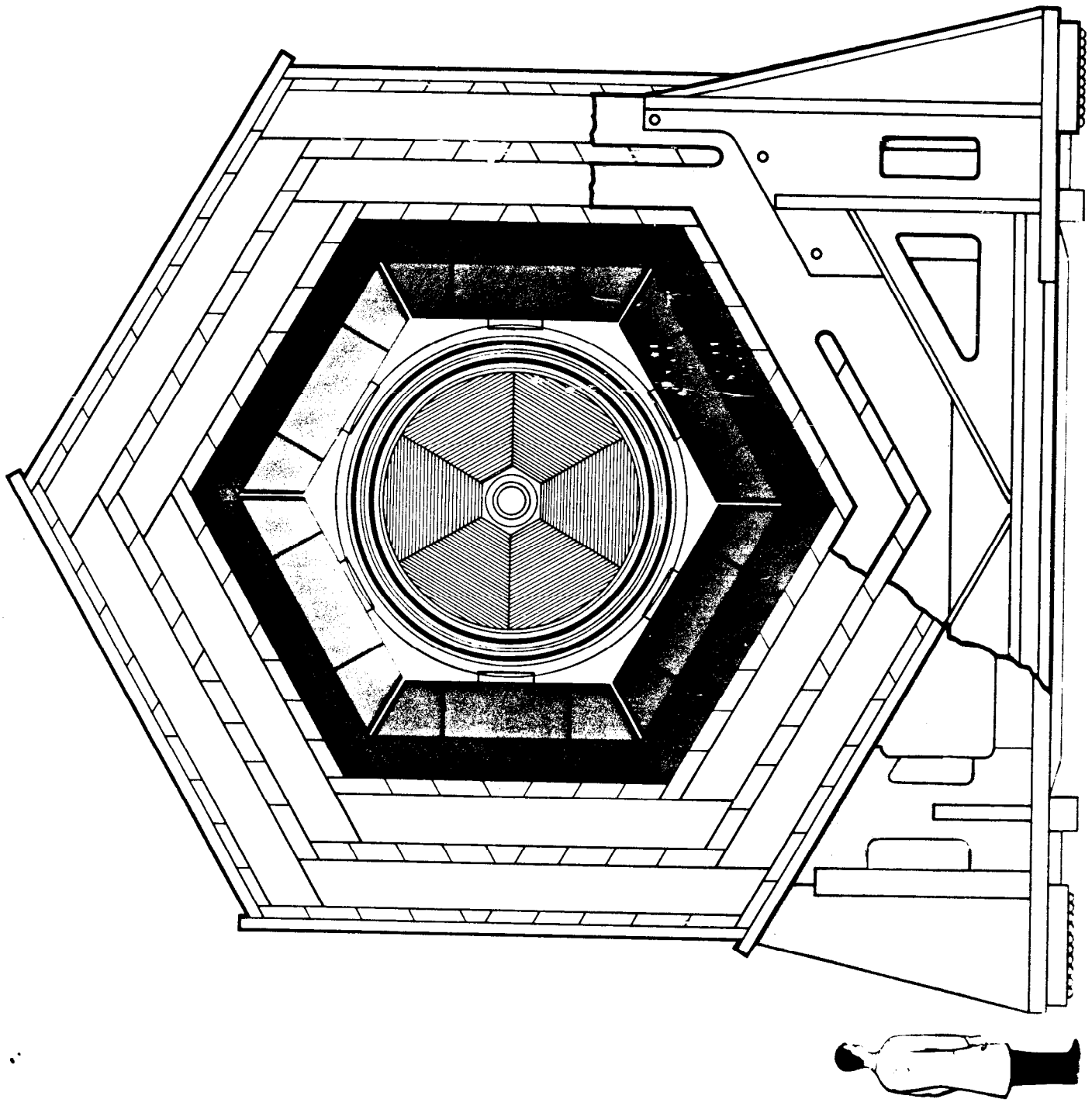

Fig. 2

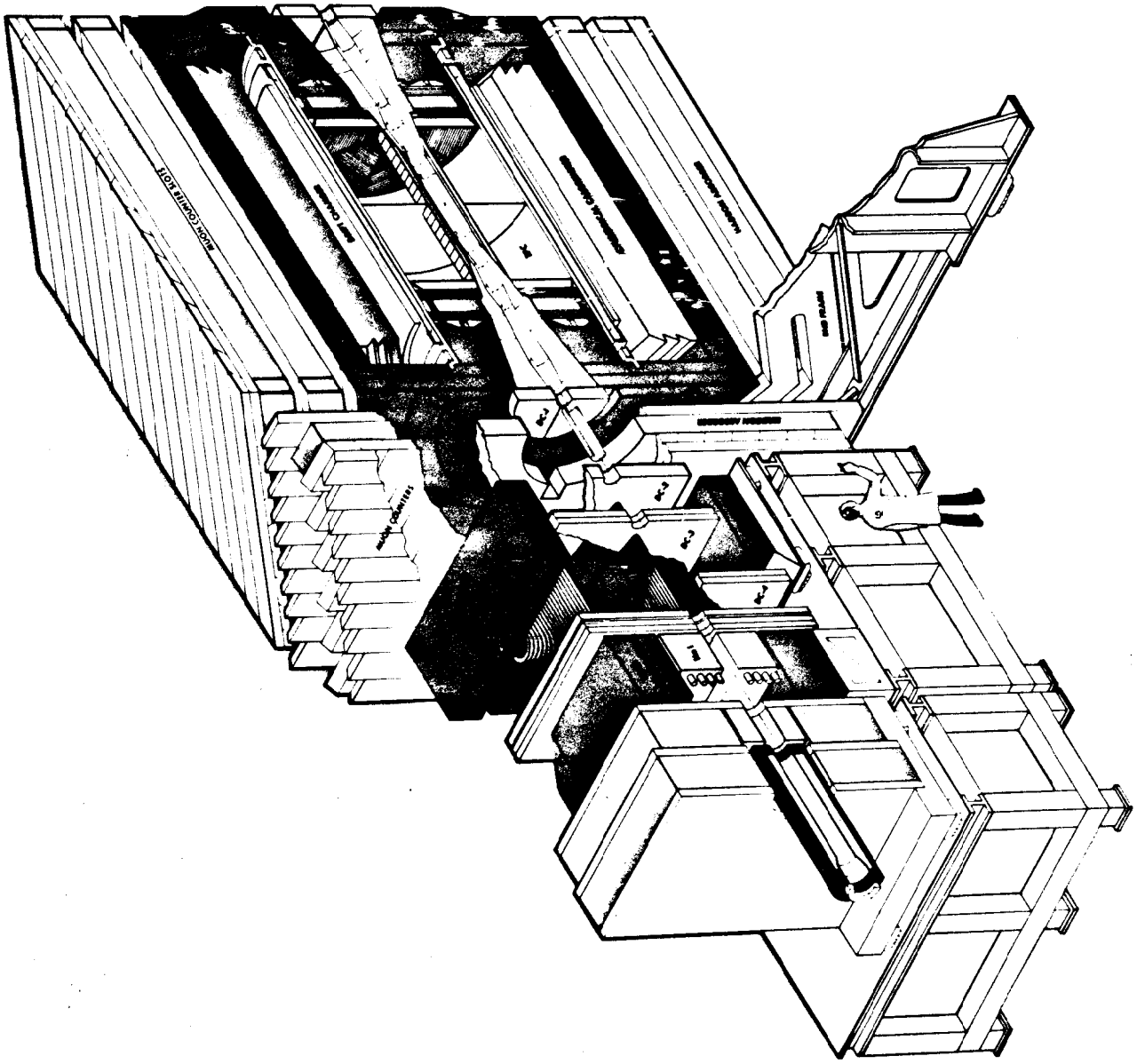

Fig. 3

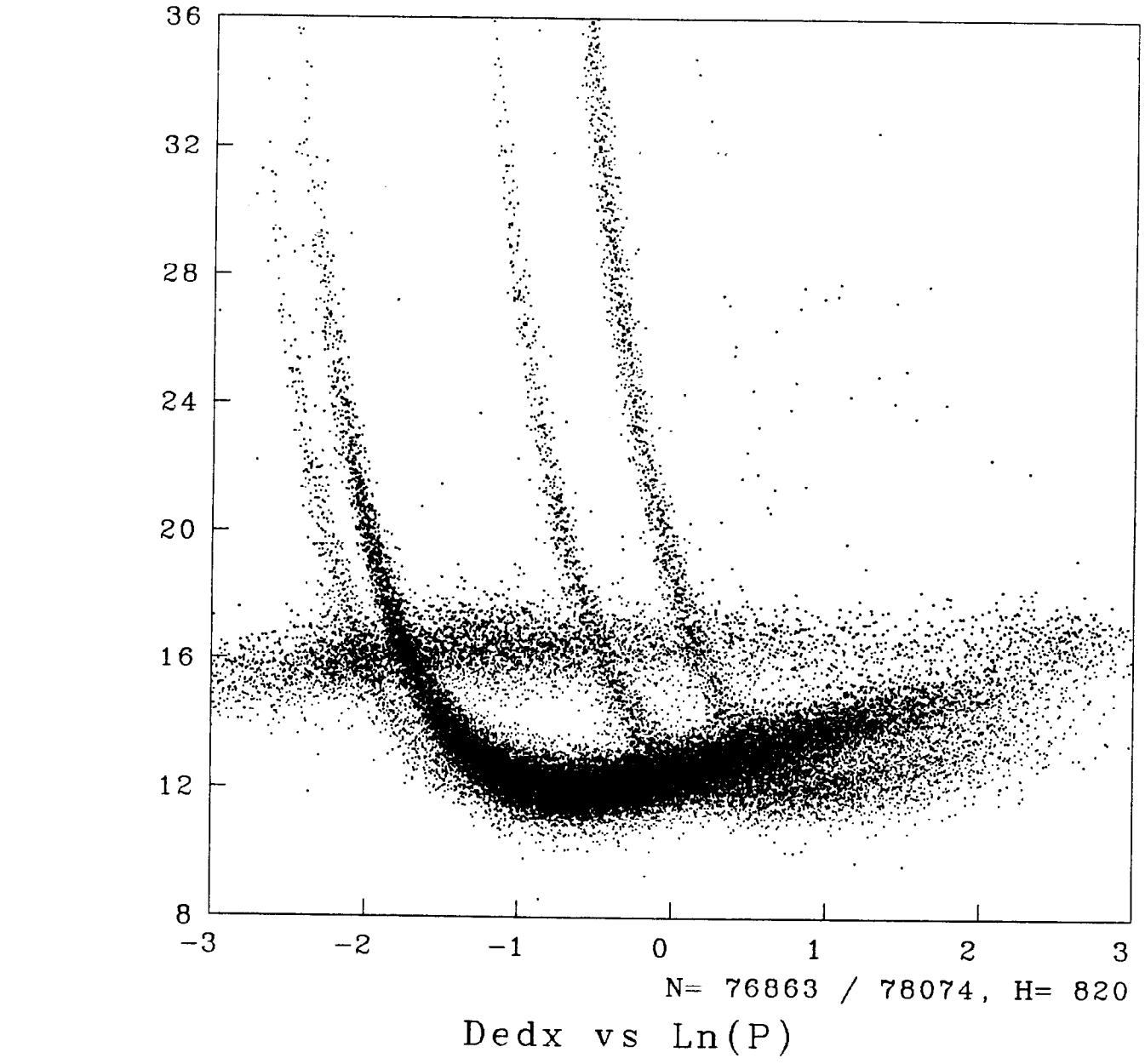
Run 15-700 06-Apr-85 13:13
36
32
28
24
20
16
12
8
-3
-2
-1
0
1
2
3
N= 76863 / 78074, H= 820
Dedx vs Ln(P)

Fig. 4

Experiments 14 and 15

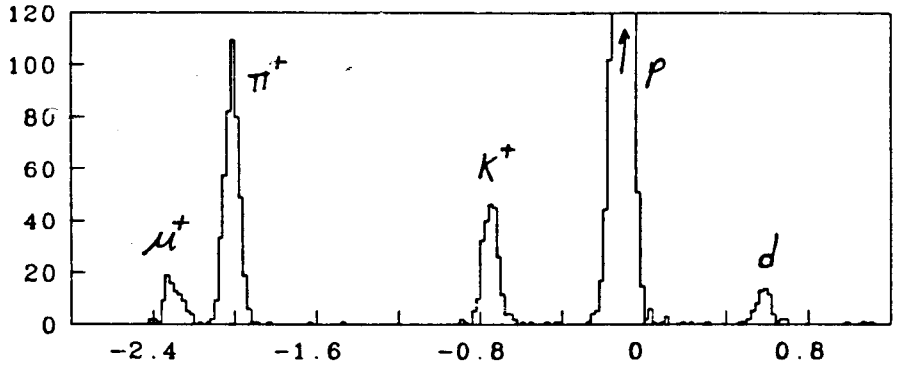

Ln Mass Positives

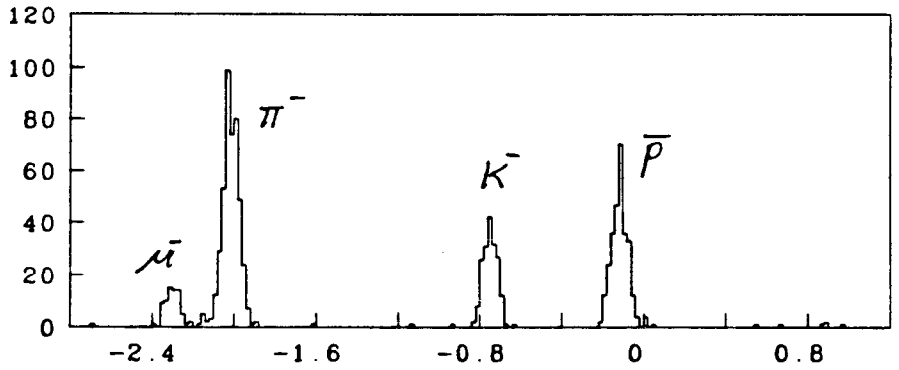

Ln Mass Negatives

Fig. 5

PEP4/9 TPC ------- PRELIMINARY

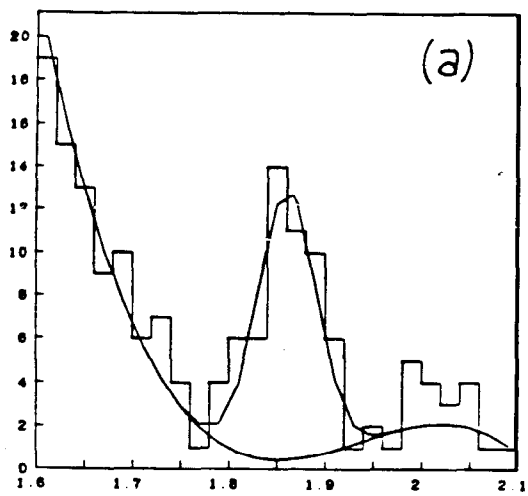

m(Kpi), p(Kpi) ⟩ 5 GeV/c
D0 --⟩ K- pi+

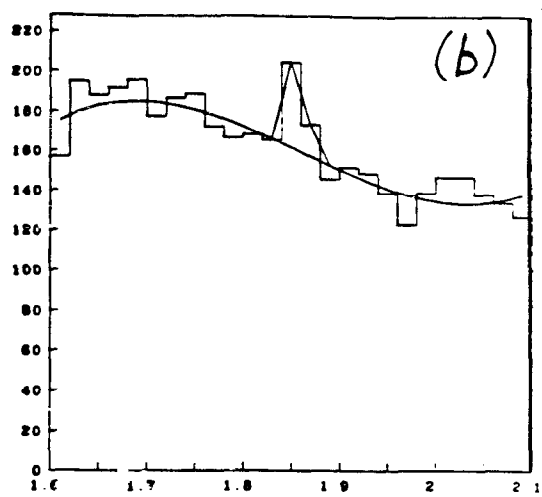

m(Kpipipi), p(Kpipipi) ⟩ 5 GeV/c
D0 --⟩ K- pi+ pi+ pi-

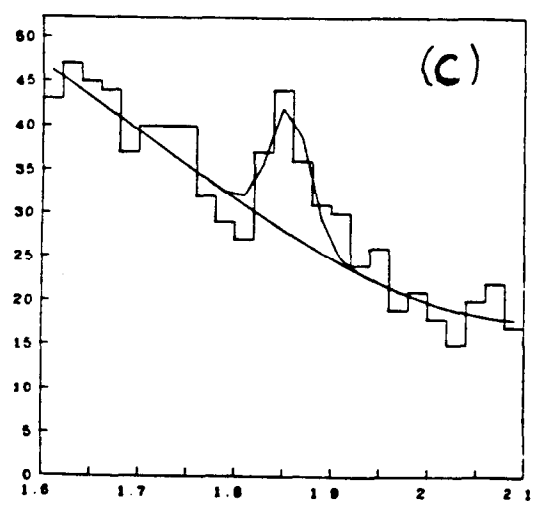

m(Kpipi), p(Kpipi) ⟩ 6 GeV/c
D+ --⟩ K- pi+ pi+

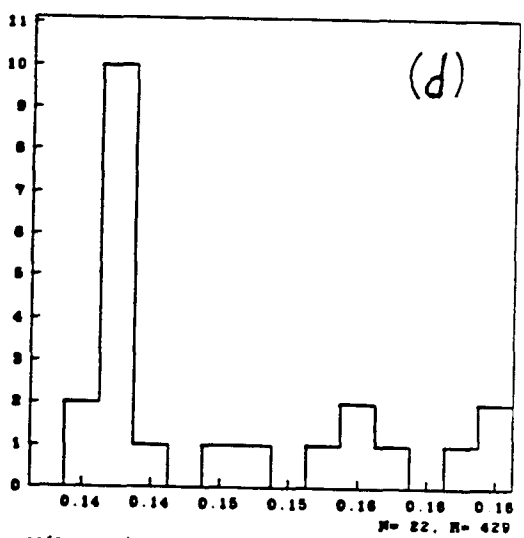

M(Kpipi) - M(Kpi), p(Kpipi) ⟩ 4 GeV
D*+ --⟩ D0 pi+, D0 --⟩ K- pi+

Fig. 6

PEP4/9 TPC ------- PRELIMINARY

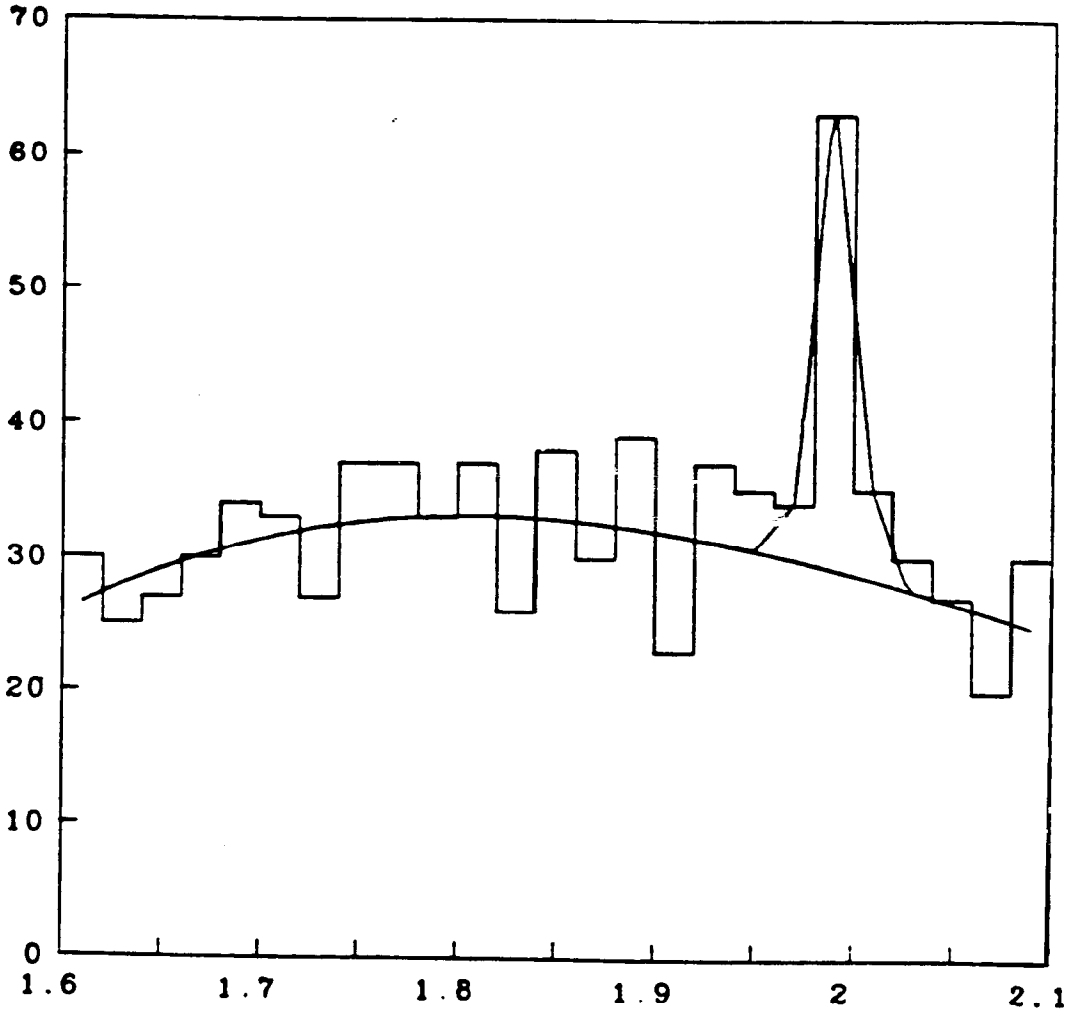

m(KKpi), p(KKpi) ⟩ 7 GeV/c
$F^{\mp}$ --⟩ K+ K- $pi^{\mp}$

Fig. 7

Lambda Candidates : Old(29.1K) vs New(7.0K)

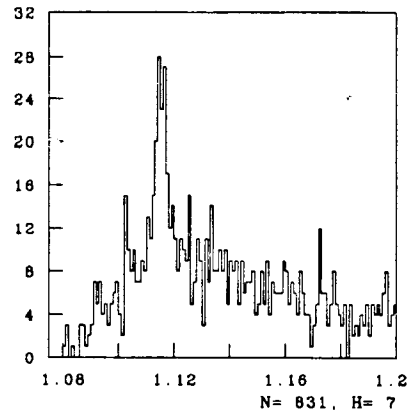

New Lmbd : P=1-2

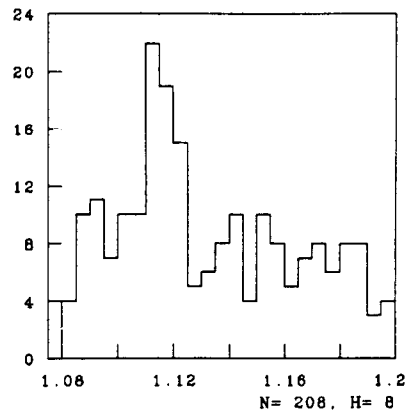

New Lmbd : P=5-10

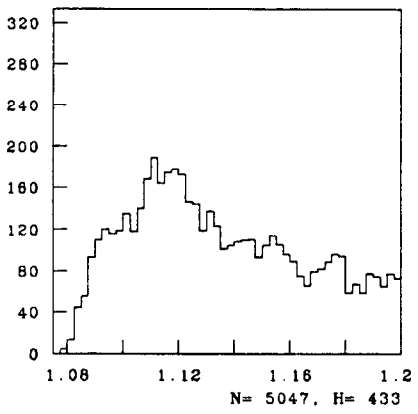

Old Lmbd : P=1-2

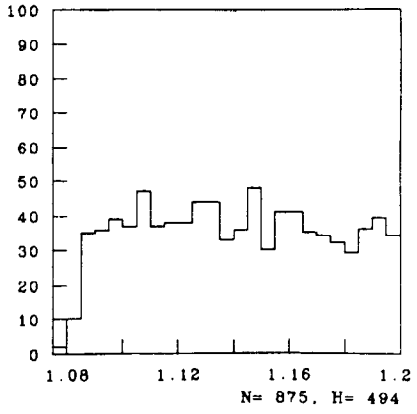

Old Lmbd : P=5-10

Fig. 8

Phi

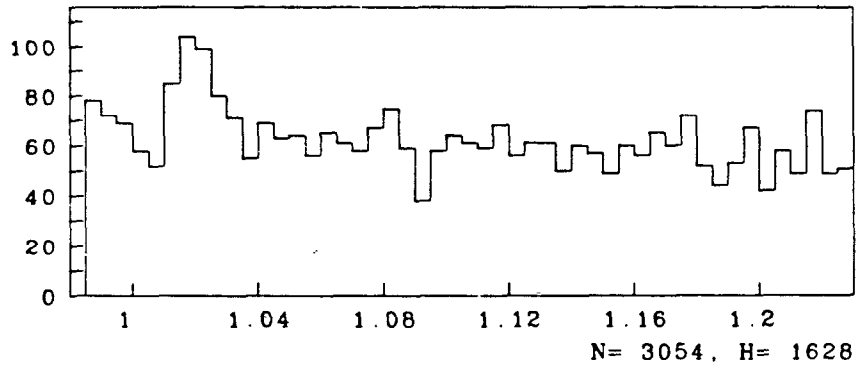

KK mass at 3.9 Kg

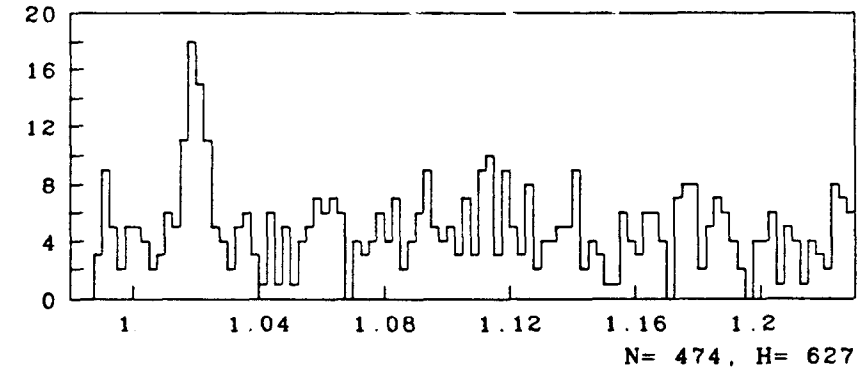

KK Mass at 13.25 Kg

Using tracks for which K is most probable choice

Fig. 9

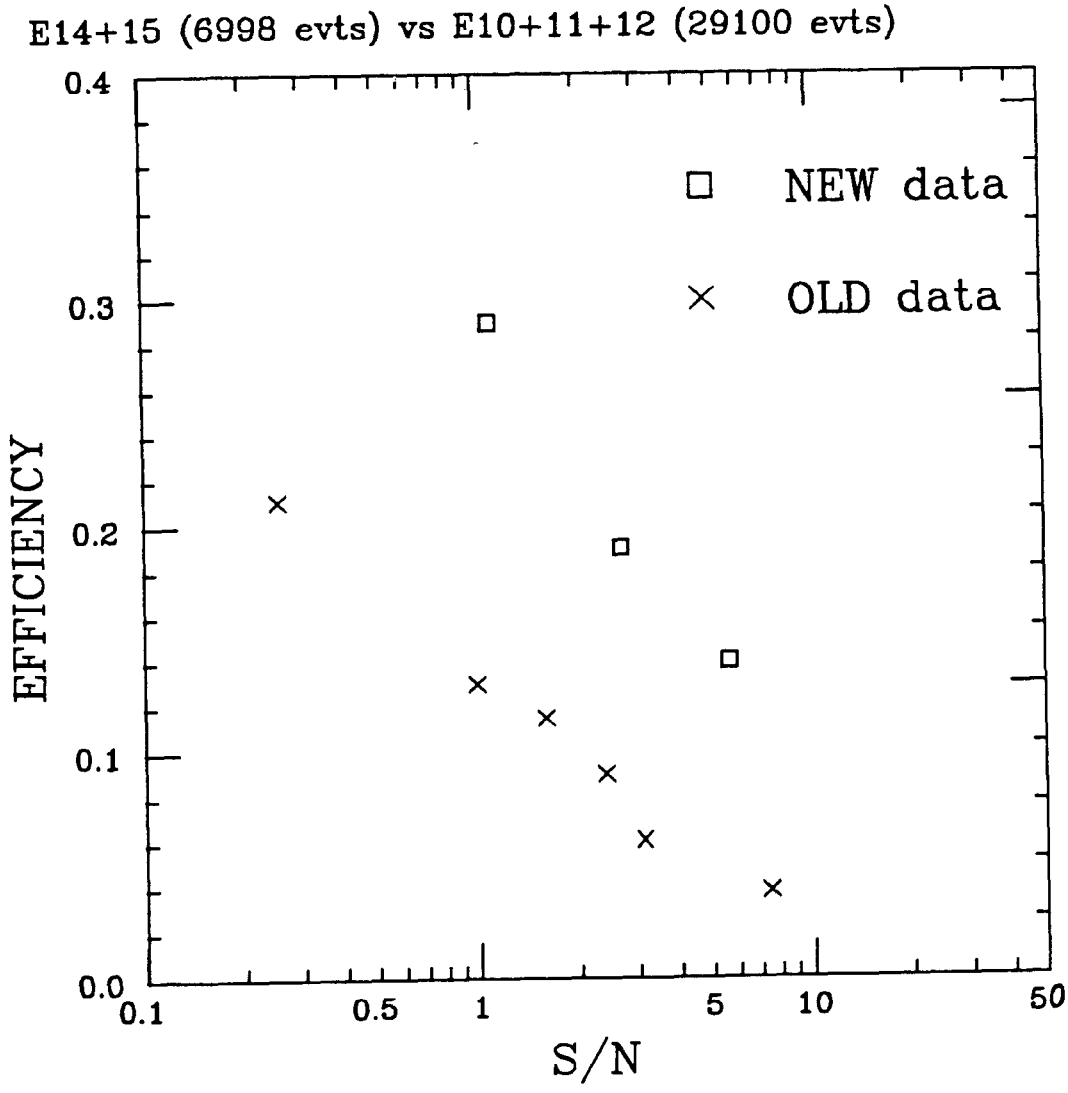
E14+15 (6998 evts) vs E10+11+12 (29100 evts)
EFFICIENCY
S/N
NEW data
OLD data
0.4
0.3
0.2
0.1
0.0
0.1
0.5
1
5
10
50

Fig. 10

Xi Candidates : E14+15(7.0K) vs E10+11+12(29.1K)

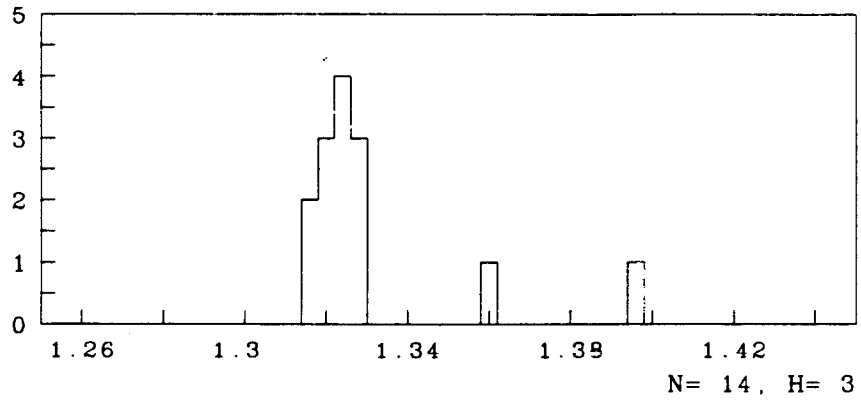

New Xi : P = 1-6 GeV/c

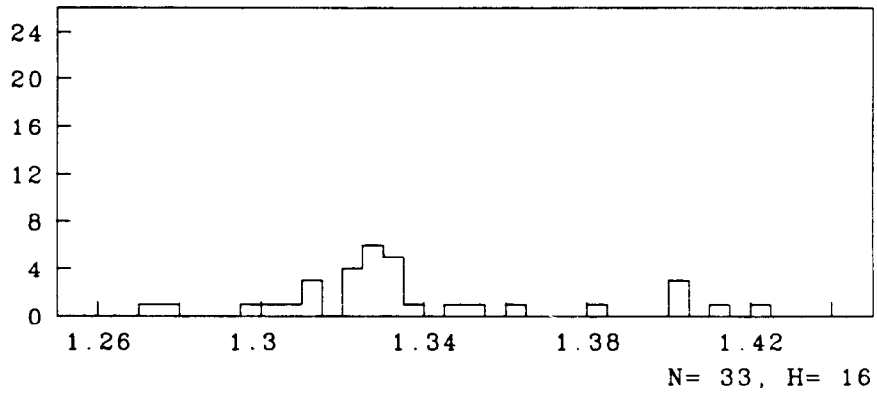

Old Xi : P = 1-6 GeV

Fig 11

Exp 15 data (NEW)

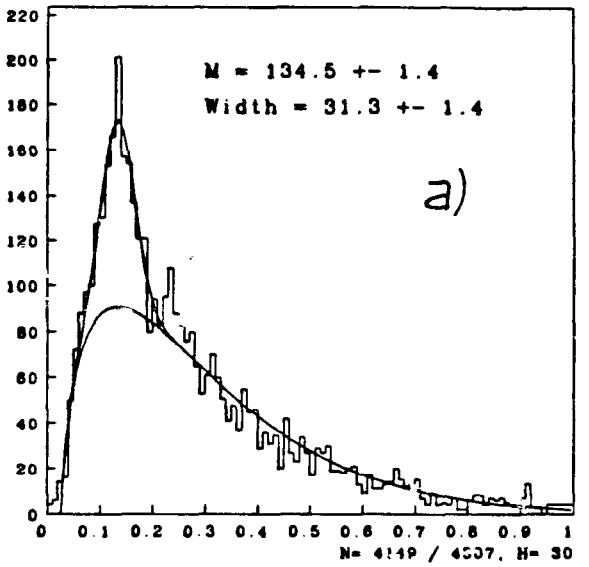

Hex calorimeter photons
Pi0 fit: E 15 data

E 12 data (OLD)

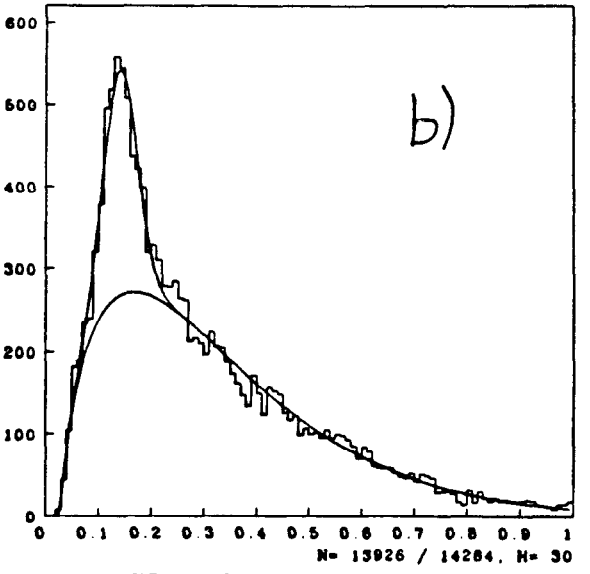

HEX calorimeter photons
Pi0 fit: E 12 data

Fig. 12

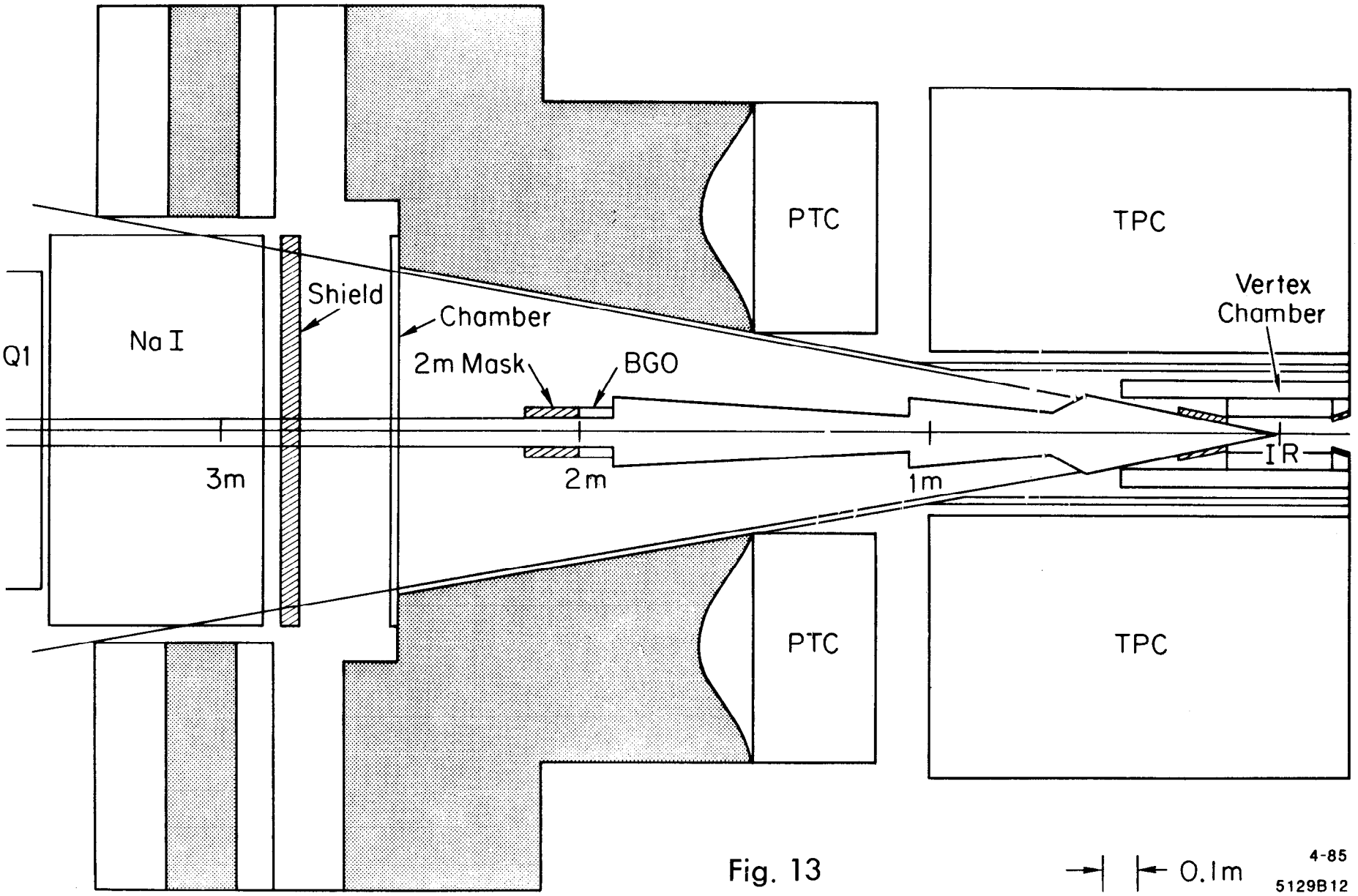
PTC
TPC
Vertex
Chamber
Shield
Chamber
Q1
Na I
2m Mask
BGO
IR
3m
2m
1m
PTC
TPC
0.1m
4-85
5129B12

Fig. 13

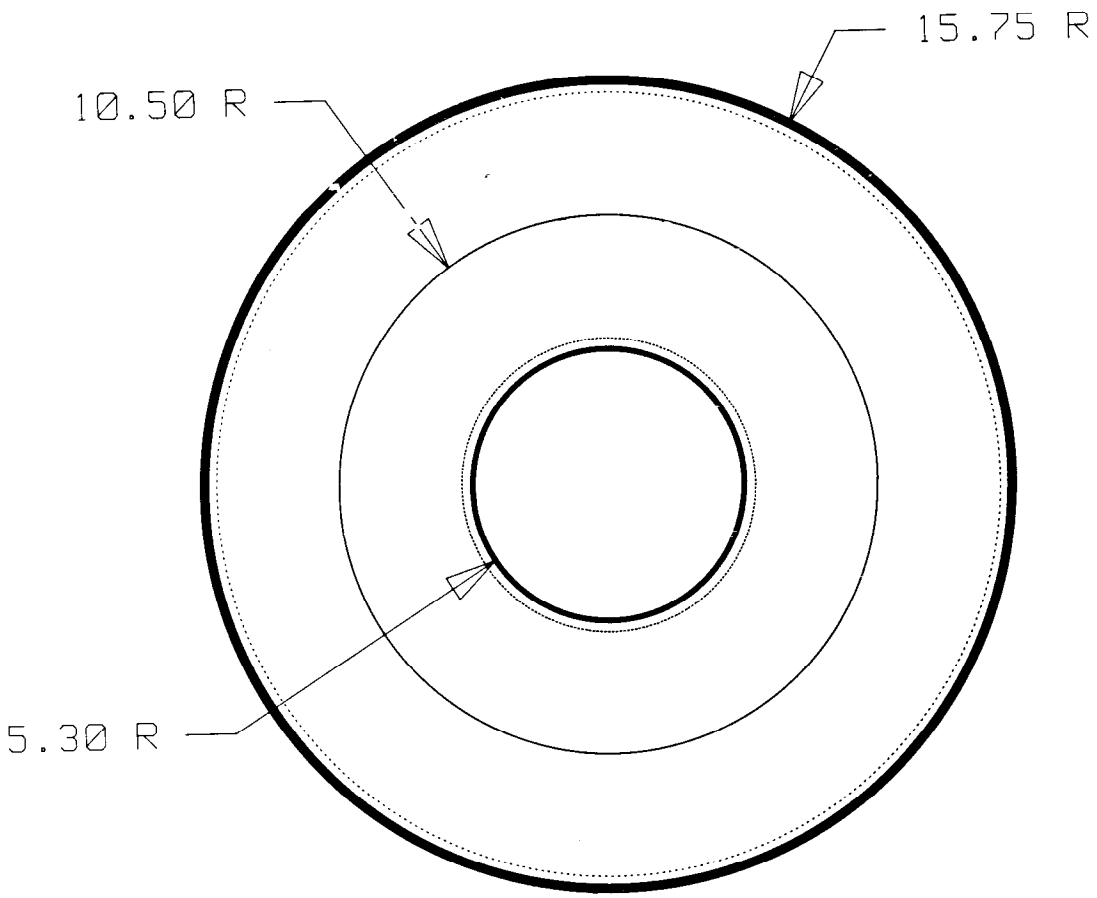

XBL 853-1905

Fig. 14

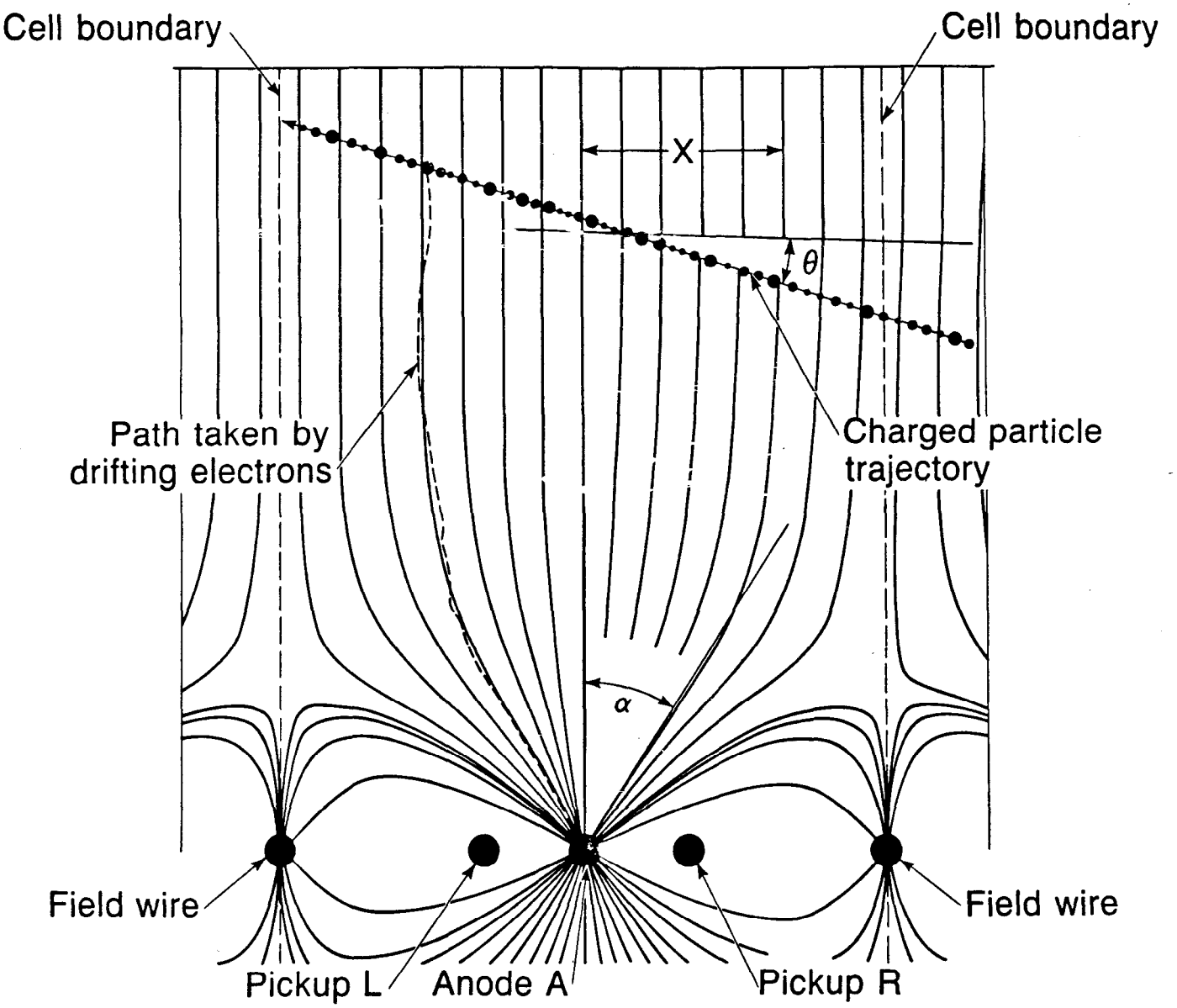
Cell boundary
Cell boundary
X
θ
Path taken by
drifting electrons
Charged particle
trajectory
α
Field wire
Field wire
Pickup L
Anode A
Pickup R
XBL 854-11065

Fig. 15

$n_e = 200$

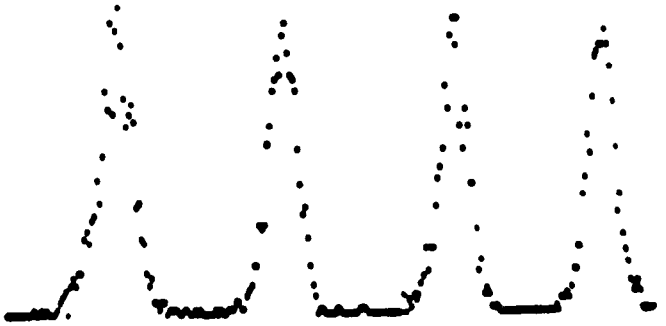

$n_e = 50$

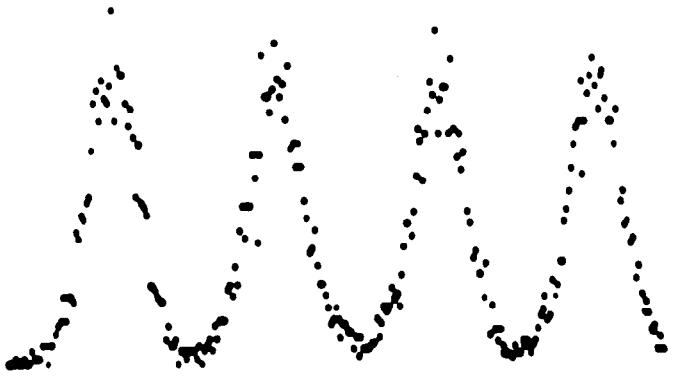

$n_e = 8$

Fig. 16

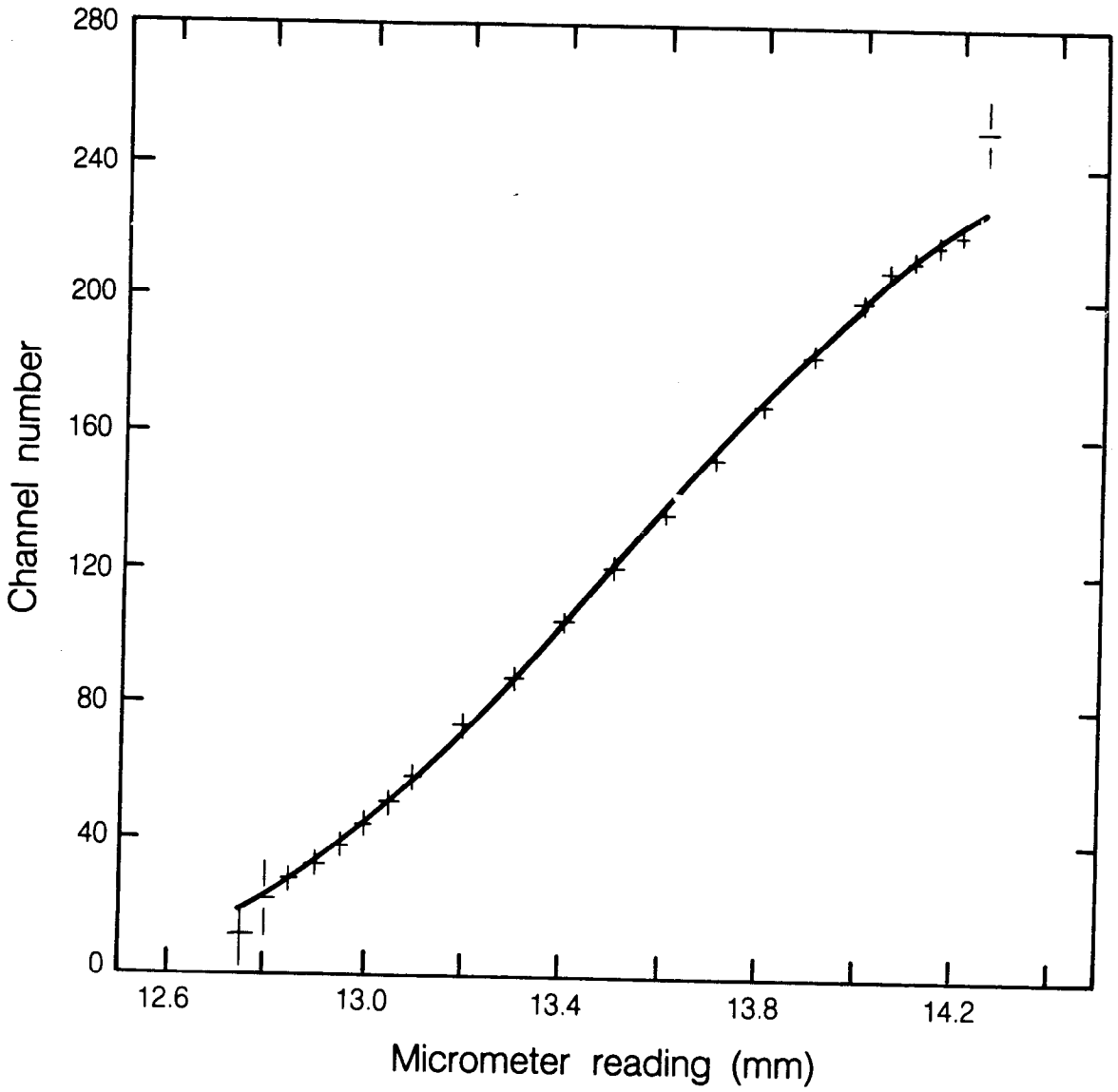

XBL 854-9527

Fig. 17

CHAPTER VIII
THE HIGH RESOLUTION SPECTROMETER IN STUDIES OF e^+e^- ANNIHILATION AT $\sqrt{s} = 29$ GeV

M. DERRICK

and

THE HRS COLLABORATION

CHAPTER VIII.
THE HIGH RESOLUTION SPECTROMETER IN STUDIES OF e^+e^- ANNIHILATION AT $\sqrt{s} = 29$ GeV

CONTENTS

VIII.1 The General Goals of the Experimental Program

The goals of the program of research with the High Resolution Spectrometer at PEP divide naturally into three areas:

(a) Measurements of the electroweak couplings of the quarks and leptons. All known partons except for the top quark are produced within the PEP energy range.

(b) Studies of the strong interactions of the quarks. This area is guided by QCD and a major objective is to understand to what extent this theory can be considered a quantitative guide.

(c) Search for qualitatively new phenomena. Although it is difficult to predict such things, by definition, there are several obvious directions in which to explore.

VIII.2 Brief Description of the High Resolution Spectrometer

The HRS[1], shown in Fig. 1, is a general-purpose spectrometer which measures both charged particles and electromagnetic energy over 90% of the solid angle. The detection elements are in a 1.62-T magnetic field with a cylindrical volume of 4.45 m in diameter by 3.88 m long. The field uniformity is such that $\Delta B/B_0$ is less than 1.5% over the main tracking region, where B_0 is the central field value.

During the first year of operation, the detector elements of the HRS consisted of a central drift chamber, an outer drift-chamber system, a barrel shower counter, and an end-cap shower-counter system.

The central drift chamber tracks charged particles using 15 cylindrical layers of drift cells. In seven of the layers the wires are oriented axially, and in the remaining eight layers they are at a stereo angle of ± 60 mr. The innermost layer is at a radial distance of 21 cm from the beam line, and the outermost layer is

at 103 cm. The outer drift chamber was designed to significantly improve the spectrometer momentum resolution for charged tracks. It consists of two layers of drift tubes comprising a cylinder 1.89 m in radius and 3.5 m in length. The tubes are 2.58 cm in diameter. The drift-chamber systems have a total of 3344 cells with a measured spatial resolution of 200 μm. The predicted momentum resolution of the HRS including and excluding the outer-drift-chamber information is shown in Fig. 2.

As seen in Fig. 2, the high-momentum tracks have a resolution which is set by measuring error whereas multiple scattering dominates at low momentum. To minimize the latter effect the storage ring vacuum pipe was made of 0.14-cm-thick beryllium with a 0.025-cm aluminum coating to absorb synchrotron photons. The chamber support structures were also designed to minimize multiple scattering of the outgoing particles. The result is that a typical track traverses 0.02 radiation lengths of material. This unique combination of high magnetic field, extensive tracking range, low multiple scattering, and precise spatial measurement, yielded a momentum resolution of

$$\frac{\sigma_p}{p} = 1.0 \times 10^{-3} p \text{ (p in GeV/c)}$$

for $|\cos\theta| < 0.7 >$ and p $>$ 5 GeV/c. The charge of a 14.5-GeV/c particle is unambiguously identified for $|\cos\theta| < 0.91$.

The momentum accuracy of the HRS can be checked using Bhabha-scattered events since they provide a sample of particles of known momentum. Figure 3 shows the momentum distribution of Bhabha-scattering electrons including points measured in the outer drift chamber and with the tracks constrained to the known vertex. The width of the distribution is due predominantly to measuring error. The contributions from the beam-energy spread and radiative effects are negligible.

The barrel shower-counter system is used to identify and measure the location of electromagnetic energy and determines the time-of-flight for particles that

traverse the spectrometer. The barrel system consists of 40 modules arranged as the staves of a barrel inside the magnet cryostat with an inner radius of 194.3 cm. The active length of the system is 304.8 cm and it covers 62% of the solid angle. Each module contains three distinct detector segments. The front section consists of a $2X_0$ layer of lead followed by a 1.27-cm-thick layer of scintillator followed by $1X_0$ of lead and another 1.27-cm-thick layer of scintillator. This section of each module is read out with a phototube at each end and provides both time-of-flight information and shower information. The second section of the module is a layer of proportional tubes, made from 3.66-m-long aluminum extrusions, each with 14 cells, 1.9 cm square. the chambers are instrumented for current division measurements and are able to locate a shower position along the wire to an accuracy of ± 2 cm. The last section of the module consists of alternating layers of $1X_0$ of lead and 0.79 cm of scintillator and is read out with a single phototube at each end of the module. For normal incidence, the total number of radiation lengths in the system is $11X_0$.

The time-of-flight measurement for minimum-ionizing particles has a RMS error of 360 psec. The error for electrons is 160 psec which is a measure of the stability of the system. The energy resolution for showering particles was measured in a test beam to be $\sigma_E/E = 0.16\sqrt{E}$ (E in GeV) for energies less than 5 GeV. As the energy increases beyond 5 GeV, a significant fraction of the shower leaks out the back of the counter, the resolution is degraded and levels off at about $\sigma_E/E = 7\%$. Monte Carlo simulations indicate that 30% of the energy in a 14.5 GeV shower is lost because of leakage. Figure 4a shows the energy distribution of minimum-ionizing particles. The peak for minimum-ionizing particles is at 200 MeV. Figure 4b shows the measured energy distribution of 14.5 GeV Bhabha-scattering positrons and electrons. The distribution has a full width at half maximum of 3.5 GeV because tracks hitting near cracks and edges have not been excluded.

The end-cap shower counters provide electromagnetic calorimetry and time-of-flight information over 27% of the solid angle. The end caps cover the ends

of the solenoid at a distance of +1.48 and −1.65 m from the mid-plane of the detector. The system contains 40 pie-shaped modules, each of which uses a wave shifter to transmit scintillation light through a light pipe to a single photomultiplier tube. The modules are $8.7X_0$ thick, consisting of eight layers of lead and scintillator. A single $1.7X_0$ thick sheet of lead makes up the first layer of the counters, followed immediately by a single layer of proportional wire chambers, which have characteristics identical to those in the barrel shower-counter system. The energy resolution for showers with E < 5 GeV is $\sigma_E/E = 0.20/\sqrt{E}$. The energy distributions for minimum-ionizing particles and Bhabha-scattered electrons and positrons are shown in Figs. 5a and 5b.

The recorded events were required to satisfy at least one of several triggers. A primary trigger resulted from hits in at least 12 of the 15 layers of the inner drift chamber, or at least four of the innermost eight layers in addition to a hit in the end caps. A secondary trigger required that the curvature processor identify two tracks with momenta greater than 3 GeV/c and be in time with the beam crossing. Small angle tracks had to be accompanied by a hit in the end cap. The high efficiency (>99%) of the central drift chamber guarantees a uniform acceptance by the charged trigger for events in which both tracks exit the chamber beyond the seventh drift-chamber layer ($|\cos\theta| < 0.92$).

Cracks in the shower counter time-of-flight system reduce the efficiency in well-defined regions. Triggers having only two found tracks required at least one barrel counter to be in time with the beam crossing to within 20 nsec. Two neutral triggers were also used. The first required that more than 4.8 GeV be deposited in the shower counters. The threshold for the second neutral trigger was set at 2.4 GeV, but at least one charged track was required in addition.

Subsequent to the first year of operation, two additions were made to the HRS hardware. A 704 cell Cerenkov counter system covering the angular range $|\cos\theta| < 0.55$ was installed in the summer of 1982 and became operational halfway through the FY1983 running period. The counters have been logging

data since that time with the pion and kaon thresholds set at 1.5 GeV/c and 6 GeV/c respectively. The average efficiency for the operating channels is 72% which is too low for these threshold counters to be used for positive identification of kaons. The signals are useful in providing a modest veto capability against pions. At the time that the 11 Cerenkov torii were installed both end cap shower counters were positioned at ± 1.48 m from the median plane hence minimizing the gap between the barrel and end cap shower systems. Only an annulus of $\sim 2°$ is not covered by any shower detection.

The multiple scattering in the material of the Cerenkov counter degrades the momentum resolution for charged tracks by about a factor or two over that shown in Fig. 2.

A four layer vertex chamber with 330 cells, shown in Fig. 6 was added in the summer of 1983 and all data logged subsequent to that time has improved vertex information. The vertex chamber provides a useful veto against cosmic rays. We are now operating with a primary trigger rate of $\sim$ 70 Hz of which 1.3 Hz is written out on magnetic tape. The latter is a factor of three lower than was typical for the first year of operation. The point reconstruction accuracy in the vertex chamber is $\sigma = 110\mu$ in the x, y plane; no z measurement is provided. Extrapolations of Bhabha scattered electrons to the vertex show that the vertex reconstruction accuracy for 14.5 GeV/c tracks is 170μ A typical event is shown in Fig. 7 at two different magnifications.

Including the vertex chamber and a layer of titanium added inside the 0.05 mm PEP vacuum pipe, the total radiation thickness up to the first layer of the main tracker is $0.015X_0$.

The HRS has no muon identification system.

Table I gives the integrated luminosity numbers for the four years of HRS operation. These numbers correspond to processed data available for physics analysis.

Table I HRS Luminosity Log	
Fiscal Year	Integrated Luminosity
	pb^{-1}
1982	20
1983	90
1984	74
1985 (to date)	50
Total	234 pb^{-1}

VIII.3 The Capability of the Detector as Exemplified in the Physics Program

(a) Studies of the electroweak interactions of leptons and quarks

We have reported results[1,2,3] on the reactions $e^+e^- \to \mu^+\mu^-$ and $e^+e^- \to \tau^+\tau^-$: we are currently carrying out a detailed study of Bhabha scattering $e^+e^- \to e^+e^-$ and the reaction $e^+e^- \to \gamma\gamma$.

The angular distributions for about 5000 events of each of the $\mu^+\mu^-$ and $\tau^+\tau^-$ final state are shown in Fig. 8. Since there is no muon identification, the e^+e^- and $\mu^+\mu^-$ final states are separated by pulse height in the shower counters as seen in Fig. 9. This means that regions not so instrumented cannot be used and so the overall detection efficiency is about two thirds of that of the full solid angle MAC detector.

The HRS current results on lepton pair production which are summarized in Table II may be compared to the expectation from the standard model of $A_{\ell\ell} = -5.9\%$ and $R_{\ell\ell} = 1.00$. Our data give $g_a^\ell = 0.22 \pm 0.05 \pm 0.03$ assuming e,μ,τ universality.

The high momentum precision allows us to see effects that are masked in other detectors. For example, Fig. 10 shows the momentum spectrum of Bhabha

Table II Results on Lepton Pair Production				
Final State	Number of Events	$\int L\mathrm{dt}$ pb^{-1}	$A_{\ell\ell}$	$R_{\ell\ell}$
$\mu^+\mu^-$	5057	106	$-(4.9 \pm 1.5 \pm 0.5)\%$	$0.99 \pm 0.017 \pm 0.03$
$\tau^+\tau^-$	5300	184	$-(5.2 \pm 1.7 \pm 0.5)\%$	$1.09 \pm 0.02 \pm 0.04$
	Standard Model		-5.9%	1.00

scattered electrons compared to the α^3 QED prediction of Berends and Kleiss.[4] It is clear that an α^4 calculation is needed. This difference can effect the measurement of the luminosity for detectors with lower momentum precision since a momentum cut is applied to select the events.

The production asymmetry of the reaction $e^+e^- \rightarrow c\bar{c}$ has also been measured. This can be done through the observation of the $D^{*+} \rightarrow D^\circ\pi^+$ decay chain.[5] The low Q value in the $D^{*\circ} \rightarrow D^\circ$ decay provides a strong constraint and the events can be isolated with essentially no background, as seen in Fig. 11. The HRS can also measure and isolate the $D^\circ \rightarrow K^-\pi^+$ and $D^+ \rightarrow K^-\pi^+\pi^+$ decays themselves[6] without the need for a $D^* - D^\circ$ transition as shown in Fig. 12.

An analysis of all such data gives $A^{cc} = -(12 \pm 8)\%$ based on 110 pb^{-1} as compared to the expected value of -9.5%. Although twice as many events have now been collected, higher detection efficiency for the $c\bar{c}$ final state is needed to make a decisive measurement of the electroweak couplings of the charm quark. We are studying various possibilities of doing this.

We are currently working on isolating a sample of b quark events, where the asymmetry is expected to be twice as large.

With sufficient data it should also be possible to tag the $s\bar{s}$ final state using $K^{*\circ}$ mesons and/or Λ hyperons. For example Fig. 13 shows the predicted asymmetry, using the Lund model, for Λ production as a function of the z cut. The HRS data with 184 pb^{-1}, also shown, does not yet have sufficient statistical precision to experimentally establish this effect.

The second area of weak interaction studies is provided by τ lepton decay measurements. The topological branching ratios of τ decay to one, three and five particles have been measured.[7] Since all four topologies 1-1, 1-3, 3-3 and 1-5 were measured, and B_5 is very small, the branching ratios B_1 and B_3 are overconstrained and only weakly dependent on the integrated luminosity.

Our value of $B_3 = 0.130 \pm 0.003 \pm 0.003$ is compared to other published results in Table III. A recent MAC value of $B_3 = 0.133 \pm 0.003 \pm 0.006$ is in good agreement with the HRS result. The good track separation provided by the large magnetic bending in the HRS leads to a smaller systematic error than is the case for MAC.

Table III Measured Values for B_3

Detector	B_3
HRS	$0.130 \pm 0.003 \pm 0.003$
Mark II	$0.14 \pm 0.02 \pm 0.01$
TPC	$0.148 \pm 0.009 \pm 0.015$
CELLO	$0.147 \pm 0.015 \pm 0.013$
TASSO	$0.153 \pm 0.011 \pm ^{+0.016}_{-0.013}$

The resulting value of $B_1 = 0.869 \pm 0.003 \pm 0.003$ is larger than the sum of the individually measured one prong modes by $\sim 9\%$. A systematic program of re-measuring these modes, in particular the leptonic decays $\tau \rightarrow e, \mu\nu\bar{\nu}$ is needed in order to see if there is new physics in τ decays or merely inadequate experimentation.

The first observation of the τ decay to five charged particles was made in the HRS.[8] The value of $B_5 = (1.3 \pm 0.4)\ 10^{-3}$ is consistent with the theoretical expectations. An example of such a decay is shown in Fig. 14. Of the 10 events observed, five have associated electromagnetic radiation and so are presumably

examples of the decay $\tau^{\pm} \rightarrow 5\pi^{\pm}\pi^{\circ}\nu_{\tau}$ and five are $\tau^{\pm} \rightarrow 5\pi^{\pm}\nu_{\tau}$ decays. These events allow an improved upper limit to be placed on the mass of the tau neutrino.

The HRS vertex chamber gives us the capability to make lifetime measurements. We have preliminary results on the lifetime of the τ lepton and on the D° meson observed via the $D^{*} - D^{\circ}$ decay chain with no background. Figure 15 shows the proper time distribution of 37 such events with the D° decaying to $K^{-}\pi^{+}$. The combination of good mass resolution, the vertex chamber and high statistics means that we can also measure the D^{+} and F^{+} mesons in addition to the D°. We expect also to measure the B meson lifetime via the decay $B^{\circ} \rightarrow D^{*+}$ which gives a D^{*} at low z. Figure 16 shows the measured z distribution of the D^{*} together with the prediction of the B decay component. It is possible that a similar technique can be used to look at the B_s meson via the decay to F^{+}.

All of these fundamental measurements are dominated by statistics: an order of magnitude more data is needed, and could be utilized, before the systematics would limit the result.

(b) Studies of the strong interactions of the quarks

The situation with the strong interaction is quite different from the electroweak interaction. Although we have a general and successful framework provided by QCD, quantitative confrontation between theory and experiment has yet to fully develop. The subject has three themes: the first (the stamp collecting phase) is the establishment of a data base; the second is the comparison of results with fragmentation models both to improve their representation of the data and to probe the mechanisms underlying the parton-hadron transition; the third phase is the quantitative comparison with QCD. Questions such as the measurement of α_s and its Q^2 dependence and a quantitative comparison of the ggg and $q\bar{q}g$ vertices can be addressed.

The current work mostly focuses on the first two aspects of the subject since these are essential preliminaries to a quantitative understanding. Such data also

provides essential input to understanding jets at the high energy hadron colliders and so is a foundation for SSC physics[9].

In the HRS program we first measured the global properties of jets,[10] giving things like sphericity, thrust and transverse momentum distributions and comparing with other data from e^+e^- annihilation, neutrino interactions and hadronic collisions. For example, Fig. 17 shows the HRS sphericity distribution compared to TASSO measurements and ISR beam jets. The behavior of the fragmentation function at low z shown in Fig. 18 is sensitive to the question of coherent gluon bremsstrahlung. To resolve this question, the data must be extended to identify heavier stable particles and resonances.

The HRS data[11] on $\pi^{\pm}$, $K^{\pm}$ and p cross sections, identified by time-of-flight, are given in Fig. 19. We cover only limited range of momenta with this technique. For the K° and Λ particles however the full momentum range is accessible although with lower efficiency.[11] Figure 20 shows the peaks observed in the $\Lambda \rightarrow p\pi^-$ and $K^{\circ}_s \rightarrow \pi^+\pi^-$ decays. The fragmentation functions are given in Fig. 21.

The charged particle multiplicity distribution of Fig. 22 is another global variable that probes the fragmentation models.[12] The absence of forward: backward multiplicity correlations in the two jets that characterize the vast majority of events, is in marked contrast to hadron physics, but is trivial result of the fragmentation models.

The unique HRS measurement[13] of the shape of the single particle fragmentation function near z=1 is a discriminator against cluster models and in favor of the Lund string ideas. The cluster models fall for below the data at high z whereas the $(1-z)^2$ power low dependence seen in Fig. 23 agrees well with the Lund model prediction.

Baryon production provides additional constraints on the models. The mechanism of baryon production is not well understood and there are some differences between our high statistics data and the Lund predictions.[14]

These studies must be extended to resonance production. We have made precise measurements of the ϕ production[15] as shown in Fig. 24. In analyzing this data we used the TOF system and the Cerenkov counters to veto pions. It is clear that good momentum resolution results in small errors on the cross section.

To measure ρ° and $K^{*\circ}$ production we have made the subtracted (charge zero less charge two) $\pi\pi$ and $K\pi$ mass distributions[16] shown in Fig. 25. Fitting these spectra to a background plus decays of the known resonances gives the ρ° and $K^{*\circ}$ fragmentation functions. Combining these data with our K° measurements[11] and the Cello π° cross sections enables us to measure the vector(v) to pseudo scalar(p) ratio for the strange and non-strange quarks as well as the SU(3) suppression of the strange sea — the s/u ratio. The results are given in Table IV and compared to other measurements. There is some evidence for tensor meson production $f^\circ(1270)$ and $K^*(1400)$ in the mass plots of Fig. 25. The Lund model currently ignore such a possibility.

Table IV Measurements of Lund Model Parameters

Parameter	JADE	TPC	TASSO[a]	HRS
s/u	0.27±0.03±0.05	0.25±0.02		0.34±0.03
$\frac{v}{v+p}(u,d)$	0.51±0.10±0.15		0.58±0.08±0.15	0.54±0.06
$\frac{v}{v+p}(s)$	0.70±0.15±0.11	0.47± 0.11±0.09		0.66±0.08
$\frac{v}{v+p}(c)$				$1.0^{+0.2}_{-0.3}$

[a] Assuming the Field-Feynman model

Such measurements will provide additional tests of the cluster versus string ideas since the suppression of heavy particles occurs in the cluster models as a result of phase space. Comparison of heavy mesons and baryon (plus baryon resonance) production is a powerful discriminator.

These studies are being extended to separated samples of light quark (u,d,s) strange quark and bottom quark annihilations. Data samples of $\sim$ 500 events

of each quark flavor have been obtained. We have already compare the global properties of c quark and light quark events and find some differences.[17]

The second extension is to three jets —events that include a hard gluon jet. Figure 26 shows the energy flow of a three jet sample. The mean charged particle multiplicity as a function of event sphericity, shown in Fig. 27 indicates a slow rise above S = 0.5 as the three jet fraction increases. So far, even the qualitative expectation that a gluon jet multiplicity should be 9/4 of that of a quark jet as a result of the gluon color charge, has not been seen; nor has the expected softer fragmentation function of gluon jets.

In heavy quark studies the unique capability of the HRS to isolate direct D° D^+ and F^+ production is well known.[3,15] Figure 28 shows the $F \rightarrow \phi\pi$ mass peaks, and Fig. 29 the F fragmentation function. A detailed comparison of the shape of the heavy quark z distribution at several energies could measure α_s with minimal uncertainties from non-perturbative effects.

(c) Search for new phenomena

Although the standard model is a remarkable result of decades of work in particle physics, it is clearly an incomplete representation of the world. Despite the many suggestions that are extant about the missing links within the standard model as well as extensions beyond it, no hard experimental evidence exists.

We have reported three negative results of specific searches for new particles. An early search[1] for the SUSY scalar electron via the reaction

$$e^+e^- \rightarrow \tilde{e}^+\tilde{e}^- \rightarrow \tilde{\gamma}e^+\tilde{\gamma}e^-$$

found one candidate event and so placed limits on the mass of the $\tilde{e}$ between 1.8 GeV and 14.2 GeV as seen in Fig. 30 The experiment consisted of searching for acoplanar e^+e^- pairs with no converted photons: the background comes from radiative Bhabha scattering. This technique, which was also used by other groups, is limited to masses less than or equal to the beam energy. The HRS

cannot search for single $\tilde{e}$ production because of the non-instrumented regions near the beam pipe.

The second search was for heavy neutral leptons.[18] Although the charged leptons and quarks of a possible fourth generation are known to be beyond PEP energies this is probably not the case for the associated neutrino. The reaction $e^+e^- \rightarrow Z \rightarrow \nu\bar{\nu}$ will then occur with a rate given by:

$$\sigma = \frac{G_F M_z \Gamma}{\sqrt{2}(m_z^2 - s)^2}(1 - 4\sin^2\theta_\omega + 8\sin^4\theta_\omega)B = 6B \text{ pb}$$

where B is the branching ratio of $Z \rightarrow \nu\bar{\nu}$, expected to be 6% per generation.

The experiment consisted in looking for isolated $e^\pm X^\pm$ pairs which could result from the decay of a neutral lepton $L^\circ \rightarrow e^\pm X^\mp \nu$ where X is any minimum ionizing particle such as a pion or muon. Six candidates events were found, a rate consistent with known backgrounds and corresponding to σB limits at 90% C.L. varying from 0.08 pb to 0.2 pb for L° masses from 1 to 7 GeV. This experiment was based on 106 pb^{-1} of data.

The third search experiment consisted in looking for prompt monojets.[19] Monojets are defined as a cluster (jet) of particles populating a single hemisphere with no balancing p_T. One such event was found which is shown in Fig. 31. The main background comes from $e^+e^- \rightarrow \gamma q\bar{q}$: annihilation following a catastrophic brem. of one of the initial electrons. About 160 such monojet events with a balancing hard photon were found. The small cracks between the barrel shower counter modules leads to an inefficiency of ~1.5% and so an expected background of 3.3 ± 1.5 events.

The observed candidate, if considered real, leads to the upper limit at 90% confidence for the reaction

$$e^+e^- \rightarrow Z \rightarrow X_1X_2$$

where X_2 decays to give the monojet and X_1 is unseen, shown in Fig. 32. On SUSY models X_1 would be a photino. Independently of any model, the HRS

result of Fig. 32 eliminates the possibility that the monojet events seen in the UA1 detector at CERN[20] are coming from anomolous Z decays for X_2 masses between 2 and 9 GeV.

A specific calculation of a SUSY model in which X_1 is a photino and X_2 a linear combination $\lambda^2\tilde{Z} + (1-\lambda^2)\hat{H}^\circ$ produced by scalar electron exchange, as shown in Fig. 33, gives the limits on the scalar electron mass shown in Fig. 34. For reasonable values of $\lambda^2 B$ ($X_2 \rightarrow q\bar{q}\tilde{\gamma}$), $\tilde{e}$ mass limits ranging from 40 to 70 GeV are obtained.

The final topic of new physics concerns the mass limits of the τ neutrino. Tau lepton decays to 5 $\pi^\pm\nu_\tau$ in the HRS have typical effective mass errors of 15 MeV and occur with high mass for the hadron system. The observation of one or two events with $M(5\pi^\pm)$ near the tau mass of 1784 MeV would than limit the mass of the tau neutrino to similar values. The events of the final state $5\pi^\pm\pi^\circ$ have a spread of errors, depending on the π° energy varying from 15 to 60 MeV.

A limit on the tau neutrino mass below the muon mass would eliminate the decay $\nu_\tau \rightarrow \mu^- e^+ \nu_e$. Fits to the spectra of Fig. 35 using different models give a 95% C.L. upper limit to ν_τ of 89 MeV. It is likely that this limit can be substantially improved with data already taken but not yet analyzed. This result, when combined with arguments based on astro-physics, then limits all neutrino masses to < 1 MeV.

A mass limit of the tau neutrino in the 10 to 20 MeV range would be extremely interesting, independently of the considerations from astro-physics. Since, on left-right symmetric models, the natural scaling of neutrino masses goes as m_ν/m_ℓ^2 a 10 MeV limit for the tau neutrino corresponds to less than 1 eV for the electron neutrino.

We are currently searching for the decay of a heavy neutrino from the fourth generation by looking for jets with a separated vertex. A search region from a few mm to ~50 cm is being used. According to the astrophysical abundance of helium and deuterium such massive neutrinos (in the mass range 1 to 10 GeV)

must decay and be in an accessible lifetime range at PEP.

VIII.4 Detector Upgrades

Because the HRS was a second round detector approved after the first complement of PEP detectors (MARK II, TPC and 2γ and MAC) the available equipment funds were limited and so a number of compromises were made in the complement of detection elements. If the program is to continue in the second, minibeta phase of PEP operations some detector improvements are called for.

After more than five years of operation of both PEP and PETRA, we now know in detail the features of the physics in this energy range. The detector updgrades can equip the HRS to match the new physics that a substantial increase in luminosity will make available. The large open magnet allows a range of options to be implemented. The improve detector can be different from, but equal to the TPC in overall capability. The exact choice of new elements will rest with the new collaboration that will be needed to continue the program.

VIII.5 Summary of Event Rates

Since the results presented in this paper came from data samples with varying integrated luminosities, a summary of the event numbers that will be collected by the HRS in the present phase and in a future high luminosity operation are given in Table V.

Table V Event Numbers				
Final State	Published Results		Data Expected	Luminosity PEP
	$\int \mathcal{L}dt$	# events	Through 1986	1000 pb^{-1}
			300 pb^{-1}	
$\mu^+\mu^-$	106	5057	14300	47700
$\tau^+\tau^-$	184	5300	8640	28800
$\gamma\gamma$	18	1604	26700	89000
e^+e^-	18	9722	162000	40000
Inclusive hadrons	20	6342	94800	316000
$b\bar{b}(s\bar{s})$			8820	28700
$c\bar{c}$			34500	115000
$K_s^\circ \rightarrow \pi^+\pi^-$	184	3750	6000	20000
$\Lambda \rightarrow p\pi^-$	184	1800	2900	9800
$D^{*+} \rightarrow D^\circ\pi^+$	110	182	500	1670
$D^\circ \rightarrow K^-\pi^+$	110	144	390	1300
$D^+ \rightarrow K^-\pi^+\pi^+$	110	123	339	1090
$F^\pm \rightarrow \phi\pi^\pm$	184	120	196	650
$\phi \rightarrow K^+K^-$	184	1000	1630	5400
$\rho \rightarrow \pi^+\pi^-$	184	~25000	41000	136000
$K^{*\circ} \rightarrow K^+\pi^-$	184	~12000	20000	65000
3 jet events	184	1500	2500	8000
Identified light				
quark	110	265	723	2400
Identified charm				
quark	110	111	300	1000

REFERENCES

1. D. Bender *et al., Phys. Rev.*, D30, 515 (1984).
2. M. Derrick *et al., Phys. Rev.*, D31, (1985).
3. K.K. Gan *et al., Phys. Lett.*, 153B, 116 (1985).
4. F.A. Berends and R. Kleiss, *Nucl. Phys.*, B177, 237 (1981), F.A. Berends, R. Kleiss and S. Jadach, *ibid,* B202, 63 (1983).
5. M. Derrick *et al., Phys. Lett.* 146B, 261 (1984).
6. S. Ahlen *et al., Phys. Rev. Lett.*, 51, 1147 (1983). M. Derrick *et al., Ibid,* 53, 1971 (1984).
7. M. Derrick *et al., Phys. Rev. Lett.*, (Submitted).
8. I. Beltrami *et al., Phys. Rev. Lett.* (Accepted).
9. M. Derrick and T. Gottschalk, Proceedings of 1984 Snowmass Study of SSC Physics.
10. D. Bender *et al., Phys. Rev.*, D31, 1 (1985).
11. M. Derrick *et al., Phys. Rev. D.* (to be submitted).
12. M. Valdata-Nappi Proceedings XIV Symposium on Multiparticle Dynamics, Lake Tahoe (1984)
13. M. Derrick *et al.,* Paper submitted to Leipzig Conference.
14. P. Baringer, Ph.D. Thesis Indiana University (1985).
15. M. Derrick *et al., Phys. Rev. Lett.* (Submitted).
16. M. Derrick *et al., Phys. Lett.* (to be submitted).
17. M. Derrick, Proceedings of XV Symposium on Multiparticle Dynamics Lund (1985).
18. D. Errede *et al., Phys. Lett.*, 51, 519 (1984).
19. C. Akerlof *et al., Phys. Lett.*, (Accepted).
20. G. Arnison *et al., Phys. Lett.*, 139B, 115 (1984).

FIGURE CAPTIONS

1. The High Resolution Spectrometer.
2. Calculated momentum resolution.
3. The observed momentum distribution of fully constrained Bhabha-scattering events.
4. The observed energy distribution in the barrel shower-counter system for (a) minimum-ionizing tracks and (b) Bhabha-scattered tracks.
5. The observed energy distribution in the end-cap shower-counter system (a) minimum-ionizing tracks. (b) Bhabha-scattered tracks.
6. HRS vertex chamber.
7. D^* event in the main tracker and in the vertex chamber.
8. Production angular distribution for the $\mu^+\mu^-$and $\tau^+\tau^-$ final states.
9. Energy distribution of single tracks as measured in the barrel shower counter.
10. Momentum distribution of Bhabha scattered electrons.
11. The quantity δ, (a) for $D^\circ \rightarrow K^-\pi^+$ with $1.81 \leq M_{K\pi} \leq 1.92$ GeV and $Z \geq 0.4$, (b) for $D^\circ \rightarrow K^-\pi^+\pi^+\pi^-$ with $1.18 \leq M_{K3\pi} \leq 1.92$ GeV and $Z \geq 0.6$, (c) for $D^\circ \rightarrow K^-\pi^+\pi^\circ$ with $1.55 \leq M_{K\pi} \leq 1.70$ GeV and $Z \geq 0.6$, (d) for $D^\circ \rightarrow K^-\pi^+$ with $1.81 \leq M_{K\pi} \leq 1.92$ GeV and $0.2 \leq Z \leq 0.4$ and $|\cos\theta^*_\pi| \leq 0.8$.
12. (a) Invariant $K\pi$ mass distribution for $z_D \geq 0.5$ and $|\cos\theta^*| < 0.7$. (b) Invariant $K_{\pi\pi}$ mass distribution for $z_D \geq 0.5$ and $|\cos\theta^*| > 0.3$.
13. Forward:backward asymmetry of Λ° production compared to predictions of Lund model.
14. Five prong tau decay.
15. Proper time distribution for D° decays.

16. A comparison of HRS D* Fragmentation data with the Webber Monte Carlo (solid line) and the 10 GeV Peterson, et al. form with ϵ of 0.19.

17. (a) Sphericity distribution compared to the TASSO measurements. (b) Comparison of HRS sphericity distribution with that of the ACDHW collaboration.

18. Fragmentation function shown as $(1/N_{ev})\ zdN^h/dz$ for e^+e^- annihilation at 29 GeV to illustrate the behavior of the cross section at low z.

19. Invariant cross sections for stable particle production.

20. Effective mass distributions showing $K^\circ_s \rightarrow \pi^+\pi^-$ and $\Lambda^\circ \rightarrow p\pi^-$ peaks.

21. Invariant cross sections for Λ° and K° production.

22. Charged particle multiplicity distribution and forward:backward multiplicity correlations.

23. Charged particle and π° invarient distributions compared to $(1-z)^2$ and $(1-z)^3$ variations. The π° data are displaced dowards for clarity.

24. ϕ meson fragmentation function.

25. Subtracted two body effective mass spectra together with the best fit histogram.

    (a) $\pi^\pm\pi^\mp,\ x > 0.05$ (b) $K^\pm\pi^\mp,\ x > 0.05$
    (c) $\pi^\pm\pi^\mp,\ x > 0.45$ (d) $K^\pm\pi^\mp,\ x > 0.45$

    The inserts in (a) and (b) show the ρ° and $K^{*\circ}$ components.

26. Energy flow in selected three jet events.

27. Mean charged multiplicity as a function of event sphericity.

28. The $\phi\pi$ invariant mass spectrum for events with (a) $0.2 < z(\phi\pi) < 0.4$ and (b) $z(\phi\pi) > 0.4$. The lower histograms are selected in particular ranges of the decay angles to emphasize the 0^- component.

29. The F fragmentation function. The solid curve is the Peterson form fit to our D^* fragmentation for $z(D^*) > 0.4$. The dashed curve is the sum of the solid curve and the estimated contribution from the B decay.

30. (a) Scalar electron event candidate. (b) Scalar electron mass limits.

31. Monojet candidate.

32. Detection efficiencies, expected cross sections, and 90% C.L. cross section limits for prompt, hadronic monojets from the production and decay of scalar particles.

33. SUSY production.

34. Limits on the mass of the scalar electron from the process $e^+e^- \rightarrow X_1X_2$ as a function the mass of the neutral fermion X_2 and the parameter λ^2 $BR(X_2 \rightarrow q\bar{q}\tilde{\gamma})$.

35. Five and six pion effective mass distributions from tau decay.

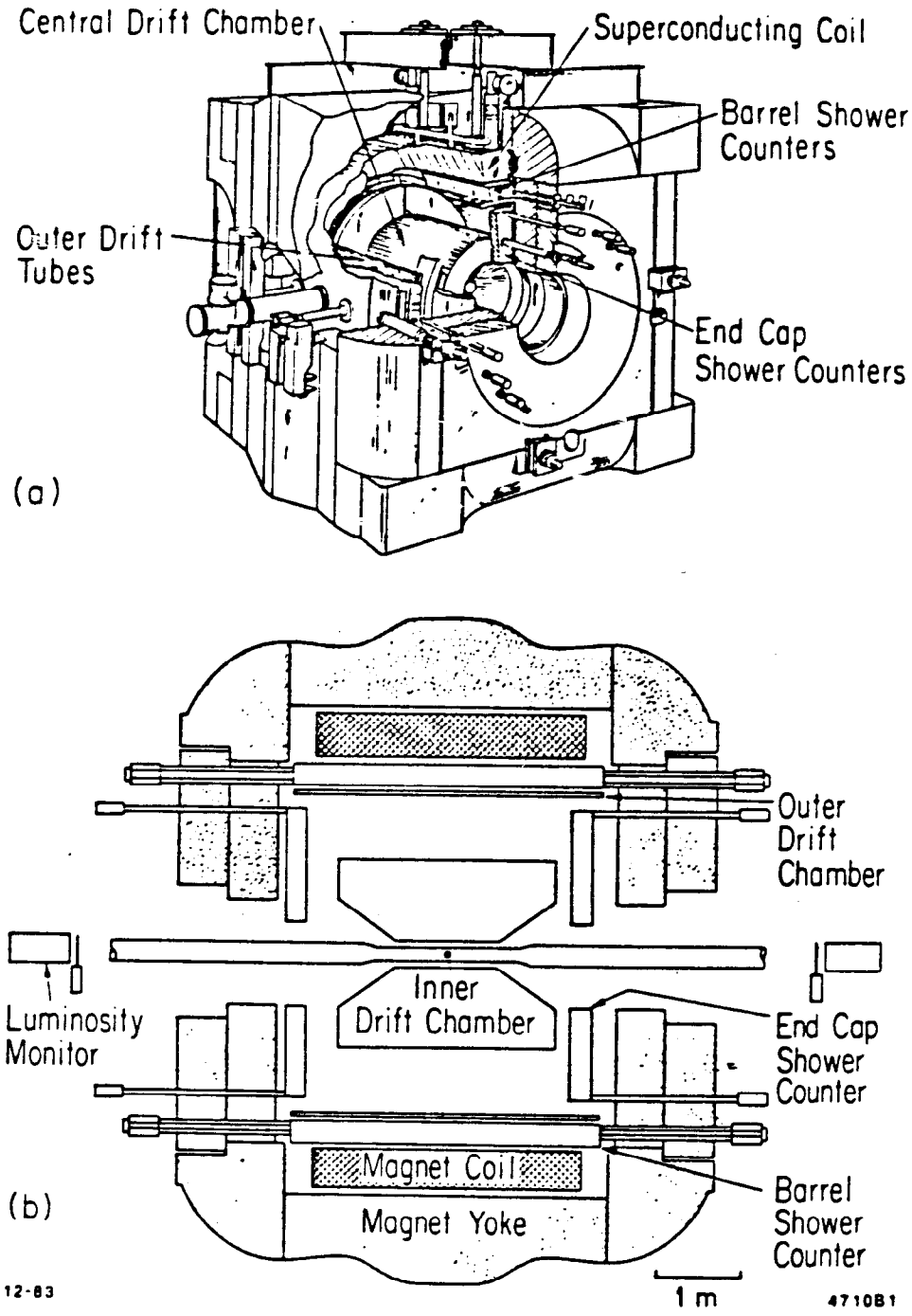
Central Drift Chamber
Superconducting Coil
Barrel Shower Counters
Outer Drift Tubes
End Cap Shower Counters
(a)
Outer Drift Chamber
Inner Drift Chamber
Luminosity Monitor
End Cap Shower Counter
Magnet Coil
Magnet Yoke
Barrel Shower Counter
(b)
1 m
12-83
4710B1

Fig. 1

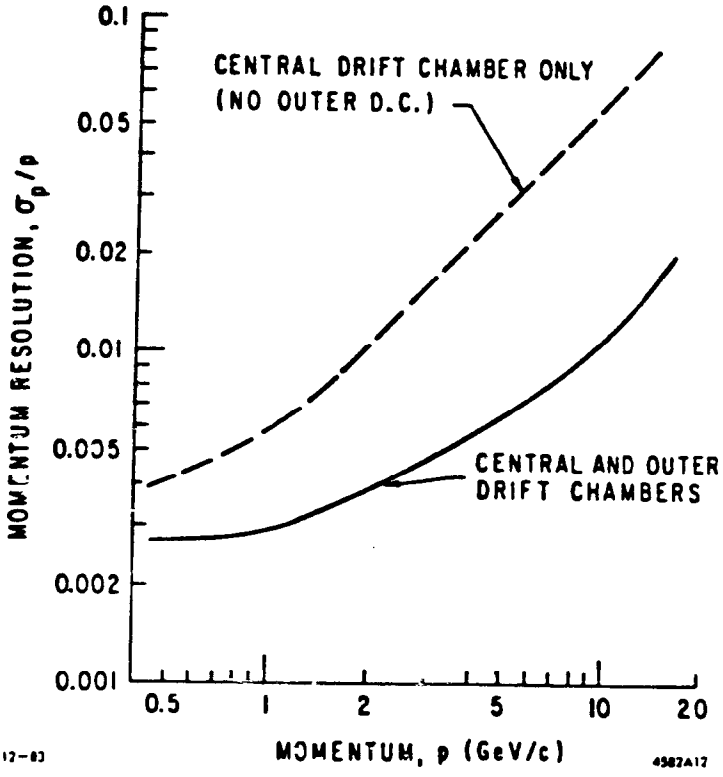

Fig. 2

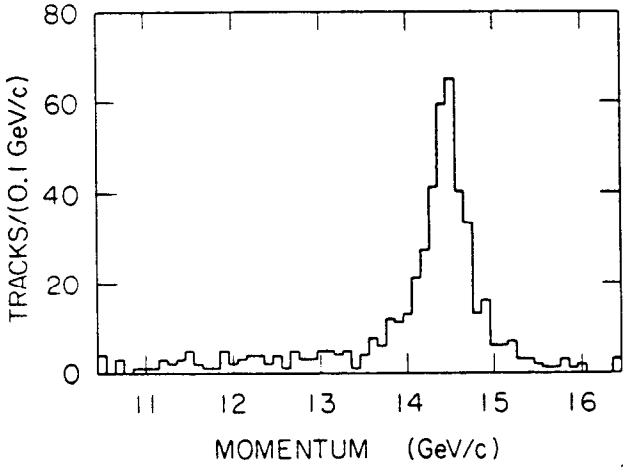

Fig. 3

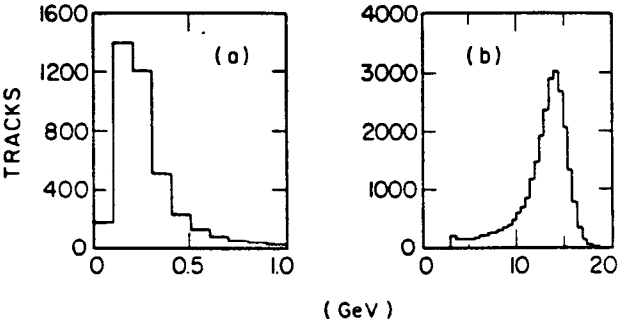

Fig. 4

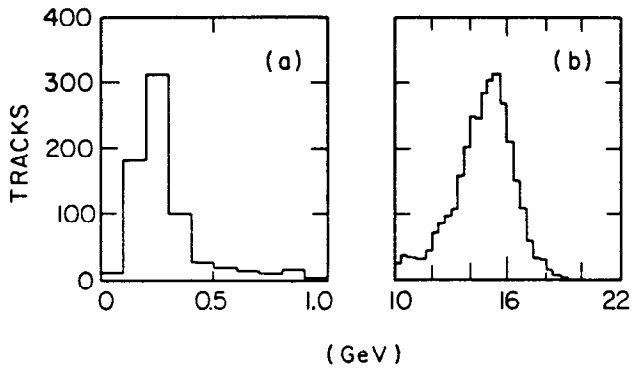

Fig. 5

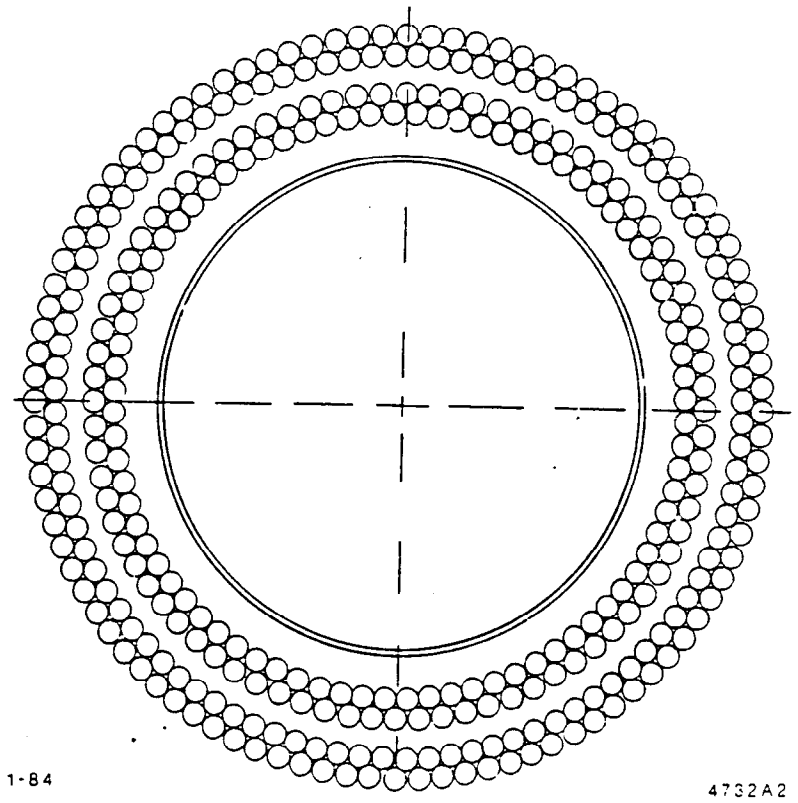

Fig. 6

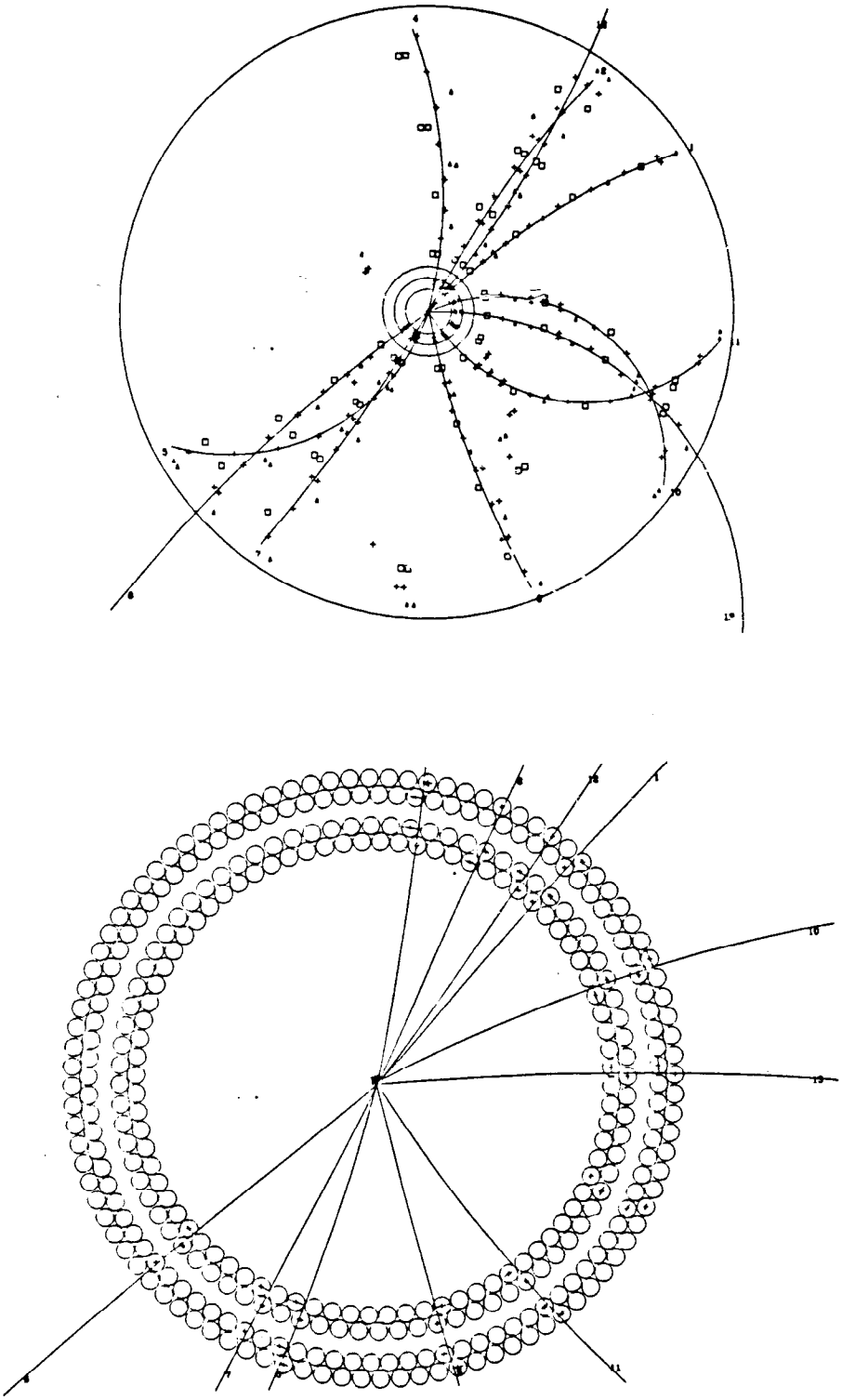

Fig. 7

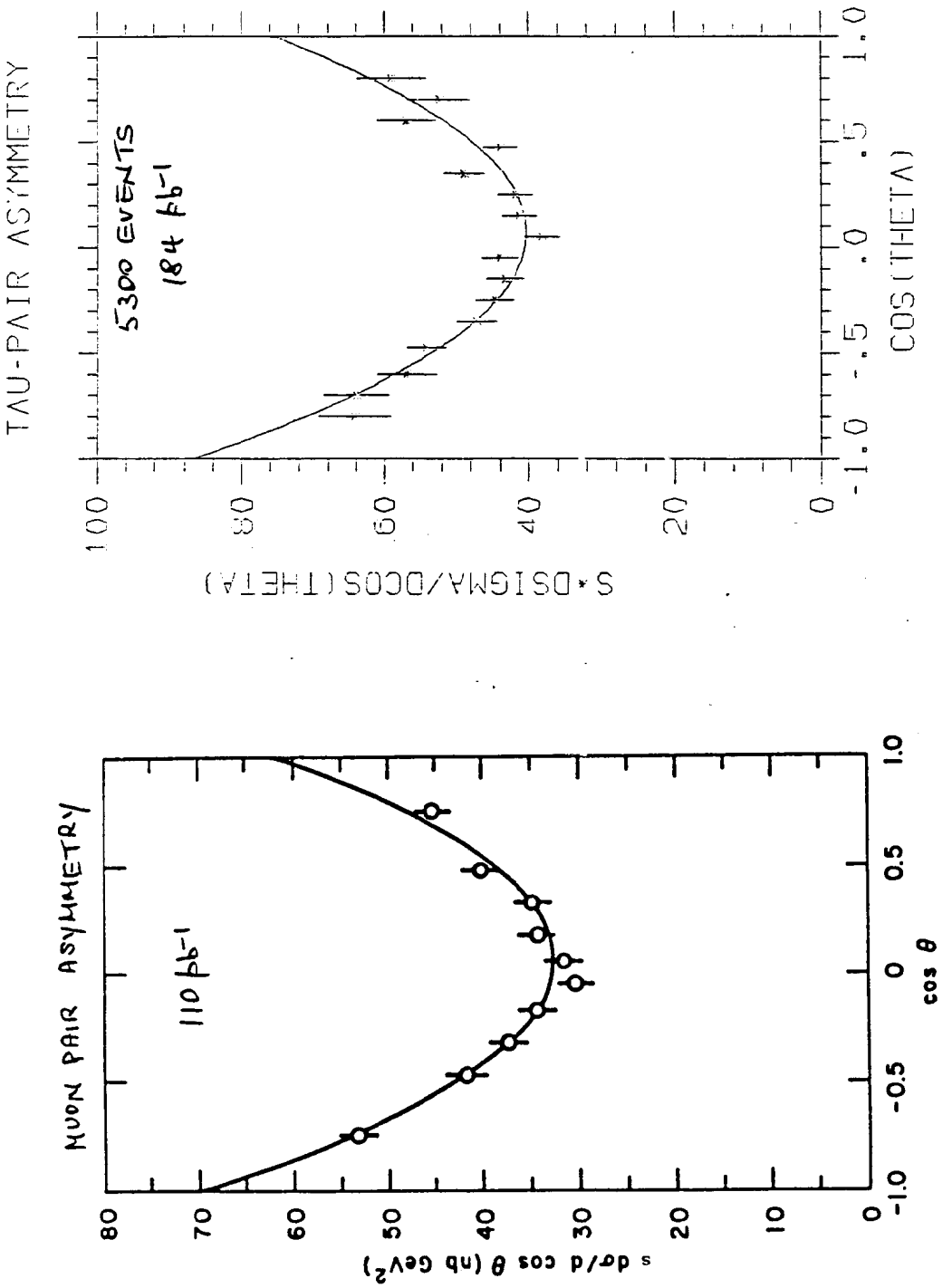
TAU-PAIR ASYMMETRY
5300 EVENTS
184 pb-1
S*DSIGMA/DCOS(THETA)
COS(THETA)
MUON PAIR ASYMMETRY
110 pb-1
s dσ/d cos θ (nb GeV²)
cos θ

Fig. 8

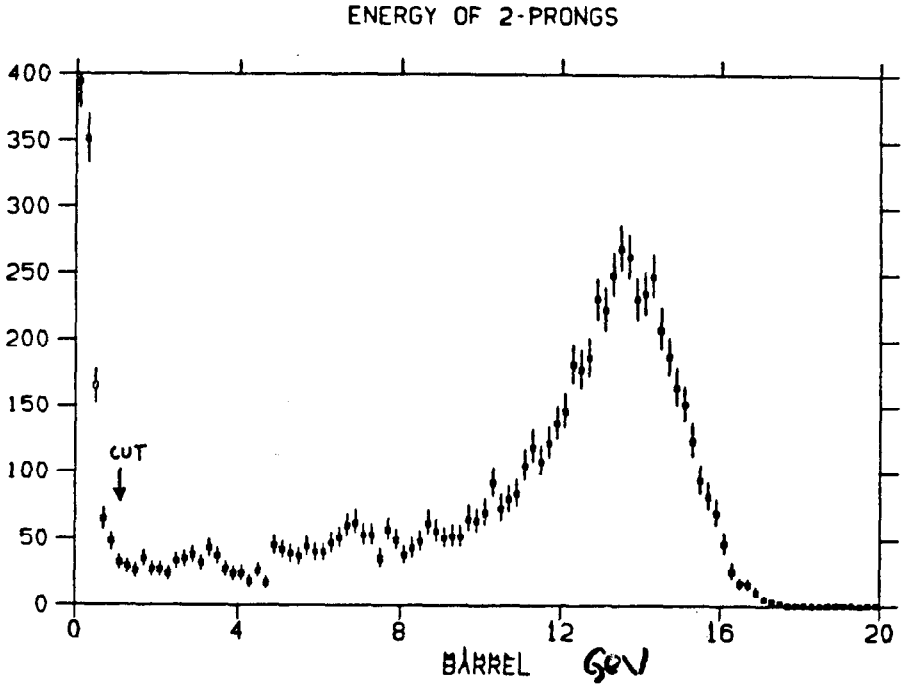
ENERGY OF 2-PRONGS
400
350
300
250
200
150
100
50
0
CUT
0
4
8
12
16
20
BARREL
GeV

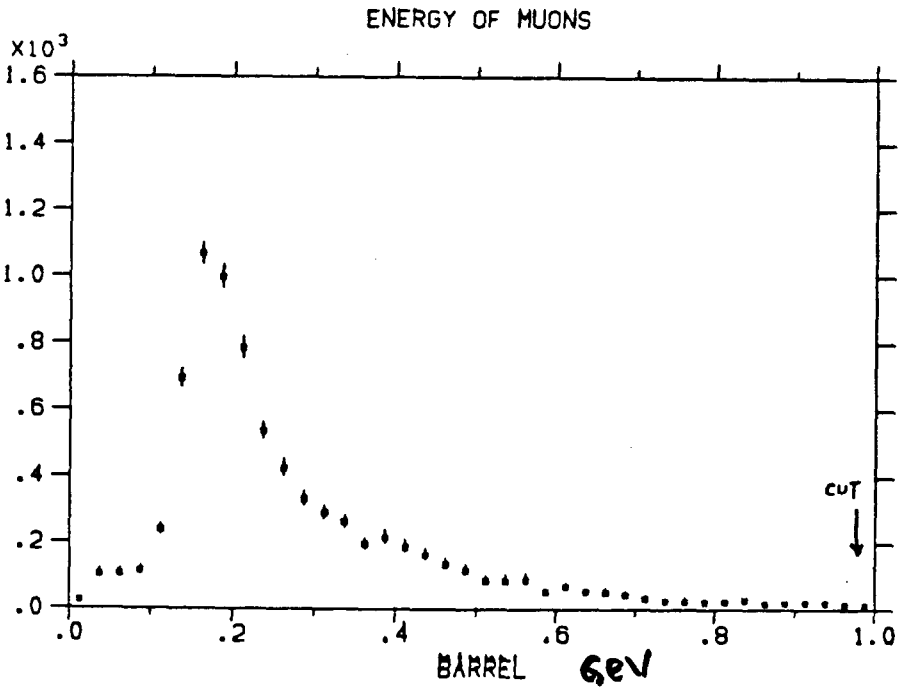
ENERGY OF MUONS
X10³
1.6
1.4
1.2
1.0
.8
.6
.4
.2
.0
CUT
.0
.2
.4
.6
.8
1.0
BARREL
GeV

Fig. 9

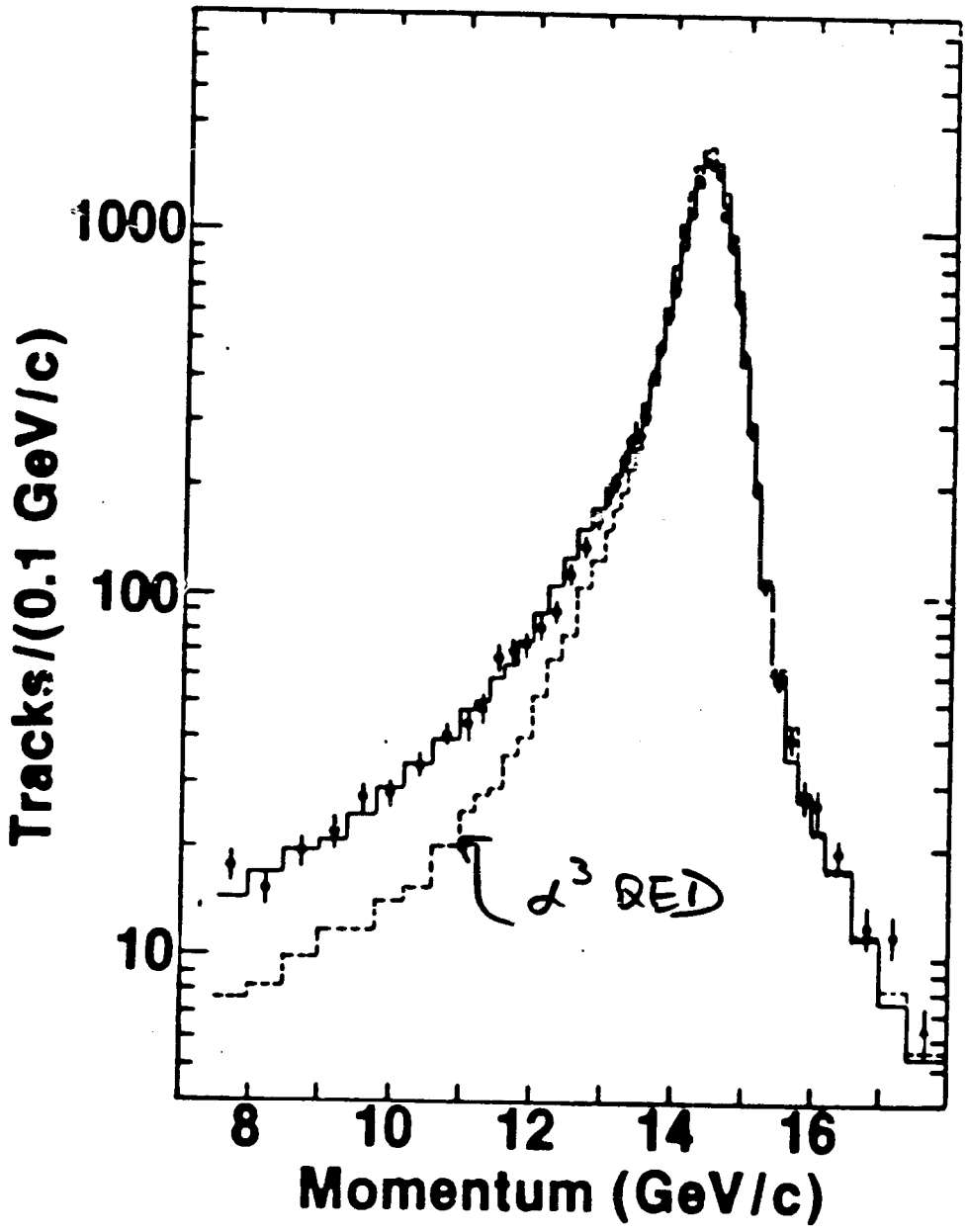
1000
100
10
Tracks/(0.1 GeV/c)
8
10
12
14
16
Momentum (GeV/c)
α^3 QED

Fig. 10

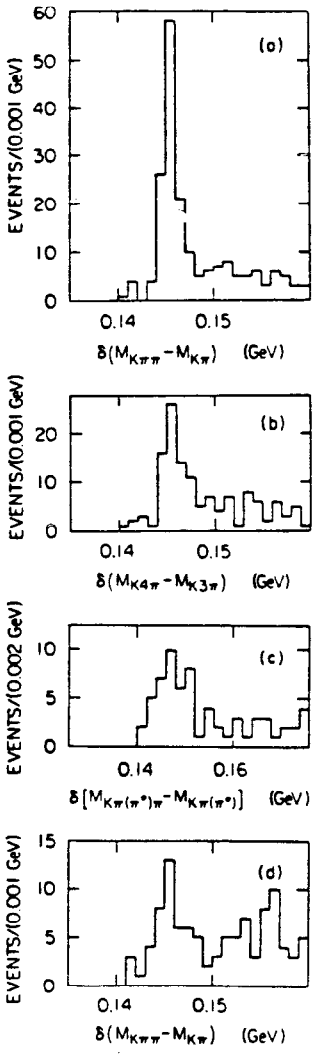
(a)
EVENTS/(0.001 GeV)
δ(M_Kππ − M_Kπ) (GeV)
(b)
EVENTS/(0.001 GeV)
δ(M_Kππ − M_Kπ) (GeV)
(c)
EVENTS/(0.002 GeV)
δ[M_Kπ(π°)π − M_Kπ(π°)] (GeV)
(d)
EVENTS/(0.001 GeV)
δ(M_Kππ − M_Kπ) (GeV)

Fig. 11

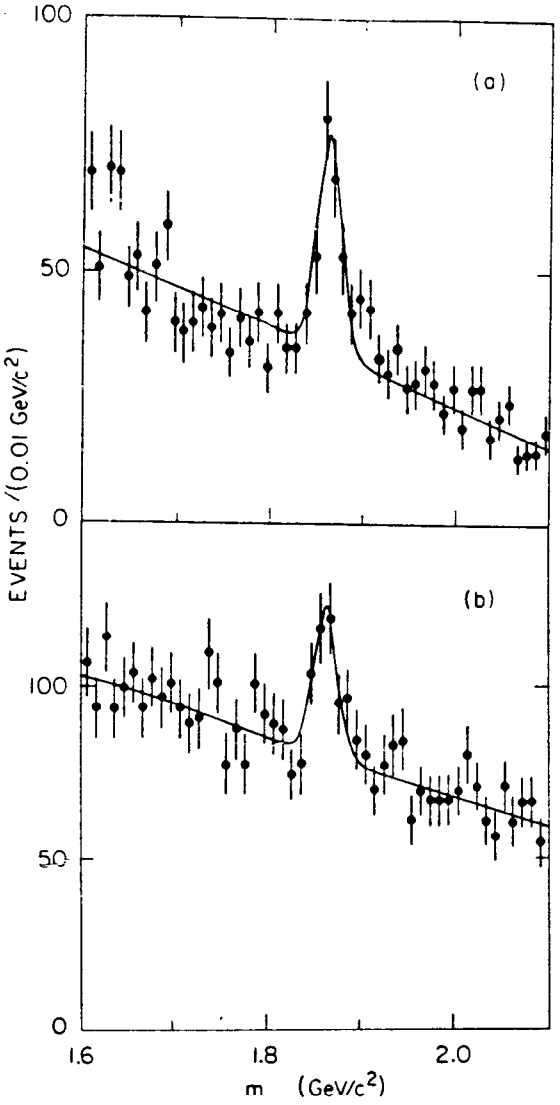
(a)
(b)
EVENTS /(0.01 GeV/c²)
m (GeV/c²)

Fig. 12

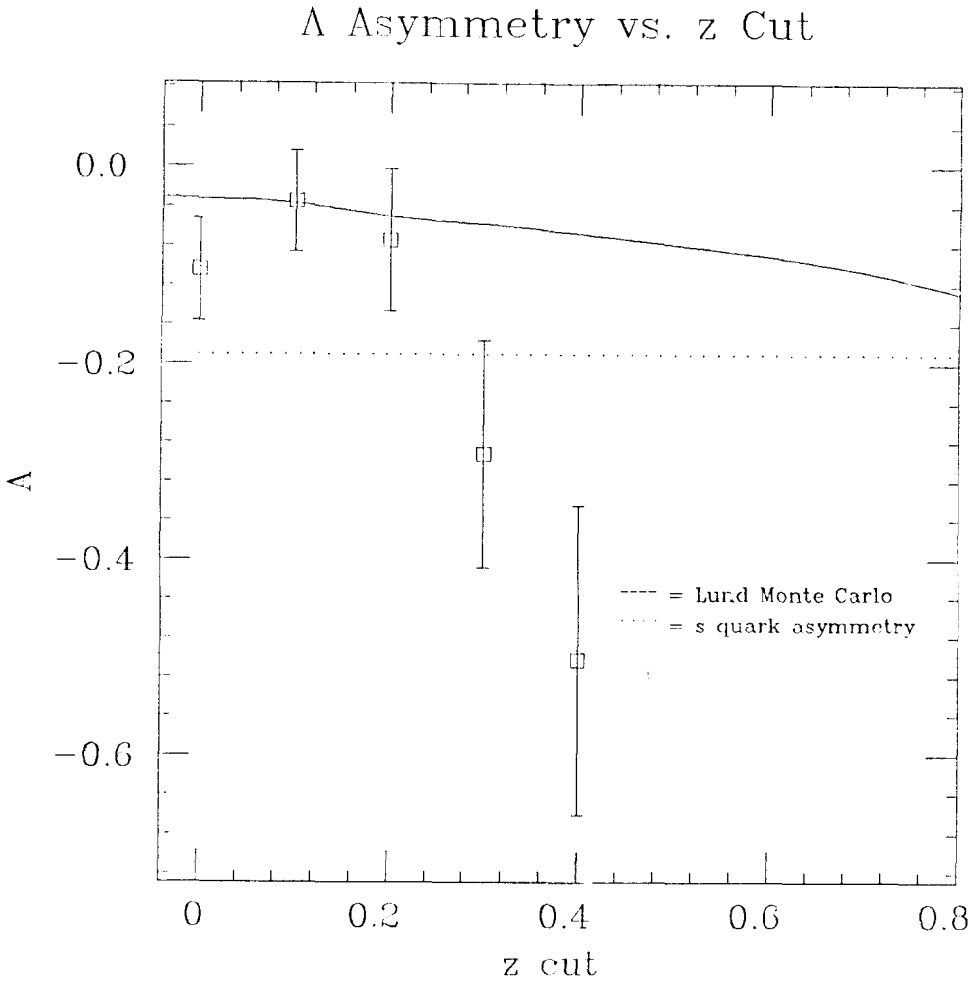
Λ Asymmetry vs. z Cut
0.0
−0.2
−0.4
−0.6
A
0
0.2
0.4
0.6
0.8
z cut
= Lund Monte Carlo
= s quark asymmetry

Fig. 13

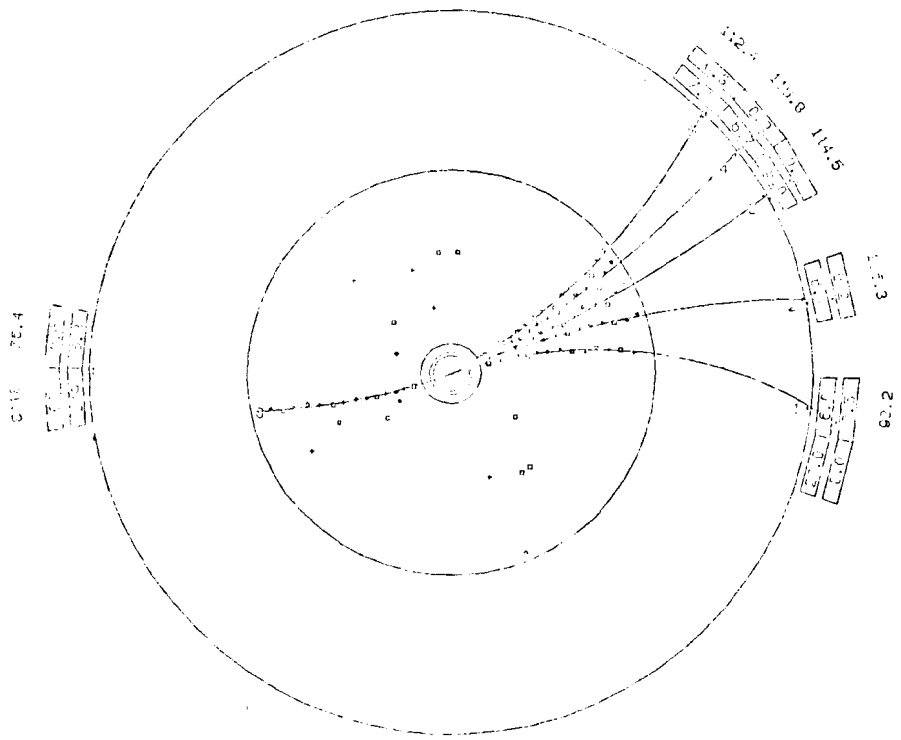

F R S RUN= 1526

EVENT= 7835
DCHITS = 121
PPPNO = 0
SH SUM= 2.8 + 0.0

TRACK	MOMENTUM	THETA
1	1.1	93.3
2	2.3	103.4
3	-4.1	110.8
4	-3.0	115.8
5	-1.7	112.1
6	1.6	81.5

PCODE = 52 PPRNG TOT. ENRGY

TRIG.= F2 F3 S6 A2 D1 D2

Fig. 14

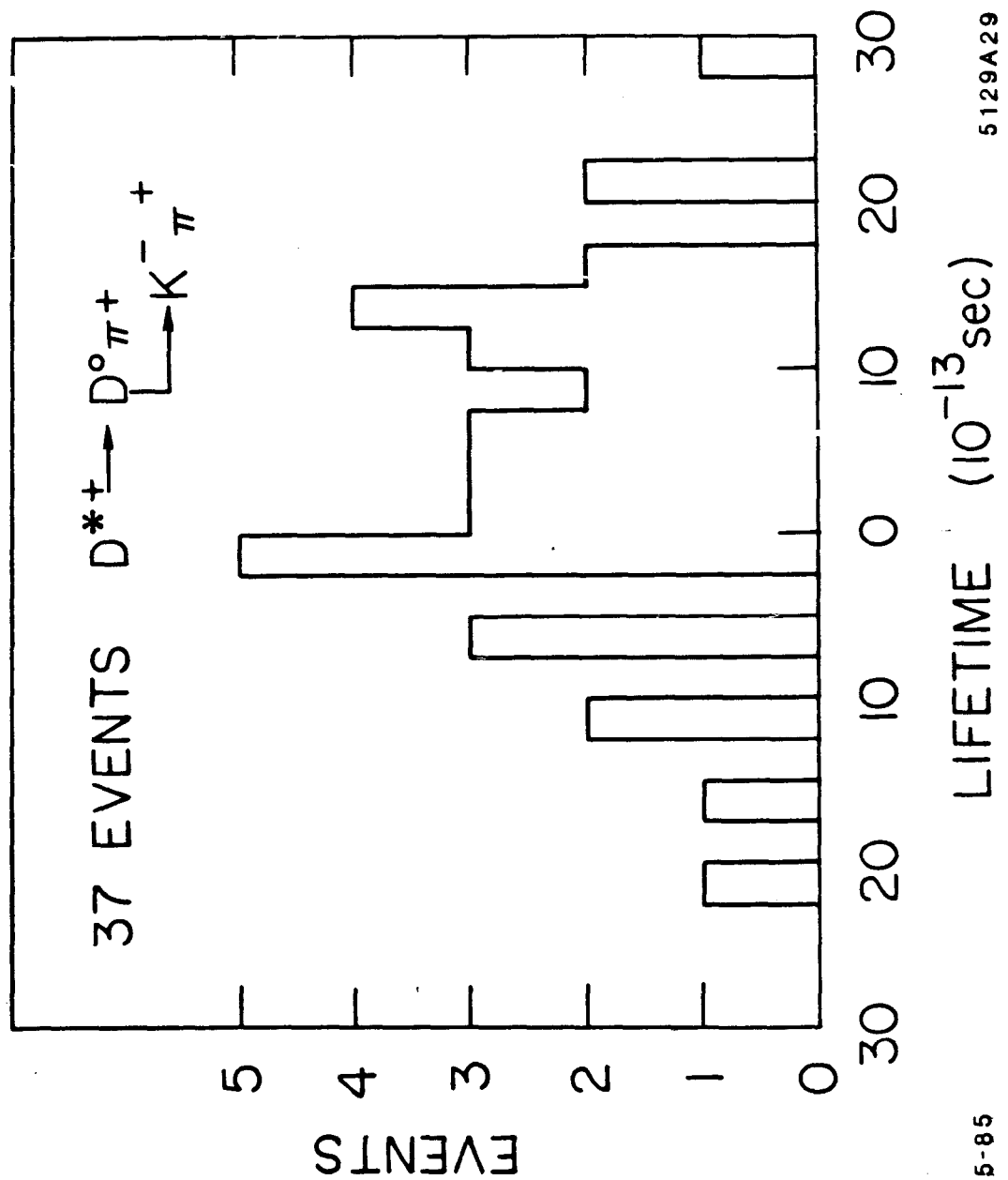

Fig. 15

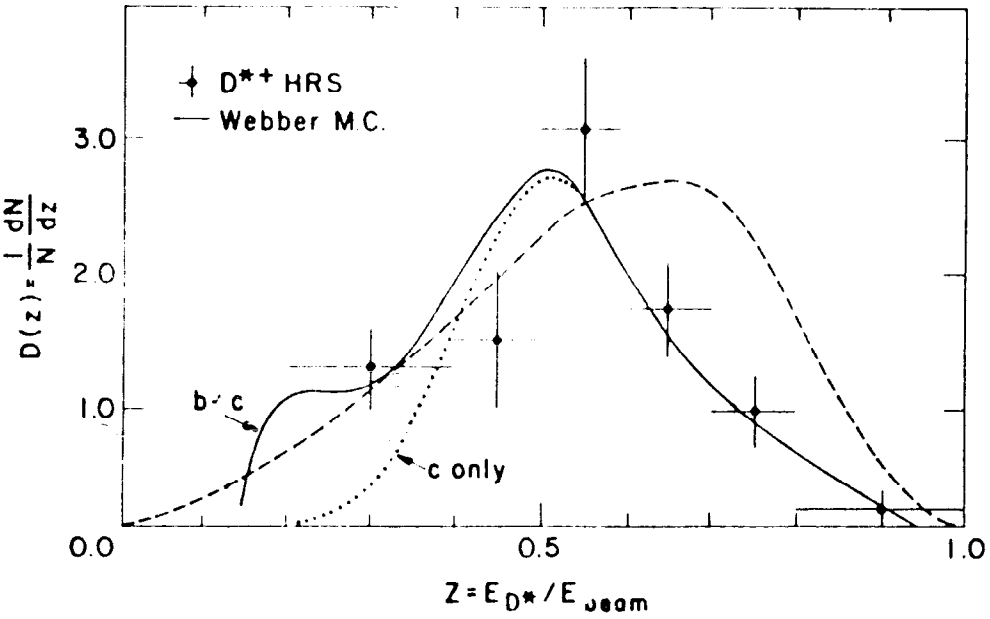

Fig. 16

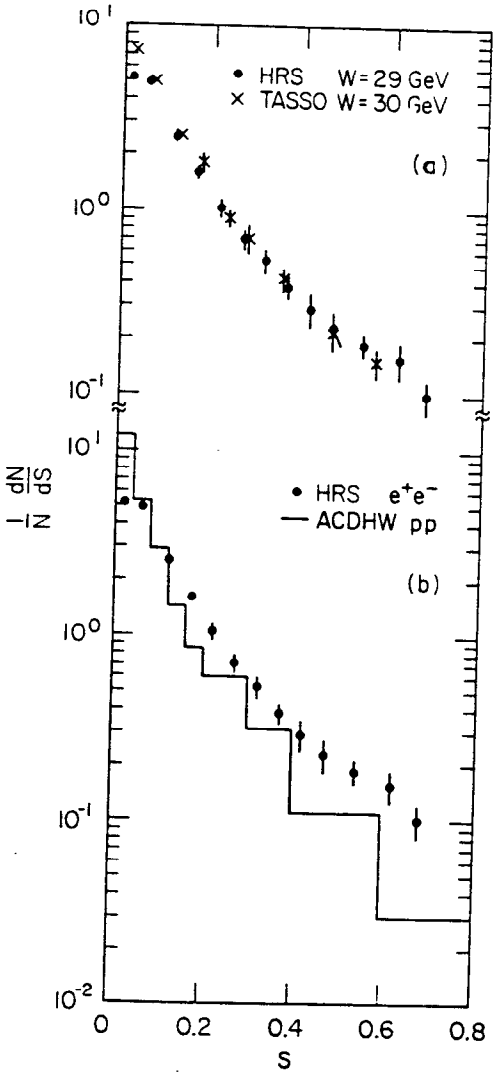

Fig. 17

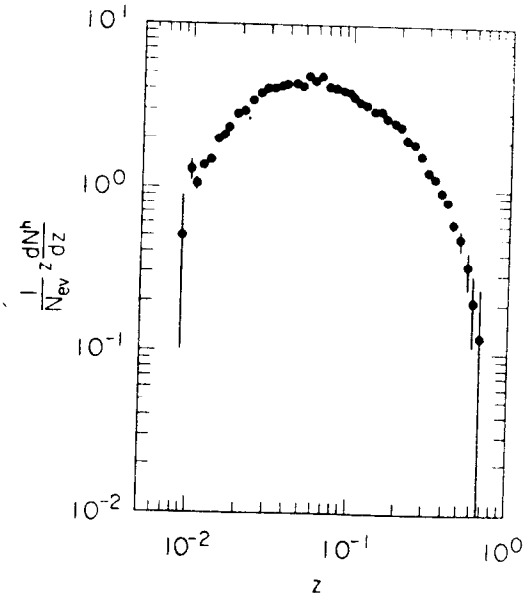

Fig. 18

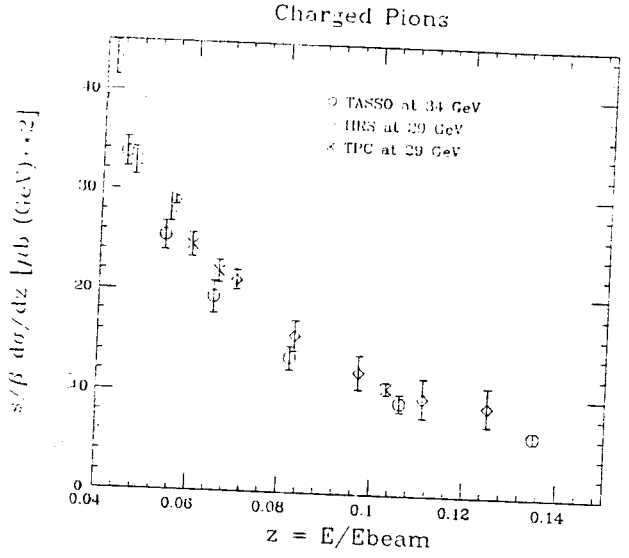
Charged Pions
TASSO at 34 GeV
HRS at 29 GeV
TPC at 29 GeV
s/β dσ/dz [μb (GeV)**2]
z = E/Ebeam

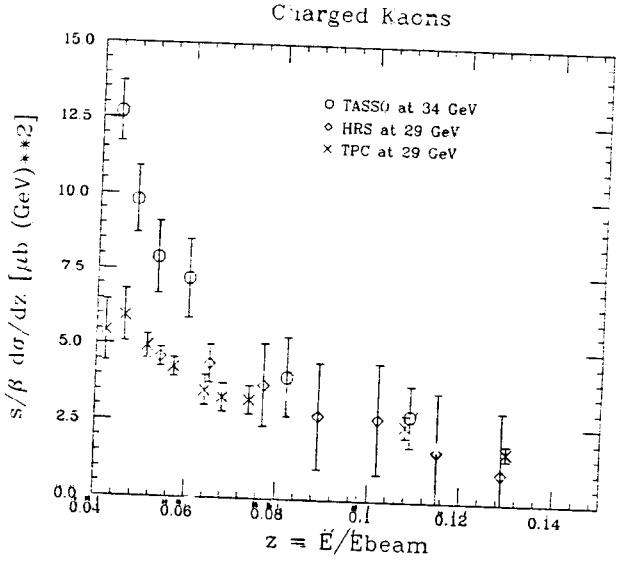
Charged Kaons
TASSO at 34 GeV
HRS at 29 GeV
TPC at 29 GeV
s/β dσ/dz [μb (GeV)**2]
z = E/Ebeam

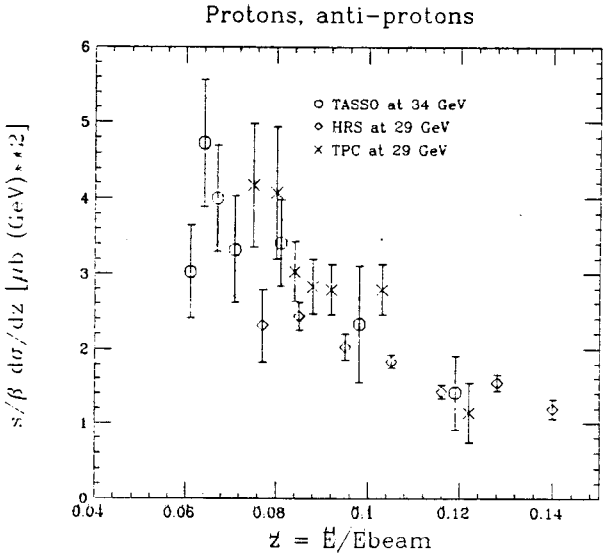
Protons, anti-protons
TASSO at 34 GeV
HRS at 29 GeV
TPC at 29 GeV
s/β dσ/dz [μb (GeV)**2]
z = E/Ebeam

Fig. 19

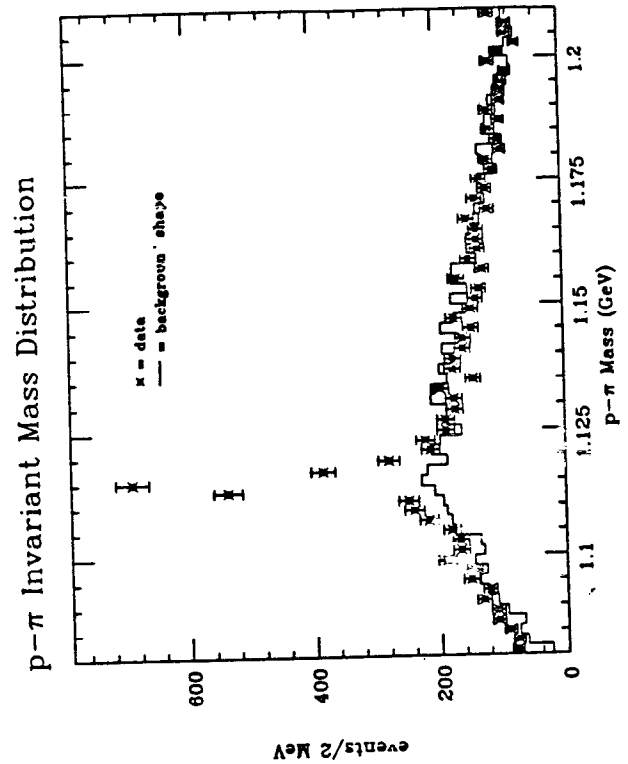
p−π Invariant Mass Distribution
x = data
— = background shape
events/2 MeV
0
200
400
600
1.1
1.125
1.15
1.175
1.2
p−π Mass (GeV)

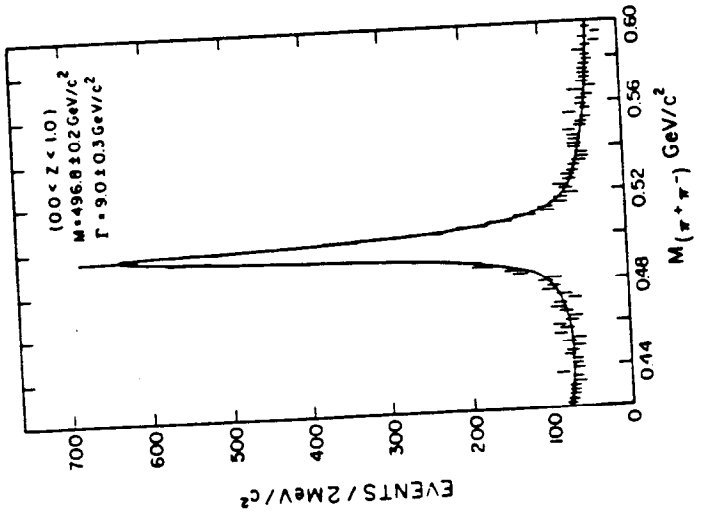
(0.0 < Z < 1.0)
M=496.8±0.2GeV/c²
Γ = 9.0±0.3GeV/c²
EVENTS / 2MeV/c²
0
100
200
300
400
500
600
700
0.44
0.48
0.52
0.56
0.60
M(π⁺π⁻) GeV/c²

Fig. 20

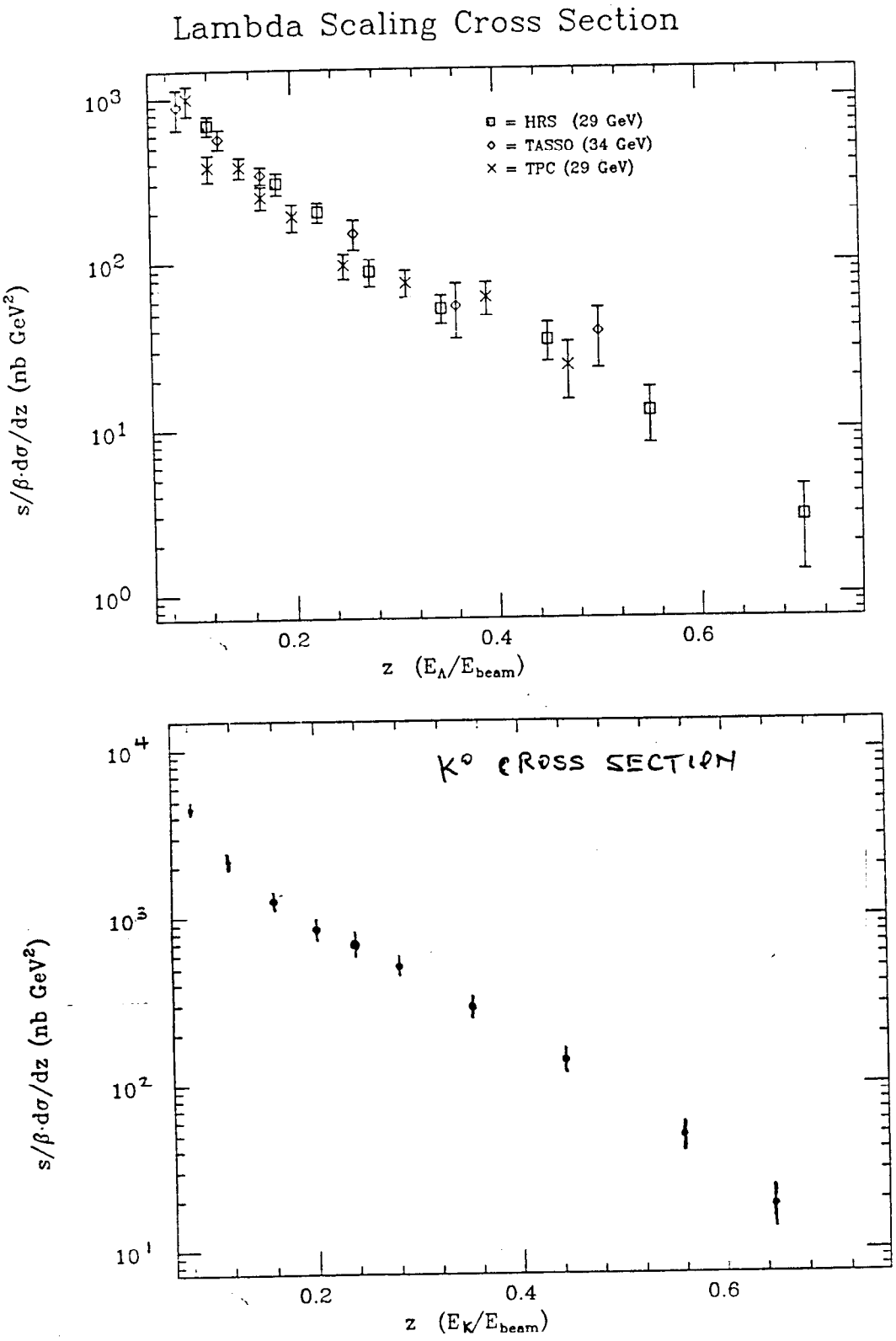
Lambda Scaling Cross Section
□ = HRS (29 GeV)
◇ = TASSO (34 GeV)
× = TPC (29 GeV)
$s/\beta \cdot d\sigma/dz$ (nb GeV^2)
10^3
10^2
10^1
10^0
0.2
0.4
0.6
z (E_Λ/E_{beam})
K° CROSS SECTION
10^4
10^3
10^2
10^1
$s/\beta \cdot d\sigma/dz$ (nb GeV^2)
0.2
0.4
0.6
z (E_K/E_{beam})

Fig. 21

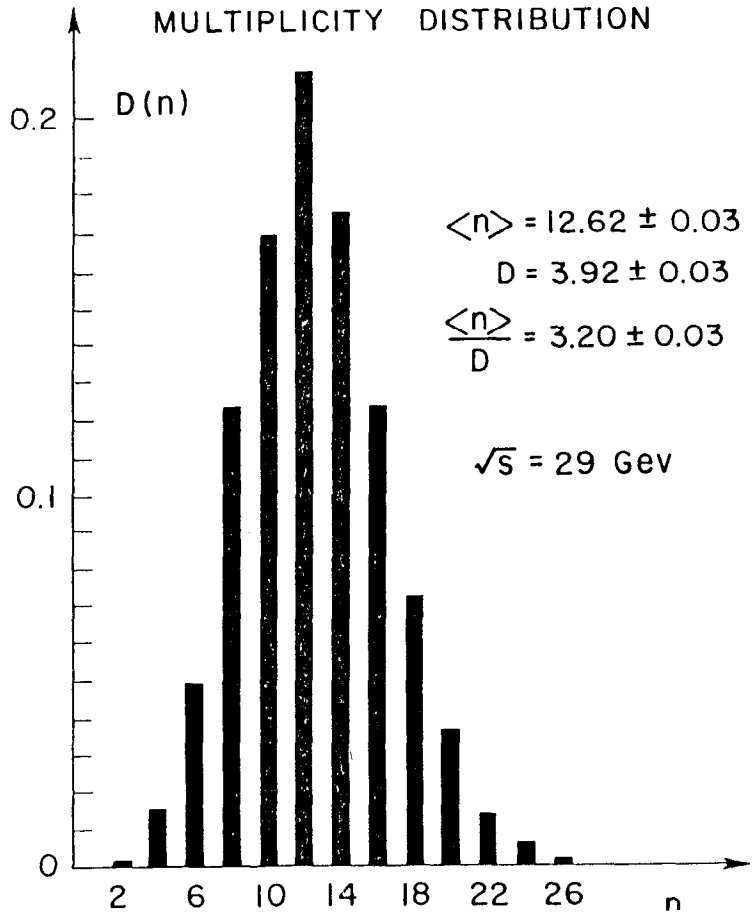
MULTIPLICITY DISTRIBUTION
D(n)
0.2
0.1
0
2
6
10
14
18
22
26
n
⟨n⟩ = 12.62 ± 0.03
D = 3.92 ± 0.03
⟨n⟩/D = 3.20 ± 0.03
√s = 29 Gev

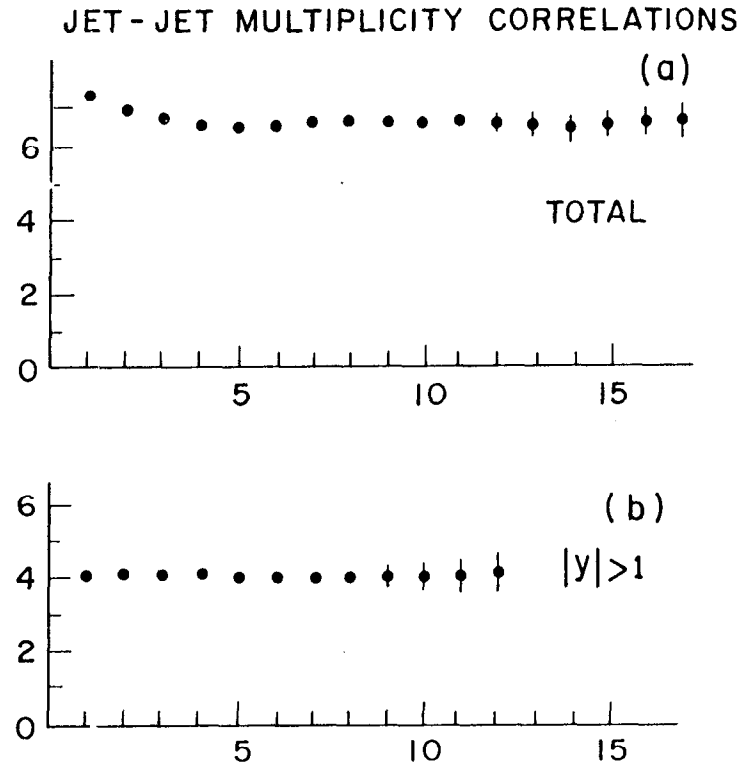
JET-JET MULTIPLICITY CORRELATIONS
(a)
TOTAL
6
4
2
0
5
10
15
(b)
|y|>1
6
4
2
0
5
10
15

Fig. 22

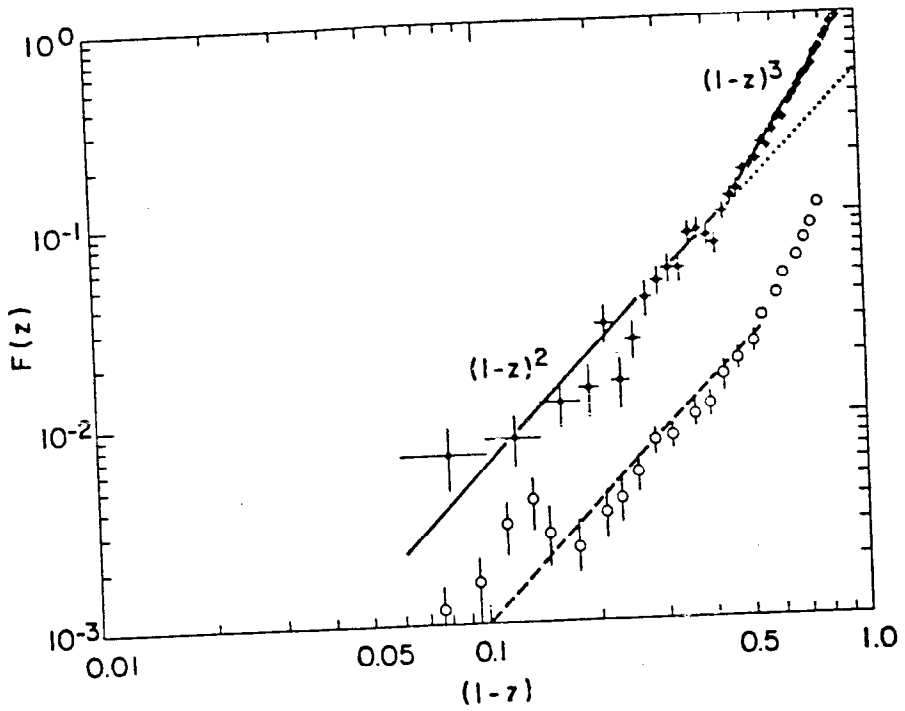
10^0
10^{-1}
10^{-2}
10^{-3}
F(z)
$(1-z)^3$
$(1-z)^2$
0.01
0.05
0.1
0.5
1.0
(1-z)

Fig. 23

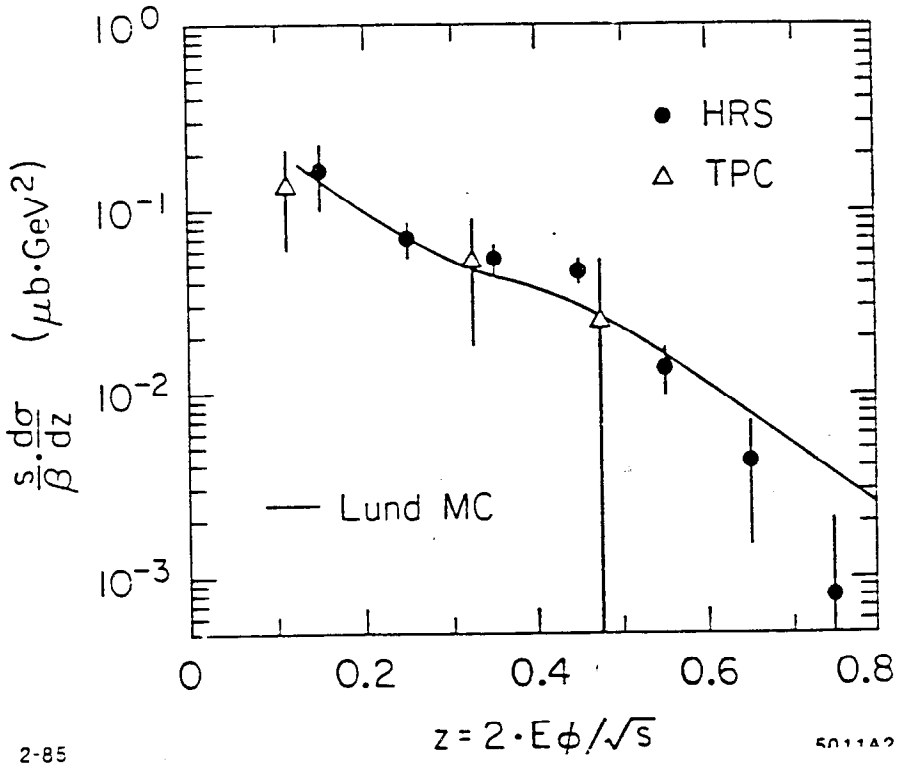
10^0
10^{-1}
10^{-2}
10^{-3}
$\frac{s}{\beta}\frac{d\sigma}{dz}$ (μb·GeV^2)
HRS
TPC
Lund MC
0
0.2
0.4
0.6
0.8
$z = 2 \cdot E\phi/\sqrt{s}$
2-85

Fig. 24

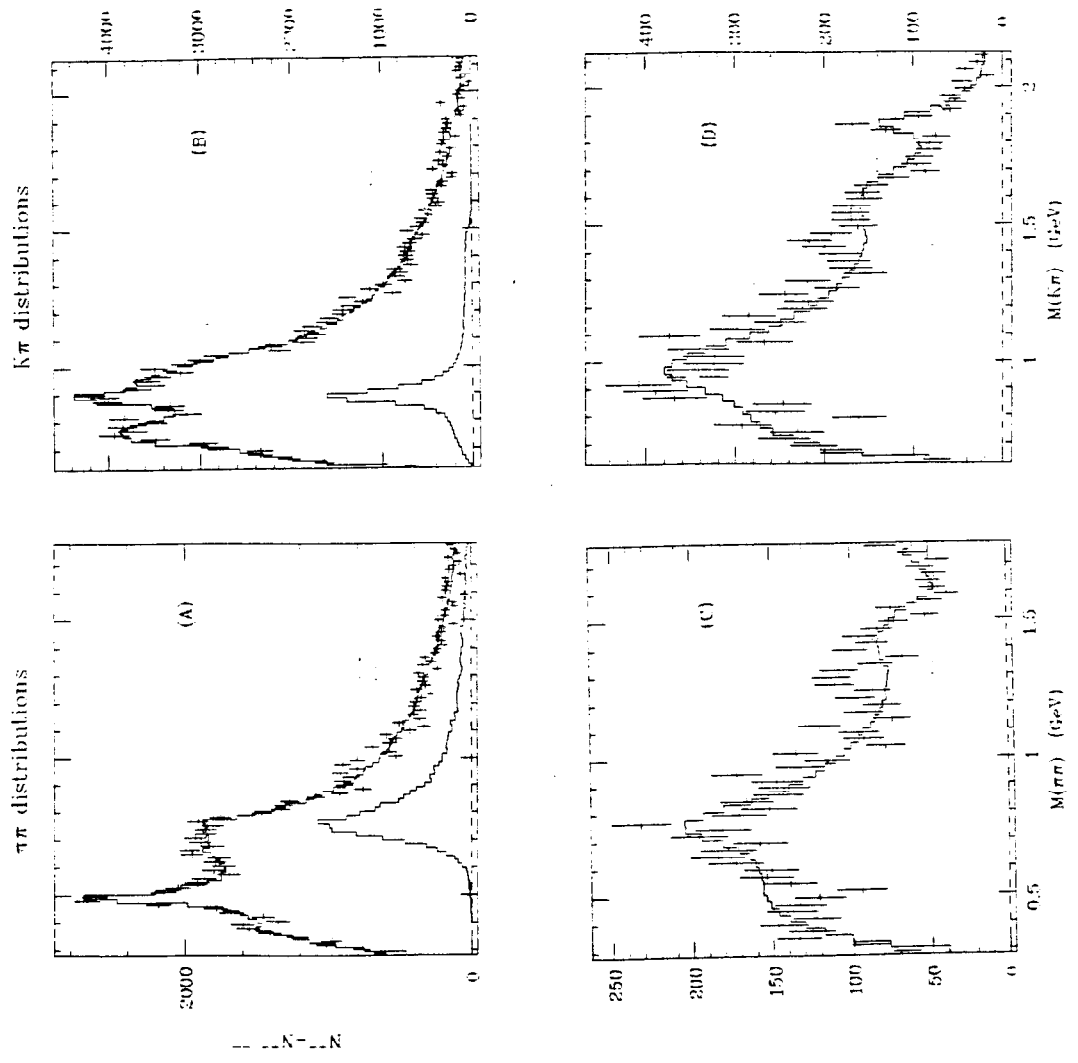

Fig. 25

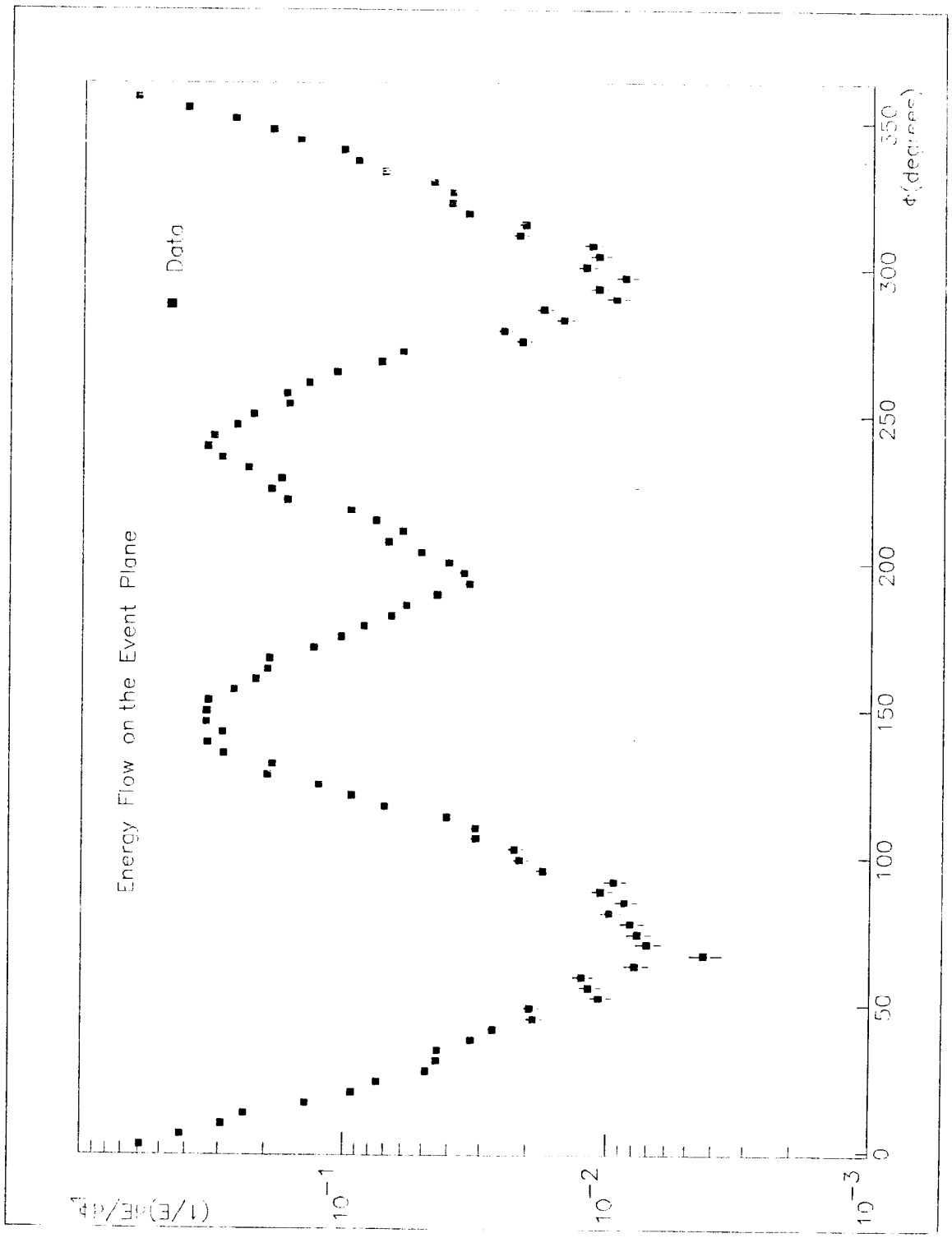
Energy Flow on the Event Plane
Data
$(1/E)dE/d\Phi$
10^{-1}
10^{-2}
10^{-3}
0
50
100
150
200
250
300
350
Φ (degrees)

Fig. 26

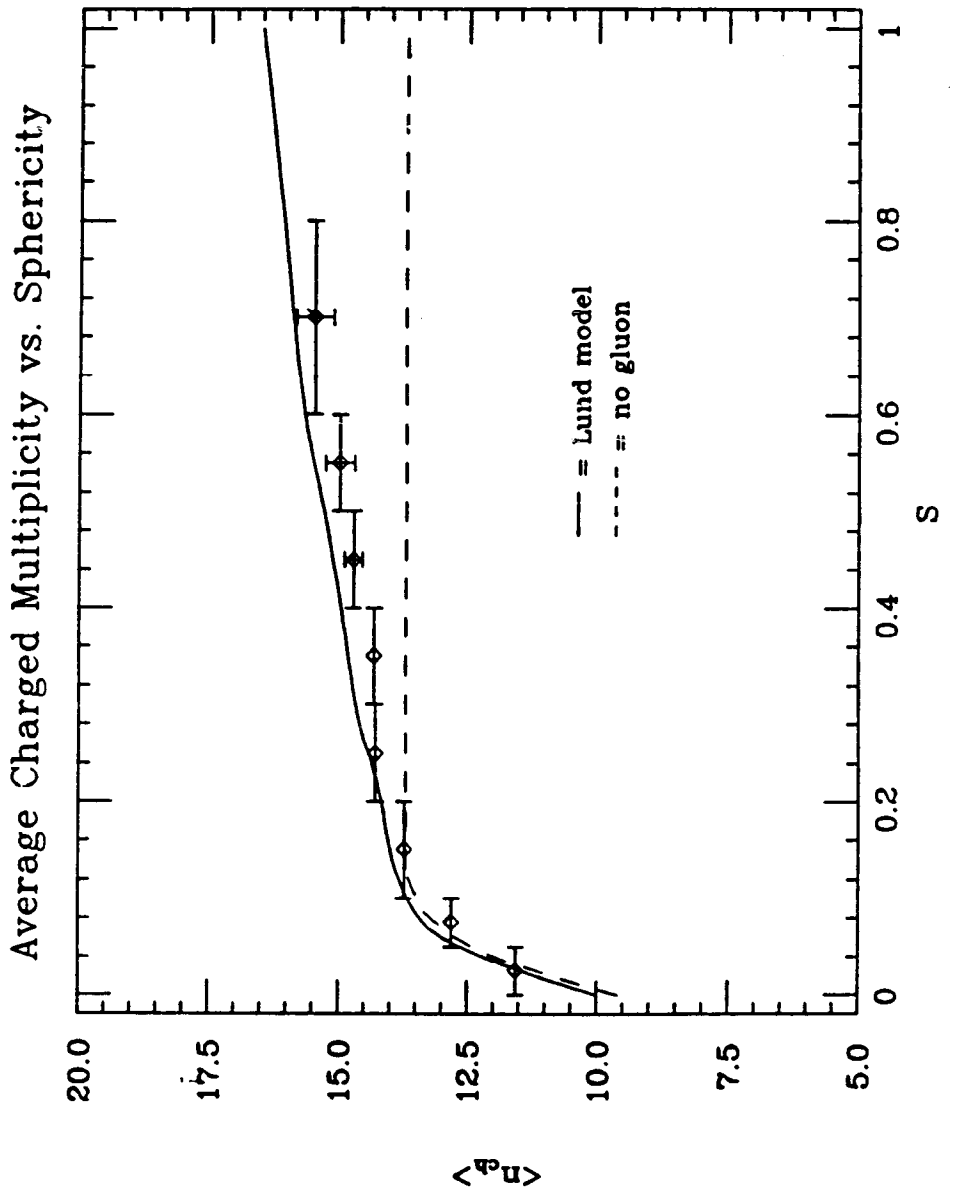
Average Charged Multiplicity vs. Sphericity
20.0
17.5
15.0
12.5
10.0
7.5
5.0
0
0.2
0.4
0.6
0.8
1
S
<n_ch>
= Lund model
= no gluon

Fig. 27

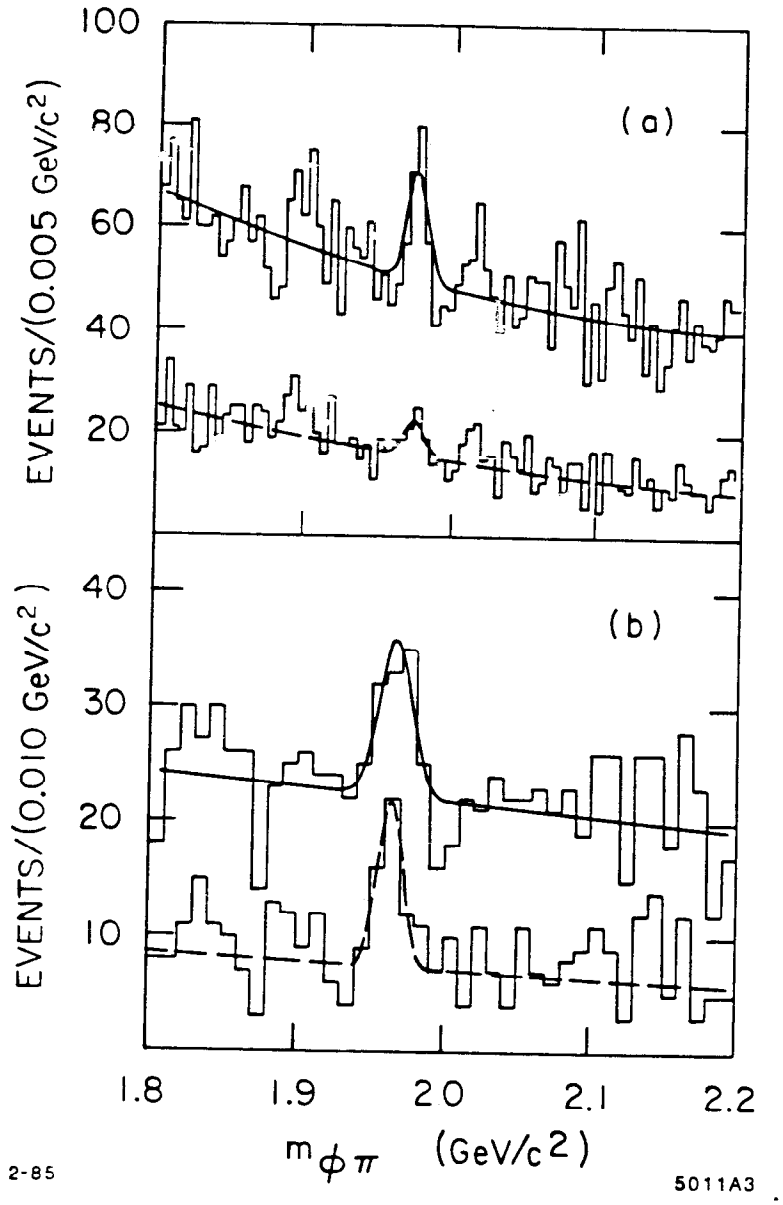
100
80
60
40
20
EVENTS/(0.005 GeV/c²)
(a)
40
30
20
10
EVENTS/(0.010 GeV/c²)
(b)
1.8
1.9
2.0
2.1
2.2
$m_{\phi\pi}$ (GeV/c²)
2-85
5011A3

Fig. 28

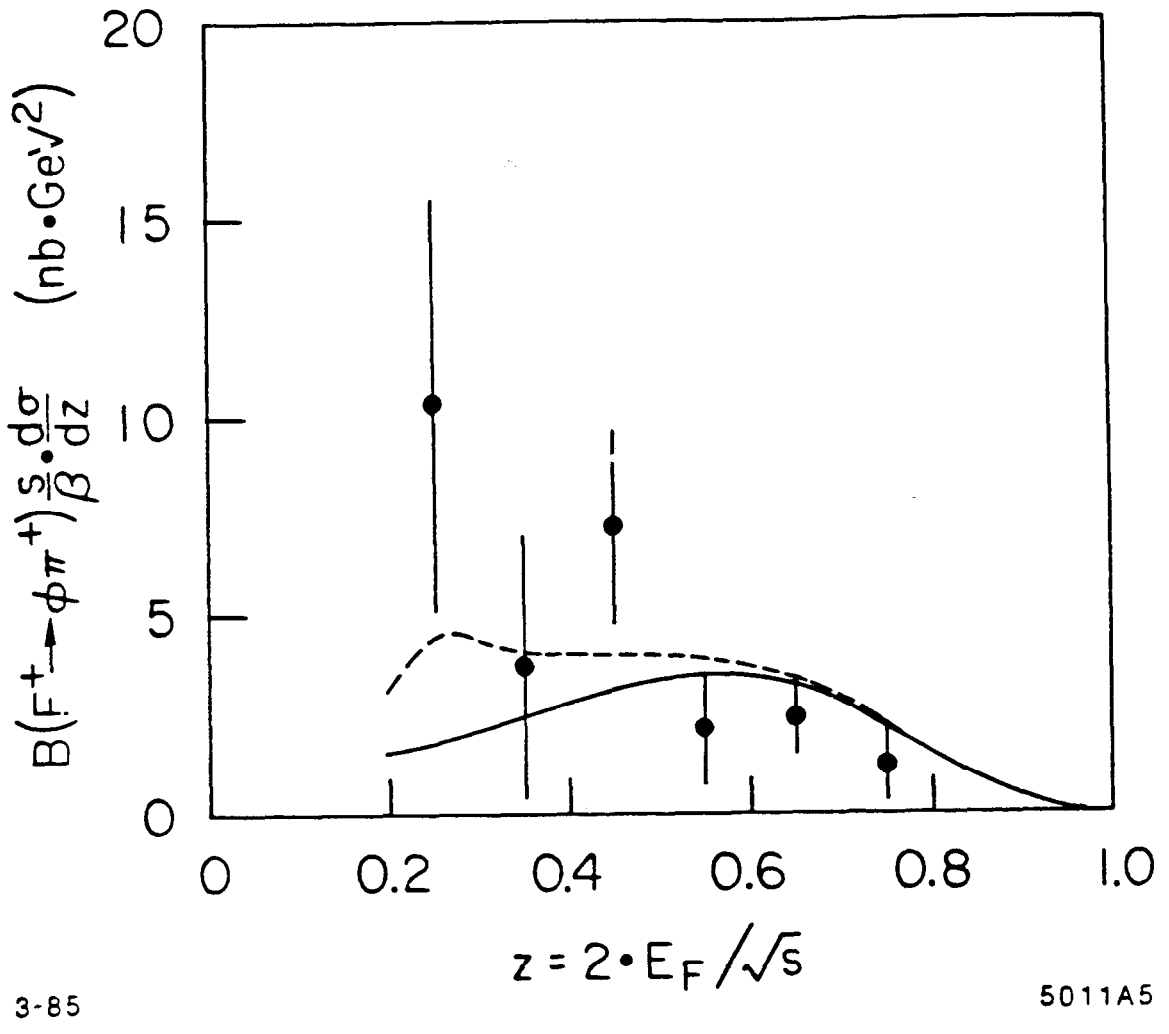
20
15
10
5
0
0
0.2
0.4
0.6
0.8
1.0
$B(F^+ \to \phi\pi^+)\frac{s}{\beta}\cdot\frac{d\sigma}{dz}$ (nb·GeV^2)
$z = 2\cdot E_F/\sqrt{s}$
3-85
5011A5

Fig. 29

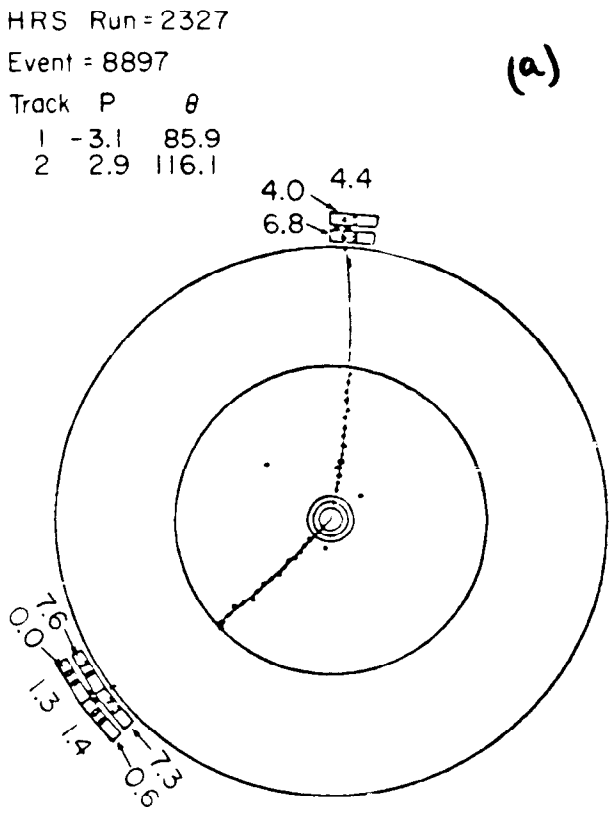

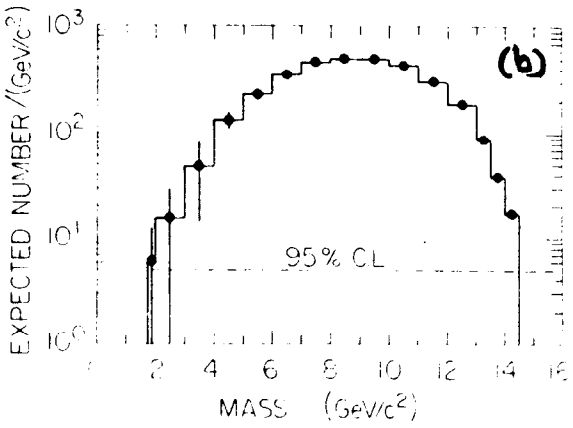

Fig. 30

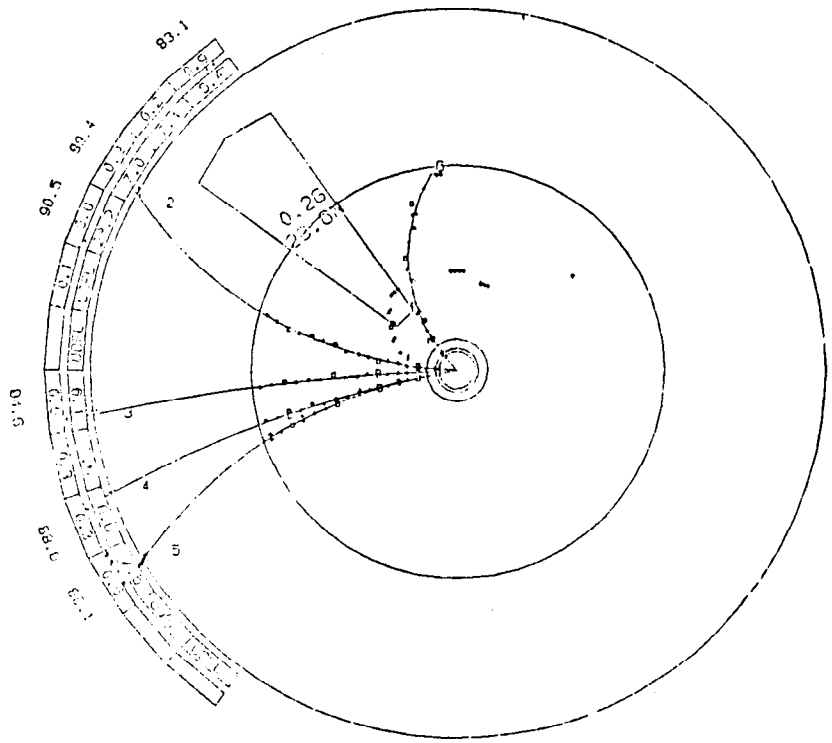

H R S RUN=0100

EVENT= 8692
DCHITS = 138
NPRNG = 6
SH SUM= 3.1 · 0.2

TRACK	MOMENTUM	THETA
2	1.0	85.9
3	-5.0	94.9
4	-2.8	87.9
5	-1.1	89.3
6	0.5	59.0

TRIG.= F2 F3 S6 A2 D1 D2

Fig. 31

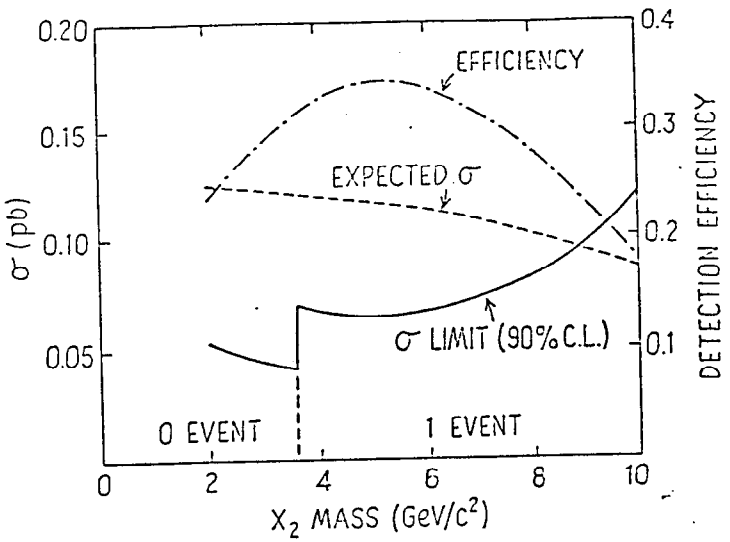

Fig. 32

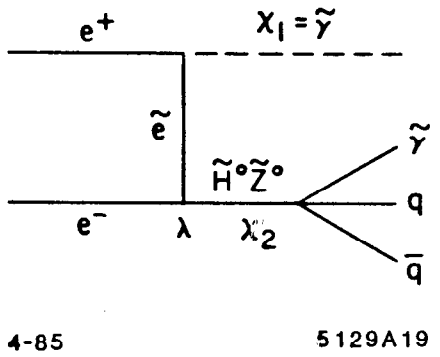

Fig. 33

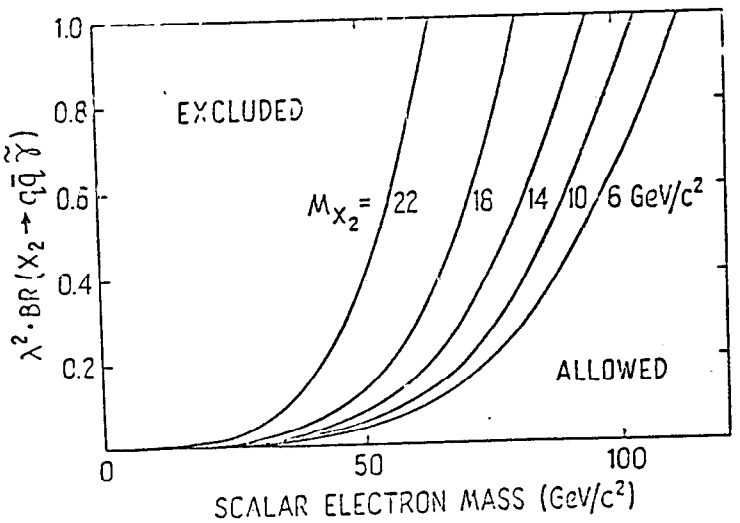

Fig. 34

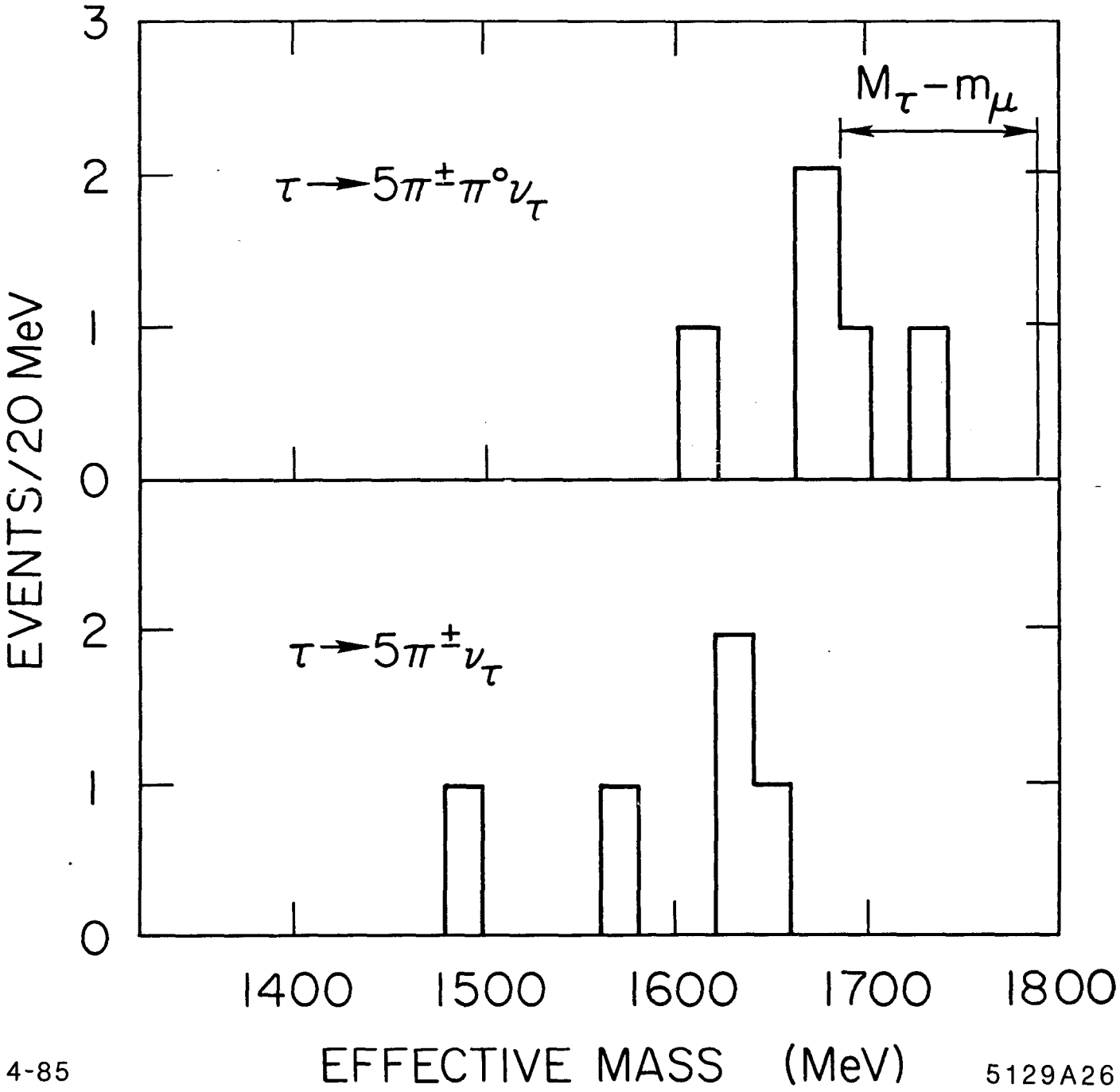
3
2
1
0
$M_\tau - m_\mu$
$\tau \rightarrow 5\pi^\pm \pi^\circ \nu_\tau$
2
1
0
$\tau \rightarrow 5\pi^\pm \nu_\tau$
EVENTS/20 MeV
1400
1500
1600
1700
1800
EFFECTIVE MASS (MeV)
4-85
5129A26

Fig. 35

APPENDIX A

B PHYSICS – SEARCHING GROUND FOR NEW PHYSICS

I.I. BIGI

There is wide spread suspicion in the high energy physics community that the Standard Model which is based on the gauge group $SU(3)_c \times SU(2)_L \times U(1)$ and which contains three fermion families plus a Higgs doublet is incomplete even at energies well below the unification mass. These are two complementary ways to establish the existence of new dynamical elements, namely

a. by producing and identifying the corresponding quanta in the lab or

b. by showing that the Standard Model is not able to reproduce fully the magnitude of some observables.

The credibility of this second, or indirect approach rests strongly on one's ability to perform calculations in a reliable way. This is exemplified by our inability to draw quantitative conclusions from the observed CP violation in K_L decays.

Detailed studies of B decays will test the Standard Model in a novel and very sensitive way and might reveal the existence of new dynamical degrees of freedom. I will concentrate on those phenomena that can be analyzed with a sample containing several ten thousand B mesons.

$B^0 - \overline{B^0}$ mixing will make its presence felt via like-sign di-lepton events (or via a reduction in the expected size of the forward-backward asymmetry of bottom jets). In the Standard Model one predicts

$$R = \frac{N(l^+l^+) + N(l^-l^-)}{N(l^+l^-)} \approx \begin{cases} 0.001 - 0.02 & \text{for } B_d \text{ mesons;} \\ 0.12 - 0.55 & \text{for } B_s \text{ mesons.} \end{cases}$$

The major uncertainty in these numbers is generated by our ignorance concerning the top quark mass m_t – R goes like m_t^4/M_W^4 for $m_t \sim$ 30-40 GeV – and the KM angle $U(b \to u)$. I estimate the remaining theoretical uncertainty to be not more than a factor of four.

A major ingredient in the computation is the decay constant f_B. Present theoretical calculations tend to converge towards $f_B \sim$ 170-220 MeV (while in

most treatments of $B^0 - \overline{B^0}$ mixing, $f_B = 150$ MeV is used). Observing the decay $B \to \tau\nu$ would allow to determine f_B once $|U(b \to u)|^2$ is known and vice versa. Using $\tau_B = 10^{-12}$ sec, one finds

$$BR(B \to \tau\nu) \simeq 10^{-3} \left(\frac{f_B}{200\ \text{MeV}}\right)^2 \left(\frac{|U(b \to u)|}{0.014}\right)^2$$

For $|U(b \to u)| < 0.005$ as suggested by the CESR results on semi-leptonic B decays one obtains

$$BR(B \to \tau\nu) \simeq 1.3 \times 10^{-4} \left(\frac{f_B}{200\ \text{MeV}}\right)^2$$

which is presumably too small to be observable.

If on the other hand $BR(R \to \tau\nu) \sim 10^{-3} - 5 \times 10^{-3}$ were observed one had to check critically, the previous determination of $U(b \to u)$. Next one would raise the possibility of $f_B \simeq 500$ MeV. This could be tested in charm meson decays where one predicts quite unambigously

$$BR(F \to \tau\nu) \sim 1.3\% \left(\frac{f_F}{200\ \text{MeV}}\right)^2$$

$f_F \simeq 500$ MeV would lead to a huge branching ratio

$$BR(F \to \tau\nu) \sim 8\%$$

If such an enhanced signal were not seen in F decays, one had to turn to 'New Physics' to explain the observed enhancement in $B \to \tau\nu$: non-minimal Higgs models could be made in order to enhance $B \to \tau\nu$ by a factor of ten while only doubling $F \to \tau\nu$.

Whatever the outcome of searches for $B \to \tau\nu$ and $F \to \tau\nu$ is, it should be kept in mind that a value of $f_B \sim 500$ MeV would strongly increase $B^0 - \overline{B^0}$ mixing.

Due to the unitarity constraints of the 3 × 3 KM matrix $|U(b \to u)|^2 \ll |U(b \to c)|^2$ implies $|U(t \to d)|^2 \ll |U(t \to s)|^2$. Thus the Standard Model – independent of many details – predicts stronger $B_s - \overline{B}_s$ than $B_d - \overline{B}_d$ mixing:

$$R_d \ll R_s$$

CP violation in semileptonic B decays is tiny within the Standard Model:

$$a_d = \frac{N(l^+) - N(l^-)}{N(l^+) + N(l^-)} < 10^{-4} - 10^{-3}$$

both for B_d and B_s mesons.

Non-leptonic B^0 decays are expected to exhibit large asymmetrics in certain channels yet the required statistics is presumably beyond PEP's reach.

The expected pattern of B_d vs. B_s mixing could be completely changed by the existence of a non-minimal Higgs sector. In general this sector would contain neutral states whose couplings violate flavor conservation. The $K_L - K_S$ mass difference requires such states to have a mass exceeding several TeV. Even so, they could enhance B_d and B_s mixing considerably; typically one finds

$$R(B_d) \sim R(B_s) \sim 0.1 - 0.5$$

The strength of CP violating phenomena is either not affected or considerably decreased.

Supersymmetric (SUSY) models with relatively light gluinos – $m_g \sim$ 20-40 GeV – and moderately light squarks – $M_g \sim$ 40-60 GeV – would affect $B^0 - \overline{B^0}$ mixing very significantly: while B_s mixing is still expected to be stronger than B_d mixing, the difference would go down considerably; even

$$R(B_d) \sim 0.1 - 0.2$$

could hold in these models.

Furthermore, there is a region in parameter space where CP violation in semi-leptonic B_s decays is enhanced to levels that could be obserable at PEP.

$$a_l(B_s) = \frac{N(l^+) - N(l^-)}{N(l^+) + N(l^-)} \sim 2[5?]\%$$

To summarize:

a. Dedicated searches for $B^0 - \overline{B^0}$ mixing at PEP would test the Standard Model in a novel and highly sensitive way.

b. Observation of the expected pattern would estalish major progress in our understanding of fundamental dynamics.

c. The numerical precision of our predictions will be enhanced significantly once m_t, $|U(b \rightarrow u)|$ and, possible, $BR(B \rightarrow \tau\nu)$ and $BR(F \rightarrow \tau\nu)$ are known.

d. It is <u>not</u> a foregone conclusion that B_d mixing will indeed be much weaker than B_s mixing: the former could actually be comparable to the latter. Such an observation would be clear evidence for an incompleteness of the Standard Model and point towards SUSY models or a non-minimal Higgs sector.

e. SUSY allows for an observable CP asymmetry in semi-leptonic B_s decays.

f. Never rule out surprises like CP violation observed in non-leptonic B^0 decays.

APPENDIX B

ON THE OBSERVABILITY OF $B^0 - \bar{B}^0$ MIXING IN THE $e^+e^- \to B\bar{B}X$ REACTION AT $\sqrt{s} \approx 15 - 30$ GeV

A. FRIDMAN AND A. SCHWARZ

APPENDIX B

ON THE OBSERVABILITY OF $B^0 - \bar{B}^0$ MIXING IN THE $e^+e^- \rightarrow B\bar{B}X$ REACTION AT $\sqrt{s} \approx 15 - 30$ GeV

CONTENTS

B1 INTRODUCTION

The possibility of observing mixing in the $B^0\bar{B}^0$ system has been rather widely discussed.[1-11] In particular theoretical estimates have been made for the case of $B^0\bar{B}^0$ production in the $e^+e^- \to \Upsilon(4S) \to B^0\bar{B}^0$ reaction. Mixing in this specific channel is expected to appear as a small effect and might thus be hardly measurable. Here we will therefore consider the $e^+e^- \to B\bar{B}X$ reaction (X meaning anything) well above the $B\bar{B}$ threshold where any combination of $B\bar{B}$ mesons[12] ($B_u\bar{B}_u$, $B_u\bar{B}_d$, $B_u\bar{B}_s$, etc.) can be produced. This reaction might be advantageous as mixing is expected to be almost complete for the B_s mesons.[5,9] In this respect the study of mixing effects in the $e^+e^- \to B\bar{B}X$ reaction is complementary to that in the $e^+e^- \to \Upsilon(4S) \to B_d^0\bar{B}_d^0$ process.

In Section B.2 we recall briefly the parameters used to describe the $B\bar{B}$ mixing and in Section B.3 we give estimates for the mixing effects which could be observed in the $e^+e^- \to B\bar{B}X$ reactions as well as in the $\Upsilon(4S)$ decays. We have also evaluated the influence of a non-spectator component in the B-decay on the observability of the mixing phenomenon. Finally, in Section B.4 we give estimates for the number of signal and background events which could be observed in an e^+e^- experiment with an accumulated luminosity of 1000 pb^{-1}.

B2 MIXING PARAMETERS

As suggested previously[13] the mixing can be measured by either of the following ratios:

$$R = \frac{N^{++} + N^{--}}{N^{+-} + N^{++} + N^{--}} \qquad \text{or} \qquad R' = \frac{N^{++} + N^{--}}{N^{+-}}$$

Here $N^{++} + N^{--}$ denotes the number of events having two leptons of the same charge in the final state, arising from the mixing process and the subsequent semileptonic decays of B^0B^0 or $\bar{B}^0\bar{B}^0$ pairs. The number of events with two leptons of opposite charge is given by N^{+-}. The latter is either due to the

semileptonic decays of the B and $\bar{B}$ mesons, $B \to l^- \nu X$ and $\bar{B} \to l^+ \nu X$, or to a double mixing process $B^0 \to \bar{B}^0 \to l^+ \nu X$ and $\bar{B}^0 \to B^0 \to l^- \nu X$. Usually the R and R′ ratios are given in terms of the Pais and Treiman parameters[14]

$$r = \frac{N(B^0 \to \bar{B}^0 \to l^+ \nu X)}{N(B^0 \to l^- \nu X)}$$

$$\bar{r} = \frac{N(\bar{B}^0 \to B^0 \to l^- \nu X)}{N(\bar{B}^0 \to l^+ \nu X)}$$

where as before N denotes a number of events. For our present discussion we will ignore eventual CP violation effects, hence $r = \bar{r}$. One has then[1,6,9]

$$r = \bar{r} = \frac{x^2 + y^2}{2 + x^2 - y^2}$$

with $x = \Delta M/\Gamma$ and $y = \Delta\Gamma/\Gamma$. Here ΔM ($\Delta\Gamma$) is the mass (width) difference between the physical B_H and B_L (H ≡ heavy, L ≡ light) state and Γ is the total width of the B meson. One obtains[15]

$$R = \frac{r + \bar{r}}{1 + \bar{r} + r + r\bar{r}} \quad \to \quad \frac{2r}{(1+r)^2}$$

$$R' = \frac{r + \bar{r}}{1 + r\bar{r}} \quad \to \quad \frac{2r}{1 + r^2} \quad .$$

In Section B.3 we will also consider the more experimental oriented parameter

$$R_m = \frac{N^{++} + N^{--}}{N_t}$$

where N_t is here the total number of events containing B's in the final state. This ratio is very convenient as it is straightforward to obtain from it the statistical significance with which a signal can be observed in a given experiment.

It has been shown[4,10] that the above formula giving R and R′ cannot be used in the case of the $e^+e^- \to \Upsilon(4S) \to B_d^0\bar{B}_d^0, \bar{B}_d^0\bar{B}_d^0$ reactions as the relative orbital momentum L between the B's has allways the odd value L=1. Therefore the influence of the Bose-Einstein statistics has to be taken into account. This leads to a reduction of the mixing effect[16] and gives[4]

$$R \to R_{odd} = \frac{r}{1+r} \qquad \text{and} \qquad R' \to R'_{odd} = r \ .$$

In order to appreciate the importance of the mixing, one needs to know the values of x and y which may be estimated within the box diagram approximation.[17] The numerical results depend on several parameters such as the mass m_t of the top quark, the value of the CP violating phase δ in the Kobayashi Maskawa matrix, and the product f^2B_b. Here f is the B meson decay constant and B_b is the so called bag parameter which usually are taken in the range of $f \approx 150$-500 MeV and $B_b \approx 0.5$-1.5 (Ref. [18]). Despite the uncertainties in the above parameters it has been shown that for the $B^0_{s,d}$ case the mixing depends essentially on the x parameter[8,9] as $x^2 \ll y^2$ (or $|\Delta\Gamma| \ll \Delta M$). Taking $y = 0$ and the formula given above we present in Fig. 1 the variation of R′ and R'_{odd} as a function of x. One sees from this plot the suppression introduced by the constraint due to the Bose-Einstein statistics. As in the current estimates[6,9] x is small ($x \lesssim 0.4$), one can see that in this range the mixing parameter R'_{odd} for the $e^+e^- \to \Upsilon(4S) \to B_d^0\bar{B}_d^0$ process is predicted to be rather small. In contrast the mixing for B_s^0 is expected[6,9] to be nearly complete. Moreover the reaction $e^+e^- \to B\bar{B}X$ at high c.m. energy has the advantage that no suppression due to Bose-Einstein statistics occurs since many relative orbital momenta should be present.[4,10,16] In the following we will therefore study the observability of mixing in the 15-30 GeV region where $B_s^0(\bar{B}_s^0)$ can be produced. The results will be compared with the mixing effects which are expected to be observed on the $\Upsilon(4S)$ resonance.

B3 THE $e^+e^- \to B\bar{B}X$ PROCESS

This reaction well above the $B\bar{B}$ threshold should lead to events having two nearly back-to-back jets due to the decays of the B mesons. These jets will be accompanied by particles due to the fragmentation of the b quarks believed to be produced via the elementary process $e^+e^- \to b\bar{b}$. In this c.m. energy region the decay products of the two B-mesons are well separated and the $e^+e^- \to b\bar{b}$ cross section is still sizeable (128 to 32 pb). The mixing can be estimated by using the ratio $R_m = (N^{++} + N^{--})/N_t$. Denoting by P_i the probability to produce a B_i (or a $\bar{B}_i$) in the final state, namely

$$P_i = \frac{b \to B_i}{b \to \text{all}} = \frac{\bar{b} \to \bar{B}_i}{\bar{b} \to \text{all}}$$

one has

$$\begin{aligned} R_m \equiv \frac{N^{++} + N^{--}}{N_t} &= 2P_uP_dBr(B_u \to l)Br(B_d \to l)\frac{r}{1+r} \\ &+ 2P_d{}^2Br(B_d \to l)Br(B_d \to l)\frac{r}{(1+r)^2} \\ &+ 2P_s{}^2Br(B_s \to l)Br(B_s \to l)\frac{r_s}{(1+r_s)^2} \\ &+ 2P_sP_uBr(B_u \to l)Br(B_s \to l)\frac{r_s}{1+r_s} \\ &+ 2P_dP_sBr(B_d \to l)Br(B_s \to l)\frac{r_s}{(1+r)(1+r_s)} \\ &+ 2P_dP_sBr(B_d \to l)Br(B_s \to l)\frac{r}{(1+r)(1+r_s)} \end{aligned}$$

neglecting B_c-production.[19] Here r_s represents the Pais and Treiman parameter for the B_s^0 meson and $Br(B_i \to l)$ is the B_i semileptonic branching ratio into an electron or a muon ($l \equiv e, \mu$). For simplicity we neglect in the present discussion the $B \to \tau\nu X$ decay which is small because of phase space suppression.[20] Note that for the $e^+e^- \to \Upsilon(4S) \to B_d^0\bar{B}_d^0$ reaction one has

$$R_m \equiv \frac{N^{++} + N^{--}}{N_t} = f_r \left[Br(B_d^0 \to l\nu X\right]^2 \frac{r}{1+r}$$

where f_r is the fraction of $B_d^0\bar{B}_d^0$ produced at the $\Upsilon(4S)$.

The possibility to pick up an $s\bar{s}$ pair from the sea is usually assumed to be around 0.1-0.2 (Ref. [19]), a value which is supported by a recent evaluation of the data taken at $\sqrt{s} = 34$ GeV by the TASSO collaboration.[21] Taking $P_s = 0.17$ and $P_u = P_d = (1 - 0.17)/2$, we estimate $R_m = (N^{++} + N^{--})/N_t$ as a function of the phase δ using $m_t = 45$ GeV, $f^2B_b = (0.20\ \text{GeV})^2$ and $\Gamma(b \to l\nu u)/\Gamma(b \to l\nu c) = 0.01$ (Γ is here the $b \to l\nu q$ decay width). The r and r_s values for our parameters were obtained from Refs. [9] and [6], respectively, which incorporate in their analyses the latest results on the B meson lifetime. The B meson was assumed to decay according to the spectator model, the semileptonic branching ratio being $Br(B \to l\nu X) = 2 \times 0.116$ as obtained at the $\Upsilon(4S)$ (Ref. [22]). As a recent analysis of experimental data has shown that δ should be confined to the $0° - 180°$ range,[23] we have only considered this interval. For the values of the parameters chosen above, R_m (not shown) varies by about 20% when δ changes from 0° to 180°. As an example we give in Table I the R_m value for $\delta = 90°$ which corresponds to $r \simeq 2.8 \times 10^{-2}$ and $r_s \simeq 0.89$. In the same table we also present the values of R_m calculated with various P_s ($P_s = 0.17$ and the limit $P_u = P_d = P_s = 1/3$), f^2B_b and m_t values. We utilize the fact that $y \approx 0$ and that x scales approximately[24] with $f^2B_bm_t^2$. One sees from this table that the mixing parameter is expected to be around 10^{-2} (first two rows in Table I). It does not depend very much on the value chosen for $\Gamma(b \to l\nu u)/\Gamma(b \to l\nu c)$. An increase by a factor of 3 changes R_m by only $\simeq 2\%$.

Recently an investigation of the available data on B decays and on lifetime measurements lead to the hypothesis that non spectator contributions may be important in the B decay mechanism.[25] An important difference between the lifetime of the B_d^0 (τ_0) and the $B^\pm$ ($\tau_\pm$) was thus predicted, namely $\tau_\pm/\tau_0 =$ 1.4-1.8. This would correspond to a non-spectator contribution α_{ns} of 29 to 44% to the total width of the B_d^0 (Refs. [26,27]). The increase of the total $B_d^0(\bar{B}_d^0)$ width will lead to a decrease of the $B_d^0(\bar{B}_d^0) \to l\nu X$ branching ratio as semileptonic decays proceed essentially via the spectator mechanism.[25,27] It is usually assumed that it is the diagram shown in Fig. 2a with $B_d^0 \to gc\bar{u}$ which is

Table I. For the phase $\delta \simeq 90°$ estimates of the mixing parameter $R_m = (N^{++} + N^{--})/N_t$ obtained with various values of α_{ns}, P_i, m_t and f^2B_b. Here α_{ns} is the fraction of the non-spectator contribution to the B^0 decay, P_i is the probability $P_i = (b \to B_i)/(b \to \text{all})$ and m_t is the top quark mass. In the product f^2B_b, f represents the B meson decay constant and B_b the bag parameter (see text). For $\alpha_{ns} \neq 0$ we recalculate the $B^{\pm}$ and B_d^0 semileptonic branching ratios using as input the experimental $Br(B \to l\nu X) = 2 \times 0.116$ value. In these cases, R_m was calculated assuming successively that $Br(B_s^0 \to l\nu X) = Br(B^{\pm} \to l\nu X)$ (next to the last column) and $Br(B_s^0 \to l\nu X) = Br(B_d^0 \to l\nu X)$ (last column).

α_{ns}(%)	P_s $P_u = P_d$ $P_c = 0$	$Br(B^{\pm} \to l\nu X)$	$Br(B_d^0 \to l\nu X)$	$B_b f^2$ (GeV)^2	m_t (GeV)	$\frac{(N^{++}+N^{--})}{N_t}$ $\Gamma(B_s^0) = \Gamma(B^{\pm})$	$\Gamma(B_s^0) = \Gamma(B_d^0)$
0.0	0.170	2×0.116	2×0.116	$(0.20)^2$	45	$\approx 8.9\ 10^{-3}$	—
				$(0.15)^2$	45	$\approx 7.4\ 10^{-3}$	—
				$(0.20)^2$	35	$\approx 7.7\ 10^{-3}$	—
	0.333	2×0.116	2×0.116	$(0.20)^2$	45	$\approx 1.5\ 10^{-2}$	—
				$(0.15)^2$	45	$\approx 1.3\ 10^{-2}$	—
				$(0.20)^2$	35	$\approx 1.3\ 10^{-2}$	—
20.0	0.170	2×0.126	2×0.101	$(0.20)^2$	45	$\approx 9.0\ 10^{-3}$	$\approx 7.0\ 10^{-3}$
				$(0.15)^2$	45	$\approx 7.8\ 10^{-3}$	$\approx 5.6\ 10^{-3}$
				$(0.20)^2$	35	$\approx 8.1\ 10^{-3}$	$\approx 5.9\ 10^{-3}$
	0.333	2×0.126	2×0.101	$(0.20)^2$	45	$\approx 1.6\ 10^{-2}$	$\approx 1.2\ 10^{-2}$
				$(0.15)^2$	45	$\approx 1.4\ 10^{-2}$	$\approx 1.0\ 10^{-2}$
				$(0.20)^2$	35	$\approx 1.5\ 10^{-2}$	$\approx 1.0\ 10^{-2}$
40.0	0.170	2×0.138	2×0.083	$(0.20)^2$	45	$\approx 9.4\ 10^{-3}$	$\approx 5.0\ 10^{-3}$
				$(0.15)^2$	45	$\approx 8.4\ 10^{-3}$	$\approx 3.8\ 10^{-3}$
				$(0.20)^2$	35	$\approx 8.6\ 10^{-3}$	$\approx 4.0\ 10^{-3}$
	0.333	2×0.138	2×0.083	$(0.20)^2$	45	$\approx 1.7\ 10^{-2}$	$\approx 8.6\ 10^{-3}$
				$(0.15)^2$	45	$\approx 1.6\ 10^{-2}$	$\approx 6.7\ 10^{-3}$
				$(0.20)^2$	35	$\approx 1.6\ 10^{-2}$	$\approx 7.1\ 10^{-3}$

responsible for the bulk of the non spectator contribution to the B_d^0-decay.[27] For the B_s^0 the process $B_s^0 \to gc\bar{u}$ (Fig. 2b) is Cabibbo-suppressed while the $B_s^0 \to gc\bar{c}$ is expected to be small due to phase space considerations. We will, therefore, first assume that the total B_s^0 decay width, $\Gamma(B_s^0)$, will not be affected by the non spectator contribution ($\Gamma(B_s^0) = \Gamma(B^{\pm})$). Then in order to be conservative we will also consider the case where both, $\Gamma(B_s^0)$ and $\Gamma(B_d^0)$, are increased by the same amount.

As examples we will take for α_{ns} the values of 20% and 40%. One then has to extract from the $Br(B \to l\nu X)$ value (measured on the $\Upsilon(4S)$) the semileptonic $B^0 \to l\nu X$ and $B^{\pm} \to l\nu X$ branching ratios. To this end, we assume that $B_d^0\bar{B}_d^0$ and B^+B^- are produced in the $e^+e^- \to \Upsilon(4S) \to B\bar{B}$ reaction in the ratio of

$$N(B_d^0\bar{B}_d^0) \; : \; N(B^+B^-) \; = \; 40\,\% : \; 60\%$$

as a consequence of the $B_d^0, B^{\pm}$ mass difference[28-30] $M(B_d^0) - M(B^{\pm}) \approx 4$ MeV.

Using the above ratio and the assumed α_{ns}, one obtains the $Br(B_d^0 \to l\nu X)$ and $Br(B^{\pm} \to l\nu X)$ as given in Table I. Correcting then the B_d^0 (and eventually the B_s^0) total width in order to take into account the non spectator contribution, we recalculate the $x = \Delta M/\Gamma$ values for $\alpha_{ns} = 20,\ 40\%$ (taking $y = \Delta\Gamma/\Gamma = 0$). We obtain thus the new values for R_m also given in Table I. As can be seen from this table the values obtained for R_m do not depend dramatically on the chosen values of the parameters and have the same order of magnitude.

For comparison we give in Table II the R_m values expected for the the $e^+e^- \to \Upsilon(4S) \to B_d^0\bar{B}_d^0$ reaction. One notices that they are an order of magnitude smaller than the corresponding values obtained from the $e^+e^- \to B\bar{B}X$ process. However, the cross section for producing $B_d^0\bar{B}_d^0$ at the $\Upsilon(4S)$ is much larger ($\approx$ 1 nb, see Ref. [31]) than the $e^+e^- \to B\bar{B}X$ cross section in the $\sqrt{s}$ = 15-30 GeV region. (Note also, that if δ reaches a value near 180°, R_m for the $\Upsilon(4S)$ could be increased by a factor of $\lesssim 3$). Not accounting for any detection efficiency or background contributions, the product $\sigma(b\bar{b})R_m$ can be used

to compare both cases. For $\alpha_{ns} = 0.20$, $B_b f^2 = (0.20\ \text{GeV})^2$ and $m_t = 45$ GeV one has $\sigma(b\bar{b})R_m \approx 0.3$ pb for the $\Upsilon(4S)$ whereas in the $\sqrt{s} = 15$-30 GeV region one obtains $\sigma(b\bar{b})R_m \approx 1.1$-0.3 pb (using $P_s = 0.17$). In this respect the two methods are nearly equivalent. On the other hand they are complementary since in one case one measures the mixing properties of the $B_d^0 - \bar{B}_d^0$ system and in the second case primarily those of the $B_s^0 - \bar{B}_s^0$ system. Indeed, in the $\sqrt{s} = 15$-30 GeV region, $\sim 84\%$ of the mixing effect comes from the B_s^0 and $\bar{B}_s^0$ production (as obtained from the formula giving R_m for the $e^+e^- \to B\bar{B}X$ reaction with $P_s = 0.17$).

Table II. For the phase $\delta \simeq 90°$ estimates of $R_m = (N^{++} + N^{--})/N_t$ for the $e^+e^- \to \Upsilon(4S) \to B_d^0\bar{B}_d^0$ reaction using $f_r = 0.40$ for the fraction of $B_d^0\bar{B}_d^0$ produced at the $\Upsilon(4S)$. Note that if $\delta \simeq 180°$, R_m could be increased by a factor of $\lesssim 3$.

$\alpha_{ns}(\%)$	$Br(B^\pm \to l\nu X)$	$Br(B_d^0 \to l\nu X)$	$B_b f^2$ $(GeV)^2$	m_t (GeV)	$\frac{(N^{++}+N^{--})}{N_t}$
0.0	2×0.116	2×0.116	$(0.20)^2$	45	$\approx 5.5\ 10^{-4}$
			$(0.15)^2$	45	$\approx 1.8\ 10^{-4}$
			$(0.20)^2$	35	$\approx 2.1\ 10^{-4}$
20.0	2×0.126	2×0.101	$(0.20)^2$	45	$\approx 2.7\ 10^{-4}$
			$(0.15)^2$	45	$\approx 8.7\ 10^{-5}$
			$(0.20)^2$	35	$\approx 1.0\ 10^{-4}$
40.0	2×0.138	2×0.083	$(0.20)^2$	45	$\approx 6.7\ 10^{-5}$
			$(0.15)^2$	45	$\approx 2.1\ 10^{-5}$
			$(0.20)^2$	35	$\approx 2.6\ 10^{-5}$

B4 B-TAGGING AND MIXING

In the following we estimate the signal and background obtained by measuring the mixing with like sign dileptons. Apart from mixing, same sign dileptons can also arise from the following decays:

$$B(\bar{B}) \rightarrow l^{\mp}\nu X$$

and

$$\bar{B}(B) \rightarrow \bar{D}(D)X \qquad \text{where} \qquad \bar{D}(D) \rightarrow l^{\mp}\nu X\ .$$

This is illustrated by Fig. 3 which presents at the quark level the various ways of producing leptons. In practice one counts only those events having two leptons of the same charge in opposite hemispheres (the latter being defined with respect to the thrust axis) where both leptons exceed a certain momentum cut (we will take successively 1.0 GeV/c and 1.5 GeV/c). This momentum cut will lead to an additional source of background due to asymmetric π^0 Dalitz decays where one of the $e^{\pm}$ has a momentum below the chosen threshold or escapes detection.

Note that if one parameterizes the mixing by R or R′ instead of R_m (see Section B.2) additional backgrounds will be generated. This is because one has to determine also N^{+-}, which is contaminated by:

$$e^+e^- \rightarrow B\bar{B}X \qquad \begin{bmatrix} B \rightarrow DX, & D \rightarrow l^+\nu X \\ \bar{B} \rightarrow \bar{D}X, & \bar{D} \rightarrow l^-\nu X \end{bmatrix}$$

and

$$e^+e^- \rightarrow D\bar{D}X \qquad \begin{bmatrix} D \rightarrow l^+\nu X \\ \bar{D} \rightarrow l^-\nu X \end{bmatrix}$$

(The background due to τ decays and two photon interactions can be easily eliminated by a multiplicity and total energy cut, respectively).

In order to estimate the number of events for signal and background we used the Lund Monte Carlo program.[19,32] We generated $e^+e^- \rightarrow b\bar{b}$ events at three different c.m. energies, $\sqrt{s} = 15, 22, 30$ GeV and at the c.m. energy corresponding to the $\Upsilon(4S)$. We also estimated the possible additional background induced by the $e^+e^- \rightarrow q\bar{q}$ processes (where q = u,d,s,c) by applying the same cuts as those used for selecting the B's.

To appreciate the importance of the detector properties we assumed that the identification of electrons and muons poses no severe problems and we take a lepton detection efficiency of $\epsilon_{lep} = 90\%$ for lepton momenta $p_l > 1.0$ GeV/c. In addition we require that the leptons should have $|\cos\theta_l| < 0.90$ (where θ_l is the emission angle of the lepton with respect to the beam direction). The results are given in Table III for an accumulated luminosity of 1000 pb^{-1} and $R_m = 8.9 \times 10^{-3}$ (see Table I). The $e^+e^- \rightarrow b\bar{b} \rightarrow B\bar{B}X$ cross sections at 15, 22 and 30 GeV were taken as 128, 60 and 32 pb, respectively. Also listed in this table are the signal to background ratio as well as the corresponding significance of the signal. One notices that the background coming from the $e^+e^- \rightarrow b\bar{b}$ process ($B(\bar{B}) \rightarrow l\nu X$ and $\bar{B}(B) \rightarrow \bar{D}(D)X \rightarrow l\nu X$, asymmetric π^0 Dalitz decays) are much more important than those induced by $e^+e^- \rightarrow q\bar{q}$ (q = u, d, s, c). For comparison we give in the same table the results expected from the $\Upsilon(4S)$, using $\sigma(b\bar{b}) = 1$ nb and $R_m = 5.5 \times 10^{-4}$ (see Table II). Clearly in this case we do not require the leptons to be in opposite hemispheres as the B's are almost emitted at rest.

In the present study the signal to background ratio is the largest at $\sqrt{s} \simeq 15$ GeV. The number of standard deviations (s.d.) quoted in the table might however be somewhat misleading. This is because in the actual experiment one has to evaluate an unknown background which comprises an important part of the observed event sample. Unless the background can be measured somehow, one has to rely on Monte Carlo calculations thus introducing systematic uncertainties.

Table III. Estimates of the number of events due to mixing and to background using the tagging procedure described in the text. The numbers were obtained at $\sqrt{s}$= 15, 22 and 33 GeV for an integrated luminosity of 1000 pb^{-1} and $R_m = 8.9 \times 10^{-3}$. For the $\Upsilon(4S)$ we took $R_m = 5.5 \times 10^{-4}$. Here N_{mix} represents the number of events due to mixing before applying any tagging method.

	15 GeV N_{mix}=1139 events lepton momentum (GeV/c)		22 GeV N_{mix}= 534 events lepton momentum (GeV/c)		30 GeV N_{mix}= 285 events lepton momentum (GeV/c)		$\Upsilon(4S)$ N_{mix}= 550 events lepton momentum (GeV/c)	
	≥ 1.0	≥ 1.5	≥ 1.0	≥ 1.5	≥ 1.0	≥ 1.5	≥ 1.0	≥ 1.5
$l^{\pm}/l^{\pm}$ tagging	423	214	267	170	161	120	262	99
background $(b\bar{b})$	529	120	710	280	494	261	2346	230
background $(c\bar{c})$	47	14	52	14	34	12	<63	<27
signal/ background	0.7	1.6	0.4	0.6	0.3	0.4	>0.1	>0.4
# of s.d.	13	12	8	8	6	6	>5	>5
$l^{\pm}K^{\pm}/l^{\pm}K^{\pm}$ tagging	34	25	27	22	18	16		
background $(b\bar{b})$	<40	<19	50	30	41	27		
background $(c\bar{c})$	<11	<5	<6	<6	<5	< 4		
signal/ background	>0.7	>1.0	>0.5	>0.6	>0.4	>0.5		
# of s.d.	>4	>4	>3	>3	> 2	>2		
$l^{\pm}K^{\pm}/l^{\pm}K^{\pm}$, no $K^{\mp}$ (tagging)	29	22	18	14	12	10		
background $(b\bar{b})$	<11	<11	< 13	<11	<13	<13		
background $(c\bar{c})$	< 7	< 5	< 2	< 2	< 2	< 2		
signal/ background	>1.6	>1.4	>1.2	>1.1	>0.8	>0.7		
# of s.d.	>4	>4	>3	> 3	> 2	>2		

Therefore, we would like to discuss here an alternative method for tagging the $e^+e^- \rightarrow B\bar{B}X$ process. In addition to the cut in the momentum p_l we propose to detect in each jet a kaon of the same charge as the lepton. This is because in the Cabibbo allowed $b \rightarrow c \rightarrow s$ ($\bar{b} \rightarrow \bar{c} \rightarrow \bar{s}$) quark decay chain, the charged kaon has the same charge as the lepton if the latter originates from the b decay as can be seen from Figs. 3 and 4. Note that the diagram in Fig. 4b gives a contribution to the l^-K^- production which is about 5 times smaller than that of Fig. 4a because of phase space suppression.[33] We have also presented in Fig. 4c a background process due to the decay of a $\bar{b}$ quark leading to an l^-K^- pair among the $\bar{B}$ decay particles.

The $B\bar{B}$ tagging efficiency is obtained by counting the number of events having their l^+K^+ and l^-K^- emitted in opposite hemispheres. We also count the number of events having l^+K^+ (l^-K^-) in one hemisphere and another l^+K^+ (l^-K^-) pair in the opposite one. These events represent part of the expected background to the mixing signal as no mixing effects have been implemented in the used Monte Carlo program. In fact this background is coming mainly from the processes of the type shown in Fig. 4c. We assume that the identification of kaons can be obtained with a combination of dE/dx, time of flight, and Čerenkov counters. We consider that $0.2 \leq p_K \leq 2.4$ GeV/c is the $K^\pm$ momentum window in which identification can be achieved. Assuming that the contamination of π(K) in the K(π) sample is $\sim 1\%$ between 0.9 and 1.0 GeV/c (a good π/K separation is assumed below 0.9 GeV/c with the dE/dx and time of flight devices) and that $\sim 4\%$ of the produced $\pi^\pm$ can fake $K^\pm$ in the 1.0-2.5 GeV/c region (a typical value for threshold Čerenkov counters) we obtain the results given in Table III. The signal to background ratio did not improve with respect to the method that required only the identification of leptons. The efficiency however drops drastically in the $l^\pm K^\pm / l^\pm K^\pm$ tagging.

In order to decrease the background due to the diagram of Fig. 4c we refined the above tagging method by requiring that in one hemisphere at least one $l^\pm K^\pm$ pair should not be accompagnied by an additional $K^\mp$. The tagging efficiency is

decreased somewhat (Table III) but one obtains almost in all cases a significantly larger signal to background ratio with a still acceptable statistical significance. The $\sqrt{s} \approx 15 - 22$ GeV c.m. energy range appears thus to be a promising region in which $B^0\bar{B}^0$ mixing might be experimentally accessible.

P5 CONCLUSIONS

We studied the possibility of measuring $B^0\bar{B}^0$ mixing in the $e^+e^- \to B\bar{B}X$ reaction by detecting like sign dileptons belonging to opposite jets. We considered the $\sqrt{s}$ = 15-30 GeV region where any type of B meson can be produced.

Using current values for the unknown parameters governing the mixing phenomenon (such as the mass of the top quark, the bag parameter, the B meson decay constant) we investigated the observability of mixing in e^+e^- experiments with an accumulated luminosity of 1000 pb^{-1}. The performed Monte Carlo calculations have shown that by selecting leptons with momenta $p_l > 1.0$, 1.5 GeV one can expect signal to background ratios ranging from 0.3 to 1.6. We have also carried out a brief comparison of our predictions with the mixing effects which could be observed at the $\Upsilon(4S)$. The numbers obtained for the ratio of signal to background appear to be comparable. On the other hand both measurements are complementary since in one case one measures primarily the mixing of the $B_s^0 - \bar{B}_s^0$ and in the other case that of the $B_d^0 - \bar{B}_d^0$ system.

As the subtraction of a large background from the observed signal may introduce further uncertainties we have also investigated additional methods for tagging the $e^+e^- \to B\bar{B}X$ process. They are based on the fact that in the Cabibbo allowed $b \to c \to s$ ($\bar{b} \to \bar{c} \to \bar{s}$) quark decay chain, $K^\pm$ and $l^\pm$ have the same charge if the lepton comes from the $B \to l^\pm \nu X$ decay. The proposed tagging methods lead to a drastic decrease in the detection efficiency but tend to increase the signal to background ratio. In this respect these tagging methods are useful and could be applied for a further measurement of mixing phenomena.

It appears that the observable effects of mixing phenomena at the $\Upsilon(4S)$ and in the $e^+e^- \to B\bar{B}X$ reaction are of comparable size within the discussed framework. The $e^+e^- \to B\bar{B}X$ reaction has however the additional advantage that all the current theoretical models predict the mixing of the $B_s^0(\bar{B}_s^0)$ to be almost complete. This means that the observable effects will not depend crucially on the exact values of unknown parameters such as the top quark mass, the bag parameter, etc. In conclusion the $\sqrt{s} \simeq 15$ GeV region appears in this study as the most promising one for detecting mixing.

ACKNOWLEDGEMENTS

We would like to thank the DESY and SLAC directorates for their support. It is a pleasure to thank A. Ali, L.L. Chau, F. Gilman, G. Godfrey, M. Peskin and S. Stone for useful discussions.

REFERENCES

1. J.S. Hagelin, M.B. Wise, Nucl. Phys. B189, 87 (1981),
   J.S. Hagelin, Nucl. Phys. B193, 123 (1981).
2. A. Ali, Z.Z. Aydin, Nucl. Phys. B148, 165 (1979).
3. E. Franco, M. Lusignoli, A. Pugliesi, Nucl. Phys. B194, 403 (1982).
4. I.I. Bigi,A.I. Sanda, Nucl. Phys. B193, 85 (1981).
5. L.L. Chau, W.Y. Keung, M.D. Tran, Phys. Rev. D27, 2145 (1983).
6. L.L. Chau, W.Y. Keung, Phys.Rev.D29, 592 (1984);
   See also the summary of L. L. Chau, Phys Rep. 95, No 1, 1 (1983).
7. S.-H.H. Tye, Proceedings of the CLEO Collaboration Workshop, Cornell Report CLNS 51/506 and CLEO 81/106, July 1981.
8. A. Ali, C. Jarlskog, Phys. Lett. 144B, 266 (1984).
9. A.J. Buras, W. Slominski, H. Steger, Nucl. Phys. B246, 45 (1984),
   A.J. Buras, H. Steger, Private Communications.
10. I.I. Bigi, A.I. Sanda, Phys. Rev. D29, 1393 (1984).
11. L. Wolfenstein, Nucl. Phys. B246, 45 (1984).
12. We define the quark content of the B mesons in the following way: $B_d \equiv b\bar{d}$, $B_u \equiv b\bar{u}$, $B_s \equiv b\bar{s}$ and $B_c \equiv b\bar{c}$. In a similar manner we use $D^0 \equiv c\bar{u}$ and $D^+ \equiv c\bar{d}$.
13. L.B. Okun, V.I. Zakharov, B.M. Pontecorvo, Nuovo Cim. Lett. 13, 218 (1975).
14. A. Pais, S.B. Treiman, Phys. Rev. D12, 2744 (1975).
15. See for instance (1), (6) and (9).
16. Note that for even L one has an enhancement factor. This occurs for instance for the $e^+e^- \to B^*\bar{B} \to B\bar{B}\gamma$ process near threshold where the

relative $B\bar{B}$ orbital momentum is L = 0; see (4) and (10). We thank I.I. Bigi for an enlightening discussion about these effects.

17. See for instance (1), (4) and (9).

18. See for instance (5), (8) and (9).

19. T. Sjöstrand, Computer Phys. Communications 28, 229 (1983) and references quoted therein.

20. In the spectator model one has $Br(B \to \tau\nu X)/Br(B \to l\nu X) \approx 0.07$ and $Br(\tau \to l\nu\bar{\nu}) \approx 0.36$.

21. TASSO Collaboration, M. Althoff et al., Phys. Lett. 136B, 130 (1984).

22. See: S. Stone, Proceedings of the International Symposium on Lepton and Photon Interactions at High Energies, Ithaca, New York, 1983, edited by D.G. Cassel and D. L. Kreinick (Cornell University Press, Ithaca, 1983).

23. F.J. Gilman, J.S. Hagelin, Phys. Lett. 126B, 111 (1983).

24. For the B^0 the parameter $x \equiv \Delta M/\Gamma = 2Re\sqrt{(M_{12} - i\Gamma_{12}/2)\,(M_{12}^* - i\Gamma_{12}^*/2)}/\Gamma$ becomes $x \approx 2|M_{12}|/\Gamma$. In the first approximation one has $|M_{12}| \propto B_b f^2 \left[m_t^2 + 3/4 m_b^2 \ln(m_t^2/m_b^2)\right] \propto B_b f^2 m_t^2$, where m_b is the b quark mass; see (9) and (11).

25. A. Soni, Phys. Rev. Lett. 53, 1407 (1984).

26. The non-spectator contribution to the B^- decay is assumed to be negligible as the $b\bar{u}$ $(\bar{b}u) \to W \to q'\bar{q}$ decay is Cabibbo supressed.

27. J.P. Leveille, Proceedings of the CLEO Collaboration Workshop, Cornell Report CLNS 51/506 and CLEO 81/106, July 1981.

28. See for instance the talk of S.-H.H. Tye at the Workshop on e^+e^- Physics at High Luminosities held at SLAC, November 30-December 1, 1984.

29. CLEO Collaboration, R. Gilles at al, Phys. Rev. Lett. 50, 887 (1983).

30. E. Eichten, Phys. Rev. D22, 1819 (1980).

31. CLEO Collaboration, see for instance R. Plunkett, Cornell Ph.D. thesis, 1982.

32. T. Sjöstrand, Computer Phys. Communications 27, 243 (1982).

33. J. Cortes, X. Pham, A. Tounsi, Phys. Rev. D25, 188 (1982).

FIGURE CAPTIONS

1. The distributions of R' and R'_{odd} as a function of $x = \Delta M/\Gamma$.

2. Non spectator processes which may contribute to the B^0 decays (see Ref. [27]). Note that among the combinations of "outgoing" quarks only c-quarks have been considered because of the dominance of the $b \to c$ over $b \to u$ transitions.

3. Schematic representation of quark decays which may lead to lepton production in the case of the $e^+e^- \to b\bar{b}$ process.

4. Some b and $\bar{b}$ quark decay processes leading to l^-K^- pairs in the final state.

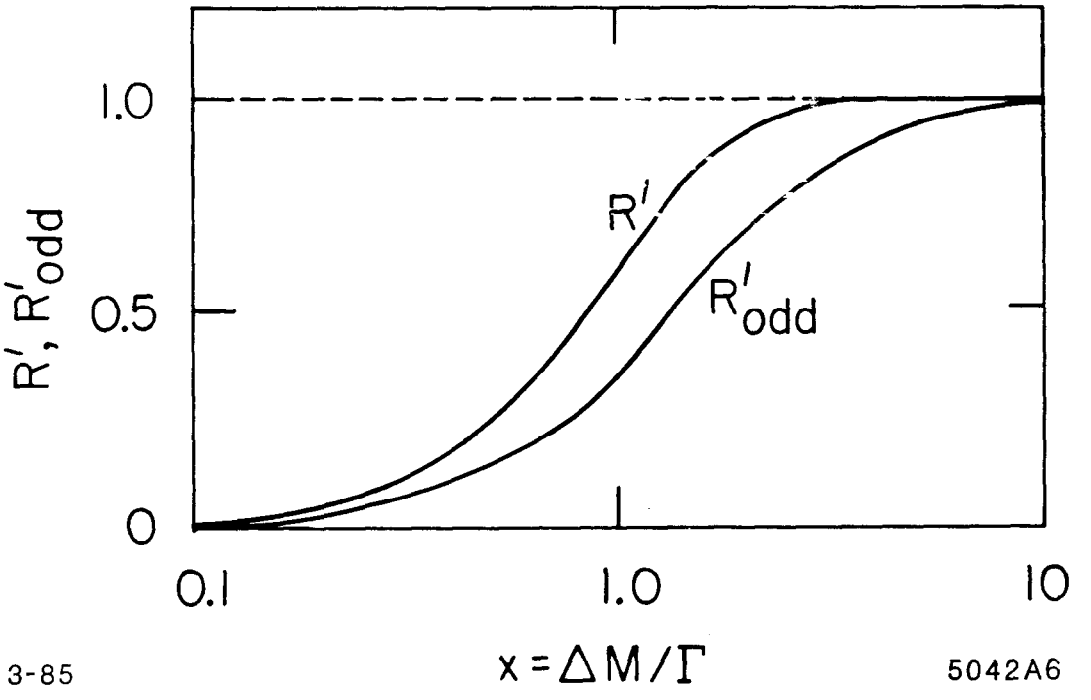

Fig. 1

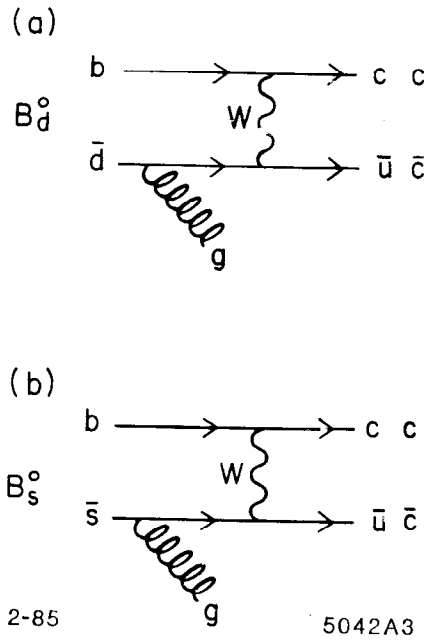
(a)
b
c c
B_d^0
W
$\bar{d}$
$\bar{u}$ $\bar{c}$
g
(b)
b
c c
W
B_s^0
$\bar{s}$
$\bar{u}$ $\bar{c}$
g
2-85
5042A3

Fig. 2

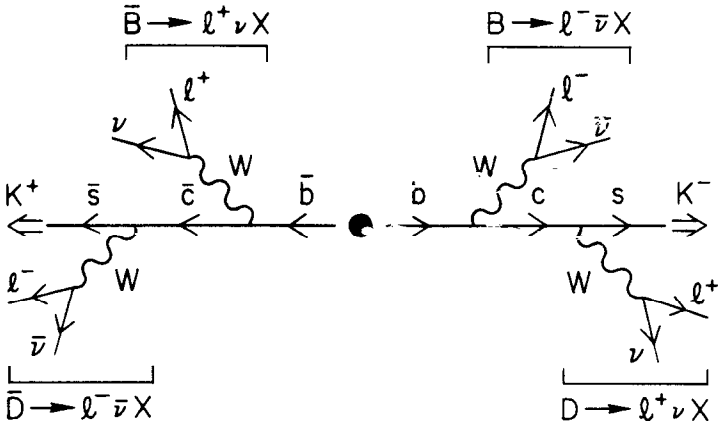
$\bar{B} \to \ell^+ \nu X$
$B \to \ell^- \bar{\nu} X$
ℓ^+
ν
W
ℓ^-
$\bar{\nu}$
W
K^+
$\bar{s}$
$\bar{c}$
$\bar{b}$
b
W
c
s
K^-
ℓ^-
W
$\bar{\nu}$
W
ℓ^+
ν
$\bar{D} \to \ell^- \bar{\nu} X$
$D \to \ell^+ \nu X$
2-85
5042A5

Fig. 3

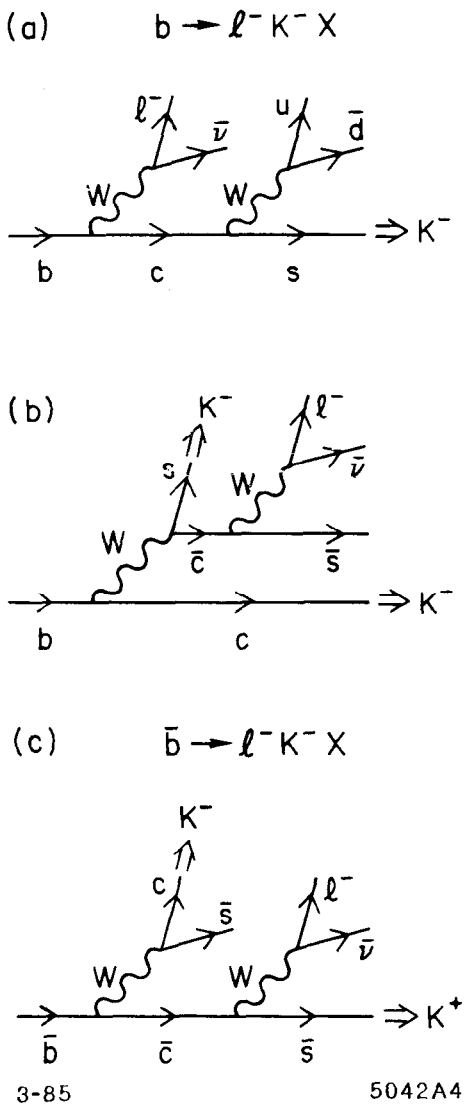
(a) b → ℓ⁻ K⁻ X
ℓ⁻
ν̄
u
d̄
W
W
K⁻
b
c
s
(b)
K⁻
ℓ⁻
s
W
ν̄
W
c̄
s̄
K⁻
b
c
(c) b̄ → ℓ⁻ K⁻ X
K⁻
c
ℓ⁻
s̄
ν̄
W
W
K⁺
b̄
c̄
s̄
3-85
5042A4

Fig. 4

APPENDIX C

LIST OF PARTICIPANTS

S. Abachi	LBL
C. Akerlof	U. of Michigan
B. Anderson	LBL
I. Antoniadis	SLAC
C. Bachas	SLAC
P. Baringer	Indiana
T. Barker	UCSB
B. Barnett	Johns Hopkins
D. Bauer	UCSB
I. Beltrami	Purdue
H. Bengtsson	UCLA
K. Berkelman	Cornell
L. Berkhart	U. of Munich
I. Bigi	Aachen
M. Block	Northwestern
D.L. Blockus	Indiana
E. Bloom	SLAC
G. Bobbink	Carnegie-Mellon
A. Bodek	U. of Rochester
T. Bolognese	LBL
G. Bonneaud	SLAC
M. Bosmon	SLAC
B. Brabson	Indiana
S. Brodsky	SLAC
A. Bross	LBL
C. Buchanan	UCLA

A. Buijs	NIKHEF
B. Bylsma	Purdue
T. Camporesi	SLAC
M. Carter	SLAC
R. Cence	U. of Hawaii
G. Chadwick	SLAC
D. Cline	U. of Wisconsin
D. Cords	SLAC
B. Cork	LBL
D. Crane	Johns Hopkins
M. Cvetic	SLAC
R. De Bonte	Purdue
M. Derrick	ANL
S. Drell	SLAC
A. Eisner	U.C. IIRPA
D. Errede	U. of Michigan
G. Feldman	SLAC
E. Fernandez	U. of Colorado
C. Field	SLAC
A. Fridman	SLAC
D. Fryberger	SLAC
H. Galic	SLAC
L. Galtieri	LBL
K.K. Gan	Purdue
M. Garnjost	LBL
F. Gilman	SLAC
T. Glanzman	SLAC
T. Gottschalk	Caltech
D. Groom	U. of Utah
T. Hansl-Kozanecki	SLAC

G. Hanson	SLAC
J. Hauptman	Iowa State
B. Herrnannsfeldt	SLAC
W. Hoffman	LBL
R. Holiebeek	SLAC
E.B. Hughes	Stanford
J. Hylen	Johns Hopkins
J. Jaros	SLAC
C. Jung	Indiana
R. Kass	Ohio State
S. Kaye	LBL
K. Kees	UCSD
L. Keller	SLAC
R. Kenney	LBL
W. Kirk	SLAC
R. Kofler	U. of Massachusetts
D. Koltick	Purdue
T. Kondo	KEK
P. Kooijman	ANL
Y. Kubota	Cornell
W. Langeveld	U.C. Riverside
J. Layter	U.C. Riverside
D. Leith	SLAC
A. Litke	SLAC
C.H. Lo	U. of Alberta
J. Loos	ANL
E. Low	Purdue
G. Lynch	LBL
R. Madaras	LBL
U. Mallik	SLAC

T. Maruyama	U. of Wisconsin
G. Masek	UCSD
S. Maxfield	U. of Massachusetts
S. Melnikoff	U.C. Riverside
R. Messner	SLAC
D.H. Miller	Purdue
E. Miller	UCSD
G. Mills	Caltech
A. Minten	CERN
K.C. Moffeit	SLAC
J. Moromisato	Nordista
R. Ng	Purdue
B. Niczyporuk	SLAC
D. Nygren	LBL
P. Oddone	LBL
H. Ogren	Indiana
R. Ong	SLAC
H. Paar	NIKHEF
W. Panofsky	SLAC
R. Panvini	Vanderbilt
S. Parker	U. of Hawaii
J.M. Paterson	SLAC
D. Pellett	U.C. Davis
M. Perl	SLAC
M. Peskin	SLAC
R. Prepost	U. of Wisconsin
L. Price	ANL
L.K. Rangan	Purdue
L. Read	DOE
B. Richter	SLAC

J. Ritchie	SLAC
D. Ritson	Stanford
L. Rosenberg	SLAC
H. Rubinstein	Weizmann Inst.
D. Rust	Indiana
M. Sakuda	Caltech
A. Sanda	Rockfeller
A. Schwarz	SLAC
K. Schwitkis	UCSB
J. Seeman	SLAC
J.C. Sens	NIKHEF
M. Sher	UCSB
E.I. Shibata	Purdue
M. Soldate	SLAC
A. Soni	UCLA
J. Spencer	SLAC
M.L. Stevenson	LBL
D. Stork	UCLA
K. Sugano	ANL
M. Sullivan	IIRPA
T. Takahashi	LBL
F. Takasaki	KEK
R. Taylor	SLAC
G. Trilling	LBL
P. Tsai	SLAC
H. Tye	Cornell
G. VanDalen	U.C. Riverside
J. Va'Vra	SLAC
M. Veltman	U. of Michigan
J. Venuti	SLAC

W. Vernon	UCSD
W. Wagner	U.C. Davis
B. Ward	SLAC
A. Wattenberg	U. of Illinois
A.E. Weidemann	U. of Tennessee
J.M. Weiss	ANL
A.W. Westaan	U. of Tennessee
M. Willutsky	U. of Michigan
H. Yamamoto	Caltech
H. Yamamoto	LBL
P. Zerwas	SLAC

2/80